UNIVERSITY OF CALIFORNIA,
IRVINE

Probing the Strength of Non-Standard Interactions Between Solar Neutrinos and Up or Down Quarks in Matter Using Recoil Electron Spectra Measured by Super-Kamiokande

DISSERTATION

submitted in partial satisfaction of the requirements
for the degree of

DOCTOR OF PHILOSOPHY

in Physics

by

Pierce Ben Weatherly

Dissertation Committee:
Professor Henry W. Sobel, Chair
Professor Simona Murgia
Professor Kevork N. Abazajian

2019

DEDICATION

This work is dedicated to my God and Savior, Jesus Christ, first and foremost. To my wife, Janelle, whom I love so very much and am continually blessed by, and to our future family. To my parents Mike and Monell Weatherly, who kept me sane and focused, and who gave me the opportunity to follow this path. To my siblings Choyce Weatherly and Cymber Kooker. To Ryan, Mike, and Rosemary Clark for being my surrogate California family and taking me in as a son. To my in-laws Jeff and Gail Goehle for allowing my wife and I to live with them and for all of their support. To my grandmother Dorotha Houston and to my uncle Phil Houston for encouraging me. To the people of Liberty Baptist Church, Mizuhashi Bible Church, and Compass Bible Church Tustin for their constant encouragement. Finally, to my friends Jeremy Pope, Cory Bourland, Matt Scarborough, Kyle Baker, and Ryan Clark who distracted me when necessary.

TABLE OF CONTENTS

LIST OF FIGURES

LIST OF TABLES

ACKNOWLEDGMENTS

I would like to thank all those to whom this work is dedicated to. I also would like to thank Professor Hank Sobel for taking me on as a graduate student and to Dr. Michael Smy for his mentoring and support. I am very appreciative of all the opportunities they have given me in learning new things and presenting my work around the world. Thanks to Scott Locke, and I wish him good luck with his analysis and finishing up his Ph. D. quickly. I would like to thank Dr. Andrew Renshaw, for all of his support and well-wishes, as well as Dr. Volodymyr Takhistov, Dr. Yukki Nakano, Professor Yasuo Takeuchi, Dr. Motoyasu Ikeda, Professor Mark Vagins, Dr. Lluis Marti Magro and all of the other Super-Kamiokande collaborators I have worked with. I am very appreciative of the leadership of Professor Masayuki Nakahata and Professor Yoichiro Suzuki. I would like to thank Jeff Griskevich for all of his help and support in teaching me about machine shop techniques and water systems. Thanks to Roy Hall for teaching me the arts of water purification systems. Thanks to my committee members Professor Simona Murgia and Professor Kevork N. Abazajian for taking time to read and comment on my dissertation. A very special thanks to my folks and my mother-in-law for their assistance in proof-reading this long dissertation. Also, thanks to the United States Department of Energy for their financial assistance through the group grant.

CURRICULUM VITAE

Pierce Ben Weatherly

EDUCATION

PhD, Physics **2019**
University of California Irvine *Irvine, CA*

Masters of Physics **2011**
The University of Texas at Arlington *Arlington, TX*

Bachelor of Science in Physics **2009**
The University of Texas at Arlington *Arlington, TX*

Bachelor of Science in Mathematics **2009**
The University of Texas at Arlington *Arlington, TX*

RESEARCH EXPERIENCE

Graduate Research Assistant **2012–2019**
University of California, Irvine *Irvine, California*

Graduate Research Assistant **2010–2011**
University of Texas, Arlington *Arlington, TX*

Undergraduate Research Assistant **2004–2009**
University of Texas, Arlington *Arlington, TX*

TEACHING EXPERIENCE

Lab Teaching Assistant **2011–2012**
University of California Irvine *Irvine, CA*

Teaching Assistant **2011**
University of California Irvine *Irvine, CA*

Lab Teaching Assistant **2009–2010**
The University of Texas at Arlington *Arlington, TX*

Physics Department Tutor **2005–2009**
The University of Texas at Arlington *Arlington, TX*

Mathematics Department Tutor **2007–2009**
The University of Texas at Arlington *Arlington, TX*

REFEREED JOURNAL PUBLICATIONS

Systematically Searching for New Resonances at the Energy Frontier using Topological Models **2014**
Phys. Rev. D 89, 095002

Search for Trilepton Nucleon Decay via $p \to e + \nu\nu$ and $p \to \mu + \nu\nu$ in the Super-Kamiokande Experiment **2014**
Phys. Rev. Lett. 113, 101801

Test of Lorentz invariance with atmospheric neutrinos **2015**
Phys. Rev. D 91, 052003

Limits on sterile neutrino mixing using atmospheric neutrinos in Super-Kamiokande **2015**
Phys. Rev. D 91, 052019

Search for dinucleon decay into pions at Super-Kamiokande **2015**
Phys. Rev. D 91, 072009

Search for Nucleon and Dinucleon Decays with an Invisible Particle and a Charged Lepton in the Final State at the Super-Kamiokande Experiment **2015**
Phys. Rev. Lett. 115, 121803

First Measurement of radioactive isotope production through cosmic-ray muon spallation in Super-Kamiokande IV **2016**
Phys. Rev. D 93, 012004

Real-Time Supernova Neutrino Burst Monitor at Super-Kamiokande **2016**
Astropart. Phys. 81 39-48

Solar Neutrino Measurements in Super-Kamiokande-IV **2016**
Phys. Rev. D 94, 052010

Search for Neutrinos in Super-Kamiokande associated with Gravitational Wave Events GW150914 and GW151226 **2016**
The ApJL 830 L11

Measurements of the atmospheric neutrino flux by Super-Kamiokande: energy spectra, geomagnetic effects, and solar modulation **2016**
Phys. Rev. D 94, 052001

Super-Kamiokande Solar Neutrino Results and NSI Analysis **2017**
J. Phys.: Conf. Ser. 888, 012190

Search for Proton Decay via $p \to e^+ \pi^0$ and $p \to \mu^+ \pi^0$ in 0.31 megaton-years exposure of the Super-Kamiokande Water Cherenkov Detector Phys. Rev. D 95, 012004	**2017**
Search for an excess of events in the Super-Kamiokande detector in the directions of the astrophysical neutrinos reported by the IceCube Collaboration APJ, 850, 166	**2017**
Search for nucleon decay into charged antilepton plus meson in 0.316 megaton-years exposure of the Super-Kamiokande water Cherenkov detector Phys. Rev. D 96, 012003	**2017**
Search for Boosted Dark Matter Interacting With Electrons in Super-Kamiokande Phys. Rev. Lett. 120, 221301	**2018**
Atmospheric neutrino oscillation analysis with external constraints in Super-Kamiokande I-IV Phys. Rev. D 97, 072001	**2018**
Search for Neutrinos in Super-Kamiokande associated with the GW170817 neutron-star merger ApJL 857 L4	**2018**
Measurement of the tau neutrino cross section in atmospheric neutrino oscillations with Super-Kamiokande Phys. Rev. D 98, 052006	**2018**
Measurement of the neutrino-oxygen neutral-current quasielastic cross section using atmospheric neutrinos at Super-Kamiokande Phys. Rev. D 99 032005	**2019**
Atmospheric Neutrino Oscillation Analysis With Improved Event Reconstruction in Super-Kamiokande IV arXiv: 1901.03230	**2019**

REFEREED CONFERENCE PUBLICATIONS

Calibration of Special Asymmetric Cells in the Sample Layer A of the [ATLAS] End Barrel Tile Calorimeter using Cosmic Ray Data — **Aug 2010**
Fourth ATLAS Physics Workshop of the Americas

GADZOOKS! & EGADS: Supernova Relic ν_e^- Detection in Gadolinium Doped Super-Kamiokande — **Dec 2013**
27th Texas Symposium on Relativistic Astrophysics

Measuring Light Attenuation and Scattering in Water at UCI — **Sep 2014**
Advances in Neutrino Technology

Parallel Talk: Solar Neutrino Results from Super-Kamiokande — **June 2015**
25th International Workshop on Weak Interactions and Neutrinos

Super-Kamiokande Solar Neutrino Results and NSI Analysis — **July 2016**
27th International Conference on Neutrino Physics and Astrophysics

Results from Super-Kamiokande — **May 2017**
11th International Conference on Interconnections between Particle Physics and Cosmology

ABSTRACT OF THE DISSERTATION

Probing the Strength of Non-Standard Interactions Between Solar Neutrinos and Up or Down Quarks in Matter Using Recoil Electron Spectra Measured by Super-Kamiokande

By

Pierce Ben Weatherly

Doctor of Philosophy in Physics

University of California, Irvine, 2019

Professor Henry W. Sobel, Chair

Non-Standard Interactions (NSI) between neutrinos and matter affect neutrino flavor oscillations. Due to the high matter density in the core of the Sun, solar neutrinos are well suited to probe these interactions. Using the 277 kton-yr exposure of Super-Kamiokande to ^{8}B solar neutrinos, we search for the presence of NSI. Our data favors the presence of NSI with down quarks at 1.8σ, and with up quarks at 1.6σ, with the best-fit effective NSI parameters being $(\epsilon^{\mathrm{d}}_{11}, \epsilon^{\mathrm{d}}_{12})$ = (-3.3, -3.1) for d-quarks and $(\epsilon^{\mathrm{u}}_{11}, \epsilon^{\mathrm{u}}_{12})$ = (-2.5, -3.1) for u-quarks. After combining with data from the Sudbury Neutrino Observatory and Borexino, the significance increases by 0.1σ.

Chapter 1

Introduction

1.1 The History, Prediction, and Discovery of the Neutrino

The events that led to the prediction and eventual discovery of the neutrino started with the campaign to characterize radioactivity at the end of the nineteenth and beginning of the twentieth century [1][2]. Distinctive differences between the three types of radiation emitted from the nucleus of the atom, $\alpha = {}^4\text{He}$ nucleus, $\gamma =$ photon, and $\beta =$ electron, drove the pursuit to characterize the emitted radiation and sources, i.e. the decays responsible for their emission. This effort resulted in the discovery by Lise Meitner and Otto Hahn that, instead of a mono-energetic β being emitted in a radioactive process, the β-decay electrons have a continuous spectra. The implications of the continuous β spectra along with the requirement of energy and momentum conservation led Wolfgang Pauli (December 1930 [3]) to postulate the existence of a yet to be discovered particle inside the nucleus alongside protons, which he called the neutron. This new particle would have the following properties: it would be electrically neutral and have a spin of $\frac{1}{2}$; it would have a speed less than the

speed of light and have a mass similar to that of an electron. It would be emitted along with the electron during the β-decay, carrying away the excess energy and momentum, and subsequently producing the continuous β spectrum that was being observed.

Later, in 1932, James Chadwick discovered a neutral particle emitted from ^{9}Be decay. This neutral particle, which acquires the name neutron, is seen to have the same approximate mass as the proton, though it differed from Pauli's neutral particle because it has such a large mass. Because of this large mass, the neutron cannot be the solution to the β-decay energy spectrum problem. In the mean time (1931), Enrico Fermi adopted Pauli's ideas of a yet-to-be-discovered, light and electrically neutral, spin 1/2 particle to construct a successful model of β-decay, which he published in 1934 [4]. In several conferences in 1932 and 1933, and again in his paper, he re-christened the particle the "neutrino," or "small neutral one" in Italian, to differentiate this particle from the heavier neutron. His model has the neutron discovered by Chadwick decaying into three particles (a proton, a β-ray electron, and the (anti-)neutrino) via the reaction $n \rightarrow p^+ + e^- + \bar{\nu}_e$. Although Fermi did not believe that it would be possible for the particle to be detected, this model launched the field of neutrino physics.

With a new particle theoretically motivated, Hans Bethe and Rudolf Peierls (1934) determined the cross section between neutrinos and matter to be incredibly small, about 10^{-6} smaller than the cross section between electrons and matter. This small cross section means that the neutrino could travel through a light year of lead before being absorbed, or, more practically, pass through the Earth without a deviation of its trajectory. The small cross section would make neutrinos very difficult to detect, unless sources with extremely high fluxes could be found or incredibly large volume detectors built, allowing for the statistical nature of quantum mechanics to give a few neutrino-matter interactions on a reasonable timescale in order to prove their existence.

1.2 The First Detection of Neutrinos and Antineutrinos

In 1954, Ray Davis Jr. approached the neutrino detection problem by following the suggestion made by Pontecorvo in 1946 to use the radiochemical process $^{37}\mathrm{Cl}(\bar{\nu}, e^-) \rightarrow {}^{37}\mathrm{Ar}$ [5]. The number of neutrino interactions can be determined by counting the number of $^{37}\mathrm{Ar}$ decays back to $^{37}\mathrm{Cl}$, which has a half-life of 34 days. Davis placed his detector filled with carbon tetrachloride (dry cleaning fluid) near a nuclear reactor to achieve a high neutrino flux and attempted to count the number of interactions by extracting any produced $^{37}\mathrm{Ar}$. Since the fission rate of the reactor was known by measuring its power output, the theoretical rate of (anti)neutrino production could be determined from nuclear fission models. Davis' first detector was a 200 L steel drum shielded by concrete, which he replaced with an unshielded 3900 L tank. The experiment produced a null result, since the reactors emit only antineutrinos and thus cannot produce $^{37}\mathrm{Ar}$ in the detector. The possible explanations for this result based on knowledge at the time were that either the interactions of neutrinos and antineutrinos with matter were truly different, or that Fermi's β decay model was incorrect or incomplete [6]. While Davis did not detect neutrinos with this experiment, he did place an upper limit for neutrinos produced by CNO fusion in the Sun [5], and would later be the first to detect solar neutrinos in the Homestake Experiment [7] (Sec. 3.3.1).

Fred Reines and Clyde Cowan decided to tackle the problem of direct detection of neutrinos using the inverse β decay reaction $p^+ + \bar{\nu}_e \rightarrow n + e^+$ [8]. The antineutrino source originally was going to be from the detonation of a nuclear bomb. A detector would be placed under the blast and be allowed to free-fall away from the explosion through a vacuum tunnel before coming to rest on a bed of feathers and foam rubber. Fig. 1.1 shows a schematic of the proposed nuclear explosion-sourced neutrino experiment. However, it would be very difficult to create a detector that would survive a nuclear blast and be able to capture the

burst of antineutrinos in the very short time window the blast provides.

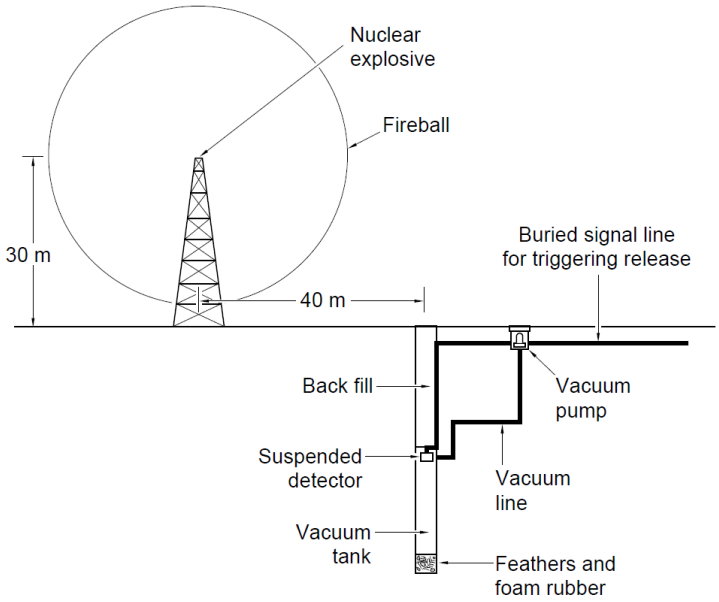

Figure 1.1: Illustration of the experiment proposed by Reines and Cowan for detecting antineutrinos from a nuclear explosion with a liquid scintillator detector. Figure from [8].

Reines and Cowan turned instead to Davis' approach, using the large and sustained flux of antineutrinos from the nuclear fission process produced in a nuclear reactor. Their new detector for this task had two tanks filled with 200 L of water. Water has a characteristic time associated with the light produced downstream by the products produced in the inverse β decay: prompt γ-rays emitted from the annihilation of the positron, and the γ emitted by the de-excitation of the nucleus that captures the neutron. The water tanks were sandwiched above and below by tanks filled with an organic liquid scintillator, that, after being excited by the γ-rays, emitted flashes of light. This light was detected by photomultiplier tubes on both the sides of the liquid scintillator tanks. The delay between the two sets of γs is on the order of 200 microseconds, allowing for a delayed coincidence criteria that can be used to verify the inverse β reaction and to veto background.

After realizing that cosmic rays were a significant background on the surface, Reines and Cowan moved the experiment in 1956, placing it under the Savannah River reactor

located in South Carolina [9][8]. The experiment was placed 11 m away from the reactor, and the massive concrete building housing the reactor provided 12 m of overburden, adequately shielding the detector from cosmic rays. They modified their experiment by doping the water with cadmium chloride to take advantage of the neutron-philic property of cadmium to increase the neutron capture efficiency, further reducing the characteristic delay time and allowing for the possibility of a clear delayed coincidence signal. As the reactor had a regular on/off cycle to maximize plutonium production, they compared their data between the on and off periods to prove the counts (and thus the incident antineutrinos) were coming from the reactor. With the reactor off, they observed a fifth the number of delayed coincidence events compared to the reactor-on rate [9]. With the successful detection of the first antineutrinos, the Fermi model of β decay was confirmed, and the difference between interactions of matter with neutrinos and antineutrinos was established [10].

In 1953, E. J. Konopinski and H. M. Hahmoud [11] applied the interaction law for β decay to muon processes. They argued that the two neutrinos produced in muon decay would necessarily need to be distinct from one another: $\mu^- \rightarrow e^- + \bar{\nu}_e + \nu_\mu$ and $\mu^+ \rightarrow e^+ + \nu_e + \bar{\nu}_\mu$. This framework led to the eventual establishment of a quantity for particle physics processes known as lepton number. The distinction between the two types of neutrinos was experimentally verified in 1962 by Leon Lederman, Melvin Schwartz, and Jack Steinberger [12] using a technique developed by Schwartz to create a pure neutrino beam. Schwartz's technique is still used to this day. This technique involves firing relativistic protons at a fixed target, beryllium in their experiment, which produces a shower of particles, similar to the process that seeds cosmic ray showers. A beam dump of 13.5 m of steel harvested from naval battleships was set up behind the target, which absorbs almost all of the shower while the neutrinos passed right on through. The neutrinos originate from pions, created in the proton-target collisions, decaying to muons through the process $\pi^+ \rightarrow \mu^+ + \nu_\mu$. A ten-ton spark chamber comprised of aluminum plates and gas was placed downstream of the neutrino beam, allowing for the neutrinos to capture on protons in the aluminum plates. The

charged leptons produced by the interaction between the neutrino and the proton would be distinguishable between muons and electrons by whether or not the charged lepton escapes the spark chamber (with a large enough track length). Electrons would not be able to escape due to interactions in the chamber, but muons minimally interact and would escape. Their experiment verified that the neutrinos produced in the pion decay subsequently create muons in the spark chamber, differentiating that type of neutrino from the neutrino produced in β decay. The neutrinos were given their designations based on the charged lepton associated with them in the particle interaction: electron neutrino ν_e for the neutrinos involved in β decay and muon neutrino ν_μ for the neutrinos involved with pion decay.

With the charged leptons (e^-, e^+, μ^-, and μ^+) and the neutrinos (ν_e, $\bar{\nu}_e$, ν_μ, and $\bar{\nu}_\mu$ respectively) now firmly associated, the experimental evidence pointed to a conservation of lepton family number similar to what Konopinski and Hahmoud argued for previously. In an interaction involving leptons, the lepton numbers $L_{e,\mu}$ are set to +1 for leptons and -1 for antileptons; L_e and L_μ must be conserved in an interaction. The number of lepton families would increase by one in 1975, with the discovery by Martin Perl of another heavier charged lepton, the tau. Its neutrino partner, ν_τ, was eventually found by the DONUT experiment twenty-five years later in 1997 (announced in 2000 [13][14]) at Fermilab, via the decay of charmed mesons.

As of early 2019, only three flavors of leptons have been discovered: the electron (e), the muon (μ), and the tau (τ). These three lepton families have been incorporated into the theoretical framework of the Standard Model of Particle Physics (SM). Various theories beyond the standard model predict one, two, or more neutrinos, usually right-handed (the opposite chirality of normal neutrinos) sterile neutrinos that do not interact with particles outside of the leptonic sector, solely interacting with the neutrinos themselves.

1.3 ν's and the Standard Model of Particle Physics

The Standard Model of Particle Physics is the theoretical framework in which particle interactions are described through three of the four known fundamental forces: Electromagnetism, Strong, and Weak interactions; the force of Gravity is not included in the SM. The SM unifies the non-Abelian gauge theories of electroweak and strong interactions. Left-handed neutrinos (ν_e, ν_μ, ν_τ) and right-handed antineutrinos ($\bar{\nu}_e, \bar{\nu}_\mu, \bar{\nu}_\tau$) enter into the SM along with the charged leptons ($e^\pm$,$\mu^\pm$,$\tau^\pm$) through the Glashow-Weinberg-Salam (GWS) model.

The GWS model is the direct product of the groups SU(2) $\otimes$ U(1), where SU(2) belongs to the weak isospin and U(1) belongs to the hypercharge [10]. The leptons are all fermions with a spin angular momentum of $\hbar/2$. The effective gauge bosons from the SU(2) $\otimes$ U(1) group are the charged gauge bosons $W^\pm$ that mediate the charged current (CC) interactions in radioactivity, the Z^0 that mediates the neutral current (NC) interactions in radioactivity, and the massless photon that mediates electromagnetic (EM) interactions. The $W^\pm$ are formed by the doublets from the SU(2) group. The photon and the Z^0 are formed by combinations of the U(1) field and the singlet from the SU(2) group mixed together by the Weinburg weak mixing angle θ_W.

The Z and $W^\pm$ bosons are very massive (O(100) GeV) compared to the leptons, and especially so compared to neutrinos. Since neutrinos are electrically neutral particles, they do not interact directly with the electromagnetic force but only have interactions through weak processes in the SM. Since the neutrino cross section with matter goes as $G_F^2 E_\nu \propto E_\nu / M_{W,Z}^4$, weak interactions involving neutrinos are heavily suppressed by the masses of the W and Z bosons [15]. This allows for the neutrino to take on the almost incorporeal property of being able to travel through vast quantities of matter without any discernible interactions occurring along the way, lending to the neutrino's nickname: the "ghost" particle. As stated previously, each generation (or flavor) of leptons are given a quantum number, known as its

lepton number, whose values are $L_\alpha = +1$ for leptons, and $L_\alpha = -1$ for antileptons, where $\alpha = e, \mu, \tau$ denotes the generation and flavor. In the SM, the total lepton numbers for each family are all conserved in a particle interaction, and, consequently, so is the total lepton number $L = \sum_\alpha L_\alpha$.

Because neutrinos have been shown experimentally to have small but non-vanishing mass, they can interact via gravity, though on scales other than cosmological ones, this effect can be neglected. The SM assumes neutrinos are massless, and there is no mass term present for the Higgs field to couple to unless right-handed neutrinos ν_R (left-handed antineutrinos $\bar{\nu}_L$) are introduced into the SM. However, if the neutrino is its own antiparticle, i.e. the neutrino is a Majorana field and not a Dirac field, the mass can be generated in a similar way to adding in ν_R. Other possible methods of generating neutrino mass exist as well.

Within the SM, the neutrinos undergo elastic scattering with the charged leptons, leading to an effective matter potential due to the local electron density. Because neutrinos have been experimentally determined to have mass, the neutrinos will oscillate between flavor states, violating the family lepton number conservation, though the total lepton number will be conserved. The SM Lagrangian pertaining to weak interactions for α-flavored neutrinos with matter in the low-energy regime is given by [10]:

$$-\mathcal{L}_{\nu_\alpha} = \frac{G_F}{\sqrt{2}} \nu_\alpha^\dagger (1 - \gamma_5) \nu_\alpha \sum_f N_f \left\{ \delta_{\alpha f} + I_{3f_L} - 2Q_f \sin^2 \theta_W \right\}. \tag{1.1}$$

In this equation, G_F is the Fermi coupling constant and θ_W is the Weinberg angle. The index f denotes the fermions with left-handed fields (f_L) and electrical charge Q_f present in the matter. The term I_{3f_L} is the eigenvalue for the third weak isospin component of f_L. The eigenvalues for the fermions are: $Q_e = -1, I_{3e_L} = -\frac{1}{2}$ for electrons, $Q_p = +1, T_{3p_L} = +\frac{1}{2}$ for protons, and $Q_n = 0, I_{3n_L} = -\frac{1}{2}$ for neutrons. For the up (u) and down (d) quarks

that make up protons and neutrons, their quantum numbers are $Q_u = +\frac{2}{3}, T_{3u_L} = +\frac{1}{2}$ and $Q_d = -\frac{1}{3}, T_{3d_L} = -\frac{1}{2}$ respectively. Since the CC interactions occur through the δ_α term, the fermionic content of the matter will set the CC interactions available to ν_α. Specifically the Kronecker delta is only non-zero for electron neutrinos: $\alpha = f = e$.

With the introduction of non-standard interactions (NSI) between neutrinos and matter, new four-fermion terms will appear as additions to the SM Lagrangian and appear in the neutrino propagation Hamiltonian as terms that add in interactions between (anti)neutrinos and quarks [16][17]. Additional flavor-violating interactions between electrons and neutrinos is also possible depending on the nature of the NSI introduced [16]. Because ordinary solar and terrestrial matter is dominated by protons, neutrons, and electrons, the NSI that pertain to neutrino propagation will be due to the up (u) and down (d) quark densities, as well as the electron density. Both the solar plasma and the Earth matter are electrically neutral, meaning the number density of protons and electrons is the same, though the neutron content can vary relative to the other two. The effects on neutrino oscillations due to introduction of NSI between neutrinos and matter into the SM will be discussed in Sec. 2.4.

1.4 Neutrino Sources

There are various sources throughout the universe that produce neutrinos, from the origin of the universe itself to natural and man-made processes that occur here on Earth. Neutrinos produced in the early universe, known as the cosmic neutrino background, were created during the inflationary period of the early universe as they separated from matter while the universe cooled down, about one second after the Big Bang. These Big Bang neutrinos are believed to exist, though they have yet to be directly detected. Other, high-energy neutrinos produced in the cosmos are known as astrophysical neutrinos. Electron neutrinos are produced in the core of stars from the fusion processes that drive the nuclear furnace in

their cores. Neutrinos coming from our Sun are called solar neutrinos, and are a rich source used to study the properties of both the Sun and neutrinos.

Additionally, both neutrinos and antineutrinos are produced in vast quantities during certain types of supernovae (core-collapse), with almost 99% of the energy of the explosion carried away by neutrinos. In 1987, a burst of supernova (anti)neutrinos was detected by several terrestrial experiments. The neutrinos and antineutrinos produced by all of the supernovae throughout the history of the universe are still flying around and create a diffuse supernova neutrino background (DNSB) [18]. The detection of the DSNB is one of the primary physics goals for Super-Kamiokande (SK) [19], in addition to supernova burst antineutrinos. Other astrophysical neutrino sources exist. Recently, the IceCube collaboration has reported that blazars are a source of high energy astrophysical neutrinos [20], though the flux from blazars are not yet well understood.

Here on Earth, atmospheric neutrinos come from the collisions of cosmic rays (either highly relativistic protons or other light nuclei) with nuclei in the atmosphere. These collisions produce many neutrinos and antineutrinos of both electron and muon flavors through charged pion ($\pi^{\pm}$) and kaon ($K^{\pm}$) decay. Rarely, tau atmospheric (anti)neutrinos from the cosmic seeding event are produced as well. Harnessing the same production mechanisms from cosmic rays that produce (anti)neutrinos, man-made (anti)neutrino beams give a controlled source for the study of high energy muon accelerator (anti)neutrinos, using the same methods as pioneered by Schwartz. Within the Earth itself, geoneutrinos are produced from the nuclear fission of radioisotope decays within the crust and mantle. Geoneutrinos are predominantly $\bar{\nu}_e$s with a very small ν_e component due to ^{40}K beta capture [21]. Additionally, the fissionable materials in man-made nuclear reactors, as well as those in nuclear explosions, produce large quantities of electron antineutrinos known as reactor antineutrinos.

Because the reactions that produce neutrinos are known, including the number and flavor content an interaction produces, their rates and fluxes from various sources can be

predicted. This allows one to test the theories governing the fundamental interactions and properties of neutrinos. The only caveat to this approach is if some process occurs which changes what would be seen in a detector away from the source, assuming details about the source are well enough understood. If the medium interacts with neutrinos in ways not expected by the theory, or if neutrinos contain additional properties not covered by the theory that cause them to behave differently even in vacuum, then what would be predicted will not match the results coming from the detector. Situations like these have driven the field of neutrino physics forward, leading to the discovery of neutrino mass and oscillations.

Solar neutrinos serve as proof that the energy production in the Sun is due to *pp* fusion. Measurements of solar neutrinos, specifically the spectral data for ^{8}B, show neutrinos interact with matter in the core of the Sun and hint of ν_e regeneration due to terrestrial matter.

Chapter 2

Neutrino Propagation, Oscillations, and Interactions

To more conveniently discuss topics related to solar neutrinos, the formalism for neutrino propagation, oscillation, and interactions is gathered and discussed first in this chapter. This discussion includes the properties of solar neutrinos in vacuum and in matter, with and without Non-Standard Interactions (NSI), as well as their their interactions in Super-Kamiokande (SK). First, details about the propagation and oscillation of neutrinos through vacuum and matter will be discussed. The cross section calculations for neutrino-electron elastic scattering (ES) in SK will then be covered. Finally, the inclusion of NSI into the neutrino propagation formalism and its effects on neutrino oscillation. In this chapter, the book Neutrino Physics, 2^{nd} Ed. by Kai Zuber [10] is used to cross-check or as a reference for details of the mathematics for the topics discussed here.

2.1 Neutrino Propagation in Vacuum: Neutrino Mass and Oscillations

Theories predicting the existence of a non-zero neutrino mass and the phenomenology that would result if neutrinos are massive were first proposed by Pontecorvo in 1958 in the context of Majorana neutrinos, where neutrinos alternated between their normal and antimatter states ($\nu \leftrightarrow \bar{\nu}$). The framework for neutrino flavor mixing was established by Maki, Nakagawa, and Sakata in 1962 [22] and requires non-zero neutrino mass as well. With a non-zero rest mass, the mass and weak eigenstates do not need be the same, and can be connected with a unitary mixing matrix in a similar manner to what occurs in the quark sector with the Cabibbo-Kobayashi-Masakawa (CKM) matrix. This unitary mixing matrix is known as the Pontecorvo-Maki-Nakagawa-Sakata (PMNS) matrix, denoted by U_{PMNS}. Neutrinos are created in a definite flavor state (a superposition of the mass states) based on the type of interaction that produced the neutrino. Due to the time evolution of the mass eigenstates, the superposition of the flavor eigenstates changes, resulting in the phenomenon of neutrino oscillation.

Assuming there are n orthonormal mass eigenstates $|\nu_i\rangle$, we can rotate them into n orthonormal flavor eigenstates $|\nu_\alpha\rangle$ with a unitary $n \times n$ mixing matrix U. Since each eigenstate basis is an orthonormal basis, and because U is unitary, we have the following identities:

$$\langle \nu_\alpha | \nu_\beta \rangle = \delta_{\alpha\beta} \quad \text{and} \quad \langle \nu_i | \nu_j \rangle = \delta_{ij} \tag{2.1}$$

and

$$U^\dagger U = 1, \qquad (U^\dagger)_{i\alpha} = U^\star_{\alpha i}, \qquad \sum_\alpha U_{\alpha i} U^\star_{\alpha j} = \delta_{ij}, \qquad \sum_i U^\star_{\alpha i} U_{\beta i} = \delta_{\alpha\beta} \tag{2.2}$$

where δ_{ab} is the standard Kronecker delta. Then, the rotational transformation between the

neutrino bases are

$$|\nu_\alpha\rangle = \sum_i U_{\alpha i} |\nu_i\rangle , \quad \text{and inverting} \quad |\nu_i\rangle = \sum_\alpha U^\star_{\alpha i} |\nu_\alpha\rangle . \tag{2.3}$$

In the case of antineutrinos, the unitary matrix becomes conjugated, i.e. $U_{\alpha i} \leftrightarrow U^\star_{\alpha i}$ swap places in Eq. 2.3. Since U is an $n \times n$ unitary matrix, it has the additional properties that there are $(n-1)^2$ independent parameters, which will be separated into $\frac{n}{2}(n-1)$ neutrino mixing angles of an $n \times n$ rotational matrix and $\frac{1}{2}(n-2)(n-1)$ CP-violating phases.

Let the neutrino $|\nu_i\rangle$ be approximated as a plane wave emitted at time $t = 0$ with momentum p from a source located at the origin. Then the neutrino wavefunction at position x is

$$|\nu_i(x,0)\rangle = e^{ipx/\hbar} |\nu_i\rangle . \tag{2.4}$$

The vacuum Hamiltonian acting on the neutrino wave function gives the time evolution for $|\nu_i(x,0)\rangle$, which is given by

$$H_{vac} |\nu_i(x,t)\rangle = i\hbar \frac{\partial}{\partial t} |\nu_i(x,t)\rangle = E_i |\nu_i(x,t)\rangle , \tag{2.5}$$

since the neutrino energy E_i should not change after emission into vacuum. Now, rewriting the above equation using the time evolution operator and inserting the plane wave approximation from Eq. 2.4 gives

$$|\nu_i(x,t)\rangle = e^{-iE_it/\hbar} |\nu_i(x,0)\rangle = e^{-iE_it/\hbar} e^{ipx/\hbar} |\nu_i\rangle . \tag{2.6}$$

For relativistic neutrinos with non-zero mass and the same momentum p, each neutrino will have a different energy E_i due to Einstein's equation $E_i^2 = (cp)^2 + m_i^2c^4$. Because the neutrino mass is so small when compared to the momentum of the relativistic neutrino, the neutrino energy is approximately equal to the magnitude of the neutrino momentum,

$E_i \simeq cp$. This is demonstrated in Eq. 2.7 after Taylor expanding E_i in $\left(\frac{m_i c}{p}\right)^2$:

$$E_i = \sqrt{p^2c^2 + m_i^2c^4} \simeq |p|c\left(1 + \frac{1}{2}\left[\frac{m_i c}{p}\right]^2\right) = |p|c + c^4\frac{m_i^2}{2c|p|} \tag{2.7}$$

The pc term ends up being just an overall phase factor in the Hamiltonian and will cancel out, meaning that it can be neglected to simplify the form of the vacuum Hamiltonian for Schrödinger's equation:

$$H_{vac}\,|\nu_i(x,t)\rangle = E_i\,|\nu_i(x,t)\rangle = \frac{m_i^2c^4}{2cp}\,|\nu_i(x,t)\rangle \quad \Rightarrow \quad H^i_{ij} = \delta_{ij}\frac{c^4m_{ij}^2}{2cp} \tag{2.8}$$

where H^i_{ij} are the matrix elements of the Hamiltonian mass matrix H^i, which is diagonal in the mass basis $|\nu_i\rangle$. Converting to the flavor basis using U, the mass matrix for the flavor eigenstates can be determined

$$H^\alpha = UH^iU^\dagger. \tag{2.9}$$

Now, to look in greater detail at the time evolution of the flavor states, let $L = x = ct$ be the distance between the source of the emitted neutrino and the point of detection, and let $E = cp$ denote the energy of the emitted neutrino for $p \gg m_i$, which is the case for the relativistic neutrino. Then, using Eq. 2.7, one defines the phase for the massive neutrinos $-i\phi_i$ as the argument of the exponential term in Eq. 2.6, which can be simplified as

$$\phi_i \equiv [E_it/\hbar] - px/\hbar = \left[E + \frac{m_i^2c^4}{2E}\right]\frac{L}{\hbar c} - \frac{EL}{\hbar c} = \frac{m_i^2c^4}{2c\hbar}\frac{L}{E} \tag{2.10}$$

after factoring out $-i$. Assuming the flavor eigenstates of the neutrino are coherent superpositions of the mass eigenstates, one can use the mixing matrix U and Eq. 2.3 to transform the flavor state to the mass bases. Then one can propagate the neutrino via Eq. 2.6 to get

$$|\nu_\alpha(x,t)\rangle = \sum_i U_{\alpha i}\,|\nu_i(x,t)\rangle = \sum_i U_{\alpha i}\exp\{-i\phi_i\}\,|\nu_i\rangle\,, \tag{2.11}$$

where Eq. 2.10 was used to simplify the exponential. Transforming the result of Eq. 2.11 back into the flavor basis, one obtains

$$|\nu_\alpha(x,t)\rangle = \sum_i U_{\alpha i} \exp\{-i\phi_i\} \left(\sum_\beta U^\star_{\beta i} |\nu_\beta\rangle \right) = \sum_{i,\beta} U_{\alpha i} U^\star_{\beta i} \exp\{-i\phi_i\} |\nu_\beta\rangle . \tag{2.12}$$

If the neutrino masses are different and non-zero, then the phase factor $\exp\{-i\phi_i\}$ in Eq. 2.12 will create interference terms in the final state transition and survival probabilities, which means that the flavor content of the neutrino is different between the initial and final states. The survival probability for a neutrino is the probability that the neutrino is detected in the same flavor state it was produced in, whereas the transition probability is the probability that the neutrino has oscillated away from the flavor state it was produced in. Both are a function of time or distance. To see the conversion between neutrino flavor states $\nu_\alpha \to \nu_\beta$, we form the time dependent transition amplitude $A(\alpha \to \beta)$ (Eq. 2.13), and determine the transition probability $P(\nu_\alpha \to \nu_\beta)(t)$ (Eq. 2.14):

$$A(\alpha \to \beta) = \langle \nu_\beta | \nu_\alpha(x,t) \rangle = \sum_i U_{\alpha i} U^\star_{\beta i} \exp\{-i\phi_i\} \tag{2.13}$$

$$P(\nu_\alpha \to \nu_\beta)(t) = |A(\alpha \to \beta)|^2 = \sum_{i,j} U_{\alpha i} U^\star_{\beta i} U^\star_{\alpha j} U_{\beta j} \exp\{-i\Delta\phi_{ij}\}, \tag{2.14}$$

where the term $\Delta\phi_{ij} \equiv \phi_i - \phi_j$. Writing out $\Delta\phi_{ij}$:

$$\Delta\phi_{ij} = (E_i - E_j)t/\hbar = \frac{\Delta m^2_{ij} c^4 L}{2cE\hbar}, \tag{2.15}$$

the position term cancels and the dependence on the squared mass splitting term,

$$\Delta m^2_{ij} \equiv m^2_i - m^2_j, \tag{2.16}$$

is explicit. The $\Delta\phi_{ij}$ term can be rewritten in terms of natural units ($c = \hbar = 1$) to give

$$\Delta\phi_{ij} \simeq 2.534 \times \Delta m^2_{ij} \frac{L}{E}, \tag{2.17}$$

where Δm^2_{ij} is in square electron Volts (eV^2), L is in meters, and E has units of MeV.

As can be seen when rewriting Eq. 2.14 in terms of the squared mass splittings, if the neutrino mass is zero, or when the neutrino masses are all degenerate ($\Delta m^2_{ij} = 0$), the transition probability reduces to just $P(\nu_\alpha \to \nu_\beta)(t) = \delta_{\alpha\beta}$, which means that there would be no mixing of the flavor states. For non-degenerate, non-zero neutrino masses, the neutrino flavor survival probability is:

$$P(\nu_\alpha \to \nu_\alpha)(t) = 1 - \sum_{\alpha \neq \beta} P(\nu_\alpha \to \nu_\beta)(t), \tag{2.18}$$

using the fact that the total probability must be equal to unity.

2.1.1 Oscillations with Three Neutrinos

With the experimental verification that there are (at least) three flavors of neutrinos, the weak eigenstates are ν_e, ν_μ, and ν_τ and have three corresponding mass eigenstates ν_1, ν_2, and ν_3. The U_{PMNS} mixing matrix (Eq. 2.21) will be a 3×3 matrix with a single CP-violating phase δ_{CP}, and three mixing angles θ_{12}, θ_{23}, and θ_{13}, producing the mass eigenstate superpositions for the flavor eigenstates.

$$\begin{pmatrix} \nu_e \\ \nu_\mu \\ \nu_\tau \end{pmatrix} = U_{\text{PMNS}} \begin{pmatrix} \nu_1 \\ \nu_2 \\ \nu_3 \end{pmatrix} = \begin{bmatrix} U_{e1} & U_{e2} & U_{e3} \\ U_{\mu 1} & U_{\mu 2} & U_{\mu 3} \\ U_{\tau 1} & U_{\tau 2} & U_{\tau 3} \end{bmatrix} \begin{pmatrix} \nu_1 \\ \nu_2 \\ \nu_3 \end{pmatrix} \tag{2.19}$$

The U_{PMNS} matrix can be decomposed into three submatricies (2.20), corresponding to the sources whose transition probabilities the parameters primarily impact: solar neutrinos (left matrix), atmospheric and reactor neutrinos (central matrix), and atmospheric neutrinos and neutrino beams (right matrix):

$$U_{\text{PMNS}} = \begin{bmatrix} c_{12} & s_{12} & 0 \\ -s_{12} & c_{12} & 0 \\ 0 & 0 & 1 \end{bmatrix} \begin{bmatrix} c_{13} & 0 & s_{13}e^{-i\delta_{CP}} \\ 0 & 1 & 0 \\ -s_{13}e^{i\delta_{CP}} & 0 & c_{13} \end{bmatrix} \begin{bmatrix} 1 & 0 & 0 \\ 0 & c_{23} & s_{23} \\ 0 & -s_{23} & c_{23} \end{bmatrix} = \tag{2.20}$$

$$\begin{bmatrix} c_{12}c_{13} & c_{12}c_{13} & s_{13}e^{-i\delta} \\ -s_{12}c_{23} - c_{12}s_{23}s_{13}e^{i\delta} & c_{12}c_{23} - s_{12}s_{23}s_{13}e^{i\delta} & s_{23}c_{13} \\ s_{12}s_{23} - c_{12}s_{23}s_{13}e^{i\delta} & -c_{12}s_{23} - s_{12}c_{23}s_{13}e^{i\delta} & c_{23}c_{13} \end{bmatrix} \tag{2.21}$$

where $c_{ij} = cos(\theta_{ij})$ and $s_{ij} = sin(\theta_{ij})$, and $\delta = \delta_{CP}$. The three squared mass splittings are then

$$\Delta m^2_{21} = m^2_2 - m^2_1, \quad \Delta m^2_{31} = m^2_3 - m^2_1, \quad \text{and} \quad \Delta m^2_{32} = m^2_3 - m^2_2. \tag{2.22}$$

The measured value of Δm^2_{21} for the ν_1 and ν_2 neutrinos is on the order of 10^{-5} eV. It is usually referred to as Δm^2_{sol}, since it plays the dominant part in the study of solar neutrinos (discussed later). Likewise, $\theta_{12} = \theta_{sol}$ is often referred to as the solar mixing angle. From atmospheric neutrino studies, it has been seen that the mass squared splittings between ν_3 and the other mass states are approximately the same, i.e. $\Delta m^2_{31} \approx \Delta m^2_{32}$ and are of order of 10^{-3} eV. The atmospheric mass splitting is assigned as $\Delta m^2_{atm} = \Delta m^2_{32}$.

Based on the solar neutrino data, $m_2 > m_1$. Because the magnitude of Δm^2_{atm} is known but not the sign of the splitting, there is an issue of knowing whether the ν_3 mass state is heavier or lighter than ν_1 and ν_2. This gives a choice to the mass ordering of the neutrinos: either the normal ordering $m_1 < m_2 < m_3$ or the inverted mass ordering $m_3 < m_1 < m_2$. The neutrino mass ordering is important for atmospheric and neutrino beam analyses, since

it alters the oscillation transition probabilities due to their dependence on the sign of Δm^2_{atm}, especially in the presence of matter. Because the analysis presented in this work considers only solar neutrinos, a simplification to studying oscillations in a two-neutrino approximation is used, and little else about the three-neutrino framework will be discussed unless necessary.

2.1.2 Oscillations in the Two-Neutrino Approximation

Solar neutrinos are created in purely the electron neutrino flavor eigenstate ν_e via charged current (CC) reactions. As the Sun does not produce antineutrinos, solar neutrino measurements are insensitive to δ_{CP}. When studying solar neutrinos, the neutrino mass ordering and atmospheric mass splitting are not so important, but there is a slight dependence on the θ_{13} mixing angle. The reactor long baseline antineutrino experiment Daya Bay [23] gives $\sin^2\theta_{13} \simeq 0.0215$, and other reactor antineutrino experiments, RENO [24][25] and Double Chooz [26] [27], measure similar values, all of which are summarized in Table 2.1. Because $\theta_{13} \simeq 8.3°$, and thus U_{e3} is relatively small, the resulting contribution to ν_e from the mass eigenstate ν_3 is small as well, though non-zero [10][28]. By inverting Eq 2.19, we get

$$|\nu_3\rangle = c_{13}\left[s_{23}\,|\nu_\mu\rangle + c_{23}\,|\nu_\tau\rangle\,\right] + s_{13}e^{i\delta_{CP}}\,|\nu_e\rangle \simeq s_{23}\,|\nu_\mu\rangle + c_{23}\,|\nu_\tau\rangle\,, \tag{2.23}$$

which shows that ν_3 is predominantly a superposition of ν_μ and ν_τ, and in almost equal amounts since $\theta_{23} \approx \frac{\pi}{4}$ based on the current global measurements [29]. The θ_{23} mixing angle has the largest errors of the neutrino mixing angle and carries an additional dependence on the mass ordering. With the lack of significant contribution from the θ_{23} mixing angle and third mass state, as well as the large difference in scales between Δm^2_{solar} and Δm^2_{atm}, the three-flavor framework can be reduced to two flavors using the assumption of taking $\Delta m^2_{31} \to \infty$, while correcting for the effects the neglected neutrino state has on the neutrino oscillations through θ_{13} [28].

Table 2.1: The experimental measurements of $\sin^2(2\theta_{13})$ from the reactor long baseline antineutrino experiments Daya Bay [23], RENO [25] and Double Chooz [27]. A combined value of the measurement based on experimental errors and ignoring correlations is given. Daya Bay has also made an independent measurement of $\sin^2(2\theta_{13}) = 0.083 \pm 0.018$ based on hydrogen capture of antineutrino-induced neutrons [30].

Experiment	$\sin^2(2\theta_{13})$
Daya Bay	$0.0841 \pm 0.0027(\text{stat}) \pm 0.0019(\text{syst})$
RENO	$0.086 \pm 0.006(\text{stat}) \pm 0.005(\text{syst})$
Double Chooz	$0.090^{+0.032}_{-0.029}(\text{total})$
Combined	$0.0844 \pm 0.0042(\text{total})$

For two-flavor eigenstates (ν_e, ν_μ) and mass eigenstates (ν_1, ν_2), the mixing matrix is reduced to a 2×2 rotation matrix of a single angle $\theta \equiv \theta_{12}$ without any CP-violating complex phases:

$$\begin{pmatrix} \nu_e \\ \nu_\mu \end{pmatrix} = \begin{bmatrix} \cos(\theta) & \sin(\theta) \\ -\sin(\theta) & \cos(\theta) \end{bmatrix} \begin{pmatrix} \nu_1 \\ \nu_2 \end{pmatrix} = U \begin{pmatrix} \nu_1 \\ \nu_2 \end{pmatrix} \tag{2.24}$$

Then the mixed waveforms for the flavor states are

$$|\nu_e\rangle = \cos(\theta)\,|\nu_1\rangle + \sin(\theta)\,|\nu_2\rangle \quad \text{and} \quad |\nu_e\rangle = -\sin(\theta)\,|\nu_1\rangle + \cos(\theta)\,|\nu_2\rangle\,. \tag{2.25}$$

The Hamiltonian mass matrix H^i is now

$$H^i = \frac{1}{2E} \begin{bmatrix} m_1^2 & 0 \\ 0 & m_2^2 \end{bmatrix} \tag{2.26}$$

and transforming in the flavor basis representation

$$H^\alpha_{vac} = \frac{1}{2E} \begin{bmatrix} m^2_{ee} & m^2_{e\mu} \\ m^2_{\mu e} & m^2_{\mu\mu} \end{bmatrix} = U H^i_{vac} U^\dagger = \tag{2.27}$$

$$H^{\alpha}_{vac} = \frac{1}{2E}\begin{bmatrix} c_\theta^2 m_1^2 + s_\theta^2 m_2^2 & s_\theta c_\theta (m_2^2 - m_1^2) \\ -s_\theta c_\theta (m_2^2 - m_1^2) & s_\theta^2 m_1^2 + c_\theta^2 m_2^2 \end{bmatrix} \tag{2.28}$$

where $c_\theta = \cos(\theta)$ and $s_\theta = \sin(\theta)$.

Rewriting Eq. 2.14 in terms of real components, the oscillation transition probability from ν_e to ν_μ in vacuum is

$$P(\nu_e \to \nu_\mu) = -4(U_{e1}U_{\mu 1}U_{e2}U_{\mu 2})\sin^2\left(\frac{\Delta m^2_{21} c^4 L}{4cE\hbar}\right) \tag{2.29}$$

which is just

$$P(\nu_e \to \nu_\mu) = \sin^2(2\theta)\sin^2\left(\frac{\Delta m^2_{21} c^4 L}{4cE\hbar}\right). \tag{2.30}$$

Since there is no δ_{CP} phase, the transition probabilities for the two-neutrino case are all equal, regardless if the particle is a neutrino or antineutrino:

$$P(\nu_e \to \nu_\mu) = P(\nu_\mu \to \nu_e) = P(\bar{\nu_e} \to \bar{\nu_\mu}) = P(\bar{\nu_\mu} \to \bar{\nu_e}). \tag{2.31}$$

Finally, the two-flavor electron neutrino survival probability P^{2f}_{ee} is simply given by

$$P^{2f}_{ee} \equiv P(\nu_e \to \nu_e) = 1 - P(\nu_e \to \nu_\mu). \tag{2.32}$$

To account for the effect the third generation of neutrinos has on the electron survival probability, the two-flavor survival probability P^{2f}_{ee} is modified by "three-flavorizing" it [31][28][32] via

$$P^{3f}_{ee} \equiv \cos^4(\theta_{13})P^{2f}_{ee} + \sin^4(\theta_{13}), \tag{2.33}$$

which just returns $P^{3f}_{ee} = P^{2f}_{ee}$ when $\theta_{13} \to 0$. Now that the necessary equations for vacuum oscillations in the two neutrino flavor approximation have been developed, the effects on the neutrino wavefunction due to matter need to be incorporated.

2.2 Neutrino Propagation in Matter in the Two-Flavor Approximation

While neutrinos can be produced in vacuum, and space-faring neutrinos propagate through vacuum to reach Earth, many neutrinos are produced in matter. Regardless of the source, neutrinos will travel through matter to reach terrestrial detectors here on Earth, be it the Earth's atmosphere (which has a negligible effect on the neutrinos due to the low density) or the "Earth matter" that makes up the crust, mantle, and core. For neutrinos propagating through the Sun or the Earth, based on the Lagrangian in Eq. 1.1, matter affects the neutrino propagation via coherent forward ES [10]. All neutrino flavors can experience NC ES interactions, which is diagonal and symmetric in the Hamiltonian and leads to an overall phase shift whose effect on the oscillation washes out [33]. However, only ν_e can undergo CC ES interactions with the electrons in the matter, and, as such, ν_e feel an effective potential V on their wavefunction from the electron number density N_e in matter, since ν-fermion interactions occur in the flavor basis. The form of the potential can be determined from the contribution of CC ES in matter to the interaction Hamiltonian:

$$H_{CC} = \frac{G_F}{\sqrt{2}}\Big[\bar{e}\gamma^\mu(1-\gamma_5)\nu_e\Big]\Big[\bar{\nu}_e\gamma_\mu(1-\gamma_5)e\Big]. \tag{2.34}$$

By noting that only the zero'th component of the averaged electron four-current density survives and is N_e, and also replacing the $(1-\gamma_5) \to 2$ for left-handed neutrinos, Eq. 2.34 can be reduced to

$$H_{CC} = \sqrt{2}G_F N_e \bar{\nu}_e\gamma_0\nu_e = V\bar{\nu}_e\gamma_0\nu_e \tag{2.35}$$

using a Friez transformation [10]. The potential is then $V = \sqrt{2}G_F N_e$.

The effective ν_e mass m^2_{ee} from H^α_{vac} (Eq. 2.27) is therefore modified in the presence of

matter by V:

$$m_{ee}^2 \to m_{ee,eff}^2 = m_{ee}^2 + A \qquad \text{where} \qquad A = 2EV, \tag{2.36}$$

and H^α becomes

$$H_{mat}^\alpha = \frac{1}{2E}\begin{bmatrix} m_{ee}^2 + A & m_{e\mu}^2 \\ m_{\mu e}^2 & m_{\mu\mu}^2 \end{bmatrix} = H_{Vac}^\alpha + V_{mat}, \tag{2.37}$$

where V_{mat} is the matter potential for the two-neutrino flavor case (ν_e, ν_μ):

$$V_{mat} = \frac{A}{2E}\begin{bmatrix} 1 & 0 \\ 0 & 0 \end{bmatrix}. \tag{2.38}$$

The rows and columns of V_{mat} are indexed corresponding to incoming/outgoing ν_e and ν_μ.

For three neutrino flavors, the matter potential still only has interactions of electrons with electron neutrinos. Then the matrix V_{mat} is simply extended to include the third generation, i.e. $V_{mat} \to V_{mat}^{3f}$:

$$V_{mat}^{3f} = \frac{A}{2E}\begin{bmatrix} 1 & 0 & 0 \\ 0 & 0 & 0 \\ 0 & 0 & 0 \end{bmatrix}, \tag{2.39}$$

where the rows and columns are indexed to additionally include the incoming/outgoing ν_τ. Properly including the effect from three neutrino flavors ($\theta_{13} \neq 0$) in the two-flavor approximation, V_{mat} can be three-flavorized (Eq. between Eq. 9 and 10 in [28]). This is done by taking

$$N_e \to N_e \cos^2\theta_{13} \Rightarrow A = 2\sqrt{2}G_F E N_e \cos^2\theta_{13}. \tag{2.40}$$

Writing V_{mat} explicitly to show the dependence on θ_{13}:

$$V_{mat} = \sqrt{2}G_F N_e \begin{bmatrix} \cos^2\theta_{13} & 0 \\ 0 & 0 \end{bmatrix}. \tag{2.41}$$

The $\cos^2\theta_{13}$ term will be kept separate from the extra parameters introduced by NSI to keep them independent of one another. It is worth noting that the matter potential V_{mat} does not have a dependence on the other neutrino oscillation parameters (θ_{23}, δ_{CP}, and Δm^2_{atm}) from the three-flavor scenario, and returns to a pure two-flavor scenario for $\theta_{13} \to 0$.

Transforming H^{α}_{mat} to the mass basis ν_1, ν_2, the effective mass basis Hamiltonian is now

$$H^{i}_{mat} = U^{\dagger} H^{\alpha}_{mat} U = H^{i}_{vac} + \frac{A}{2E} U^{\dagger} \begin{bmatrix} 1 & 0 \\ 0 & 0 \end{bmatrix} U \tag{2.42}$$

where the second term becomes

$$\frac{A}{2E} U^{\dagger} \begin{bmatrix} 1 & 0 \\ 0 & 0 \end{bmatrix} U = \frac{A}{2E} \begin{bmatrix} \cos^2(\theta_{12}) & \frac{1}{2}\sin(2\theta_{12}) \\ \frac{1}{2}\sin(2\theta_{12}) & \sin^2(\theta_{12}) \end{bmatrix}. \tag{2.43}$$

Therefore, H^{i}_{mat} can be written as

$$H^{i}_{mat} = \frac{1}{2E} \begin{bmatrix} m_1^2 + A\cos^2(\theta_{12}) & \frac{A}{2}\sin(2\theta_{12}) \\ \frac{A}{2}\sin(2\theta_{12}) & m_1^2 + A\sin^2(\theta_{12}) \end{bmatrix} \tag{2.44}$$

which shows that H^{i}_{mat} is not diagonal. To get the eigenstates $\nu^{mat}_{1,2}$ of the effective mass Hamiltonian in matter, one needs to diagonalize H^{i}_{mat}, where the eigenvalues are $\lambda = \left(\frac{m^2_{1,mat}}{2E}, \frac{m^2_{2,mat}}{2E} \right)$ for the neutrinos in matter. In the usual way, the eigenvalues are obtained from

$$\mathrm{Det}\big\{ H^{i}_{mat} - \lambda I_2 \big\} = 0, \tag{2.45}$$

which gives the characteristic equation:

$$0 = (2E\lambda)^2 + (2E\lambda)\big\{ m_1^2 + m_2^2 + A \big\} + m_1^2 m_2^2 + A(m_2^2 c_{12}^2 + m_1^2 s_{12}^2). \tag{2.46}$$

Again, $s^2_{12} = \sin^2\theta_{12}$ and $c^2_{12} = \cos^2\theta_{12}$. Solving the quadratic equation piece by piece, we

get that $-b = A + m_1^2 + m_2^2$, and $c = m_1^2 m_2^2 + A(m_2^2 \cos^2\theta_{12} + m_1^2 \sin^2\theta_{12})$, and the radical expression is

$$\begin{aligned} b^2 - 4c = (m_1^4 + m_2^4 - 2m_1^2 m_2^2) + 2Am_1^2(1 - 2s_{12}^2) + 2Am_2^2(1 - 2c_{12}^2) + A^2 = \\ \Delta m_{21}^4 + 2Am_1^2\{\cos(2\theta_{12})\} + 2Am_2^2\{-\cos(2\theta_{12})\} + A^2 = \\ \Delta m_{21}^4\{\cos^2(2\theta_{12}) + \cos^2(2\theta_{12})\} - 2A\cos(2\theta_{12})\Delta m_{21}^2 + A^2 = \\ [A - \Delta m_{21}^2\cos(2\theta_{12})]^2 + [\Delta m_{21}^2 \sin(2\theta_{12})]^2. \end{aligned} \tag{2.47}$$

Then, the effective masses for a neutrino propagating through matter are given by:

$$\begin{aligned} m_{1,mat}^2 &= \tfrac{1}{2}\left(m_1^2 + m_2^2 + A - \sqrt{[A - \Delta m_{21}^2\cos(2\theta_{12})]^2 + [\Delta m_{21}^2\sin(2\theta_{12})]^2}\right) \\ m_{2,mat}^2 &= \tfrac{1}{2}\left(m_1^2 + m_2^2 + A + \sqrt{[A - \Delta m_{21}^2\cos(2\theta_{12})]^2 + [\Delta m_{21}^2\sin(2\theta_{12})]^2}\right) \end{aligned} \tag{2.48}$$

The effective squared mass splitting is easily written as

$$\Delta m_{12,mat}^2 \equiv m_{2,mat}^2 - m_{1,mat}^2 = \Delta m_{21}^2 \sqrt{\left(\frac{A}{\Delta m_{21}^2} - \cos 2\theta_{12}\right)^2 + \sin^2(2\theta_{12})} \tag{2.49}$$

and explicitly writing out the dependence on θ_{13}

$$\Delta m_{12,mat}^2 = \Delta m_{21}^2 \sqrt{\left(\frac{2\sqrt{2}G_F E N_e}{\Delta m_{21}^2}\cos^2\theta_{13} - \cos 2\theta_{12}\right)^2 + \sin^2(2\theta_{12})} \tag{2.50}$$

With the eigenvalues obtained, the rotation matrix for neutrinos in matter U_{mat} is defined by the matter mixing angle θ_{mat}. The angle θ_{mat} is given by treating the two parts of the radical in the effective mass splitting as legs of a triangle with the mass splitting as the hypotenuse. Then the tangent function is

$$\tan 2\theta_{mat} = \frac{\sin 2\theta_{12}}{\frac{A}{\Delta m_{21}^2} - \cos 2\theta_{12}}, \tag{2.51}$$

with the other trigonometric functions given as

$$\begin{aligned}\sin 2\theta_{mat} &= \frac{\sin 2\theta_{12}}{\sqrt{\left(A/\Delta m^2_{21} - \cos 2\theta_{12}\right)^2 + \sin^2(2\theta_{12})}} \\ \cos 2\theta_{mat} &= \frac{A/\Delta m^2_{21} - \cos 2\theta_{12}}{\sqrt{\left(A/\Delta m^2_{21} - \cos 2\theta_{12}\right)^2 + \sin^2(2\theta_{12})}}\end{aligned} \tag{2.52}$$

For constant electron density along the neutrino's trajectory, the transition and survival probabilities for neutrino oscillation due to matter can be written in the new matter basis, following the same arguments used for vacuum oscillations, to obtain

$$P^{2f}_{e\mu,mat} = P^{2f}_{mat}(\nu_e \to \nu_\mu) = \sin^2(2\theta_{mat}) \sin^2\left(\frac{L}{4E}\Delta m^2_{21,mat}\right), \tag{2.53}$$

$$P^{3f}_{ee,mat} = \left[1 - P^{2f}_{e\mu,mat}(\cos^2\theta_{13})\right]\cos^4\theta_{13} + \sin^4\theta_{13}. \tag{2.54}$$

When the neutrino is in vacuum, $A \to 0$, and the original parameters and probabilities for the mixing angle and the mass eigenvalues (and splitting) are recovered: $m^2_{i,mat} \to m^2_i$, $\Delta m^2_{21,mat} \to \Delta m^2_{21}$, $\theta_{mat} \to \theta_{12}$, and $P^{2f,3f}_{\alpha\beta,mat} \to P^{2f,3f}_{\alpha\beta}$. In Eq. 2.51, $\tan 2\theta_{mat}$ diverges when the denominator goes to zero, which occurs when a neutrino propagates through a critical electron density N^{crit}_e

$$N^{crit}_e \equiv \frac{\Delta m^2_{21}\cos 2\theta_{12}}{2\sqrt{2}G_F E\cos^2\theta_{13}}, \tag{2.55}$$

known as the resonance region. As neutrinos propagate through matter in the Sun and the Earth, the electron density is not constant, but is variable and large, especially in the solar core. This variable density can greatly affect neutrino oscillations, most importantly in the resonance region. In the resonance region, the oscillation amplitude of the transition probability is maximal and independent of θ_{12} (i.e. when $\sin^2(2\theta_{mat}) = 1$ in the case of constant N_e), meaning that the mass eigenstates are maximally mixed. The effect on neutrino oscillation due to solar neutrinos propagating through a resonance region in solar matter is known as the MSW effect and MSW resonance respectively. The MSW effect and resonance

is named after L. Wolfenstein, who first theorized of the effect in [33], and after S. P. Mikheyev and A. Y. Smirnov, who further refined the theory in [34].

2.3 Neutrino-Electron Elastic Scattering

Solar neutrinos interact via elastic scattering with the electrons in the water of SK [35], with electrons in the heavy water (D_2O) of the Sudbury Neutrino Observatory (SNO) detector [36], and with the electrons in the liquid scintillator in the Borexino detector [37]. Details pertaining to these detectors will be discussed in the next chapter. The neutrino-electron elastic scattering, ($\nu\ e$), is an electroweak process described by the reaction

$$\nu + e^- \rightarrow \nu + e^- \quad (\nu\ e), \tag{2.56}$$

and involves the three active neutrino flavors, ν_e, ν_μ and ν_τ. Elastic scattering can happen through neutral current (NC) interactions mediated by the neutral Z^0 gauge boson, while only the ν_e can ES through charge current (CC) interactions mediated by the charged gauge boson W^-. When discussing the axial (g_A) and vector (g_V) couplings, they will be written in forms from the predictions of the Glashow-Salam-Weinberg (GSW) model ([38][39][40] respectively).

The Lagrangian for electron-neutrino NC ES interactions in Eq. 2.34 can be re-written in terms of the axial and vector couplings as

$$\mathcal{L} = -\frac{G_F}{\sqrt{2}}[\bar{\nu}\gamma_\alpha(1-\gamma_5)\nu][\bar{e}\gamma_\alpha(g_V - g_A\gamma_5)e], \tag{2.57}$$

where

$$g_V = -\frac{1}{2} + 2\sin^2\theta_W \quad \text{and} \quad g_A = -\frac{1}{2}, \tag{2.58}$$

and where θ_W is the Weinberg angle ($\sin^2\theta_W = 0.2317$ [41]). For electron-ν_e CC ES interactions, after applying a Fierz transformation [10], the Lagrangian can be written as

$$\mathcal{L} = -\frac{G_F}{\sqrt{2}}[\bar{\nu}_e\gamma_\alpha(1-\gamma_5)\nu_e][\bar{e}\gamma_\alpha(1-\gamma_5)e]. \tag{2.59}$$

The differential cross section for (ν e) ES is then

$$\frac{\mathrm{d}\sigma}{\mathrm{d}y} = c_0 E_\nu[\Upsilon_1^2 + \Upsilon_2^2(1-y)^2 + \frac{m_e}{E_\nu}\Upsilon_3 \times y], \tag{2.60}$$

where m_e is the electron mass, and the coefficient $c_0 = G_F^2 m_e/(2\pi) = 4.31\times10^{-45}$ cm^2/MeV. The inelasticity y is the ratio between the electron kinetic energy T_e and the neutrino energy E_ν, $y \equiv T_e/E_\nu$, which has the range $0 \leq y \leq 1$. It is also useful to define two additional couplings for the (ν_e e) cross section:

$$G_V = g_V + 1 \quad \text{and} \quad G_A = g_A + 1. \tag{2.61}$$

The Υ_i parameters are different for (ν_e e) and ($\nu_{\mu,\tau}$ e) ES cross sections. This difference comes from (ν_e e) ES interactions having both NC and CC components, while ($\nu_{\mu,\tau}$ e) ES interactions only occur through NC interactions. For ν_e, they are defined as

$$\Upsilon_1 = G_V + G_A, \quad \Upsilon_2 = G_V - G_A, \text{ and } \Upsilon_3 = G_A^2 - G_V^2, \tag{2.62}$$

while for $\nu_{\mu,\tau}$, they are defined as

$$\Upsilon_1 = g_V + g_A, \quad \Upsilon_2 = g_V - g_A, \text{ and } \Upsilon_3 = g_A^2 - g_V^2. \tag{2.63}$$

For antineutrinos, the signs on the G_A and g_A terms in Υ_1 and Υ_2 can be flipped to obtain the proper ($\bar{\nu}$ e) ES cross sections.

The differential cross sections in Eq. 2.60 are modified for SK analyses to include radiative corrections from one-loop electroweak, QCD and QED processes by numerical methods, based on the work by Bahcall et al. [41]. The radiative-corrected cross sections for the case of an incident neutrino with $E_\nu = 10$ MeV is shown in the left of Fig. 2.1 for (ν_e e) elastic scattering (the solid line), and ($\nu_{\mu,\tau}$ e) elastic scattering (the dashed line). As seen in Fig. 2.2, the cross section for ($\nu_{\mu,\tau}$ e) ES (dashed line), which occurs via NC interactions only, is about a factor six smaller than that for (ν_e e) ES (solid line), since the (ν_e e) ES includes CC interactions in addition to the NC interactions. The total cross section is obtained by integrating the differential cross section from $T_e = 0$ to $T_{\max}$, where $T_{\max}$ is the limit from conservation of four momentum:

$$T_{\max} = \frac{2E_\nu^2}{2E_\nu + m_e}. \tag{2.64}$$

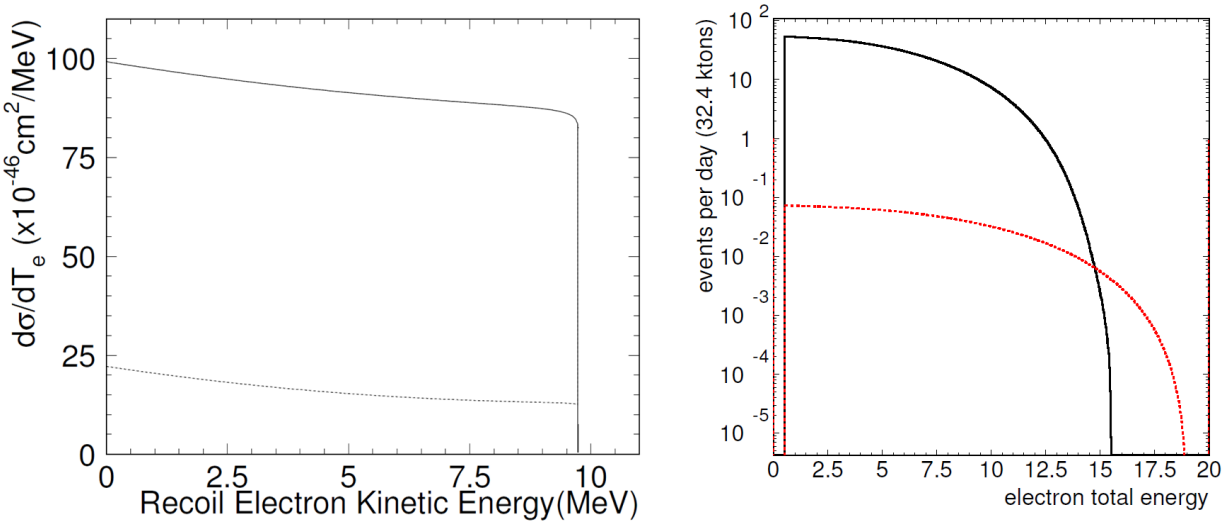

Figure 2.1: Left: The differential cross sections including radiative corrections from [41] of (ν_e e) elastic scattering (ES), solid line, and ($\nu_{\mu,\tau}$ e) ES, dashed line, for an incident neutrino energy of $E_\nu = 10$ MeV, with the x-axis being the recoil electron kinetic energy T_e [42]. Right: The expected number of (ν e) ES events per day in SK as a function of T_e due to ^{8}B (black) and *hep* (red) neutrinos [43].

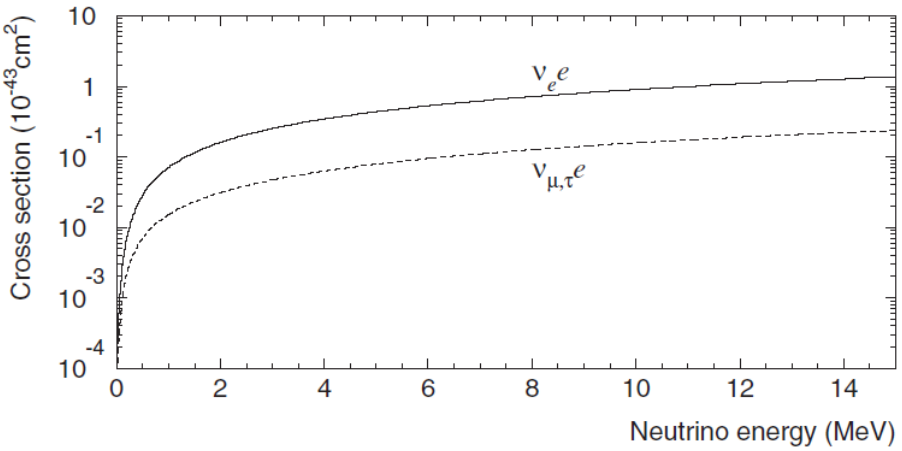

Figure 2.2: The elastic scattering cross section for (ν_e e) interaction (solid line), and for ($\nu_{\mu,\tau}$ e) interaction (dashed line) as a function of neutrino energy [44].

The energy spectrum for the recoil electrons from solar neutrinos with energy E_ν observed by SK is described by the differential equation

$$F_S(T_e)dT_e = \int_0^{E_\nu} \phi_S(E_\nu)\frac{d\sigma}{dT_e}dE_\nu dT_e, \tag{2.65}$$

where $\phi(E_\nu)$ is the solar neutrino spectrum of a given solar neutrino "species" S ($S = {}^8$B and *hep* for SK). For a given reaction in the thermonuclear fusion process in the Sun, the neutrino produced in that stage may be referred to as a "species" in this work and named after the parent particle(s) involved in the reaction. For example, the neutrino species produced in the ^{8}B decay is known as a "Boron-8 neutrino," while a neutrino produced by ^{3}He-proton fusion is known as a "*hep*" neutrino. For the neutrino produced by β capture on ^{7}Be in the *pp*-fusion chain, these neutrinos are called "Beryllium-7 neutrinos." The production mechanisms for the solar neutrinos will be discussed in Sec. 3.2. SK uses the *hep* neutrino spectrum predicted by Bachall in [41] and the ^{8}B neutrino spectrum measured by Winter et al. [45], which will be described in Sec. 3.2.1. The right side of Fig. 2.1 shows the recoil electron spectrum expected to be seen in SK using these two neutrino spectra. The total rate due to ES of incident solar neutrinos of species S is obtained by integrating the recoil electron energy spectrum in Eq. 2.65 out to infinity ($T_e \to \infty$) and multiplying by both

the flux for the species, assuming a particular Standard Solar Model (SSM) ($\Phi_S^{\rm SSM}$), and the number of targets N in a detector:

$$R_S = \Phi_S^{\rm SSM} N \int_{T_e=0}^{\infty} \int_{E_\nu=0}^{\infty} \phi_S(E_\nu) \frac{d\sigma(E_\nu)}{dT_e} dE_\nu dT_e. \tag{2.66}$$

For electrons in SK's 32.5 kton inner detector, $N = N_e = 1.086 \times 10^{34}$. For the solar neutrino fluxes predicted by the BP2004 SSM [46], the ^{8}B flux is 5.79×10^6 cm^{-2}s^{-1} and the *hep* flux is 7.88×10^3 cm^{-2}s^{-1} (see Sec. 3.2 and Table 3.2). The Sudbury Neutrino Observatory (SNO) measures a ^{8}B flux of 5.25×10^6 cm^{-2}s^{-1} via the NC interaction rate [47] (see Sec 3.3.4 and Table 3.5).

The energy spectrum described in Eq. 2.65 determines the energy distribution of the recoil electrons in the SK detector Monte Carlo simulation of ^{8}B and *hep* solar neutrinos (see Sec. 6.1). Since the angle between an incident neutrino and a recoil electron in (ν e) ES is given by

$$\cos\theta_{ES} = \frac{1 + (m_e/E_\nu)}{\sqrt{1 + 2(m_e/T_e)}}, \tag{2.67}$$

Eq. 2.65 can be modified to obtain the angular distribution of the recoil electrons:

$$F(\theta_{ES}) d\theta_{ES} = \int_0^{E_\nu} \phi(E_\nu) \frac{d\sigma}{dT_e} \frac{dT_e}{d\theta_{ES}} dE_\nu d\theta_{ES}. \tag{2.68}$$

For the solar neutrino energies SK is sensitive to, the angular distribution in Eq. 2.68 will be concentrated at zero, and the recoil electron will scatter along the same direction as the incident neutrino. However, recoil electrons undergo multiple Coulomb scattering in the water in various amounts, which has an affect on the reconstructed direction, discussed later in Sec. 6.4.1 and Sec. 7.5.

The expected distribution in the recoil angle θ_{ES} in SK based on Eq. 2.68, is shown in Fig. 2.3 for four recoil electron energies (T_e) (color, dashed lines) where the y-axis is

the events in the fiducial volume per day per degree; the solid black line is the event rate integrated over the full ^{8}B and *hep* spectra. This angular distribution is used to simulate the response of the SK detector to solar neutrinos (see Ch. 6), and as a handle for statistically selecting the solar neutrino signal from the background in the final data sample.

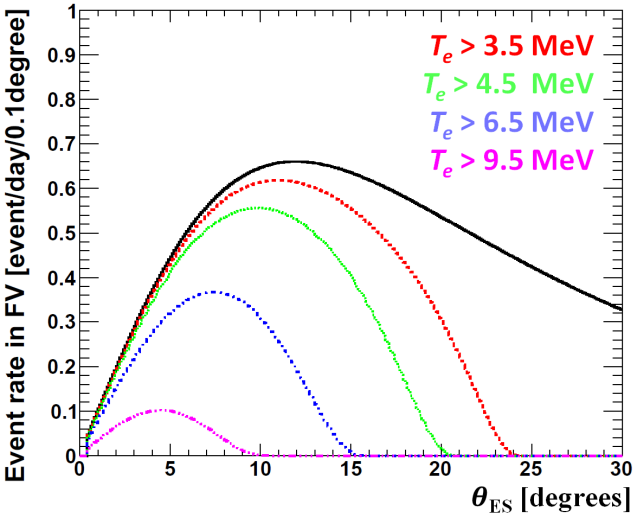

Figure 2.3: The expected distribution in the recoil angle θ_{ES} in SK based on Eq. 2.68 for four recoil electron energies (T_e) (color, dashed lines) where the y-axis is the events in the fiducial volume per day per degree [48]. The solid black line is the event rate integrated over the full ^{8}B and *hep* spectra [46].

2.4 Non-Standard Neutrino-Matter Interactions

In this section, the formalism for non-standard interactions (NSI) for neutrinos will be discussed. NSI is a generalized extension to the interactions between neutrinos and fermions in matter beyond the electroweak interactions allowed by the SM for neutrino interactions [16][17]. These interactions can be described by an effective four-fermion operator of the form

$$\mathcal{L} = -2\sqrt{2}G_F\epsilon^{f,P}_{\alpha\beta}(\bar{\nu}_\alpha\gamma^\mu\nu_\beta)(\bar{f}\gamma_\mu Pf), \tag{2.69}$$

where P is the parity operator ($P = L, R$) and the indices $\alpha, \beta = e,\ \mu,\ \tau$. The index f corresponds to the fermions within the traversed matter: electrons (e), up-quarks (u), and down-quarks (d). The chiral couplings from the standard ($\nu\ e$) ES Lagrangian in Eq. 2.57, g_L and g_R, are defined as

$$g_L = \frac{1}{2}(g_V + g_A) = -\frac{1}{2} + \sin^2\theta_W \quad \text{and} \quad g_R = \frac{1}{2}(g_V - g_A) = \sin^2\theta_W, \tag{2.70}$$

and the vector and axial couplings from Eq. 2.58 can be re-written in terms of the chiral couplings:

$$g_V = g_L + g_R \quad \text{and} \quad g_A = g_L - g_R. \tag{2.71}$$

The vector and axial couplings of the NSI parameters $\epsilon^{f\mathrm{P}}_{\alpha\beta}$ are defined in an analogous way to Eq. 2.71:

$$\epsilon^{f,V}_{\alpha\beta} = \epsilon^{f,L}_{\alpha\beta} + \epsilon^{f,R}_{\alpha\beta} \quad \text{and} \quad \epsilon^{f,A}_{\alpha\beta} = \epsilon^{f,L}_{\alpha\beta} - \epsilon^{f,R}_{\alpha\beta}. \tag{2.72}$$

As it is the vector couplings that will have an effect on the neutrino propagation and oscillations, $\epsilon^{f}_{\alpha\beta} \equiv \epsilon^{f,V}_{\alpha\beta}$, unless otherwise stated.

When the matter potential of the Hamiltonian in Eq. 2.39 is expanded to include NSI described by Eq. 2.69, it becomes

$$H^{NSI}_{mat} = \sqrt{2} G_F N_e(r) \begin{bmatrix} 1+\epsilon_{ee} & \epsilon_{e\mu} & \epsilon_{e\tau} \\ \epsilon^*_{\mu e} & \epsilon_{\mu\mu} & \epsilon_{\mu\tau} \\ \epsilon^*_{\tau e} & \epsilon^*_{\tau\mu} & \epsilon_{\tau\tau} \end{bmatrix} \tag{2.73}$$

where the diagonal (off-diagonal) terms are real (complex). These $\epsilon_{\alpha\beta}$ parameters are the sum of the contributions from each fermion-neutrino interactions scaled by Y_f, the ratio of the local fermion density N_f by the local electron density N_e:

$$\epsilon_{\alpha\beta} = \epsilon^{e}_{\alpha\beta} + \epsilon^{d}_{\alpha\beta} Y_d + \epsilon^{u}_{\alpha\beta} Y_u = \sum_{f=e,u,d} Y_f \epsilon^{f}_{\alpha\beta} \tag{2.74}$$

and

$$Y_f = \frac{N_f}{N_e}. \tag{2.75}$$

It is important to note that each NSI parameter $\epsilon^f_{\alpha\beta}$ can be allowed to take on differing values relative to one another. The $\epsilon^f_{\alpha\beta}$ can be rotated into the mass basis ϵ^f_{ij} using U_{PMNS}:

$$\epsilon^f_{ij} = \sum_{\alpha\beta} U_{i\alpha} U^*_{\beta j} \epsilon^f_{\alpha\beta}. \tag{2.76}$$

After reducing the NSI matter potential to the two-flavor approximation for solar neutrinos, the effective NSI matter potential in Eq. 2.73 becomes

$$V_{\text{NSI}} = \frac{G_F N_e}{\sqrt{2}} \begin{bmatrix} \cos^2\theta_{13} + \epsilon_{11} & \epsilon_{12} \\ \epsilon^*_{12} & -\cos^2\theta_{13} - \epsilon_{11} \end{bmatrix}, \tag{2.77}$$

which is the NSI analogue of Eq. 2.41. This notation follows the convention for the two-flavor NSI parameters ϵ_{11} and ϵ_{12} established by Friedland et al. in [16], though the three-neutrino derivation of these effective NSI parameters from the work of Gonzalez-Garcia and Maltoni [17] is used in the analysis presented in this work. The other difference between Eq. 2.77 and in [16] is the choice of conjugation for ϵ_{12}, where we follow here the choice in [17]. In this notation, the contribution from each fermion to the NSI parameter $\epsilon_{1j}, (j = 1, 2)$ is formed in the same way as in Eq. 2.78:

$$\epsilon_{1j} = \epsilon^e_{1j} + \epsilon^d_{1j} Y_d + \epsilon^u_{1j} Y_u = \sum_{f=e,u,d} Y_f \epsilon^f_{1j}, \tag{2.78}$$

where the Y_f are the same fermion-to-electron ratios defined in Eq. 2.75. The condition for the two-flavor approximation for solar neutrinos is that $\theta_{13} \ll 1$ is satisfied by the choice that $\sin^2\theta_{13} = 0.020$, the analysis bin corresponding to reactor neutrino measurements (see Sec. 2.1.2). However, a second condition arises due to the NSI that must be satisfied to use

the two-flavor NSI approximation [16][17]. This second condition is that, in the presence of NSI, $G_F \sum_f \epsilon^f_{\alpha\beta} \ll \Delta m^2_{31}/E_\nu$. In the approximation of ν_3 single mass state domination ($\Delta m^2_{31} \to \infty$), this additional condition is satisfied.

With NSI present, the effective squared mass splitting in matter $\Delta m^2_{21,mat}$ in Eq. 2.50 becomes

$$\Delta m^2_{\rm NSI} = \sqrt{\left[(A(cos^2\theta_{13} + \epsilon_{11}) - \Delta m^2_{21}\cos(2\theta_{12})\right]^2 + \left[A\epsilon_{12} + \Delta m^2_{21}\sin(2\theta_{12})\right]^2}, \quad (2.79)$$

where, here, A is defined slightly differently to remove the dependence on $\cos^2\theta_{13}$: $A = 2\sqrt{2}G_F N_e E_\nu$. Similarly, in the presence of NSI the effective mixing angle in matter θ_{mat} from Eq. 2.51 becomes

$$\tan(2\theta_{\rm NSI}) = \frac{A(\cos^2\theta_{13} + \epsilon_{11}) - \Delta m^2_{21}\cos(2\theta_{12})}{A\epsilon_{12} + \Delta m^2_{21}\sin(2\theta_{12})}. \quad (2.80)$$

Taking both $\epsilon_{11} \to 0$ and $\epsilon_{12} \to 0$ returns the squared mass splitting and the effective mixing angle back to their original forms in Eq. 2.50 and Eq. 2.51 respectively.

This characterization of the effective NSI parameters can be transformed into the notation used by Gonzalez-Garcia and Maltoni in [17] via the following equations:

$$\epsilon^f_{11} = -2\epsilon^f_{\rm D} \quad \text{and} \quad \epsilon^f_{12} = 2\epsilon^f_{\rm N}, \quad (2.81)$$

where D (N) stands for diagonal (non-diagonal), and, from their work, the full three-flavor NSI contributions to the two-flavor effective parameters $\epsilon^f_{\rm D}$ and $\epsilon^f_{\rm N}$ is given by

$$\begin{aligned}\epsilon^f_{\rm D} = -\tfrac{1}{2}\epsilon^f_{11} = c_{13}s_{13}{\rm Re}[e^{i\delta_{\rm CP}}(s_{23}\epsilon^f_{e\mu} + c_{23}\epsilon^f_{e\tau})] - (1+s^2_{13})c_{23}s_{23}{\rm Re}[\epsilon^f_{\mu\tau}] \\ -\tfrac{c^2_{13}}{2}(\epsilon^f_{ee} - \epsilon^f_{\mu\mu}) + \tfrac{s^2_{23} - s^2_{13}c^2_{23}}{2}(\epsilon^f_{\tau\tau} - \epsilon^f_{\mu\mu})\end{aligned} \quad (2.82)$$

and

$$\epsilon^f_{\rm N} = \frac{1}{2}\epsilon^f_{12} = c_{13}(c_{23}\epsilon^f_{e\mu} - s_{23}\epsilon^f_{e\tau}) + s_{13}e^{-i\delta_{\rm CP}}[s^2_{23}\epsilon^f_{\mu\tau} - c^2_{23}\epsilon^{f*}_{\mu\tau} + c_{23}s_{23}(\epsilon_{\tau\tau} - \epsilon^f_{\mu\mu})], \qquad (2.83)$$

where s_{ij} (c_{ij}) $= \sin\theta_{ij}$ ($\cos\theta_{ij}$). Taking $\theta_{13} \to 0$ and also setting the muon-related terms to zero, the equations for ϵ^f_{1j} in [16] are recovered from $\epsilon^f_{\rm N,D}$, up to the factor of ± 2 denoted in the relations in Eq. 2.81. Setting the muon-related terms to zero is motivated by experimental constraints from atmospheric neutrino data and neutrino beam data, an argument used in Friedland et al. [16], and will discussed in Ch. 11.

As for modifications to SM neutrino interactions, the NSI Lagrangian described in Eq. 2.69 leaves neutrino-nucleon CC reactions unchanged, such as the processes that produce neutrinos in the Sun [16]. This means that detectors using the same kind of neutrino-nucleon CC reactions to observe neutrinos will also remain unchanged, such as the radiochemical experiments, SNO, and KamLAND, all of which are described in the next chapter. Conversely, NC reactions are dependent on the axial current could be affected by NSI, such as those reactions measured in SNO for the ^{8}B solar neutrino flux. Also, the extra coupling of all neutrino flavors with electrons, the $\epsilon^e_{\alpha\beta}$ term can modify the (ν e) ES cross sections and affect the (ν e) ES rates one would expect to observe in the water of SK or in the heavy water (D_2O) in SNO.

Because of these possible effects on the ES rates in SK and SNO, as well as on the NC interaction rate in SNO, two assumptions are made about the NSI parameters so that the data from these experiments can be used for the analysis presented in this work. Specifically, the first assumption is that all electron-related NSI terms are set to zero: i.e. $\epsilon^{e,L}_{\alpha\beta} = \epsilon^{e,R}_{\alpha\beta} = 0$, so that the ($\nu$ e) cross sections and the ES rate in SK (and SNO) remain unaffected. The second assumption is that only the vector component of the NSI parameters can be extracted from the effective parameters ϵ^f_{11} and ϵ^f_{12} tested in this analysis (i.e. $\epsilon^{f,A}_{\alpha\beta} = 0$), which is the

same procedure used in [17]. Further details on why these assumptions are necessary will be described in Ch. 11, as will current constraints to $\epsilon^f_{\alpha\beta}$ from experiments.

While the reduction of the parameter space to only two additional sets of effective NSI parameters ϵ^f_{11} and ϵ^f_{12} ($f = u, d$) simplifies things somewhat, this still amounts to a total of four additional parameters on top of the three from the PMNS matrix (and the neutrino energy) when determining the different neutrino oscillation probabilities:

$$P(\theta_{13}, \theta_{12}, \Delta m^2_{21}/E_\nu, \epsilon^d_{11}, \epsilon^d_{12}, \epsilon^u_{11}, \epsilon^u_{12}). \tag{2.84}$$

To test the NSI experimentally, only the effect from one quark in matter on the neutrino wavefunction and resulting oscillations will be considered at a time. That is, only NSI interactions between solar neutrinos and u-quarks (d-quarks) are considered so that the other interaction is turned off, i.e. $\epsilon^d_{1j} = 0$ ($\epsilon^u_{1j} = 0$).

Chapter 3

Solar Neutrinos

Neutrinos are produced in the core of stars during the fusion of four protons into a ^{4}He nucleus (an α particle), two ν_es, and two positrons

$$4p \rightarrow {}^4\mathrm{He} + 2e^+ + 2\nu_e. \tag{3.1}$$

The daughter positrons annihilate with electrons in the solar plasma, yielding photons (γs) that carry away the rest of the energy in the fusion reaction. The net release of energy Q from this process is

$$Q = 4m_p - m_{^4\mathrm{He}} + 2m_e = 26.73 \text{ MeV}. \tag{3.2}$$

The neutrinos created from this thermonuclear fusion process in the Sun are the only way to study the chemical composition and the processes that govern the mechanisms for energy production in the Sun's core.

This process occurs in the majority of stars through the Carbon-Nitrogen-Oxygen (CNO) fusion chain, first described by C. F. von Weizsächer in 1937 [49] and 1938 [50], and later developed independently by Hans Bethe in 1939 [51]. Based on Bethe's work in [51],

another possible way this process can occur in the Sun is via initial fusion by sets of proton pairs, known as *pp*-fusion, since the Sun is of lower than average stellar mass. Based on current knowledge, the *pp* chain (Fig. 3.4) produces 98.4% of the solar luminosity, with the CNO cycle (Fig. 3.5) making up the remaining luminosity [51]. These processes will be discussed in Sec. 3.2.

3.1 The Standard Solar Model and Neutrino Production in the Sun

Before discussing neutrino production in the Sun, it is useful to discuss Standard Solar Models (SSMs). SSMs are constructed to replicate measurements of the Sun's current radius and mass, as well the surface luminosity, spectroscopy, and temperature, based on using fundamental knowledge from thermodynamics and nuclear and particle physics in conjunction with the process described in Eq. 3.1 [52][53].

The assumptions that are used when constructing the SSMs include:

- Helium production from hydrogen fusion (Eq. 3.1) via the *pp*-fusion chain (98%) and with a small contribution from the CNO-cycle (2%).
- A spherical sun
- Quasi-static evolution in hydrodynamic equilibrium taking place over 4.6 billion years
- Thermal equilibrium
- When entering the main sequence, the sun was highly convective and had a uniform composition
- Reproduce the current state of the Sun

The quasi-static evolution requires the inward attraction of gravity to be balanced out by the radiation pressure (hydrodynamic equilibrium), which requires the equation of state to be a function of temperature, density, and isotopic chemical composition. The thermal equilibrium requires that the energy output from the luminosity corresponds to the rate of energy that is generated from the fusion processes, and that radiation and convection processes transport energy through the Sun [10]. In the equation of state, the ratio of initial ^{4}He/H is tuned to reproduce the present day measurements. Additionally, the oscillations of the Sun's surface and shape (helioseismology) are used to test the description of the solar core predicted by SSMs [54].

Since SSMs attempt to accurately model the behavior of the solar core, they predict the rates and locations of nuclear processes that produce solar neutrinos, and, consequently, predict the relative amount of neutrino production at those locations and the resulting total flux for each solar neutrino species. The production mechanisms for the solar neutrinos will be discussed in Sec. 3.2. Each SSM predicts as a function of the solar radius ($r = R/R_{\text{Sun}}$) the isotopic chemical abundances, fraction of neutrino species production, and electron density, as well as other important parameters (matter density, temperature, pressure, etc.).

Using measurements from solar neutrino experiments and adhering to a specific neutrino theory or model, the predictions of a given SSM can be tested to ascertain its accuracy, or conversely, assuming the validity of a specific SSM, a neutrino theory can be investigated. To test the strength of NSI between solar matter and solar neutrinos, the validity of the BP2004 SSM developed in 2004 by John N. Bahcall and Marc H. Pinsonneault [46] will be assumed (tables from Bahcall's website [55]). The temperature (matter density) radial profile derived from BP2004 is shown on the left (right) in Fig 3.1.

The electron density profile drives the matter effects to the neutrino oscillations in the MSW resonance region of critical electron density (for given oscillation parameters). The density in the Sun's core is approximately 100 times that of water. For reference, the Earth's

solid inner core is ∼10 times that of water. Because of the large pathlengths solar neutrinos may take through the high density environment in the solar core, this environment makes an excellent place to test the effects that matter may impose on neutrino oscillations. As the majority of higher energy solar neutrinos are produced in the high densities of the solar core, the adiabatic transition of high electron density in the solar core to the lower density farther out in the Sun causes adiabatic flavor conversion for solar neutrinos, which is the MSW effect referred to earlier. The MSW effect leads to a suppression of the P_{ee} for higher energy ^{8}B (and *hep*) solar neutrinos compared to the P_{ee} expected by vacuum-dominated oscillations, especially in the Large Mixing Angle (LMA) solution of the $U_{\rm PMNS}$ parameter space associated with solar neutrinos. While all solar neutrinos are created purely in the ν_e flavor eigenstate by the CC fusion processes in the Sun, most ^{8}B and *hep* neutrinos are produced in the ν_2 mass eigenstate. Most ^{8}B and *hep* neutrinos also leave the Sun in the ν_2 mass eigenstate.

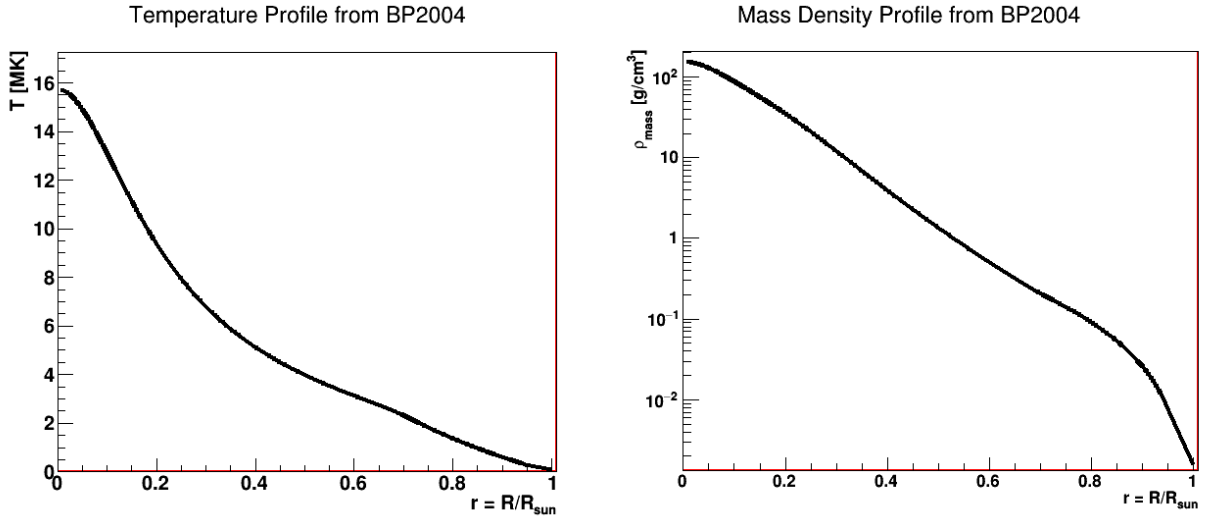

Figure 3.1: The temperature (left) and mass density (right) profiles as a function of $r = R/R_\odot$ in the BP2004 SSM [55].

The prediction by the BP2004 SSM of the distribution of isotopes in the Sun (by mass fraction X_i) as a function of r is illustrated in Fig 3.2, as well as the integrated mass profile (the integral of the mass within radius r divided by the total solar mass $M_{\rm Sun}$). The electron

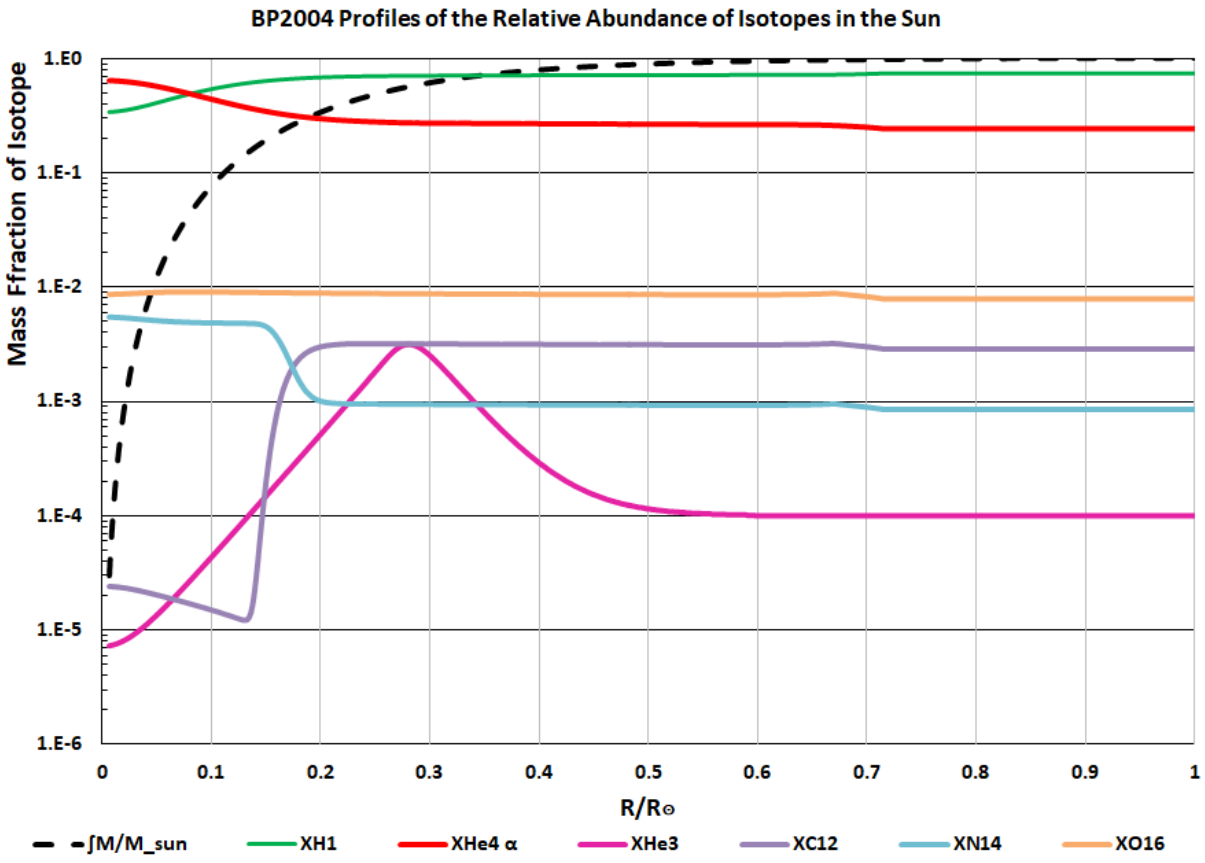

Figure 3.2: The mass fractions X_i from the BP2004 SSM for each isotope i as a function of $r = R/R_\odot$. The y-axis values for the solid colored lines are the fractions each isotope contributes to the mass shell at r, and the dashed black line represents the fractional integrated mass of the Sun $\int_0^r M/M_\odot$ up to r [55].

number density N_e is derived from the local mass fractions $X_i(r)$ of an isotope i and matter density $\rho_m(r)$ for the spherical shell defined by the radial bin r, and is given by the equation:

$$N_e(r) = N_A \rho_m(r) \sum_i X_i(r) \frac{Z_i}{A_i} \tag{3.3}$$

where Z_i (A_i) is the atomic number (atomic weight) for a given isotope and i runs over the isotopes relevant in the Sun which are listed in Table 3.1. The radial profiles for the number density for down quarks (d) and up quarks (u), $N_d(r)$ and $N_u(r)$ respectively, are derived in a similar fashion to $N_e(r)$ and are important when introducing NSI effects to solar neutrino oscillations:

$$N_q(r) = N_A \rho_m(r) \sum_i n_i^q X_i(r) \frac{Z_i}{A_i} \tag{3.4}$$

where q = d, u, n_i^q is the number of q-quarks for a given isotope i found in Table 3.1. The left plot in Fig 3.3 shows the radial profile for electron number density $N_e[\mathrm{MeV}^{-3}]$, while the right plot in the same figure shows the ratios of the quark-to-electron number densities in (solid colored lines) and the up-to-down quark ratio (dotted line) as a function of r.

Table 3.1: Information for Isotopes Used in the BP2004 SSM. The parameters Z (A) correspond to the Atomic Number (Weight) of the isotope. The number of up (down) quarks n^u (n^d) per isotope are given as well, relevant for NSI. Color corresponds to Fig. 3.2.

Isotope	Z	A	Z/A	n^u	n^d	Color
^{1}H	1	1.0078	0.9922	2	1	Green
^{3}He	3	3.0160	0.6631	5	4	Magenta
^{4}He	4	4.0026	0.4997	6	6	Red
^{12}C	12	12.0	0.5	18	18	Purple
^{14}N	14	14.0031	0.4999	21	21	Teal
^{16}O	16	15.9949	0.5002	24	24	Orange

Other SSMs, including some newer models, were investigated in the context of neutrino oscillations due to non-zero neutrino mass and no NSI, to determine the impact the solar model has on the NSI and standard Super-Kamiokande Solar Neutrino Oscillation analyses.

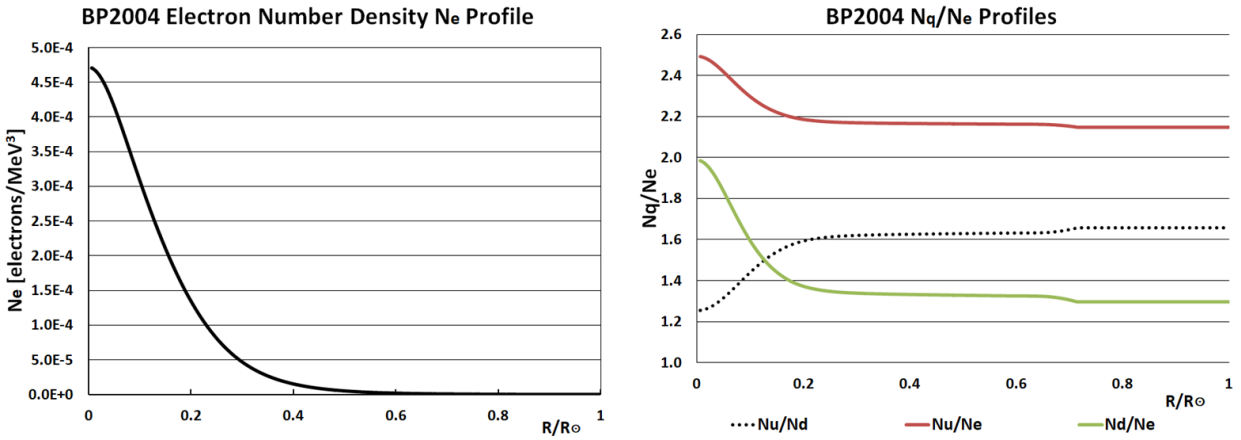

Figure 3.3: The electron and quark density profiles derived from the matter density and isotopic mass fractions (X_i) given in the BP2004 SSM tables available in [55]. Left: The electron number density profile N_e derived from Eq. 3.3. Right: The ratio of the number density of d-quarks N_d (green) and u-quarks N_u (red) to the electron number density N_e as a function of r; the dotted line is the radial profile of N_u/N_d.

However, since the SNO neutral current measurement is used as a constraint, the difference in the one, two, and three σ included regions of the $(\sin^2\theta_{12}, \Delta m^2_{21})$ parameter space (for the no-NSI case) are not affected.

3.1.1 The Solar Neutrino Problem

The original solar models by Bahcall in 1964 [56] and by Kuzmin and Zatsepin in 1965 [52] were designed to use neutrino spectroscopy to understand the core of the Sun. Soon after, Ray Davis Jr. led a team to measure the solar neutrino flux with the Homestake Experiment and compared their results to Bahcall's solar model. It was found that the predicted flux was three times larger than what was seen in Homestake [7]. This discrepancy became what is known as the Solar Neutrino Problem.

Davis' group led a campaign to determine where their knowledge of their detector was lacking, and to better understand the experiment's efficiencies. However, this endeavor by Davis' group did not resolve the discrepancy between the flux predictions and measurements.

Meanwhile, the theorists worked on cross-checking the SSM. It was found that the neutrino flux dependence in the SSM on the temperature and pressure profile was not correct, though fixing it did not resolve the discrepancy either [54].

As time moved on, various other experiments with differing detection media, energy thresholds, and systematics were conducted to resolve this problem (see Sec 3.3). However, the correlations between the fluxes of different solar neutrino species from the SSMs complicates the picture further. It was found that, for the lower energy neutrinos with $E_\nu \lesssim 1$ MeV (namely the *pp* neutrinos), the flux agreed better with the SSM predictions [10], although the measurements of the ^{7}Be solar neutrino flux was nearly zero at the time ($\Phi_{^7\mathrm{Be}} \simeq 0$) [54]. However, for the ^{8}B neutrinos, the discrepancy became larger. Rectifying the ratio of the $\Phi_{^7\mathrm{Be}}/\Phi_{^8\mathrm{B}}$ solar neutrino fluxes by adjusting parameters in the SSMs had the effect of increasing the ratio, as opposed to decreasing the ratio to near zero [54].

This implied that the problem lay not so much with variations in the solar models, but with some assumption of the particle physics for neutrinos. Specifically, the problem pointed to an energy-dependent effect on the fluxes, which non-zero neutrino masses could solve. Eventually, in the 21st century, the Borexino experiment measured the ^{7}Be solar neutrino flux and found it to be in agreement with the predictions from the SSMs (Sec. 3.3.5).

3.2 Neutrino Production in the Sun

The elemental composition of the Sun determines the percentage of the luminosity produced by either the *pp* or CNO branch of the solar fusion process. If the number of heavier elements (the metalicity) is larger, as it is in the case of more massive stars, the contribution from the CNO cycle will also be larger. Likewise, the production rate of each neutrino species

will follow the rate of the thermonuclear process which creates that specific neutrino species. Since the *pp*-chain dominates in the Sun, the neutrinos it produces dominate the total flux, while the CNO neutrinos are produced at a significantly reduced rate. Table 3.2 summarizes the labels, reactions, end-point or mono-energy, and the expected flux at Earth for each neutrino species.

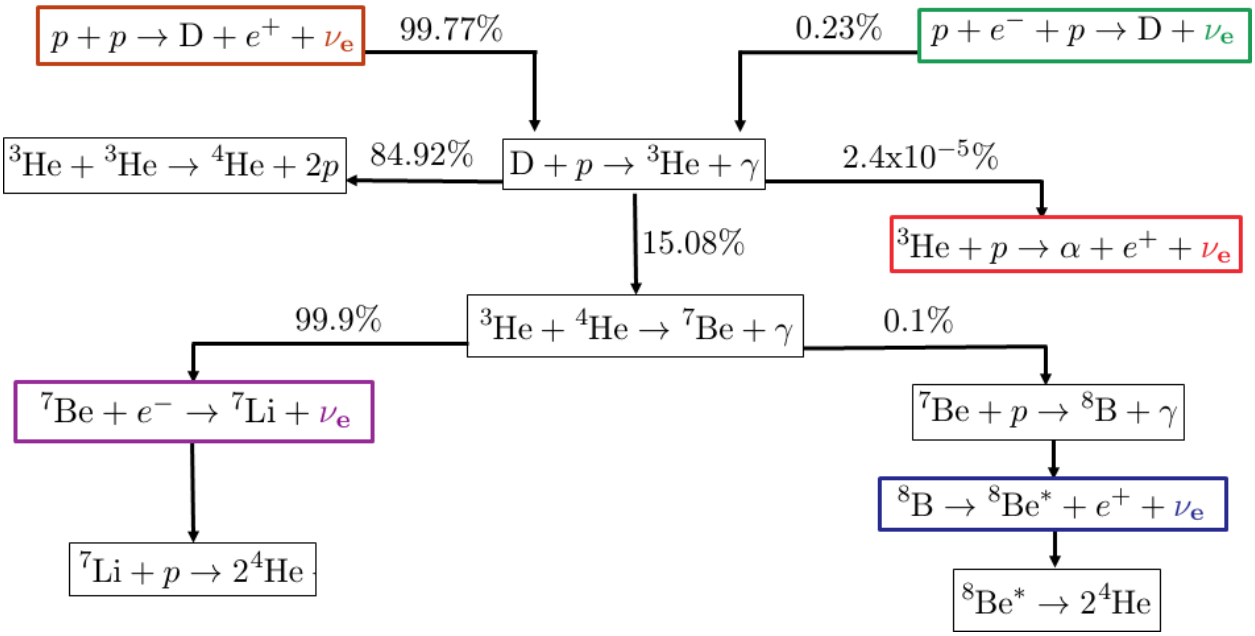

Figure 3.4: The proton-proton (*pp*) fusion chain, which produces about 98.4% of the energy in the Sun. The reactions that produce neutrinos are colored and correspond to Table 3.2

The neutrino production is very sensitive to the temperature profile of the Sun (i.e. how the temperature changes as a function of r) because the temperature drives the nuclear reactions, as well as the pressure and density profiles, which determine what neutrino species (if any) are produced. If the temperature drops too low, the rate of fusion processes slows down and eventually stops. The low neutrino production in the center of the Sun is due to the small amount of material within the shell, and therefore we see a drop-off of neutrino production reflected in Fig 3.6. This figure shows the fraction of neutrino flux production within the spherical shell with radius r for each species in the *pp*-chain [55].

The width of each curve in Fig 3.6 shows the strength of the temperature dependence.

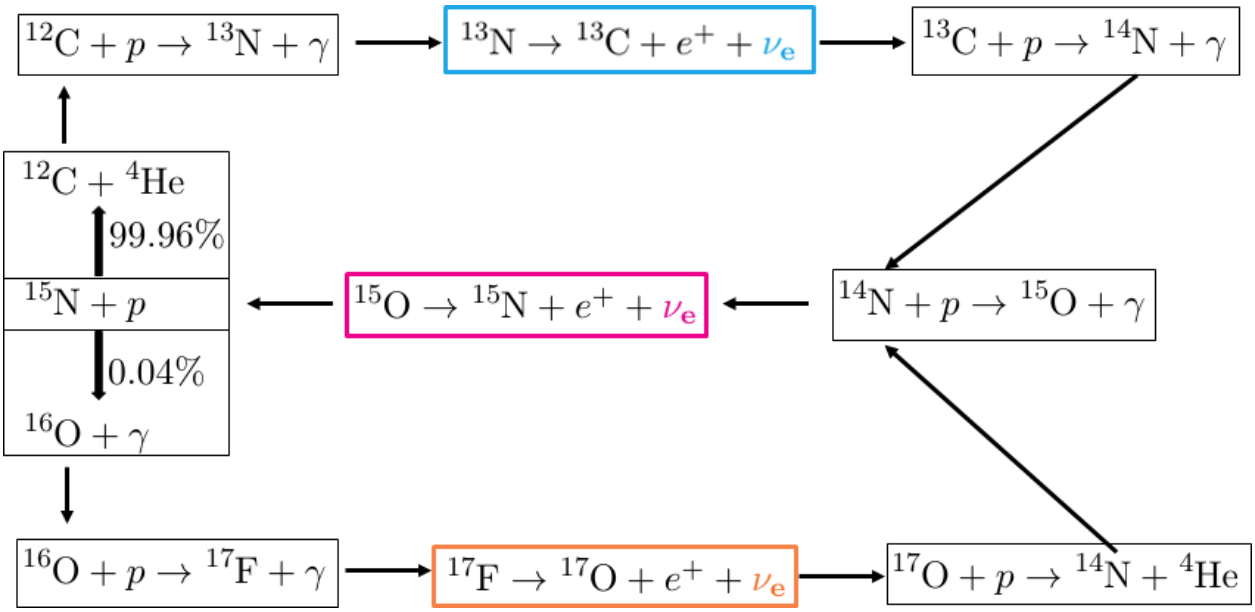

Figure 3.5: The Carbon-Nitrogen-Oxygen (CNO) fusion cycle in stars. The CNO fusion cycle is important for higher mass stars, but only accounts for 1.6% of the energy production in the Sun. The reactions that produce neutrinos are colored and correspond to Table 3.2.

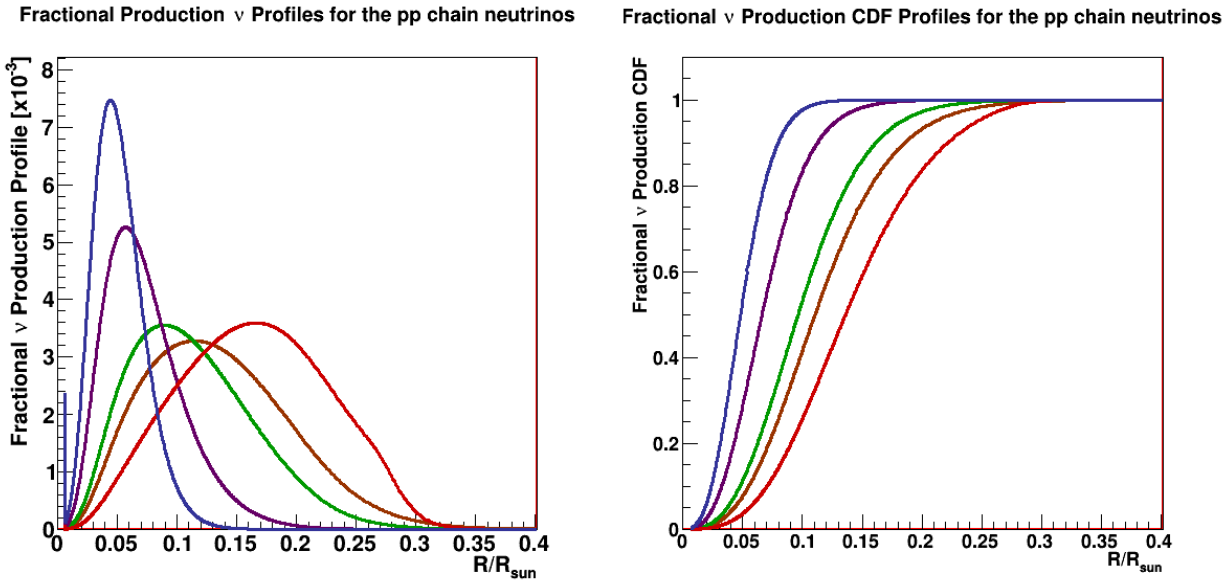

Figure 3.6: The relative flux fraction profiles for each spherical shell of radius r predicted by the BP2004 SSM [55] for the *pp*-chain neutrino species. The color corresponds to Table 3.2, where *pp* (brown), *pep* (green), ^{7}Be (purple), ^{8}B (blue) and *hep* (red) are all shown in this figure.

Table 3.2: The *pp* and CNO reactions, the neutrino species produced, their mono-energetic or endpoint energies E_ν [10], and predicted flux from BP2004 [46]. The last column is the reference color related to Fig. 3.4, Fig. 3.5, and Fig. 3.6.

ν_e Species	Reaction	mono/endpoint E_ν [MeV]	Flux [$\mathrm{cm^{-2}s^{-1}}$]	Reference Color
pp Chain				Fig. 3.4
pp	$p + p \rightarrow \mathrm{D} + e^+ + \nu_e$	≤ 0.42	$5.94(1\pm0.01)\mathrm{x}10^{10}$	Brown
pep	$p + e^- + p \rightarrow \mathrm{D} + \nu_e$	$= 1.442$	$1.40(1 \pm 0.02)\mathrm{x}10^{8}$	Green
^{7}Be	$^7\mathrm{Be} + e^- \rightarrow {}^7\mathrm{Li} + \nu_e$	$= 0.862,\ 0.384$	$4.86(1 \pm 0.12)\mathrm{x}10^{9}$	Purple
^{8}B	$^8\mathrm{B} \rightarrow {}^8\mathrm{Be}^* + e^+ + \nu_e$	≤ 14.06	$5.79(1 \pm 0.23)\mathrm{x}10^{6}$	Blue
hep	$^3\mathrm{He} + p \rightarrow \alpha + e^+ + \nu_e$	≤ 18.77	$7.88(1 \pm 0.16)\mathrm{x}10^{3}$	Red
CNO Cycle				Fig. 3.5
^{13}N	$^{13}\mathrm{N} \rightarrow {}^{13}\mathrm{C} + e^+ + \nu_e$	≤ 1.27	$5.71(1^{+0.37}_{-0.35})\mathrm{x}10^{8}$	Cyan
^{15}O	$^{15}\mathrm{O} \rightarrow {}^{15}\mathrm{N} + e^+ + \nu_e$	≤ 1.73	$5.03(1^{+0.43}_{-0.39})\mathrm{x}10^{8}$	Magenta
^{17}F	$^{17}\mathrm{F} \rightarrow {}^{17}\mathrm{O} + e^+ + \nu_e$	≤ 1.74	$5.91(1 \pm 0.44)\mathrm{x}10^{6}$	Orange

The radial window defined by the curves and therefore the production zones of the neutrino species directly corresponds to the temperature over which the reactions can occur to produce neutrinos. The ^{8}B neutrinos (as well as ^{7}Be neutrinos) are especially sensitive to the temperature profile, and to the corresponding density profiles of ^{4}He, ^{3}He in the Sun, given as the width of the zone is very narrow.

3.2.1 Solar Neutrino Energy Spectrum

The resulting energy spectrum for the solar neutrino fluxes seen at Earth for each of the different solar neutrino species is shown in in Fig. 3.7, which is derived from a later SSM by Bahcall and A. M. Serenelli, the BS2005 OPAL Opacity Project SSM (BS05 OP or BS2005 OP)[57] .

In Super-Kamiokande, the ^{8}B neutrinos dominate the solar neutrino signal, with a less significant contribution by *hep* neutrinos. These are the only solar neutrino species who have endpoint energies high enough to produce a signal above the energy threshold for the

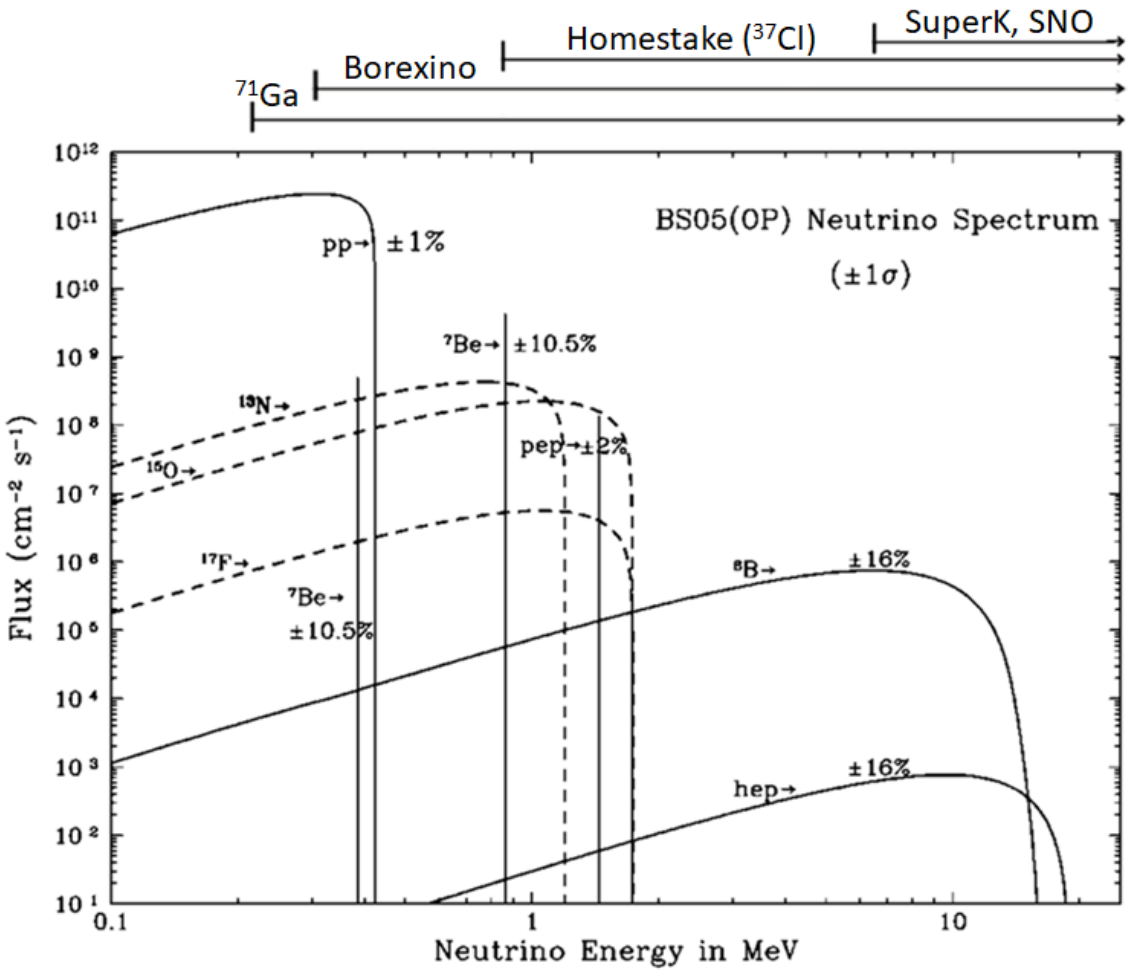

Figure 3.7: The Energy Spectrum for Solar Neutrino Fluxes from the BS2005 OP SSM (Figure 2 in [57]), with the neutrino energy range for the solar neutrino experiments shown above.

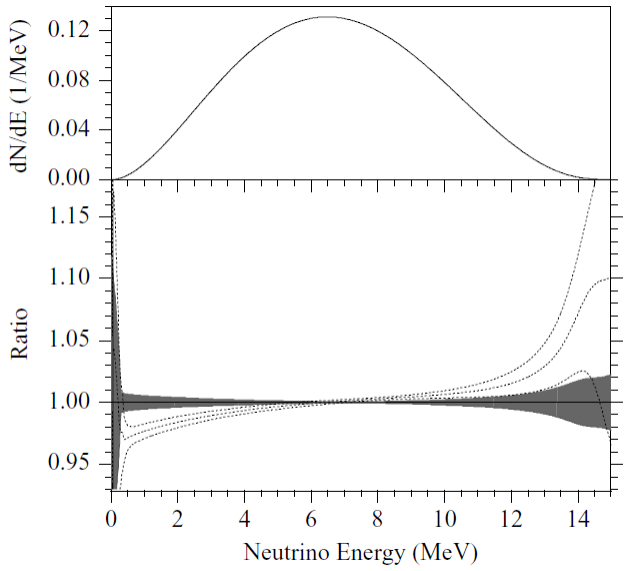

Figure 3.8: Top Panel: The Winter06 ^{8}B normalized neutrino energy spectrum. Bottom Panel: The ratio between the Winter06 spectrum and the measurement by Ortiz et al. [58] with $\pm 1\sigma$ experimental uncertainty (dashed lines) and the $\pm 1\sigma$ experimental uncertainty of the Winter06 spectrum (dark gray band) [45].

detector (Sec. 3.3.7, Ch. 6, and Ch. 8 through Ch. 10). Similarly, the ^{8}B neutrinos are the primary signal in the Sudbury Neutrino Observatory (SNO). To understand the spectrum for this solar neutrino species, W. T. Winter, S. J. Freedman, K. E. Rehm, and J. P. Schiffer [45] measured the broad α energy spectra resulting from the ^{8}B decay to the unstable excited state ^{8}Be*, and its subsequent de-excitation to two α particles, a method pioneered by J. Napolitano, S. J. Freedman and J. Camp [59]. While doing this, Winter et al. simultaneously measured the β^+ energy spectrum to accurately predict the ^{8}B neutrino spectrum. This ^{8}B neutrino spectrum will be referred to by the label "Winter06 spectrum," which is plotted in the top panel of Fig. 3.8. The bottom panel shows the ratio between the Winter06 spectrum and the α spectrum measurement of ^{8}B decay performed by Ortiz et al. in [58]. The figure also displays the $\pm 1\sigma$ experimental uncertainty of the Winter06 (Ortiz) spectrum as a dark gray band (as dashed lines).

The Winter06 spectrum is adopted in the Super-Kamiokande (SK) solar neutrino analysis and in this analysis as the predicted spectrum for ^{8}B solar neutrinos. For the *hep* solar

neutrino spectrum, the prediction by J. N. Bahcall et al. [41] is used.

3.3 Solar Neutrino Experiments

Experiments designed to detect solar neutrinos usually fall into two different categories, radiochemical and real-time experiments. Both types of experiments have their strengths and drawbacks, and have differing sensitivities to the various solar neutrino species. Radiochemical experiments include the Davis Homestake Experiment, which used ^{37}Cl in cleaning fluid as the target, and the Gallium experiments GALLEX/GNO and SAGE. The real-time experiments include Kamiokande, SK, SNO, and Borexino. Each experiment will be discussed here, though a detailed discussion of SK will begin after this chapter.

Solar neutrino radiochemical experiments count the number of daughter isotopes produced through neutrino capture on the parent nuclei via CC processes. These daughter isotopes could be unstable, but must be long enough lived to survive extraction from the parent bulk material to be counted via their subsequent decay. The total rate of production of the unstable daughters is the product of the number of parent atoms in the bulk material with the energy integral of the neutrino flux and the neutrino cross section on the parent isotope. The drawback to this method is that only the time-averaged flux due to the measured production rate of the daughter isotopes can be determined. One benefit is that the radiochemical experiments are sensitive to the lower energy solar neutrinos, and can have, in general, lower energy thresholds than real-time experiments (prior to Borexino). A second benefit is that the radiochemical experiments have powerful background reduction techniques.

The measurements by real-time experiments record the time, energy, and direction of the neutrino interaction in the detection medium. The real-time experiments based on water

or heavy water look for the Cherenkov light created by electrons moving at super-luminal speeds in the detector medium or for de-excitation gammas from downstream processes. In water (SK) and heavy water (SNO), the incident neutrino can elastically scatter (ES) off an electron causing the electron to recoil. If the velocity of the recoil electron is high enough that it is super-luminal, it is above Cherenkov threshold and emits Cherenkov light until it slows down to sub-luminal speeds relative to the index of refraction in the water (or heavy water). In heavy water, the neutrino can also either break up the deuterium through a CC or a NC process producing an electron, or it can scatter via the NC process. The real-time experiments SK and SNO are sensitive to the higher energy solar neutrino species, ^{8}B and *hep*, as the energy threshold is higher for these experiments. The ^{8}B flux is very low and the *hep* rate is much lower when compared to the other solar neutrino species. SK and SNO must be scaled to the kiloton range or larger to measure these high energy solar neutrinos. The size of a detector depends on the neutrino cross sections relative to interactions with the detection medium. The other real-time experiment Borexino, on the other hand, looks instead at scintillation light from the elastic scattered events in liquid scintillator, which lowers the energy threshold for detecting solar neutrinos while losing the directional information.

3.3.1 The Davis Homestake Experiment

The Chlorine experiment by Ray Davis Jr. [60][7] ran from 1968 to 1994 in the Homestake gold mine located in South Dakota. This mine provided the experiment an overburden equivalent to having of 4100 meters of water above it (meter water equivelent or mwe), shielding it from the majority of cosmic rays. The detector was filled with 615 tons of the cleaning fluid perchloro-ethylene (C_2Cl_4), specifically having the target of ^{37}Cl which has a natural abundance of ∼24%. Neutrinos interact with the target ^{37}Cl and produce ^{37}Ar via the reaction $^{37}\mathrm{Cl} + \nu \rightarrow {}^{37}\mathrm{Ar} + e^-$. The energy threshold for this reaction (and the

experiment) is 0.814 MeV, which is above the *pp* neutrino detection threshold.

To extract the ^{37}Ar from the C_2Cl_4 bulk, helium was bubbled through the cleaning fluid approximately every nine to ten weeks. Then the argon was collected in cold charcoal traps and further purified. After purification, the argon was injected into proportional counters which were placed into low activity lead shielding to perform the counting experiment of argon decays. Detection of ^{37}Ar, which has a half-life of 35 days, occurs by looking for a 2.82 keV γ or an Auger electron with the proportional counters, either of which is emitted from the atom as it decays back to chlorine: $^{37}\mathrm{Ar} \rightarrow {}^{37}\mathrm{Cl} + \nu_e + e^-$. Both the energy and pulse shape information acquired by the proportional counters were used to further reduce any remaining background [10].

The final result [7] from the Homestake's data set spanning more than twenty years is

$$2.56 \pm 0.16(\mathrm{stat}) \pm 0.15(\mathrm{sys})\ \mathrm{SNU} \tag{3.5}$$

where

$$1\ \mathrm{SNU} = 10^{-36}\ \text{captures per target atom per second.} \tag{3.6}$$

Homestake's measurement of the solar flux disagreed with Bahcall's SSMs, consistently measuring a third of the SSMs' predicted rate, and started the issue of the Solar Neutrino Problem described earlier.

3.3.2 Kamiokande

The Kamioka Nucleon Decay Experiment (KamiokaNDE), the predecessor to Super-Kamiokande, was located within the same mine as SK and also had a 1000 mwe overburden from the mountain. The Kamiokande experiment was a 3-kton water Cherenkov detector employing 948 twenty-inch (50 cm) photomultiplier tubes (PMTs), which gave the detector

a photocathode coverage of 20% and allowed for efficient detection of Cherenkov light. The first run of Kamiokande had large backgrounds at low energies due to radon within the water sourced from within the mine, as well as gamma rays coming from the rock surrounding the cylindrical tank. This background swamped any solar signal, as the endpoint of the background is tens of MeV, above the endpoint energies of solar neutrinos. Additionally, Kamiokande-I had no timestamps for its events, so it would not be able to correlate the direction of the Sun relative to any ES recoil electron events it would record.

Several upgrades between the experiment's first and second phase (Kamiokande-II [61]) were implemented to allow for the detection of solar neutrinos. To combat the radon background coming from the water, a water purification system was constructed to clean and recirculate water from the tank to keep the water transparent and remove radioactive contaminants like uranium, radium, and radon. After the radon from the initial filling of the detector with the mine water decayed away, the only significant source of radon diffusing into the water would be from the air above the tank or the rock surrounding it. New electronics assigned timestamps to events and had improved timing. This yielded better time resolution for events and allowing researchers to better distinguish between events in the detector. Additionally, an instrumented 1.5 m veto layer was introduced, allowing additional shielding from and a veto tag for the background gamma rays. Kamiokande-II ran from November 1985 to April 1990, with a live time, i.e. the total amount of time the detector was "live" and collecting data, of 1043 days. The experiment had an initial threshold of 9.3 MeV, which was reduced to 7.5 MeV following a campaign of increasing the gain on the PMTs.

For their solar neutrino analysis, the experiment looked for Cherenkov light produced by the electrons recoiling from the ES of neutrinos within the inner 680-ton fiducial volume. The ES reaction

$$\nu_f + e^- \to \nu_f + e^- \quad \text{where} \quad f = e, \mu, \tau \quad \text{(ES)} \tag{3.7}$$

and its cross sections are described in Sec. 2.3. This reaction does not have a lower energy

threshold. However, the recoil electrons must have enough energy not only to produce Cherenkov light, but to produce enough light that will make it to enough of the PMTs in order to reconstruct the event. The recoil electron direction and the incident neutrino direction are highly correlated, and the electron will recoil away from the incoming neutrino. With these upgrades, Kamiokande was able to detect electrons recoiling away from the direction of the Sun in real time, showing clear evidence that the Sun does indeed produce neutrinos, specifically ^{8}B ν_es.

In 1990, Kamiokande underwent an additional upgrade for its third phase (Kamiokande-III [62]), where newer electronics were once again installed. Additionally, an aluminized plastic cone was placed around each inner detector PMT to increase light collection and increase the coverage of the detector to 25%. All of the PMTs that had died during the course of the experiment up to this point were also replaced. Kamiokande-III had an analysis threshold of 7.5 MeV and ran until February 1995, with a live time of 1036 days.

Table 3.3: Measurements reported by the Kamiokande Collaboration [63] of the average ^{8}B flux in terms of the ratio between measurement and theory ($\frac{Data}{SSM}$) and the measured flux. The theoretical flux is the prediction from an SSM assuming no neutrino oscillations. The live time for each phase is given as well.

Experimental Phase	$\frac{Data}{SSM} \pm \text{stat} \pm \text{sys}$	Flux $\pm$(Stat)$\pm$(Sys) $\times 10^6$ [cm^{-2}s^{-1}]	Live Time [days]
Kamiokande-II	$0.46 \pm 0.05 \pm 0.06$	$2.67 \pm 0.29 \pm 0.35$	1043
Kamiokande-III	$0.496^{+0.044}_{-0.042} \pm 0.048$	$2.82^{+0.25}_{-0.24} \pm 0.27$	1036
Combined	$0.492^{+0.034}_{-0.033} \pm 0.058$	$2.80 \pm 0.19 \pm 0.33$	2079

The final results reported by Kamiokande [63] after Kamiokande-III concluded are in the form of a ratio between the measured flux from the data divided by the theoretical flux from the SSM, all averaged over the recoil electron energy: $\frac{Data}{SSM}$, where the SSM ^{8}B flux assumes no neutrino oscillations. For Kamiokande-II, the SSM flux value $\phi_\nu^{\text{SSM}}(^8\text{B}) = 5.8 \times 10^6$ cm^{-2}s^{-2} from the J. N. Bahcall and R. K. Ulrich SSM [64] is used, while Kamiokande-III uses the SSM flux value $\phi_\nu^{\text{SSM}}(^8\text{B}) = 5.7 \times 10^6$ cm^{-2}s^{-2} from the J. N. Bahcall and M.

H. Pinsonneault SSM [65]. The final results from Kamiokande-II and Kamiokande-III are consistent and are summarized in table Table 3.3.

Interestingly, measurements performed by the first half of Kamiokande-II overlapped with measurements performed by the Homestake experiment from August 1986 to March 1988, which meant that the flux measurements by the two were directly comparable as they were measuring the "same" Sun, i.e. the instantaneous state of the Sun was the same for both experiments. Homestake measured a flux of 4.2 ± 0.7 SNU, which is consistent with the Kamiokande-II measurement from the this period. This deepened the Solar Neutrino Problem even though the ^{8}B neutrinos had a deficit of around one-half instead of one-third [61].

3.3.3 The ^{71}Ga Experiments: GALLEX/GNO and SAGE

The Gallium experiments all have similar technology and methodology [10]. The bulk target material for the solar neutrinos is a gallium doped compound or solution. The specific reaction for solar neutrinos is the CC-mediated transmutation of ^{37}Ga, which has a relative abundance of 39.9%, into ^{71}Ge via inverse beta decay:

$$^{71}\mathrm{Ga} + \nu_e \rightarrow {}^{71}\mathrm{Ge} + e^-, \quad E_{\mathrm{threshold}} = 233 \text{ keV}. \tag{3.8}$$

Similar to the Homestake experiment, the unstable ^{71}Ge isotope is extracted periodically. It is counted by employing proportional counters to capture both the energy and pulse shape of the decay of the germanium back to gallium. The proportional counters were injected with a mixture of a noble gas (xenon and/or argon) and germane gas (GeH_4), where the germane came from the chemical purification of the germanium. The signature of this decay is as follows: two mono-energy lines at 1.2 keV and 10.37 keV from the Auger electrons, and

γ-rays produced in the decay:

$$^{71}\mathrm{Ge} + e^- \rightarrow {}^{71}\mathrm{Ga} + \nu_e. \tag{3.9}$$

The SSM from Bahcall, Pinsonneault, and Basu [66] predicts the rate of ^{71}Ga transmutation to ^{71}Ge to be 128^{+9}_{-7} SNU.

The GALLium EXperiment (GALLEX) [67] ran from 1991 to 1997 in the underground Gran Sasso National Lab (LNGS) in Italy. The target mass was 101 tons of $GaCl_3$ solution containing 30.3 tons of gallium. Every three weeks, nitrogen gas was flushed through the tank to extract the $GeCl_4$, which was then concentrated chemically into germane gas before being combined with argon/xenon gas and pumped into the proportional counters. The original GALLEX analysis used the rise time (RT) of the pulses read out from proportional chambers to count the germanium isotopes, thereby measuring the *pp* solar neutrino induced production of ^{71}Ge. The final GALLEX(RT) result [67] is shown in Table 3.4.

GALLEX had four experimental phases over its run period before being shut down in 1997 for maintenance and upgrades. Simultaneously, the collaboration reformed into the Gallium Neutrino Observatory (GNO) [68], which collected data between 1998 and 2003 in three periods. For the GNO analysis, the full pulse shape (PS) data and the energy measurements collected by the proportional counters were used to determine the production rate of ^{71}Ge. A re-analysis of the GALLEX data was published in 2010 [69], after performing source calibrations to the proportional counters used in these experiments, as well as analyzing GALLEX pulse shape (PS) data with the same method as GNO to reduce errors and use the full information recorded. The results for the production rate of ^{71}Ge agree with the original analysis. The final result from the GNO experiment and the combined results with GALLEX RT and PS analyses are given in Table 3.4.

The other gallium experiment, the Soviet-American Gallium Experiment (SAGE) [70],

Table 3.4: Results from GALLEX rise-time (RT) analysis, GALLEX re-analyzed pulse shape (PS) analysis, GNO, and SAGE for the measure of ^{71}Ge from ^{71}Ga transmutation induced by *pp* solar neutrinos via Eq. 3.8. An expected value of 128^{+9}_{-7} SNU from Bahcall, Pinsonneault, and Basu's SSM [66] (assuming no oscillations), with the central value of the Data/SSM ratio given in the third column. The last column contains the live time for each experiment in days. For the All Gallium Experiments Combined weighted result, the statistical and systematic errors are combined in quadrature.

Experiment	Rate ± Stat ± Sys. [SNU]	$\frac{Data}{SSM}$	live time [days]
GALLEX(RT)	$77.5 \pm 6.2\ ^{+4.3}_{-4.7}$	0.605	1687
GALLEX(PS)	$73.4\ ^{+6.1}_{-6.0}\ ^{+3.7}_{-4.1}$	0.573	-
GNO	$62.9\ ^{+5.5}_{-5.3} \pm 2.5$	0.491	1594
GALLEX(RT)+GNO	$69.3 \pm 4.1 \pm 3.6$	0.541	3281
GALLEX(PS)+GNO	$67.6 \pm 4.0 \pm 3.2$	0.528	-
SAGE	$65.4\ ^{+3.1}_{-3.0}\ ^{+2.6}_{-2.8}$	0.511	1999.8
All Ga Combined (PS)	66.1 ± 3.1	0.516	-

was located under the Russian Caucasus mountains in the Baksan Neutrino Observatory. The experiment had a 4700 mwe overburden and ran from 1990 until 2007, with 57 tons of molten gallium-germanium alloy (50 tons of gallium) contained in seven chemical reactors as the target material. In a similar process to GALLEX/GNO, the ^{71}Ge was extracted from the alloy monthly, chemically refined into germane, and injected into the proportional counters in a mixture with xenon gas. The SAGE analysis uses both pulse shape and energy measurements, and the current results from SAGE [70] are given in Table 3.4. In order to combine with the results from GALLEX/GNO, the last line in the table, SAGE was calibrated in a similar manner. A preliminary result from the re-analysis thesis in [69] was used to obtain the combined result, where the central value for the GALLEX results was 73.1 SNU instead of 73.4 SNU.

The Gallium experiments provided the first observations of *pp* neutrinos, which experimentally confirmed that hydrogen thermonuclear fusion is the driving process powering the Sun, specifically through the *pp*-fusion chain [10]. Additionally, the deficit of $\sim\frac{1}{2}$ in the flux

measured by the Gallium experiments relative to the SSM predictions indicates the transformation of *pp* neutrino states between their production in the solar core and arrival at Earth due to neutrino vacuum oscillations arising from non-zero neutrino masses [68].

3.3.4 The Sudbury Neutrino Observatory (SNO)

The Sudbury Neutrino Observatory (SNO) [36] was a real-time Cherenkov detector designed by University of California Irvine professor Herb Chen [71] to simultaneously measure both the total flux of all active neutrino flavors and the electron flavor component independently for ^{8}B (and *hep*) solar neutrinos [47]. To achieve this simultaneous measurement, SNO employed a target of 1 kt of heavy water (D_2O, where D is the deuteron D=^{2}H) purified to 99.92% for the first experimental phase (Phase-I). The heavy water was held in a transparent acrylic vessel (diameter = 12 m), which was surrounded by a stainless steel geodesic structure (diameter = 17.8 m) that acted as the support for the PMT array (9456 inward-facing and 91 outward-facing 20 cm PMTs). To increase the 4π photocathode coverage, each PMT was mounted with a non-imaging light collector, bringing the total coverage to 55%.

The two concentric structures were housed in a 30 m barrel-shaped cavity filled with purified water that both acted as a shield against the external radioactive background from the mine rock and as a veto against cosmogenic sources (muons). The water between the PMT array and the acrylic vessel served as an additional buffer and veto against radioactivity originating from the support structure and PMTs. The PMT array detected the Cherenkov light from the heavy water in the acrylic vessel and from the purified water in the veto region. The experiment was located at the SNOLAB facility in the Creighton mine near Sudbury, Ontario, Canada at a depth of 2092 m with a 5890 ± 94 mwe overburden. This overburden reduced the muon rate from cosmic radiation to $\sim$3 events per hour. Both the D_2O and H_2O were purified to get rid of radioisotope impurities and bacteria while also ensuring good

transparency for light collection. It was important for SNO to have stringent limits on their radioactive backgrounds, as gammas with energy $\geq$ 2.2 MeV will have enough energy to overcome the deuteron's binding energy and cause it to break up, releasing a neutron which would be a background to their NC measurement.

During the life of the SNO experiment, three separate phases were performed, with the first phase (SNO Phase-I, Nov 1999 to May 2001) only using ultrapure D_2O as described earlier. The later two phases were designed to improve the NC flux measurement by increasing the efficiency of neutron detection in SNO. In SNO Phase-II, sometimes referred to as the "Salt" phase (July 2001 to Aug 2003), 2 tons of NaCl was added to the heavy water. In SNO Phase-III, or the SNO-NCD phase (Nov 2001 to Nov 2006), a Neutral Current Detection (NCD) array comprised of helium-filled proportional counters was introduced into the D_2O after removing the NaCl used in Phase-II.

By using heavy water, the SNO detector is sensitive to solar neutrinos through three kinds of reactions: NC (CC) interactions between all active (electron flavor) neutrinos and the deuterium in the medium, and through neutrino-electron ES interactions between neutrinos and the atomic electrons in the medium (Sec. 2.3). The total flux for ^{8}B neutrinos (Φ_{NC}) can be determined regardless of the flavor state of the neutrinos (unless the neutrino oscillates into a sterile neutrino state) by measuring the rate of NC reactions,

$$d + \nu \rightarrow p + n + \nu \quad E_{\text{threshold}} = 2.225 \text{ MeV}. \tag{3.10}$$

This channel is sensitive to all the active flavor states $f = e, \mu, \tau$ equally, making it independent of any oscillation effects between the active neutrino flavor states. The ejected neutron captures on the heavy water deuterons, which releases a single 6.25 MeV photon that creates Compton electrons or pair produces e^-e^+. These $e^{\pm}$ produce Cherenkov radiation, which is picked up by the PMTs. The electron neutrino flux can be directly measured through the

CC reactions

$$d + \nu_e \rightarrow p + p + e \quad E_{\text{threshold}} = 1.442 \text{ MeV}, \tag{3.11}$$

which are only sensitive to the ν_e state. The energy resolution of SNO for the protons produced by two reactions is very tight, meaning the correlation between neutrino energy and the effective energy seen by the detector is strong. By comparing the NC to the CC reaction rates, the amount of oscillation away from the ν_e flavor eigenstate can be directly measured independently of the flux. Furthermore, by comparing the energy dependence of the two measurements while considering the energy dependence of the respective reaction cross sections, the energy dependence of the solar neutrino survival probability $P_{ee}(E_\nu)$ can be determined.

Additionally, in the same way Kamiokande and SK detect neutrinos, SNO sees the Cherenkov light from the ES of neutrinos with electrons in the heavy water (Eq. 3.7), which are predominantly due to ^{8}B ν_es. This allows for the comparison against other (light) water Cherenkov detectors and a measurement of the flux independent from the deuterium NC and CC processes. The Cherenkov radiation produced by the ES recoil electrons is picked up by the PMT array and correlated to the incident neutrino energy through the total amount of light detected.

The results for the 306.4 days of live time of SNO Phase-I are published in [72], where the analysis had an energy threshold of $T_{eff} = E_{eff} - m_e > 5.0$ MeV, corresponding to the recoil electron kinetic energy. The fluxes are measured under the assumption that the solar ^{8}B flux is solely comprised of ν_es and has an undistorted spectrum (no flavor oscillations). Then the fluxes for the three reactions in SNO Phase-I are given in Table 3.5. The total flux Φ_{NC} measured by SNO agrees well with the SSMs, while the Φ_{ES} flux still agrees well with Kamiokande and Super-Kamiokande. Also, since Φ_{NC} is so much larger than Φ_{CC}, the solar neutrino flux must have additional active flavor components. SNO decomposed their

measurements into the flavor components, yielding

$$\Phi_{\nu_e} = 1.76 \pm 0.05(\text{stat}) \pm 0.09(\text{sys}) \times 10^6 \text{ cm}^{-2}\text{s}^{-1}, \tag{3.12}$$

and

$$\Phi_{\nu_\mu,\nu_\tau} = 3.41 \pm 0.45(\text{stat})^{+0.48}_{-0.45}(\text{sys}) \times 10^6 \text{ cm}^{-2}\text{s}^{-1}. \tag{3.13}$$

The independent measurements of the three reactions and the relative flavor composition of the flux, all independent of SSMs, confirmed the SSM predictions and confirmed that the solar neutrino problem was due to neutrino oscillations.

The addition of the NaCl to the heavy water in SNO Phase-II allowed for neutron capture on ^{35}Cl which has a larger neutron capture cross section than deuterium. This neutron capture process results in ^{36}Cl and a γ-cascade with 8.6 MeV of energy to be released. The higher energy and number of photons released from this process are more likely to be picked up by the PMTs than in the case of neutrons capturing on deuterons, allowing for an increase in the efficiency of identifying NC events via more efficient neutron detection. The SNO Salt Phase measurements of the relevant fluxes are published by the SNO collaboration in Table XXII of [73] and aggregated into Table 3.5. The results for the combined analysis of Phase-I and Phase-II with a low energy threshold of $T_{eff} = 3.5$ MeV while simultaneously fitting the rates for all interactions are published in [74]. SNO measures a total ^{8}B solar neutrino flux of $\Phi^{\text{I+II}}_{\text{NC}_{uncon}} = 5.140^{+0.160}_{-0.158}(\text{stat})^{+0.132}_{-0.117}(\text{sys}) \times 10^6$ cm^{-2}s^{-1} with no constraint on the ^{8}B neutrino energy spectrum. When SNO does constrain the ^{8}B neutrino energy spectrum using the energy-dependent P_{ee} and A_{ee} from Eq. 3.16, they measure $\Phi^{\text{I+II}}_{\text{NC}} = 5.046^{+0.159}_{-0.152}(\text{stat})^{+0.107}_{-0.123}(\text{sys}) \times 10^6$ cm^{-2}s^{-1}.

The NDC array introduced in SNO Phase-III is another relatively independent way of measuring the ^{8}B solar neutrino NC rate in SNO[75][76]. The NDCs consisted of 40 proportional counters made from helium-filled nickel tubes, with thirty-six of the NDCs being

filled with ^{3}He and the remaining four filled with ^{4}He. The ^{3}He facilitates the detection of neutrons via tritium production

$$^3\mathrm{He} + n \rightarrow {}^3\mathrm{H}^- + p \tag{3.14}$$

with a total kinetic energy of 764 keV, and a back-to-back emission of the negatively charged triton and proton [75]. The neutrons come from the breakup of the deuterium in SNO's heavy water through the NC reaction in Eq. 3.10. The anode wires of the NDCs were held to 1950 V, which results in a gain of ∼220 for the gas. Since the daughter particles have charge, the helium gas is ionized by the interaction. This primary ionization causes an avalanche of secondary set of ionizations, leading to a current pulse in the anode of the NDC. The resulting set of waveforms for the measured current are read out and stored, and analyzed offline. The four NDCs that were filled with ^{4}He are used for background studies, as ^{4}He is insensitive to the neutrons.

The analysis to measure the NC flux in SNO Phase-III has a higher energy threshold of $T_{eff} = 6.0$ MeV to further reduce the backgrounds for the measurement. With the NDC's, SNO Phase-III measured $\Phi^{\mathrm{III}}_{\mathrm{NC}_{uncon}} = 5.54^{+0.33}_{-0.31}(\mathrm{stat})^{+0.36}_{-0.34}(\mathrm{sys}) \times 10^6$ cm^{-2}s^{-1} with a live time of 385.17 ± 0.14 days. The measurements of the ^{8}B solar neutrino flux based on NC, CC, and ES interactions in SNO Phase-III were published by the collaboration in [75] and again in Table XVII of [76], and are transcribed here in Table 3.5. The successor to SNO, SNO+ [77], has also measured the ^{8}B ν_e flux as $2.53^{+0.31}_{-0.28}(\mathrm{stat})^{+0.13}_{-0.10}(\mathrm{sys}) \times 10^6$ cm^{-2}s^{-1} with 0.9 kt × 76.89 days exposure using ultrapure water [78].

Table 3.5: Experimental Results from SNO for the measured fluxes of the specific interactions (NC,CC,ES) for each experimental phase (I,II,III) and the measured flavor component of the flux for ^{8}B neutrinos. The NC measurements for the reactions assume the constraint of an undistorted ^{8}B neutrino energy spectrum comprised solely of ν_e, while the flavor components are extracted directly from the reactions in SNO. The subscript "*uncon*" corresponds to not using the above constraint to the ^{8}B energy spectrum for measuring the fluxes. The effective energy threshold $T_{eff} = E_{eff} - 0.511$ MeV is given in the second to last column. The live time for the measurement is given in the last column. All three SNO phases have a maximum energy cutoff of $T_{eff} = 20.0$ MeV for their analyses.

Flux Measurement	SNO Phase	Flux$\pm$(stat)$\pm$(sys) $\times 10^6$ cm^{-2}s^{-1}	T_{eff} [MeV]	Live Time [days]
CC	I[72]	$1.76\ ^{+0.06}_{-0.05} \pm 0.09$	5.0	306.4
ES	–	$2.39\ ^{+0.24}_{-0.23} \pm 0.12$	–	–
NC	–	$5.09\ ^{+0.44\ +0.46}_{-0.43\ -0.43}$	–	–
ν_e	–	$1.76 \pm 0.05 \pm 0.09$	–	–
$\nu_{\mu,\tau}$	–	$3.41 \pm 0.45\ ^{+0.48}_{-0.45}$	–	–
CC	II[73]	$1.72 \pm 0.05 \pm 0.11$	5.5	391
CC$_{uncon}$	–	$1.68 \pm 0.06\ ^{+0.08}_{-0.09}$	–	–
ES	–	$2.34 \pm 0.23\ ^{+0.15}_{-0.14}$	–	–
ES$_{uncon}$	–	$2.35 \pm 0.22 \pm 0.15$	–	–
NC	–	$4.81 \pm 0.19\ ^{+0.28}_{-0.27}$	–	–
NC$_{uncon}$	–	$4.94 \pm 0.21\ ^{+0.38}_{-0.34}$	–	–
NC	I+II [74]	$5.140\ ^{+0.0.160\ +0.132}_{-0.158\ \ -0.117}$	3.5	697.4
NC$_{uncon}$	–	$5.046\ ^{+0.159\ +0.107}_{-0.152\ -0.123}$	–	–
CC$_{uncon}$	III [75][76]	$1.67\ ^{+0.05\ +0.07}_{-0.04\ -0.08}$	6.0	385.17 ± 0.14
ES$_{uncon}$	–	$1.77\ ^{+0.24\ +0.09}_{-0.21\ -0.10}$	–	–
NC$_{uncon}$	–	$5.54\ ^{+0.33\ +0.36}_{-0.31\ -0.34}$	–	–
NC$_{\rm ML}$	I+II+III [47]	$5.25 \pm 0.16\ ^{+0.11}_{-0.13}$	$\begin{matrix}\text{I \& II} & 3.5\\ \text{III} & 6.0\end{matrix}$	1053.9

SNO 3-Phase Results: $\Phi^{\rm SNO}_{\rm NC_{MLL}}$, P_{ee}, A_{DN}, and Oscillation Contour Results

The combined analysis of all three phases was published in [47] in 2013 and gives a total ^{8}B neutrino flux of

$$\Phi^{\rm SNO}_{\rm NC_{ML}} = 5.25 \pm 0.16({\rm stat})^{+0.11}_{-0.13}({\rm sys}) \times 10^6\ {\rm cm}^{-2}{\rm s}^{-1} \tag{3.15}$$

(also listed at the end of Table 3.5) using a maximum likelihood (ML) fit method. All three phases have a maximum energy cutoff of $T_{eff} = 20.0$ MeV, while the 3.5 MeV low energy

Table 3.6: The SNO collaboration combined result for all three experimental phases, published in [47]. The units for the ^{8}B flux $\Phi_{^8\mathrm{B}}$ are $\times 10^6$ cm^{-2}s^{-1}. The quadratic parameterization to the day survival probability spectrum P_{ee}^D and the linear parameterization for the day-night asymmetry spectrum A_{ee} are both functions of the neutrino energy E_ν centered around 10 MeV and are given in Eq. 3.16. The parameterizations are all independent of any solar model, and are determined by a maximum likelihood fit to an average day and night flux, the survival probability spectra for day and night, and the day-night asymmetry spectrum. The correlation matrix from the maximum likelihood fit for the parameters is given in the right-hand side of the table.

Parameter	Best Fit $\pm$ (stat) $\pm$ (sys)	$\Phi_{^8\mathrm{B}}$	c_0	c_1	c_2	a_0	a_1
$\Phi_{^8\mathrm{B}}$	$5.25 \pm 0.16^{+0.11}_{-0.13}$	1.000	-0.723	0.302	-0.168	0.028	-0.012
c_0	$0.317 \pm 0.016 \pm 0.009$	-0.723	1.000	-0.299	-0.366	-0.376	0.129
c_1	$0.0039^{+0.0065}_{-0.0067} \pm 0.0045$	0.302	-0.299	1.000	-0.206	0.219	-0.677
c_2	$-0.0010 \pm 0.0.0029^{+0.0014}_{-0.0016}$	-0.168	-0.366	-0.206	1.000	0.008	-0.035
a_0	$0.046 \pm 0.0.031^{+0.014}_{-0.013}$	0.028	-0.376	0.219	0.008	1.000	-0.297
a_1	$-0.016 \pm 0.0.025^{+0.010}_{-0.011}$	-0.012	0.129	-0.677	-0.035	-0.297	1.000

threshold analysis for Phase-I and Phase-II and the 6.0 MeV energy threshold for Phase-III are used in this combined flux analysis. The total Day (Night) live time of SNO for Phase-I is 119.9 (157.4) days, 176.5 (214.9) days for Phase-II, and 176.6 (208.6) days for Phase-III.

To parameterize the ^{8}B solar neutrino signal, SNO performs a ML fit to extract the signal from the following data:

- An average $\Phi_{^8\mathrm{B}}$ for both day and night.
- The day (night) solar ν_e survival probability P_{ee}^D (P_{ee}^N) spectrum as a function of E_ν.
- The day-night asymmetry spectrum $A_{ee}(E_\nu)$ defined by $A_{ee}(E_\nu) = 2\frac{P_{ee}^N(E_\nu) - P_{ee}^D(E_\nu)}{P_{ee}^N(E_\nu) + P_{ee}^D(E_\nu)}$.

It should be noted that SNO's definition of A_{ee} is opposite in sign than the definition used by SK, and is based on the survival probabilities instead of the day and night rates like in SK. A constant value of $A_{ee} = 0$ ($a_0 = a_1 = 0$) corresponds to an absence of matter effects on solar neutrino oscillations as neutrinos traverse through Earth's matter on their way to the detector (during the night). SNO also uses the assumption of a constant flux for ^{8}B solar

neutrinos in this combined analysis. The use of the neutrino energy, E_ν in units of MeV, is to disentangle the fit results from the detector response. To be independent of theoretical models, a quadratic (linear) fit of the day survival probability $P_{ee}^D(E_\nu)$ (day-night asymmetry $A_{ee}(E_\nu)$) spectrum, centered around 10 MeV, is used:

$$\begin{aligned} P_{ee}^D(E_\nu) &= c_0 + c_1(E_\nu - 10) + c_2(E_\nu - 10)^2 \\ A_{ee}(E_\nu) &= a_0 + a_1(E_\nu - 10) \end{aligned} \tag{3.16}$$

For the survival probability spectrum, the SNO energy resolution of T_{eff} is broad and makes the measure of $P_{ee}^D(E_\nu)$ insensitive to sharp distortions.

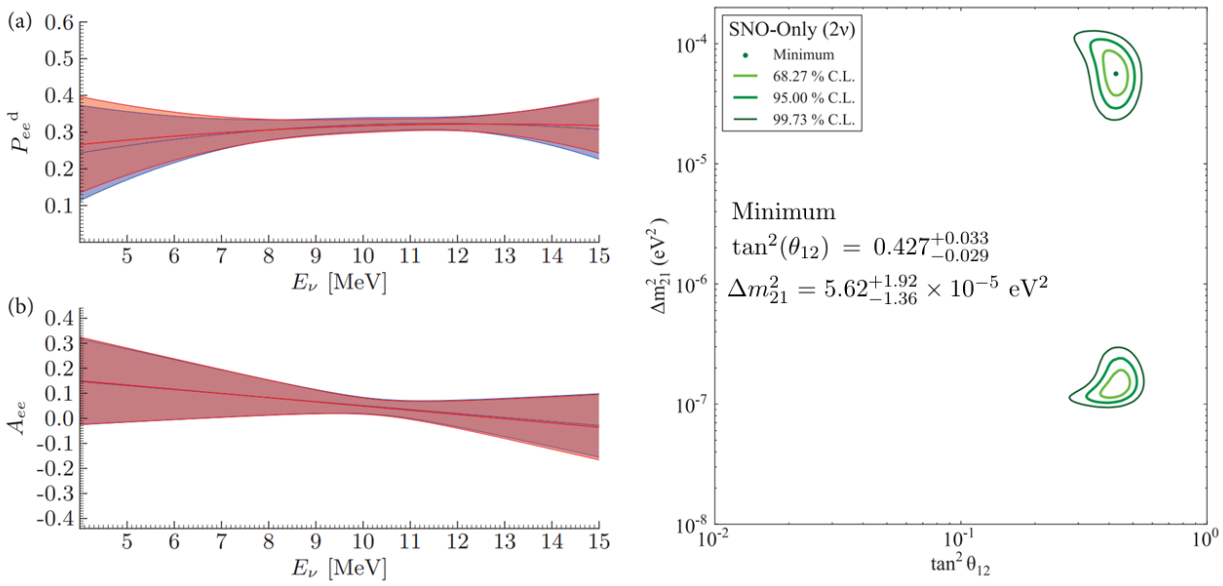

Figure 3.9: **SNO Results** - The combined results of all 3 phases of the SNO experiment. These results are published in [47]. Left: The day survival probability spectrum P_{ee}^D (top) and the day-night asymmetry spectrum A_{ee} (bottom). The solid lines corresponding to the best fits from Table 3.6 and the bands representing the root mean square (RMS) spread due to the correlated uncertainties from the parameters. The colors correspond to the maximum likelihood (Bayseian) fit in red (blue). Right: The resulting 1, 2, and 3-σ contours for the SNO 2-flavor solar neutrino oscillation analysis using only SNO data and assuming the BS2005(OP) SSM.

The parameterized results and correlation matrix for the ^{8}B solar neutrino data from the maximum likelihood fit, sometimes referred to as SNO-Poly, are listed in Tables VII and

VIII of [47], and are listed in Table 3.6, as these results are used for including SNO data into the SK NSI analysis (SK+SNO), which is one of the primary results of the analysis presented in this work. The SNO-Poly results for $P_{ee}^{D}(E_\nu)$ and $A_{ee}(E_\nu)$ are shown on the left side of Fig 3.9 (Fig. 10 of [47]) with the solid lines corresponding to the best fits from Table 3.6 and the bands representing the root mean square (RMS) spread due to the correlated uncertainties from the parameters. The colors correspond to the maximum likelihood (Bayesian) fit in red (blue).

Using the SNO-Poly result, SNO performs a χ^2 fit to the P_{ee}^{D} and A_{ee} predictions from SSMs based on the neutrino oscillation parameters, taking the minimum χ^2 as their best fit and the uncertainties from the corresponding deviations in χ^2. SNO checked the consistency of the best fit oscillation parameters using the SNO-Poly method by simulating their data and comparing the best fit and uncertainties. In these tests, SNO found that the $\Delta\chi^2$ method from fitting expectations to the SNO-Poly data resulted in unbiased best fit neutrino oscillation parameters with consistent uncertainties [47]. The resulting contours for SNO's two-flavor solar neutrino oscillation analysis ($\theta_{13} = 0$) is displayed on right side of Fig. 3.9 (Fig. 14 of [47]). The best fit oscillation parameters assuming the BS2005(OP) SSM [57] to this fit are $\tan^2(\theta_{12}) = 0.427^{+0.033}_{-0.029}$, or $\sin^2(\theta_{12}) = 0.299^{+0.016}_{-0.014}$, and $\Delta m^2_{21} = 5.62^{+1.92}_{-1.36} \times 10^{-5}$ eV^2 where the uncertainties are the $\pm 1\sigma$ errors after profiling (or minimizing) over the other parameters.

3.3.5 Borexino

The Boron solar neutrino Experiment (Borexino [37]) is located at LNGS in Italy and has been running since 2007 [79][80][81][82][83]. The experiment is a calorimeter filled with 278 tons liquid scintillator in its spherical nylon film (radius = 4.25 m), and is designed to perform real-time measurements of low energy solar neutrinos.

The scintillation light comes from (ν_e e) ES events and from NC interactions (all flavors) in Borexino's 100-ton fiducial volume. Scintillation light in Borexino is recorded by 2212 PMTs on the surface of the spherical stainless steel vessel (radius = 6.85 m) that encloses the non-scintillating buffer material, an additional nylon outer film (radius = 5.50 m), and the inner nylon film containing the liquid scintillator. The energy, position, time, and the pulse shape of each event are recorded by the timing and number of photons hitting the PMTs, which is then used to reconstruct events. The stainless steel vessel is immersed in a water tank that acts as a veto for cosmic rays and as a shield from excess radiation from the surrounding mine environment.

One of the primary goals for the experiment is low-energy solar neutrino spectroscopy, specifically the flux measurement of the ^{7}Be solar neutrino line at 862 keV [80] and the corresponding day-night asymmetry rate [84]. To do this, Borexino has been made as clean as possible, resulting in the most radio-pure liquid scintillator calorimeter in the world. This feat was accomplished by constructing the detector out of low activity materials (Phase-I). The results from Borexino Phase-I for their measurement of the 862 keV ^{7}Be solar neutrino flux of $(4.43 \pm 0.22) \times 10^9/(\text{cm}^2\ \text{s})$ [79] agrees with the BP2004 SSM prediction of $(4.86 \pm 0.58) \times 10^9/(\text{cm}^2\ \text{s})$ [46]. In 2010, Borexino began undertaking a lengthy campaign to purify the liquid scintillator in order to improve their measurements by reducing the amount of contamination in their liquid scintillator due to ^{85}Kr and ^{210}Bi [83]. Borexino Phase-II began in December 2011 after their purification campaign was completed.

In 2018, Borexino published simultaneous fit of the rates for all of the solar neutrino species (both *pp*-chain and CNO-cycle neutrinos) in [83], by combining their unpublished analyses in [81] and [85]. In their analysis, they define a low energy region (LER) from 0.19 to 2.93 MeV (recoil electron kinetic energy) and a high energy region (HER) from 3.2 to 16.3 MeV, which is sub-divided into two regions, HER-I and HER-II, at 5.7 MeV. The highest energy region HER-II uses the total scintillator volume since the energy is above the

radioisotope backgrounds, while the HER-I region retains a $z > 2.5$ m cut. The LER has an exposure of 1291.51 days $\times$ 71.3 tons, using Borexino Phase-II data taken from December 2011 to May 2016, after their purification campaign completed. The HER-I (HER-II) data set includes the data from Phase I and additional data from Phase-II through December 2016, resulting in an exposure of 2062.4 days $\times$ 227.8 (266.0) tons. The LER is used to measure the *pep*, *pp*, and ^{7}Be neutrino fluxes, and uses either a high metalicity SSM (HZ) or low metalicity SSM (LZ) for the *pep* flux. Due to the reduction of the threshold during phase II, the combination of the 0.862 MeV and the 0.384 MeV lines from the ^{7}Be neutrinos is able to be taken into account in this fit. The relevant radio-isotope backgrounds are applied to these data sets to extract the fluxes for the solar neutrino species. The best fit MSW-LMA oscillation parameters to all other solar neutrino experiments [86] are used to predict the interaction rates and fluxes expected to be measured in Borexino. With these expected rates and fluxes, Borexino extracts their measured event rates and fluxes. Their analysis uses the following best fit values with one-sigma errors for the relevant oscillation parameters: $\sin^2(\theta_{12}) = 0.306^{+0.012}_{-0.012}$ and $\Delta m^2_{21} = 7.50^{+0.19}_{-0.17} \times 10^{-5}$ eV^2.

The Borexino measurements of the various solar neutrino rates and fluxes are given in Table II of [83] and are collected below in Table 3.7. Their global analysis also shows the first 5σ rejection of *pep* neutrino absence from the total solar neutrino flux and places an upper limit on the CNO neutrino rate of 8.1 counts per day per 100 tons (cpd/100 t) at the 95% confidence level [81].

Borexino ^{7}Be Day-Night Asymmetry Measurement

In addition to measuring the *pp*-chain neutrino fluxes, in 2012, Borexino made a measure of the 862 keV ^{7}Be solar neutrino day-night asymmetry (A_{dn}) [84]. Their analysis uses data taken between May 2007 and May 2010 (740.88 days live) in a window in recoil electron kinetic energy between 550 and 800 keV, though there is a Compton-like electron scattering

Table 3.7: Experimental Results from Borexino for the rates and fluxes of low energy solar neutrinos via global fit [83] to Borexino Phase-II data assuming the MSW-LMA oscillation parameters [81], and measurements of the ^{8}B rate and unoscillated flux from both Borexino phases [85]. The pure ν_e ^{8}B flux from the HER analysis is reported as HER(ν_e) [85]. The upper limit to the CNO measurements is given as well. The region of recoil electron kinetic energy over which the analysis was performed is given in column 2, and the last column is the exposure for the analysis in ton-years.

[t]

Solar ν Species	Energy Region	Rate $\pm$ Stat $\pm$ Sys. [cpd/100 t]	Flux: $\Phi^{ES}_{\nu_e}$ $\pm$ Stat $\pm$ Sys. [cm^{-2} s^{-1}]	Exposure [ton-year]
pp	LER	$134 \pm 10^{+6}_{-10}$	$(6.1 \pm 0.5^{+0.3}_{-0.5}) \times 10^{10}$	252.11
^{7}Be	LER	$48.3 \pm 1.1^{+0.4}_{-0.7}$	$(4.99 \pm 0.11^{+0.06}_{-0.08}) \times 10^9$	252.11
pep (HZ)	LER	$2.43 \pm 0.36^{+0.15}_{-0.22}$	$(1.27 \pm 0.19^{+0.08}_{-0.12}) \times 10^8$	252.11
pep (LZ)	LER	$2.65 \pm 0.36^{+0.15}_{-0.24}$	$(1.39 \pm 0.19^{+0.08}_{-0.13}) \times 10^8$	252.11
CNO	LER	< 8.1 (95% C.L.)	$< 7.9 \times 10^8$ (95% C.L.)	252.11
^{8}B	HER-I	$0.136 \pm 0.013 \pm 0.003$	$(5.77 \pm 0.56 \pm 0.15) \times 10^6$	1286.28
^{8}B	HER-II	$0.087^{+0.008}_{-0.010} \pm 0.005$	$(5.56^{+0.52}_{-0.64} \pm 0.33) \times 10^6$	1501.98
^{8}B	HER	$0.223^{+0.015}_{-0.016} \pm 0.006$	$(5.68^{+0.39}_{-0.41} \pm 0.03) \times 10^6$	1286.28
^{8}B	HER(ν_e)	-	$(2.55^{+0.17}_{-0.19} \pm 0.07) \times 10^6$	1286.28
hep	HER-III	< 0.002 (90% C.L.)	$< 2.2 \times 10^5$ (90%C.L.)	800

"shoulder" around 665 keV due to conservation of 4-momentum. The exposure during the day (night) is 360.25 (380.63) days $\times$ 132.5 tons, where the fiducial mass is defined by the spherical volume formed by 3.3 m radius that maximizes the detector's sensitivity to the day-night effect. The fiducial volume encloses 4.978×10^{31} electrons and gives a signal-to-background ratio of 0.70 ± 0.04 within the energy window of the analysis. The rate during the night is combined with the zenith information from the event timing, and the spectrum information is used while accounting for the low energy ^{210}Po background.

Borexino's definition and measurement of the Borexino 862 keV ^{7}Be A_{dn} is

$$A_{dn}^{^7\mathrm{Be\,862\,keV}} = 2\frac{r_N - r_D}{r_N + r_D} = 0.001 \pm 0.012(\mathrm{stat}) \pm 0.007(\mathrm{sys}). \tag{3.17}$$

This formula for A_{dn} is opposite in sign to the way SK measures the day-night asymmetry (Eq. 3.19), where the day (night) rate is given by $r_D(r_N)$. This lack of a difference in day

and night rates agrees with the MSW hypothesis, as the ^{7}Be neutrinos are too low in energy to incur measurable effects on the survival probability due to matter in the Sun, much less in the Earth.

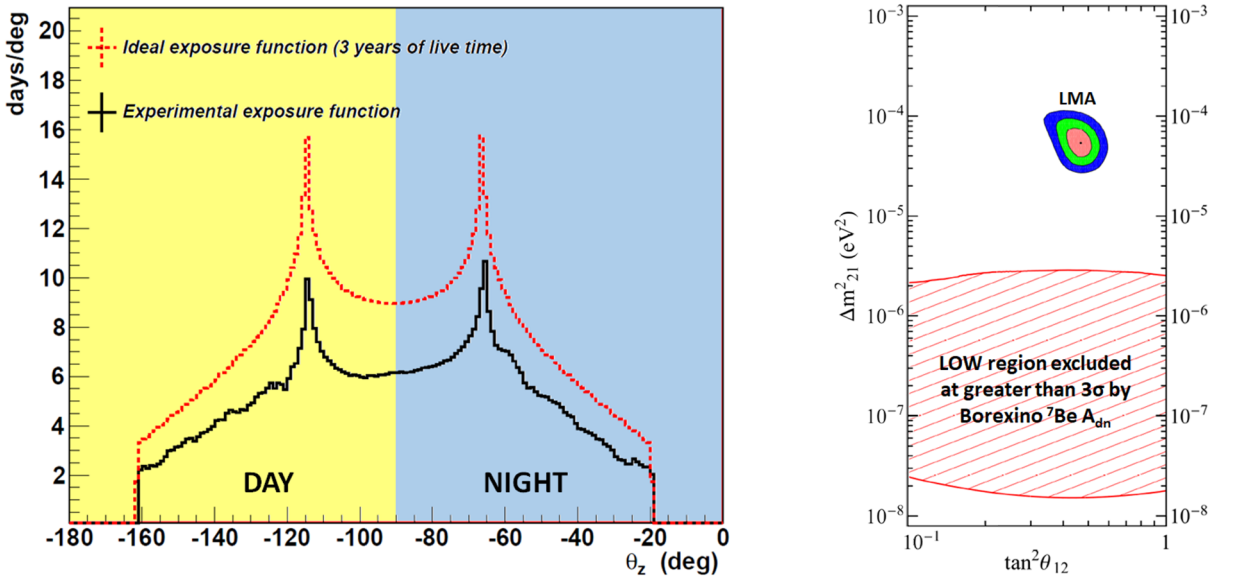

Figure 3.10: **Borexino ^{7}Be** A_{dn} - Borexino's live time dependence on the solar zenith angle and the solar neutrino oscillation parameter space allowed regions without (center) and with (right) Borexino's A_{dn} fit. Both figures from [84]. Left: The solar zenith angle θ_Z [deg] dependence of Borexino's live time (or exposure) in days. Right: The resulting 1, 2, and 3-σ contours (as of 2012) for all solar neutrino experiments after including the Borexino ^{7}Be A_{dn} fit. Only the LMA region survives at 3σ, while the LOW region is excluded at greater than 3σ.

The effect from the 384 keV ^{7}Be solar neutrinos is taken into account in the systematic error by lowering the lower energy bound to 250 keV and taking the difference in the central values. It was found that the A_{dn} measurement with the 250 keV lower energy bound is consistent with A_{dn} measurement with the 550 keV lower energy bound. Borexino's resulting A_{dn} measurement disfavors the region $\Delta m^2_{21} < 2\times10^{-6}$ eV^2 at greater than 3σ by itself, with the LOW solution being excluded at greater than 8.5σ, while being in agreement with the LMA solution (which gives a χ^2 fit of approximately zero). Fig. 3.10 shows the distribution of the exposure Borexino has to solar neutrinos as a function of degrees in zenith angle

(left), and the allowed 1 to 3 σ regions of the solar neutrino oscillation parameter space after including Borexino's A_{dn} fit (right).

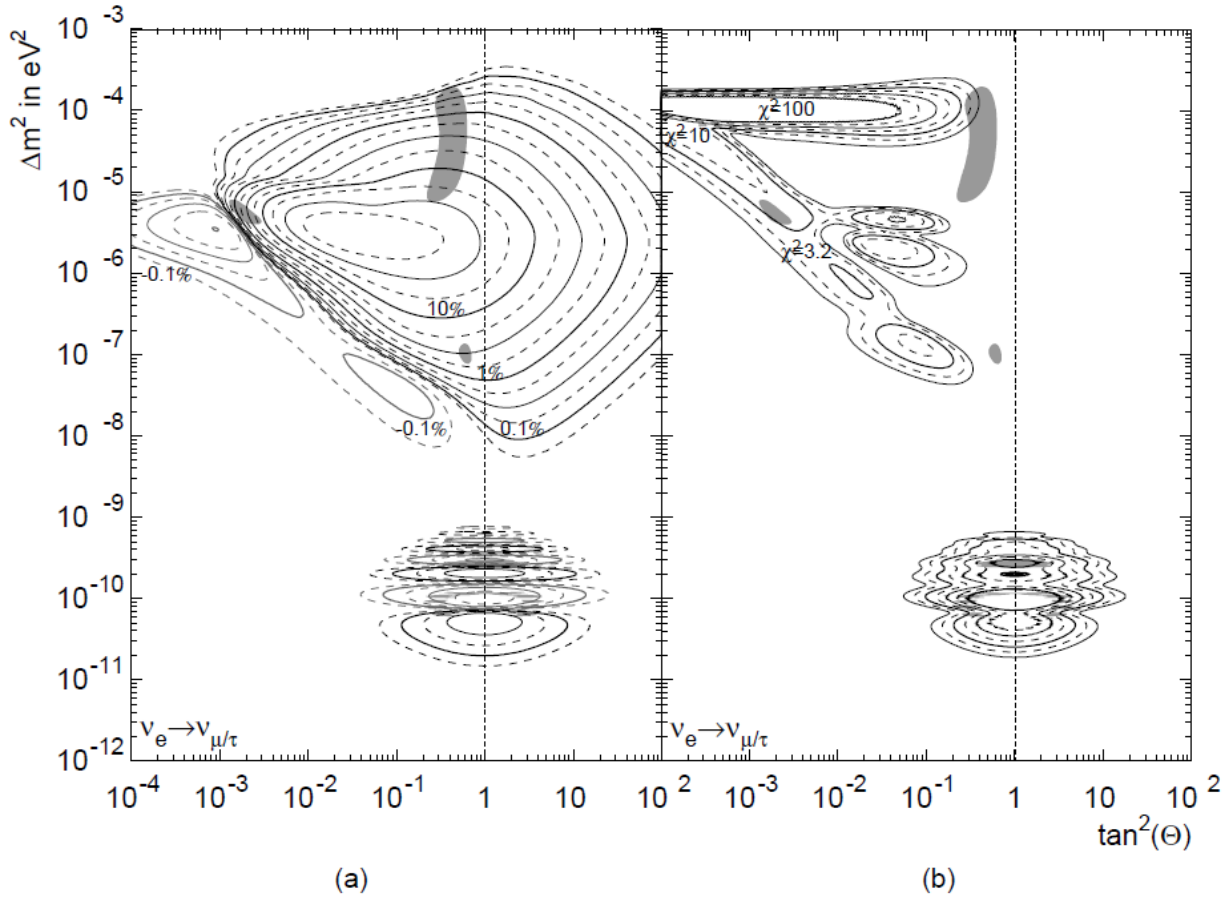

Figure 3.11: Oscillation predictions of A_{DN} (a) and the spectral distortion of the elastic scattering rate (b) [87].

The measurement of the day-night asymmetry A_{DN} from the solar neutrino analysis of Super-Kamiokande, which uses an unbinned maximum log-likelihood fit to all signal and background events extracted from SK, excludes the LOW solution at greater than 3σ through the zenith information. However, in the work presented here, this measurement is neglected in favor of a quicker computation of the integrated (in energy and zenith angle) ES rate during the day and night, which is then used to form A_{DN}. Using the integrated A_{DN} has the unfortunate effect of returning the LOW solution, as the zenith information is what leads to ruling it out. To exclude the LOW solution again without the large computational

resources necessary for implementing the A_{DN} likelihood measurement, the Borexino ^{7}Be A_{dn} measurement is used. Because the predicted asymmetry of the elastic scattering rate (left side in fig 3.11) is of the order of one to ten percent in the LOW solution region, the sub-percent asymmetry and incredibly small errors of Borexino's measurement (Eq. 3.17) are able to strongly exclude this region independently of SK, which further restricts the allowed regions of both the solar oscillation parameter space and the NSI parameter space. Further details of these three day-night asymmetries, including how they are predicted and fit in the NSI analysis, will be discussed in Ch. 10.

3.3.6 KamLAND Reactor Antineutrinos and Solar Neutrino Flux Measurements

While itself not designed as a solar neutrino experiment, the Kamioka Liquid Scintillator Antineutrino Detector, or KamLAND [88][89], has contributed to the study of solar neutrinos through the precise measurement of the mass splitting Δm^2_{21} and mixing angle θ_{12} using nuclear reactor antineutrinos. KamLAND also published a measurement of the solar neutrino fluxes for ^{7}Be [90] and for ^{8}B [91] using their detector. KamLAND sits in the experimental cavern that once housed the Kamiokande Detector, in the Kamioka mine of Gifu, Japan, where the experiment collected data from March 2002 to September 2011. While employing similar liquid scintillator (LS) technology as Borexino, the detector is much larger though not as radio-pure. The inner detector (ID) weighed in at 1 kiloton of ultrapure LS and the experiment's outer detector (OD) was a 3.2 kton pure water buffer. The OD was used for shielding against mine backgrounds (neutrons and γs) and as muon veto by utilizing the muon-induced Cherenkov light. The LS was contained in a transparent balloon (radius = 6.5 m) suspended in a stainless steel shell (radius = 9 m) filled with mineral oil. The shell acts as the structure for the array of 1879 PMTs that provide 34% photocathode coverage. The detector employs two different PMT setups in the array to pick up the scintillation light

from the LS: 554 twenty-inch PMTs recycled from Kamiokande and 1325 new PMTs with better single-photoelectron and timing resolution than the Kamiokande tubes. The newer style tubes are also 50 cm (20 inches) in diameter, but have had their photocathode masked to reduce the diameter to 43.2 cm. The fiducial volume of KamLAND is defined by a sphere with a radius of 6 m concentric with the LS balloon. The 2011 Japanese earthquake and disaster at Fukushima resulted in all the Japanese commercial nuclear reactors to be shut off. The lack of a reactor antineutrino flux allowed KamLAND to take pure background data for their reactor antineutrino measurement. It also allowed KamLAND to better study low energy geological antineutrino (geoneutrinos) fluxes.

The KamLAND experiment sees electron antineutrinos $\bar{\nu}_e$ produced by the 56 Japanese nuclear power reactors, and several additional reactors on the Korean peninsula, with the nominal distance (baseline) to the reactors being approximately 180 km based on the flux weighted average. Detailed proprietary operational data for each commercial reactor was given to KamLAND by a Japanese power company consortium, including fuel replacement, fuel reshuffling, and the time variation of thermal power output. This detailed reactor information allowed KamLAND to make accurate predictions of the $\bar{\nu}_e$ flux at the detector from each of the reactors. KamLAND detects scintillation light produced by the $\bar{\nu}_e$ through the inverse β-decay

$$\bar{\nu}_e + p \rightarrow e^+ + n. \tag{3.18}$$

This process has a delayed coincidence signature in KamLAND due to prompt Cherenkov light and subsequent γs from e^+e^- annihilation of the ejected positron and the delayed light from the neutron capture on a proton or ^{12}C nucleus in the scintillator. The average capture time for neutrons in KamLAND is $207.5 \pm 2.8\mu$s. The analysis in [89] uses an un-binned maximum-likelihood fit (UMLF) to both the event rate and prompt energy (E_p) spectrum shape. The UMLF extracts the neutrino oscillation parameters and the fluxes for the reactor antineutrinos and geoneutrinos. The time variation of both the event rate and the prompt

energy spectrum shape are considered. The E_p for events lie in the range of 0.9 to 8.5 MeV. The results of this analysis are summarized in Table 3.8.

Table 3.8: KamLAND-only measurements from [89] for the neutrino oscillation parameters θ_{12}, θ_{13} and Δm^2_{21} are shown with the total error of the measurement. KamLAND extracts these parameters using an unbinned maximum-likelihood fit to the antineutrino event rate and energy spectrum shape, including time variations. The electron antineutrino sources are Japanese nuclear reactors and geoneutrinos, both of which are fit to simultaneously in the analysis.

$\sin^2(\theta_{13})\pm$ total	$\Delta m^2_{21}\pm$ total $\times 10^{-5}$ [eV^2]	$\tan^2(\theta_{12})\pm$ total	$\sin^2(\theta_{12})\pm$ total
$0.010^{+0.033}_{-0.034}$	$7.54^{+0.19}_{-0.18}$	$0.481^{+0.092}_{-0.080}$	$0.325^{+0.042}_{-0.036}$

3.3.7 Super-Kamiokande

The Super-Kamiokande experiment [35] is the world's largest ring imaging water Cherenkov detector and is the successor to the Kamiokande and the Irvine-Michigan-Brookhaven (IMB) experiments. SK observes neutrinos of all kinds from a multitude of sources, as well as searches for nucleon decay and other rare processes. The experiment is located in the Kamioka mine in the Gifu prefecture of Japan, 1 km underground, the same mine that housed the Kamiokande experiment previously. The detector is filled with 50 kilotons of ultrapure water in which the neutrinos and antineutrinos interact (as well as muons sourced by cosmic radiation) and is the bulk material under observation from which nucleon decay may occur.

The SK experiment has been running over twenty years, with data collection starting in 1996. The experiment has gone through four experimental phases, SK-I, SK-II, SK-III, and SK-IV. The SK-IV phase ended in May 2018 to refurbish the detector and upgrade the experiment to the SK-Gd Experiment. The SK-Gd experiment entails doping the SK ultrapure water with Gadolinium Sulfate $Gd_2(SO_4)_3$ to better search for and measure the

Diffuse Supernova Neutrino Background (DSNB). The idea for SK-Gd was proposed by John Beacom and Mark Vagins [19].

SK was the first experiment to show evidence that neutrino flavor oscillations induced by non-zero neutrino mass are the reason for the difference between measurements and predictions of atmospheric neutrinos originally hinted at by Kamiokande data. SK also was the first experiment to show that at least one of the neutrinos has a finite neutrino mass [92]. Together with SNO, SK also gave the first experimental indication of neutrino flavor conversion in the Sun, due to non-zero neutrino mass and the MSW effect, could solve the Solar Neutrino Problem. These two sets of evidence have shown that neutrino oscillations arise from non-zero neutrino mass which is not predicted by the Standard Model of Particle Physics. Arthur McDonald of the SNO collaboration and Takaaki Kajita of the Super-Kamiokande collaboration won the 2015 Nobel Prize in Physics for this work [93] . A detailed discussion of the detector will be covered in later chapters, where we discuss its calibration, data acquisition, and the data analysis for solar neutrino measurements and results.

The results for SK-I [44], SK-II [94], SK-III [95], and the 1664 day data set from SK-IV [42] are given in Table 3.9, with the flux values extracted from Table VI in the SK-IV paper. The revised SK-III values are used in Table 3.9. The ^{8}B ν_e flux measurements from the SK, SNO, and Borexino experiments, as well as KamLAND and SNO+, are plotted in Fig. 3.13.

The day-night asymmetry values given in the table are calculated from the day-night rate asymmetry

$$A_{DN} = 2\frac{r_d - r_n}{r_d + r_n}, \tag{3.19}$$

where r_d (r_n) is the energy averaged day (night) scattering rate in SK and $A_{DN} = 0$ corresponds to no Earth-matter effects on neutrino oscillations. The values of A_{DN} for each SK-Phase in Table 3.9 are taken from [96] for SK-I/II/III, and from the SK-IV(1664d) so-

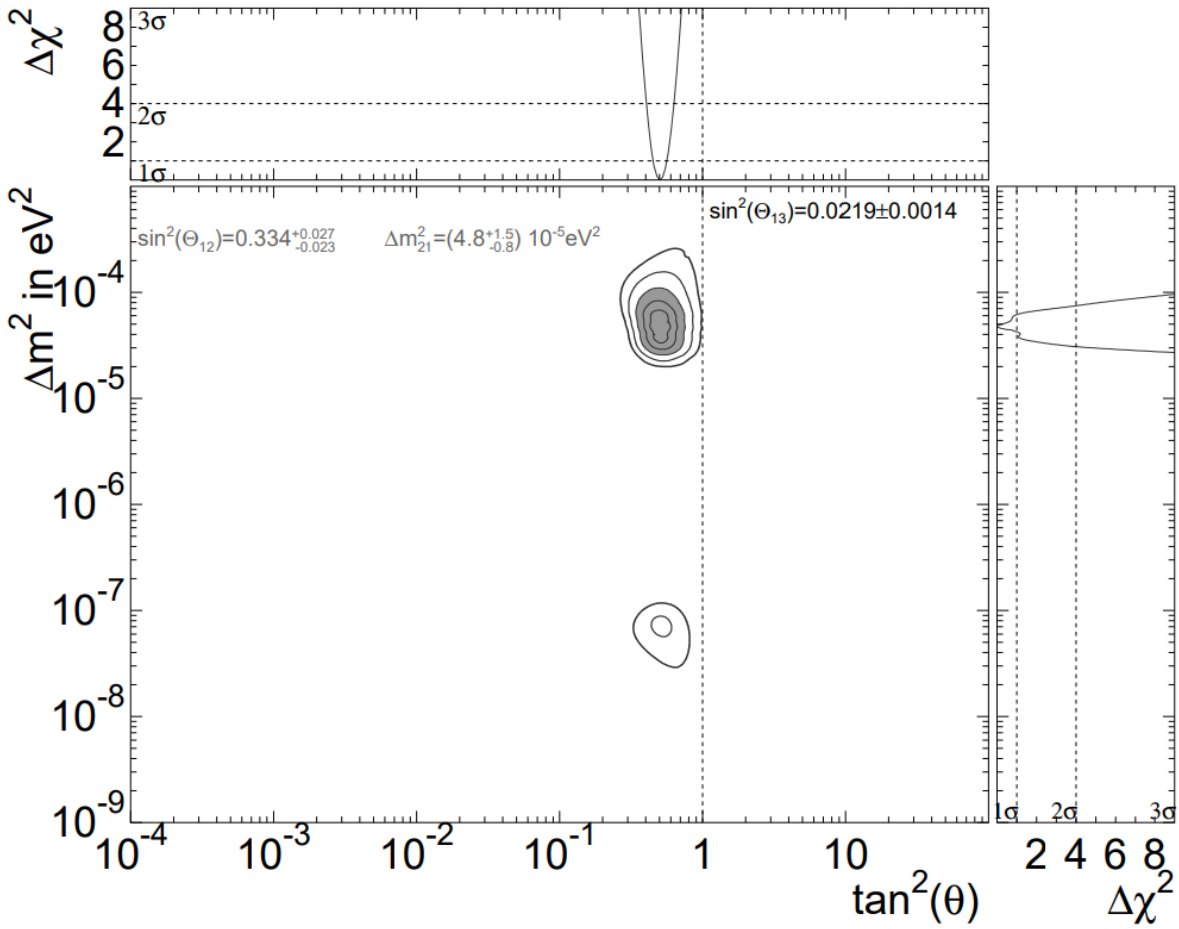

Figure 3.12: **Combined Results for the Super-Kamiokande Solar Oscillation Analysis** - Solar neutrinos oscillation parameter constraints using SK recoil electron spectrum and day-night data from SK-I/II/III/IV(1664d) data set. The 1–5σ confidence levels are shown, with 1–3σ region shaded. The NC is constrained to the SNO results, and θ_{13} is constrained by short baseline measurements of reactor antineutrinos $(\frac{\sin^2\theta_{13}-0.0219}{0.0014})^2$. Fig. 33 of [42].

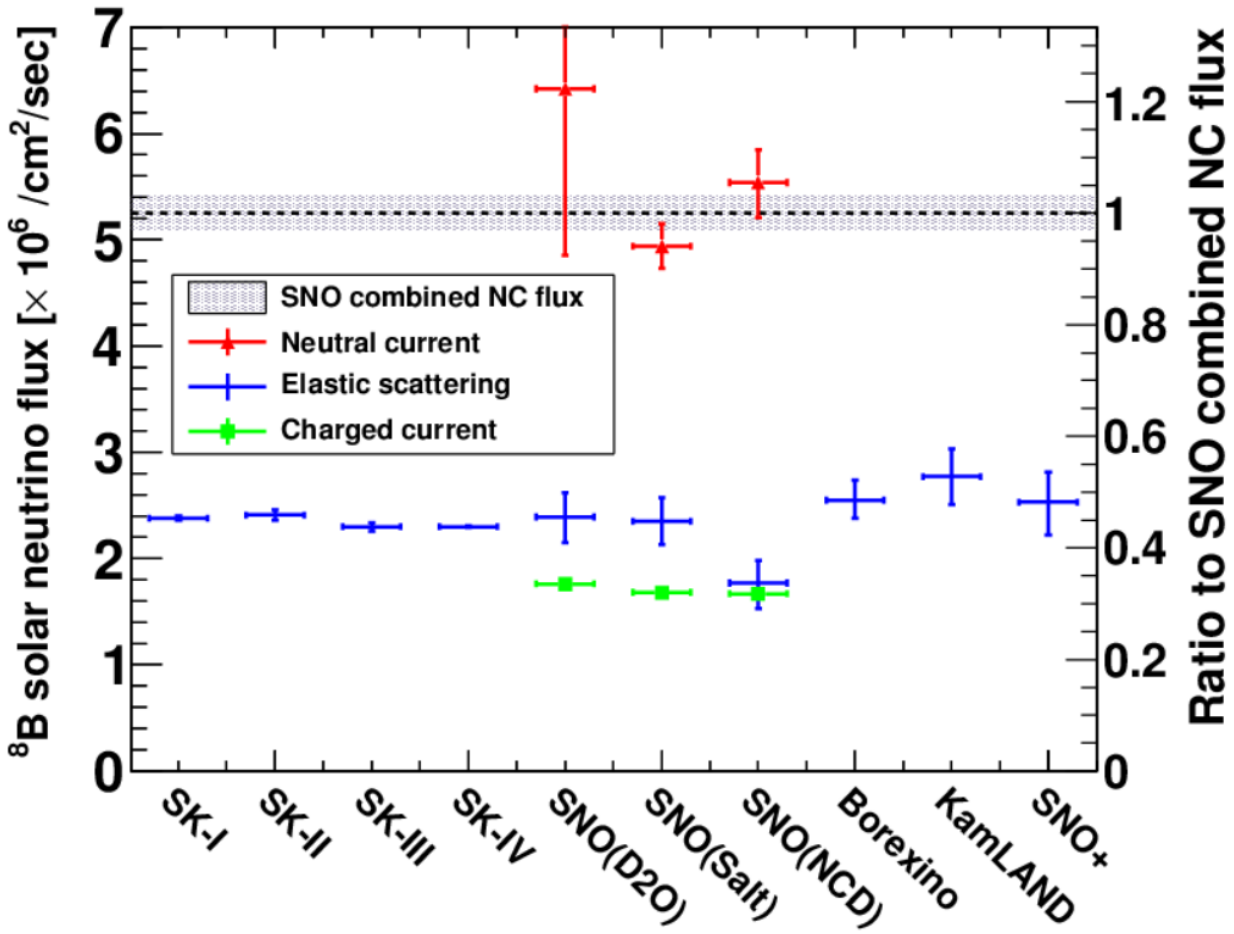

Figure 3.13: The ^{8}B flux measurements for SK, SNO, and Borexino solar neutrino experiments (and KamLAND). The initial SNO+ measurement is provided as well. Figure courtesy of Y. Nakano. These values are reported in the corresponding section for each experiment in this chapter.

Table 3.9: Super-Kamiokande results from the Solar Neutrino Analysis and Solar Neutrino Oscillation Analysis for each experimental phase [42]. The total live time for each phase, the energy averaged ^{8}B flux and corresponding number of extracted signal events from the recoil electron data are given in the top table. The bottom table gives the energy averaged day-night rate asymmetry, as well as the live time for the day and night data sets for each SK-Phase. The energy window over which the measurements are averaged for each SK-Phase is given in each table.

Solar Neutrino Flux & Signal Events

SK Phase	Live Time [days]	Energy Window E_{total} [MeV]	$\Phi^{ES}_{^8\mathrm{B}}\pm(\mathrm{stat})\pm(\mathrm{sys})$ $\times 10^6[\mathrm{cm}^2\mathrm{s}^{-1}]$	# Signal Events $N_{sig}\pm(\mathrm{stat})\pm(\mathrm{sys})$
SK-I	1496.12	5.0 – 20	$2.380 \pm 0.024\ ^{+0.084}_{-0.076}$	$22,404 \pm 226\ ^{+784}_{-717}$
SK-II	791.79	7.0 – 20	$2.41\ \pm 0.05\ ^{+0.16}_{-0.15}$	$7212\ ^{+152.9\ +483.3}_{-150.9\ -461.6}$
SK-III	548.53	5.0 – 20	$2.404 \pm 0.039 \pm 0.053$	$8148\ ^{+133}_{-131} \pm 176$
SK-IV(1664d)	1663.91	4.0 – 20	$2.308 \pm 0.020\ ^{+0.039}_{-0.040}$	$31,891\ ^{+283}_{-281} \pm 543$
SK Combined	4500.34	≤ 20	$2.345 \pm 0.014 \pm 0.036$	$69,655^{+794.9+1986.3}_{-788.9-1879.6}$

Day-Night Rate Asymmetry

SK Phase	live day [days]	live night [days]	Energy Window E_{total} [MeV]	$\%A_{DN}$ $\pm(\mathrm{stat})\pm(\mathrm{sys})$
SK-I	733.15	762.97	5.0 – 20	$-2.1 \pm 2.0 \pm 1.3$
SK-II	383.58	408.21	7.0 – 20	$-5.5 \pm 4.2 \pm 3.7$
SK-III	264.05	284.47	5.0 – 20	$-5.9 \pm 3.2 \pm 1.3$
SK-IV(1664d)	797.43	866.48	5.0 – 20	$-4.9 \pm 1.8 \pm 1.4$
SK Combined	2178.21	2322.13	≤ 20	$-4.1 \pm 1.2 \pm 0.8$

lar analysis [42] for SK-IV and the combined result. SK obtains the measurements of the solar neutrino oscillation parameters by fitting to the recoil electron spectral data combined with the day-night data from all four phases, while constraining the total average ^{8}B solar neutrino flux and $\sin^2\theta_{13}$. The total average ^{8}B solar neutrino flux is constrained to SNO's NC measurement of $5.25 \pm 0.16^{+0.11}_{-0.13} \times 10^6$ cm-2 s^{-1} [47]. The neutrino mixing angle θ_{13} is constrained to the short baseline measurements of antineutrinos from nuclear reactors: $\sin^2\theta_{13} = 0.0219 \pm 0.0014$ for the SK-IV 1664d solar analysis in [42]. Fig. 3.12 shows the $1 - 5\sigma$ confidence level contours of the solar neutrino oscillation parameters Δm^2_{21} and $\tan^2(\theta_{12})$. The resulting best fit values and the total error for the oscillation parameters are $\sin^2(\theta_{12}) = 0.334^{+0.027}_{-0.023}$, and $\Delta m^2_{21} = 4.8^{+1.5}_{-0.8} \times 10^{-5}$ [eV^2].

3.4 Combined Results from all Solar Neutrino Experiments with KamLAND

Combining all the solar neutrino experimental data together (Solar) along with KamLAND [42] yields a value of $\sin^2\theta_{13} = 0.028 \pm 0.015$, which is in good agreement with measurements from experiments measuring antineutrinos produced by nuclear reactors at shorter baselines [23][24][25][26][27] (see Table 2.1). Constraining the value of θ_{13} to these short baseline measurements, the Solar + KamLAND data yields measurements for the solar mixing angle of $\sin^2\theta_{12} = 0.307^{+0.013}_{-0.012}$ and the solar squared mass splitting of $7.49^{+0.19}_{-0.18} \times 10^{-5}$ [eV^2].

The allowed contours for $\sin^2\theta_{12}$ and $\sin^2\theta_{13}$ are shown in the Fig. 3.14 (Fig. 35 of [42]) where green corresponds to the fit to the Solar data (1–5σ lines, 1–3σ shaded), blue to KamLAND (1–3σ), red is the combined result (1–3σ). The reactor neutrino constraint on θ_{13} is denoted by the gold lines. Fig. 3.15 (Fig. 34 of [42]) shows the allowed contours for $\sin^2\theta_{12}$ and Δm^2_{21} which includes the reactor antineutrino constraint to θ_{13}. The solid green lines are again from the fit to the Solar data (1–5σ lines, 1–3σ shaded), blue to KamLAND (1–3σ), red is the combined result (1–3σ). The dashed green lines correspond to the SK+SNO combined fit and are shown for comparison. The SK+SNO combined fit in Fig. 3.15 show that the driving force behind the solar neutrino oscillation parameter fit from the Solar data set is dominated by these two experiments when using the reactor neutrino constraint on θ_{13}.

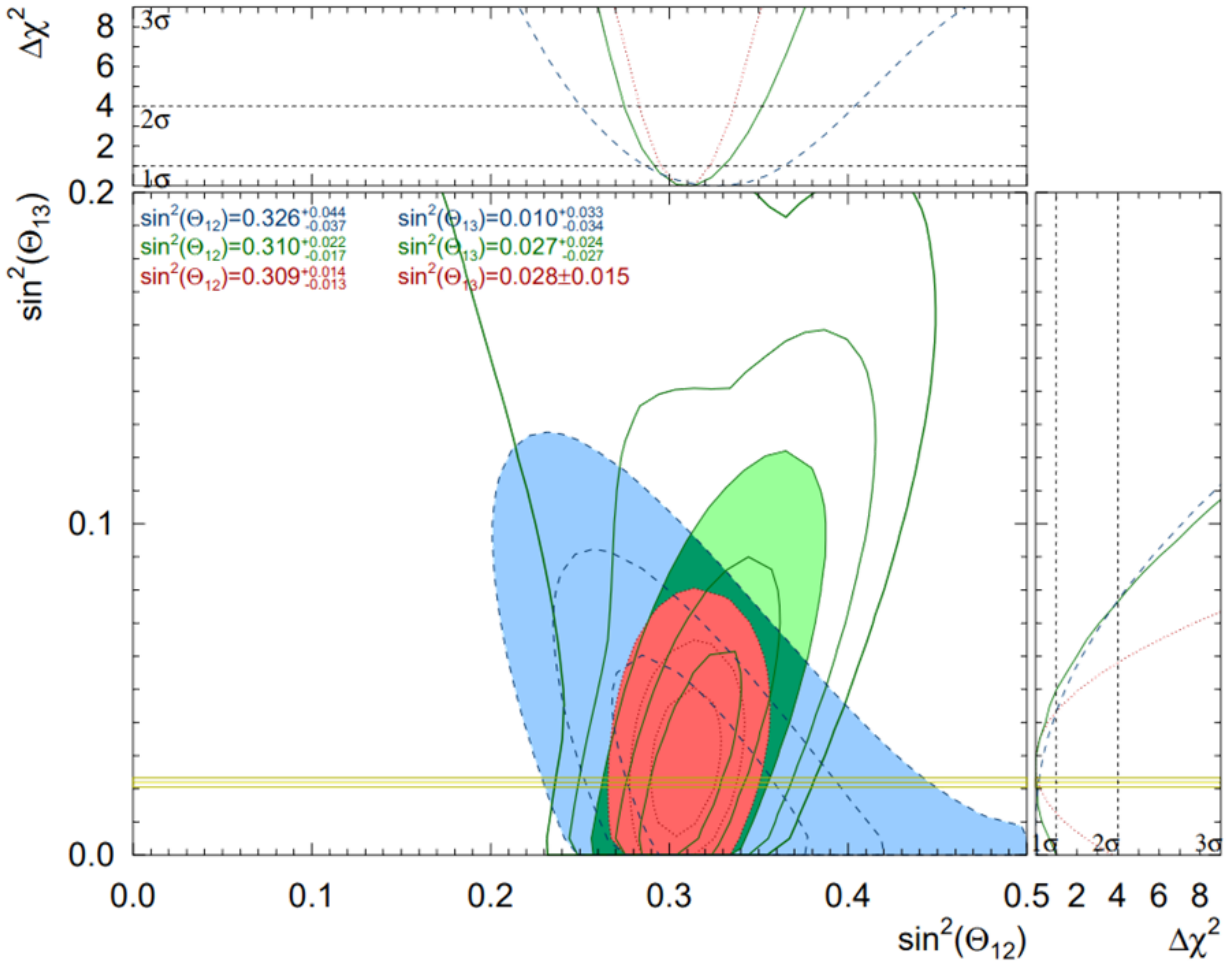

Figure 3.14: The allowed regions for the neutrino mixing angles $\sin^2\theta_{12}$ and $\sin^2\theta_{13}$ from the global fit to all Solar and KamLAND data (Fig. 35 of [42]). Contour lines (shaded regions) represent the $1--5\sigma$ ($1--3\sigma$) allowed region confidence levels. The colors correspond to all Solar data (green), KamLAND data only (blue), and Solar+KamLAND data (red). The best fit to the oscillation parameters is given in the plot. The gold lines are the reactor antineutrino data measurement of $\sin^2\theta_{13} = 0.0219 \pm 0.0014$, which is used as a constraint in 3.15.

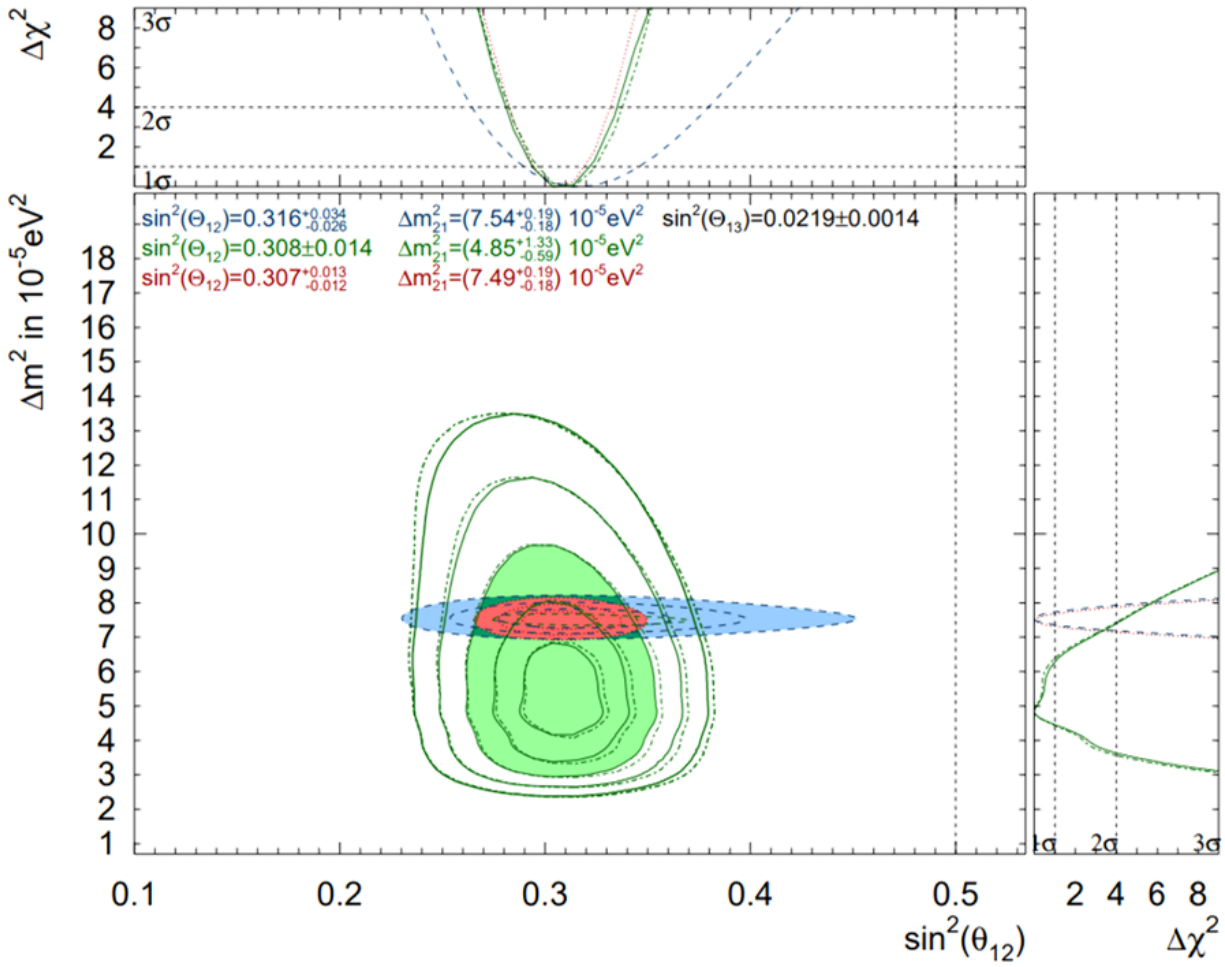

Figure 3.15: The allowed regions for the solar neutrino oscillation parameters $\sin^2\theta_{12}$ and Δm^2_{21} from the global fit to all Solar and KamLAND data with the reactor antineutrino constraint on θ_{13} (Fig. 34 of [42]). Contour lines (shaded regions) represent the 1–5σ (1–3σ) allowed region confidence levels. The colors correspond to all Solar data (green), KamLAND data only (blue), and Solar+KamLAND data (red). The best fit to the oscillation parameters is given in the plot. The solid green lines correspond to the fit to the Solar data. The dashed green lines correspond to the SK+SNO combined fit and are shown for comparison.

Chapter 4

The Super-Kamiokande Experiment

4.1 Overview

Super-Kamiokande (SK) [35] is a 50-kiloton, ultrapure water Cherenkov detector built 1000 m (2700 meters-water-equivalent) underground within the Japanese mountain Ikenoyama. It resides in the "Kamioka mine", a zinc mine owned by the Kamioka Mining and Smelting Company. The experiment has been running since April 1996 and has just begun its fifth phase, SK-V. As relativistic charged particles traverse through the ultrapure water in SK, Cherenkov light is emitted from them while their velocity is greater than the speed of light in the water. This Cherenkov light is observed by photomultiplier tubes (PMTs) which are set into the detector structure and arranged in so-called "super module" sub-structures, denoted by a rectangle inside the SK tank in Fig. 4.2. A layer, or super-layer, in SK refers to the 2.1 m tall band of super modules that make up the PMT support structure of SK.

SK is divided into an Inner Detector (ID) and an Outer Detector (OD) which are optically separated from each other. During SK-III, SK-IV, and SK-V, the ID is observed by 11,129 inward-facing 50 cm diameter PMTs, while the OD employs 1885 outward-facing PMT

assemblies composed of a 20.3 cm diameter PMT and a wavelength shifting plate. During SK-I (SK-II), the number of ID PMTs was 11,146 (5182). Each super module contains two OD PMT assemblies and a four-by-three array of ID PMTs, with the exception of special super modules near the corners of the cylinder. The OD is used as a veto trigger and as a buffer from environmental backgrounds. The ID PMTs are used to detect the Cherenkov light or light-cones produced, for example, by recoil electrons from elastic scattering (ES) of neutrinos or from muons entering the detector. Their phtotcathode covers 40% (19%) of the cylindrical surface of the detector structure for SK-I/III/IV/V (SK-II).

The Kamioka mine is located in Japan in the Gifu prefecture near the city of Kamioka, shown in Fig. 4.1. The detector itself is located at 36°25'33" N, 137°18'37" E, 371.8 m above sea level. The underground experimental areas in the mine form the Kamioka Observatory, overseen by the University of Tokyo's Institute for Cosmic Ray Research (ICRR). In addition to SK, the Kamioka Observatory contains several high-precision low-energy experiments. With the exception of the KAGRA experiment [97], a gravity wave interferometer experiment which has its own dedicated tunnel system, the underground experiments are all accessed via a 1.8 km horizontal tunnel. The overburden reduces the cosmic muon rate to 2.2 Hz ($6 \times 10^{-8}/\mathrm{cm}^2$ s sr), and only muons with an energy above 1.3 TeV will penetrate to the detector, greatly reducing overall backgrounds to many of the SK analyses [35].

Other than SK and KAGRA, ICRR manages many other noteworthy experiments in the mine, including the following: the XMASS experiment [98], a low-mass dark matter detector; CANDLES [99], which searches for double beta decay via ^{48}Ca; NEWAGE [100], a small, direction-sensitive dark matter detector; and the EGADS experiment [101]. EGADS stands for Evaluating Gadolinium's Action on Detector Systems and it is a gadolinium sulfate ($Gd_2(SO_4)_3$) doped water Cherenkov detector whose detector components are the same as in SK. As its name suggests, EAGDS has been an R&D test bed for the planned upgrade of Super-Kamiokande during its fifth experimental phase. EGADS also serves as

Figure 4.1: The location of the Super-Kamiokande Experiment within Japan [35].

a supernova burst monitor and is a part of the SNEWS network, described later, alongside SK. The EGADS experiment has shown that with long-term exposure to 0.20% $Gd_2(SO_4)_3$ solution, the detector components used in SK are unaffected. Of equal importance, EGADS has shown that the optical transparency of the water can be maintained at similar levels to the ultrapure water transparencies in SK by the "Band-Pass" water system, described later.

The Kamioka Observatory originally housed the predecessor to SK, the Kamioka-Nucleon-Decay-Experiment (KamiokaNDE), whose name SK pays homage to. However, the "NDE" at the end of Super-Kamiokande now has a dual meaning: the original acronym, as well as Neutrino Detection Experiment. The reactor antineutrino experiment KamLAND, a separate institutional entity from ICRR, now occupies the experimental cavern once home to Kamiokande. There are four primary SK experimental areas, with Fig. 4.2 showing the schematic layout of the SK experiment in the mine. The first area is the SK cavern in which the detector tank sits, with the dome above the tank housing the front-end electronics, calibration devices, and other detector systems. The second area houses the linear accelerator (LINAC), a medical particle accelerator used for energy calibrations, along with its control room. The third area is the SK control room, where shift workers reside and is the location

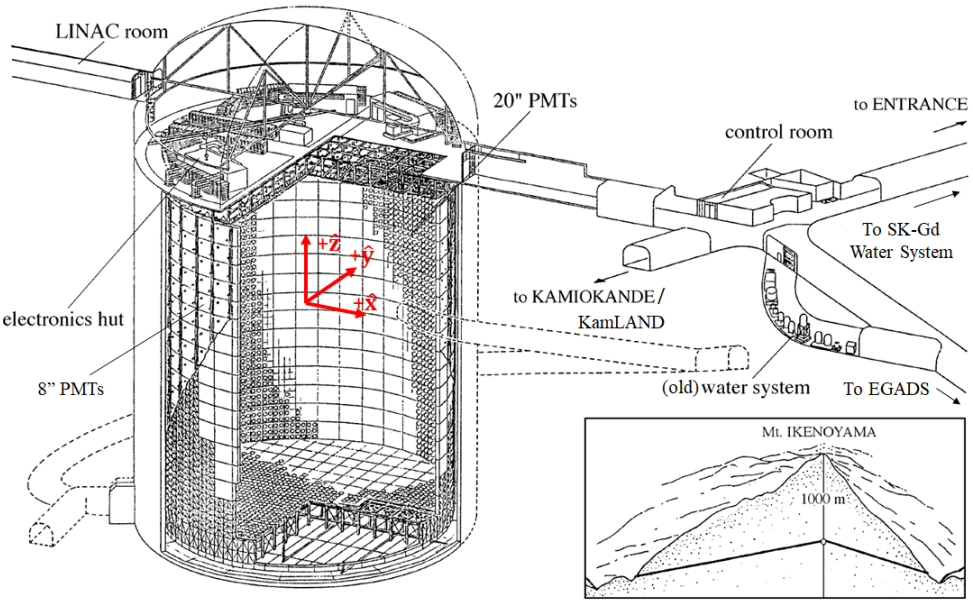

Figure 4.2: The layout of the Super-Kamiokande Experiment within the Ikenoyama Kamioka mine [35]. The rectangular coordinate system used in SK is inset into the detector for reference.

of the online computer system. The online computer system builds the detector events by collecting data coming from the front-end electronics on top of the tank. After building the events, the system ships the data to storage computers for further processing and analysis. These storage computers are located in the ICRR office-laboratory, or the Kenkyuto, located in Higashi-Mozumi down Route 41 toward Toyama City. The final area is the SK water system which cleans the water to minimize contaminants and maintain the ultrapure water transparency. While this water system was used prior to 2019, a new water system for SK-Gd has been constructed that will purify the water without removing the added $Gd_2(SO_4)_3$.

The inner surface of the dome, as well as the entrance area and control room, is covered in "Mineguard," a polyurethane epoxy made by the Canadian company Urylon Plastics Incorporated and the Mining Industry Research Organization of Canada [102]. The coating has two primary components: Polyol Resin and Diphenylmethane Disocyante. It is used as a

seal against the radon gas emitting from the rock in the mine, which is a serious background in low energy analyses like the solar neutrino analysis. Radon gas is also a health hazard for humans. While Mineguard blocks the radon gas produced in the mine rock from entering into the SK dome, it itself produces radon in much smaller quantities. Because Mineguard produces radon, a special formulation of Mineguard-C6 was created for in-tank use in SK to seal the water leak in the tank walls (see Sec. 4.2.1 and Sec. 4.2.2.).

The SK collaboration was created by the union of the Kamiokande and Irvine-Michigan-Brookhaven (IMB) collaborations. Both collaborations performed searches for proton decay theorized from grand unified theory models and had the serendipity to see supernova burst neutrino events from the 1987a type-IIa supernova. They additionally made measurements related to atmospheric neutrinos produced in cosmic ray showers, and Kamiokande made measurements of solar neutrinos. SK was designed as a scaled up version of Kamiokande to improve searches for nucleon decay, as well as to detect neutrinos from various sources, including supernova neutrinos, the ^{8}B solar neutrinos produced in the core of the Sun from fusion processes, atmospheric neutrinos, and neutrinos produced in man-made neutrino beams (i.e. by the K2K and T2K experiments [103]).

In addition to external collaborations with the T2K (and previously the KEK) experiment, SK sends signals to the SuperNova Early Warning System (SNEWS [104]), as the neutrino burst from a supernova arrives prior to the optical component. SNEWS is a collaboration between many neutrino, gravity wave, and telescope experiments that alert the community of astronomers and physicists that a supernova burst has been detected. When SK detects a supernova burst, the collaboration gives the community the reconstructed direction of the supernova in order for the optical telescope experiments to train their "eyes" on the supernova in time to catch the full optical component of the explosion.

Currently, the Super-Kamiokande Collaboration has $\sim$150 collaborators, with scientists and engineers from Japan, the United States, Canada, China, Korea, Poland, Spain, France,

the United Kingdom, and Italy. The primary funding for the SK experiment comes from Japan's Ministry of Education, Culture, Sports, Science and Technology, with additional significant support by the U.S. Department of Energy and National Science Foundation. Additional funding is provided by the Spanish Ministry of Science and Innovation, the National Science Foundation of China, the Research Foundation of Korea, and the Korean Ministry of Science and Technology. Though a detailed, but limited, overview of the SK Experiment will be described here, further details can be found in [35].

4.2 The Experimental Phases of Super-Kamiokande

The SK experiment has been collecting data since 1996 over the course of four completed experimental phases known as SK-I through SK-IV and just recently began SK-V. The experiment has made many measurements of the properties of solar and atmospheric neutrinos, as well as searched for neutrino sources from the cosmos, sterile neutrinos, and nucleon decay. SK has been the far detector for two different neutrino beam experiments: the KEK to Kamioka (K2K) experiment (June 1999 to November 2004) and currently for the Tokai to Kamioka (T2K) experiment. Details of each SK-Phase prior to SK-V which are relevant to SK low energy analyses are summarized in Table 4.1. Because it takes several months to fully clean the water to the ultrapure status desired for analyses, the actual data period is delayed by several months relative to the start of each SK-Phase.

The SK-I Phase ran for five years, starting in April 1996 and ending in July 2001. The SK-I phase had 11,146 ID PMTs yielding a photocathode coverage of 40% and 1885 OD PMTs. At the end of this phase, the tank was drained to refurbish the detector and to replace bad PMTs that were either dead or had a high dark rate. Once the refurbishment work was completed in September 2001, the detector began refilling with water. During this refilling, one of the 50 cm PMTs on the bottom imploded and created an energetic

shockwave, setting off a chain reaction that destroyed all of the PMTs below the waterline. As the detector was about 30 m full, almost 6800 ID and 1100 OD PMTs were destroyed. The tank was drained, and the glass and photocathode residue was cleaned up. To collect data while the Hamamatsu Company manufactured replacement PMTs, the surviving ID PMTs and spares were redistributed throughout the detector, and destroyed or damaged OD PMTs were replaced with new ones. To prevent a chain reaction from occurring again, protective cases, also called PMT housings, were manufactured to encapsulate and shield the 50 cm PMTs. These cases consist of a fiber reinforced plastic (FRP or fiberglass) hull and an acrylic window. The PMT cases were installed in the process of redistributing the ID PMTs.

This second phase, SK-II, ran for three years from October 2002 to October 2005. The reduction in the number of PMTs, 5182 ID tubes and 1885 OD tubes, resulted in a reduced photocathode coverage of 19%, similar to the original Kamiokande Experiment, and an increase in the energy threshold for low energy analyses. Once Hamamatsu finished with the production of the new 50 cm PMTs in October 2005, the SK-II phase ended, and the detector was once again reopened to install the new tubes, along with newly made PMT housings for them. This once again brought the photocathode coverage back up to the 40% mark from SK-I. This refurbishment period is known as the full reconstruction and lasted until July 2006, when the refilling of the tank with pure water had been completed and data collection began. At that time, the SK-III data period started, lasting for three years. In August 2008, the detector was turned off to upgrade the front-end electronics. A method of precision control of the water temperature within the water system and the SK tank to prevent convection within the ID was developed during SK-III, reducing backgrounds for the SK low energy analyses.

The original front-end electronics, specifically the data acquisition system (DAQ), were replaced with upgraded Ethernet capable electronics after the end of SK-III. More on the SK

Table 4.1: Summary of the pertinent information of each SK-Phase for the SK Solar Neutrino and NSI analysis, with the live time of the solar neutrino data set given in days for the day, night and total data sets. The dates given in the Phase Start (Data Start) row are the beginning dates for the respective SK-Phase (Solar data set). The details of these analyses per SK-Phase, including the SK day-night rate asymmetry A_{DN}, is given in Table 3.9. SK-V started in Feb. 2019, but the official Data Start date has yet to be determined. In the analysis presented in this work, the published results of SK-IV(1664d) are used (up to Feb. 1, 2014), as the data set and results for the whole of SK-IV have yet to be finalized.

Information	SK-I	SK-II	SK-III	SK-IV	SK-V
Phase Start	April 1996	Oct. 2002	July 2006	Sep. 2008	Feb. 2019
Data Start	Nov. 1996	Dec. 2002	Oct. 2006	Oct. 2008	···
End Date	July 2001	Oct. 2005	Aug. 2008	Dec. 2018	···
Live time	1496.12	791.79	548.53	2859.68	···
Day Live	733.15	383.58	264.05	1381.32	···
Night Live	762.97	408.21	284.47	1478.36	···
# ID PMTs	11,146	5182	11,129	11,129	11,129
PMT Coverage	40%	19%	40%	40%	40%
# OD PMTs	1885	1885	1885	1885	∼1865
DAQ	ATM	ATM	ATM	QBEE	QBEE

electronics and DAQ will be discussed later in Sec. 4.5. Once the upgrade to the front-end electronics was complete in September 2008, the SK-IV phase started. SK-IV saw several additional improvements to the overall detector and data quality, including a replacement of the high voltage system for the ID PMTs and further improvement of the water temperature control method began in SK-III.

The Wideband Intelligent Trigger (WIT) [105][106], an ultra-low energy DAQ system, was introduced during this phase. The WIT system is used to push the trigger threshold down as low as possible. It simultaneously triggers on and reconstructs low energy recoil electrons down to 2.5 MeV in kinetic energy with almost 100% efficiency, while rejecting events near the PMT structure. Although WIT is currently running and collecting data, the data it has collected for SK-IV has not yet been analyzed and merged into the official SK solar neutrino analysis.

SK-IV also saw the radon measurement system in the mine upgraded, and saw the

removal of the membrane degasifier system from the SK water system since it had been been discovered to be a radon source. In February 2018, the water system was intentionally altered to better understand water convection in SK. Because of this work and subsequent calibrations preparing for the next SK-Phase, the data from 2018 is currently excluded from the low energy analyses. The preliminary full data set for the low energy analyses includes all data collected from October 2008 until December 31, 2017.

The SK-IV phase officially ended in May 2018 to perform detector maintenance and to prepare to upgrade the detector to the SK-V phase, the SK-Gd Experiment. SK-V officially started in February 2019. A goodly portion of my time during my PhD has been involved in performing R&D at UCI and in Japan at EGADS for the SK-Gd upgrade for SK, including the efforts in preparing for and participating in the 2018 SK detector maintenance.

4.2.1 The 2018 SK Detector Maintenance

The 2018 detector maintenance lasted from the end of May 2018 until mid October 2018, with many more tasks than previous maintenance periods. UCI led the effort for the replacement of OD PMTs, the cleaning of the structure, and the replacement of the OD Tyvek. While most collaborators outside of ICRR participated in the maintenance for one to three weeks, UCI maintained a presence on-site the full time. For myself, I spent ten weeks working 100% time in the tank as a specialist, while training and leading teams in the OD work.

Work began on the top of the detector after some initial draining of the water to expose the top and initial portions of the detector wall. Continued periods of draining allowed for access to all of SK from floating platforms and inflatable rafts in the ID, and an annulus-shaped floating floor in the OD that spanned the entire OD region, similar to previous maintenances. Since only the OD top could be reached from the tank top by ladders, four hoist-operated window-washing baskets, or "gondolas," were used to access the various parts

of SK during the maintenance. Two of the gondolas granted access into the detector from the tank top, one for an ID floating platform and the other for the OD floating floor which brought workers and equipment in and out of the tank. The other two gondolas were set up inside the OD on a track that allowed them to scroll azimuthally in addition to their movement up and down. The azimuthal gondolas provided access to the whole height of the OD barrel above the floating floor. After the tank was fully drained, the bottom of the detector, the OD bottom, was accessed by both the ID and OD gondolas, as well as the inclined pit, a tunnel outside the detector that starts near the SK water system and winds its way down to the access hatch at the bottom of the SK tank wall (the dashed tunnel shown in Fig. 4.2).

The primary maintenance task was to prepare the detector for the introduction of the gadolinium sulfate during the upcoming SK-V phase, the SK-Gd experiment. This included sealing a long-standing leak in the stainless steel walls of the detector, so that no gadolinium sulfate would seep into the environment (see Sec. 4.2.2), and removing any rust found in the tank. With the addition of the $Gd_2(SO_4)_3$ into the SK water, the pH of the resulting solution will drop, thus becoming an acidic environment. This could liberate the rust off of the stainless steel of the structure and into the water, drastically decreasing the transparency of the water. Other tasks included the usual replacement of dead or noisy ID and OD PMTs, though it was found that for about twenty OD PMTs the signal cable had been flooded with water, and it was decided not to recover them.

The majority of the work during this refurbishment occurred in the OD, including detector upgrades and a painstaking cleaning of the stainless steel detector support structure and stainless steel outer wall. The black-white Tyvek that serves as an optical barrier between the dead region of the PMT support structure and aids in light collection in the OD was largely left in place in the OD top, but was completely removed in the OD barrel and bottom regions to clean the support structure. The white Tyvek that is used as a reflector on the

outer surface of the OD was also fully removed and replaced.

With the various Tyvek removed, the exposed support structure and outer wall were wiped down to remove any biologically produced films (bio-film) and to remove diesel fume residue originating from the original detector construction. The PMT glass left over from the 2001 accident, itself a radioactive source and a sharps danger for the cleaners wiping down the structure, was removed as best as possible by vacuum cleaners. The residue on the structure was very dark in color, and measurements with a germanium detector found it to be very radioactive. This residue is a source that contributes to the radioactive backgrounds in the SK low energy analysis. Because of the drop in pH that will occur when adding in the $Gd_2(SO_4)_3$, the dark radioactive substance would spread through the detector. It would lead to reduction in the quality of the transparency in SK and an increase in radioactive backgrounds away from the PMT wall. To alleviate this danger, as much of the residue was removed from the structure as was possible.

All the rust found in the tank was removed and the affected areas re-passivated by electric rust-removal machines. The outer wall was steam-cleaned to further sterilize and remove any residual bio-film. A special tape was used to remove any excess residue, glass, and lint left over from the wiping and steam-cleaning of the structure and outer wall. Once the outer wall was clean, workers from Mitsui & Co., the company that built the SK steel structure, applied a special epoxy, Mineguard-C6 (see Sec. 4.2.2), to the weld seams to seal any holes. With all cleaning and PMT replacement work completed on the support structure, the black-white Tyvek was replaced for the exposed layer.

Every three days the water was drained by $\sim$2 m to expose the next horizontal weld seam, which could include part or all of the next super-layer, and maintenance would commence for the newly exposed parts of the detector. Once the detector was fully drained and the work on the bottom was finished, the outer white-white wall Tyvek was replaced, and the detector was sealed up to begin the refilling process. The top OD region took about

three-and-a-half weeks to complete in total, while the bottom OD region, due to the extensive application of Mineguard-C6 on the entire OD floor, took almost a month and a half to complete. With the tank drained and the OD floor work complete, the black-white Tyvek on the floor was replaced, as well as the white Tyvek on the outer walls of the OD.

On the top and bottom of the OD, plumbing was removed, added, or altered for the installation of the new water purification system. A new light injection system used for calibration purposes was also installed into the structure along the whole height of the detector, as well as along the top and bottom. This new light injection system uses optical fiber guides to direct laser light of varying wavelengths into the ID at the PMT wall at various heights. The broken fiber optic cables in the OD light injection system that was already in place were replaced. The OD light injection system is used for OD calibrations.

In the ID, the SK Calibration working group photographed the orientation of the dynode for each PMT to better understand and simulate their response. They also took measurements of the residual B-field in the ID region near the PMTs at every water level with the compensation coils used to negate the Earth's magnetic field turned on. These coils negate the Earth's B-field within the tank as to ensure the electrons produced by the PMT photocathode make it to the PMT dynode, which will be discussed in greater detail later (Sec 4.4). These two tasks were performed to better simulate these aspects of the detector and to reduce systematic uncertainties.

Once all the maintenance work was completed, the tank was refilled, and the final work on the OD top was completed in late December of 2018.

4.2.2 The SK-Gd Upgrade for Super-Kamiokande

The SK-Gd experiment is an idea proposed by John Beacom and Mark Vagins [19] that entails doping the SK ultrapure water with 0.2% $Gd_2(SO_4)_3$ to better search for and measure the Diffuse Supernova Neutrino Background (DSNB) [18]. Both neutrinos and antineutrinos are produced by all core-collapse supernova throughout the history of the cosmos and comprise the DSNB. The DSNB antineutrinos interact in SK via the β-decay reaction

$$\bar{\nu}_e + p \rightarrow e^+ + n, \tag{4.1}$$

where the Cherenkov light from the prompt positron will be detected by the PMTs. The γs produced from the annihilation of the positron are below Cherenkov and thus invisible to SK. Due to the lack of a magnetic field in the tank, positrons and electrons are indistinguishable from one another in SK.

Without a positive identification of the prompt positrons, these inverse β-decay (IBD) events are difficult to distinguish from events caused by radioactive β-decays due to spallation (or solar neutrino elastic scattering recoil electrons). The detection of the associated neutron in the IBD event, within the expected capture time, would uniquely identify the event. The neutron will eventually ($\sim$200 μs) capture on the hydrogen in the water, but the long capture time and the small amount of energy released (a 2.2 MeV γ) make for a small detection efficiency ($\sim$20%) in SK. Gadolinium has a much higher neutron capture cross section, so the addition of a small concentration of Gd results in a shorter capture time and a larger light yield from the neutron capture (8 MeV γ cascade). This increases the overall neutron detection efficiency and lower backgrounds to the DSNB analysis [19]. The percent of neutron captures as a function of Gd concentration in water is plotted in Fig. 4.3, where the horizontal axis is in logarithmic scaling. Since approximately half of the mass of gadolinium sulfate is due to the Gd, 0.10% Gd corresponds to a solution of 0.20%

$Gd_2(SO_4)_3$).

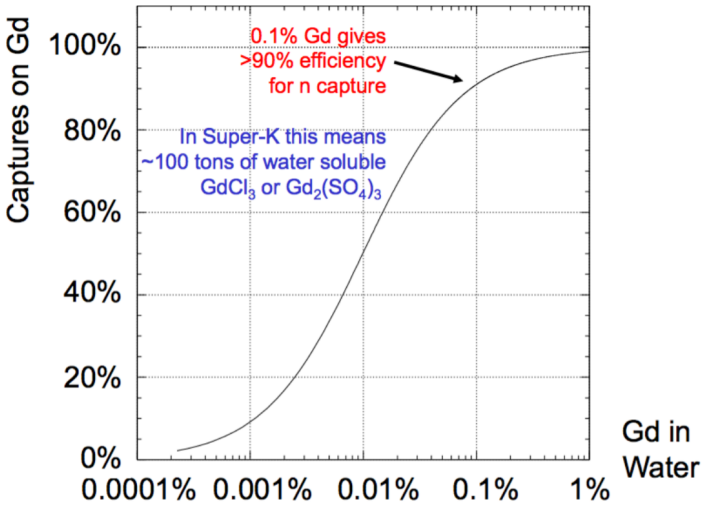

Figure 4.3: The percent of neutron captures on gadolinium in water as a function of Gd concentration [107]. A concentration of 0.10% Gd corresponds to a solution of 0.20% $Gd_2(SO_4)_3$.

The Band-Pass Water System

While details of the SK water system are described in Sec. 4.6.1, it is useful to briefly discuss them here as well, prior to discussing the Band-Pass water system. Standard ultrapure water systems, like the one SK employed prior to SK-V, consist of de-ionization resin (DI), ultraviolet light (UV) to kill bacteria, and several types of filters to remove particulates, including the bacteria, and even ions from the water. Mechanical filters are passive elements made from polypropylene that catch particles larger than the filter's pore size. The ultrafilter (UF) is a membrane filter with a pore size of $\sim$ 10 nm, smaller than the 0.2-micron mechanical filter used to catch bacteria. Reverse osmosis membranes filter water by pressurizing water against a semipermeable membrane high enough to overcome osmotic pressure, which allows the solvent (water) through but not the solute (inorganic materials). Water systems sometimes employ "total organic carbon" 185 nm lamps (TOC) tuned to the typical energy level of the chemical bonds in organic compounds to ionize them. With the organic

compounds ionized, the DI will remove them. A schematic of the standard SK water system used during SK-I – SK-IV is given in Fig. 4.21. At UCI, a simplified version of the standard water system, where the UF and RO membranes have been removed from the water system, has been used for SK-related studies (described later).

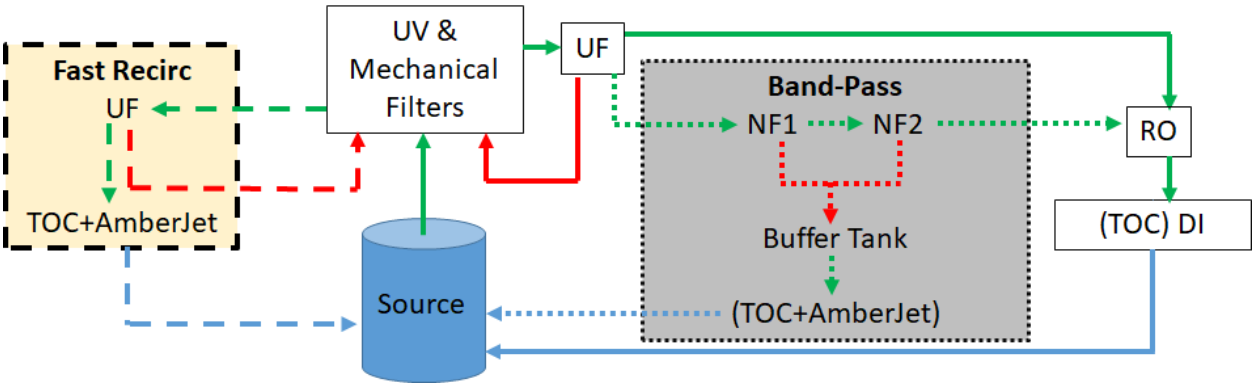

Figure 4.4: Illustration of a standard water system, the Band-Pass water system, and the Fast Recirc water system. The solid lines correspond to a standard water system and the dotted lines correspond to the addition of the Band-Pass system to a standard water system. The dashed lines on the left side of the figure correspond to the Fast Recirc system. The red lines correspond to the water stream rejected by the UF and NF membranes. Blue lines denote purified water. A schematic of the standard SK water system used during SK-I – SK-IV is given in Fig. 4.21.

While the standard water system maintains ultrapure quality water, the design also removes Gd^{+3} ions by the DI. A new type of water filtration system that retains the $Gd_2(SO_4)_3$ while maintaining the ultrapure water quality was conceptualized by Mark Vagins and designed by Roy Hall of South Coast Water. This new water system is known as the Band-Pass system. In addition to mechanical filters, the Band-Pass system employs stages of membranes, UF and nanofilters (NF), that allow only a specific range of particle sizes through, similar to an electronic band pass filter. The UF membrane has a larger pore size than the Gd and sulfate ions, allowing these ions to pass through, while trapping impurities larger than the ions in a continuous loop. The NF membranes filter out the Gd and sulfate ions, as their pore sizes are smaller than these ions. Two stages of NF membranes are used to ensure as much of the gadolinium sulfate is removed from the water stream prior to using

RO, TOC and DI to achieve the ultrapure quality. The Gd and sulfate ions removed by the NF are sent to a collection tank where they are recombined with the purified water. The water in the collection tank is then sent through TOC and a special anion resin before returning the now cleaned solution to the tank. The original intent behind using this anion resin, AmberJet, is to extract any uranium introduced with the gadolinium sulfate through absorption into the resin beads. It was found that AmberJet also improves the water quality. The AmberJet is treated so that it leaves the Gd alone, while still removing anions from the water. A prototype system was built at UCI and demonstrated that water transparency could be maintained at levels comparable to the SK-III and SK-IV measured values.

An independent, fast re-circulation water system (Fast Recirc) that uses UF, UV, TOC, and AmberJet has also been used with the EGADS detector as an alternative method of maintaining the water transparency. Both the Band-Pass and Fast Recirc can be used simultaneously, producing the highest water transparency. An illustration of these three types of water systems is shown in Fig. 4.4.

EGADS Water Transparency Tests

The EGADS experiment, described previously, uses a scaled up version of the UCI Band-Pass system prototype to maintain high levels of water transparency with both ultrapure water and 0.2% $Gd_2(SO_4)_3$ solution. The detector is fully instrumented with the same equipment and materials as SK, and ran with the 0.2% $Gd_2(SO_4)_3$ solution continuously for $\sim$3 years. UCI, along with Roy Hall, is responsible for maintaining the EGADS water systems.

The water transparency for the detector is measured with the Underground Device Evaluating Attenuation Lengths (UDEAL) designed by Michael Smy. UDEAL works by firing seven lasers of different wavelengths through a vertical water column of variable height (a maximum height of 8.2 m). The laser beams traverse the water, and the amount of light

lost in the water is determined by two integrating spheres which measure the light intensity before and after passing through the water column. Before injection into the water, a beam-splitter sends 10% of a laser beam into the 4 inch diameter integrating sphere as a reference, while the lower 12 inch integrating sphere receives the light transmitted through the water column. The integrating spheres sample the laser light intensity using photodiodes. The light extinction curve for each laser is formed through taking these measurements as a function of height. The curve is fitted with an exponential function from which the attenuation length $1/\alpha(\lambda)$ is extracted, where α is the attenuation coefficient.

The parameter used to describe the water transparency measurement from UDEAL is the percent of Cherenkov light left after traveling through 15 m of water (%LL15m), as 15 m is the average distance Cherenkov light travels in SK. To construct this parameter, the $\alpha(\lambda)$ measurements of the seven lasers from a run are combined with weights based on the convolution of the Cherenkov spectrum with the PMT response illustrated in Fig. 4.14. The %LL15m value is given by

$$\%\text{LL15m} = 100 \sum_{i}^{7} w_i \times e^{-L \cdot \alpha(\lambda_i)} \tag{4.2}$$

where $L = 15$ m, the index i runs over the lasers of wavelength λ, w is the weight for a given laser, and α is the measured attenuation coefficient for a given laser. The list of the λ and w for each laser used in UDEAL is given in Table 4.2.

Table 4.2: The wavelength of the lasers used in UDEAL and their weights in the %LL15m calculation (Eq. 4.2).

λ [nm]	337	375	405	445	473	532	595
w	0.252	0.253	0.206	0.141	0.106	0.039	0.003

While I continually monitor the UDEAL system, in 2012 I upgraded it to automatically run every day, sampling positions in the bottom, middle, and top of the detector volume.

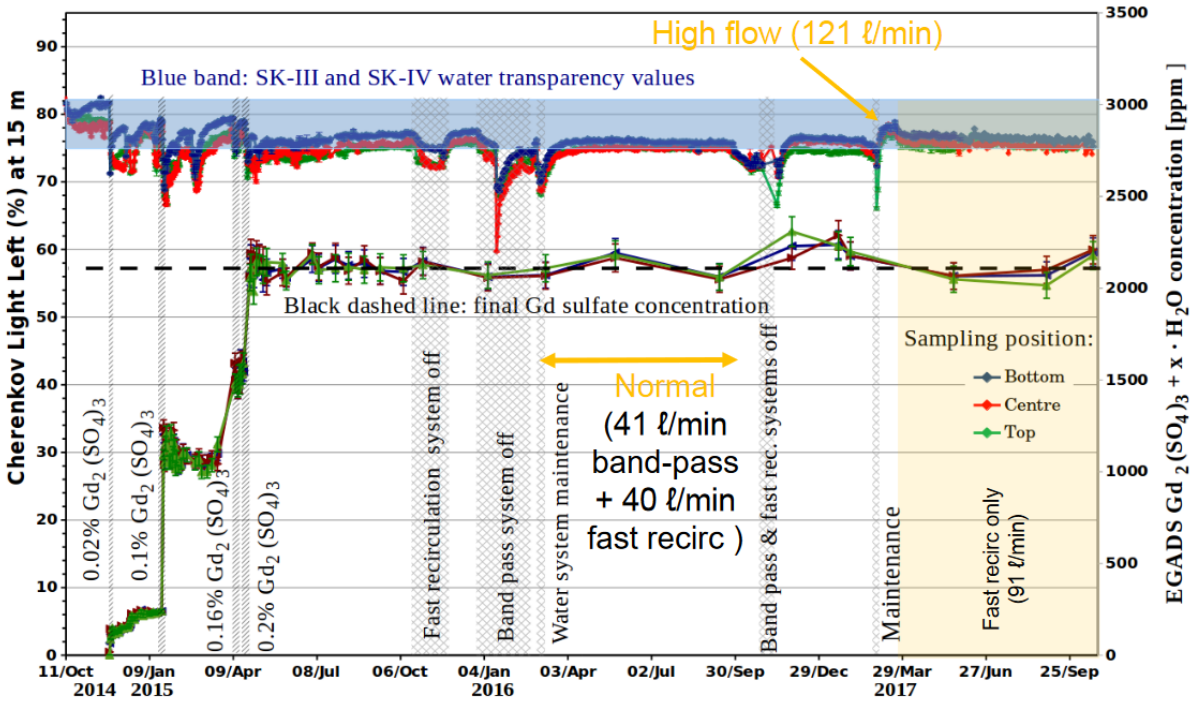

Figure 4.5: Water transparency %LL15m and gadolinium sulfate concentration measurements in EGADS. The dense set of data points arranged higher on the plot correspond to the UDEAL %LL15m measurements (left axis) at various positions (marker and line colors) while the blue band corresponds to the SK-III and SK-IV. The slightly sparser set of data points are measurements of the gadolinium sulfate concentration of the solution in EGADS in ppm for the same sampling points. Other details related to maintenance and how the Band-Pass and Fast Recirc were running are also denoted in the figure. Figure courtesy of Lluis Marti Magro and Mark Vagins.

The results of these daily runs for a recently completed EGADS phase are shown in Fig. 4.5 and demonstrate the ability of the EGADS water systems to maintain the same water transparency as the ultrapure water in SK-III and SK-IV. In the figure, the dense set of data points arranged higher on the plot correspond to the UDEAL %LL15m measurements (left axis) at the top (green), center (red) and bottom (blue), while the blue band corresponds to the SK-III and SK-IV measured values. The slightly sparser set of data points below the %LL15m data are concentration measurements in ppm of the gadolinium sulfate solution in EGADS for the top, center, and bottom sampling points. Other details related to maintenance and how the Band-Pass and Fast Recirc were running are also denoted in the figure. These results were used when simulating the effect that a 0.2% $Gd_2(SO_4)_3$ solution would have on light propagation in SK, described in Sec. 5.2.1.

Soak Study Tests at UCI

For the SK-Gd experiment, the small leak in the SK tank wall, amounting to a loss of ∼3 tons of water per day, had to be sealed during the 2018 maintenance to ensure that no gadolinium sulfate introduced into the detector will leak into the environment. Several new cracks and holes were discovered in the weld seams and steel plates of the OD during the maintenance. To stop any leaks, all of the weld seams in the OD wall and the entire surface of the OD floor needed to be covered with a sealing material like a glue or an epoxy. The sealing material needed to meet the four requirements for use in SK:

- It will not dissolve in ultrapure water or the 0.2% $Gd_2(SO_4)_3$ solution.
- The optical transparency of the water with and without Gd must be maintained with the introduction of the sealing material. Any emanations from the sealing material must be removable by the water system.
- It must have very low radioactivity so that it does not add significant additional back-

grounds into the detector.

- It must have the proper mechanical properties, and it must adhere to the stainless steel wall. It must maintain its integrity if it stretches for several millimeters due to pressure-induced distortions of the tank wall.

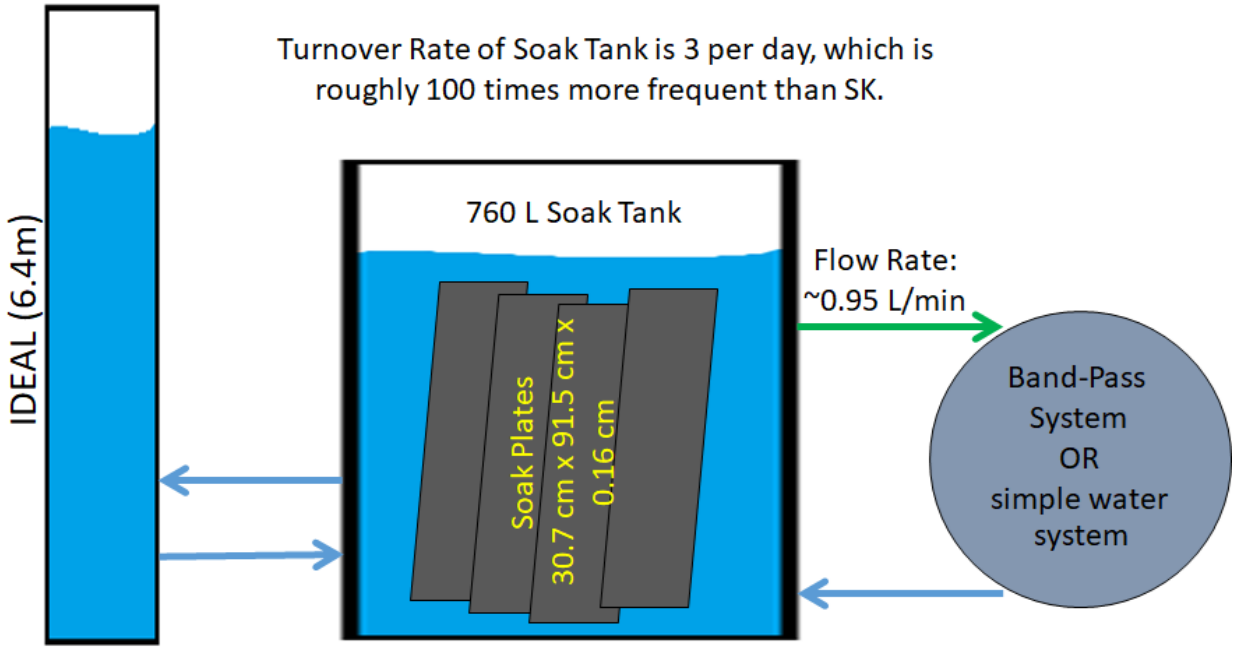

Figure 4.6: Illustration of the setup for the UCI soak studies including IDEAL, the Soak Tank with inserted soak plates covered in sealing material, and the water purification sytem.

Extensive soak studies (optical transparency measurements for various sealing materials) were carried out at UCI by myself over the course of several years using the Irvine Device Evaluating Attenuation Lengths (IDEAL) and the UCI water systems. An illustration of the UCI soak study is given in Fig. 4.6. IDEAL is the prototype for UDEAL and works in the same way, though it has a 6.4 m pipe. The water column in the IDEAL pipe comes from the "soak" tank in the UCI water system. The soak tank houses stainless steel plates covered in the sealing material to be soaked and studied. The surface area of the plates, water volume of the tank, and turnover rate for cleaning of the water are designed to scale to the same parameters in SK. The UCI water system is designed to mimic either SK's standard "simple" water system or to clean the water with the Band-Pass system.

The various UCI water systems were upgraded and maintained in large part by myself since 2012, along with the help of our project engineer Jeff Griskivich. The %LL15m results of soak studies for various sealing materials performed at UCI with ultrapure water cleaned by a simplified water system (described previously) are given in Fig. 4.7.

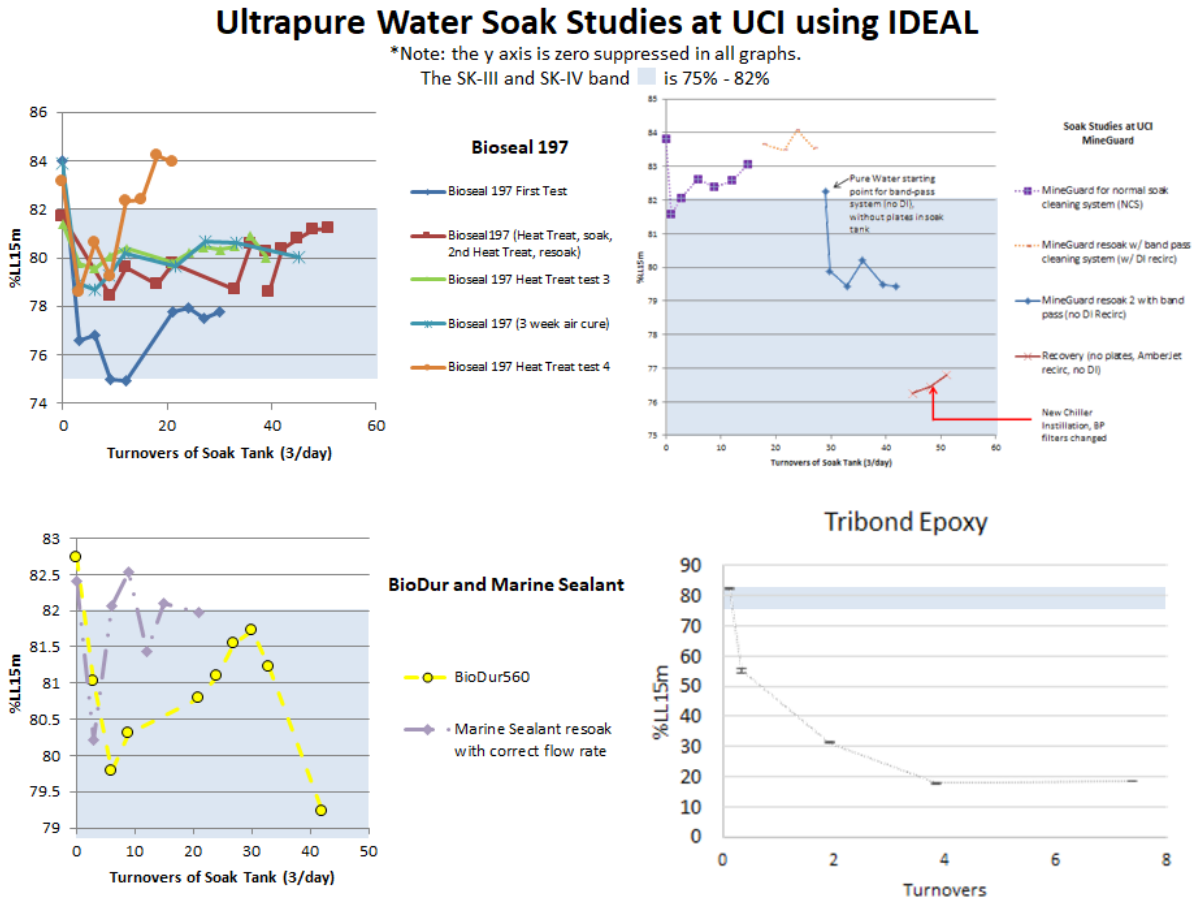

Figure 4.7: %LL15m results for various UCI soak studies using sealing materials immersed in ultrapure water. The ultrapure water was cleaned by a simplified water system for these studies using only UV, mechanical filters, TOC and DI. The light blue band corresponds to the SK-III and SK-IV water transparency measurements.

The sealing material candidate that was used to seal the leak in SK during the 2018 maintenance is a type of Mineguard epoxy known as Mineguard-C6, specially designed to meet the four criteria previously described. Mineguard-C6 replaces some of the materials in the original formulation. It uses fumed silica and calcium carbonate to reduce the epoxy's

radioactivity. Additionally, polyurea is used in the Mineguard-C6 instead of polyeurothane to avoid issues with hydrolysis as polyeurothane breaks down in water. In the first test soaking Mineguard-C6 plates in ultrapure water, the simple water system was used and maintained SK level water transparencies. A second long-term test was performed using the Band-Pass. New Mineguard-C6 plates were soaked in ultrapure water and in the three progressively stronger concentrations of $Gd_2(SO_4)_3$ solution that mimic the planned introduction of gadolinium sulfate into SK for the SK-Gd experiment. The results from these studies (Fig. 4.8) showed that the effects on the water transparency due to the Mineguard-C6 were minimal in ultrapure water.

While the initial results for the Mineguard-C6 in various concentrations of gadolinium sulfate were acceptable, it was found that the TOC lamp used in conjunction with the AmberJet in the Band-Pass system had been burned out for a long time. After replacing the quartz housing and the bulb, the %LL15m measurements of Mineguard-C6 plates soaked in a 0.2% $Gd_2(SO_4)_3$ solution returned to SK quality transparency levels. To verify the lamp replacement is what had brought the transparency up, the lamp was turned off manually, resulting in the drop in the transparency on the right of the figure. This showed the necessity of using TOC to remove emanations from the Mineguard-C6.

Current Status of SK-Gd

Currently, SK is operated with pure water, utilizing a Fast Recirc water system that also employs DI resin. In this way, the SK water has been returned to ultrapure quality as quickly as possible. Baseline detector calibration measurements to determine the results of the 2018 refurbishment are currently being performed with in SK with ultrapure water. Gadolinium sulfate will be added once the new Band-Pass water system for SK-Gd is completed. The leak has been reduced at least by a factor of 200 ($\sim$17 L per day), about a factor of ten lower than the target rate. After the pure water phase, the detector will be loaded with enough

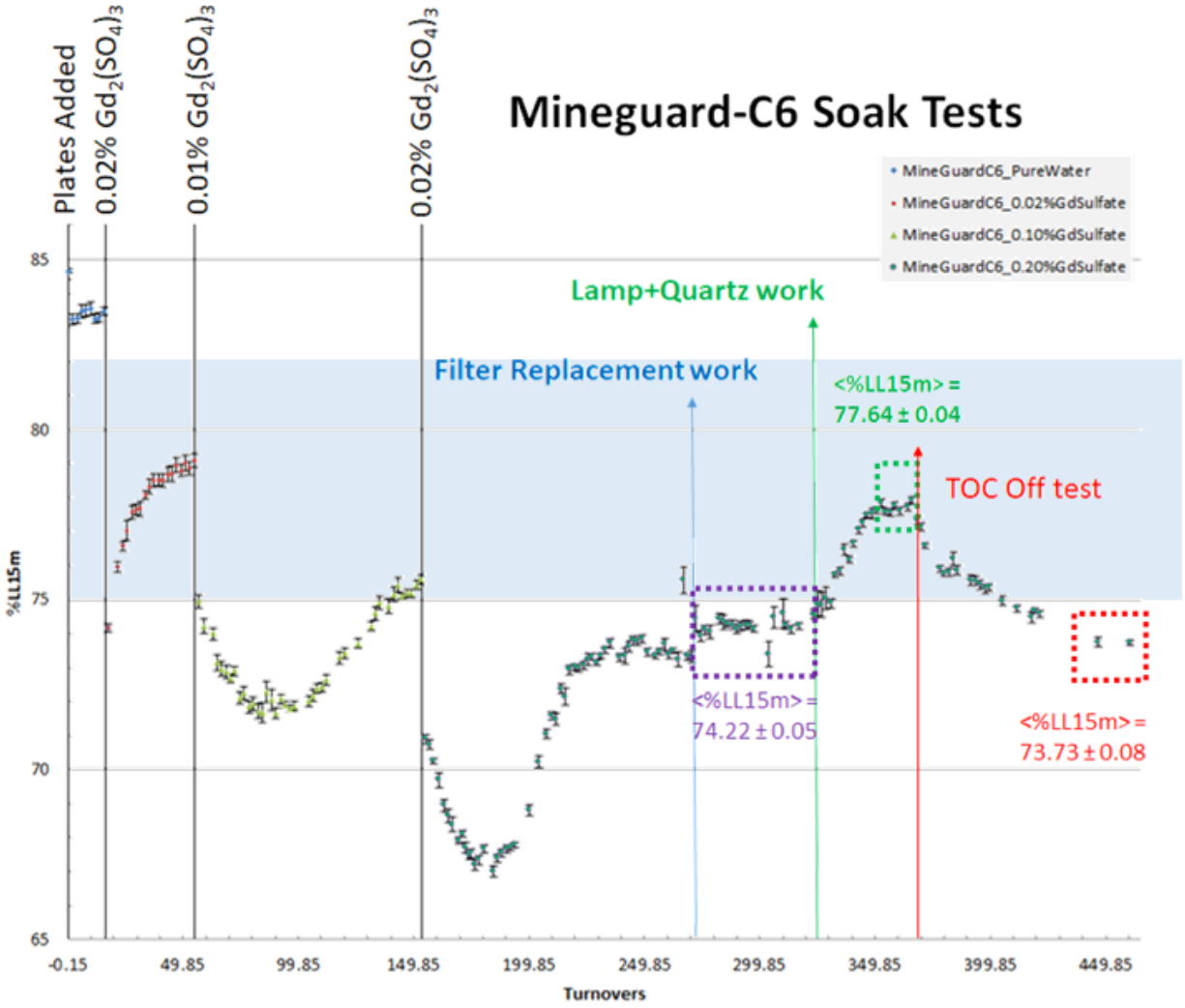

Figure 4.8: The Mineguard-C6 soak study at UCI utilizing the Band-Pass water system and IDEAL. The x-axis is the number tank turnovers, i.e. the number of times the soak tank volume was cleaned. The light blue band corresponds to the SK-III and SK-IV water transparency measurements.

gadolinium sulfate to bring it to a 0.02% $Gd_2(SO_4)_3$ solution first, then increased to 0.1%, and finally to the target concentration of 0.2%.

4.3 Detector Tank and Structure

The 50,000 m^3 tank is an upright cylinder with a height of 41.4 m and a diameter of 39.3 m, filled with ultrapure water during SK-I/II/III/IV, as well as currently in SK-V. The structure and outer wall of SK are made from SUS 304 stainless steel (SS) alloy. The coordinate systems used in SK are shown in Fig. 4.9, where x, y, and z are the standard rectangular Cartesian coordinates, and r ,z, and ϕ are the standard cylindrical coordinates. The remaining spherical coordinate θ is not shown but is important when determining background shapes (Sec. 8.1) in the SK solar neutrino analysis.

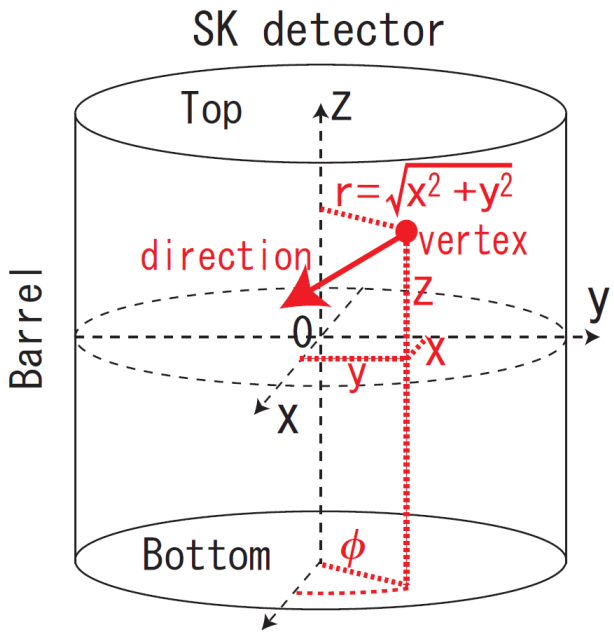

Figure 4.9: The definition of the Cartesian and cylindrical coordinate systems used in Super-Kamiokande [43].

The SS plates that make up the cylinder's outer surface are between 3 to 4.5 mm thick.

The wall behind the plates was back-filled with 40 to 50 cm thick reinforced concrete that was applied to the excavated cavity to provide structural integrity. A large domed cavity above where the tank sits was included in the excavation. As stated previously, many detector systems and calibration-related devices/equipment are housed within the dome, including the trays for the PMT cables, the electronic huts and their air conditioning systems, and areas for storage. The structure for a heavy lift crane used during the initial detector construction resides about 4 m from the tank top and has been procured for the ID and OD gondolas used during SK detector maintenance.

A cylindrical SS support structure is concentric within the SK-tank and holds in place the PMT assemblies for both the ID and OD tubes. The support structure is 55 cm thick with a height (width) of 2.1 (2.8) m and provides support to the SS plates of the tank top. The 55 cm width of the support structure is a "dead" region, as both the ID (OD) PMTs face inward (outward) from the dead region, and it is sealed light tight to optically isolate the ID from the OD. The support structure resides approximately 2.5 m from the outer wall in the barrel region and has a 2.6 m region above (below) the tank floor (ceiling). The ID region defined by the support structure has a height (diameter) of 36.2 (33.8) m, and has a volume of 32,000 m^3. A cross section of the SK tank and dome is shown in Fig. 4.10 where details of the SK dome, tank, and PMT support structure can be seen.

Super modules are the individual building blocks of the support structure, and provide the support frame for the PMT assemblies. Each ID PMT assembly is made of three 50 cm PMTs arranged in a row and fixed together by attaching the fiberglass tube housings to stainless steel bars. Four of these assemblies are bolted into the super module next to one another, as shown in Fig. 4.11, and the gaps between the PMTs are covered with opaque black sheets. The black sheets are made from polyethylene terephthalate (PET) and help to optically separate the ID and OD and also reduce the low energy background events emanating from the PMT housings in the dead region. The OD PMT assemblies are

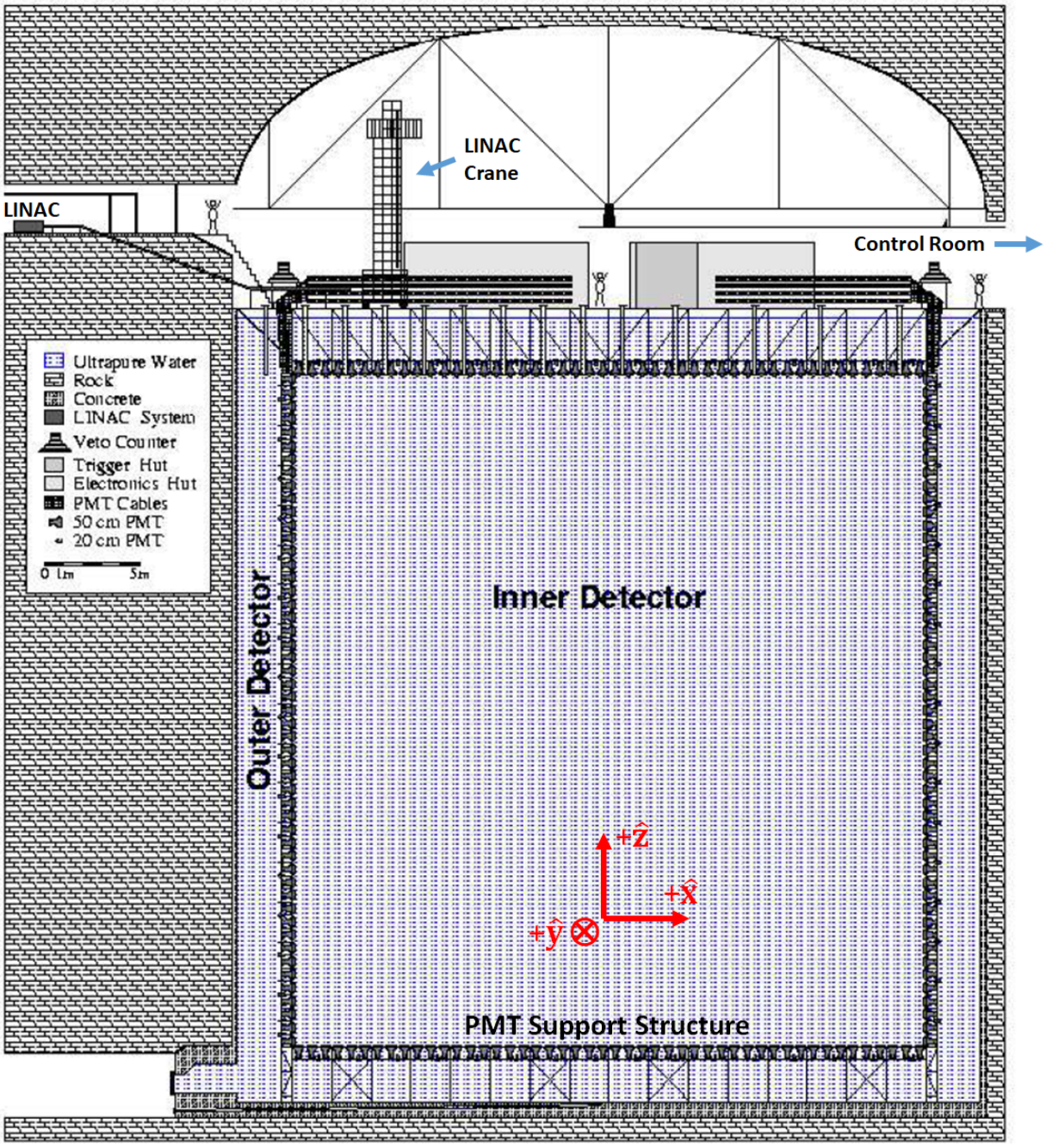

Figure 4.10: A cross section of the Super-Kamiokande detector [35].

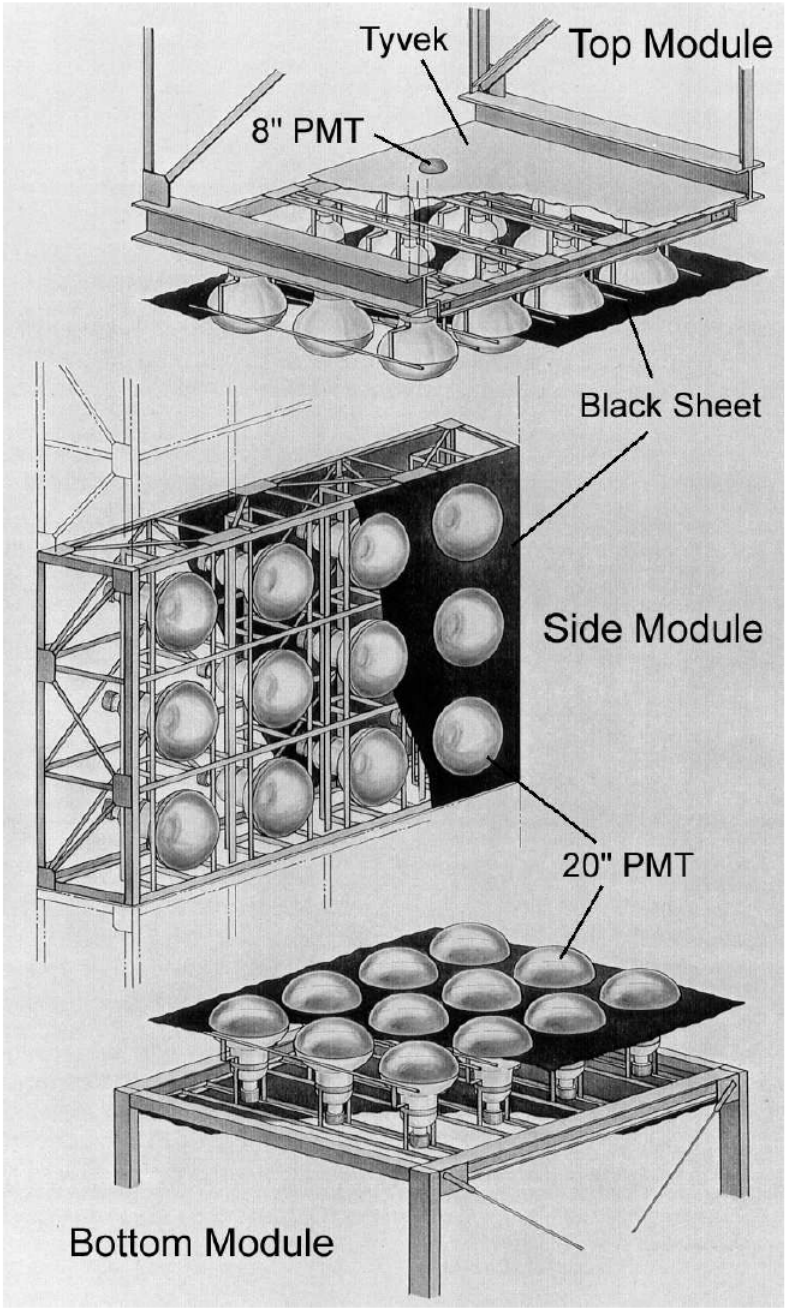

Figure 4.11: Schematic view of super modules that comprise the PMT support structure in SK, with the black sheet (black-white Tyvek) for the ID (OD) shown as well. The wavelength shifter plate for the OD PMTs and the FRP housings, acrylic windows for the ID PMTs are not shown [35].

attached in several different ways. In general, the OD PMT is either bolted to a wavelength shifter plate (waveplate) adjoined to the face of the 20.3 cm PMT or is bolted directly to the super module structure. In the first case, it is the waveplate that is bolted to the super module. Details about the OD PMT assembly will be described later in Sec. 4.4. A square sheet of black-white Tyvek is placed between the waveplate and the PMT and is mated to the super-module-sized black-white Tyvek that is hung on each super module in the OD region.

Two types of Tyvek manufactured by the DuPont company are used in SK:

- White Tyvek: Hung on the outside wall, the ceiling, and the floor of the detector.
- Black-white Tyvek: Hung on OD side of the PMT structure and helps to optically separate the ID and OD.

The white Tyvek (Type 1073B Tyvek) is a standard product which is made from high-density polyethylene fibers pressed together to form thick, paper-like sheets [35]. It reflects between 80% to 90% of light for wavelengths between 340 nm and 400 nm respectively and is deployed in the OD to maximize the amount of light the OD PMTs acquire. While the Tyvek allows for multiple reflections of Cherenkov photons, primarily diffuse reflections, the detection efficiency in the OD is more important for fulfilling the veto task the OD is designed for than having a precise pattern reconstruction. The black-white Tyvek is custom manufactured for us by DuPont. It is a laminate of three fabrics: the white Tyvek previously described, and a central (outer) layer of white (black) low-density polyethylene. The black side of the black-white Tyvek faces the dead region of the support structure, while the white side faces the OD region to enable light reflection.

4.4 Super-Kamiokande Photomultiplier Tubes

As stated previously, SK employs two types of PMTs, 50 cm (20 inch) PMTs in the ID, and 20.3 cm (8 inch) PMTs in the OD, developed by Hamamatsu Photonics K.K. The back of the PMT is coated with silver reflector up to the hemisphere of the tube where the photocathode coat begins for the PMT's forward region. The silver reflector blocks light from the backwards region of the PMT. When a photon hits the photocathode, a photoelectron (pe) is produced and flies to the first dynode, located at the back of the PMT. The high voltage (HV) on the dynodes, provided by the HV power supplies on the tank top in the electronic huts, causes an avalanche of secondary electrons. This avalanche cascades from the front dynode through the dynode chain liberating more and more electrons until, finally, it reaches the anode with enough current (or charge) to send a signal up the PMT cable for readout to the front-end electronics.

The cables of the PMTs are run up through the OD region along the support structure wall between the super modules. These cables are run out of the tank through sealed, light-tight cable ports, along cable trays to take up any excess cable, and finally into the electronic huts where the cables are plugged into the front-end electronics. The PMT cables provide both the HV needed for the PMTs to work and the path for the PMT signal extraction. All of the PMT cables in SK are of the same length, and the length acts as a physical signal delay for the detector readout. By constructing the detector with a uniform PMT cable length, the signal attenuation of all the PMTs is the same, which ensures that the detector response is uniform. The known length of the cables ensures the timestamp precision for a PMT "hit." A "hit PMT" is a PMT that has a signal sent to the front-end electronics which passes the charge threshold described in Sec. 4.5.

ID PMTs: Hamamatsu 50 cm PMT

The ID PMTs are 50 cm (20 inch) diameter Hamamatsu R3600 PMTs and are described in detail in [108]. The ID PMTs have bialkali (Sb-K-Cs) photocathodes with a quantum efficiency that is maximized in the UV region (360 nm – 400 nm) at 21%. Their total range of acceptance is from 280 nm to 660 nm, sufficiently covering the relative Cherenkov spectrum in pure water, both of which are shown in Fig. 4.14. A "Venetian blind"-style dynode is employed in the 50 cm PMT, which has an optimized voltage step-up ratio across the plates in the dynode to minimize the response time. This setup results in a good 1 pe peak, but loses the 2 pe peak from the recharging time of the dynode. These PMTs are run at a voltage between 1.7 – 2 kV to ensure a gain of 10^7. The average transit time for the ID PMTs is around 100 ns, seen in Fig. 4.13. By fitting this distribution with an asymmetric Gaussian, the spread in the timing is 2.2 ns (1σ), though, in general, the average spread in the transit time is $\sim$3 ns [108].

The acrylic window on the PMT housing is UV transparent (95% for $\lambda > 350$ nm [48]) and has holes in it to allow water to fill the housing, which is necessary to prevent total reflection of the Cherenkov light. The ID PMT cable has a dedicated HV line and a separate coaxial signal cable bound within the cable jacket which runs up into the electronic hut for the detector quadrant that the PMT is located in.

Within the tank, on the outer surfaces, a series of 26 coils are arranged in an enclosed grid-like pattern to counter adverse effects on the PMTs the Earth's geo-magnetic field can cause. The reduction of the Earth's B-field is especially important for the 50 cm tubes due to the photoelectron's long transit distance between the photocathode and the dynode. The larger B-field would curl the photoelectron trajectory and cause the photoelectron to miss hitting the dynode and thus being lost. The Earth's B-field has a strength of 450 mG at SK, oriented an angle of 45° with respect to the x-y plane of SK. After the compensation,

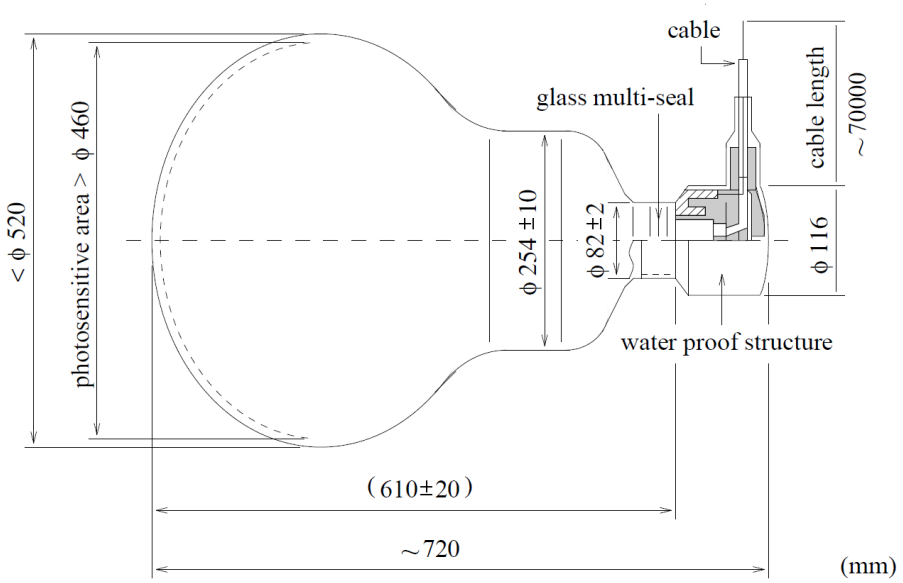

Figure 4.12: Schematic of a Hamamatsu 50 cm (20 inch) diameter PMT [108][35]. All numbers in the figure are in units of mm.

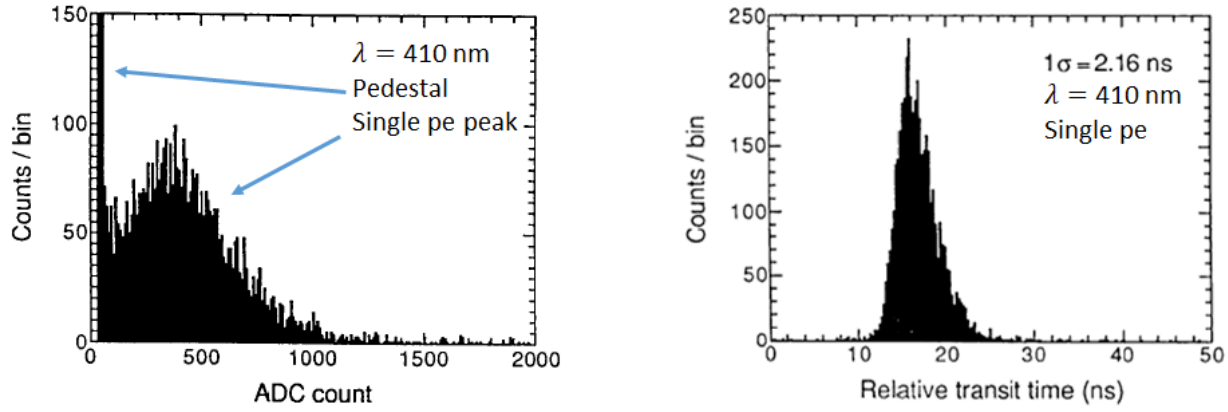

Figure 4.13: Left: Distribution of the single photoelectron (pe) pulse height from the SK 50 cm PMTs, with the pedestal shown. Right: The distribution for a 50 cm PMT of the relative transit time for single pe measurements of 410 nm light. Both figures taken from [108].

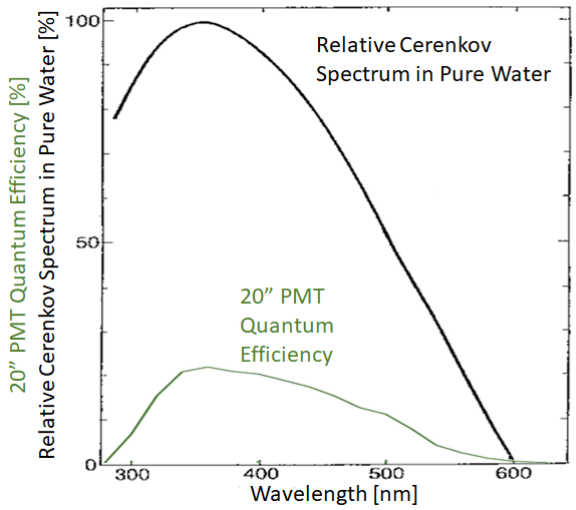

Figure 4.14: The quantum efficiency as a function of wavelength for the Hamamatsu 50 cm (20") PMT photocathode (green) [35] and the relative Cherenkov spectrum in pure water [43].

the field is reduced by a factor of nine to an average of 50 mG.

Hamamatsu 20.3 cm PMTs and OD PMT Assembly

The OD PMTs are 20.3 cm (8 inch) diameter Hamamatsu PMTs, with two PMTs set into the diagonal of the external face of the super module, providing a photocathode coverage of ∼0.5%. Several different models of the Hamamatsu 20.3 cm PMTs are currently used: model R1408, the only OD PMT type used in SK-I, were originally were deployed in IMB; model R5902 are a newer generation from Hamamatsu and were purchased as a replacement for dead OD PMTs. The OD PMTs have a single coaxial cable that delivers the HV to the PMT and carries the analog signal to the DAQ. To increase the efficiency of the light collection in the OD, wavelength shifter plates (waveplates) are attached to each PMT. Reflective tape on the outside edges of the plates increase its efficiency.

Originally, the PMTs and waveplates deployed in the OD had seen use in the IMB detector. Many of the IMB PMTs eventually failed due to either leaks in the housings,

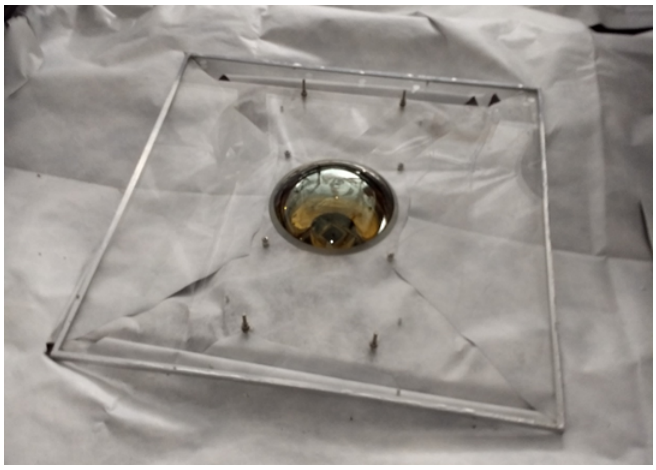

Figure 4.15: Super-Kamiokande 20.3 cm (8 inch) PMT in the OD top with wavelength shifting plate and black-white Tyvek.

which introduced water into the PMT base region, or due to nicks in the cable jacket caused by flying glass from the 2001 accident, which allowed water into the PMT base and cable. In either case, this led to dead PMTs and flooded cables, as found during the various detector refurbishments. Due to the failure rate of the unpotted IMB-style housings, replacement OD PMTs have their bases potted to the PMT with epoxy by Hamamatsu, which results in a water-tight seal. The potting of the bases was a success, as the failure rate of the newer potted base PMTs is very low, especially compared to the OD PMTs with IMB-style bases.

The square waveplates are doped acrylic panels 60 cm on edge and 1.3 cm thick. They are coupled to the PMTs by physical contact and partially through the water which fills the gap. The waveplates increase the coverage of the PMTs to $\sim$10% of the OD surface. The doping material, 50 mg/l of bis-MSB, absorbs UV light and isotropically re-emits 55% of the photons into a wavelength in the blue-green region [35]. A study of bis-MSB doped wavelength shifter plastic was performed by L.P. Boivin and D.S. Hanna in [109]. In their study, they measured the normalized spectral distribution of the shifted light emitted from the other end of a 12 cm doped wavelength shifter plastic bar being irradiated by 365 nm light. This distribution is shown in Fig. 4.16.

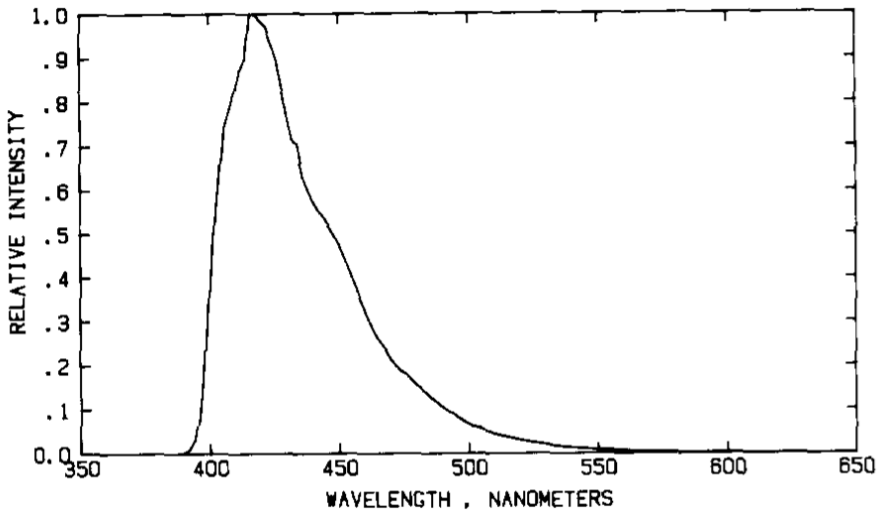

Figure 4.16: The normalized spectral distribution of light emitted by bis-MSG doped wavelength shifter plastic when exposed to 365 nm light [109].

The 20.3 cm PMTs have a different wavelength sensitivity than the ID PMTs and are less sensitive to the UV Cherenkov photons. The waveplates shift the UV light to wavelengths more appropriate for these PMTs, increasing the collection efficiency by 150% [35]. A black plastic sheet is wrapped around the back of the PMT to block light and low energy background events coming from the dead region. Fig. 4.15 is a photo taken during the 2018 detector refurbishment of an OD PMT assembly installed on the top face of the OD with the black-white Tyvek. The OD PMTs are important as a veto and calorimeter system for SK high energy analyses. However, for SK low energy analyses, the OD PMTs are primarily used only as a Boolean veto for events, while the OD itself is used as a buffer against γs from the rock that would be a source of background.

4.5 Super-Kamiokande Front-end Electronics, Data Acquisition and Triggering Systems

The front-end electronics for SK include an HV system for the PMTs and the data acquisition system (DAQ) that digitizes the analog signal from the PMTs. The original front-end electronics used prior to SK-IV were Analogue Timing Modules (ATMs) that collected the time and charge information from the PMTs. The ATMs were replaced at the beginning of SK-IV with QBEEs, charge-to-time based electronics that use Ethernet readout modules. The basic information in SK data is the charge (Q), time (T), and PMT cable number. The cable number corresponds to the physical location of a PMT in the detector. The electronic crates that power the ATM and QBEE boards are designed via Tristan KEK Online (TKO) Standards, and are referred to as TKO crates. In the case of the ATM boards, TKO crates also receive the data from the ATMs and pass it on to the central electronics hut.

The electronics are housed in four electronics huts on the detector top, one per detector quadrant, and the information is sent to the trigger system located in the fifth central electronics hut that also houses the control electronics. The trigger system delivers the relevant information, ID and OD Q-T information along with trigger flags and timestamps, to online event builder computers in the control room. The online event builders merge all of the data streams to form a completed full-detector event and then send the information to the Kenkyuto via fiber optic lines.

Because precise real-world timing is necessary for many real-time analyses, like the K2K/T2K neutrino beam, supernova, and gamma ray burst analyses, SK also employs two Global Positioning Systems (GPS) that provide timestamps for data in SK. The GPS antennae were originally located on the roof of the Radon Hut, but were moved to the roof of the Kenkyuto during SK-IV to achieve better communication with the GPS satellites. The GPS timestamps are sent to the central hut via fiber optic lines, and the resulting accuracy

between the two GPS clocks is approximately 60 ns.

4.5.1 SK-I to SK-III DAQ and Hardware Trigger

For SK-I, SK-II, and SK-III, the DAQ, illustrated in Fig. 4.17, consists of 946 ATMs, each of which integrates the T and Q information for 12 ID PMTs which is then digitized with an onboard Analog to Digital Converter (ADC) module. At the ATM board, each PMT signal is amplified by a factor of 100 before being divided into four signals (quarter-signals).

One of the quarter-signals is summed with the corresponding quarter-signals from the other eleven PMTs to form the PMTSUM signal for the ATM board. The PMTSUM signal is then sent to a flash ADC to save the PMTSUM waveform information. Onboard discriminators receive the second quarter-signal from the PMTs and will generate two -15 mV deep, 200 ns wide square-wave pulses if the signal is above a threshold corresponding to 0.23 p.e., for each of the 12 PMTs. The timing width of the first (second) pulse is 200 ns (900 ns). The timing of the first pulse is set to 200 ns, as that time span is the upper duration for the light from events in SK to take the longest path in the ID (the full diagonal) and hit the PMTs. The 200 ns pulse from each PMT is then summed together to form the HITSUM pulse, which is then sent to the hardware trigger system in the central hut. The top third of Fig. 4.18 shows schematically the PMT analog signal passing the ATM thresholds and being added into the HITSUM. The DC component due to dark noise is filtered out by a capacitor, so that only the AC component is passed and makes it into the HITSUM. In the central hut, all of the HITSUM pulses from the various ATM boards are summed together. If the level of this summed HITSUM is above the hardware trigger threshold, the hardware trigger issues a global trigger, saving the collected event data and sending it to the online computers.

The global trigger has three trigger levels it will issue, dependent on whether the

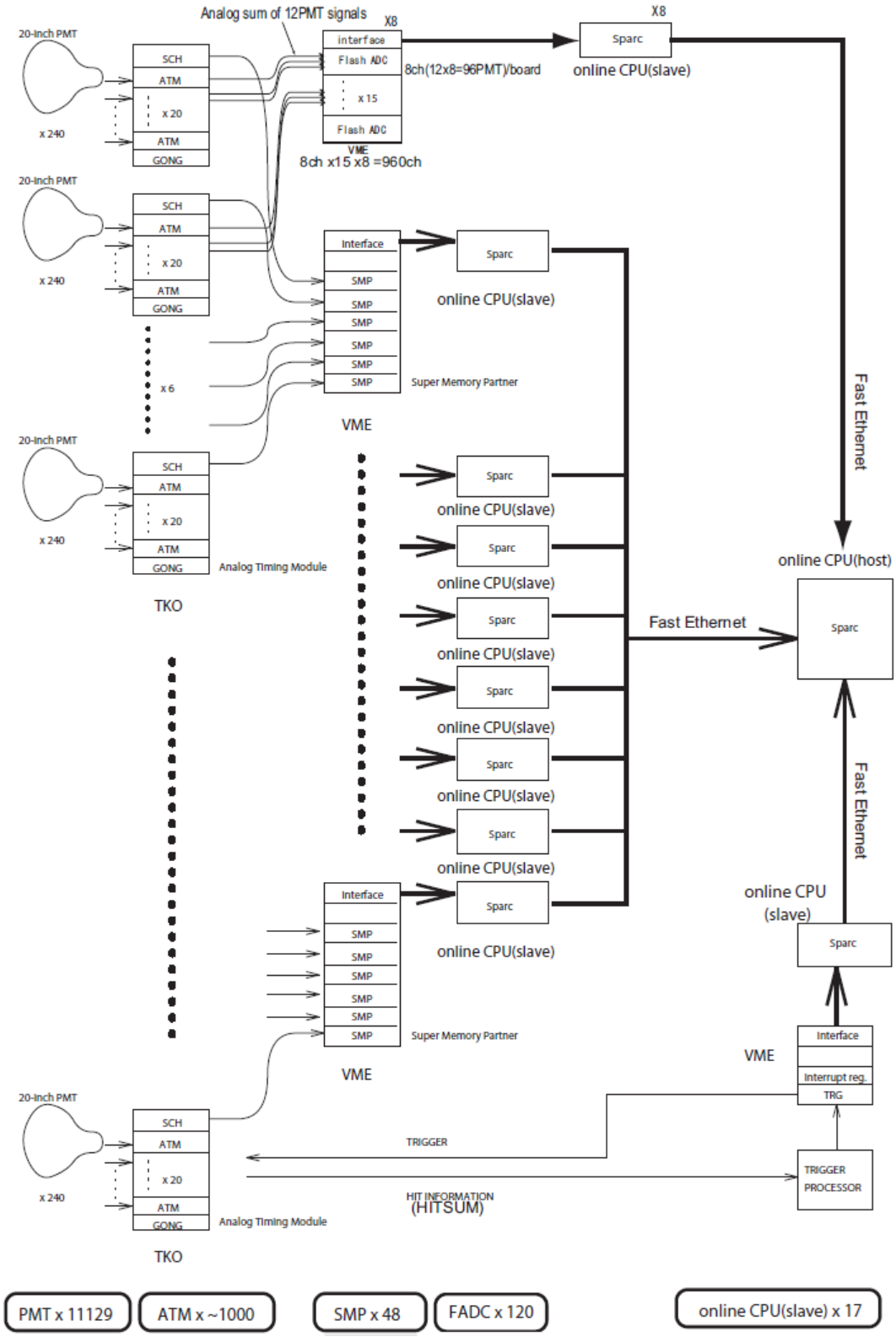

Figure 4.17: A schematic of the SK-I/II/III ID DAQ [43].

summed HITSUM voltage passes their threshold: the super low energy (SLE) trigger, the low energy (LE) trigger, and the high energy (HE) trigger. The average number of ID PMT hits, or simply hits for short, that is due to dark noise within 200 ns is ∼19 hits, and the trigger thresholds are set to take these dark hits into account. The voltage thresholds for the HE, LE, and SLE triggers are set corresponding to the number of hits above dark noise: 31, 28, and 15 hits respectively. Other global triggers exist as well, such as for calibration flags, OD activity, etc., but they will be described only as necessary and when the need arises. Table 4.3 lists the threshold values, both voltage and total hits, for each SK-Phase, though the last threshold value for the SLE trigger is listed. The SLE threshold was changed often as the background changed during SK-I and SK-III. An overview of the waveform signals and the timing process that generates a global trigger is shown in Fig. 4.18.

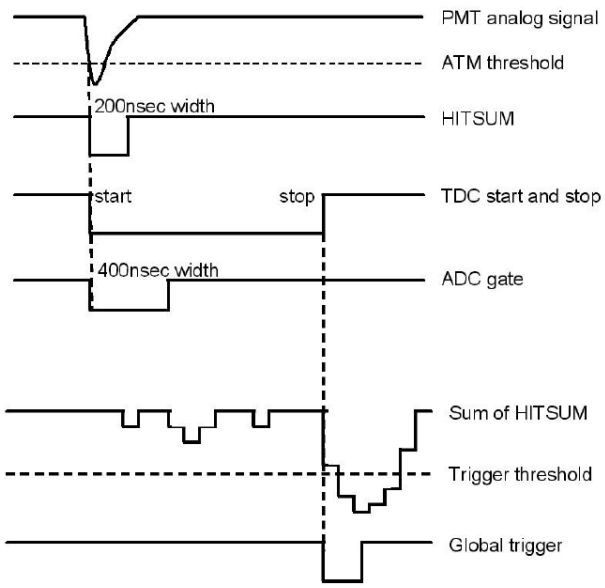

Figure 4.18: An illustration of the waveforms and timing that generate the global trigger [43].

The 900 ns pulse generated by the ATM discriminators is known as the "selfgate signal" and is used as a trigger to initiate signal integration with the charge-to-analog converter (QAC) and time-to-analog converter (TAC). The remaining two PMT quarter-signals are sent to the QAC and TAC. The QAC integrates the charge of one of the quarter-signals for

Table 4.3: The final trigger thresholds of the global trigger for each SK-Phase in mV for SK-I/II/III and total PMT hits for SK-IV. The SK-IV QBEE Discriminator Threshold is -0.69 mV, which is the same for all trigger levels, as the trigger levels are software based instead of hardware based as in SK-I/II/III. The number of coincident PMT hits within a 200 ns sliding time window for the SK-IV thresholds are set as to mimic the hardware trigger in the previous SK-Phases. *As the SK-IV SLE threshold was lowered two thirds of the way through the data period, both are listed.

Phase	HE	LE	SLE
SK-I	-340 mV	-320 mV	-186 mV
SK-II	-180 mV	-152 mV	-110 mV
SK-III	-320 mV	-302 mV	-186 mV
SK-IV	50 hits	47 hits	34/31* hits

400 ns when triggered by the selfgate signal, and the TAC generates the timing information for the hit PMTs. The QAC and TAC output is then digitized by an ADC if a global trigger has been issued within 1.3 μs.

4.5.2 SK-IV DAQ and Software Trigger

As the ATMs were no longer supported by the manufacturing company, and to further reduce the dead time (time during which the detector does not collect data), the ATMs were replaced with the QBEE boards [110]. The QBEE boards were designed to use the same LeCroy MQT200 charge-to-time conversion (QTC) modules used in the OD and to be swapped with the ATM boards in the TKO crates. While the TKO crate powers the QBEE boards, the readout uses the faster Ethernet output. Each QBEE board has 8 QTC chips, with three input channels per QTC chip.

The QTC chips have three gain ranges for the PMT readout (small, medium, and large) and cover a dynamic charge range of 0.2 to 2500 pC, wider than that of the ATMs, though the T and Q resolutions are comparable. The QTC output is a square waveform whose leading edge corresponds to the hit arrival time, and the width to the PMT's integrated

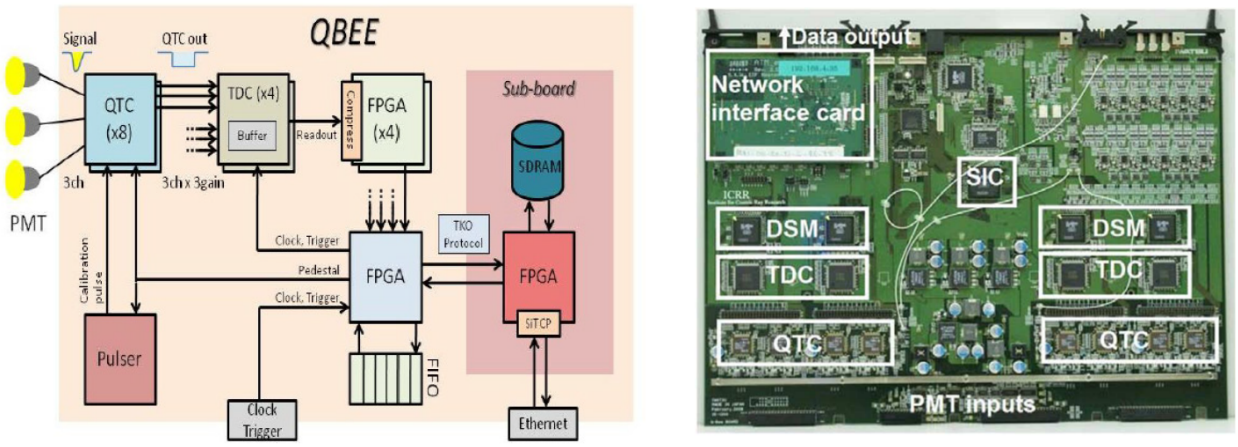

Figure 4.19: Left: A block diagram of the QBEE signal processing flow [43]. Right: A picture of the QBEE board with the components labeled [110]. The sub-board on the left is the network interface card on the right. The System Interface Control (SIC) and Data Sort Mapping (DSM) arrays in the right picture are Field Programmable Gate Arrays (FPGAs) and correspond to the blue FPGA and olive colored FPGAs respectively in the diagram on the left.

charge. The output is sent via Ethernet to the central hut, where the data flow for issuing a global trigger, assigning flags, etc., resumes.

In addition to the front-end electronics, the online computers responsible for building the events were upgraded. A block diagram of the data flow for the signal processing in the QBEE is shown on the left side of Fig. 4.19, and a labeled picture of the QBEE board is shown on the right. A schematic view of the SK-IV DAQ and Online System is illustrated in Fig. 4.20.

With the new electronics, a software trigger was implemented to check for the number of coincident PMT hits within a 200 ns sliding time window. The SK-IV trigger thresholds, the minimum required number of coincident PMT hits, are set as to mimic the HITSUM hardware trigger used in the previous SK-Phases. The effective energy threshold from the software trigger threshold is directly correlated, as the number of coincident hit PMTs are used to determine the energy estimator N_{eff} for low energy events (see Sec. 6.2). Although lowering the trigger threshold means that more low energy events can be acquired, the

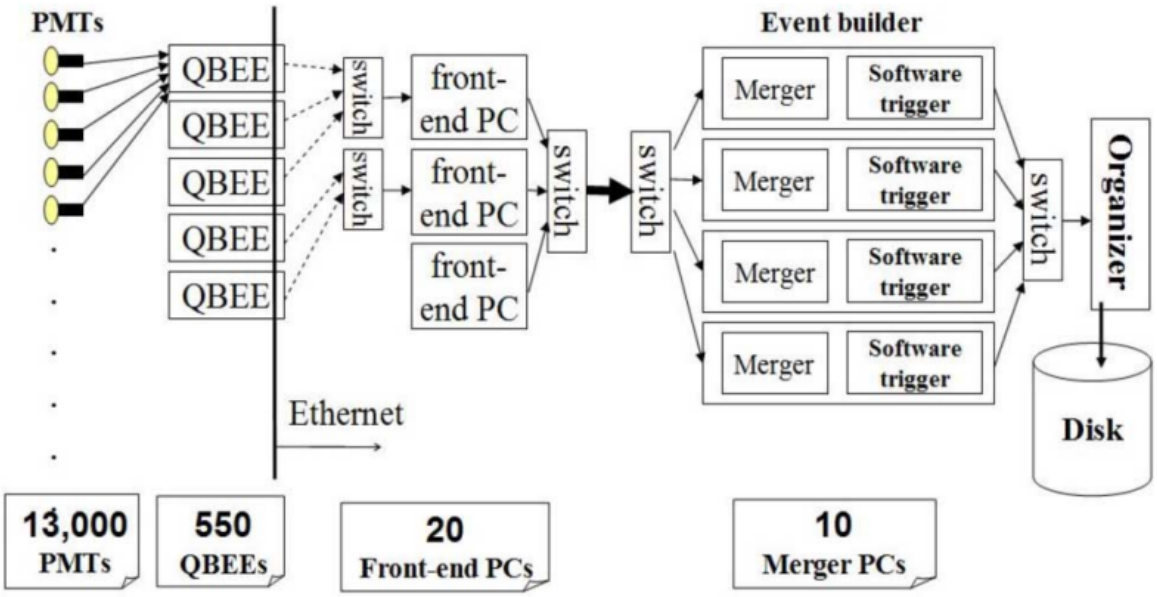

Figure 4.20: A schematic view of the SK-IV DAQ and Online System [110].

background rate in the detector rises exponentially with decreasing energy.

4.5.3 High Voltage Systems

The HV supply system for the ID PMTs originally consisted of CAEN Coċomponents installed in 1995: a distributor (A933K), a controller (SY527), and an interface module (V288). While the CAEN system had good performance, the failure rate was high for HV modules, and the company dropped repair support. The HV system was upgraded due to these issues during SK-IV in 2013 and replaced with "iSeg" modules made by the German manufacturer iseg Spezialelektronic GmbH. As both the CAEN system and iSeg modules have the feature that the individual PMT voltages can be set and turned off independently, each PMT has its HV set individually to ensure that the gain is the same for all PMTs, while the HV system monitors the status. For both HV systems, the HV monitor gives updates every 10 minutes to SK "shifters" (collaborators who monitor the detector systems live) as part of a

slow control system that warns shifters of any major problems.

The average dark rate for the ID PMTs depends on when the PMTs were manufactured, corresponding to their installation in SK, and varies as a function of time. In SK-IV, the running averages for each batch vary between 3.8 kHz and 7.4 kHz. For a random 50 ns time window (used to determine the energy estimator N_{eff} in Sec. 6.2), this dark rate corresponds to $\sim$3 accidental hits. The dark rate is implemented in the detector simulations for SK analyses based on the measured average dark rate of $\sim$5.94 kHz, or the measured dark rate for a given time period. Because it has been seen that the gain for the PMTs has varied, this problem is addressed via an offline correction and will be discussed in Sec 6.2.2.

The HV system for the OD PMTs uses a LeCroy 1454 HV Mainframe in each of the four electronics huts. Forty of the HV channels in each OD HV supply are connected to "paddle cards" that deliver HV to 12 OD PMTs, making the OD HV system somewhat complicated. When the HV is off, individual OD PMTs can be turned off via dip switches on paddle cards in the OD HV electronics. In general, the supplied HV is approximately 1.8 kV. To match the optimal operating voltage for each PMT, Zener diodes are inserted into the paddle cards to scale down and regulate the supplied HV. The signals from the OD PMTs that pass threshold are transferred from the paddle cards to the OD DAQ.

In SK-I to SK-III, the QTCs were used to measure the hit time and charge and pass the information to time-to-digital converters (TDCs). At the beginning of SK-IV, the OD DAQ was upgraded to use the QBEE boards described earlier, which have the OD QTCs integrated into them. The information from the OD DAQ is collected and sent to the central hut, where the data is aggregated with the various trigger and timestamp information. The central hut then sends the OD information to the online event builder computers in the control room, where it is merged with the ID data. The OD trigger threshold is 19 (22) hits within 200 ns for SK-I/II/III (SK-IV), and, after a global trigger is issued, the OD data saved for a window of 10 μs before to 6 μs after the global trigger. The OD trigger is important

for the solar neutrino analysis, as a cut is applied based if an OD trigger was issued and also based on the number of hit OD PMTs if no OD trigger was issued. Details of this cut are described in Sec. 7.4.5

4.6 Background Reduction

To reduce the backgrounds for the various analyses, both the water in SK and the air in and around the detector are purified. Every component in the water system is there to increase the optical transparency of the water and remove anything that would contribute to the radioactive backgrounds, especially radon. The environment in the mine outside of the experimental areas is rich in radon gas, which can work its way into the water in the detector. The air system itself is employed specifically to reduce the radon concentration in and around the detector.

For the low energy analyses, radioactive contaminants in the ID water volume can add to the backgrounds, such as the radioactive daughters of ^{222}Rn. ^{222}Rn is produced from the decay of ^{238}U, and has a half-life of $\tau = 3.8$ days, after which it α-decays. In the ^{222}Rn decay chain, ^{214}Bi ($\tau = 20$ min) is produced, which β-decays with a Q-value of 3.272 MeV [111]. It is possible that the β decay of ^{214}Bi is one of the main backgrounds for the solar neutrino analysis, as the β is indistinguishable from a recoil electron. The radioactive backgrounds from the decay of ^{222}Rn in the SK water are collectively referred to as the "radon background" or shorthanded to radon. The Rn background in SK-IV has been studied in [48].

4.6.1 Super-Kamiokande Water System

Because SK is a very large water Cherenkov detector whose PMTs need to receive the light from events that occur within the ID, the light in the water must be able to make it to the

PMTs. The average path length for light in SK is ∼15 m, but it can travel up to 50 m, the diagonal of the ID. To maximize the measured light intensity, i.e. the observed number of photons that hit PMTs, impurities that often scatter or absorb the light in the water must be removed. Bacteria is introduced into the detector through the contact of people or by objects inserted into the detector and will grow in the water. The bacteria's waste products can impair the water transparency and can create bio-film that may adhere to the surfaces of detector equipment and alter the equipment's optical response to Cherenkov light.

The SK water purification system (SK water system) removes these contaminants from the water and additionally removes radioactive backgrounds. The SK water system is shown schematically in Fig. 4.21. SK continually recirculates its water through the water system at 60 tons per hour to maintain the high optical transparencies and low radioactive backgrounds needed for quality data collection. Rain and melt water from snow on the mountain seep into the mine, creating several streams that maintain a temperature between 10.5 and 11 °C, several of which are used to cool the water treated by the water system via a heat exchanger, discussed momentarily. To fill the SK tank, the water is originally sourced from two of the mine streams and passed through the water system to clean it up while filling.

During normal SK operation, the water from the water system is injected at the tank bottom after it is cooled to between 13.24 and 13.06 °C. The introduction of the cooled water at the bottom of the detector reduces convection in the detector volume and limits the distance that the Rn background influences. The Rn comes from the support structure and PMT housings and can also come from leaks in the water system and from the air. The Rn reduction is leveraged to maximize the fiducial volume for SK low energy analyses. Controlling the input water temperature and reducing convection creates a laminar flow in the upper 3/4 of the detector ($z > -10$). This restricts the detector-based radon backgrounds to the bottom of the detector ($z < -7.5$) where they decay away, while creating a low background region in the upper half of the detector. The The water system finally extracts

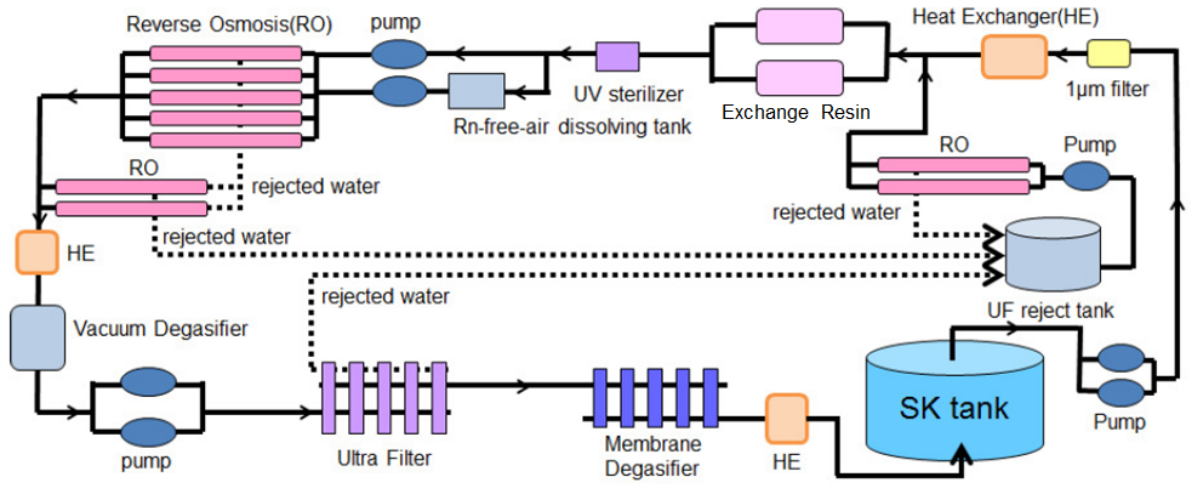

Figure 4.21: A schematic diagram of the SK water purification system used in SK-I – SK-IV [43]. The Membrane Degasifier was bypassed in the middle of the SK-IV Phase as it was found to be a source of radon.

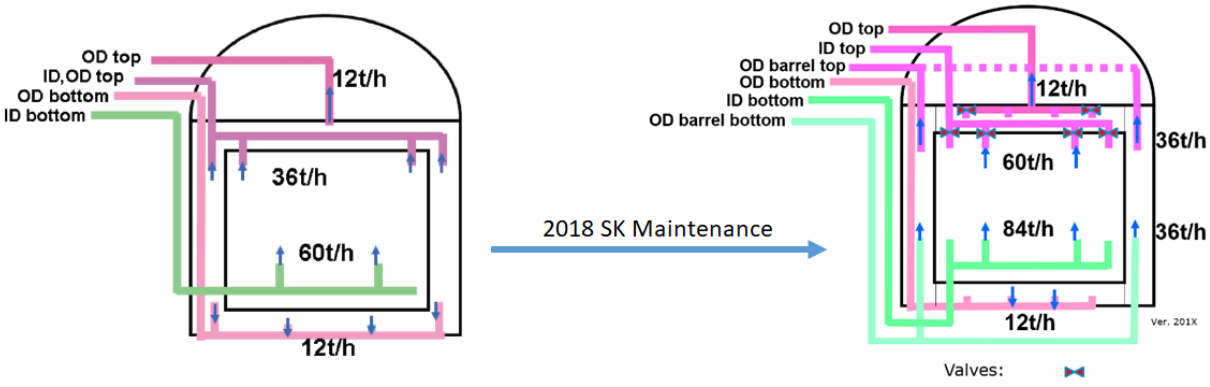

Figure 4.22: Left: The rates and locations of the water injection and extraction points in the SK tank [112]. Right: The water injection and extraction for SK after the plumbing upgrades performed during the 2018 detector maintenance; figure courtesy of H. Sekiya.

the aged water from the top of the tank, shown in Fig. 4.22. The flow rates allow the water system to clean a full ID volume, called a turnover, in ∼1 month.

The temperature of the supply water from the water system that feeds the SK tank is plotted in in Fig. 4.23 for the SK-III and SK-IV periods. The control over the supply water temperature during SK-III and the beginning of the SK-IV period was too chaotic to reduce convection, and a new temperature control system was installed in 2009 which controls the temperature to within an accuracy of 0.01 °C. At the end of SK-IV, as stated previously, convection studies were performed by raising the water temperature.

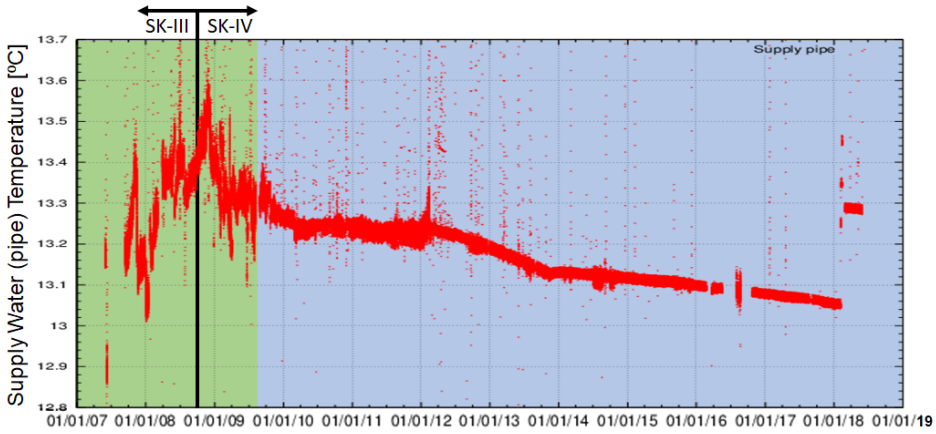

Figure 4.23: The variation of the supply water temperature as a function of time. The blue background denotes the new temperature control system installed in November 2009, and the green background denotes use of the prior system. Figure courtesy of H. Sekiya and R. Wendell.

The primary components of the SK water system, following the extraction of water from the SK tank, are as follows:

- 1 μm Filters: Several polypropylene mesh filters with pore sizes of ∼1 μm that removes small particles and dust that degrade the water transparency and are radon sources.
- Heat Exchanger (HE): As stated earlier, the water temperature in the ID is controlled very precisely to reduce convection. Several heat sources, such as the pumps and friction in

the filtration units of the water system, the PMTs, and rock that surrounds the tank emit heat into the water, etc., continually supply heat to the water. To combat this, heat exchangers are used in various locations in the water system to regulate the water temperature and precisely control it using the cooler mine stream water. Additionally, with the water temperature below 13.5 °C, bacterial growth is suppressed and PMT dark noise is reduced.

- Exchange Resin: an ion exchange resin bed that removes lighter and heavy ions from the water. The original ion exchange resin system removed ions like Na^{+}, Cl^{-}, Ca^{+2}, but was found to be a significant radon source. It was swapped for the Cartridge Polisher sometime in SK-I, whose resin eliminates these lighter ions, as well as heavy ions that include radioactive species.

- UV Sterilizer: A UV lamp sits along the central axis of a shell through which the water flows. The UV light delivered by the lamp (254 nm) kills bacteria in the water.

- Rn-free-air Dissolving Tank: dissolves air with very low radon concentration from the radon-reduced air purification system (Sec. 4.6.2) into the water to increase the vacuum degasifier's radon removal efficiency.

- Reverse Osmosis (RO): Installed in SK-III, this staged membrane filtration system has hollow shells containing a cloth membrane. The membrane has a pore size of $\sim$1 nm that rejects contaminants heavier than 1000 the molecular weight of water into a waste stream known as the reject stream. The stream of RO water that passes through the membrane is known as the product stream.

- Vacuum Degasifier: Removes dissolved gasses like CO_2 from the water that can impact water transparency, the radon gas that adds to the background event rate in the low energy region, and oxygen that encourages bacterial reproduction in the water.

- Ultra Filter (UF): A membrane filtration system similar to the RO system but whose

membrane pore size is ∼10 nm. The UF removes ultra-fine particles from the water. Anything that makes it through the UF is removed by the RO.

- UF Reject Tank: The reject stream of the RO and UF membranes are sent to this tank. When filled, the water is sent through another set of ROs, and the reject stream of this system is sent back to the tank, effectively trapping and concentrating the waste into this tank.

- Membrane Degasifier: An additional, large vacuum degasifier system that employs membranes to remove any leftover radon dissolved in the water. The system was installed during the first refurbishment between SK-I and SK-II. It has been bypassed in the water system since May 2014, as rubber seals critical to the system were found to be themselves a radon source.

4.6.2 Air Purification Systems for Radon Reduction

The level of radon gas is very high in the Kamioka mine. It is both a health hazard for workers in the ICRR experimental areas including at SK and a major background for low energy analyses. Because of this, several steps have been taken to reduce the concentrations of Rn in and around SK. The walls of the SK experimental area are sealed with Mineguard, and the access to the mine is restricted by two sets of doors to form simple airlocks. The SK experimental area has two sets of Rn-reducing airlocks: one in the LINAC room area and one at the entrance next to the control room.

Located in the "Radon Hut" at the entrance of the mine, a massive air blower intakes fresh air with low radon concentrations through a 10-micron filter. Since the mine stays approximately the same temperature all year, the seasons affect the air flow through the mine. In the winter, air is sucked into the mine from the Mozumi entrance, and in the summer the airflow is reversed, causing a large concentration of radon rich air at the mine entrance.

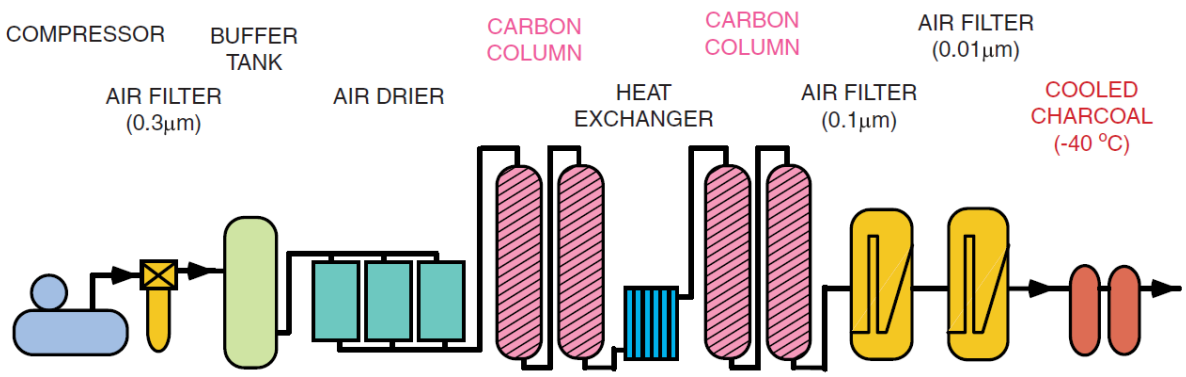

Figure 4.24: Schematic view of the SK radon reduced air purification system [35].

To ensure the air pumped into the ICRR experimental areas has a low concentration of radon year round, the intake for the air system is located up the side of the mountain away from the mine entrance. UCI maintains the Radon Hut, performing maintenance of the system bi-annually or more frequently, depending on the weather and environmental factors that affect the system (bugs, pollen, snow, rain, etc.). The ICRR experimental areas, including the

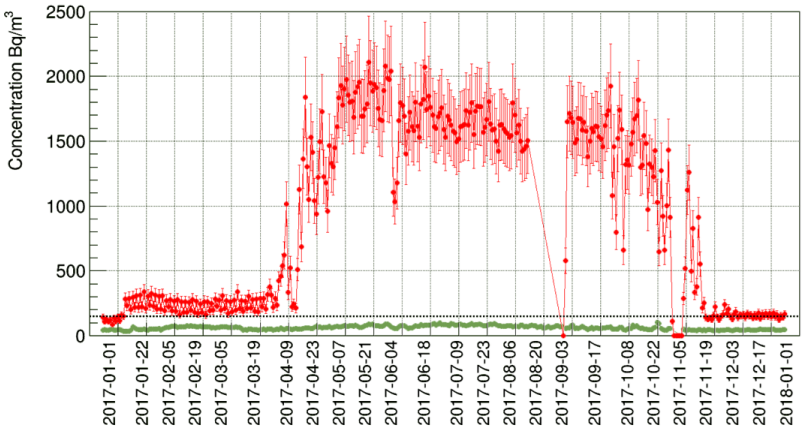

Figure 4.25: Rn gas levels in the air in the mine near the SK entrance (red) and in the SK Dome (green). The readings are from the year 2017 and show the seasonal variation of the radon level. The dotted black line is the maximum radon concentration allowed in the ICRR experimental areas (150 Bq/m^3). The dropout in the mine tunnel data between mid Aug. and Mid Sep., as well as the period around early Nov. is due to maintenance. Figure courtesy G. Pronost.

dome above the SK tank and connected areas, are over-pressurized with this good air. This allows the double-door system in SK, described earlier, to function properly as an airlock,

reducing the flow of radon-rich air from the mine to drift into SK and the tank.

An additional system, the radon-reduced air purification system, conditions the air supplyied from the Radon Hut with additional filtration using activated charcoal. This system lowers the radon concentration to a few mBq/m^3, then pumps it into the top of the SK tank above the water. The air is supplied at over-pressure to create a buffer against the dome air that has a residual radon level between 30 and 100 Bq/m^3. It additionally supplies air to the water system Rn-free-air Dissolving Tank, discussed earlier. The radon concentration in the buffer gas is constantly monitored by a highly sensitive detector system to determine where sources of Rn backgrounds in SK may originate and to what extent they contribute [113].

A new radon monitoring system [114] was deployed in 2016 throughout the ICRR experimental areas, including SK, as well as in the mine and Radon Hut. This system measures the radon concentration in the air in real-time using 21 one-liter radon detectors and Raspberry Pi electronic readouts. With this system, both the seasonal and day-night variations in the radon concentration can be monitored. Fig. 4.25 shows the daily averaged radon levels in the SK dome and outside the front SK entrance in the mine.

Chapter 5

Super-Kamiokande Calibration

Details for the calibration of the SK detector for SK-I are reported in [35] and for SK-IV in [112]. A specific focus on the LINAC calibration (Sec. 5.3.1) is reported in [115], and a report on using ^{16}N produced by the deuterium-tritium fusion neutron generator as a calibration source (Sec. 5.3.2) is detailed in [116]. All calibration in SK involves simulating aspects of the detector and/or the detector in full, such as the behavior of Cherenkov light in water, the behavior and response of the PMTs, or how to understand the relationship between Chereknov light produced by an event and its energy. The SK detector simulator is a heavily customized Geant3 [117] Monte Carlo (MC) simulation, called SKDETSIM. In this work, the SKDETSIM MC simulated data will be simply referred to as MC. A description of SKDETSIM and how it is used to generate solar neutrino MC is given in Sec 6.1.

5.1 PMT Calibration

The timing behavior of PMTs depends on the height of the measured pulse. As PMTs are the active detection equipment in SK (see Sec. 4.4), the behaviors of their timing (T) and

charge (Q) are very important to characterize. In high energy analyses, the combined T and Q behavior of a PMT is important. For low energy analyses, T and Q are treated fairly independently, as these analyses use single photoelectron (pe) statistics, and the occupancy (density distribution of hit PMTs) is more important than Q. While the general methods apply to both the ID and OD PMTs, only the calibrations related to the ID will be discussed. The OD is generally only used as a veto for some of the SK low energy analyses.

Because low energy events in SK produce single pe PMT hits, low energy analyses heavily rely on PMT calibration to make sense of the data, specifically the "QE" calibration. QE refers to the product of the PMT quantum efficiency, the fraction of incident photons that produce photoelectrons in the photocathode via the photoelectric effect, and the PMT's collection efficiency. The collection efficiency is the fraction of the number of photoelectrons produced in the PMT to the corresponding amount of charge eventually read out by the front-end electronics. Photoelectrons must make it to the first dynode to start an avalanche (or cascade) of electrons in the dynode chain, and the subsequent charge must pass the read-out threshold in order for the PMT hit to be measured by the front-end electronics. Each PMT is hand made and may have a unique QE, as the environment in which PMTs were produced varied from one production run to another. As such, it is necessary to calibrate this parameter for each individual PMT.

The second important parameter to discuss when talking about PMTs is the "gain," defined as the conversion factor from the number of photoelectrons to the charge (in units of pC). The gain is divided into the absolute gain, which is applied to all the ID PMTs in SK, and the relative gain specific to individual ID PMTs. First, the absolute gain calibration will be discussed.

5.1.1 Absolute Gain

The absolute gain translates from the charge obtained from the electronics that read out the PMT signals to the number of pe. The number of pe for an event is important, as it is used in SK analyses as a measure of an event's energy. This absolute gain is dependent on the HV that is supplied to the PMTs, which is established at the beginning of both SK-II and SK-III. For SK-V, a similar procedure has been adopted.

The initial HV was determined by guiding the light from a Xe flash lamp into a scintillator ball to produce a uniform light source. The light from the Xe source is filtered to pass only UV light, which is then injected into several fiber optic lines. One of these lines is used as a reference monitor for the light intensity. The other line is connected to the scintillator ball which has been placed in a dark box containing the ID PMT that will be tested and installed in SK. The scintillator ball itself is 5 cm in diameter and made of acrylic. It is doped with 15 ppm of POPOP used as a wavelength shifter that causes the ball to emit the light at 440 nm, and with 2000 ppm MgO that acts as a diffuser. The scintillator ball has an angular uniformity of better than 1%. The HV for each ID PMT was set to ensure the same observed charge response Q^{obs} (Eq. 5.1) as signal output for the same incident light intensity. The incident light intensity emitted from the scintillator ball produces ∼30 photoelectrons in an ID PMT. For PMT j in SK, the charge response Q_j^{obs} is proportional to the product of the PMT's QE_j, the total (or absolute) gain A_j, and the number of photons N_j^{γ} from the Xe source that strike the photocathode and cause an avalanche in the PMT's dynode:

$$Q_j^{\text{obs}} \propto N_j^{\gamma} \times A_j \times \text{QE}_j. \tag{5.1}$$

For SK-III, only 420 "standard" reference PMTs underwent this procedure. These standard PMTs are strategically mounted in the ID to understand the geometrical relationship between PMTs in similar positions in the detector and the Xe scintillator ball used

in-tank [112], shown schematically in Fig. 5.1. The setup for the Xe scintillator ball source was relocated to the tank after initial testing of the standard PMTs. The monitor dark box was placed on the tank top and the scintillator ball was installed in the detector tank near the center: $(x, y, z) = (353.5, -70.7, 0.0)$ cm. After the system was installed into SK, the HV settings for the rest of the ID PMTs were calibrated *in situ* in similar fashion using the Xe light source and scintillator ball. Their HV values were set to give the same Q^{obs} as the reference PMTs corresponding to their geometric position relative to the scintillator ball. The scintillator ball remains in the tank to enable real-time monitoring of the relative gain for the ID PMTs during years of continuous running.

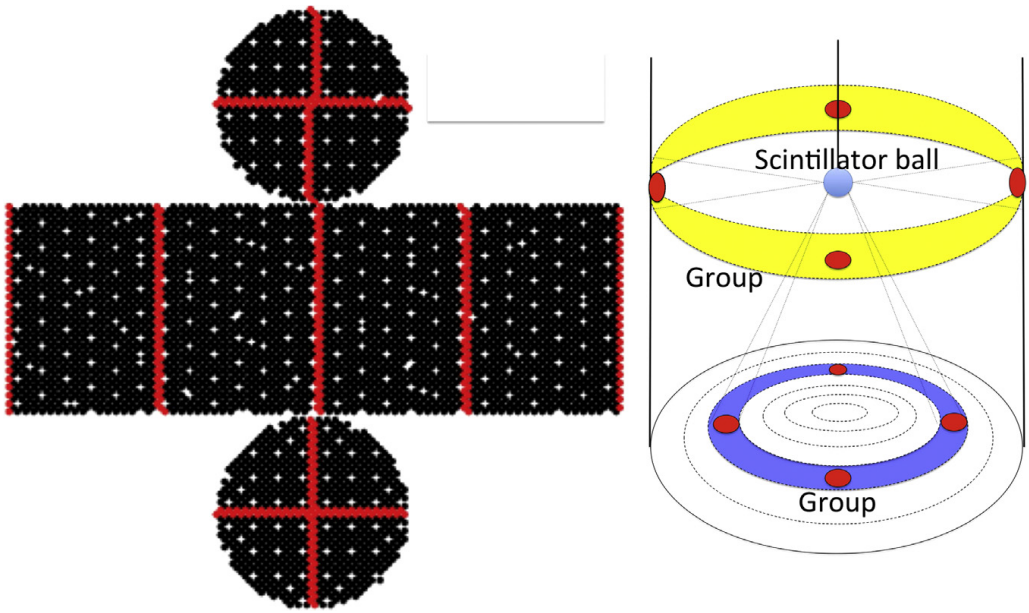

Figure 5.1: The "standard PMTs" used as reference PMTs in SK-III and SK-IV, and their grouping relationship with other PMTs [112]. Left: location of the 420 standard ID PMTs in red, with the other ID PMTs in black. Right: The standard reference PMTs (red) and the PMTs they are correspondingly grouped with on the detector wall (yellow) at the same z-position, and on the detector top/bottom (blue) at the same r position.

After setting the HV for all of the PMTs in SK, the absolute gain of the detector is determined using a Ni-Cf source. This is referred to as the "nickel source" calibration. The Ni source is a 3.5 kg polyethylene ball containing 6.5 kg of NiO wool surrounding a ^{352}Cf source inserted into the center of the sphere. This sphere is small and light enough to be

deployed in any free calibration port on the detector top via a small hand-operated crane. When the Ni source is submersed, it fills with water. The ^{352}Cf has a half life of 2.65 years and decays by either α-decay (96.9%) or by spontaneous fission (3.1%) that has an average of 3.8 neutrons per decay. The neutrons emitted by the ^{352}Cf thermalize in the water inside the ball and capture on the Ni. The reaction $^{58}\mathrm{Ni}(n,\gamma)^{59}\mathrm{Ni}$ isotropically produces 9 MeV gamma rays (67.9%). The Ni source provides a stable and uniform light source in the range of Cherenkov light with 99% of the observed signal being single photoelectrons. A typical distribution of charge due to single-pe from the Ni source calibration data taken during the SK-III is plotted in Fig. 5.2.

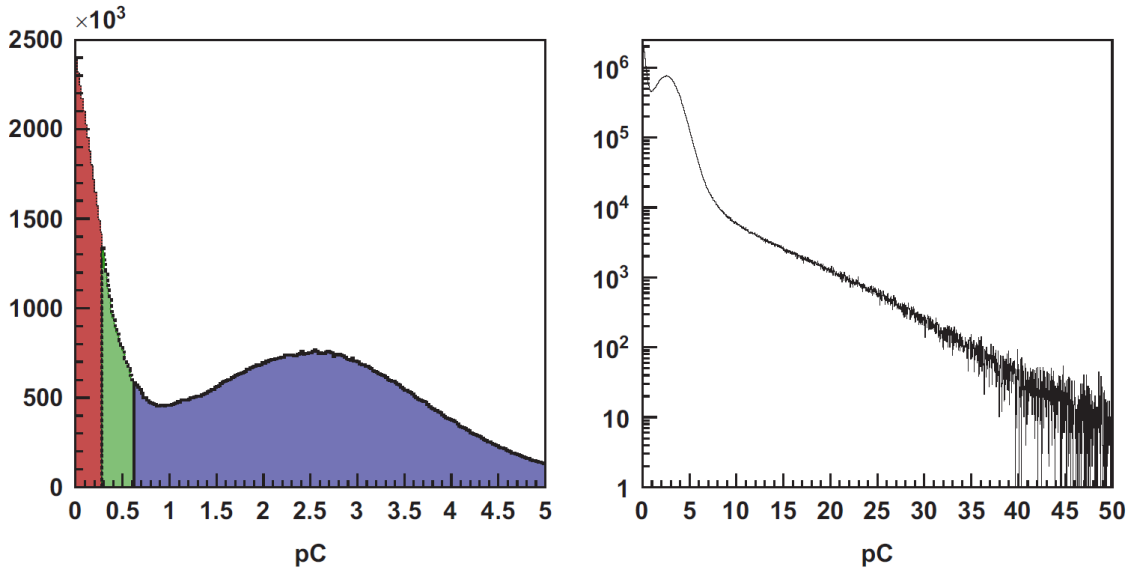

Figure 5.2: Charge distribution in pC for single photoelectrons resulting from Ni-Cf source ("nickel source") calibration in SK-III [112]. The left (right) is the linear (logarithmic) distribution of the charges after the relative gain correction is applied. In the left figure, the blue region represents the distribution with normal PMT gain, while the green region results from doubling the gain while lowering the trigger threshold by half; the red, lower region below 0.25 pC is linearly extrapolated from the higher charge region.

This calibration is performed once a month to keep track of the drift in the absolute gain of the detector. The results of the calibration are summarized in Table 5.1 for each phase. Differences between SK-II and SK-III arise from the different PMTs produced before

and after the accident, with the newer PMTs having a lower gain than that of the older ones. Between SK-III and SK-IV, differences arise due to the differing performances of the front-end electronics, as well as a steady increase in the long-term gain during SK-IV. The increase in gain amounts to ∼2-3% per year relative to the initial value for SK-IV.

Table 5.1: The absolute gain for each SK-Phase in pC/photoelectron

Phase	Absolute Gain [pC/pe]
SK-I	2.055
SK-II	2.297
SK-III	2.243
SK-IV	2.645

Gain Drift in SK-IV

The increasing drift in the gain causes the observed hit rate of a PMT to increase due to Q^{obs} passing the hit-based trigger threshold for readout in the readout electronics more quickly and/or more often. For an event, this means that the calculated number of effective hit PMTs (N_{eff}) increases, and so does Q^{obs} per hit PMT. The N_{eff} is used by low energy analyses to determine the observed total energy for physics events, while accounting for corrections to the hit rate and minimizing any detector-related factors (PMTs, the water transparency, or geometrical dependencies).

The drift in the gain during the latter half of SK-IV has led the low energy group of SK to apply a time-dependent gain correction to both the data and MC. This is determined by assuming the fractional difference in the hit rate (HR) and the gain (G) are linearly correlated, i.e.

$$C_G = \frac{F_{\mathrm{HR}}}{F_G}, \tag{5.2}$$

where

$$F_{\mathrm{HR}} \equiv \frac{\mathrm{HR}(t) - \mathrm{HR}(0)}{\mathrm{HR}(0)} \quad \text{and} \quad F_G \equiv \frac{G(t) - G(0)}{G(0)}. \tag{5.3}$$

The gain correction parameter C_G is tuned for each different PMT manufacturing batch separately using the decay-e sample (Sec. 5.2.2) and MC to minimize the time variation of the water transparency and N_{eff} [118]. The best fit for the gain correction is $C_G = 0.226 \pm 0.003$. Sec. 6.2 discusses how N_{eff} is derived, and the gain correction of N_{eff} is discussed in Sec. 6.2.2.

5.1.2 Relative Gain

For each individual PMT, the relative gain is determined by normalization with the average gain over all the PMTs. The gain of each PMT is obtained using a single light source with a high and a low intensity setting. The light source for the relative gain calibration is a nitrogen-laser-driven dye laser with a neutral density filter wheel containing two different filters for the low and high intensity settings. The filter wheel is set between the fiber optical cable that feeds into the diffuser ball and the dye laser. This "laser calibration" is also used in the timing calibration (Sec. 5.1.4).

The high intensity setting corresponds to Q_j^{obs} for the j'th ID PMT from Eq. 5.1, and the low intensity setting is low enough to only have a few hit PMTs record the flash. In the low intensity case, PMT hits are considered to be single-pe hits independent of the total absolute gain A_j and are set in photon counting mode, i.e.

$$N_j^{\mathrm{obs}} \propto N_j^{\gamma} \times \mathrm{QE}_j \quad \text{where} \quad N_j^{\gamma} = I \times a_j. \tag{5.4}$$

The parameter a_j is the acceptance of the j'th ID PMT, and I corresponds to the intensity of the light source for either the low or high setting. The charge threshold for the electronics

is set low enough so that any relative change in gain makes minimal impact on $N_j^{\rm obs}$, with $\Delta N_j^{\rm obs} = 1.5\%$ for a 10% change in the gain G_j. The gain for the j'th ID PMT is given by $G_j \propto Q_j^{\rm obs}/N_j^{\rm obs}$.

The relative gain distribution for all of the ID PMTs at the start of SK-III can be seen in Fig 5.3, where the mean lies at G=1. The RMS of the distribution (5.9%) is assumed to be due to differences in the QE of each PMT, as $Q^{\rm obs}$ was set to be the same across all PMTs at the beginning of SK-III. The relative gain factors G_j are used as a fine correction to the absolute gain to more accurately convert $Q_j^{\rm obs}$ into the number of observed pe in the j'th PMT for each event. Once the relative gain is determined for each PMT, the absolute gain is determined using the nickel source calibration and correcting for the relative gain correction for each PMT.

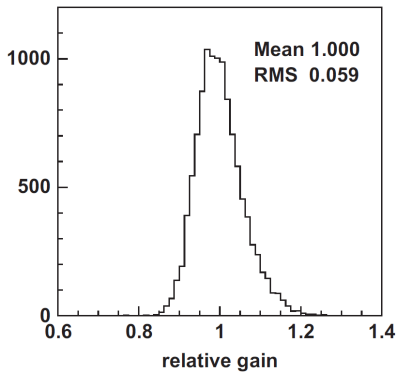

Figure 5.3: The distribution of the relative gain for each PMT at the beginning of SK-III measured with laser calibration data [112].

5.1.3 QE Calibration

As stated earlier, QE refers to the product of the PMT quantum efficiency, the fraction of incident photons that produce photoelectrons in the photocathode via the photoelectric effect, and the PMT's collection efficiency. The wavelength dependence of the quantum efficiency for the 50 cm PMTs as measured by Hamamatsu is shown in Fig. 4.14.

To determine the QE for each PMT, the effect from the gain for a given PMT needs to be mitigated, and the number of photons reaching the PMT must be reasonably well known. The nickel source described in the previous subsection (Sec. 5.1.2) is able to satisfy these criteria and is employed in this calibration. In order to use Eq. 5.4 to extract QE_j, SKDETSIM is used to predict the number of incident photons, and the ratio between observation and prediction is formed. Additional requirements on the stability of the water transparency throughout the detector is absolutely necessary. Any non-uniformity in the water quality and transparency will alter the probability of a photon striking a PMT, if it makes it to the PMT wall at all. These non-uniformities can cause a deviation along the photon track as it propagates through the detector to the j'th PMT and will cause discrepancies between the observations from calibration data and the predictions from SKDETSIM.

Other complications to this calibration come in the form of PMT dark noise and radioactive backgrounds. To remove (or minimize) these effects, hit PMTs are removed from consideration if the timing for their registered hits falls outside the timing window of an event. For each PMT hit, the time-of-flight (TOF) is calculated from the vertex subtracted timing distribution: T-TOF in nanoseconds. The timing of the hits is separated into several categories to facilitate the background subtraction. The T-TOF distribution is the distribution of the timing residuals for an event with vertex $\vec{v}$ in the tank and is given by:

$$t_{\mathrm{residual}} = (t_j - t_0) - \frac{|\vec{v} - \vec{h}_j|}{c_{\mathrm{water}}}, \tag{5.5}$$

where t_j is the hit time for the j'th PMT, t_0 is the emission time (adjusted to minimize all timing residuals), $\vec{h}$ is the distance vector to each PMT, and c_{water} is the group velocity of light in the SK water [94]. Consequently, $\mathrm{T} = (t_j - t_0)$, and $\mathrm{TOF} = |\vec{v} - \vec{h}_j|/c_{\mathrm{water}}$. So-called "on-time hits" occur within a 300 ns wide time window, and so-called "off-time hits" occur 150 ns to 450 ns after the end of the on-time hit period. The difference in the on-time and off-time hits gives the true hit rate, i.e. the true number of hits for the total time window.

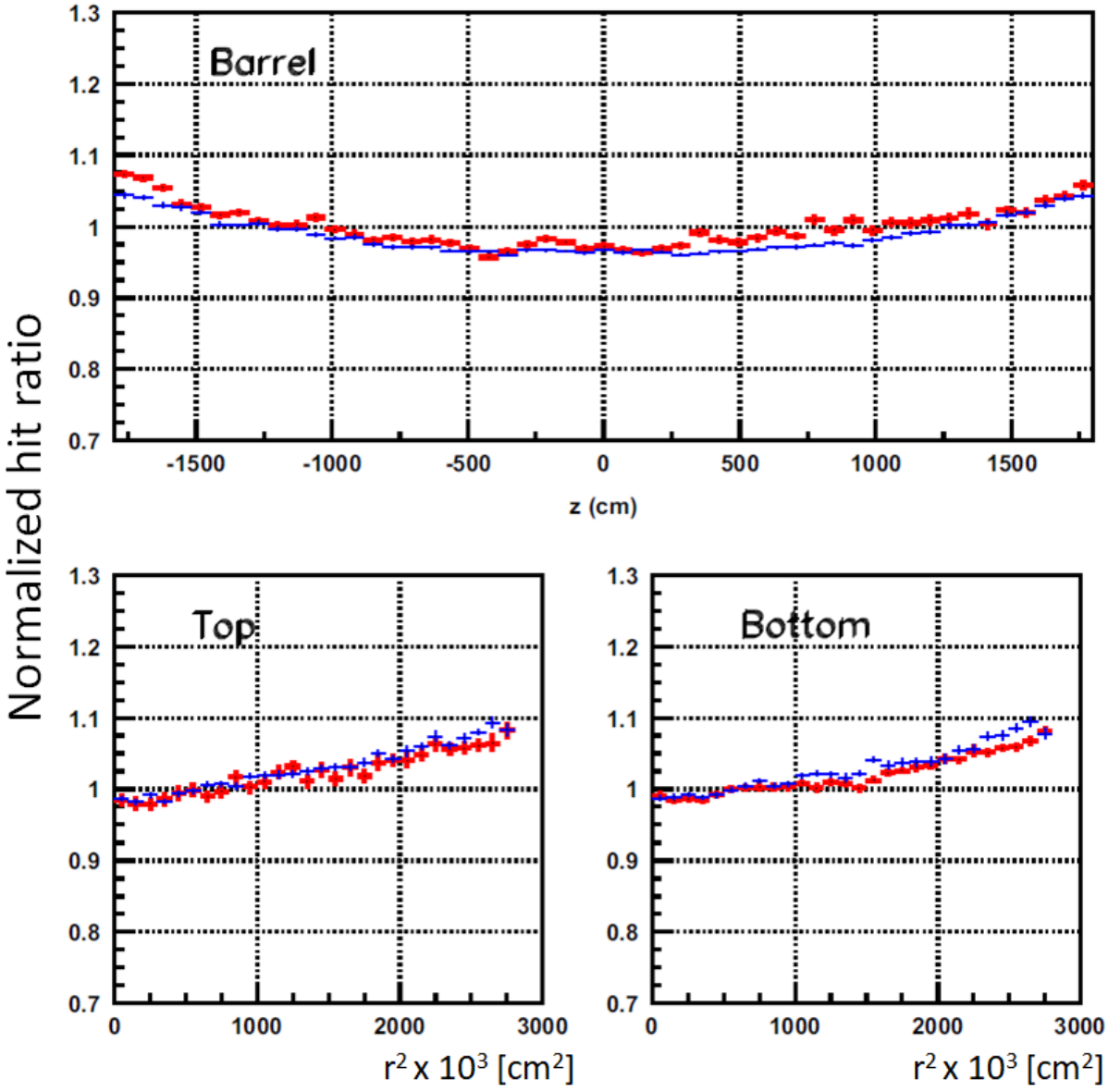

Figure 5.4: The positional dependence of the PMT hit "probability" for data (red) and MC (blue) [112]. The vertical axis is the number of hits after normalizing to the average value of all PMTs. The upper figure corresponds to the barrel PMTs as a function of height z, and the bottom figures are the top (left) and bottom (right) PMTs as a function of r^2. Here, MC is not corrected by the QE factor.

Additional effects due to the relative geometry between the nickel ball and the j'th PMT are taken into account as well. To account for any position dependence, the hit probability is corrected by the factor:

$$N_j^{\text{obs}} \times \frac{R_j^2}{a(\theta_j)}, \tag{5.6}$$

where R_j is the distance between the source and the PMT. The dependence of the j'th PMT's acceptance a on the incident angle θ_j is

$$a(\theta_j) = 0.205 + 0.524\cos\theta_j + 0.39\cos^2\theta_j - 0.132\cos^3\theta_j. \tag{5.7}$$

Any scattering or absorption in the water, or reflection from neighboring PMT glass or from the black sheet is not included in this correction. The corrected hit probabilities are shown in Fig. 5.4 after normalizing to the average number of hits in all PMTs. After accounting for these additional effects in MC, all remaining differences are absorbed into the QE_j factor for each PMT. In creating MC for the QE calibration, the QE of each PMT is set to the same number. After forming the ratio of the nickel calibration data to the QE calibration MC for each PMT, these values are stored in the "QE-table." The table is used in data analyses and in SKDETSIM to weigh the production of photoelectrons for each PMT.

Additional differences between PMTs used in SK-I/II and SK-III/IV exist, due in large part to differences in the manufacturing process. These differences are considered when creating the QE_j and the relative gain G_j factors. Discussion of these details is beyond the scope of this analysis. For further details, please see [112].

5.1.4 PMT Timing Calibration

To have an accurate and precise reconstruction of the track directions and vertices for events in SK, both the PMTs and the readout electronics must be calibrated properly. Several factors contribute to the response time of the readout electronics:

- Timing responses due to the spread in the transit time of the photoelectrons in the PMTs.
- The length of the signal cable connecting the PMT and readout electronics.
- The time it takes the electronics to process the received PMT signal.

During signal processing in the readout electronics, the rise time for larger pulses is quicker than that of smaller pulses, causing the stronger pulse to cross the threshold for readout earlier. This leads to a dependence in the readout time for a given pulse based on the pulse's height. This effect is known as the "time-walk" effect and is shown schematically in Fig. 5.5.

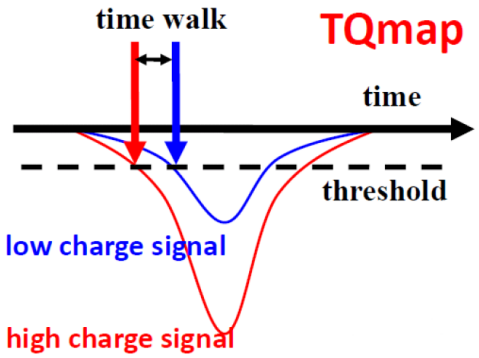

Figure 5.5: The "time-walk" effect due to higher charged signals passing the discriminator threshold more quickly than lower charged signals, which leads to an offset in the readout time for a given PMT and readout electronic set [43].

To account for the time-walk effect, the "timing calibration system" injects fast light pulses into SK at varying intensities through a small diffuser ball located in the center of the

tank. A schematic of the timing calibration system is shown in Fig. 5.6. The laser used to calibrate the TQ-map in the PMT timing calibration at the beginning of SK-IV is a gas flow nitrogen laser designed by Usho Optical Systems Company (USHO KEC-100). This laser is a fast pulse laser (0.4 ns at FWHM) with a wavelength of 337 nm. It is used to pump a dye that shifts the light to 398 nm, approximately corresponding to the maximum response of the convolution of the Cherenkov spectrum, the PMT quantum efficiency, and the light absorption spectrum. The dye pulse has a width of 0.2 ns FWHM, and a variable optical filter is used to control the intensity. The variable intensity 398 nm light is monitored by a 2-in PMT, and the light is transported to the diffuser ball in the center of the SK detector via optical fiber. The diffuser ball is designed to emit light isotropically and has a variation in photon emission time of less that 0.2 ns.

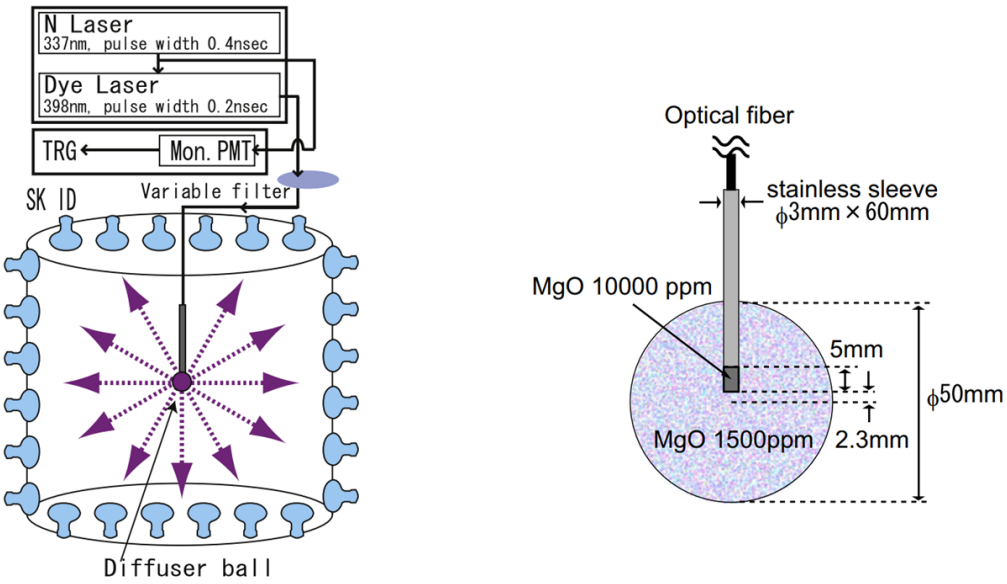

Figure 5.6: Left: Schematic overview of the SK timing calibration system. Right: Cross-section of the diffuser ball used in the timing calibration system, seen in the figure on the right. Both plots are taken from [112].

The variable intensity light produced by the timing calibration system leaves an imprint in the T and Q information read out by the front-end electronics. The calibration data is used to map the strength of the variability in the T and Q information for each pair of

PMT and readout electronics. Doing this forms a unique set of calibration constants for each PMT called the "TQ-map." Here, T is the signal response time from the time when a PMT is hit to the time of electronic readout. T is determined by subtracting the readout time by the time-of-flight subtraction (T-TOF) from the source position to the PMT, as the emission time of the calibration light is known. In this way, the TQ-map takes into account the overall process time and time-walk effect.

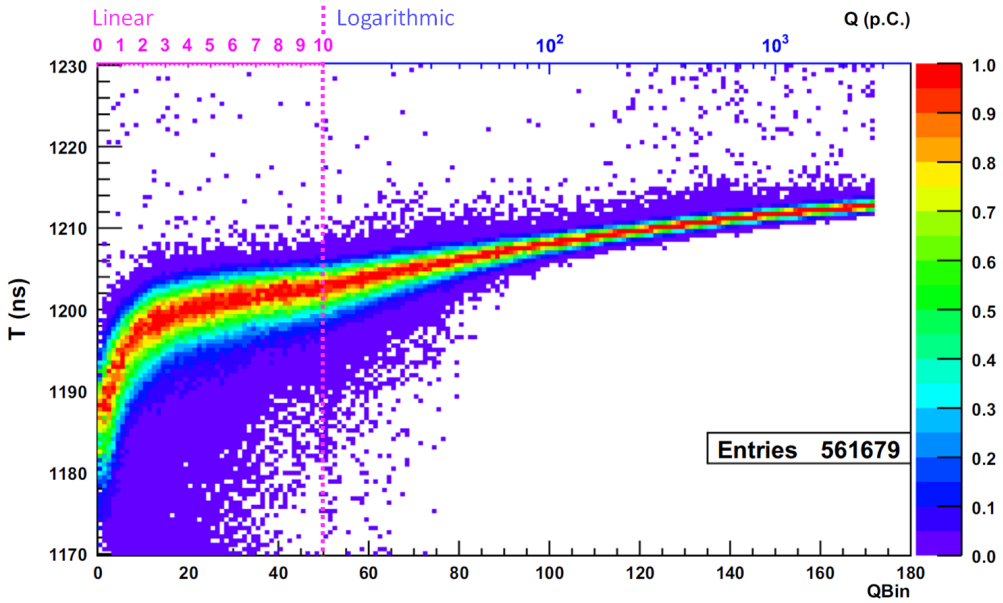

Figure 5.7: A typical TQ-map for readout channel (cable) number 10 [112]. The horizontal top axis is the charge Q in pC with a combined linear and log scale corresponding to the bottom horizontal axis (Qbin). The vertical axis is the time-of-flight subtracted timing T for the hits, where larger (smaller) T correspond to earlier (later) hits.

To create the TQ-map for a given PMT, the Q-axis (in units of pC) of the two-dimensional TQ distribution is divided into 180 "Qbins." The Qbins are defined in the following way: linearly from 0 to 10 in 0.2 pc wide bins and logarithmically from 10 to 3981 pC in $50 \times \log(\text{pC})$ wide bins [112]. For reference, the amount of Q [pC] per pe is 2.645 during SK-IV (see Table 5.1). The two-dimensional TQ distribution for the PMT corresponding to cable (or channel) number 10 is plotted in Fig 5.7. The timing distribution of each Qbin is fit with an asymmetric Gaussian, where the asymmetry comes in due to early (late) hits from

from direct (indirect) light and from asymmetric time responses of the PMTs themselves. The set of peaks and standard deviations from these asymmetric Gaussian fits are themselves fit with different polynomials for certain ranges of Qbins. The fits for the ranges of Qbins are given by:

$$\begin{aligned} F_1(x) &\equiv P^3(x) && \text{Qbin} \leq 10 \\ F_2(x) &\equiv F_1(10) + (x-10) \times \left[F_1'(10) + (x-10) \times P^3(x-10)\right] && 10 \geq \text{Qbin} \leq 50 \\ F_3(x) &\equiv F_2(50) + (x-50) \times P^6(x-50) && \text{Qbin} \geq 50 \end{aligned} \tag{5.8}$$

where x is a continuous parameter corresponding to the Qbins. F_1' is a derivation of F_1 introduced to enforce continuity between F_1 and F_2 at Qbin = 10. The three polynomial functions are constructed to satisfy the boundary conditions at $x = 10$ and $x = 50$, i.e. $F_1(10) = F_2(10)$ and $F_2(50) = F_3(50)$. These fifteen fit parameters, four from the first and second region each and seven from the last region, are saved as the functional TQ-map for each PMT. The TQ-maps are used to correct the time response for each set of PMT and readout electronics.

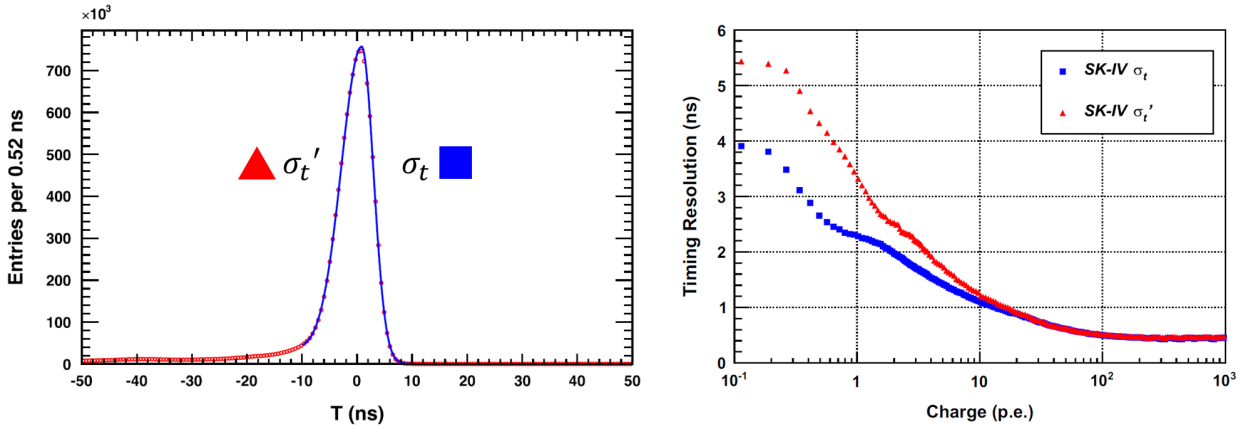

Figure 5.8: Left: The fitted asymmetric Gaussian (blue) for data (red) from the timing distribution of all PMTs for Qbin = 14. Right: The asymmetric timing resolutions σ_t for late hits (blue square) and σ_t' for early hits (red triangle) as a function of charge (in units of photoelectrons) for SK-IV. Both figures are taken from [112].

Once the final TQ-map for each PMT has been created from these polynomial fits,

the timing resolution of SK is evaluated after applying each PMT's TQ-map. The timing distribution using all ID PMTs is formed for each Qbin and is fit by an asymmetric Gaussian f^{Qbin}. This asymmetric Gaussian fit is a separate procedure from the asymmetric Gaussian fit to the timing of individual PMTs described earlier. For a given Qbin, the fit f^{Qbin} is described by two Gaussian fits f_i^{Qbin}:

$$f_i^{\mathrm{Qbin}} = A_i \times \exp\left[\frac{-(t - T_{\mathrm{peak}})^2}{\sigma_i^2}\right] + B_i, \tag{5.9}$$

where the index $i = 1$ (2) denotes the later (earlier) hits. The two Gaussian functions are matched at $t = T_{peak}$ by requiring $A_1 + B_1 = A_2 + B_2$. The results of this fit (blue) to the timing distribution data (red) in Qbin = 14 are shown in the left side of Fig. 5.8. The two timing resolutions σ_i from Eq. 5.9 are designated as $\sigma_1 = \sigma_t$ and $\sigma_1 = \sigma_t'$, and the timing resolution for SK-IV is plotted in the right side of Fig 5.8. The SKDETSIM software takes advantage of both σ_i to more accurately reproduce the timing distributions found in the data. The asymmetry is especially important in being able to produce accurate MC simulations with SKDETSIM for calibration sources like the LINAC.

For continuous monitoring of the TQ-map in real-time, the laser component of the timing calibration system was replaced with a laser that is better suited for continuous running. The new laser component consists of a sealed nitrogen gas laser (Laser Science Instruments VSL-337 N^2) and dye (DLM-120). The N^2 laser emits 337.1 nm light, and the dye shifts it to the desired 398 nm. For continuous running, the intensity is held at a constant level that achieves ∼99% occupancy in the ID PMTs with a maximum average Q of ∼20 pe per PMT. This calibration occurs with a frequency of approximately 0.03 Hz, and the long-term stability of the timing response in SK-IV is within ±0.1 ns.

5.2 Water Transparency and Photon Tracking Calibration

As stated early on, the detection medium of SK is water that has been purified to minimize the loss of light from physics events in the detector propagating to the PMTs. Small changes in the water transparency (WT) can cause greater attenuation of the light and impact physics results. To accurately simulate events using SKDETSIM, the various behaviors of photons in the water (scattering, absorption, and reflection) must be well understood. This includes reflections off the black sheet and PMT surfaces described earlier.

The WT is tracked using two separate methods: (1) data from real-time laser calibration light at various wavelengths is used to obtain the wavelength dependence of the attenuation coefficients for scattering and absorption in light propagation; (2) Michel electrons produced by muon decays within the ID are used to track the time variation of the absorption coefficient. Michel electrons will be referred to as "decay-e." An additional parameter for the variability in the WT as a function of height, known as the top-bottom asymmetry, is also determined to better understand data and to more accurately simulate the photon propagation in SKDETSIM.

The path length for photons is modeled as an exponential $I(\lambda) = I_0(\lambda)\exp[L \times \alpha_{total}(\lambda)]$, where L is the track length and $\alpha_{total}(\lambda)$ is the total attenuation coefficient. The wavelength-dependent water transparency is defined as $L_{WT}(\lambda) = 1/\alpha_{total}(\lambda)$. The total attenuation coefficient α_{total} is defined as

$$\begin{aligned} \alpha_{total}(\lambda) &= \alpha_{abs}(\lambda) + \alpha_{sct}(\lambda), \quad \text{where} \\ \alpha_{sct}(\lambda) &= \alpha_{sym}(\lambda) + \alpha_{asym}(\lambda). \end{aligned} \tag{5.10}$$

In SKDETSIM, the components of the α_{total} correspond to the total absorption α_{abs}, the

symmetric component of scattering α_{sym} (symmetric Mie scattering plus Rayleigh scattering), and the asymmetric component of Mie (forward) scattering α_{asym}. The attenuation coefficients for water are referred to in this work as "WT coefficients." The three WT coefficients are described in SKDETSIM through WT parameters that are tuned to match MC to results from calibration data. The SK WT is generally quoted at a reference wavelength of $\lambda = 400$ nm, with the average value of the WT for SK-IV being 120 m.

5.2.1 Real-time Tracking of the Water Transparency by Laser Light

The laser injection system fires a collimated laser beam into the top of the SK detector at multiple wavelengths using either a nitrogen laser (337.1 nm) or laser diodes (LD) with wavelengths 375 nm, 405 nm, 445 nm, and 473 nm. Previously, in addition to the 337 nm wavelength produced by the nitrogen laser, the other wavelengths (365 nm, 400 nm, and 420 nm) used in the calibration were produced by a N^2 dye-laser system. The dye-laser system was replaced in 2009 with the current set of LDs. The 473 nm LD was installed at that time as well. When performing the WT calibration, laser light is injected once per minute into the detector. Hit patterns in six individual regions of the ID are analyzed to extract the WT coefficients. These regions of the detector correspond to the top PMTs and PMTs in the five regions of the barrel (B1 - B5). The barrel regions are illustrated in Fig. 5.9. This figure illustrates the setup for the light injection system for the WT calibration. By grouping the PMTs by region, the scattering and reflection angle with respect to the PMTs is indirectly measured in aggregate. The laser light is used to determine $\alpha_{sym}(\lambda)$, $\alpha_{asym}(\lambda)$, and $\alpha_{abs}(\lambda)$ by comparing the timing and spatial distributions between the laser data and corresponding MC. Before applying WT corrections in the reconstruction of physics events, the WT is fixed to $L_{WT}(400\text{nm}) = 90$ m, as the correct WT can only be applied offline after the calibration data has been analyzed.

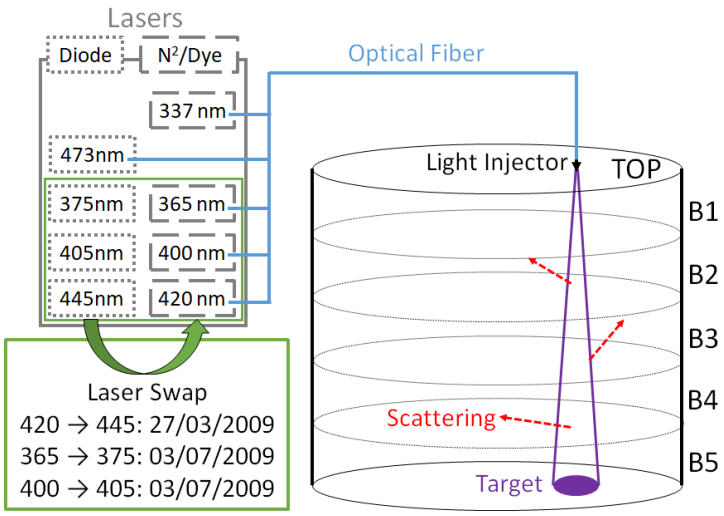

Figure 5.9: Illustration of the real-time light injection system used for water transparency measurements. The definition of the barrel regions are shown, along with the laser wavelengths. The dates for the exchange of each dye laser with a laser diode and the corresponding wavelength change due to the exchange. Figure modified from [112].

The data for each of the six regions shown in Fig. 5.10 are compared against MC for PMT T-TOF hit distributions. In the figure, the data (black circles) for the 405 nm LD is shown, along with the best-fit tuned MC (red). The green region is due to scattered light. The number of scattered photons and shape of their distribution are used to tune the WT parameters that describe the WT coefficients α_{abs}, α_{sym}, and α_{asym} in SKDETSIM. The peak in the yellow region is due to the reflected light of the beam-spot off the bottom black sheet and PMTs. The distribution of the reflected light is used in SKDETSIM to model and tune reflection effects due to these surfaces.

A second calibration for determining the angular dependence of the black sheet reflectivity is used to tune the corresponding model in SKDETSIM. More information on the measurements and modeling of light reflection off the black sheet and PMTs in SK can be found in [112].

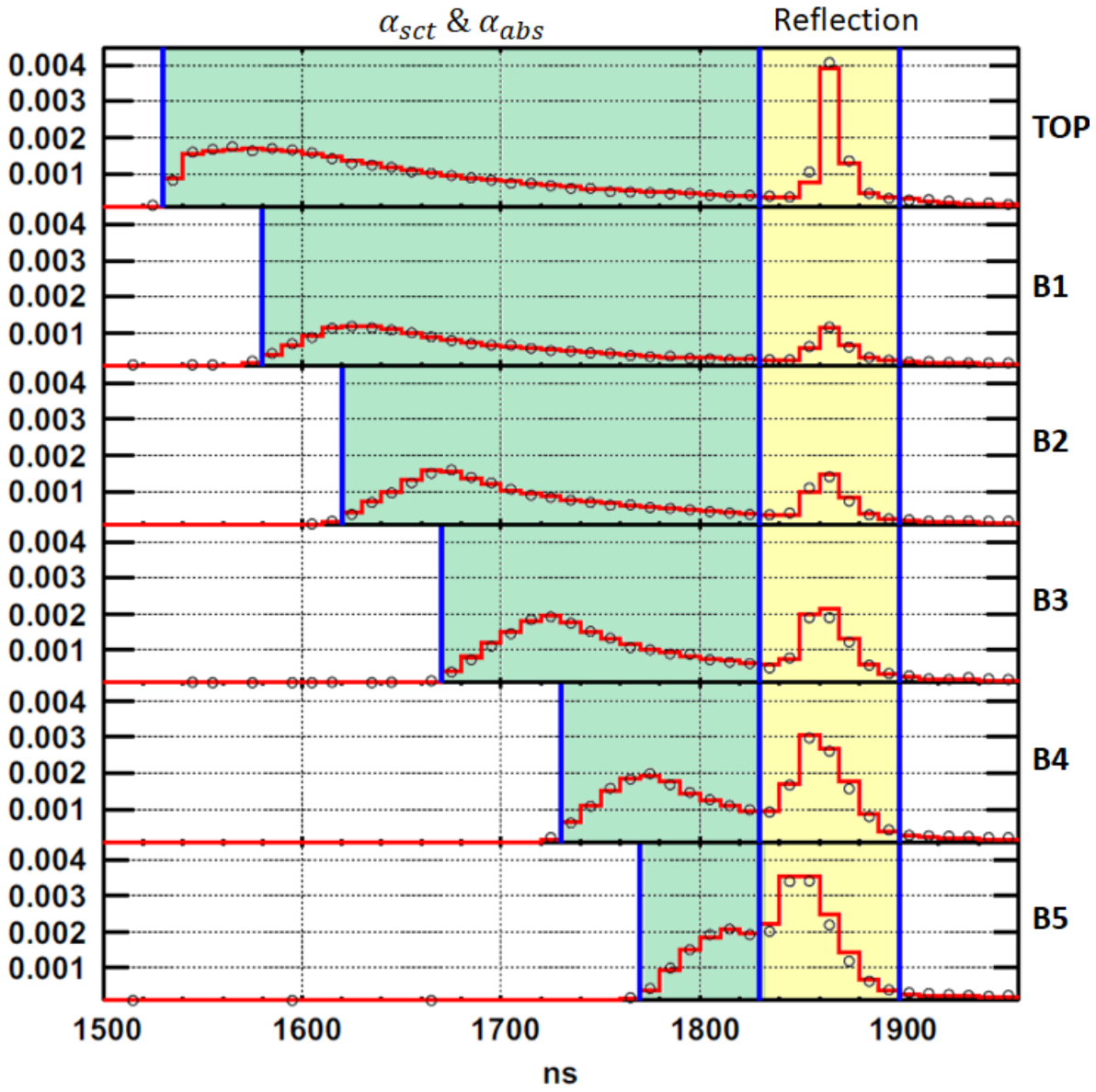

Figure 5.10: Typical result for the T-TOF PMT timing distributions from the 405 laser diode for the water transparency calibration [112]. The data (black) and MC (red, best fit tune) for each region (listed on the right next to the plot) is shown. The shape of the distribution and number of photons in the green region is used to extract the best fit tune for the parameters of functions that model the water transparency coefficients $\alpha_{abs}, \alpha_{sym}$, and α_{asym} in SKDETSIM. The information in the yellow region is used to model in SKDETSIM the reflection off the PMT glass and the black sheet in the detector.

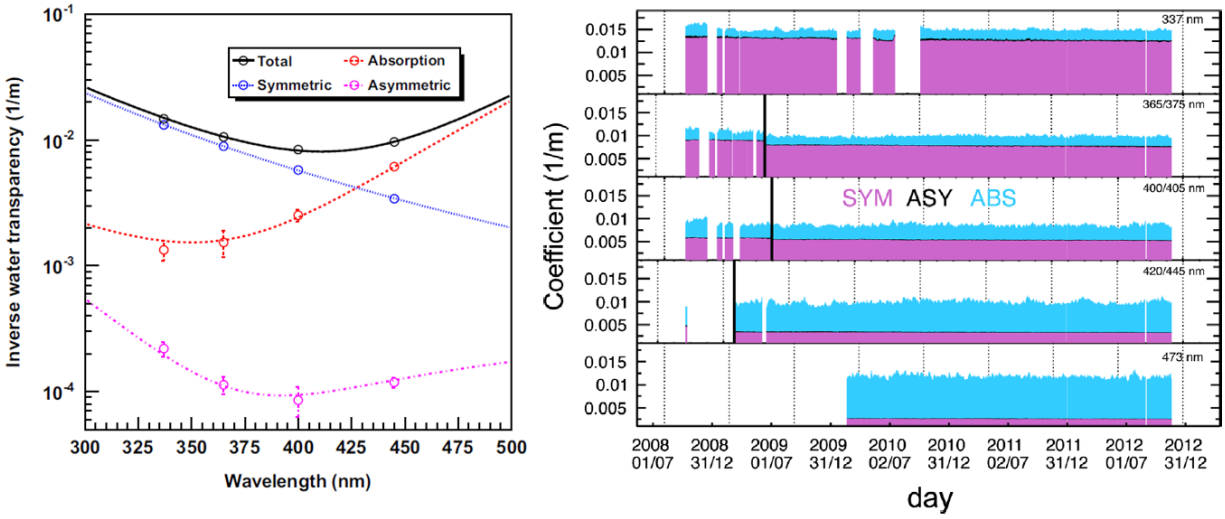

Figure 5.11: Left: The various fitted functions (lines) of each water transparency coefficient. These coefficients are based on the best fit water transparency parameters obtained from the measured coefficient data (circles) taken in April 2009. The total attenuation coefficient, defined in Eq. 5.10, is shown in black. Right: The time dependence for the measured water transparency coefficients as a function of the date in SK-IV for each laser wavelength. The vertical black line represents the change in the wavelength due to the exchange of the laser diodes in the calibration system. The overall height for each data period is the total attenuation coefficient. The symmetric scattering (purple) dominates for lower wavelengths, while the absorption (blue) dominates for larger wavelengths. The contribution due to asymmetric Mie scattering (black) is an order of magnitude smaller than the other two effects. The symmetric scattering coefficient is considered to be stable, though the absorption coefficient varies with time. Both figures taken from [112].

Water Transparency Coefficients and Parameters

Functions are used to describe each WT coefficient in order to obtain the proper wavelength dependence outside of the calibration wavelengths. The functions are fit to the calibration data using sets of WT parameters A_i, S_i, and M_i that describe $\alpha_{abs}(\lambda)$, $\alpha_{sym}(\lambda)$, and $\alpha_{asym}(\lambda)$ respectively. The function used to describe the absorption WT coefficient is an ad hoc piecewise function:

$$\alpha_{abs}(\lambda) = \begin{cases} A_0 \times \left[\frac{A_1(t)}{\lambda^4} + A_2(\frac{\lambda}{500})^{A_3}\right] & \text{if } \lambda \leq 463.9\text{nm} \\ \frac{A_0 \times A_1(t)}{\lambda^4} + \text{PF}(\lambda) & \text{if } \lambda \geq 463.9\text{nm} \end{cases} \tag{5.11}$$

where the WT parameter $A_1(t)$ is varied with time based on decay electron data, described in Sec. 5.2.2. The function $\text{PF}(\lambda)$ has been experimentally measured by Pope and Fry using their integrating cavity absorption meter (ICAM) device [119]. The symmetric scattering WT coefficient is given by the function

$$\alpha_{sym}(\lambda) = \frac{S_0}{\lambda^4}\left(1 + \frac{S_1}{\lambda^2}\right), \tag{5.12}$$

while the asymmetric scattering WT coefficient is given by the function

$$\alpha_{asym}(\lambda) = M_0\left[1 + \frac{M_1}{\lambda^4} \times (\lambda - M_2)^2\right]. \tag{5.13}$$

To tune the parameters for SKDETSIM, many timing distributions are created based on various sets of WT parameters, and the set that minimizes the χ^2 value when taking the difference between data and MC is selected.

Typical values for the WT parameters based on laser calibration data from April 2009 are listed in Table 5.2. The fitted functions of the WT coefficients based on Table 5.2 are shown in the left side of Fig. 5.11, while the time dependence of the measured WT

Table 5.2: Standard values of the water transparency parameters used to describe the various water transparency coefficients. These values are based on the April 2009 laser calibration data.

α_{abs}			
A_0	A_1	A_2	A_3
0.624	2.961×10^7	3.24×10^{-2}	10.94

α_{sym}	
S_0	S_1
8.514×10^7	1.138×10^6

α_{asym}		
M_0	M_1	M_2
1.002×10^{-4}	4.623×10^6	392

coefficients for SK-IV is shown on the right side of the figure. Figure 5.12 shows the actual time variation of the three WT coefficients for each laser wavelength during the whole of SK-IV. Since the majority of the Cherenkov spectrum is below 445 nm, the dominant effect on the total attenuation WT coefficient is due to the symmetric scattering WT coefficient. The symmetric scattering WT coefficient is stable, with the $\frac{\text{RMS}}{\text{mean}} = 0.3\%$ between October 2008 and November 2012 (see the purple contribution in the right plot of Fig. 5.11).

All but one of the WT parameters are fixed to the value in Table 5.2. The absorption WT coefficient has a higher variation with time and has a strong impact on SK low energy analyses. The WT parameter $A_1(t)$ is adjusted to account for variations in light absorption, based on the decay electron measurements around a given time period. In the SK low energy analyses, all of the WT parameters are tracked and averaged in approximately five-day intervals to model the actual WT conditions for a given date. For low energy events, the WT variations affect the number of effective hits N_{eff} and subsequent reconstructed energy (Sec. 6.2), as well as the reconstructed vertex (Sec. 6.3) and directional information (Sec. 6.4). The time-dependent WT is used in simulating events for specific dates in SKDETSIM or when reconstructing and analyzing data.

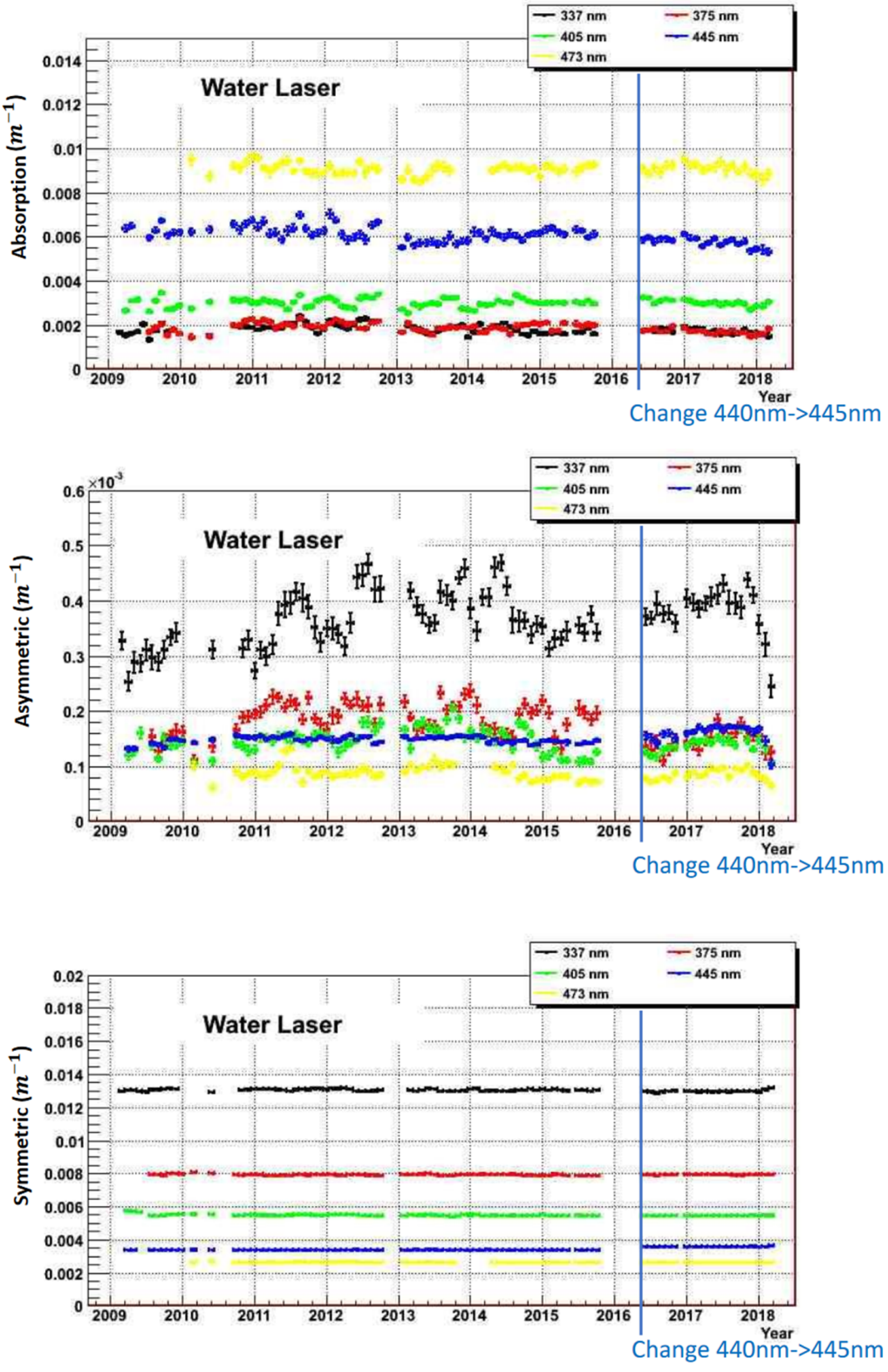

Figure 5.12: The time variation of the three water transparency coefficients for each wavelength used in the laser calibration system for all of SK-IV. The top, center, and bottom plot is of $\alpha_{abs}, \alpha_{asym}$, and α_{sym} respectively.

Effects of Gadolinium Sulfate on Water Transparency for SK-V/SK-Gd

As an aside, for SK-Gd, enough gadolinium sulfate ($Gd_2(SO_4)_3$) will be added into the SK water to form a 0.2% solution. The resulting effect on the WT, the "Gd-effect," has been estimated using wavelength-dependent WT measurements performed by myself in the EGADS experiment. The effect on the WT of introducing gadolinium sulfate in EGADS is discussed in Sec. 4.2.2, and the WT results are plotted in Fig. 4.5. The total attenuation coefficient is measured daily at three tank positions (top, center, bottom) for $Gd_2(SO_4)_3$ solutions in EGADS with the UDEAL system described in Sec. 4.2.2. UDEAL measures $\alpha_{total}(\lambda)$ at the same wavelengths as the laser calibration system in SK, plus two additional wavelengths, 532 nm and 595 nm. By measuring the amount of light lost when transmitting the laser beams through the water column (supplied from EGADS) at various heights, the extinction curve of each wavelength can be formed and $\alpha_{total}(\lambda)$ extracted. Below 337 nm, an atomic absorption spectrometer (AAS) is used to measure the total attenuation coefficient by scanning across multiple wavelengths. The AAS measurement is then matched up to the UDEAL measurement at 337 nm.

The Gd-effect on the WT is determined by subtracting the total attenuation coefficient for ultrapure EGADS water ($\alpha^{\mathrm{UP}}_{total}(\lambda)$) from the average stable value with the 0.2% gadolinium solution:

$$\Delta\alpha^{\text{Gd-effect}}_{total}(\lambda) = \alpha^{0.2\%\ Gd_2(SO_4)_3}_{total}(\lambda) - \alpha^{\mathrm{UP}}_{total}(\lambda). \tag{5.14}$$

The wavelength dependence between the reference measurements provided by UDEAL is approximated by linear interpolation. Above 445 nm, the overall effect is small. The EGADS collaboration measured the scattering component of the light attenuation for 0.2% gadolinium sulfate solution to be approximately 10%. The rest of the WT loss is due to absorption.

I have implemented the wavelength dependence of the Gd-effect in SKDETSIM by

modifying the WT coefficients α_{abs} and α_{sym}. To include the measured scattering component, 90% (10%) of the Gd-effect is added to the WT coefficient α_{abs} (α_{sym}). However, absorption lines that occur below 337 nm are treated as purely absorption without any scattering component. Fig. 5.13 shows the application of the Gd-effect to the WT coefficients in SKDETSIM.

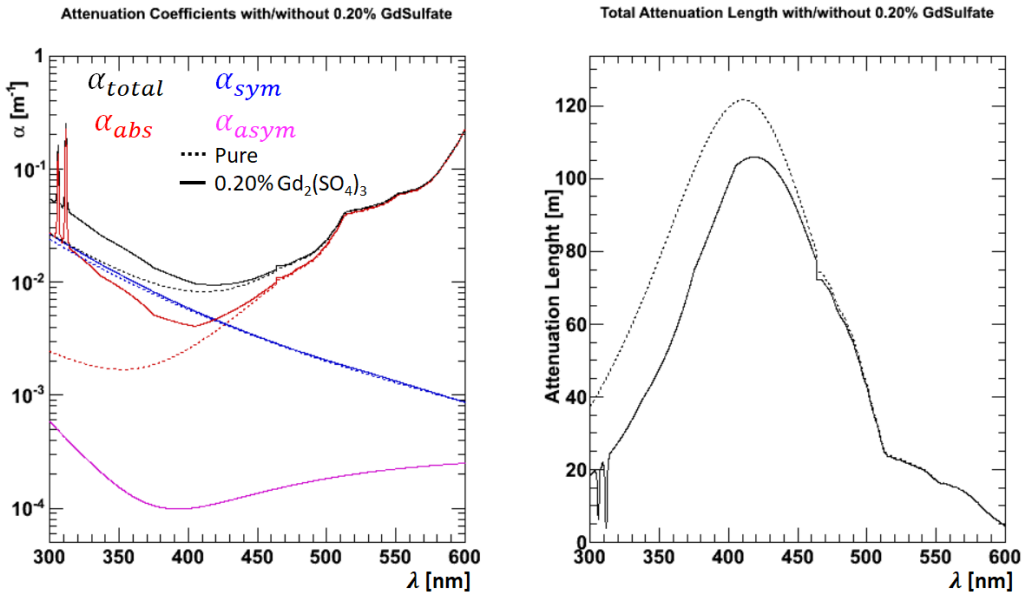

Figure 5.13: The water transparency coefficients from SKDETSIM with pure water (dotted lines) and with the 0.20% $Gd_2(SO_4)_3$ "Gd-effect" measured in EGADS applied (solid lines).

5.2.2 Time Dependence of Water Transparency using Decay Electrons

The WT is checked independently from the laser calibration using electrons produced by muon decay within the SK detector:

$$\mu \rightarrow \nu_\mu + \bar{\nu_e} + e^-. \tag{5.15}$$

The decay electrons (decay-e), also known as Michel electrons, have a well known energy spectrum. The overburden of rock cuts the muon rate down to about two per second in the detector. The time dependence of the mean energy of the decay-e is measured to track the time variation of the WT. To properly select decay-e, the following criteria must be met for a candidate event:

- The time difference (Δt) between the parent muon event and the decay-e candidate is 3.0 μs $\leq \Delta t \leq$ 8.0μs.
- The candidate decay-e must lie in the 22.5-kiloton fiducial volume, i.e. the reconstructed vertex must be farther than 2 m away from the PMT structure.
- The number of hit PMTs must be greater than 50.
- The distance between the reconstructed vertex of the candidate decay-e and the stopping point of the cosmic-ray muon is less than 2.50 m [118].

Around 1500 decay-e events per day pass the selection criteria. For these selected decay-e events, the distance between each hit PMT and the event vertex is calculated.

The PMT selection criteria for the decay-e WT measurement is illustrated on the left of Fig. 5.14 [120]. In the figure, d_j is the distance between j'th hit PMT, and N_{eff}^j is the effective hit value of that PMT (Eq. 6.5 in Sec. 6.2). N_i is the number of hit PMTs within a 10° wedge of the ring defined by the Cherenkov cone. To remove hits due to noise and indirect light, only PMTs whose hits have a residual timing (T-TOF) within 50 ns are considered. To ensure only direct light is used, only PMTs within the Cherenkov light cone relative to the reconstructed direction of the decay-e are considered. The Cherenkov light cone is azimuthally symmetric with an opening angle between 32° and 52°, which defines a ring as shown in Fig. 5.14. This ring is broken into 36 equal bins, and the hit PMTs on this

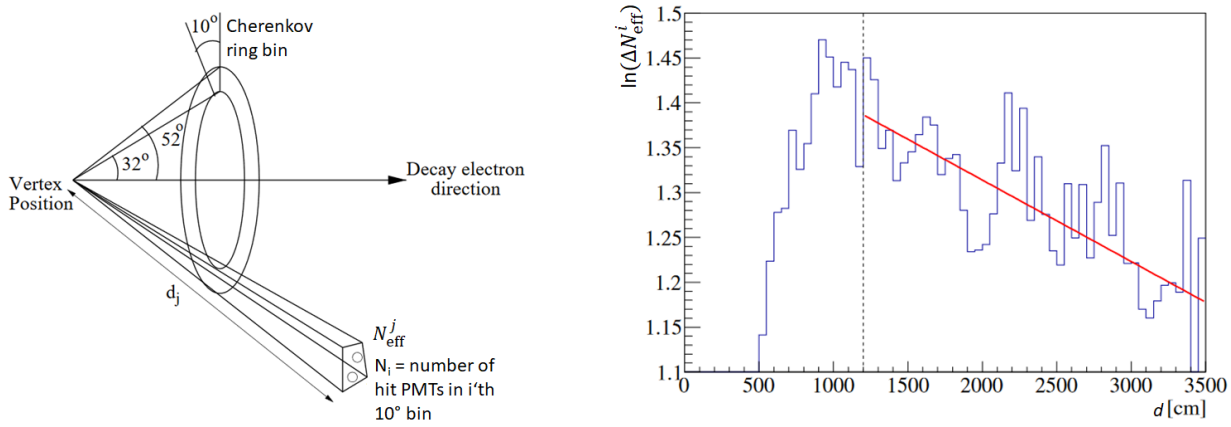

Figure 5.14: Left: An illustration of the parameters used in the decay-e water transparency measurement, modified from [120]. d_j is the distance between j'th hit PMT, and N^j_{eff} is the effective hit value of that PMT. N_i is the number of hit PMTs within a 10° wedge of the ring defined by the Cherenkov cone. Right: A typical ΔN^i_{eff} distribution in d from decay-e (blue histogram) [118]. The red line is a linear fit to the distribution between 1200 cm and 3500 cm, from which the water transparency is extracted.

ring are grouped together to get:

$$\Delta N^i_{\text{eff}} = \sum_{j=1}^{N_i} N^j_{\text{eff}} \exp(d_j/\lambda_e), \tag{5.16}$$

where λ_e is the relative water transparency. By assuming the size of each 10° bin is small, the average distance is $\bar{d}_i = \sum_{j=1}^{N_i} d_j/N$ and total N_{eff} is $N_{\text{eff}}(\bar{d}_i) = \sum_{j=1}^{N_i} N^j_{\text{eff}}$. Using the average distance, the exponential in Eq. 5.16 can be factored out of the sum, yielding:

$$\Delta N^i_{\text{eff}} = N_{\text{eff}}(\bar{d}_i) \times \exp\left(\bar{d}_i/\lambda_e\right). \tag{5.17}$$

Since the effective hit value for the PMTs in each 10° bin have been corrected by the attenuation due to the water transparency, $\exp\left(\bar{d}_i/\lambda_e\right)$, each of the ΔN^i_{eff} should be equal. By using the ΔN^i_{eff} from all the decay-e events in a single day, the collected effective hit values can be averaged over the Michel spectrum. The aggregate $\ln(\Delta N^i_{\text{eff}})$ distribution for a given day is then binned in d. An example $\ln(\Delta N^i_{\text{eff}})$ distribution is plotted on the right side

of Fig. 5.14 [118]. This distribution is fit with a linear function in the range between 1200 and 3500 cm. The resulting slope is, by definition, the inverse of the attenuation length λ_e. After averaging over a week of data, λ_e is used as an input to track the WT coefficient α_{abs} through the WT parameter $A_1(t)$.

To extract α_{abs} from λ_e, many mono-energetic electron MC samples are generated across a wide range of energies. The λ_e value and A_i WT parameters are varied independently while generating these MC samples. The energy is reconstructed for all sets of MC, and the consistency of the reconstructed energy to the true energy is used to establish the correlations between α_{abs} and λ_e. The results must also be consistent with the WT from the laser calibration. By doing this, α_{abs} can be tracked with the measurement of λ_e. The actual change in α_{abs} from the original absolute energy scale calibration can be determined, illustrated as the fractional change of the absorption coefficient in Fig. 5.15.

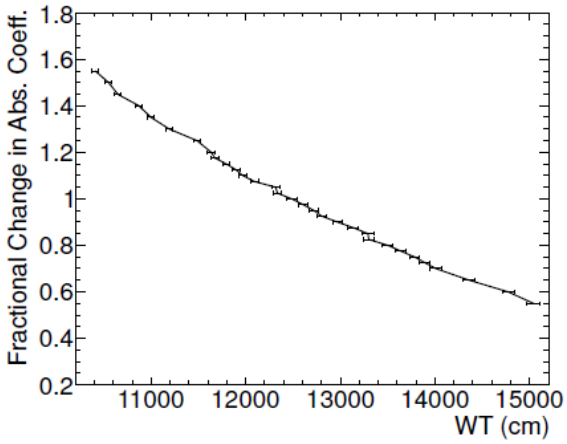

Figure 5.15: Fractional change of α_{abs} between the original absolute energy scale calibration and the WT measured by decay-e [42].

For low energy events, the WT is used not only for SKDETSIM but also for offline reconstruction of the event data recorded by SK. The WT affects, among other physical parameters, the reconstructed vertex, direction, and energy of data and MC events. This method requires a sliding window of seven days before and after the day one desires to simulate WT conditions, and it is also affected by PMT gain. The impact on the effective

number of PMTs N_{eff} hit from decay-e is shown for a period of SK-IV in Fig. 5.16 when using the standard WT assumption of 90 m (black) and after applying the correction due to the measured WT (red).

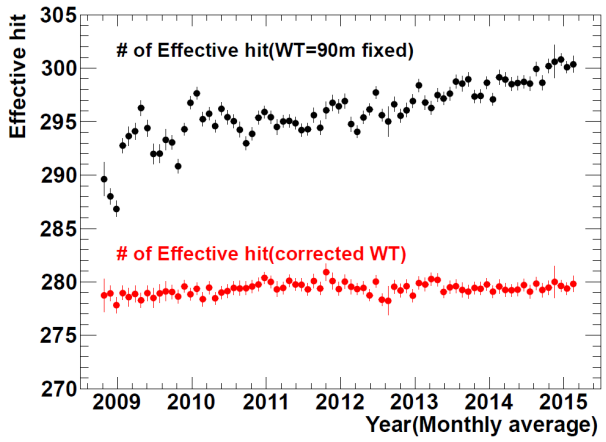

Figure 5.16: Time variation of the number of effective hit PMTs N_{eff} before (black) and after (red) applying the water transparency corrections derived from decay electron data in SK-IV [48].

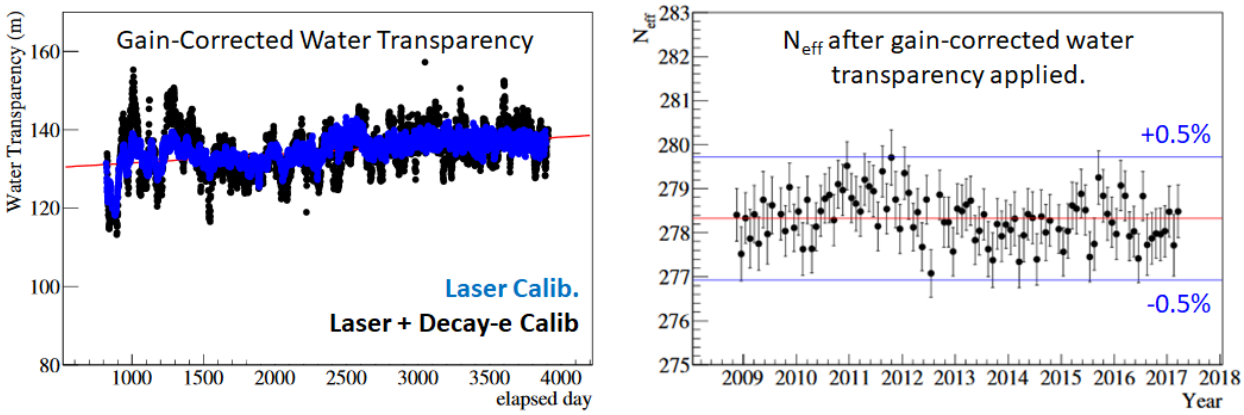

Figure 5.17: Left: The measured water transparency after applying the gain correction, using laser calibration data (blue) and the WT after combining the laser calibration data with the decay electron data (black). Right: The time variation of N_{eff} after applying the gain-corrected WT. The N_{eff} is stable within 0.5%. Figures courtesy of L. Wan.

The amount of observed charge each PMT contributes will change with any drift in its gain. The number of effective PMT hits N_{eff} and resulting reconstructed energy for events is also slightly affected. For the discussion on the determination of the N_{eff} and energy

reconstruction for events, please refer to Sec. 6.2 on event energy reconstruction. It is relevant to say here that the energy estimator N_{eff} and the resulting reconstructed energy are calculated using the WT information. During the second half of the SK-IV period, the gain of the PMTs began to drift upwards. This increase in the gain can cause the number of PMTs that pass the readout threshold to increase. That would cause more PMTs to be considered in an event than would have been with the original level of gain, and more events would pass the hit-based trigger threshold. This effect has a small, though significant, impact on low energy analyses because the energy reconstruction is highly dependent on the number of hit PMTs (Sec. 6.2). Much work has gone into correcting for the drift in the PMT gain (see the discussion in the last paragraph of Sec. 5.1.1), and the mean energy of the decay-e becomes stable after this correction is applied. Likewise, after applying the gain correction, the WT (N_{eff}) is stable, as can be seen on the left (right) side of Fig. 5.17. With a stable gain-corrected WT, the WT-corrected mean energy of the decay-e sample is stable within $\pm 0.5\%$.

5.2.3 Position Dependence and Top-Bottom Asymmetry

After correcting the various calibration data sets for the WT, an asymmetry between the number of hit PMTs in the top and bottom of the detector is still seen. Both Ni source calibration data and Xe lamp calibration data show the average hit rate in the top region is $\sim$5% less than the bottom region (Fig. 5.19). This position dependence is called the Top-Bottom Asymmetry (TBA) and can vary in time. The water transparency of SK retains a z-dependence due to injection of fresh, clean water from the water purification system at the bottom and removal of the older water by the purification system at the top of the tank. While it is thought that the TBA is due to the WT, the TBA correction is applied separately from WT corrections. Fig. 5.18 shows the effect the TBA has on the calibrations that set the SK absolute energy scale, described in the next section (Sec. 5.3). The left figure is the

z-position dependence of the LINAC calibration at two x-positions and two energies when comparing data and MC without TBA correction applied. The right figure is similar to the left but is for the DT calibration at all positions.

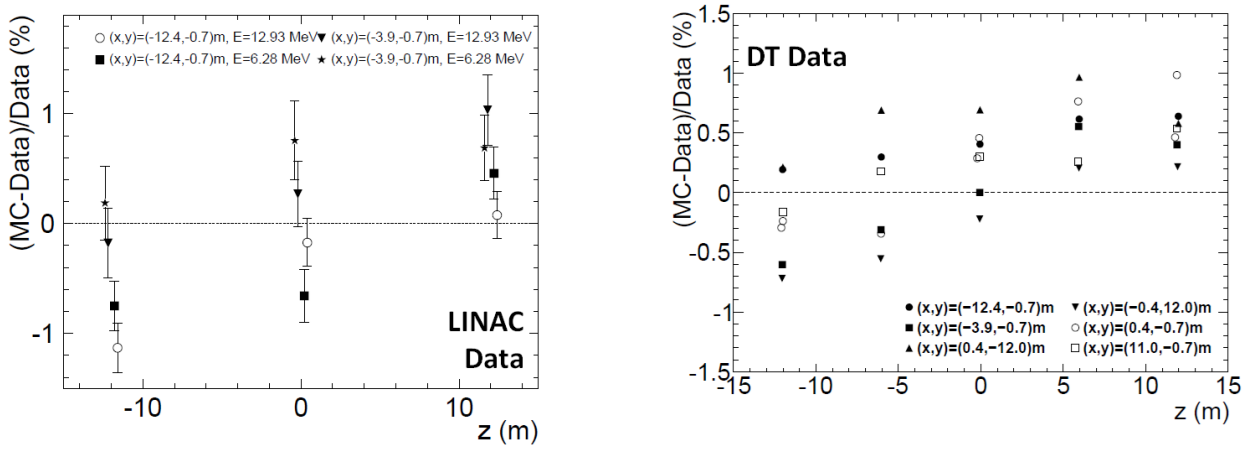

Figure 5.18: The z-position dependence for the calibrations that determine the absolute energy scale of SK-IV [42]. Both figures compare data and MC without TBA correction applied. Left: the z-position dependence of the LINAC calibration for two x-positions and two energies. Right: The z-dependence of the DT calibration at all positions.

The TBA is determined using the monthly Ni source calibration and monitored using the real-time Xe lamp system (Sec. 5.1.1), which occurs once every second. Using the Ni source calibration data, the TBA is formed by evaluating the difference between the average hit rate (HR) in the top and bottom regions of the detector divided by the average HR in the barrel region:

$$\mathrm{TBA} = \frac{< \mathrm{HR_{top}} > - < \mathrm{HR_{bottom}} >}{< \mathrm{HR_{barrel}} >}. \tag{5.18}$$

When using the Xe lamp data to track the TBA, the average HR in Eq. 5.18 is replaced with the average charge Q. This analysis is similar to the QE measurement previously described, but the QE_j for each PMT is applied here. The TBA results, shown in Fig. 5.19, from the nickel source (red dots) and Xe lamp (blue line) calibration data are consistent with one another and show the same variation in time. A similar z-dependence for the WT is found in the decay-e data.

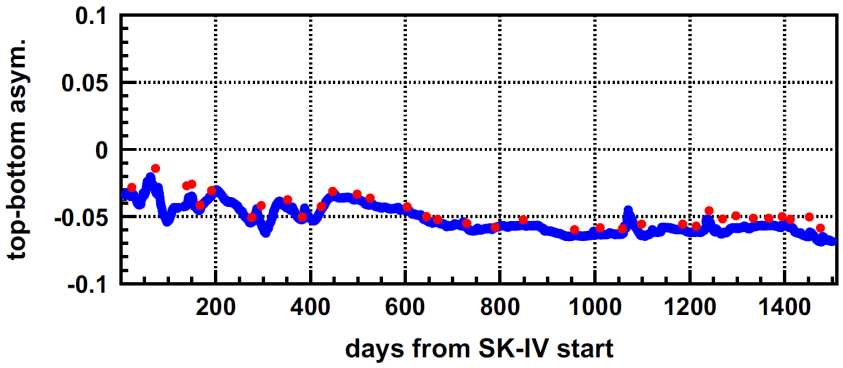

Figure 5.19: The time variation of the top-bottom asymmetry since the start of SK-IV [112]. The red dots (blue line) represents the nickel source (Xe lamp) data.

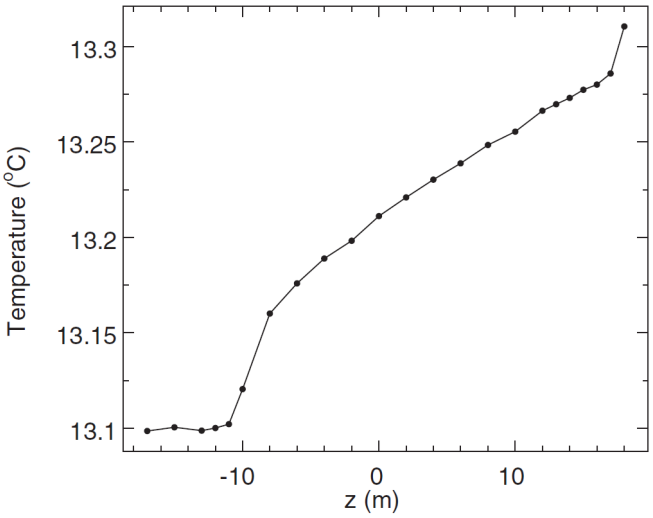

Figure 5.20: The standard z-dependence of the water temperature in the SK detector [42]. Below $z = -11$ m, the temperature is constant due to convection, and so the time-varying absorption coefficient α_{abs} is assumed to be constant in z.

Since the time dependence on the WT is primarily due to the absorption coefficient, the TBA effect is implemented by multiplying the function $A(z,t)$ to α_{abs} in the detector MC simulations, where

$$A(z,t) = \begin{cases} 1 + z \times \beta(t) & z \geq -11 \text{ m} \\ 1 - 11 \times \beta(t) & z \leq -11 \text{ m} \end{cases} \tag{5.19}$$

As seen in Fig. 5.20, below z = -11 m, the water temperature is stable in that region due to convection. Below this height, the absorption coefficient is assumed to be constant in z due to the constant temperature, while above this height, the absorption coefficient is assumed to change linearly. The functional form for $\beta(t)$ is derived from MC fits to the nickel data that incorporates the time-dependent TBA measurement:

$$\beta = \big[-0.163 \times \text{TBA}^2(t) - 3.676 \times \text{TBA}(t) \big] \times 10^{-3} \text{ m}^{-1}. \tag{5.20}$$

To model the time dependence of the TBA, the gain correction is applied here as well.

5.3 Absolute Energy Scale Calibration

The absolute energy scale is the determination of the correlation between the observed amount of Cherenkov light emitted by a charged particle, recoil electrons in the case of solar neutrinos, and the observed energy for that particle. This correlation includes position and directional dependencies, as well as the time dependence of the energy scale. The calibration of the absolute energy scale is the most important calibration for all low energy analyses. Small changes in the observed energy of a low energy event can shift the distribution of events in the associated energy spectrum, or events could be inappropriately excluded from an analysis.

As SK studies the energy spectrum of solar neutrinos through the recoil electron energy spectrum, understanding the relationship between the electron energy interpreted by SK from the PMT data and the true energy of the electron is incredibly important. The absolute energy scale tunes SKDETSIM to model the detector's response. Two calibration methods are used to calibrate the absolute energy scale, a linear accelerator (LINAC) that injects single, mono-energetic electrons into the detector and a deuterium-tritium (DT) fusion neutron generator that produces ^{16}N in the detector.

5.3.1 LINAC Calibration

The LINAC calibration [115] uses a recycled medical accelerator, a Mitsubishi ML-15MIII electron linear accelerator (the LINAC) housed above the SK tank. The schematic for the LINAC calibration system with the location of the steering magnets and the injection points in the tank is shown in Fig. 5.21. The LINAC has been modified to produce single, mono-energetic electrons with a slow rate of injection, fired downward into SK. An electron gun, steering magnets, and collimators reduce the number of electrons that make it into the tank. Approximately 0.1 electrons per bunch are injected into the tank by the LINAC, which simplifies the calibration for single electron events.

The electron gun uses a filament at the beginning stage of the accelerator to produce an electron beam. The momentum for the electron beam can be tuned to standard target energies between 4.4 and 18 MeV (total energy). The electron beam momentum is selected by tuning the current of the D1 magnet (Fig. 5.21), bending the electron beam produced by the LINAC, and narrowing down the associated collimators to only allow the part of the beam with desired momentum down the beam pipe. The actual beam energy of the electron beam is measured on the tank top by a Ge detector. During the 2016 LINAC calibration, the filament burned out and was replaced. The new filament slightly changed the available

electron energies delivered by the LINAC.

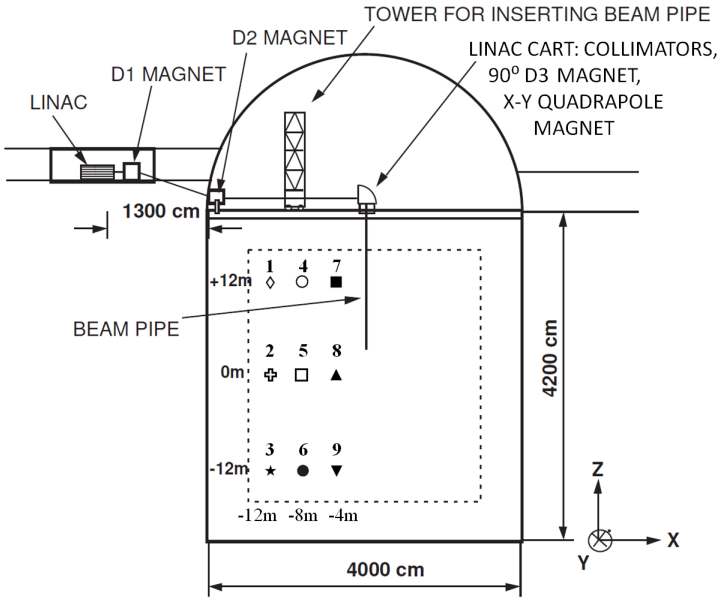

Figure 5.21: Schematic of the LINAC calibration system, including the calibration positions (labeled 1-9) of the beam pipe injection sites along the x-axis of the SK tank [115].

The 90° bending magnet, D3 in Fig. 5.21, is mounted to a cart. This cart also houses additional collimators and a set of quadrupole steering magnets that direct the e-beam toward the end of the beam pipe inside the SK tank. The beam pipe is capped by a titanium window at the end that ensures vacuum and withstands the water pressure at the bottom of the SK tank. A scintillation counter array is located toward the end of the beam pipe as well. The central counter is located just before the titanium window and records the number of electrons passing through the end of the beam pipe. Four outer counters help to guide the beam into the central counter and titanium window.

The LINAC cart is set on rails fixed to the negative x-axis of the detector tank and can be rolled over the calibration ports set between the rails on the tank top. The rail for the LINAC cart fixes the available injection sites in the y-axis to be located at $y = -70.7$ cm. Calibration ports fix the available x-positions. Due to time constraints, only two or three x-positions are used: -388.9 cm, -813.1 cm, and -1237 cm. The length of the sections

of beam pipe inserted into the tank sets the z-positions to 1197 cm, -6 cm, and -1209 cm. This results in a total of 9 in-tank positions for which the LINAC calibration is performed (see Fig. 5.21). While calibration is performed at six (1-3 and 7-9), or all nine positions, the energy settings of the electron beam are prioritized to get the best data sample across the full energy range. Due to the difficulty of getting low energy electrons down the beam pipe and into the tank, the lower energy LINAC calibration data suffers from poor statistics. This leads to a larger uncertainty in the energy scale at low energies.

LINAC calibration usually takes place over the course of approximately one month during the summer. Due to time constraints and significantly incurred "dead time" to supernova, LINAC calibration is not often performed. For SK, the dead time to supernova is when the detector is not recording data and can miss a supernova burst. Dead time can be caused by power outages, computer downtime, electronic malfunctions, a global veto signal being issued to the DAQ, or the HV to the ID is off. Inserting or extracting the LINAC beam pipe can take up to an hour depending on the z-position. During this time, the detector is open, and the HV to the PMTs must be off to protect the PMTs from over-exposure to the light in the SK dome.

During SK-IV, the initial full LINAC calibration was performed in 2009. Due to high variability in the WT, a limited calibration was performed in 2010 for only two energies. The second full calibration was performed in 2012. In 2016, another full LINAC calibration was attempted, but due to various complications, a second calibration was performed in 2017. The 2009, 2010, and 2012 calibrations only used two of the calibration ports (x = -388.9 cm and x = -1237 cm). This was enough to establish the COREPMT parameter (C_{PMT}) used in SKDETSIM to set the absolute energy scale with $C_{\mathrm{PMT}}^{2009-10}$ and determine its time variation by comparing to C_{PMT}^{2012}. The 2016 and 2017 calibrations used the three x-axis calibration ports, and the third COREPMT parameter, $C_{\mathrm{PMT}}^{2016-17}$, was derived for SK-IV, after correcting for the drift in the PMT gain in the WT and TBA described earlier.

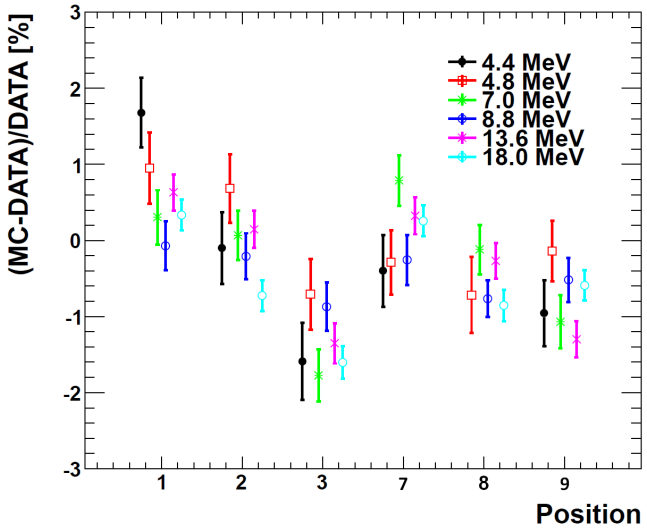

Figure 5.22: The percent difference between the N_{eff} peak position of the 2012 LINAC calibration data and SKDETSIM MC for LINAC calibration positions denoted in Fig. 5.21 [48].

The C_{PMT} parameter is obtained by using LINAC data and tuning SKDETSIM to match the response of the detector, while also comparing the peak of the N_{eff} distribution between LINAC data and MC (Fig. 5.22). Once C_{PMT} is determined, the percent difference between the N_{eff} of the LINAC data and MC is evaluated, and the energy scale is determined to be $\sim$0.53% for all LINAC energies and injection positions.

Germanium Detectors in the LINAC Calibration

A Ge crystal detector is used to independently measure the electron beam energy with high resolution. The Ge detector is calibrated using several sources:

- Natural radioactivity including ^{40}K at 1.46 MeV and ^{208}Tl at 2.61 MeV.
- A sealed ^{60}Co source (1.17 MeV and 1.33 MeV).
- A sealed ^{137}Cs source at 0.662 MeV.
- The Ni-Cf source (γs up to 9 MeV) used in the Ni calibration.

When measuring the electron beam energy, the settings for the electron beam remain the same as during injection, though the 90° bending magnet (D3) that sends the beam down into the tank is turned off to redirect the beam into the Ge detector.

The results from the Ge measurement of the beam energy at each position are used in SKDETSIM. One can then compare the MC with the LINAC calibration data and determine the uncertainty in the electron beam energy. For larger electron momenta, the penetration of the electrons into the Ge crystal could reach inactive elements. This energy loss is estimated using a Monte Carlo simulation of the Ge detector.

During the 2017 LINAC calibration, a second Ge detector with different detector geometry and materials was used to cross-check the electron beam energy. This second Ge detector was found to agree with the original one to ∼0.1%. With the Ge detector measurements, the electron beam energy is determined at the order of ∼ 0.1% level.

5.3.2 DT Generator ^{16}N Calibration

Because of the limited access and large dead time associated with the LINAC, more frequent calibrations are performed using a deuterium-tritium (DT) fusion neutron generator to produce ^{16}N in the water [116]. The DT generator can be deployed in many more locations throughout the detector by using a mobile crane. The crane raises and lowers the DT generator "torpedo" which houses the DT generator. An illustration of the DT calibration is shown in Fig. 5.23, along with a picture of the DT crane and the DT generator torpedo. A black umbilical carries the HV and signal information between the DT generator and the operational electronics on the tank top. Attached to the umbilical is the interlock that, unless submerged in water, prevents the DT generator from firing and releasing a deadly dose of neutrons. The DT calibration is performed once every three months. It is also performed immediately after each LINAC calibration to match detector conditions as best as possible.

The insertion and removal of the DT generator torpedo takes a combined ∼15 minutes, incurring much less dead time than the LINAC. Some additional dead time is incurred by the DT calibration during a global veto issued to the DAQ.

The DT generator produces neutrons through the reaction

$$^{2}\mathrm{H} + {}^{3}\mathrm{H} \rightarrow {}^{4}\mathrm{H} + n \tag{5.21}$$

with an energy of 14.2 MeV, large enough to generate ^{16}N in the water through the (n,p) reaction with ^{16}O:

$$^{16}\mathrm{O} + n \rightarrow {}^{16}\mathrm{N} + p. \tag{5.22}$$

The ^{16}N subsequently decays isotropically with a half-life of 7.13 seconds by β emission and a total endpoint energy of 10.4 MeV. The primary decay mode (66%) is via a 6.1 MeV γ and a 4.3 MeV β, with the next most common mode (28%) being a 10.41 MeV β. Because the ^{16}N decays are isotropic, where the LINAC events are only downward, they are useful to calibrate the directional and positional dependence of the energy scale. This knowledge is crucial to the solar neutrino analysis, as the neutrino events occur throughout the detector and are incident from the Sun.

DT calibration is performed for the central port, the ports used in the LINAC calibration, the corresponding ports on the positive x-axis, and the two extreme ID ports on the $\pm y$-axis. When performing the DT calibration, the DT generator torpedo is inserted in a calibration port while the detector PMT HV is turned off. Once the DT generator is far enough into the tank that the interlock is below the top of the calibration port, a light-block is installed and the HV is turned back on.

The tip of the DT generator is then lowered into the desired z-position via the crane, and a run starts (panel a in Fig. 5.23). The DT system sends a global veto signal to the SK DAQ, and the generator fires, producing a neutron cloud ($\sim 10^6$ n) at the tip of the torpedo

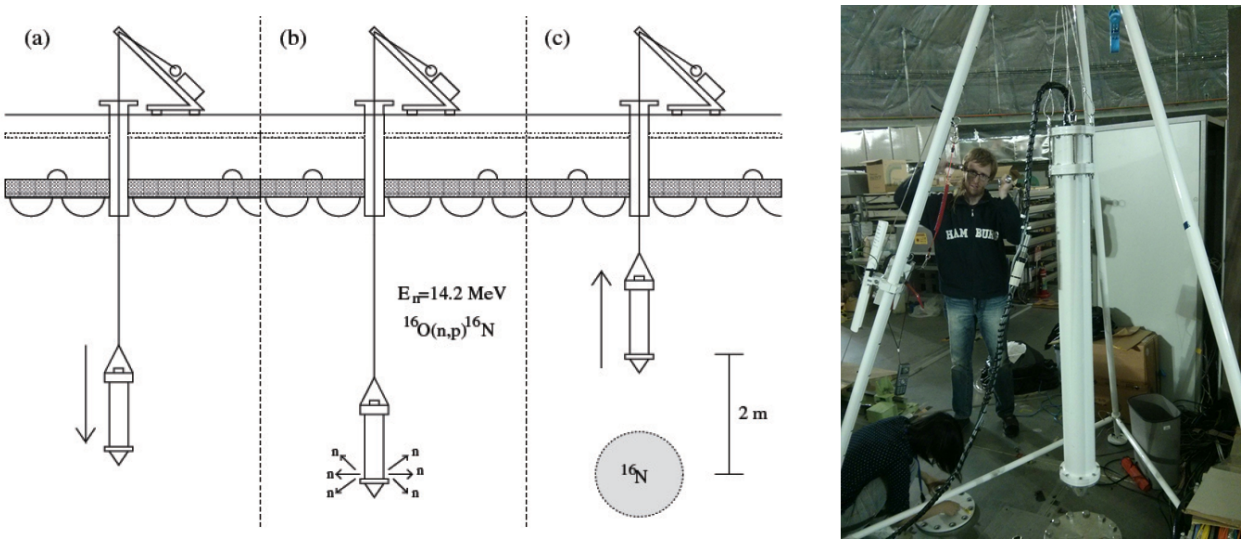

Figure 5.23: Left: Illustration of the DT generator calibration system and procedure [116]. Right: Photo of the torpedo that houses the DT generator hanging from the crane above the central SK calibration port $(x = 0, y = 0)$. The black umbilical cable bundle and interlock, housed in a white PVC pipe, are visible as well.

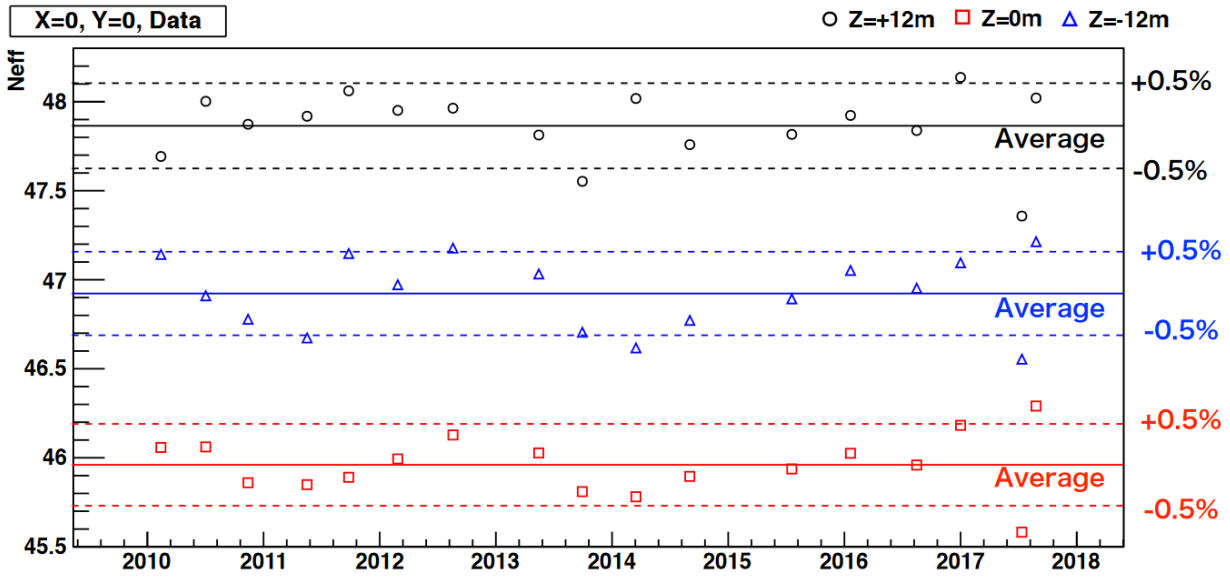

Figure 5.24: The stability of the SK-IV energy scale using the DT calibration data after applying the gain correction. The data is from the central calibration port corresponding to the z-axis of the SK detector, $(x = 0, y = 0)$, at three z-positions. The N_{eff} is stable within $\pm 0.5\%$. Figure courtesy of L. Wan.

(panel b in Fig. 5.23). The veto signal remains active for a few seconds while the crane pulls the torpedo as far back as possible to reduce shadowing of PMTs by the torpedo (panel c in Fig. 5.23). The two positions on the y-axis have shorter overhead clearance due to air ducts that cool the electronic huts, and the torpedo shadowing is much more significant for the associated DT calibration data. While the veto is active and the crane is pulling up the torpedo, the neutron cloud produces 10^4 ^{16}N events in the water (panel c in Fig. 5.23). The super low energy (SLE) event rate spikes up around 20 kHz above the average rate ($\sim$10-12 kHz), which can cause the DAQ to slow down and crash if the veto signal was turned off. After the few seconds it takes to lift the torpedo up and the ^{16}N to begin to decay, the veto is turned off and the SK DAQ starts to record the DT calibration data. This step is repeated 19 more times before moving on to the next z-position. Once data is collected for all z-positions, the DT generator torpedo is removed from the tank.

Once all the DT data is collected, the peak and shape of the reconstructed energy distribution is compared to MC to estimate the various dependencies of the energy scale on the position, direction, and time-varying detector conditions. The directional dependence of the zenith scale, with respect to the detector zenith angle, is shown in Fig. 5.25. The last two zenith bins, $0.6 \leq \cos\theta_{\mathrm{Z_{SK}}} \leq 1$, are affected by the shadowing of PMTs by the DT generator torpedo. The data is fit with an exponential plus a constant to determine the systematic uncertainty on the day-night asymmetry. The uncertainty is due to the directional dependence of the bias on the reconstructed energy and estimated to be $\pm$0.1%. After correcting for the gain variation, the variation of the energy scale using DT calibration data is stable within $\pm$0.5% for all of SK-IV. This stability of the average energy scale (N_{eff}) measured with the DT calibration data is shown Fig. 5.24 for the top (black), center (red), and bottom (blue) positions in the z-axis of the SK tank.

With the Wideband Intelligent Trigger (WIT) system [105][106] online toward the end of SK-IV and running in SK-V, an effort is underway to extract ^{16}N events produced by

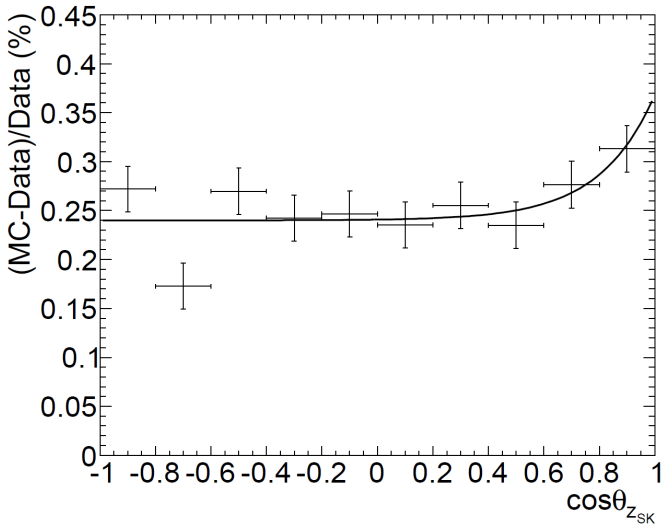

Figure 5.25: Difference in mean N_{eff} between DT calibration data and simulation for SK-IV, binned by zenith angle [42]. The aggregate uncertainty due to position dependencies correlated to the zenith direction is approximately ±0.1% after subtracting the absolute offset.

cosmic ray muons via neutron tagging techniques. Muons can create ^{16}N by being captured by the oxygen in the water and by producing spallation-induced neutrons that then capture on the oxygen nucleus (Eq. 5.22). The muon-induced ^{16}N forms a background that must be removed for the solar neutrino analysis (Sec 7.4.12). This data set of ^{16}N events would uniformly and isotropically fill the detector for the full time the WIT system is online. A clean data set of ^{16}N events would improve the ^{16}N cut that is applied in the solar neutrino analysis (Sec. 7.4.12). With a muon-induced ^{16}N sample, a third calibration method of the absolute energy scale independent of the DT and LINAC calibrations could be performed. This calibration will not suffer from the drawbacks inherent with the other two: directional dependencies, shadowing in the case of the DT generator torpedo, and the incurred dead time when opening the detector to perform the LINAC and DT calibrations.

5.3.3 Systematic Uncertainty of the Energy Scale

Four different sources contribute to the determination of the systematic uncertainty for the absolute energy scale. The uncertainty due to the energy determination for the electron beam produced by the LINAC using the Ge detector is 0.21%. During the LINAC calibration, which takes place over the course of a month, the LINAC beam pipe is being constantly inserted and removed. This causes changes to the WT beyond normal time variations. The uncertainty due to changes in the water transparency during the LINAC data collection can account for variations in the energy scale of 0.20%. The directional and position dependencies for the energy scale, which contribute 0.10% and 0.44% to the uncertainty respectively, are determined by comparing the DT calibration data and MC produced by SKDETSIM. The four errors are combined in quadrature, yielding a total estimated uncertainty of 0.54% for the energy scale, using the SK-IV 1664-day data period analyzed in [42].

After considering the total SK-IV data period and implementing the gain correction, the preliminary systematic uncertainty in the position dependence increases to 0.46%, while the preliminary systematic uncertainty in the water transparency decreases to 0.11%, giving a preliminary total systematic uncertainty for the energy scale of 0.53%. The SK-IV systematic uncertainties for the energy scale are summarized in Table 5.3.

Table 5.3: Summary of the systematic uncertainties for the energy scale [%] in SK-IV for the 1664-day period and the full SK-IV data period (preliminary).

Error	SK-IV 1664 days	All SK-IV
Position Dependence	0.44	0.46
Direction Dependence	0.10	0.10
Water Transparency	0.20	0.11
LINAC Energy	0.21	0.21
Total	0.54	0.53

Chapter 6

Event Simulation and Reconstruction

Many of the details presented in this and subsequent chapters can be found in the Super-Kamiokande solar neutrino analysis publications for SK-I [44], SK-II [94], SK-III [95], and SK-IV [42]. The systematic uncertainty for the recoil electron spectrum shape and ES rate for each phase due to the reconstructed event information will be discussed in Ch. 8.

6.1 Event Simulation

The SK detector simulation software, SKDETSIM, is a heavily customized Geant3 [117] Monte Carlo (MC) simulation that fully simulates the detector's response based on calibrations performed in the detector, or based on measurements made elsewhere. SKDETSIM includes physics descriptions of the full geometry and material makeup of each of the components of the detector, as well as including time-dependent effects such as dark noise rate, water transparency (WT), top-bottom asymmetry (TBA), live and dead PMTs, and other environmental variables. For any desired type of simulation (solar neutrinos, calibration, etc.), these time-dependent variables are set to correspond to the same period desired to be

simulated.

While data periods are described by real world time, the data is broken into chunks called "runs" to better manage everything. A run in SK is the period of time, a maximum of 24 hours, during which data is taken where all the DAQ triggering logic and PMT hit-based trigger threshold criteria are fixed. When changing the trigger logic or the threshold settings, a new run is begun in order to separate and organize data under what set of conditions the data is taken. Runs are further broken up into "subruns," where a subrun is the smallest packet of events in the data collected by the DAQ that contains all events passing trigger and threshold requirements. A subrun contains approximately 30 to 90 seconds of sequential events.

6.1.1 Solar Neutrino and Electron Simulation

Since solar neutrinos are detected by the recoil electrons induced by neutrino - electron ($\nu\ e$) elastic scattering (ES) in SK, it is necessary to simulate the detector's response to charged electrons at varying energies and the Cherenkov photons they emit. The solar neutrino data varies as a function of the date and time it is taken, based on the detector's live time. To mimic the solar neutrino data, the solar neutrino MC uses the timestamps of each subrun from SK data and tracks the position of the Sun at these times. Because the position of the Sun is well known from millennia of human observation, the true vector from the Sun can be accurately modeled. The subrun timestamps and the Sun's position at those times are used to match the zenith distribution of the MC to the data, as true solar neutrinos will always come from the Sun.

The event rate in the solar neutrino MC is generated according to the total expected number of (ν_e e) ES interactions in SK by ^{8}B and *hep* solar neutrinos. The expected rate is 325.6 events per day (assuming BP2004 SSM) before any energy threshold requirements [44].

In SK-I/II/III, the ^{8}B (*hep*) neutrinos are generated with a rate of approximately 0.2 (0.02) Hz. All events are considered to occur at the beginning of a subrun, using the timestamp of the subrun's first event. In SK-IV, the event generation rate was increased to $\sim$2 ($\sim$0.2) Hz for ^{8}B (*hep*) neutrinos to achieve better MC statistics and because of larger disk space (data storage) availability. Originally, the timing distribution of the SK-IV MC was the same as in the previous SK phases. A study has been performed on the effect that bunching the solar neutrino events at the start of a subrun has on the SK-IV solar neutrino results. It was found that this choice of having all events occur at the time corresponding to the first event in a subrun did not affect the SK-IV results. This is because the subruns have a small timing width, and SK's has poor angular resolution for recoil electrons (see Sec. 6.4). However, the MC events are now equally distributed throughout the duration of the given subrun they model in order to more accurately mimic the incident neutrino distribution corresponding to the Sun's location.

The energy spectrum of the ^{8}B solar neutrinos, shown in Fig. 3.8, is taken from the results of the Winter06 measurement [45] of the spectra of the ^{8}B decay products (2 α's and a β^+), described in Sec. 3.2.1. The neutrino energy spectrum used for the *hep* species is taken from the predictions of Bahcall et al. given in [41]. The systematic uncertainties of these flux calculations are included later when applying the energy-correlated systematic uncertainties of the recoil electron spectrum.

The angular distribution and energy spectrum of the electrons recoiling due to ($\nu\ e$) ES is modeled in SKDETSIM based on the differential cross section of this process for both the ν_e and $\nu_{\mu,\tau}$ channels. The cross section calculations include electroweak radiative corrections from [41] and are further described in Sec. 2.3. Eq. 2.68 describes the angular distribution, while the energy spectrum of the recoil electrons is described by Eq. 2.65. The angular distribution is integrated over the recoil electron kinetic energy T_e from zero to $T_{\rm max}$ (Eq. 2.64), where $T_{\rm max}$ is the maximum energy allowed by the conservation of four-momentum.

The resulting energy spectra for the ^{8}B and *hep* induced recoil electrons is shown in Fig. 2.1. The total ES rate is given by Eq. 2.66, and the fluxes are from BP2004 in Table 3.2. Only (ν_e e) ES events are generated for the solar neutrino MC used in the solar neutrino signal extraction (Sec. 8.1). The contributions from ($\nu_{\mu,\tau}$ e) NC interactions are included when determining the expected recoil electron spectra in solar neutrino oscillation analysis (Sec. 10.1).

The electron's trajectory through the water is tracked over the short path it travels (a few centimeters), and all emitted Cherenkov photons are tracked from their production until their termination. Any scattering or absorption of the Cherenkov photons in the water and any reflection from a surface in the detector (PMT or black sheet) are included in the simulation. The simulated behavior of the photons, described in Sec. 6.1.2, is modeled after the calibrations discussed in Sec. 5.2. During the simulation, the water transparency, top-bottom asymmetry, and other time-varying factors are set based on the date the simulation MC is to be modeled after.

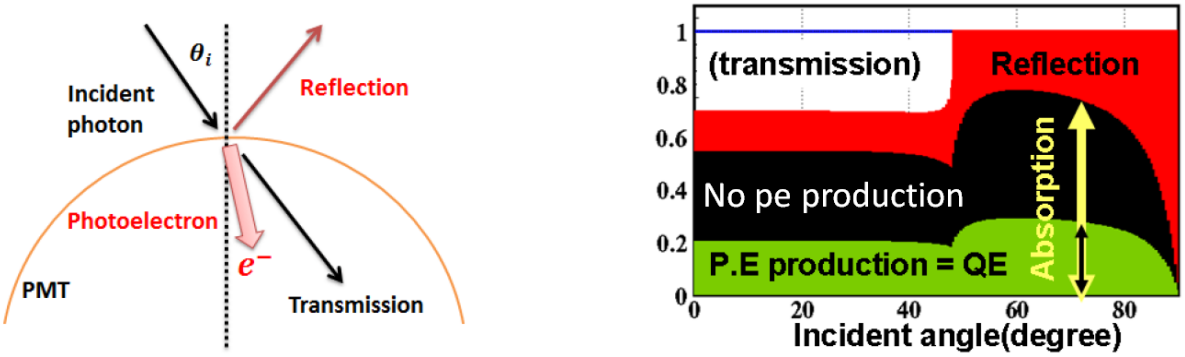

Figure 6.1: Left: Illustration of the three cases for incident photons on PMTs [48]. Right: PMT response to unpolarized 420 nm light. The black area is the case when the photon is absorbed without a photoelectron being produced. The white region is when the photon is transmitted through the PMT without being absorbed by the photocathode. Figure modified from [43].

6.1.2 Cherenkov Photon Production, Tracking, and Detection

The number of Cherenkov photons N produced per unit length dx and unit wavelength $d\lambda$, is modeled after the differential equation:

$$\frac{d^2N}{dx\ d\lambda} = \frac{2\pi\alpha}{\lambda^2 n(\lambda)}\left(1 - [n(\lambda)\beta]^{-2}\right) \tag{6.1}$$

where $n(\lambda)$ is the index of refraction for ultrapure water, $\alpha \simeq \frac{1}{137}$ is the fine structure constant, and β is the photon velocity in the medium in units of c (the speed of light in vacuum). The environmental variables that affect n, such as the water temperature and pressure, are included in the simulation based on their measurements in SK for the date desired to be simulated.

Cherenkov light is emitted by a charged particle if it is traveling faster than the speed of light relative to the medium: $\beta > 1/n$. In terms of energy, a charged particle will emit Cherenkov light only if it has a total energy greater than the Cherenkov threshold E_{CT}. For charged particles with mass m, E_{CT} is

$$E_{\mathrm{CT}} = \frac{m \times n}{\sqrt{n^2 - 1}}. \tag{6.2}$$

The opening angle θ_{C} of the Cherenkov cone is

$$\cos\theta_{\mathrm{C}} = \frac{1}{\beta n(\lambda)}, \tag{6.3}$$

which yields $\theta_{\mathrm{C}} \simeq 42^\circ$ for the water medium. For electrons, $E_{\mathrm{CT}} = 0.767$ MeV, for muons $E_{\mathrm{CT}} = 157.4$ MeV, and for pions $E_{\mathrm{CT}} = 207.9$ MeV [48].

For each photon produced that makes it through the water to a PMT, SKDETSIM determines one of three outcomes for the incident photon (see illustration on the left side of

Fig. 6.1):

1. The photon is reflected off the PMT (red area).
2. The photon transmits through the PMT without being absorbed by the photocathode (white area).
3. The photon is absorbed by the photocathode (black and green areas), and the probability of photoelectron (pe) production is considered (green area).

Each one of these processes has a dependence on the incident angle θ_j of the Cherenkov photon to the j'th ID PMT in SK. The probability that a photoelectron is created from an absorbed photon is directly related to the j'th PMT's charge response function (Eq. 5.1):

$$P(\gamma \rightarrow \text{pe}) = \epsilon_{\text{qe}(\lambda)} \times P_{(obs)}(\theta_j, \lambda) \times C_{\text{PMT}} \times \text{QE}_j, \tag{6.4}$$

where the quantum efficiency $\epsilon_{\text{qe}(\lambda)}$ is measured by Hamamatsu and shown in Fig. 4.14. The factor QE_j is obtained from the QEtable described in Sec. 5.1.3, and the COREPMT parameter C_{PMT} is derived from LINAC data (Sec. 5.3.1). The two-dimensional function $P_{(obs)}(\theta_j, \lambda)$ is the probability density function (PDF) of the PMT-response at a given wavelength for photon-PMT interaction and photoelectron production. This PDF is illustrated in Fig. 6.1. After the photoelectrons are generated, the output charge and response of the front-end read-out electronics is simulated for PMT j. Once the charge exceeds the PMT's threshold, the photon is considered to be detected. This step in the simulation takes the PMT timing resolution into account using the TQmap (Sec. 5.1.4).

6.2 Energy Reconstruction

The amount of Cherenkov photons produced by a charged particle in SK is approximately proportional to the amount of energy deposited within the detector. The reconstructed energy a particle deposits in the detector is proportional to the number of photoelectrons produced in the hit PMTs by Cherenkov photons. For electrons with energy less than 100 MeV, on average, PMTs will only see a single photoelectron per PMT, if any. For higher energy events, such as cosmic-ray muons, hit PMTs result in having a higher charge from multiple photoelectron production per PMT. For low energy events, counting the number of hit PMTs with a single photoelectron (single-pe) signal is proportional to the energy of the charged particle: $\sim$6 hit PMTs per MeV.

To reconstruct the energy of a contained event in SK, such as an electron, the information must be obtained from the PMTs hit by the light emitted from the event. A timing coincidence criteria of 50 ns between the event and the hit PMTs is established to remove dark noise and light from other low energy or background events. The PMT timing residuals relative to an event, T-TOF given by Eq. 5.5, must fall within the timing window for said event. N_{50} is the number of hit PMTs within this 50-ns window. The energy estimator $N_{\rm eff}$ is a correction to N_{50} that takes into account environmental and geometrical factors for each hit PMT [95]. The environmental factors include WT, TBA, the average dark noise rate ($R_{\rm dark}$) for the PMTs, the number of functioning PMTs in the ID ($N_{\rm alive}$), and the PMT gain. Most of these corrections are tracked as a function of time. The corrections ensure that $N_{\rm eff}$ is independent of location inside the detector.

6.2.1 The Energy Estimator N_{eff}

As stated earlier, the energy estimator N_{eff} is a correction to N_{50} determined from the effective hit of the j'th PMT (N^j_{eff}) within a 50-ns window of (T-TOF). N_{eff} and N^j_{eff} are defined by the following equations:

$$\begin{gathered} N_{\text{eff}} = \sum_j^{N_{50}} N^j_{\text{eff}} \quad \text{and} \\ N^j_{\text{eff}} = (X_j + \epsilon_{\text{tail}} - \epsilon_{\text{dark}}) \times \frac{N_{\text{all}}}{N_{\text{alive}}} \times S^{-1}(\theta_j, \phi_j) \times \exp\left(\frac{r_j}{\omega(t)}\right) \times \frac{1}{\text{QE}_j} \end{gathered} \tag{6.5}$$

where N_{all} is the total number of ID PMTs. All other components will be discussed below (see [95] for more details).

X_j: PMT Occupancy

The X_j occupancy term is used to estimate effects from multiple photoelectrons within the j'th hit PMT, which can occur when an event near the PMT is directed toward the PMT structure. In this scenario, the Cherenkov cone does not have the distance to expand and only strikes a few PMTs. X_j corrects for this effect, and is defined as

$$X_j = \begin{cases} -\log(1 - x_j)/x_j, & x_j < 1 \\ 3.0, & x_j = 1 \end{cases} \tag{6.6}$$

where x_j is the ratio of hit PMTs surrounding a central PMT (a 3×3 grid with the j'th PMT in the center) divided by the total number of live PMTs within the grid. The ratio x_j is the occupancy and is formed for each hit PMT in an event. When $x_j < 1$, the number of photons per single PMT is estimated by Poisson statistics as having a behavior approximated as $-\log(1 - x_j)$. When each PMT in the 3×3 grid is live and is hit ($x_j = 1$), X_j is set to 3. This value was determined by MC studies.

$\epsilon_{\mathbf{dark}}$: Dark Noise

To account for the time-dependent dark noise rate of the ID PMTs, the correction term ϵ_{dark} is defined as

$$\epsilon_{\text{dark}} = \frac{N_{\text{alive}} \times R_{\text{dark}} \times 50 \text{ ns}}{N_{50}}. \tag{6.7}$$

ϵ_{dark} corrects for dark noise hits within the 50-ns time window. N_{alive} and R_{dark} have the time dependence for the given data period taken into account run-by-run. The average measured dark noise rate for a run is $\sim$5.94 kHz in SK-IV.

$\epsilon_{\mathbf{tail}}$: Late Light Arrival

The ϵ_{tail} term is used to correct for the possible late arrival of Cherenkov light from an event, as some photons may arrive at a PMT outside the 50-ns time window because of scattering or reflection. Doubling the allowed time window, the number of effective hits in 100 ns (N_{100}) is formed in the same fashion as N_{50}. With these two hit rates, the correction due to late hits can be described as

$$\epsilon_{\text{tail}} = \frac{N_{100} - N_{50} - N_{\text{alive}} \times R_{\text{dark}} \times (100 \text{ ns} - 50 \text{ ns})}{N_{50}}. \tag{6.8}$$

$N_{\mathbf{all}}/N_{\mathbf{alive}}$: Dead PMT Correction

The effect of dead PMTs on N_{eff} for a given run is accounted for by this scale factor, as the photons that strike dead PMTs are not collected.

$S(\theta_j, \phi_j)$: PMT Photocathode Coverage

This term is the effective photocathode area of the j'th PMT from a given location in SK, where θ_j is the glancing angle. It includes shadowing effects from other PMTs. The function is derived from MC simulation for each SK-Phase to determine the directional cross section of each PMT as viewed from the angles (θ_j, ϕ_j). A visual definition of (θ_j, ϕ_j) is shown in the left of Fig. 6.2. The angles (θ_j, ϕ_j) are the spherical coordinates centered around the PMT. The effective photocathode coverage function $S(\theta, \phi)$ is shown in the right side of Fig. 6.2. The MC derivation $S(\theta_j, \phi_j)$ includes the PMT acrylic shielding for all phases after SK-I.

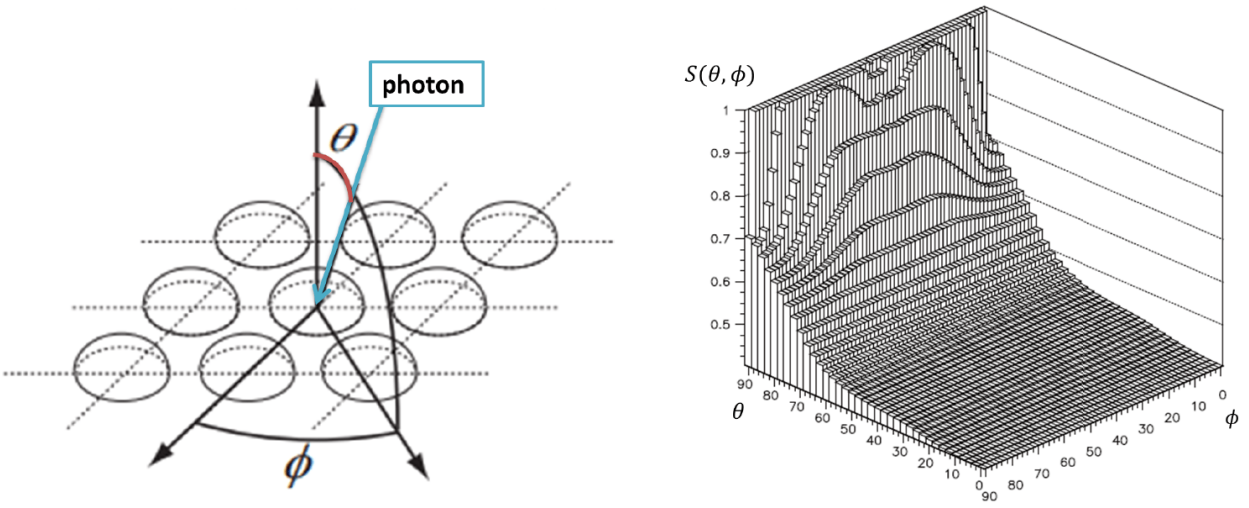

Figure 6.2: Left: Visual definition of the spherical coordinate angles (θ_j, ϕ_j) with the origin located at the center of the j'th hit PMT. Right: The correction function $S(\theta, \phi)$ that describes the effective photocathode coverage of a PMT in SK. Both figures taken from [48].

$\exp(r_j/\omega(t))$: Water Transparency Correction

The exponential term corrects for effects from the WT, described in Sec. 5.2. Here, r_j is the vector from the reconstructed vertex position to j'th PMT. The function $\omega(t)$ is the time-dependent WT based on the data or run period.

QE_j: PMT QE Correction

The final term is the correction on N_{eff} due to the QE factor of each PMT described in Sec. 5.1.3.

6.2.2 SK-IV Gain Correction to N_{eff}

Details of the SK-IV PMT gain correction for low energy analyses are discussed in [118]. To account for the drift in the gain discussed in Ch. 5, a correction is applied to the factors of N_{eff} impacted by the gain: the occupancy (X_j) and the PMT dark noise parameter (ϵ_{dark}) through the dark noise rate R_{dark}. The time-dependent fractional hit rate F_{HR} and gain drift function F_G are defined in Eq. 5.3. They are assumed to be linearly correlated, i.e. $C_G = F_{\mathrm{HR}}/F_G$ (Eq. 5.2). The factor C_G is obtained from the decay-e data sample and applied to N_{eff}, assuming an unchanged WT function $\omega(t)$. The occupancy term $X(x_j)$ in N_{eff} is modified to include the QE factor for each tested PMT and to apply the gain correction:

$$X(x_j) \rightarrow \frac{X(x_j/\mathrm{QE}_j)}{1 + F_G \times C_G}. \tag{6.9}$$

The PMT dark rate term is considered now for each PMT individually instead of a detector-averaged dark rate, in addition to applying the gain correction:

$$\epsilon_{dark} \rightarrow \frac{\epsilon^j_{dark}}{1 + F_G \times C_G}. \tag{6.10}$$

A new WT function $\omega'(t)$ is then determined using the corrected N_{eff} (assuming the old WT function) to account for the gain drift. The newly-corrected WT function (Fig. 5.17, left) is then applied in the N_{eff} calculation, and N_{eff} becomes relatively invariant in time (Fig. 5.17, right). By applying the gain correction to N_{eff}, the energy scale, WT, TBA, and

other affected parameters are stabilized.

6.2.3 Energy Reconstruction of $e^{\pm}$ from N_{eff}

After calculating N_{eff}, the reconstructed energy of an $e^{\pm}$ (an electron or positron) is acquired for different energy regimes. This boundary is at $N_{\mathrm{eff}} = 189.8$ or $E_{\mathrm{rec}} \simeq 25$ MeV. For $N_{\mathrm{eff}} < 189.8$, the function is a fourth order polynomial, while above this value the relationship is defined as a simple linear function:

$$E_{\mathrm{rec}} = \begin{cases} [0.82 + 0.13N_{\mathrm{eff}} - 1.11 \times 10^{-4}N_{\mathrm{eff}}^2 + & \\ \quad 1.25 \times 10^{-6}N_{\mathrm{eff}}^3 - 1.25 \times 10^{-9}N_{\mathrm{eff}}^4] & N_{\mathrm{eff}} < 189.8 \\ 25.0 + 0.138(N_{\mathrm{eff}} - 189.8) & N_{\mathrm{eff}} \geq 189.8 \end{cases} \tag{6.11}$$

where the values for the coefficients used here are the best fit from Fig. 6.3. The values of these coefficients are usual for SK-IV data. These coefficients are obtained through fitting to the LINAC calibration data and associated MC, as the beam energy is measured by the Ge detector (see Sec. 5.3.1). This method of determining the energy from N_{eff} assumes the charged particle emitting Cherenkov light is an $e^{\pm}$ and is not used for pions, muons, or other charged particles.

Energy Resolution and Systematic Errors

To predict the recoil electron energy spectrum that should be observed in SK, the theoretical energy spectrum $F(E)$ given in Eq. 2.65 needs to be distorted by including the detector energy resolution:

$$F(E_{obs}) = \int_0^{E_{\mathrm{max}}} F(E)R(E, E_{obs})dE, \tag{6.12}$$

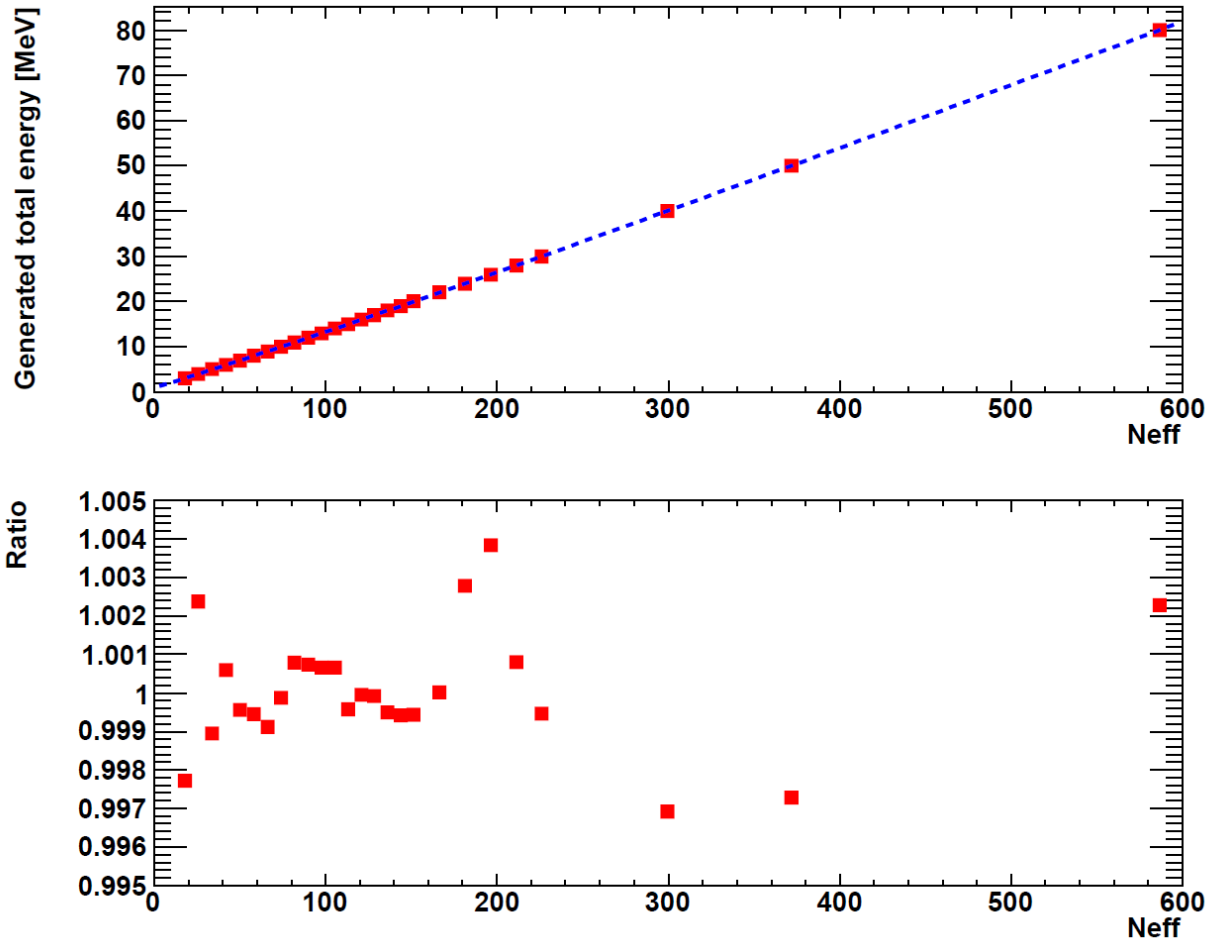

Figure 6.3: The top panel shows the relationship between true electron total energy from MC and N_{eff} (red squares) with the best fit (blue line). The bottom panel is the ratio of the fit to the MC points as a function of N_{eff}. Figure from [48].

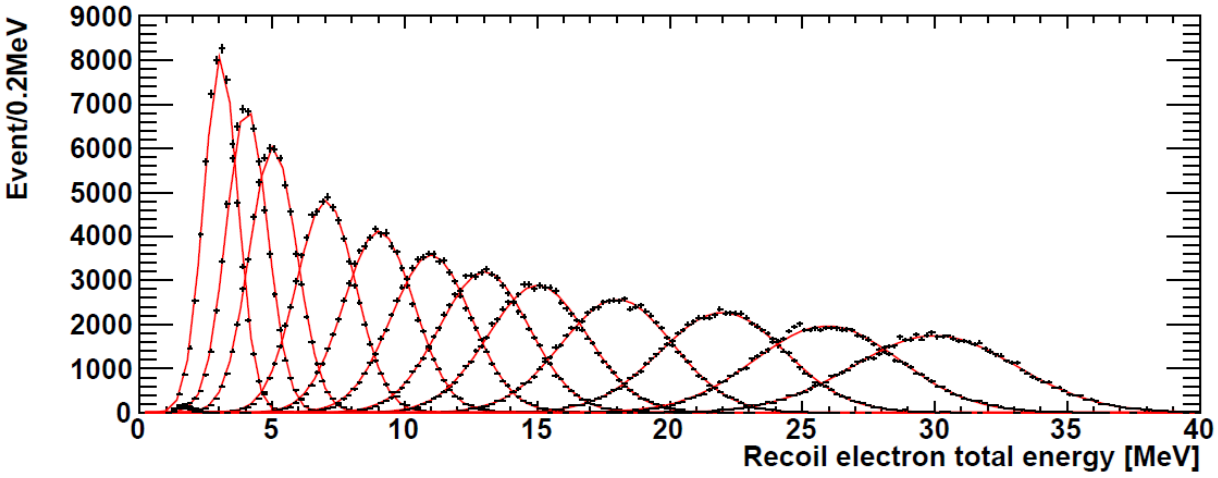

Figure 6.4: Energy distributions of recoil electrons generated for the ^{8}B solar neutrino MC [43]. The MC results (black errors) and their resulting Gaussian fit (red curve) are shown.

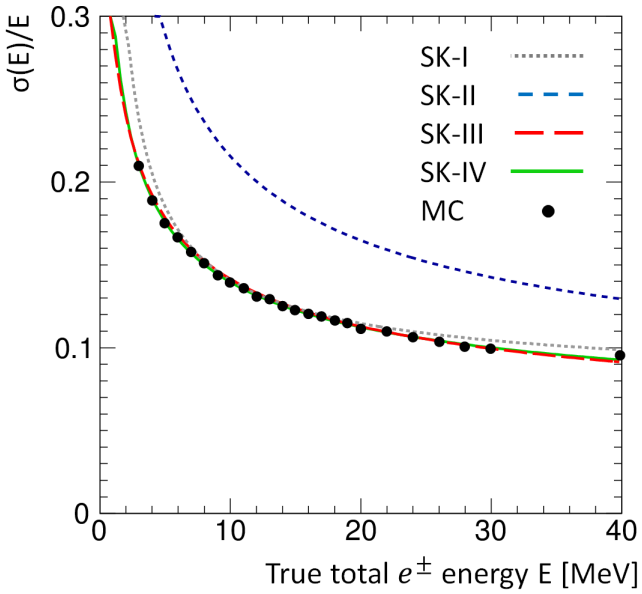

Figure 6.5: Energy resolution function (Eq. 6.14) for SK-I (dotted gray line), SK-II (short-dashed blue line), SK-III (long-dashed red line), and SK-IV (solid green line). The coefficients for each SK-Phase (Table 6.1) are obtained via sets of mono-energetic electron MC (black circles).

where, here the E is the true total energy of the $e^{\pm}$, E_{obs} is the observed total energy of the electron, and $R(E, E_{obs})$ is the detector energy response (or performance) function. The energy response function is defined as

$$R(E, E_{obs}) = \frac{1}{\sqrt{2\pi}\sigma(E)} \exp\left(-\frac{[E - E_{obs}]^2}{\sigma^2(E)}\right) \tag{6.13}$$

where the sigma function $\sigma(E$ [MeV]) is the energy resolution for each SK-Phase is

$$\sigma(E) = c_0 + c_1\sqrt{E} + c_2 E. \tag{6.14}$$

These coefficients c_k are determined using multiple mono-energetic electron MC samples (Fig. 6.4). The resulting energy distributions are fit with $R(E, E_{obs})$. Then, the energy resolution difference

$$\Delta\sigma(E_{obs}) = \frac{\sigma(E)}{E_{obs}} \tag{6.15}$$

is formed and fitted by Eq. 6.14. The coefficients c_k for each phase are given in Table 6.1, and the associated curves for the energy resolution are plotted in Fig 6.5. The 5% improvement in SK-III over SK-I is a result of the improvement in the vertex reconstruction.

Table 6.1: The coefficients of the energy resolution function $\sigma(E)$ (Eq. 6.14) for each SK-Phase.

SK-Phase	c_0	c_1	c_2
SK-I [44]	0.2468	0.1492	0.0690
SK-II [94]	0.0536	0.5200	0.0458
SK-III [95]	-0.123	0.376	0.0349
SK-IV	-0.0664	0.329	0.0422

The energy resolution is checked with the LINAC calibration by comparing the event energy and the "in-tank energy" determined by LINAC MC. The LINAC MC is a Geant3 MC simulation of the behavior for LINAC beam electrons. It simulates the effect that the

counter and titanium window have on the electron energy as it passes through to enter the tank. Once the electron enters the tank, the simulation is continued with SKDETSIM. The in-tank energy is the energy of the simulated LINAC electron when it enters the tank. The distribution of the energy for LINAC electrons (data) should peak at the same point as the in-tank energy from MC.

The percent difference in the $\Delta\sigma(E_{obs})$ between the LINAC data and MC is evaluated at several energies and used to form a function to describe the percent difference in the energy resolution:

$$\Delta\sigma_{\mathrm{LINAC}} = \begin{cases} 1.00\% & E_{obs} < 4.89 \text{ MeV} \\ 0.60\% & E_{obs} > 6.81 \text{ MeV} \\ \text{interpolation} & 4.89 \leq E_{obs} \leq 6.81 \text{ MeV} \end{cases} \tag{6.16}$$

The $\Delta\sigma(E_{obs})$ for the 2009-2010 SK-IV LINAC calibration are listed in Table 6.2 with their corresponding in-tank energies.

Table 6.2: The percent difference of $\Delta\sigma(E_{obs})$ at different in-tank energies of LINAC electron events taken during the 2009-2010 LINAC calibration.

Energy [MeV]	4.38	6.28	8.16	12.93	15.58
$\Delta\sigma(E_{obs})$ [%]	-2.53	0.90	-0.95	1.03	0.76

The systematic uncertainty of the energy resolution is given by using the ratios of the RMS and the mean from the reconstructed energy distribution at each LINAC energy for LINAC data and MC:

$$1 - \frac{\mathrm{RMS_{MC}}/\mathrm{mean_{MC}}}{\mathrm{RMS_{DATA}}/\mathrm{mean_{DATA}}} \tag{6.17}$$

After the SK-IV 1664 days solar paper, the RMS (mean) terms in the equation were replaced by using the σ (peak) information obtained by fitting the corresponding reconstructed dis-

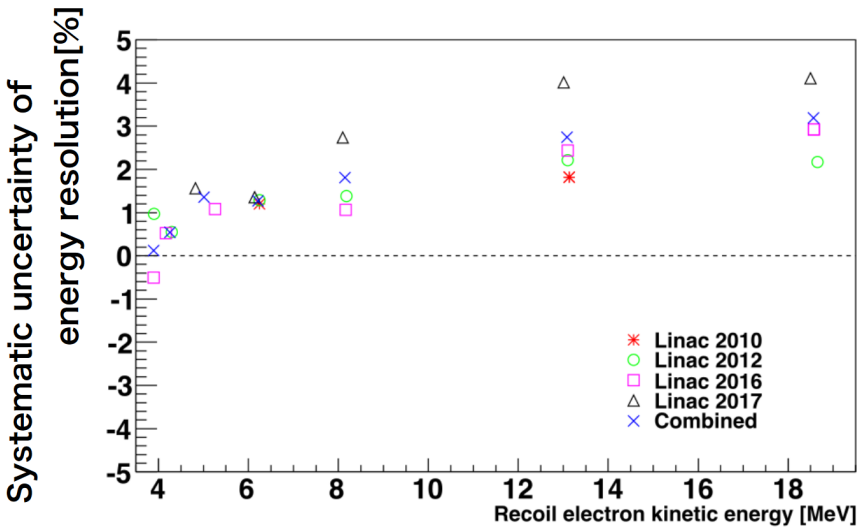

Figure 6.6: The systematic uncertainty on the energy resolution, Eq. 6.17, as a function of recoil electron kinetic energy from each LINAC calibration performed in SK-IV. Figure courtesy of M. Hasegawa.

tributions with Gaussian functions. This systematic uncertainty is plotted as a function of energy in Fig. 6.6 for all the SK-IV LINAC data, though only data from the 2009-2010 and the 2012 LINAC calibration was used in the SK-IV 1664 days solar paper [42].

6.3 Vertex Reconstruction

Inside the SK detector, electrons with $E \leq 20$ MeV only travel several to ∼10 cm. Because SK's vertex resolution is much larger (∼50 cm at ∼10 MeV), an event can be considered to be a point source. While only the times, charges, and geometry of the hit PMTs exist at the detector level, the timing and hit pattern are used to reconstruct the vertex for an event. The charge (or PMT signal pulse height) is due to a single photon for low energy events and carries no information relevant to the vertex.

The vertex fitter for SK-I uses a timing-based hit selection that employs a grid search over locations in the detector to maximize a "truncated χ^2" goodness of fit. Details about the vertex fitter used for vertex reconstruction in SK-I can be found in [44]. The vertex

fitter used after SK-I is BONSAI, or Branch Optimization Navigating Successive Annealing Iterations [121]. BONSAI uses the timing residuals to reconstruct the vertex position by maximizing a likelihood PDF based on data from the LINAC calibration described in Sec. 5.3.1. The likelihood function to be maximized is described by

$$L(\vec{v}, t_0) = \sum_{j=1}^{N_{\rm hit}} \log[P(t - t_{\rm TOF} - t_0)], \tag{6.18}$$

where the PDF $P(t - t_{\rm TOF} - t_0)$ is given in the left side of Fig. 6.7. $t_{\rm TOF}$ is the time of flight, t is the time of readout at the front-end electronics, and t_0 is the time of emission. This method uses all the hit PMTs ($N_{\rm hit}$) in an event. BONSAI maximizes the likelihood based on searching through a list of vertex positions based on PMT hit combinations of four or more. These hit combinations define a unique vertex position due to timing constraints. A version of BONSAI is used as an online vertex fitter. It reduces the amount of data stored by removing events reconstructed very close to the SK PMT structure as these events are likely to be background. The actual vertex reconstruction used in analyses is performed offline after the relevant environment information (WT, TBA, etc.) becomes available [94]. Based on the fitted vertex, one calculates the reconstructed energy, direction, and other event variables.

The resulting vertex resolution is taken as the distance for which 68% of the reconstructed LINAC event vertices agree with MC, shown in the right side of Fig. 6.7. The improvement seen in the figure between SK-I and SK-III comes from the change in the algorithm used, where the resolution is 100 (125) cm at 5 MeV in SK-III (SK-I) [95]. The greater improvement seen for the vertex resolution in SK-IV over SK-III is because of the improved front-end electronics [48] and better agreement in the timing residuals between data and MC [42]. The improved electronics result in a sharpening of the timing peak as well [43]. The poorer SK-II resolution is because of the halved photocathode coverage. The poorer vertex resolution at lower energies is a result of the reduction in the amount of Cherenkov light

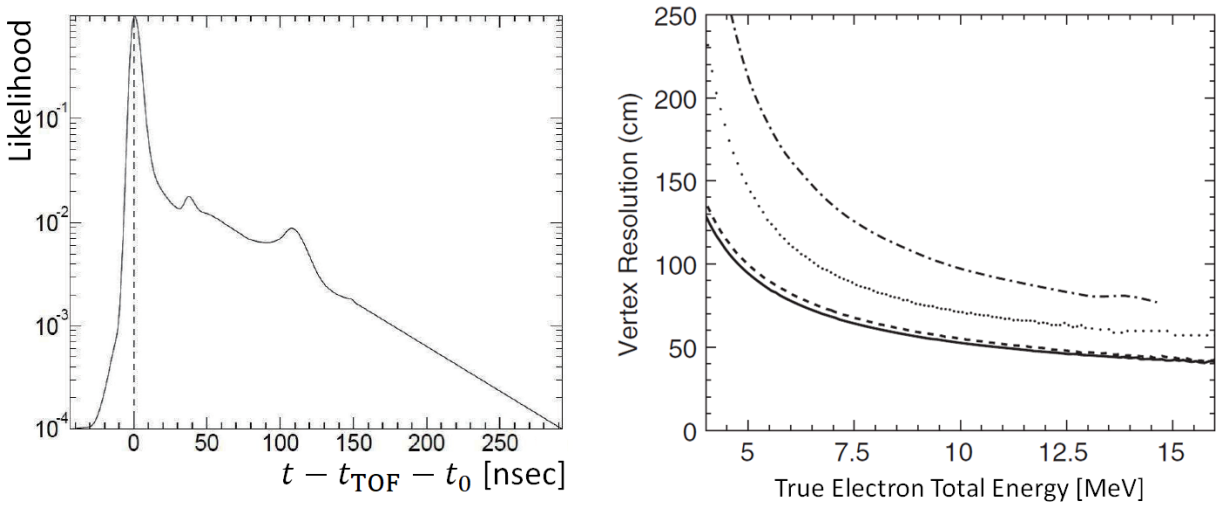

Figure 6.7: Left: The probability density function of the timing residuals (Eq. 5.5) for the single-pe signal, used in the BONSAI program for event vertex reconstruction via maximum likelihood fit. The additional peaks are a result of after-pulsing of the PMTs. Right: The vertex resolution for SK-I (dotted), SK-II (dashed-dotted), SK-III (dashed), and SK-IV (solid) data periods [42].

(number of photons) produced. The vertex resolution of SK-IV is limited by the width of the PMT timing resolution.

6.3.1 Vertex Shift

The bias in the reconstructed vertex is known as the "vertex shift." Due to the vertex shift, events near the boundary of the fiducial volume may move in or out of the allowed region. The vertex shift is checked at several positions in the tank using γs from the nickel source calibration data (see Sec. 5.1.1), as the source location is known precisely. The vertex shift measured by the Ni calibration data is plotted in Fig. 6.8. The origin of the arrows is the location of the Ni source, and the direction indicates the average vertex shift at that position. The length of the arrow corresponds to the magnitude of the vertex shift, scaled up by a factor of 20 in order to make the shift easier to see . As seen in the figure, the vertex shift is position-dependent. As an example, the far radial region of the tight fiducial volume (Sec.

7.4.11), events are shifted in the z-direction by +0.7 cm (-2.7 cm) for $z > 0$ ($z < 0$) and are then shifted radially outward by 1.78 cm.

In SK-IV, the effect is much smaller than in previous phases because of the better front-end electronics and the resulting improved understanding of the timing residuals. The effect of the vertex shift is included in the systematic uncertainty for the solar analysis results.

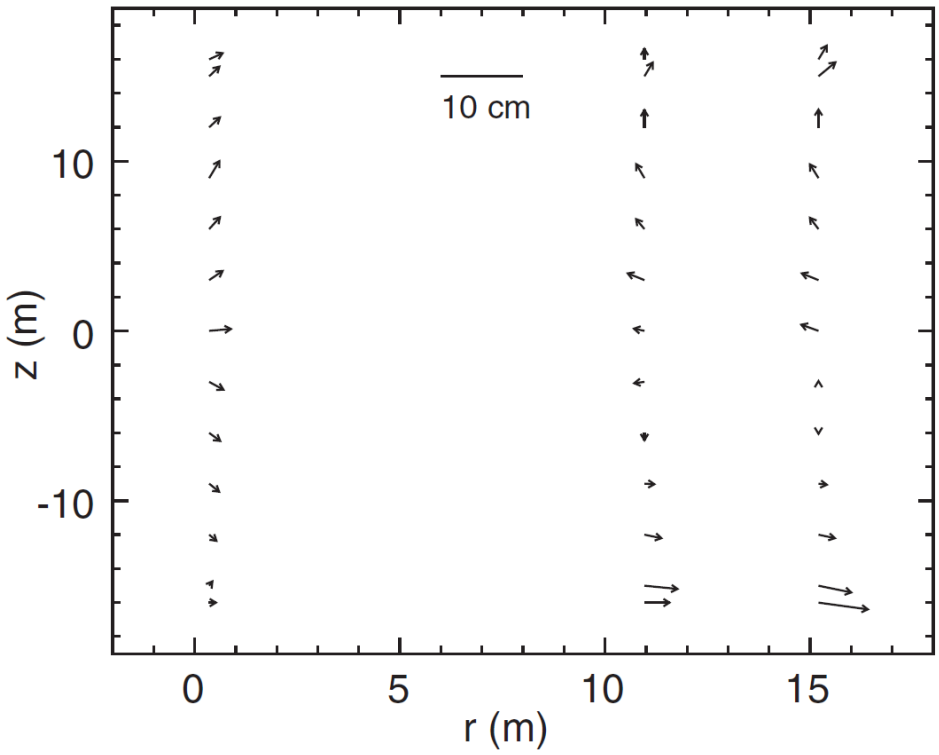

Figure 6.8: The vertex shift of Ni calibration events in SK-IV [42]. The origin of the arrows corresponds to the position of the Ni-Cf source. The direction indicates the averaged vertex shift at that position. The arrow's length corresponds to the magnitude of the shift, scaled up by a factor of 20.

6.4 Direction Reconstruction

Neutrino-electron elastic scattering is predominantly forward, i.e. the recoil electron preserves the incident direction of the solar neutrinos. This "directionality" is vital for extract-

ing a solar neutrino signal from SK. A maximum likelihood method comparing data to MC is used to reconstruct the recoil electron direction and is based on the PMT hit pattern a Cherenkov ring causes [44]. The likelihood function is

$$L(\vec{d}) \equiv \sum_{j}^{N_{30}} \log\left[f(E, \cos\theta_j)\right] \times \frac{\cos\theta_j}{a(\theta_j)}, \tag{6.19}$$

where N_{30} is the number of hit PMTs within a 30-ns window. The angle θ_j is the opening angle between the event direction and the direction from the vertex to the j'th PMT. The angular acceptance $a(\theta_j)$ for the j'th PMT is derived by MC (see Sec. 5.1.3) and given by Eq. 5.7. The likelihood function $f(E, \cos\theta_j)$ depends on the reconstructed event energy and will be discussed next. $L(\vec{d})$ is maximized using a grid search method with varying step sizes: 20°, 9°, 4°, and 1.6° [44].

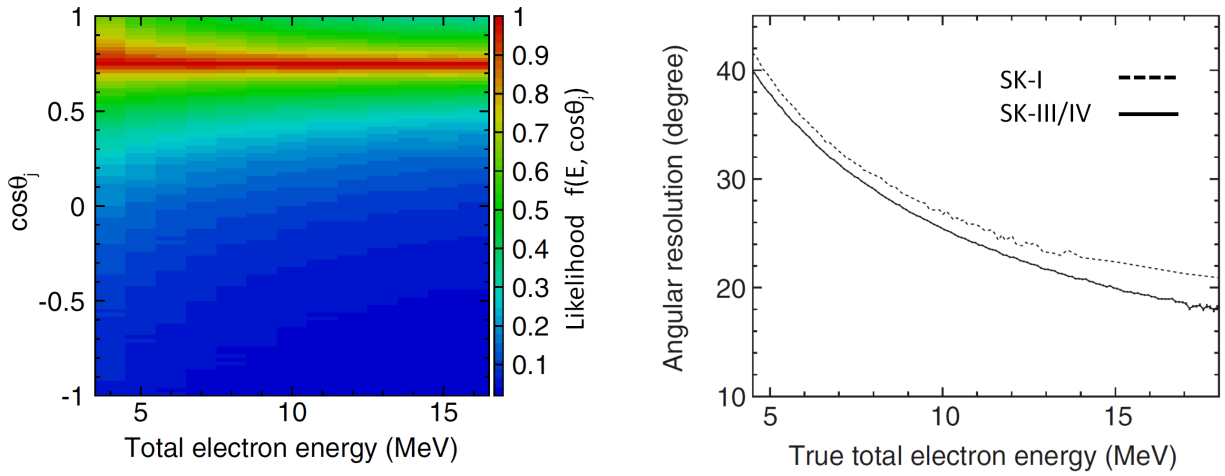

Figure 6.9: Left: The two-dimensional likelihood function used in the reconstruction of event direction. The color is the value of the likelihood function $f(E_{\rm obs}, \cos\theta_{\rm dir})$ in Eq. 6.19. The x-axis is the reconstructed energy of the recoil electron. The y-axis is the cosine of the opening angle between the reconstructed direction of an event and the direction from the vertex to each hit PMT. The red band is around the expected 42° degree opening angle of the Cherenkov cone [44]. Right: The absolute angular resolution of SK-I (dashed line) and SK-III/IV (solid line) as a function of the true total recoil electron energy from MC. Both figures taken from [95].

The two-dimensional likelihood function $f(E, \cos\theta_j)$ is constructed using the electron

MC. The function is shown in the left side of Fig. 6.9. The peak in f (red band) is around the expected opening angle of the Cherenkov cone ($\cos 42^\circ \simeq 0.74$), and the width in $\cos\theta_{\rm dir}$ is due to multiple Coulomb scattering of the recoil electrons and scattering of the Cherenkov photons [44]. The right side of the figure shows the comparison between SK-III (solid line) and SK-I (dashed line) for the absolute angular resolution as a function of true recoil electron total energy. The absolute angular resolution is defined as the angle of the cone around the true direction that contains 68.3% of the reconstructed directions [115].

The energy dependence of f was incorporated into the likelihood function during SK-III. This improved the angular resolution over SK-I by ∼10% at 10 MeV. This resolution is close to the limit one could achieve due to the multiple Coulomb scattering experienced by electrons. The improved vertex fitting BONSAI gave over the SK-I vertex fitter also contributes to the improved angular resolution, especially for the low energy region below 6.5 MeV [95].

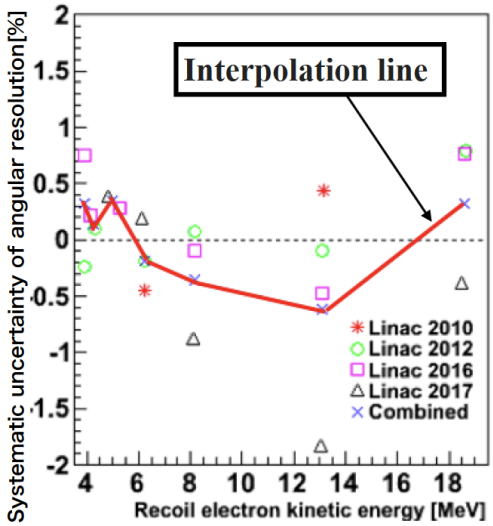

Figure 6.10: The systematic uncertainty on the angular resolution as a function of recoil electron kinetic energy from each LINAC calibration performed in SK-IV. The linear interpolation line is used to estimate the systematic uncertainty for intermediate energies. Figure courtesy of M. Hasegawa.

The angular resolution from the MC is estimated by comparing the difference between

the reconstructed directions of LINAC data and LINAC MC at various energies [115]. The angular resolution is plotted for each SK-IV LINAC calibration in Fig.6.10, and the angular resolutions for θ_j at various LINAC energies are listed for each SK-Phase in Table 6.3. These differences are used when determining the effect the angular resolution has on the systematic error of the flux and the recoil electron spectrum.

Table 6.3: The percent difference of the angular resolution between LINAC data and MC for each SK-Phase at different in-tank energies of LINAC electron events taken during the 2009-2010 and the 2012 LINAC calibrations [42].

Energy [MeV]	SK-I [%]	SK-II [%]	SK-III [%]	SK-IV [%]
4.0	...	...	...	0.64
4.4	-1.64	...	0.74	0.68
5.3	-1.38	...	...	...
6.3	2.32	5.93	...	0.02
8.2	2.33	7.10	0.40	0.06
10.3	1.52	...	...	...
12.9	1.07	6.50	-0.27	0.22
15.6	0.88	...	0.39	...
18.2	...	...	...	0.31

6.4.1 Multiple Coulomb Scattering of Recoil Electrons

Recoil electrons experience multiple Coulomb scattering in SK's water, resulting in a "wandering" of the Cherenkov cone. This wandering of the cone translates the amount of multiple scattering experienced by electrons into the PMT hit pattern [42]. The amount of multiple scattering incurred by electrons is directly correlated to their energy: lower energy electrons experience a larger amount of multiple scattering than higher energy ones. This effect causes the Cherenkov light from lower energy electrons to be emitted more isotropically than those with higher energy, which is reflected in the PMT hit pattern.

Recoil electrons induced by ^{8}B solar neutrinos tend to have higher energies than Rn

backgrounds, i.e. βs produced from the decay of ^{214}Bi (Rn background). These recoil electrons incur less multiple Coulomb scattering than the background βs. In addition to a β, most radioactive backgrounds emit multiple γs. The light due to the β and γs tends to be more isotropic than the Cherenkov light resulting from a multiply-scattered electron.

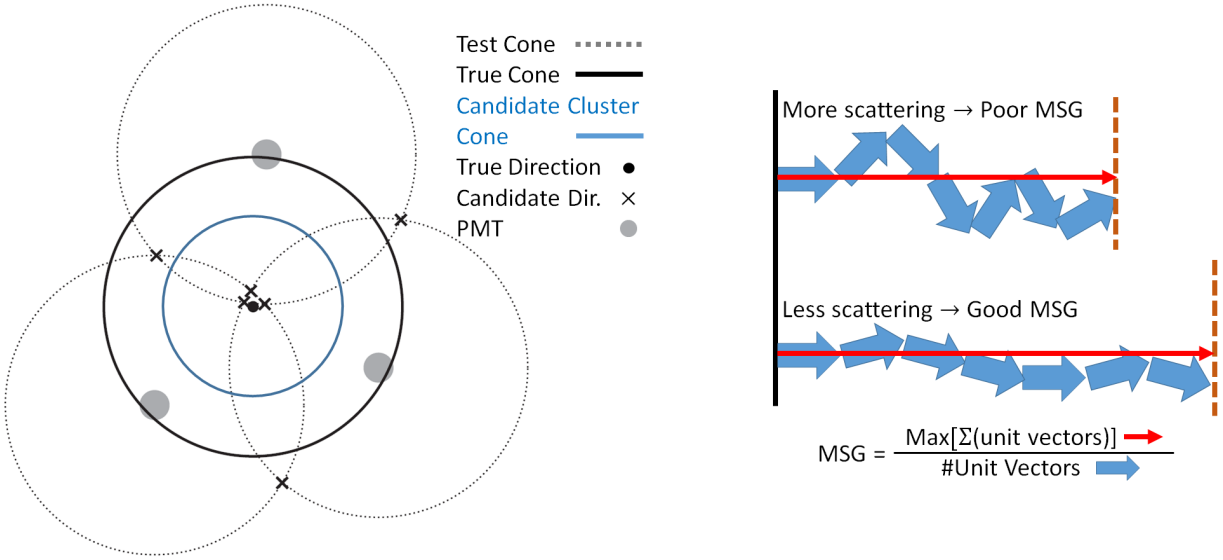

Figure 6.11: Left: Schematic for the event direction candidates used to determine the multiple scattering goodness (MSG) from Cherenkov cone projections onto the PMT surface of the SK inner detector. Figure modified from [42]. Right: Illustration of the calculation for MSG.

The multiple scattering goodness (MSG) is a directionality-based "goodness of fit" criteria that characterizes the anisotropy in the PMT hit pattern. MSG takes advantage of the difference between the hit pattern distribution due to the more anisotropic signal of recoil electrons and the more isotropic radioactive backgrounds. A schematic of the directional information used to determine MSG is shown on the left side of Fig. 6.11, where the true event direction (Cherenkov cone) is represented by the black circle (cone). Using the information in the figure, MSG is defined in the following way:

1. Multiple projections of the Cherenkov cone with an opening angle of 42° (dotted gray circles) are made. These projections originate at the reconstructed vertex and are

centered around each PMT (grey dot) with a T-TOF less than 20 ns.

2. "Event Direction Candidates" are defined by pairs of these Cherenkov cones that overlap twice (the black x's). The cone pairs are then used to construct vectors originating from the event vertex to the two points of overlap, which will be the candidate directions for the event. These candidate directions will cluster (the x's in the blue ring) around the true event direction (the black dot).

3. Direction candidates are associated with other direction candidates within a 28.4° cone (blue circle) to form a "cluster" and construct a so-called "central event direction."

4. After a direction candidate is used to form a cluster, it no longer is used to form other clusters.

5. The central event directions are then combined in a vector sum to refine the event direction.

6. This procedure is then repeated over several iterations using the refined event directions while checking other possible cluster assignments (permutations) for direction candidates, until the magnitude of the vector sum is maximized.

7. MSG is defined as the ratio of the maximized magnitude of the vector sum divided by the number of event direction candidates within the 20-ns timing window, illustrated in the right side of Fig. 6.11.

With this definition of MSG, electrons experiencing less multiple Coulomb scattering will have a larger MSG value, as the electron's path will be more directional and the Cherenkov cone pattern will be tighter, while events incurring more multiple Coulomb scattering will have a smaller MSG value. Fig. 6.12 shows this energy dependence of the MSG distribution for electrons using LINAC data (points) and MC (histogram) for two different energies: $T_e = 4.38$ MeV (filled circles and solid line) and $T_e = 8.16$ MeV (bars and

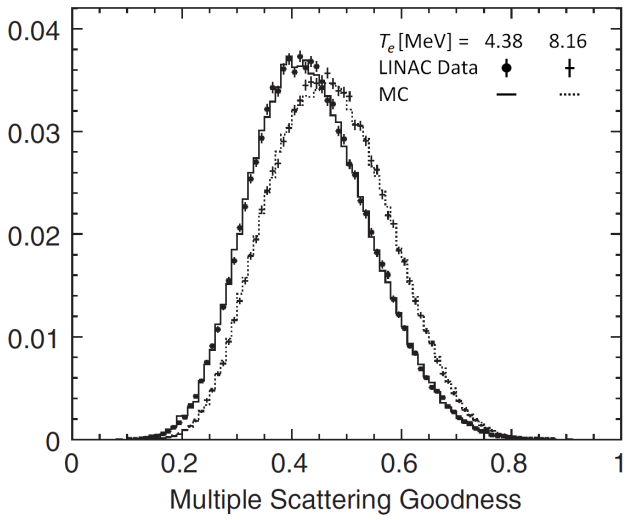

Figure 6.12: The MSG distributions from LINAC data (points) and MC (histograms) corresponding to 4.38 MeV and 8.16 MeV electrons, normalized by the number of events [42].

dotted line). The difference in the MSG distributions for each energy and the agreement between LINAC data and MC corroborate the idea that lower energy electrons experience more multiple Coulomb scattering than higher energy ones. MSG is used to improve the signal extraction for lower energy recoil electrons in the SK solar neutrino analysis, discussed in Sec. 9.1.

Chapter 7

Data Reduction

The data-taking period for each SK-Phase is given in Table 4.1, with the respective trigger threshold listed in Table 4.3. The trigger threshold for SK-I, SK-II, and SK-III is set by the discriminator voltage of the HITSUM signal (see Sec. 4.5.1). In SK-IV, the trigger threshold is defined by the minimum number of coincident PMT hits within ∼200 ns required for an event (Sec. 4.5.2). The trigger system for SK is described in Sec. 4.5. For low energy analyses, the effective number of hit PMTs (N_{eff}) in an event is directly correlated to the event's observed energy. SK has progressively lowered the trigger threshold to detect ever lower energy recoil electrons. However, lowering the trigger threshold significantly increases the super-low energy (SLE) event rate in SK.

As stated in Sec. 6.1.1, ∼326 ^{8}B-induced ν_e elastic scattering interactions per day are expected in SK. This rate ignores any detector efficiencies or energy thresholds [44]. However, even the low energy (LE) trigger rate in SK is much higher, approximately 2×10^5 events per day with the 47-hit trigger threshold in SK-IV. On average during SK-IV, the LE trigger rate is stable at ∼45 Hz, while the high energy (HE) trigger rate, which has a threshold of 50 hits, is stable around ∼11 Hz. The SLE trigger is set to a threshold of 34

hits for the first half of SK-IV, with a trigger rate of 4.4 kHz, but was lowered to 31 hits to increase the detection efficiency of recoil electrons with $3.5 < T_e < 4.5$ to 100%, and increase exposure to even lower energy events. Unfortunately, the SLE trigger rate increased to ∼11 kHz.

Because the event rate due to low energy radioactive backgrounds in SK is very high, especially near the PMT structure, obvious backgrounds are removed using pre-reduction cuts online (Sec. 7.2). For the solar analysis, more stringent cuts are applied (Sec. 7.4). The solar analysis cuts are designed to remove radioactive backgrounds, calibration events, noisy events, or bad events with poor reconstruction.

7.1 Summary of the Data Reduction Steps

Before discussing the details involved in the data reduction steps for the solar neutrino analysis, a summary will be given here. The impact each reduction step has on the recoil electron energy spectrum can be seen in Fig. 7.1.

The first reduction step is the result of applying:

1. The pre-reduction (Sec. 7.2).
2. The removal of bad runs (Sec. 7.3) and bad subruns (Sec. 7.3.1).
3. The removal of noise or calibration events:
   (a) The cut on the total number of hit PMTs (N_{hit}) (Sec. 7.4.1).
   (b) The removal of calibration triggered/source events (Sec. 7.4.2).
   (c) The removal of flashing PMTs (Sec. 7.4.3).
   (d) Muon-related event removal (Sec. 7.4.4).

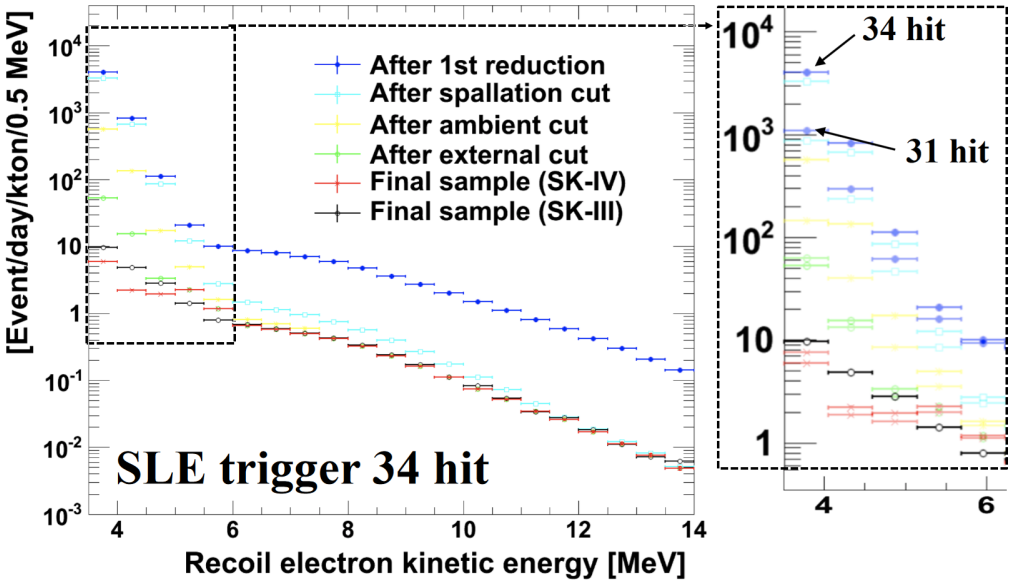

Figure 7.1: The energy spectrum after each reduction step for the 34-hit SLE trigger threshold data period of SK-IV. The final solar neutrino sample after all cuts is shown for the SK-IV 34-hit SLE trigger threshold (red) and the SK-III final data sample (black). The horizontal axis is the recoil electron kinetic energy (T_e), and the vertical axis is the number of events normalized to the exposure. The outset is the effect of the different pre-reduction criteria after changing the SK-IV SLE trigger threshold from 34 hits to 31 hits. Figure courtesy of M. Hasegawa.

(e) The removal of events that trigger the OD (7.4.5).

The second reduction step is the spallation cut described in Sec. 7.4.7. The third reduction step is the "ambient background cut," which includes:

1. The event reconstruction quality (g_R^2) cut (Sec. 7.4.6).
2. The patlik (L_{pattern}) cut (Sec. 7.4.8).
3. The tight fiducial volume cut (Sec. 7.4.11).

The fourth reduction step is the external event cut described in 7.4.10. The final reduction comes from applying the ^{16}N cut described in Sec. 7.4.12 and the small hit cluster removal from Sec. 7.4.9.

The differences between the SK-IV (34-hit trigger threshold) and SK-III final data samples in the lower energy region are due to changes in the cut criteria of the solar neutrino analysis:

- For total energy E = 4.0 - 5.0 MeV, the tight fiducial volume cut in SK-IV is more constraining than in SK-III. The corresponding SK-III (SK-IV) fiducial volume is 12.3 kton (8.85 kton). The SK-IV cut reduces the event rate by removing more events originating near the PMT structure and ID bottom.
- For E = 5.0 - 5.5 MeV, the event quality cut is looser: $g_R^2 = 0.25$ in SK-III and $g_R^2 = 0.29$ in SK-IV.
- For E = 5.5 - 6.5 MeV, the small hit cluster cut is completely removed, which increases the event rate in these two energy bins relative to SK-III.

The first two items listed above result in a lower efficiency for SK-IV than SK-III in the corresponding energy range. However, the trade-off is approximately a 40% reduction in the

corresponding background. The outset of Fig. 7.1 shows the effect of changing the software trigger threshold from 34 hits to 31 hits and tightening the pre-reduction cut criteria. The pre-reduction cut criteria were changed to handle the increase in the SLE event rate (Sec. 7.2).

7.2 Pre-Reduction

The high trigger rate must be managed properly by the DAQ and online computers. Without any data reduction, several hundred gigabytes of data would need to be recorded per day. Obvious backgrounds are removed using pre-reduction cuts via the online computers in the "real-time process." The real-time process applies a simplified reconstruction of events immediately after they are recorded by the DAQ. The reconstruction assumes a WT of 90 m because the WT data has not yet been analyzed at the time of pre-reduction. These cuts are looser versions of the cuts used in the solar neutrino analysis.

By removing the obvious background events, along with external and ambient events, the total amount of data is drastically reduced while avoiding any significant removal of true solar neutrino events. The data collected is reduced to 1% of the total event rate in the case of SK-IV for the 34-hit trigger threshold [42]. Table 7.1 gives a summary of the number of events removed for each step in the pre-reduction and the percentage of events left. This data was collected during SK-IV over a 24-hour period with the 34-hit trigger threshold.

Loose Fiducial Volume Cut

While the background events occur throughout the detector, they are heavily concentrated near the PMT structure. Additionally, the determination of the energy scale breaks down in the region close to the PMTs. A fiducial volume cut is applied requiring events to have

Table 7.1: Summary of the number of events removed by each pre-reduction step and the percentage remaining. This data was taken from a standard 24 hour run during SK-IV with the 34-hit SLE trigger threshold [43].

Pre-Reduction Step	Number of Events	% Remaining
Initial Uncut	197,524	100.0
Loose Fiducial Volume Cut	28,161	14.2
Loose External Cut	14,864	7.5
Loose Energy Cut	6,872	3.5
Loose Reco. Quality Cut	2,057	1.0

a reconstructed vertex greater than 200 cm away from the PMT structure. Otherwise the events are removed. More accurately, the loose fiducial volume cut removes events whose reconstructed vertex has a radial coordinate (r) with a magnitude $r > 14.9$ m and a z position with absolute value $|z| > 16.1$ m.

Loose External Cut

The PMTs and PMT structure produce events that predominantly point inwards into the ID. These external events are major backgrounds to the solar neutrino analysis. Their directional behavior can be leveraged to reduce this background by placing requirements on the distance (d_{eff}) between the reconstructed vertex of an event and the point on the wall (p_{wall}) backwards projection along the event direction. The definitions for d_{eff} and p_{wall} are illustrated in Fig. 7.2.

The requirement on d_{eff} for the 34-hit SLE threshold period for SK-IV is $d_{\text{eff}} > 400$ cm. Because the SLE data acquisition rate increased so dramatically by lowering the SLE trigger threshold from 34 hits to 31 hits, a separate energy-dependent cut was created for the online pre-reduction and was applied during the 31-hit SLE threshold era. For this new cut, an event is rejected if it has $E < 5.0$ MeV and $d_{\text{eff}} < 7.0$ m or if it has $5.0 \geq E < 8.0$ MeV and $d_{\text{eff}} < 5.0$ m. Here E corresponds to the total energy of an event. Table 7.2 has the

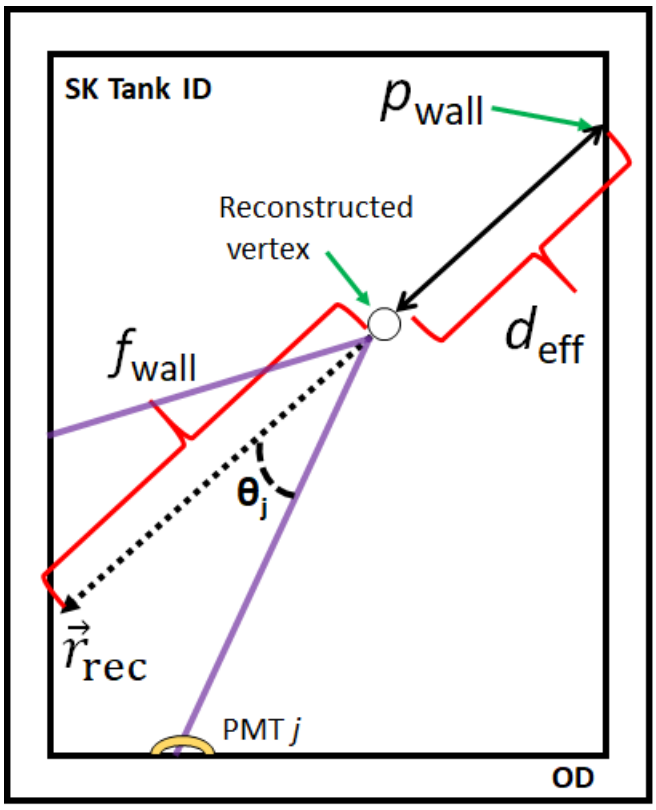

Figure 7.2: Illustration of several reconstructed parameters used in SK analyses. The angle θ_j is the angle between the reconstructed direction (dashed line) from the reconstructed vertex (circle) and the j'th hit PMT. The parameter $d_{\rm eff}$ is the distance from the reconstructed vertex to the point on the PMT structure ($p_{\rm wall}$) opposite the reconstructed direction of the event. The parameter $f_{\rm wall}$ is the effective distance between the reconstructed vertex and the PMT structure along the reconstructed direction.

summary of the external cuts used in both the pre-reduction and the solar neutrino analysis.

Table 7.2: Summary of the external event cut for pre-reduction (PRE) and for the solar neutrino analysis (SNA). The PRE criteria here is for the SK-IV 31-hit SLE trigger threshold era, as the 34-hit era only removes events with $d_{\text{eff}} < 400$ cm. Events are rejected if they meet the criteria. The first column has the energy range (total event energy E), the second column has the d_{eff} criteria for event rejection, and the final column has the p_{wall} criteria.

Energy Range [MeV]	$d_{\text{eff}} <$ [cm]	p_{wall}
	PRE	
$E \geq 8.0$	400	any
$5.5 \leq E < 8.0$	500	any
$4.0 \leq E < 5.5$	700	any
	SNA	
$E \geq 8.0$	400	any
$5.5 \leq E < 8.0$	650	any
$4.0 \leq E < 5.5$	1000	top
	1200	barrel
	1300	bottom

Loose Energy Cut

If the reconstructed total energy is too low, below 3.0 MeV total energy, the event is removed. To cut out cosmic-ray muons, events with more than 2000 pe are removed from the low energy data set. The muon data is retained elsewhere for spallation, atmospheric neutrino, and other cosmic-ray-related studies.

Loose Cut to Event Reconstruction Quality

Events with a poor quality of reconstruction or those that are mis-reconstructed (a completely bad fit) are removed by the parameter g_R^2, which is a combination of a pair of

goodness parameters [94]. The parameter g_R^2 is defined by

$$g_R^2 = g_{\rm VT}^2 - g_{\rm AD}^2. \tag{7.1}$$

The goodness parameter $g_{\rm VT}$ corresponds to the vertex reconstruction quality, and it is based on the timing information of the hit PMTs. The goodness parameter $g_{\rm AD}$ corresponds to the directional reconstruction quality, and it is based on how closely the PMT hit pattern reflects the azimuthal symmetry a Cherenkov cone should produce.

The goodness parameter $g_{\rm VT}$ is defined using two timing residual Gaussian distributions to form a weighted average Gaussian. The first timing distribution has a width of $w = 60$ ns that allows it to encompass selected PMT hits. The second timing distribution has a width of $\sigma = 5$ ns corresponding to the characteristic PMT timing resolution for single-pe statistics. The goodness $g_{\rm VT}$ is given by

$$g_{\rm VT} \equiv \sum_j^{\text{all hits}} \frac{G_j(w)}{\sum_j^{\text{all hits}} G_j(w)} \times G_j(\sigma), \quad \text{where} \quad G_j(u) \equiv \exp\left[-\frac{1}{2}\left(\frac{\tau_j(\vec{v}) - t_0}{u} \right)^2 \right], \tag{7.2}$$

and t_0 is emission time defined by the peak of the timing distribution. The effective hit time $\tau_j(\vec{v}) = t_j - |\vec{v} - \vec{h}_j|$ is the TOF between the reconstructed vertex ($\vec{v}$) and the vector location ($\vec{h}_j$) of the j'th hit PMT (see Sec. 5.1.3).

The goodness parameter $g_{\rm AD}$ is defined as

$$g_{\rm AD} \equiv \frac{\max[\phi_j^{\rm Uniform} - \phi_j^{\rm Data}] - \min[\phi_j^{\rm Uniform} - \phi_j^{\rm Data}]}{2\pi}. \tag{7.3}$$

The ordered set ϕ_j corresponds to the azimuthal angle between the best fit reconstructed direction and the direction from the vertex to the j'th PMT ($\vec{v} - \vec{h}_j$) for all hit PMTs in an event ($N_{\rm hit}$). All of the hits are ordered by their azimuthal angle from 0 to 2π, and the ordered set ϕ_j is formed. The ordered set $\phi_j^{\rm Data}$ corresponds to the actual hit PMTs in

the event. The ordered set ϕ_j^{Uniform} is formed under the assumption that the hit PMTs are uniformly distributed along a Cherenkov cone, i.e. $\phi_j^{\text{Uniform}} = 2\pi \times (j/N_{\text{hit}})$. The maximum (minimum) functions extract the maximum and minimum deviations for all PMTs in the event. A large difference in g_{AD} corresponds to a divergence from the expected hit pattern of a Cherenkov-like event and indicates background events or noisy events such as hit cluster events.

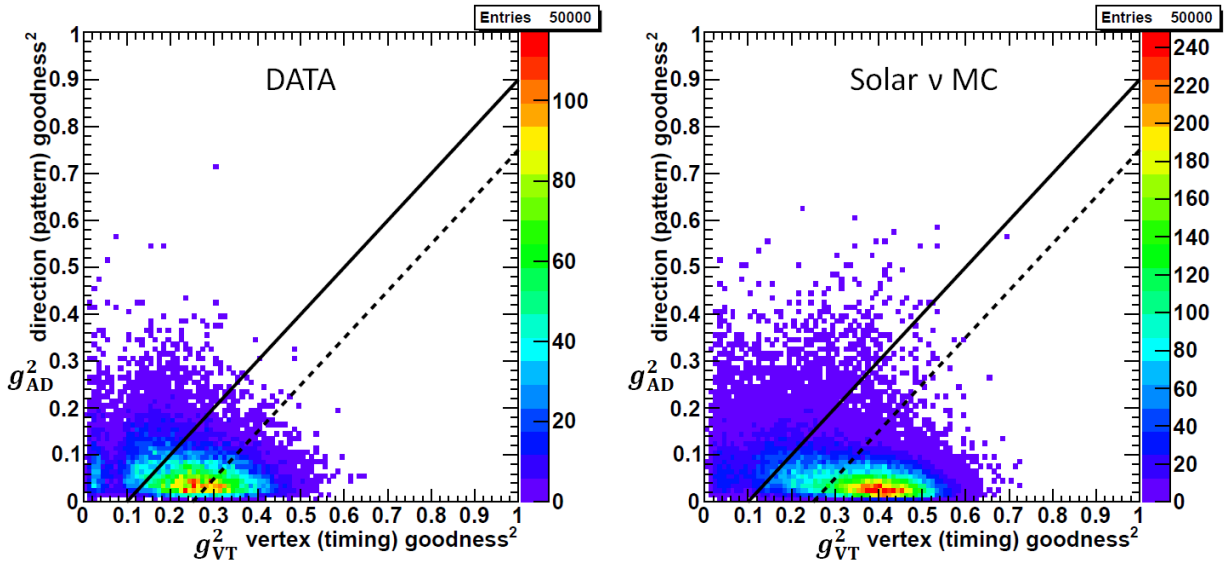

Figure 7.3: The correlation between g^2_{VT} and g^2_{AD} for background data sample (left) and solar neutrino MC (right), where the solid (dashed) line corresponds to $g^2_R = g^2_{\text{VT}} - g^2_{\text{AD}} = 0.10$ (0.25), the pre-reduction (solar analysis) cut value [48].

The values of both g_{VT} and g_{AD} range between 0 and 1. The best quality of reconstruction is when $g_{\text{VT}} = 1$ and $g_{\text{AD}} = 0$. For the pre-reduction, the requirement of $g^2_R > 0.10$ (0.15) is applied to remove poorly reconstructed events during the 34-hit (31-hit) SLE threshold period. Fig. 7.3 shows the difference between the background data sample from the solar neutrino final data sample (left) and the solar neutrino MC (right). The pre-reduction cut (solid line) for the 34-hit SLE threshold period and the solar analysis cut (dashed line) are plotted as well.

7.3 Run Selection

As previously mentioned in Sec. 6.1, the SK data stream is broken into "runs" to organize the data based on real-world time and detector conditions. Detector conditions include the detector trigger logic, the trigger threshold conditions, if T2K starts or stops the neutrino beam, detector calibration (like Ni source, LINAC, DT), etc. The maximum live time for a run is 24 hours, and runs are broken down into units called "subruns," which can last between ∼30 and ∼90 seconds. The SK-IV run period used in this analysis spans from run number 61525 to run number 72333, the same data period used in [42].

To ensure the quality of data used in analyses, several criteria are considered offline (i.e. after data has been taken and saved) when deciding if data from a given run should not be included. A run is labeled as a "bad run" if it meets the following criteria:

- If the total time for a run is less than five minutes, the run is rejected. There is insufficient pedestal data to judge whether a run is good or bad otherwise.
- If the HV has been turned back on within 15 minutes of the start of a run, the PMTs may still be too noisy.
- If there is a problem with hardware or software during a run.
- If any calibration (DT, Ni, LINAC, etc.) or detector maintenance is performed during a run.

Usually, if something happens within the detector that results in poor data quality during a short period of time, most of a run can be saved. Only subruns that meet these bad run criteria will be removed (bad subruns).

7.3.1 Bad Subrun Cut for the Solar Neutrino Analysis

To ensure other "bad run" style problems do not occur at the subrun level, three additional criteria are implemented [48]. Two are based on ID PMT channels and one on the OD trigger rate.

Bad Channel Cut

Slowly over time, the number of ID PMT channel failures increases. Two requirements are implemented based on the total number of bad ID channels in a subrun (bad channel cut) [48]:

- If the number of bad channels is less than 10, which can happen for very short runs, the subrun is removed. There is not enough information collected to determine the quality of the run or subrun.
- If a QBEE in the front-end electronics has problems, the 24 PMTs connected to the board are dead and are considered to be bad channels. The number of bad channels must not fluctuate too high above the monthly average number of bad channels: $N_{\mathrm{bad}} <$ monthly average + (1.5×24).

OD Trigger Rate

Since the OD trigger rate can fluctuate upwards because of noisy OD PMTs, a bad-subrun criterion based on the OD trigger rate is used. The average OD rate measured in SK is relatively steady at 1.954 ± 0.180 Hz and corresponds to the muon rate in the OD. If the OD rate fluctuates by 5σ to 2.847 Hz, the subrun is labeled as bad and is removed from the solar neutrino analysis.

7.4 Solar Neutrino Analysis Cuts

For the solar analysis, the cut values are tuned in different energy regions to optimize the significance:

$$\text{significance} = \frac{S}{\sqrt{BG+S}}, \tag{7.4}$$

where S (BG) is the number of signal (background) events. In the lower energy regions, the background dominates the signal, and significance $\simeq S/\sqrt{BG}$. These cuts are applied offline after determining and accounting for the various detector environment details from calibrations (noise rate, WT, TBA, gain correction, energy scale and resolution, etc.).

7.4.1 Number of Hit PMTs

Since solar neutrinos do not produce recoil electrons above ∼20 MeV, a cut is made on the total number of hit PMTs allowed for an event: $N_{\text{tot}} < 400$. This value corresponds to roughly 60 MeV for electrons. The cut helps to remove high energy events such as decay electrons, cosmic-ray muons, and atmospheric neutrinos.

7.4.2 Calibration Source Cut

Since multiple types of automated calibrations are performed routinely within SK, events caused by the calibration sources are flagged and removed. These scheduled triggers occur anywhere between once a second (laser calibration for WT measurements), 30 minutes (pedestal events), or once every several weeks (LED-bursts used for supernova burst detection system testing).

Additionally, any light emitted from the material that makes up the calibration devices or the sensors is removed. If an event has a reconstructed vertex closer than 2 m from a

calibration device or within 1 m of the cable of a device, the event is removed. The cables for all calibration devices are parallel to the z-axis. Table 7.3 lists the various calibration sources/devices removed by this cut.

Table 7.3: The positions of the automated calibration sources and devices installed in SK.

Source	x [cm]	y [cm]	z [cm]
Xenon light	353.5	-70.7	0
LED	35.5	-350	150
TQ Diffuser Ball	-176.8	-70.7	100
Supernova Burst Test	-35.3	353.5	100
Water Temp. Sensor (1)	-35	1200	-2000
Water Temp. Sensor (2)	70.7	-777.7	-2000

7.4.3 PMT Flasher Cut

Occasionally, during data collection, an arc discharge occurs on the dynode of a PMT. This causes a flash that is seen by many other PMTs around the flasher, while the flashing PMT sees a large number of pe. If the charge readout from a given PMT exceeds 50 pe while the number of hits in the 24 surrounding PMTs exceeds three, the event is labeled as a flasher event and removed. An example of a run with (without) a significant flasher is displayed in the top (bottom) of Fig. 7.4, with the red line corresponding to the flasher cut criteria. In both cases, all events in the top right are removed by the cut. Sometimes, flasher events will only occur several times within a run, and the flashing PMT will cease the flashing behavior. The lower panel is an example of a run with a minimal number of flashing PMTs.

7.4.4 Time Difference Cut to Muons

Several backgrounds in the solar neutrino analysis are caused by cosmic-ray muons. These background events can be removed by a cut on the time difference between an LE (or SLE)

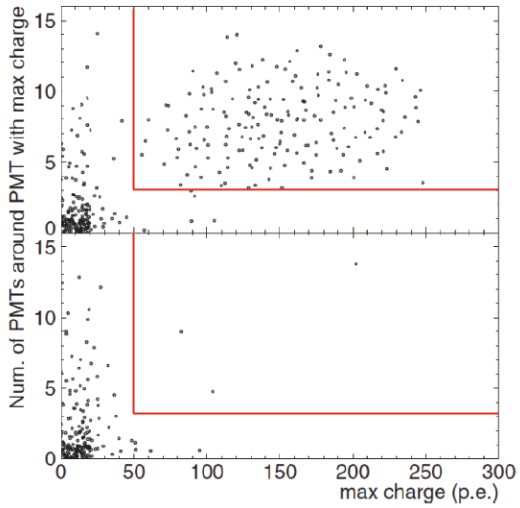

Figure 7.4: The cut criteria to remove flasher events [43]. The x-axis is the maximum charge of a hit PMT for the event, while the y-axis corresponds to the number of hits in the 24 surrounding PMTs. The top (bottom) panel shows a run with (without) flasher events.

triggered event and the previous cosmic-ray muon: $\Delta t = t_{\rm sle} - t_{\mu}$. t_{μ} is the time that the muon passes through the detector, and $t_{\rm sle}$ is the time of the low energy event.

A typical distribution of this time difference is plotted in Fig. 7.5. "Ringing" noise in the PMT cables induced by very energetic muons typically occurs around 1 μs after the muon, and after-pulsing of PMTs occurs within 15 μs. Decay-e produced by muons have a lifetime of 2.2 μs. To remove these backgrounds, any event occurring within 50 μs after the muon, $\Delta t < 50$ μs, is removed (red line). During the SK-IV phase, untagged muons, typically not energetic enough to produce Cherenkov radiation, are also taken into account when calculating the time difference to the previous event.

7.4.5 OD Event Cut

The recoil electron Cherenkov light from a solar neutrino ES should be fully contained in the ID, as the ID and OD are optically separated. Low energy events do not have enough energy to penetrate through the dead region of the PMT structure and create light in both the ID

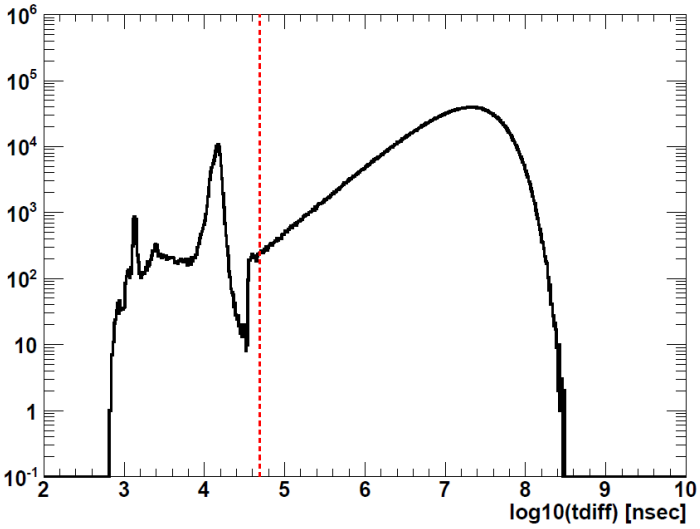

Figure 7.5: Typical distribution of the time difference between low energy events and their preceding muon [48]. Events below the 50 μs cut (red dashed line) are removed. The peak near 1 μs is caused by ringing induced by highly energetic muons. The peak around 15 μs is caused by after-pulsing.

and OD. If the total charge measured in the OD for an event is $\gtrsim 20$ pe, the OD is triggered and the event is flagged. Any event flagged with an OD trigger is due to a high energy event and not a solar neutrino, and so it is cut. Additionally, any event with $N_{hit} \geq 20$ in the OD is cut, even if a trigger is not issued by the OD.

7.4.6 Event Quality Cut

As described earlier in Sec. 7.2, the event reconstruction quality (g_R^2) (Eq. 7.1) is optimized by energy region to maximize the efficiency of extracting the solar neutrino signal, i.e. the significance (S) (Eq. 7.4). The energy dependent criteria for the cut on g_R^2 that maximizes S is found to be

$$g_R^2 > \begin{cases} 0.29, & 3.5 \leq T_e < 4.5 \text{ MeV} \\ 0.25, & 4.5 \leq T_e < 7.0 \text{ MeV} \\ 0.20, & T_e \geq 7.0 \text{ MeV} \end{cases} \tag{7.5}$$

where T_e is the recoil electron kinetic energy.

Fig. 7.3 shows the difference between the background data sample from the solar neutrino final data sample (left) and the solar neutrino MC (right), along with the solar neutrino cut (dashed line) for the 5.0 to 7.0 MeV region. The cut requirement increases in severity as the energy becomes lower because there is more background.

7.4.7 Spallation Cut

When cosmic-ray muons pass through the water of SK, there is a chance that they collide with an oxygen nucleus and break it apart. This breakup results in hadronic cascades or electromagnetic showers, and it is known as "spallation." Sometimes, multiple muons pass through SK at the same time, referred to as "muon bundles." These muon bundles are seeded by the same cosmic-ray interaction. Single muons and muon bundles are treated the same in this cut.

Besides producing n, p, $\pi^{\pm}$, etc., these collisions produce radioactive nuclei (the spallation products). These spallation products eventually $\beta^{\pm}$-decay and can also release γs and neutrons. The $\beta^{\pm}$s mimic solar neutrino ES interactions and are a major source of background for the solar neutrino analysis.

These processes are known as nuclear spallation reactions. The daughter isotopes have a wide range of lifetimes, from half-lives tens of ms long, up to 7.13 s or 13.8 s, and a broad range of energy modes available to the βs and γs (4-20 MeV). The long life of some of these isotopes makes correlations between them and their parent muon(s) difficult to form. A list of the spallation products that β decay is given in Table 7.4, and a scatter plot of those entries shown in Fig. 7.6. The horizontal axis of the scatter plot is the maximum total energy of the $\beta^{\pm}$ in MeV, and the vertical axis is the spallation product half-life in seconds.

Recent work by S. Li and J. Beacom has given the muon-induced nuclear spallation reactions seen in SK a better theoretical foundation [122]. SK has also made measurements of the production rates and half-lives of the spallation-induced isotopes [123]. The production rates from [123] are transcribed in Table 7.4. When the fitted rates are consistent with zero, the upper 90% confidence level is listed.

Table 7.4: List of possible muon-induced spallation products that can occur in SK. The primary process (fourth column) and the SK results for the fits to the production rates of selected isotopes (fifth column) are transcribed from [123]. The production rates are for all decay modes of a given isotope and integrated over their entire energy spectrum. When the fitted rates are consistent with zero, the upper 90% confidence level is listed.

Isotope	$\tau_{1/2}$ [sec]	Decay Mode	Kinetic Energy [MeV]	Primary Process	Measured Rate [kton^{-1}day^{-1}]
^{8}He	0.119	β^-	9.67 + 0.98(γ)	^{16}O(π^-, ^{3}H + 4p + n)^{8}He	< 1.4
		β^- n	16%		
^{8}Li	0.838	β^-	$\sim$13	^{16}O(π^-, α + ^{2}H + p + n)^{8}Li	$8.3 \pm 0.3 \pm 0.3$
^{8}B	0.77	β^+	13.9	^{16}O(π^+, α + 2p + 2n)^{8}B	$8.3 \pm 0.3 \pm 0.3$
^{9}Li	0.178	β^-	13.6 (50.5%)	^{16}O(π^-, α + 2p + n)^{9}Li	$0.9 \pm 0.3 \pm 0.3$
		β^- n	49.5%		
^{9}C	0.127	β^+ n	3$\sim$15	^{16}O(n, α + 4n)^{9}C	< 1.4
^{11}Li	0.0085	β^-	16$\sim$20 ($\sim$50%)	^{16}O(π^+, 5p + π^0 + π^+)^{11}Li	-
		β^- n	$\sim$16 ($\sim$50%)		
^{11}Be	13.8	β^-	11.51 (54.7%)	^{16}O(n, α + 2p)^{11}Be	< 16.9
			9.41 + 2.1(γ) (31.4%)		
^{12}Be	0.0236	β^-	11.71	^{18}O(π^-, α + p + n)^{12}Be	-
^{12}B	0.0202	β^-	13.37	^{16}O(n, α + p)^{12}B	$19.8 \pm 0.1 \pm 1.0$
^{12}N	0.0110	β^+	16.32	^{16}O(π^+, 2p + 2n)^{12}N	$2.8 \pm 0.1 \pm 0.1$
^{13}B	0.0174	β^-	13.44	^{16}O(π^-, 2p + n)^{13}B	-
^{13}O	0.0086	β^+	13.2 or 16.7	^{16}O(π^-, μ^- + p + 2n + π^-)^{13}O	-
^{14}B	0.0138	β^-	14.55 + 6.09(γ)	^{16}O(n, 3p)^{14}B	-
^{15}C	2.449	β^-	9.77 (36.8%)	^{16}O(n, 2p)^{15}C	< 6.7
			4.47 + 5.30(γ)		
^{16}C	0.747	β^- n	$\sim$4	^{18}O(π^-, n + p)^{16}C	-
^{16}N	7.13	β^-	10.42 (28.0%)	^{16}O(n, 2p)^{16}N	$39.7 \pm 3.3 \pm 2.8$
			4.29 + 6.13(γ) (66.2%)		

To statistically remove spallation-induced β events, several likelihood functions f are

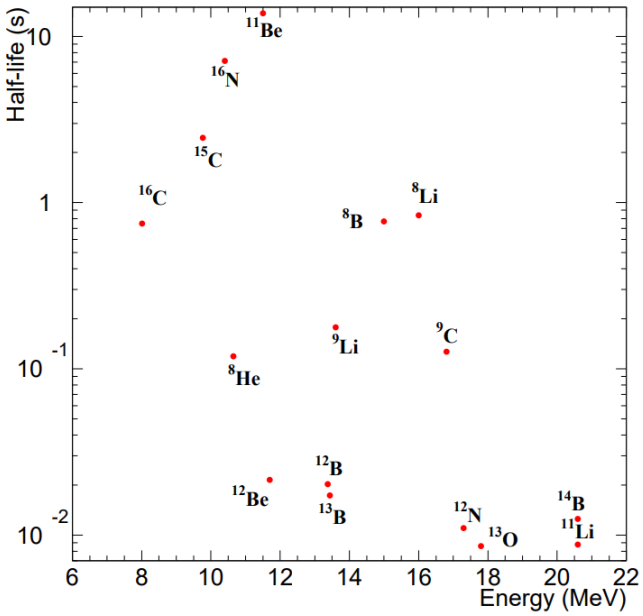

Figure 7.6: Scatter plot of the maximum total energy for the β emitted by the spallation products in Table 7.4 and the spallation radioisotope's half-life in seconds [124].

determined, and these functions are used to define the spallation likelihood:

$$L_{\text{spal}} = f(\Delta T) \times f(\Delta L) \times f(Q_{\text{res}}). \tag{7.6}$$

Here, ΔT is the time difference between the spallation candidate event and the muon event that precedes it, and the temporal likelihood function $f(\Delta T)$ is created by incorporating the various half-lives of the spallation radioisotopes. The distance between the reconstructed muon track and the candidate event vertex is ΔL. The residual charge of the preceding muon (Q_{res}) is

$$Q_{\text{res}} = Q_{\text{obs}} - d \times \frac{dQ}{dl}, \tag{7.7}$$

where Q_{obs} is the muon's observed charge, d is the distance the muon traveled in the water, and $\frac{dQ}{dl} \simeq 26.78$ pe/cm is the minimum ionizing amount of charge per unit length expected to be deposited in the water by the muon.

The spatial and residual charge likelihood functions, $f(\Delta L)$ and $f(Q_{\text{res}})$ respectively,

are determined using two sets of real data: a random sample, and a spallation-like sample. The random sample is generated by taking low energy events ($T_e < 4.5$ MeV), then randomly distributing the event vertices to mimic the signal distribution, while keeping the event timing unaltered. The spallation-like sample is generated by taking events occurring shortly after muons ($\Delta T < 0.1$s) and with higher energy ($T_e > 7.5$ MeV). The cut on $\log(L_{\text{spal}})$ is set so that the dead time of the random sample is 20%, where, for SK-IV, events with $\log(L_{\text{spal}}) \geq 4.52$ are removed. Figure 7.7 shows the distribution for $\log(L_{\text{spal}})$ of the spallation-like (random) sample in black (red) for SK-IV, where the gray region corresponds to the events removed by the spallation cut.

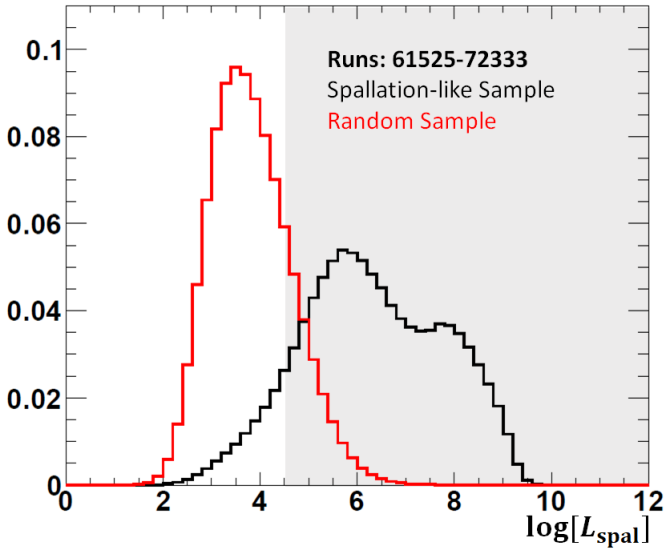

Figure 7.7: The normalized distributions for the spallation log likelihood from the spallation-like (random) sample in black (red) for SK-IV, where the gray region corresponds to the events removed by the spallation cut [48].

As the $\log(L_{\text{spal}})$ has a time dependence because of the delayed decays, it causes additional, position-dependent dead time to the solar neutrino analysis. Solar neutrino MC is used to extract the dead time as polynomial functions of the detector coordinates z and r^2

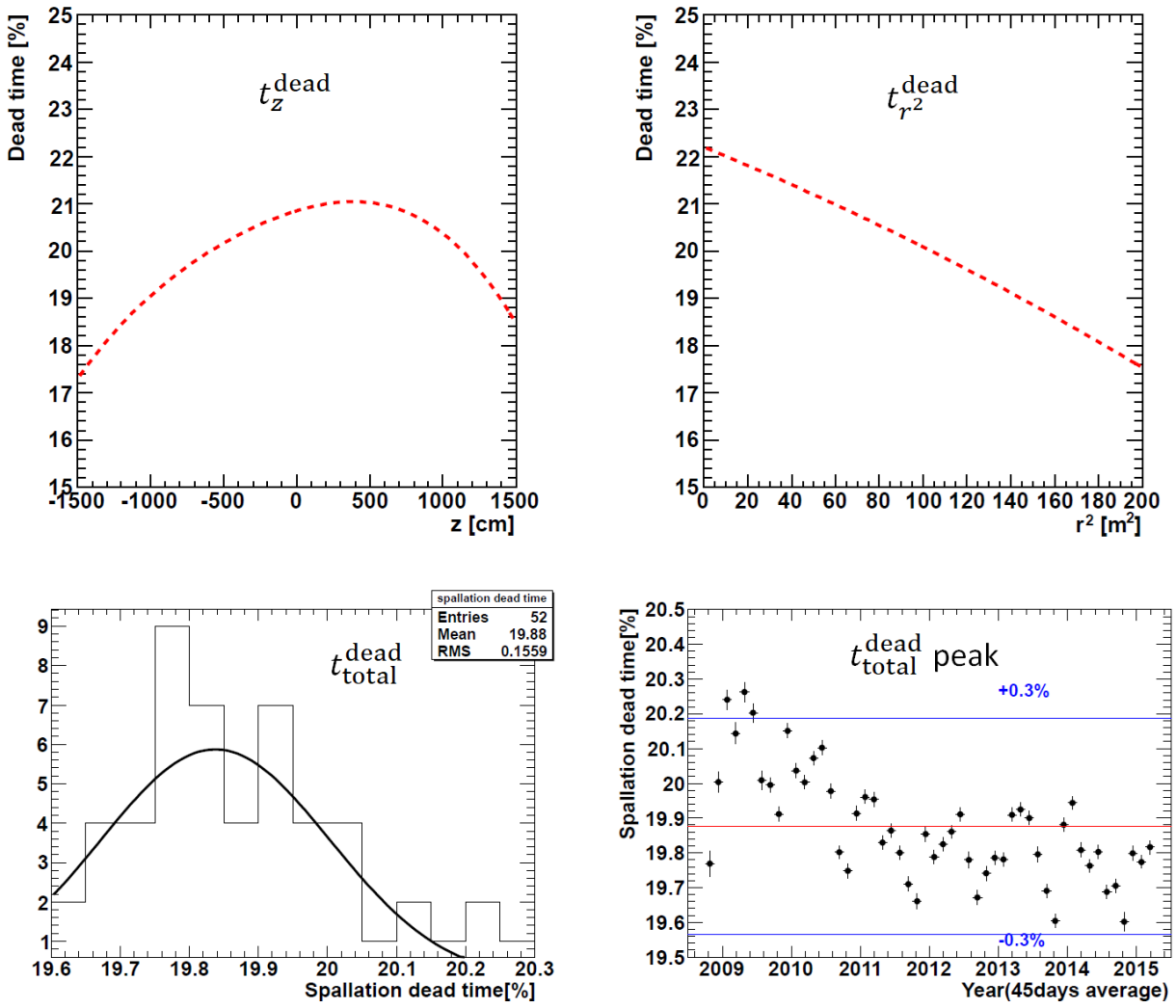

Figure 7.8: The percentage of dead time incurred in the solar neutrino analysis by the spallation cut (spallation dead time) as a function of z (r^2) is shown in the top left (right) plot of the figure. The bottom left plot is the distribution of the spallation dead time, while the bottom right plot is the time variation of the peak for the fit to the spallation dead time for the first half of SK-IV [48].

($t^{\rm dead}_{\rm total}(r^2,z)$). The spallation dead time polynomial functions are defined by:

$$1 - t_z^{\rm dead} = 0.79143 - 0.93206 \times 10^{-5} \cdot z + 0.98724 \times 10^{-11} \cdot z^2 - 0.30075 \times 10^{-11} \cdot z^3 + 0.16359 \times 10^{-14} \cdot z^4 - 0.26618 \times 10^{-18} \cdot z^5 - 0.63656 \times 10^{-22} \cdot z^6 \quad \text{and}$$
$$1 - t_{r^2}^{\rm dead} = 0.77799 + 0.18903 \times 10^{-7} \cdot r^2 + 0.22175 \times 10^{-14} \cdot r^4. \tag{7.8}$$

The resulting percent dead time as a function of detector coordinates for $t_z^{\rm dead}$ ($t_{r^2}^{\rm dead}$) is plotted in the top left (top right) of Fig. 7.8.

These functions are multiplied together and scaled by a normalization factor to form the total spallation dead time:

$$t^{\rm dead}_{\rm total}(r^2,z) = 5.08691 \times t_z^{\rm dead} \times t_{r^2}^{\rm dead}. \tag{7.9}$$

The normalization factor comes from requiring the total dead time to match the dead time of the random sample: $\int_{\rm vol} t^{\rm dead}_{\rm total}(r^2,z)) = 20\%$. The resulting distribution of the percent $t^{\rm dead}_{\rm total}$ for SK-IV is given in the bottom left of Fig. 7.8. The time variation in the percent $t^{\rm dead}_{\rm total}$ is stable within $\pm 0.3\%$ and is shown in the lower right part of the figure for the first half of SK-IV .

7.4.8 Hit Pattern Cut

Sometimes, the spallation products discussed in the previous subsection decay into multiple βs and/or γs, which causes the patterns produced by the Cherenkov light to be smeared out or poorly defined. The Cherenkov ring pattern in the hit PMTs is better defined (clearer) when only a single electron is emitting Cherenkov light. Events with multiple βs and/or γs can be distinguished from the single electron events by creating a likelihood function that accounts for these differences in the respective PMT hit pattern.

The hit pattern likelihood function, "patlik," is defined as

$$L_{\text{pattern}}(E, \vec{v}) \equiv \frac{1}{N_{50}} \sum_{j}^{N_{50}} \log[P(E, \cos\theta_j, f_{\text{wall}})], \tag{7.10}$$

where E is the total energy of an event, N_{50} is the number of hit PMTs in the T-TOF 50 ns time window, and the function P_j is the probability density function (PDF) of the hit pattern at the j'th hit PMT. P_j is a function of the event energy and the event variables θ_j and f_{wall}. These event variables are defined in Fig. 7.2.

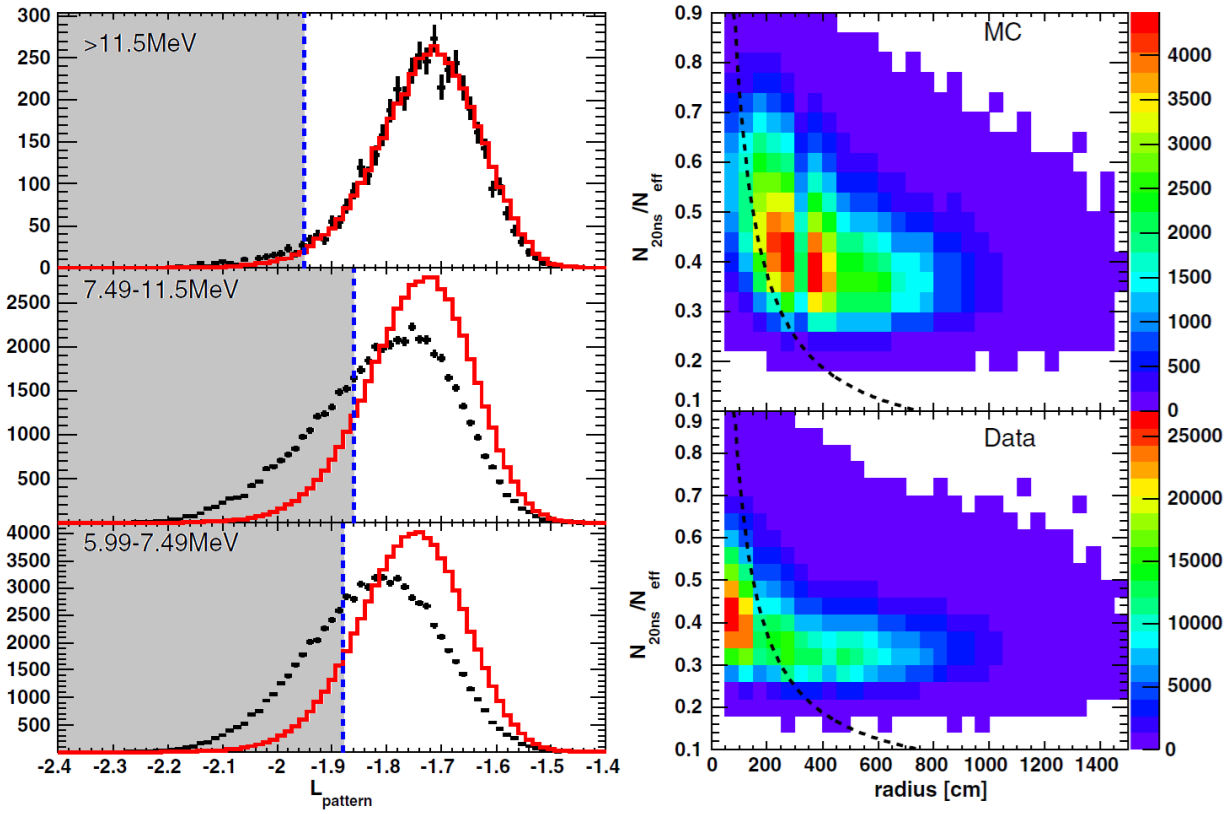

Figure 7.9: Left: The L_{pattern} distribution of data (black error bars) and solar neutrino MC (red) for the three energy regions (recoil electron kinetic energy), with the cut value (blue dashed line) and removed region (gray background) shown. Right: Small hit cluster removal (Sec. 7.4.9). The top (bottom) panel showing the cluster size of solar neutrino MC (data) events in the edge region as a function of cluster radius. Events to the left of the cut (dashed black line) are removed. Both plots from [42].

Since L_{pattern} is dependent on the event energy, different cuts on patlik are applied to

maximize the significance for three different energy ranges:

$$L_{\text{pattern}} > \begin{cases} -1.88, & 6.5 \leq E < 8.0 \text{ MeV} \\ -1.86, & 8.0 \leq E < 12.0 \text{ MeV} \\ -1.95, & E \geq 12.0 \text{ MeV} \end{cases} \tag{7.11}$$

The left side of Fig. 7.9 shows the data (black) and MC (red) patlik distributions for these three energy regions with the corresponding patlik cut value (blue dashed line) and the events removed by the cut (gray background). The patlik cut is not applied below $E = 6.5$ MeV since events do not emit enough light to form PMT hit patterns distinct enough from one another to distinguish between the classification of events with patlik.

7.4.9 Cut on Events with Small Hit Clustering

Radioactive background events that originate from the PMT glass or shielding are sometimes correlated to an upward fluctuation of PMT dark noise, causing them to pass the trigger threshold. In this situation, these events have a reconstructed vertex close to the wall with a small clustered hit pattern and with a total energy less than 5.5 MeV. Only events reconstructed within certain locations in the ID, known as the edge region, are affected by this cut. Events are retained if they meet the following criteria:

$$\begin{aligned} E_{\text{total}} = 4.0 - 5.0 \text{ MeV}: &\quad r^2 \leq 120 \text{ m}^2 \text{ and } -3.0 \text{ m} \leq z \leq +13 \text{ m} \\ E_{\text{total}} = 5.0 - 5.5 \text{ MeV}: &\quad r^2 \leq 155 \text{ m}^2 \text{ and } -7.5 \text{ m} \leq z \leq +13 \text{ m} \end{aligned} \tag{7.12}$$

where E_{total} is the total reconstructed energy of an event, and (r^2, z) is the reconstructed vertex position in the SK cylindrical coordinate system. If an event does not meet the above criteria, it is removed.

The clusters are characterized by first determining the set of PMTs with timing residuals less than 20 ns relative to the event (N_{20}). One then searches for the smallest sphere around any of the PMTs in the N_{20} set that encloses at least 20% of all the PMTs in the set. The radius of this sphere ($r_{\rm cluster}$) is used to construct the cut parameter $P_{\rm cluster}$:

$$P_{\rm cluster} \equiv \frac{N_{20}}{N_{\rm eff}} \times r_{\rm cluster}. \tag{7.13}$$

The right side of Fig. 7.9 shows the two-dimensional distribution of cluster radius versus $N_{20}/N_{\rm eff}$ for solar neutrino MC events (top plot) and data events (bottom plot) in the edge region. Real solar neutrino events in the edge region have similar characteristics as the backgrounds but have larger clusters and larger $P_{\rm cluster}$ values [95]. Events in the edge region with $P_{\rm cluster} < 75$ cm are removed. The dashed line in the two plots shows the effect of this cut, with events to the left of the line being removed.

7.4.10 External Event (γ-ray) Cut

As mentioned in the pre-reduction cuts, external radioactivity and γ-rays originate from the rock wall around SK, the PMT glass and shielding, and other detector components. These events point inward into SK, and some can be rejected using the reconstructed parameter $d_{\rm eff}$. The parameter $d_{\rm eff}$ is the minimum effective distance between the reconstructed vertex and the PMT structure opposite the event direction (see Fig. 7.2). A loose version of the cut is applied during pre-reduction. After the WT has been applied for the event reconstruction, events with $E \geq 8.0$ MeV are removed if $d_{\rm eff} < 400$ cm. The solar neutrino analysis imposes a stronger set of cuts on $d_{\rm eff}$ at energies below 8.0 MeV. For events with total energy between $5.5 \leq E < 8.0$ MeV, events are rejected if $d_{\rm eff} < 650$ cm.

For events with energy between 4.0 MeV and 5.5 MeV, the $d_{\rm eff}$ cut is tuned using a

central inner volume: $|z| < 10$ m and $r^2 < 13$ m^2. This inner volume is removed from the region in the ID where the vertices of external events are reconstructed. In this energy region, the cut is also dependent on which surface $p_{\rm wall}$ lies (top, barrel, or bottom). Again, $p_{\rm wall}$ is the position on the wall opposite of the reconstructed event direction (see Fig. 7.2). Events with $4.0 \leq E < 5.5$ MeV are rejected if:

$$\begin{aligned} &d_{\rm eff} < 1000{\rm cm}, \quad \text{for } p_{\rm wall} \text{ at top} \\ &d_{\rm eff} < 1200{\rm cm}, \quad \text{for } p_{\rm wall} \text{ at barrel} \\ &d_{\rm eff} < 1300{\rm cm}, \quad \text{for } p_{\rm wall} \text{ at bottom} \end{aligned} \tag{7.14}$$

The harsher cut for the bottom region is due to the high concentration of background in the bottom of the ID. Table 7.2 summarizes the external event cut. Because of the non-uniform distribution of backgrounds in the outer regions of the ID, further energy-dependent fiducial volume requirements will be applied next (Sec. 7.4.11).

7.4.11 Tight Fiducial Volume Cuts

While solar neutrinos are expected to interact uniformly throughout the volume of SK, regions with high event rates are likely due to radioactive backgrounds. These backgrounds are assumed to come from the PMTs, their housings, the SK structure, and the "Rn background" inside the tank. The Rn background comes from the daughters of the ^{222}Rn decay chain. In the lowest energy bin of the solar neutrino analysis, $E = 4.0$ - 4.5 MeV (total energy), the β decay of ^{214}Bi is thought to be a significant contributor to the Rn background [113]. The β-decay of ^{214}Bi has a Q-value of 3.27 MeV (the total energy released in the decay). Because of the poor energy resolution of $\sim$20% around $E \simeq 4.5$ MeV, the reconstructed energy of these βs may be well above the 4.0 MeV energy threshold.

Because the distribution of backgrounds in the ID is not uniform, further energy-

dependent fiducial volume requirements are applied to maintain the uniformity of vertex distributions. Having uniform vertex distributions helps to keep the shapes of the background distributions uniform, which allows the shapes to be modeled. Doing this helps to minimize the associated systematic uncertainties.

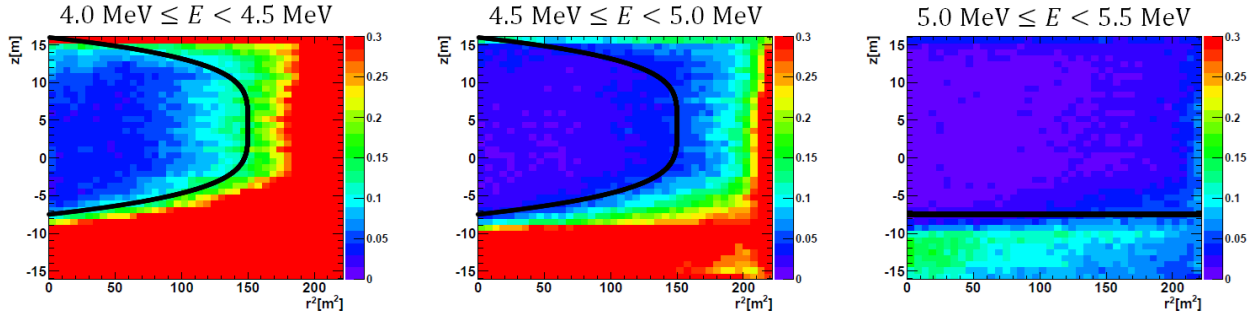

Figure 7.10: The vertex distributions in r^2 versus z for the three lowest energy bins (total reconstructed energy) in the solar neutrino analysis [48]. The fiducial volume lies to the left of the black line for the two lowest energy bins, and above the black line in the 5.0 - 5.5 MeV bin (total energy). The event rate (color) is in units of event/day/bin.

The standard fiducial volume cut is a 2-m wall cut that is applied at all energies. This cut rejects events with a reconstructed vertex less than 2 m away from the PMT structure, yielding a fiducial volume of 22.46 ktons. Below $E = 5.5$ MeV, more stringent, or "tight," fiducial volume cuts are applied to reject the increased background and reduce the systematic uncertainty. The tight fiducial volume (TFV) cut was studied in depth to simultaneously maximize the fiducial volume and the significance at low energies [48]. The TFV cut rejects events that lie outside of the following regions:

$$\begin{aligned} z > -7.5 \text{ m}, &\qquad 5.0 \leq E < 5.5 \text{ MeV} \\ r^2 + (\tfrac{150.0}{11.75^4} \times |z - 4.25|^4) < 150.0, &\qquad 4.0 \leq E < 5.0 \text{ MeV} \end{aligned} \tag{7.15}$$

Below $E = 5.0$ MeV, the TFV has a total volume of 8.85 kton, while the total volume of the TFV for the $E = 5.0$ - 5.5 MeV bin is 16.54 kton. Prior to SK-IV, the $E = 5.0$ - 5.5 MeV bin had an additional requirement that would remove events with $r^2 > 180$ m^2. This

requirement has been removed for SK-IV based on the work in [48]. The vertex distributions for the three lowest energy bins in the solar neutrino analysis are shown in Fig. 7.10 with the TFV boundary denoted by a black line.

7.4.12 ^{16}N Cut

^{16}N can be be produced in the SK water from fast neutrons produced by spallation (Sec. 7.4.7) or the DT generator (Sec. 5.3.2). It can also be produced when a low energy μ^- stops in SK by capturing on an ^{16}O nucleus [116]. Muon-induced ^{16}N occurs uniformly throughout the detector. As discussed in the DT generator calibration, ^{16}N has a half-life of 7.13 seconds and subsequently decays to βs. The radioisotope's primary decay mode (66%) is to emit a β with endpoint energy of 4.3 MeV and a 6.1 MeV γ. A secondary decay mode (28%) is to a β with an endpoint of 10.41 MeV. Since the decay modes mimic the signal of a solar neutrino, these events need to be rejected. While the spallation cut does remove some of these events, additional consideration is given to ^{16}N because of its long half-life. To remove events produced by ^{16}N, the correlation between captured (or stopping) muons and the event candidates is considered by applying the following criteria:

1. Muons in the stopping muon data sample are selected if there is not an accompanying event which occurs within 100 μs of the muon.

2. The distance between the reconstructed vertex of the candidate event and the stopping point of the muon must be less than 250 cm. The time difference between the two must be between 100 μs and 30 seconds.

If candidate events meet these criteria, they are rejected. The resulting dead time of $\sim$0.53% incurred from the ^{16}N cut is estimated by accidental coincidence between the random sample events (events that occur prior to muons) and the stopping muons that pass criterion 1. The

^{16}N cut is the final reduction step for the solar neutrino analysis on the data, after which the final solar neutrino sample data set is obtained.

7.5 Multiple Scattering Goodness (MSG)

Even after applying all the cuts in the solar neutrino analysis, background events still contaminate the final data sample. As described in Sec. 7.4.11, it is believed that the β decay of ^{214}B produced by the Rn background contributes significantly. The poor energy resolution below $E = 4.5$ MeV (total energy) can allow the β to reconstruct above the 4.0 MeV threshold. The multiple scattering goodness (MSG) parameter (Sec. 6.4.1) is used in the solar neutrino analysis. Instead of using it as a cut, it is used to bin events with $E < 8.0$ MeV. During solar neutrino signal extraction (Sec. 8.1), candidate events are further separated into MSG bins when extracting the (ν e) ES-induced recoil electron spectra (Sec. 9.1). Three MSG bins are used: low ($0 \leq$ MSG < 0.35), middle ($0.35 \leq$ MSG < 0.45), and high ($0.45 \leq$ MSG < 1). By binning in MSG, the impact of signal-like events is improved while reducing the impact of background-like events. This method of including MSG into the signal extraction has a minimal impact on the systematic error.

While the physics motivation of MSG and the Cherenkov hit pattern likelihood (patlik, Sec. 7.4.8) are different, both are based on PMT timing and hit patterns and may have good correlation. A study is currently underway to determine if the systematic error can be reduced by removing one parameter from the solar neutrino analysis by cutting or binning on the other parameter at equivalent values. Another option is to bin with the patlik parameter instead of cutting on it. Other possibilities include using the two-dimensional distribution of the parameters for various energies and form a third parameter out of the two, similar to the idea for g_R^2. The left side of Fig. 7.11 shows the two-dimensional distribution of patlik and MSG for the $E = 6.5$ - 7.0 MeV bin using the ^{8}B solar neutrino MC. The horizontal dashed

lines (green) are the bin partitions for the MSG, and the vertical line (red) is the patlik cut for that energy. Events in the gray region are removed by the patlik cut. The correlation coefficient for the plotted distribution is 0.87, assuming a linear correlation.

In one approach, I determined an equivalent MSG value to the patlik cut for each energy bin by requiring the MSG value to remove the same amount of MC events as the patlik cut. Events from the so-called "solar background region" of the final data sample are used to compare the removal efficiency of each cut. In the solar neutrino analysis, the solar background region is defined by $\cos\theta_{\rm Sun} < 0.0$. The parameter $\cos\theta_{\rm Sun}$ is the dot product of the vector pointing from the Sun and the reconstructed event direction. Signal-like events have large $\cos\theta_{\rm Sun}$ values, and events with $\cos\theta_{\rm Sun} < 0.0$ are more likely to be due to background. The removal efficiency for each energy bin in the solar neutrino analysis is plotted in Fig. 7.12. In this study, the patlik value was assumed to be the same below $E = 6.5$ MeV as for the $E = 6.5$ - 7.5 MeV bins. In general, it seems that the equivalent MSG cut has improved background reduction in some energy ranges. However, the effects on the systematic error are still being determined. Additionally, it has been found that flasher events and other poorly reconstructed events tend to lie outside of the typical MSG versus patlik distribution. This information may be leveraged to institute an automated way of cross-checking for bad subruns.

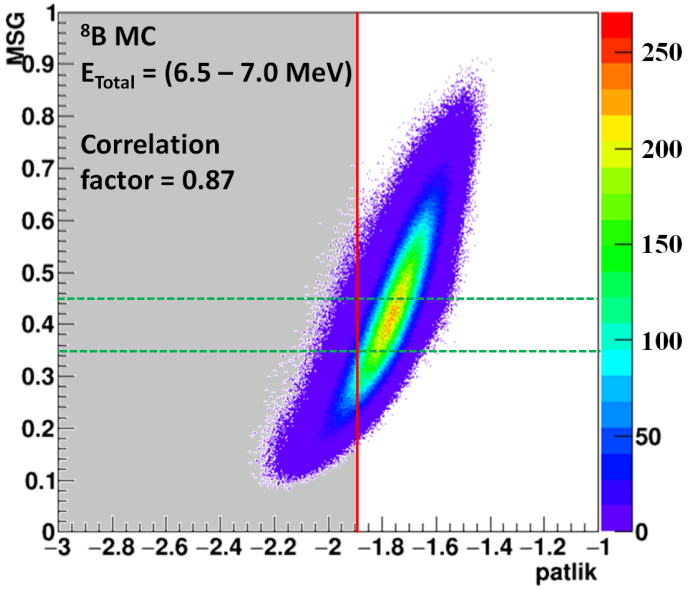

Figure 7.11: The correlation between MSG versus patlik using ^{8}B MC for the 6.5 - 7.0 MeV total energy bin. The horizontal green dashed lines are the MSG bin partitions, while the red line is the patlik cut for that energy range. The gray area is the events removed by the patlik cut. The correlation factor of 0.869 assumes a linear correlation between the two parameters.

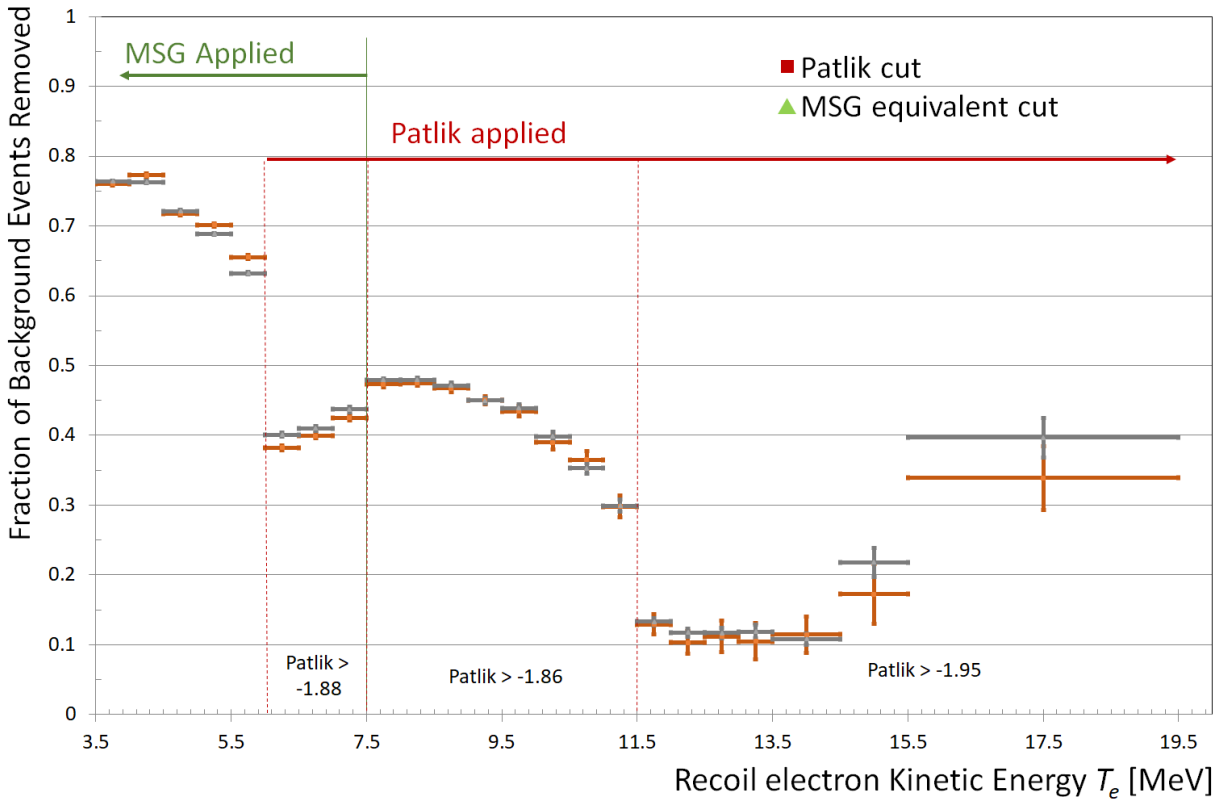

Figure 7.12: The comparison of the fraction of total background events removed in each T_e bin by the patlik cut (brown) and the equivalent MSG cut (olive). The data used is the background of the solar neutrino final sample, which corresponds to $\cos\theta_{\mathrm{Sun}} < 0.0$. The equivalent MSG cut was determined by tuning the parameter so it removes the same number of events from the ^{8}B MC as the corresponding patlik cut. The vertical axis is the fraction of events removed. Below $T_e = 5.99$ MeV, patlik is not used. The equivalent MSG cut in that energy range corresponds to patlik = -1.88.

Chapter 8

The Solar Neutrino Total Flux Analysis

When discussing energy in the solar neutrino analysis, the recoil electron kinetic energy (T_e) will be used and not the total energy, unless otherwise explicitly stated. The final solar data sample referred to in this chapter is the sample of candidate recoil electron events after all reduction cuts have been applied (see Sec. 7.1). The left side of Fig. 8.1 illustrates the various parameters that will be used to discuss solar neutrinos in this and subsequent chapters. $\theta_{\rm Sun}$ is the angle between the recoil electron direction ($r_{\rm rec}$) and the incident solar neutrino direction (r_ν). The zenith angle ($\theta_{\rm Z}$) is the angle between the upward direction along the z-axis of a detector and $r_{\rm rec}$.

8.1 Signal Extraction Method

Because the (ν e) elastic scattering (ES) process is highly forward peaked, the direction $r_{\rm rec}$ of the recoil electrons and incident solar neutrino direction r_ν are highly correlated. The

angular distribution of this process is described by Eq. 2.68. By binning candidate ES events from the final solar neutrino sample in $\cos\theta_{\text{Sun}}$, a peak in the forward region appears ($\cos\theta_{\text{Sun}} \gtrsim 0.8$). This "solar peak" is a clear signature of solar neutrinos.

The $\cos\theta_{\text{Sun}}$ distribution of the final solar data sample is plotted on the right side of Fig. 8.1. The data (black error bars) is for recoil electron events which have reconstructed energy between 3.49 and 19.49 MeV. The solar peak is clear in this distribution.

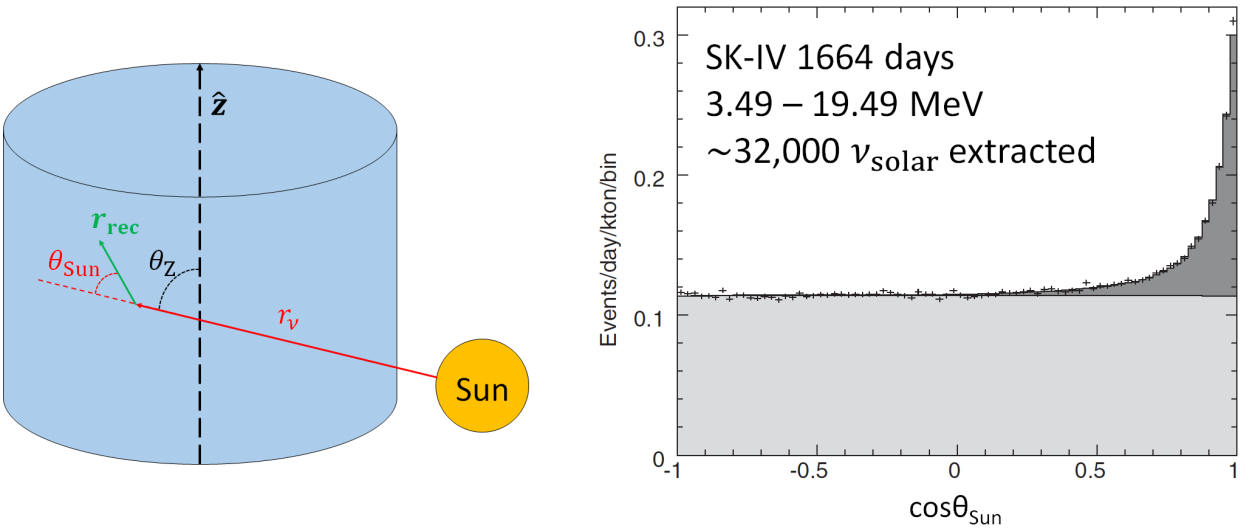

Figure 8.1: Left: Illustration of the definitions of θ_{Sun} (the zenith angle θ_{Z}), which is the angle between the solar incident neutrino direction and the reconstructed recoil electron direction (the positive z-axis). Right: The $\cos\theta_{\text{Sun}}$ distribution for the final solar data sample for recoil electrons with reconstructed energy between 3.49 and 19.49 MeV, after all cuts [42]. The data (error bars) and best fit (black line) are displayed, along with the solar neutrino signal (dark shaded region) and background (light shaded region) components of the fit.

8.1.1 Extended Maximum Likelihood Fit for Solar Neutrinos

An extended maximum likelihood fit is employed to extract the number of solar neutrino interactions from the final solar data sample. This fit is used in the solar neutrino analyses for all SK-Phases: SK-I [44], SK-II [94], SK-III [95], and SK-IV [42]. The likelihood function

is defined as:

$$L_{\text{Flux}} = e^{-(\sum_i B_i + S)} \prod_{i=1}^{N_{\text{bin}}} \prod_{j=1}^{n_i} \left(B_i \times b_{ij} + S \times Y_i \times s_{ij} \right), \tag{8.1}$$

and the fit is maximized using the free parameters S and B_i. The parts that comprise L_{Flux} are as follows:

- The index i labels the analysis bins, up to the maximum number of bins N_{bin}. These bins can correspond to energy, MSG, etc., or a combination of these parameters.
- The index j labels the observed events, up to the maximum number of observed events n_i in bin i.
- S and B_i are free parameters for the fit. S is the number of solar neutrino events summed over all bins, while B_i is the number of background events in bin i.
- Y_i is the fraction of expected signal events in bin i, determined from the solar neutrino MC.
- The background weights b_{ij} are determined from expected background shape probability density functions (PDFs). The background shape PDFs are constructed from data.
- The signal weights s_{ij} are determined from the predicted signal shape PDFs, constructed from the solar neutrino MC.

In the plot on the right side of Fig. 8.1, the best fit (black line) is shown for recoil electron events with energy between 3.49 and 19.49 MeV. The dark (light) shaded region corresponds to the signal (background) component of the fit.

The likelihood function is used in the energy spectrum analysis to extract the number of signal events S_i within each bin as well.

Solar Analysis Binning

The flux and spectrum analyses of SK-IV have a maximum of $N_{\rm bin} = 23$ bins. These bins are energy bins spanning the energy range from 3.49 MeV to 19.49 MeV. The first twenty bins range from 3.49 to 13.49 MeV with width of 0.5 MeV. Two bins with a width of 1 MeV span the range between 13.49 and 15.49 MeV. The final energy bin covers the range from 15.49 to 19.49 MeV. In SK-III, $N_{\rm bin} = 22$ as the 3.49 - 3.99 MeV bin was below the analysis threshold. In SK-I (SK-II), $N_{\rm bin} = 21$ (17) as bins below 4.49 (6.49) MeV were below the analysis threshold.

After the SK-IV 1664-day paper [42], the total flux analysis has been changed to include MSG. For SK-II/III/IV, the energy bins below 7.49 MeV are sub-divided into three MSG bins: $0 \leq \text{MSG} < 0.35$, $0.35 \leq \text{MSG} < 0.45$, and $\text{MSG} \geq 0.45$. This gives $N_{\rm bin} = 39$ for SK-IV. MSG has been incorporated into the SK solar neutrino spectrum analysis (Ch. 9) since the beginning of SK-IV.

Background PDFs

The background shape PDFs are used to determine the background weights b_{ij}. These PDFs are constructed using the zenith ($\theta_{\rm Z}$) and azimuthal background shape distributions of the final solar data sample. Sets of the background shape distributions are formed by binning the data in energy (or MSG). Below 7.49 MeV, events are collected in 0.5 MeV wide bins. Above this energy, two other energy bins are used: 7.49 - 9.49 MeV and 9.49 - 21.49 MeV. When including MSG, the energy bins below 7.49 MeV are sub-divided as previously described. These bins will be indexed here by e.

After converting the distribution of events in the detector coordinates to $\cos\theta_{\rm Sun}$, each

background shape is fit with:

$$\frac{1}{p_{e,9}} \sum_{k=0}^{8} p_{e,k} \times \cos^{k}(\theta_{j}^{\mathrm{Sun}}), \tag{8.2}$$

and the parameters $p_{e,0-8}$ are obtained during the fit to bin e. The parameter $p_{e,9}$ is a normalization factor to ensure the integral of the polynomial over the distribution equals to one. The background shape PDFs are the normalized background polynomial functions. The background weight b_{ij} is extracted from the PDFs. The background shape PDFs for each bin using the full SK-IV data set are plotted in Fig. 8.2. These background shapes are not broken down by MSG.

Signal PDFs

The signal shape PDFs used to determine the signal weights s_{ij} are created from the $\cos\theta_{\mathrm{Sun}}$ distributions of the solar neutrino MC. Similar to the background shape PDF determination, events are grouped with the same energy-MSG bins e. In a given bin e, the distribution is fit with three exponential functions plus a Gaussian function:

$$\sum_{k=0}^{2} \exp\left(c_{e,2k} + c_{e,2k+1} \times \cos\theta_{j}^{\mathrm{Sun}}\right) + c_{e,6} \exp\left(-\frac{1}{2}\left[\frac{c_{e,7} - \cos\theta_{j}^{\mathrm{Sun}}}{c_{e,8}}\right]^{2}\right), \tag{8.3}$$

where the parameters $c_{e,0-8}$ are obtained from the fit.

The two-dimensional signal shape PDFs are constructed by interpolating in energy. The signal weight s_{ij} is extracted from these signal shape PDFs. By using this method for the signal and background shape PDFs, the analysis is unbinned in energy and $\cos\theta_{\mathrm{Sun}}$.

After the SK-IV 1664-day solar analysis, the signal shape PDFs were updated to use a different fit to the MC $\cos\theta_{\mathrm{Sun}}$ distributions. The new signal shapes for each bin use a set of four polynomial functions that are fit to different regions in the $\cos\theta_{\mathrm{Sun}}$ distribution.

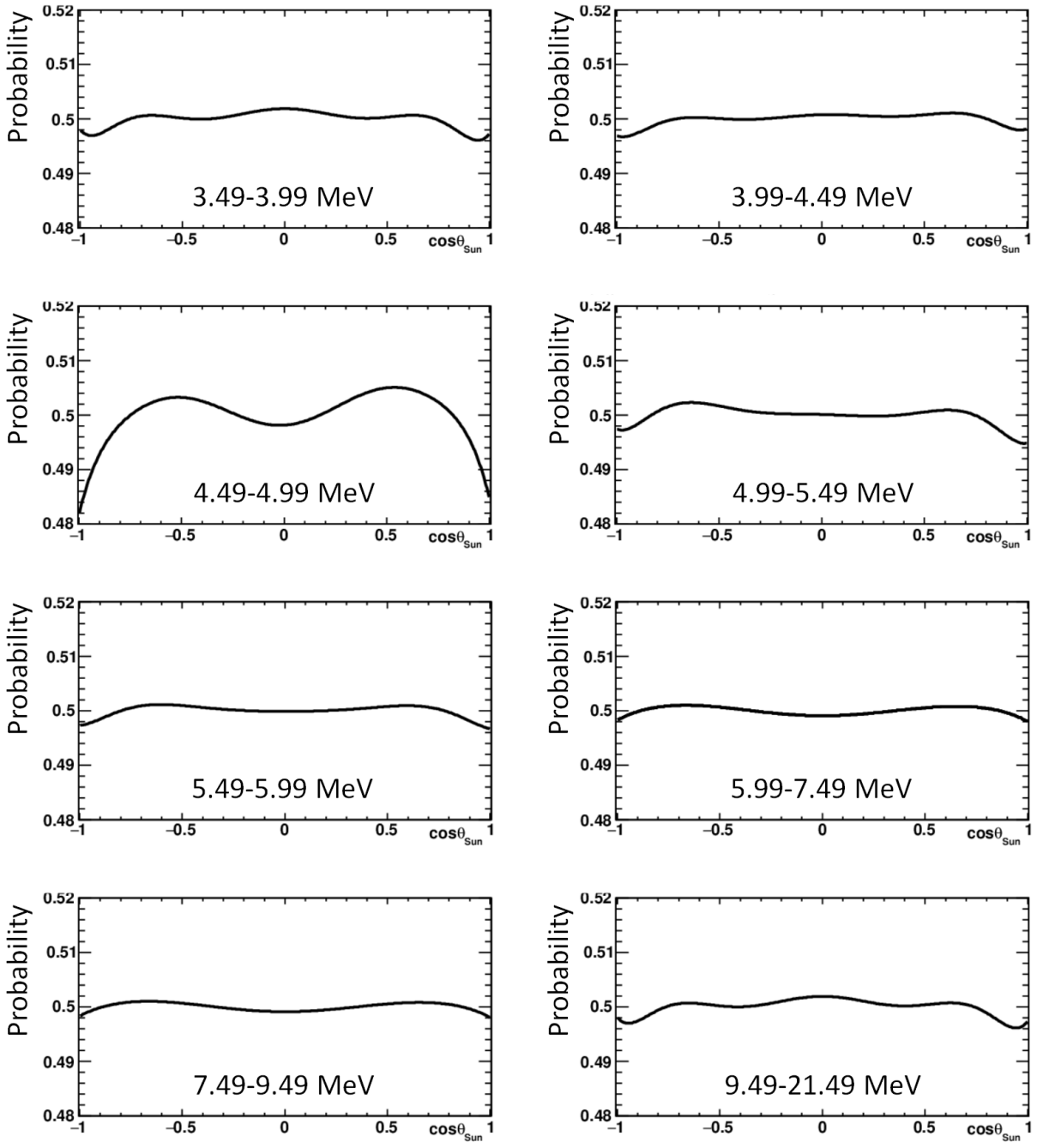

Figure 8.2: The fitted background shape PDFs in $\cos\theta_{\mathrm{Sun}}$ from which the background weights b_{ij} are extracted.

These regions overlap to allow for a transition function to smoothly go between the fitted polynomials. Table 8.1 lists the minimum, maximum, and centroid for these fits in $\cos\theta_{\rm Sun}$. The degree of a polynomial is not determined *a priori*. It is varied to optimize the fit in each region of the distribution, though the maximum degree of a polynomial is twelve. The full distribution is normalized so that the area under the curve is one. This method was adopted to better model the distribution. The effect on the systematic error is currently being investigated. The signal PDFs from this method are plotted in Fig. 8.3, and are divided at 7.49 MeV.

Table 8.1: The boundaries and centroid for the new polynomial functions used to fit the background shapes. This description for the signal shapes was applied after the 1664-day solar analysis. The values in the table correspond to $\cos\theta_{\rm Sun}$.

Lower Bound	Centroid	Upper Bound
-1.00	-0.375	0.25
0.00	0.375	0.75
0.50	0.700	0.90
0.85	0.925	1.00

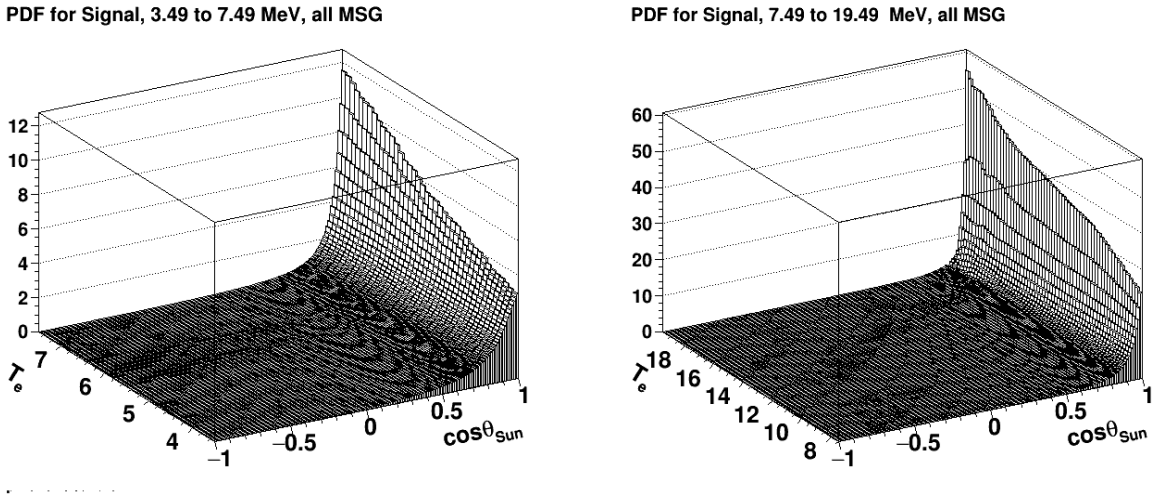

Figure 8.3: The signal shape PDFs using the new method for modeling the signal distribution from solar neutrino MC. Both distributions ignore MSG. The background shape of the 4.49-4.99 MeV bin is due to Rn backgrounds near the edges of the tight fiducial volume.

Expected Fraction of Signal Events

The expected fraction of signal events is determined from the solar neutrino MC (Sec. 6.1), using both ^{8}B and *hep* simulated events. The total number of generated events for a given bin is

$$N_i^{\text{generated}} = N_i^{^8\text{B}} + 0.1 \times N_i^{hep}, \tag{8.4}$$

where the scale factor is applied to normalize the *hep* generation rate to 0.2 Hz. The number of *hep* events is over-produced in the simulation by a factor of 10 to get good statistics (2 Hz), but needs to be scaled down to correspond to the desired generation rate. For comparison, the ^{8}B generation rate is 2 Hz.

After these events are generated, they are reconstructed in the same manner as data (Ch. 6), and the analysis cuts discussed in Ch. 7.1 are then applied. The remaining number of events in a given bin is $N_i^{\text{after cuts}}$. For a given bin, Y_i is:

$$Y_i = \frac{N_i^{\text{after cuts}}}{N_i^{\text{generated}}}. \tag{8.5}$$

In Fig. 8.4, the expected energy distribution for the Y_i divided by the exposure (live time $\times$ fiducial volume) of each energy bin is plotted.

8.2 Systematic Uncertainties of the Total Flux

The systematic uncertainty for the signal extraction method is estimated to be 0.7%. This uncertainty is determined by applying the extraction to simulated dummy data for which the total number of signal events S and background events B_i are known. The percentage difference between the true S and extracted S is taken as the uncertainty on the total flux measurement using this method.

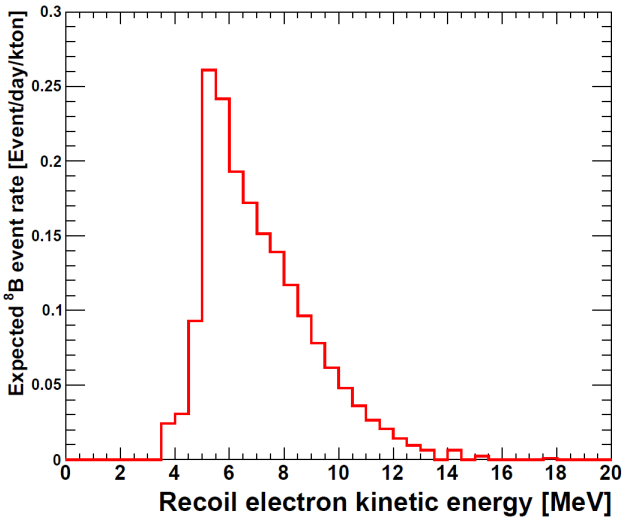

Figure 8.4: The energy distribution from MC of the expected ^{8}B event rate in SK [48]. This distribution is made from the Y_i factors multiplied by the exposure for each energy bin. The MC assumes the Winter06 ^{8}B neutrino energy spectrum [45] and the ^{8}B flux measured by SNO [47]. The drop in the expected rate below 5 MeV comes from the tighter fiducial volume cut.

The different effects that the components of the signal extraction have on the total flux are considered separately. The systematic uncertainties for SK-IV will be discussed here. Details for the other SK-Phases can be found in [44][94][95].

In general, systematic effects are determined by first considering the effect that shifting an aspect of the extended maximum likelihood method has on the recoil spectrum F. Then, the modified Y_i, s_{ij}, and/or b_{ij} are determined. Finally, L_{Flux} is re-minimized to get the modified S', which is then compared to the original result for S.

8.2.1 Energy Scale

The systematic uncertainty of the energy scale is summarized in Sec. 5.3.3 and has an estimated total uncertainty of 0.54%. To determine the impact it has on the systematic uncertainty of the total flux, the following actions are performed. The energies of the MC events are shifted by ±0.54%, and the new signal fractions ($Y_i^{\pm\text{Escale}}$) are used in the signal

extraction. This results in a difference of ±1.2% in the number of extracted signal events. The difference is taken as the systematic uncertainty on the SK-IV total neutrino flux coming from the energy scale.

8.2.2 Energy Resolution

The resolution of the reconstructed energy is detailed in Sec. 6.2.3. It is based on the relationships between the observed total energy (E_{obs}) and the true total energy (E) of the recoil electrons. To ascertain the systematic uncertainty, the energy resolution function $\sigma(E)$ (Eq. 6.14) is fluctuated by $\Delta\sigma_{\mathrm{LINAC}}$ (Eq. 6.16). $\Delta\sigma_{\mathrm{LINAC}}$ is the percentage difference of the energy resolution between the LINAC data and MC. $\sigma(E)$ is replaced in the response function $R(E, E_{obs})$ (Eq. 6.13) by $\sigma^{\pm} = \sigma(E) \times (1 \pm \Delta\sigma_{\mathrm{LINAC}})$, resulting in a shift in the energy spectrum $F^{\pm}_{\mathrm{sys}}(E_{obs})$ (Eq. 6.12).

The ratios between $F^{\pm}_{\mathrm{sys}}$ and the un-altered spectrum F are used as weights to modify the signal fractions: $Y_i^{\pm\mathrm{Eres}}$. The percentage difference between $F^{\pm}_{\mathrm{sys}}$ and F is shown on the left plot of Fig. 8.5. The signal extraction is performed with the new $Y_i^{\pm\mathrm{Eres}}$. The energy resolution uncertainty is ±1.0% below 4.89 MeV and ±0.6% above 6.81 MeV [42]. The difference in the resulting signal, ±0.15%, is taken as the systematic uncertainty on the total flux from the energy resolution.

8.2.3 ^{8}B Neutrino Spectrum Shape

There is an uncertainty in the shape of the ^{8}B neutrino spectrum due to theoretical and experimental uncertainties from Winter06 [45]. The uncertainty in the ^{8}B neutrino spectrum shape leads to a shift in its spectrum by ∼±100 keV. The effect this uncertainty has on the total flux is determined in a similar fashion as the systematic uncertainty of the energy

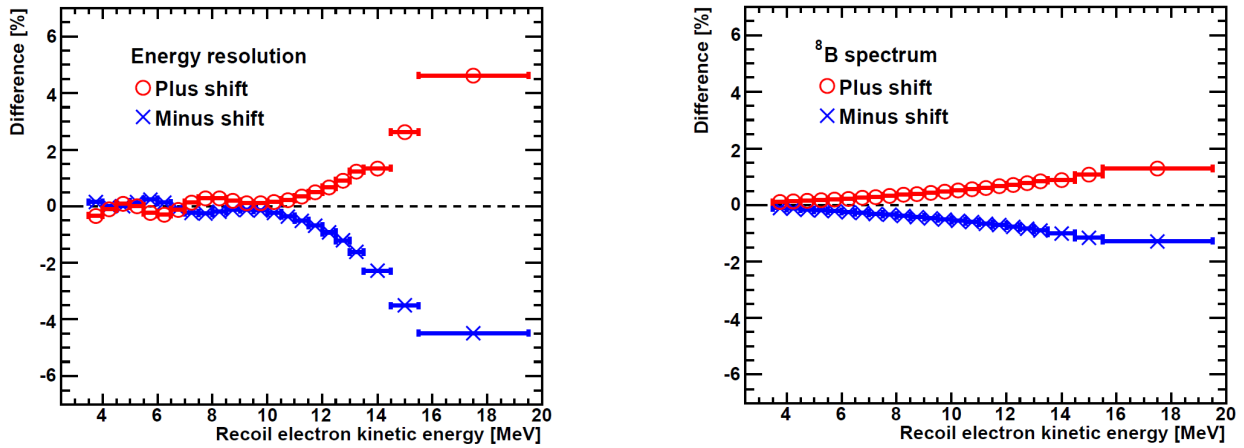

Figure 8.5: The percentage difference between the original spectrum and the shifted energy spectrum. The shift in the spectrum is the result of shifting the energy resolution (left) or the ^{8}B neutrino spectrum (right) [48]. The trigger efficiency and reduction efficiency are taken into account.

resolution (Sec. 8.2.2). Here, $\Phi(E_\nu)$ is modified in the estimation of the recoil electron spectrum $F_{\rm sys}(E_{obs})$ (Eq. 6.12). Sets of MC events are created by distorting $\Phi(E_\nu)$ based on the uncertainties of the spectrum shape. The subsequent effects of distorting the ^{8}B neutrino spectrum on F and Y_i are determined. The difference in the signal compared to the original total flux is $\pm 0.35\%$. This value is taken as the systematic error due to the ^{8}B solar neutrino spectrum. The percentage difference between F modified by the ^{8}B neutrino spectrum shape uncertainties and the original F is plotted on the right plot of Fig. 8.5.

8.2.4 Cross Section

As stated in Sec. 2.3 and in Sec. 6.1.1, the cross section calculations for the (ν e) ES process include the radiative corrections from Bahcall et al. [41]. Bahcall et al. introduce two parameters to characterize the radiative corrections in their analysis: ρ and $\kappa(T_e)$. The error on ρ is due to the lack of precision on the top quark mass and the Higgs mass. Their paper was published in 1995, prior to the improved measurements from the Large Hadron Collider experiments. The uncertainty in the $\kappa(T_e)$ function is from one-loop corrections of

the ES interaction from quantum chromodynamic processes.

The 1σ theoretical uncertainties given in their paper for the two parameters are used to shift the parameters in the cross section numerical calculation. New recoil electron MC spectra F are created, the new Y_i are determined, and the effect on the total extracted flux is analyzed. A change in S of $\pm 0.5\%$ is seen by fluctuating the cross section. This change is taken as the systematic uncertainty due to the (ν e) ES cross section uncertainties.

8.2.5 Trigger Efficiency

Low energy events in SK pass the trigger threshold after a minimum number of PMTs are hit within a certain time window (see Sec. 4.5). The trigger efficiency depends on several factors: the vertex position, the water transparency (WT), the number of hit PMTs, and the response of the front-end electronics. By comparing the difference of the trigger efficiency between Ni-source calibration data and corresponding MC, the trigger efficiency can be estimated as a function of energy. These differences in the trigger efficiency are applied to the signal extraction method by changing the extracted number of events correspondingly.

For the data used in the SK-IV 1664-day solar neutrino analysis and in the analysis presented in this work, the trigger threshold was set to 34 hits. The trigger efficiency for the two lowest energy bins in SK-IV are listed in Table 8.2, along with the difference in efficiency. The trigger efficiency is 100% with negligible uncertainty above $T_e = 4.49$ MeV [42]. The resulting systematic uncertainty for the total flux measurement due to the uncertainty of the trigger efficiency is $\pm 0.1\%$. After changing the SLE trigger threshold from 34-hits to 31-hits, the trigger efficiency is improved below $T_e = 4.49$ MeV. Above this energy, the trigger efficiency is 100% with negligible uncertainty. The preliminary systematic uncertainty for all of SK-IV remains $\pm 0.1\%$.

Table 8.2: The trigger efficiencies ($\epsilon_{\mathrm{TrgEff}}$) of the two lowest energy bins for the 34-hit threshold used in the SK-IV 1664-day solar analysis and the 31-hit trigger threshold. 34-hit table is Table 7.2 from [48]. The third column is the difference between the trigger efficiencies from Ni calibration MC and data: $\Delta\epsilon_{\mathrm{TrgEff}} = \epsilon^{\mathrm{MC}}_{\mathrm{TrgEff}} - \epsilon^{\mathrm{Data}}_{\mathrm{TrgEff}}$. $\Delta\epsilon_{\mathrm{TrgEff}}$ is used to estimate the systematic uncertainty for these bins in the solar neutrino energy spectrum analysis.

Efficiency of the 34-hit Trigger Threshold for SK-IV (1664 days) [48]

T_e [MeV]	Data[%]	MC[%]	$\Delta\epsilon_{\mathrm{TrgEff}}$
3.49 - 3.99	89.36 ± 0.22	92.42 ± 0.24	3.43 ± 0.37
3.99 - 4.49	99.18 ± 0.22	100.0 ± 0.21	0.86 ± 0.31

Efficiency of the 31-hit Trigger Threshold for SK-IV (Preliminary)

T_e [MeV]	Data[%]	MC[%]	$\Delta\epsilon_{\mathrm{TrgEff}}$
3.49 - 3.99	98.72 ± 0.22	100.0 ± 0.13	1.28 ± 0.26
3.99 - 4.49	99.31 ± 0.16	100.0 ± 0.10	0.69 ± 0.19

8.2.6 Angular Resolution

The angular resolution of the directional reconstruction is determined by comparing LINAC data and LINAC MC (Sec. 6.4). The uncertainties in the angular resolution between the LINAC data and MC are detailed in Table 6.3 for various energies and for each SK-Phase. By using the uncertainty in the angular resolution, the reconstructed directions of the solar neutrino MC are shifted. This varies the signal shape PDFs and has a corresponding effect on the signal weights: $s_{ij}^{\mathrm{ang}\pm}$. The new signal weights are then used to extract S, resulting in a shift of $\pm 0.1\%$. This uncertainty is taken as the systematic error due to the uncertainty in the angular resolution.

8.2.7 Background Shape

The background shape PDFs are dependent on the θ and ϕ detector coordinates. The background shapes in $\cos\theta_{\mathrm{Sun}}$ are not flat due to the geometry of the detector structure and a possible non-uniform distribution of background events. Prior to SK-IV, the effect

that varying background shape distributions have on solar neutrino signal extraction was determined by flattening the shape of the ϕ distribution. The background shapes in $\cos\theta_{\rm Sun}$ are then reformed, and the PDFs are remade. The background weights b_{ij} are consequently affected by this procedure. The difference in the total flux extracted using the modified and unmodified b_{ij} is $\pm 0.1\%$, which is taken as the systematic error from the uncertainty in the background shape.

Because the flat-ϕ method of determining the systematic uncertainty for the background shapes is not well motivated, two other studies have been performed to determine how the uncertainty in the background shapes affect the systematic uncertainty on the flux and energy spectrum. The impact that the correlations between the uncertainties in $\theta_{\rm Z}$ and ϕ have on the $\cos\theta_{\rm Sun}$ distribution is determined taking the 1σ uncertainties and propagating them through to the $\cos\theta_{\rm Sun}$ distribution. Fig. 8.6 shows the results of this method for the low MSG sample (MSG < 0.35) of the 3.49 - 3.99 MeV energy bin. This method is denoted by the red band and labeled as the "standard method." This bin has the poorest understood background shape. It was determined that the systematic error on the total flux by applying this method is $\pm 0.1\%$. This is the systematic uncertainty used in the SK-IV 1664-day solar analysis and the analysis presented in this work.

The second method is the "complete scramble method," which was incorporated into the solar analysis since the publication of the SK-IV 1664-day solar analysis. The standard definition of the $\cos\theta_{\rm Sun}$ distribution is $\sum_j r_j^{\rm rec} \cdot r_j^{\nu}$ over all events j. In the complete scramble method, all events within a given bin have their $r_j^{\rm rec}$ and r_j^{ν} scrambled:

$$\text{Complete Scramble Method:} \quad \frac{1}{N}\sum_{j}^{N}\sum_{k}^{N} r_j^{\rm rec} \cdot r_k^{\nu}. \tag{8.6}$$

Both j and k run over the full set of N events, and the distribution is normalized to the original number of events N. The dark black histogram in Fig. 8.6 shows the resulting

background shape from the scramble method. It was determined that the systematic error on the total flux from applying the scramble method is ∼0.2%.

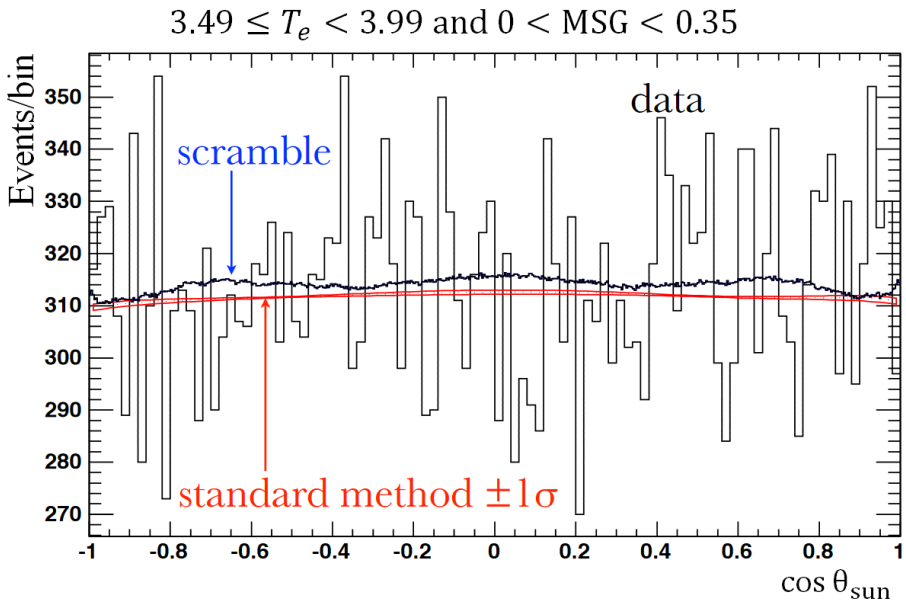

Figure 8.6: The $\cos\theta_{\mathrm{Sun}}$ distribution of data in the energy and MSG bin with the poorest understood background. The red outlined band corresponds to $\pm 1\sigma$ of the standard method, while the dark black histogram shows the shape from the scramble method. Plot courtesy of M. Smy.

8.2.8 Reduction Steps

In general, the systematic uncertainty due to the inefficiency of a reduction cut is determined with calibration data and MC by using the equation

$$\text{Systematic Uncertainty} = \frac{\epsilon_{\mathrm{Data}} - \epsilon_{\mathrm{MC}}}{\epsilon_{\mathrm{MC}}}, \quad \text{where} \quad \epsilon = \frac{\mathrm{A}}{\mathrm{B}}. \tag{8.7}$$

B (A) is the number of events before (after) a cut is applied for data and for MC.

Reconstruction Goodness and Event Quality Cut

The estimated uncertainty that the event quality cut (Sec. 7.4.6) gives to the total flux is determined using LINAC calibration data and corresponding MC. The event quality cut is based on the reconstruction goodness g_R^2 (Sec. 7.2). LINAC events must have: a reconstructed vertex <200 cm from the end of the beam pipe; reconstructed energy between 3.49 to 19.49 MeV; and a downward reconstructed direction. These events are counted (B) and then have the event quality cut criteria from the solar neutrino analysis applied. Events with $g_R^2 > 0.25$ are included and counted as part of A. These removed LINAC events correspond to equivalent recoil electron events in the solar analysis.

The systematic uncertainty of this cut can be determined from the cut inefficiency after comparing data and MC using Eq. 8.7. The systematic uncertainty from the inefficiency of the event quality cut is estimated at $\pm 0.1\%$ for the SK-IV 1664-day solar analysis.

Hit Pattern

The hit pattern cut (patlik) inefficiency is determined in the same manner as the event quality cut, but over a more restricted energy range: 5.99 to 19.49 MeV. Eq. 8.7 is used to estimate the inefficiency of the patlik cut, and the resulting systematic uncertainty in the total flux is estimated at $\pm 0.5\%$.

Small Hit Cluster

Using DT calibration data and associated MC, the systematic uncertainty of the small hit cluster cut can be estimated. The DT data is taken close to the walls and is used to create an event sample after applying the external event cut. By comparing this event sample to MC, the systematic uncertainty of the small hit cluster cut is estimated to be $\pm 0.4\%$.

Fiducial Volume and Vertex Shift

The vertex shift is discussed in Sec. 6.3.1, along with the method by which events are shifted. The effect on the elastic scattering rate is determined by artificially shifting the vertices of the solar neutrino MC events in specific ways. These shifts are based on the results of the nickel source calibration, near the boundaries of the fiducial volume, for each bin in the signal extraction. The number of events included by the fiducial volume cut are compared to the un-shifted number, and the resulting systematic effect on the total rate is ±2%. The energy dependence of the vertex shift systematic uncertainty is shown in Fig. 8.7, where the increase in the uncertainty below 4.99 MeV comes from the tight fiducial volume cut.

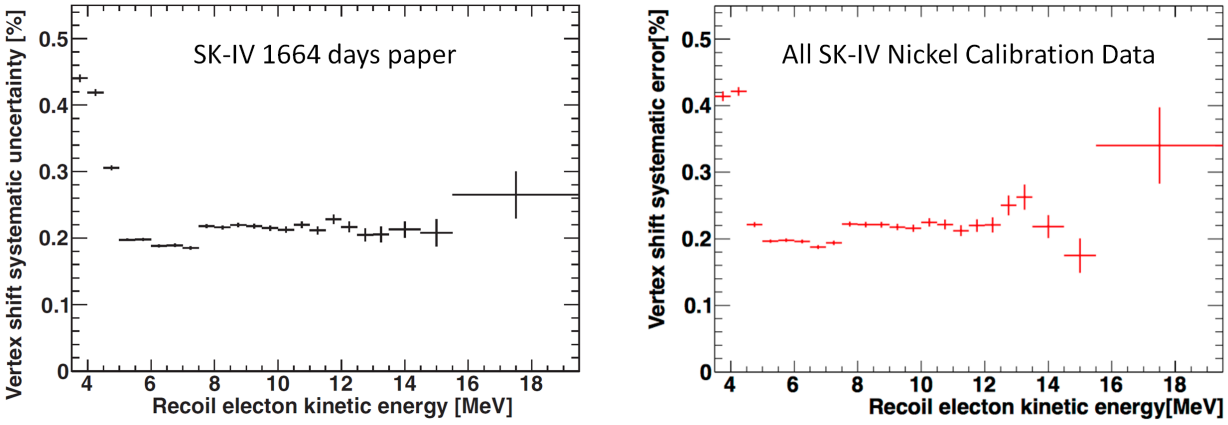

Figure 8.7: The energy dependence of the vertex shift systematic uncertainty from [42] (left) and for all of SK-IV (right).

External Event Cut

The external event cut (Sec. 7.4.10) depends on both the reconstructed vertex and direction of an event to calculate the cut parameter d_{eff} (and p_{wall}). To estimate the efficiency of this cut, the solar neutrino MC is modified by artificially shifting the reconstructed vertices and directions of the events. The vertices are shifted based on the vertex shift, and the direction is shifted based on the angular resolution. This procedure is illustrated on the left of Fig.

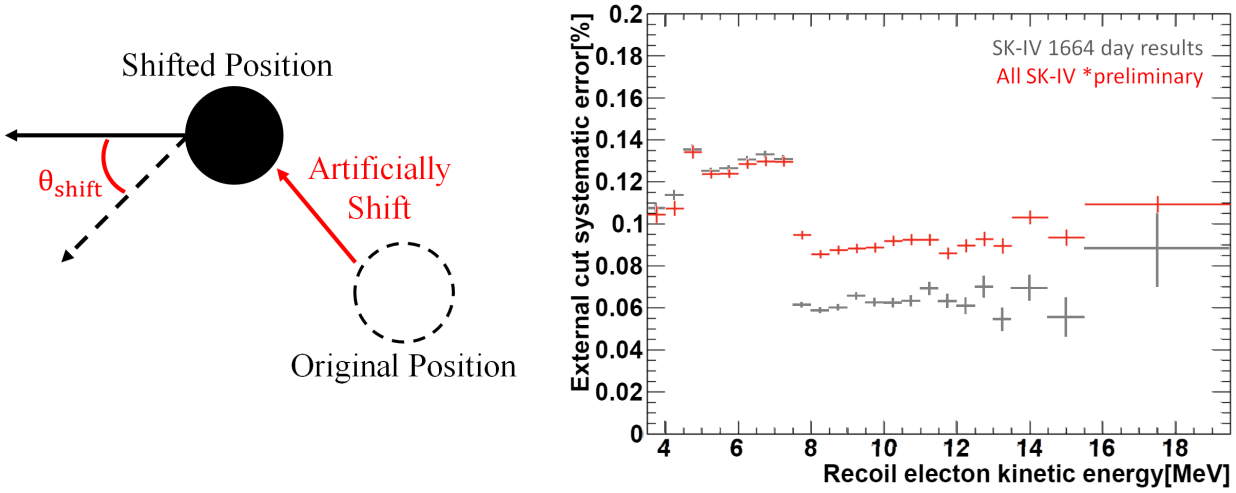

Figure 8.8: Left: The artificial shift of the reconstructed vertex and the definition of the resulting shift in the direction θ_{shift}. Right: the systematic uncertainty in the external event (γ-ray) cut. The shift in the uncertainty below 7.49 MeV is because of the differing criteria in that energy region outlined in Table 7.2. The dark gray data corresponds to the SK-IV 1664-day analysis and is published in [42] (courtesy Y. Nakano). The red data corresponds to preliminary results for the entire SK-IV data set (courtesy M. Hasegawa).

8.8. The efficiency of this cut for each energy bin is shown in the right of Fig. 8.8. The systematic uncertainty on the total flux caused by the external event cut is estimated at $\pm 0.1\%$.

Second Vertex Fit

Prior to SK-IV, a second vertex fitter (CLUSFIT) was employed to further remove ambient events. The fiducial volume cut was re-applied based on its vertex reconstruction. The estimated systematic uncertainty on the total flux from using the second fitter for SK-I, SK-II, and SK-III is $\pm 0.5\%$, $\pm 1.0\%$, and $\pm 0.5\%$ respectively.

Live time

The uncertainty in the live time calculation is caused by the event-rate-dependent timing accuracy of the main DAQ computer that receives the information from the front-end electronics [44]. The uncertainty on the total flux due to the live time calculation is estimated at $\pm 0.1\%$ for each SK-Phase, as well as for the uncertainty on the day-night asymmetry measurements.

Spallation Cut

The spallation cut is discussed in Sec. 7.4.7. It incurs a dead time, which is taken into account in the calculation of the expected number of solar neutrino events. The spallation-induced dead time for the MC is calculated by applying the position-dependent function $t_{\mathrm{total}}^{\mathrm{dead}}$ to the simulated events. The systematic uncertainty of the spallation cut is estimated by determining the difference between the dead time of the random sample and the MC simulated events. The stability of the dead time over the data period, shown in the lower right of Fig. 7.8, is used to estimate the systematic uncertainty of the cut on the total flux measurement: $\pm 0.2\%$.

8.2.9 Summary of the Systematic Uncertainty for the Total Flux

The systematic uncertainties for the total flux measurement by SK are summarized in Table 8.3. The SK-IV uncertainties for the 1664-day data period are given, and the full data period uncertainties are given in parentheses if they differ. After adding all uncertainties in quadrature, the total uncertainty in the flux measurement for SK-IV is $\pm 1.7\%$. The uncertainty of the energy scale dominates the systematic uncertainty of the total flux measurement.

Compared to the previous SK-Periods, SK-IV has the smallest uncertainty due to the

lower uncertainties from the energy scale and resolution. This improvement develops from the higher statistics below 4.49 MeV. By lowering the energy threshold and measuring a wider range of energy, the energy scale is better determined. The corresponding reduction in the uncertainty for the reconstructed energy of the recoil electron spectra lowers the systematic uncertainty in the flux and energy spectrum analysis.

The live time for the energy bins is the same across SK-IV, where as previous phases have smaller live times below 5.99 MeV. For SK-III, the live time below 5.99 MeV is approximately half of the full data period. For SK-IV, further reductions in the uncertainties are from a better understanding and control over the vertex shift, the trigger efficiency, and the angular resolution. The removal of the second vertex fit also makes the total systematic uncertainty lower in SK-IV.

Differences in the systematic uncertainties for SK-IV, between the 1664-day analysis and the (preliminary) full SK-IV data, primarily originate from the lowering of the SLE trigger threshold from 34 hits to 31 hits within 200 ns and the associated changes in the pre-reduction to deal with the increased noise rate. More calibration and statistics for the full SK-IV period also contribute. MSG was applied to the total flux after the 1664-day analysis for SK-II, SK-III, and SK-IV, and it introduced an additional 0.4% systematic uncertainty to the total flux, though the total error is not impacted.

8.3 Results of the Total Flux Measurement by SK

Using the extended maximum likelihood method for events from 3.49 MeV to 19.49 MeV, the number of solar neutrino events extracted (N_ν) from the SK-IV 1664-day solar neutrino data sample (right side of Fig. 8.1) is $31{,}891^{+283}_{-281}$(stat)$\pm$543(syst.). This is the largest number of solar neutrinos extracted from any SK-Phase. The data is denoted by the points with

Table 8.3: List of the systematic errors (in percent) on the total flux measurement for each phase of SK [42]. The threshold corresponds to the recoil electron kinetic energy. The SK-IV values are for the 1664-day solar sample. The SK-IV values in parentheses are preliminary uncertainties if there has been a change.

Uncertainty	SK-I	SK-II	SK-III	SK-IV 1664 days (all)
Threshold [MeV]	4.49	6.49	3.99	3.49
Trigger efficiency	0.4	0.5	0.5	0.1
Angular resolution	1.2	3.0	0.7	0.1
Reconstruction goodness (g_R^2)	$^{+1.9}_{-1.3}$	3.0	0.4	0.1
Hit pattern (patlik)	0.8	...	0.3	0.5
Small hit cluster	...	...	0.5	$^{+0.5}_{-0.4}$ (0.4)
External event (γ-ray) cut	0.5	1.0	0.3	0.1
Vertex shift	1.3	1.1	0.5	0.2
Second vertex fit	0.5	1.0	0.5	...
Background shape	0.1	0.4	0.1	0.1
Live time	0.1	0.1	0.1	0.1
Spallation cut	0.2	0.4	0.2	0.2
Signal extraction	0.7	0.7	0.7	0.7
Cross section	0.5	0.5	0.5	0.5
Energy scale	1.6	$^{+4.2}_{-3.9}$	1.2	$^{+1.1}_{-1.2}$ (1.0)
Energy resolution	0.3	0.3	0.2	$^{+0.3}_{-0.2}$ (0.1)
^{8}B spectrum	$^{+1.1}_{-1.0}$	1.9	$^{+0.3}_{-0.4}$	$^{+0.4}_{-0.3}$
Total	$^{+3.5}_{-3.2}$	$^{+6.7}_{-6.4}$	2.2	1.7 (1.6)

errors, and the best fit to the background (signal plus background) is given by the light gray (dark gray) region. While the live time of the SK-IV 1664-day analysis is only ∼11% longer than the live time of SK-I, the number of solar neutrinos extracted per day is much larger: ∼19.2 events per day for SK-IV compared to ∼15.0 events per day in SK-I, an increase of ∼28.0%. The higher event rate is due to the lowering of the detector threshold, relaxing the patlik cut, and the removal of the second vertex fit. The improvement in understanding the systematic uncertainties leads to smaller uncertainties in the signal extraction. The large number of events combined with the smaller errors also makes SK-IV the most precise data set of each SK-Phase.

Including the complete SK-IV data set, which includes the lower SLE threshold, the

total number of extracted solar neutrino events per day in SK-IV is ∼19.4, and the number of extracted solar neutrinos is $55{,}729^{+363}_{-361}$(stat)±543(syst.). Across all phases of the SK experiment, the total number of signal events extracted is $93{,}745^{+878.9}_{-872.9}$(stat) $^{+1986.3}_{-1879.6}$(syst.). These extracted events are predominantly ^{8}B neutrinos with a small amount of *hep* neutrinos. This is the largest data set of ^{8}B and *hep* solar neutrinos in the world. For comparison, Borexino extracts ∼0.5 ^{8}B neutrinos per day in their HER analysis [83]. The average solar neutrino extraction rate for SNO is ∼9.3 events per day, which includes NC, CC, and ES events [72][73][76][47].

The number of extracted events N_ν can be converted into a measurement of the absolute flux by comparing to the expected number of solar neutrino interactions in the SK fiducial volume $N_{\rm exp}$. $N_{\rm exp}$ can be determined by applying the total cut efficiency $\epsilon_{\rm cut}$ and live time $T_{\rm live}$ to the expected rate $R_{\rm exp}$ for SK, given Eq. 2.66:

$$N_{\rm exp} = R_{\rm exp} \times T_{\rm live} \times \epsilon_{\rm cut}, \tag{8.8}$$

where $T_{live} = 1663.91$ days for the SK-IV 1664-day data set. The total cut efficiency $\epsilon_{\rm cut} = 0.14983$ is given by the ratio of the number of solar neutrino MC events passing all solar analysis cuts divided by the total MC events generated.

Using the BP2004 SSM flux $\Phi^{^8{\rm B}} = 5.79 \pm 1.33 \times 10^6/({\rm cm}^2\ {\rm s})$ [46], the expected event rate is 326.1 events/day/kton [44]. However, for generating the SK-IV solar neutrino MC, the expected event rate was changed to correspond to the SNO NC measurement of the ^{8}B flux $\Phi_{^8{\rm B}}^{\rm SNO\ NC} = 5.25 \times 10^6/({\rm cm}^2\ {\rm s})$ [76]. The total expected rate in the SK ID fiducial volume is $R_{\rm exp} = 295.4$ events/day/32.5 kton, with ^{8}B (*hep*) neutrinos contributing a rate of 294.73 (0.64) events/day/32.5 kton. The total rate assumes 1.086×10^{34} electrons in the 32.5 kton fiducial volume, and it uses the Winter06 ^{8}B neutrino spectrum [45]. The *hep* rate assumes the BP2004 flux of $\Phi^{hep} = 7.88 \pm 1.26 \times 10^3/({\rm cm}^2\ {\rm s})$.

The number of expected events in SK for the 1664-day data set is $N_{\rm exp}$ = 73,636 events (assuming no neutrino oscillations). Dividing the number of extracted events (Table 8.4) by $N_{\rm exp}$ gives 0.433. This corresponds to a pure ν_e ^{8}B solar neutrino flux of $\Phi_{^8\rm B} = (2.308 \pm 0.020({\rm stat})^{+0.039}_{-0.040}({\rm syst})) \times 10^6/({\rm cm}^2\ {\rm s})$ [42]. The flux measurement is the most precise for SK, relative to the other phases, as shown in the right side of Fig 8.9. The figure also shows that the total flux measured in each phase of SK is consistent within 1σ of the combined SK total flux (black dashed line). The total uncertainty on the combination of the SK phases (red lines) assumes no correlations between phases except for the uncertainty on the ^{8}B neutrino spectrum.

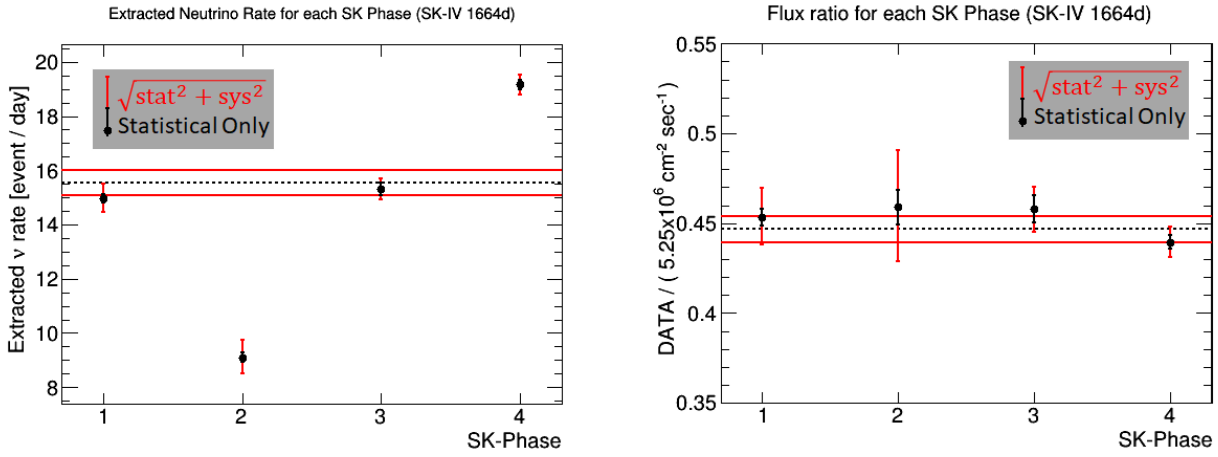

Figure 8.9: Left: The comparison of number of extracted solar neutrino events divided by the live time for each phase. Right: The comparison of the solar neutrino fluxes for each phase. The y-axis is the ratio of the observed flux divided by the expected flux from the MC assuming no oscillations and a total ^{8}B flux of $5.25 \times 10^6/{\rm cm}^2/{\rm s}$. The unit of the y-axis is Data/MC (unoscillated).

The result of the total flux measurement, assuming a pure ν_e flavor content, is given for all SK-Phases in Table 8.4, along with the number of solar neutrino signal events extracted. The live time and the lowest energy threshold for each SK-Phase is given as well. The gain correction is applied for the full SK-IV preliminary results, but not for the SK-IV 1664-day results since the gain was stable up to that time. The preliminary total flux measurement for the full SK-IV period (and corresponding SK combined total flux) uses the systematic

Table 8.4: Super-Kamiokande results from the Solar Neutrino Analysis for each experimental phase [42] and the preliminary results including all of SK-IV at the bottom. The total live time for each phase, the energy averaged ^{8}B flux assuming a pure ν_e flavor content and corresponding number of extracted signal events from the recoil electron data are given. The T_e energy threshold for each SK-Phase is given in the third column.

Solar Neutrino Total Flux & Signal Events

SK Phase	Live Time [days]	Threshold T_e [MeV]	$\Phi^{\mathrm{ES}}_{^8\mathrm{B}}\pm(\mathrm{stat})\pm(\mathrm{sys})$ $\times 10^6[\mathrm{cm}^2\mathrm{s}^{-1}]$	# Signal Events $N_{\mathrm{sig}}\pm(\mathrm{stat})\pm(\mathrm{sys})$
SK-I	1496.12	4.49	$2.380 \pm 0.024^{+0.084}_{-0.076}$	$22,404 \pm 226^{+784}_{-717}$
SK-II	791.79	6.49	$2.41 \pm 0.05^{+0.16}_{-0.15}$	$7212^{+152.9+483.3}_{-150.9-461.6}$
SK-III	548.53	3.99	$2.404 \pm 0.039 \pm 0.053$	$8400^{+137}_{-135} \pm 176$
SK-IV(1664d)	1663.91	3.49	$2.308 \pm 0.020^{+0.039}_{-0.040}$	$31,891^{+283}_{-281} \pm 543$
Combined	4500.34	$--$	$2.345 \pm 0.014^{+0.039}_{-0.040}$	$69,907^{+798.9+1986.3}_{-792.9-1879.6}$
SK-IV	2859.70	3.49	$2.289 \pm 0.015 \pm 0.036$	$55,729^{+363}_{-361} \pm 543$
Combined	5696.14	$--$	$2.330 \pm 0.013 \pm 0.036$	$93,745^{+878.9+1986.3}_{-872.9-1879.6}$

uncertainties from the SK-IV 1664-day result.

8.4 Day, Night, and Zenith Flux Measurements

The exposure of the SK detector (live time) to a given zenith direction is well understood. Since the location of the Sun relative to SK at any given time is well known, it is known what path the solar neutrino takes. The zenith angle θ_{Z} is displayed in the diagram on the left side of Fig. 8.1, with $\cos\theta_{\mathrm{Z}} \leq 0$ corresponding to the "Day" (D) time sample and $\cos\theta_{\mathrm{Z}} > 0$ corresponding to the "Night" (N) time sample. The "All" sample is the total flux results, as it contains both the Day and Night samples, i.e. it encompasses $\cos\theta_{\mathrm{Z}} \in [-1, 1]$. While the total flux analysis has a lower threshold of 3.49 MeV for SK-IV, the SK-IV zenith (and day-night asymmetry) analysis maintains a threshold of 4.49 MeV. The slightly higer threshold is due to concerns about systematic uncertainties from the background shape of the lower energies. An effort is currently underway to include data below 4.49 MeV in this

part of the solar neutrino analysis.

To extract the solar neutrino signal for the Day sample and the Night sample, the $Y_{i\mathrm{D,N}}$ are created independently of each other for each bin i. The signal shape PDFs from the total flux extraction are used to extract the Day and Night solar neutrino signals. The shape of the expected signal does not vary enough to discern between the two samples. The background shapes are correlated through the zenith binning, and are treated as such during the signal extraction. The total number of signal events extracted for the Day bin is $13{,}924.2^{+183.0}_{-181.2}$(stat.), and the total number of signal events extracted for the Night bin is $15{,}764.9^{+192.8}_{-181.2}$(stat.).

The $\cos\theta_{\mathrm{Sun}}$ distributions for solar neutrino recoil electron candidates for the Day (red) and Night (blue) samples are plotted in Fig. 8.10 for recoil electrons with kinetic energy greater than 4.49 MeV. This is the energy threshold for the SK-IV day-night asymmetry analysis. An event display of a solar neutrino candidate recoil electron event is given in Fig. 8.12. This event is very low energy and has traveled through the Earth. There is a very high likelihood this is an actual solar neutrino, as very stringent cuts were applied, including large MSG, large $\cos\theta_{\mathrm{Sun}}$, and very good event reconstruction quality. While this event is currently excluded from the zenith-dependent solar analyses, it is included in the total flux and in the spectral analysis (Ch. 9).

When solar neutrinos travel through the Earth, the effects of the matter potential on the neutrino wavefunction regenerate solar neutrinos into the electron flavor eigenstate. This regeneration causes an increase in the solar neutrino rate detected during the night. SK has three measurements of the zenith dependence on the rate. The first is the asymmetry in the day and night rate (or flux) A_{DN}, and the second is a binned zenith distribution (later sub-divided by energy and MSG in Sec. 9.3.1). The third measurement, the day-night amplitude-fit method, is described in [96]. The details of the day-night amplitude-fit measurement are beyond the scope of the analysis presented in this work and will not be

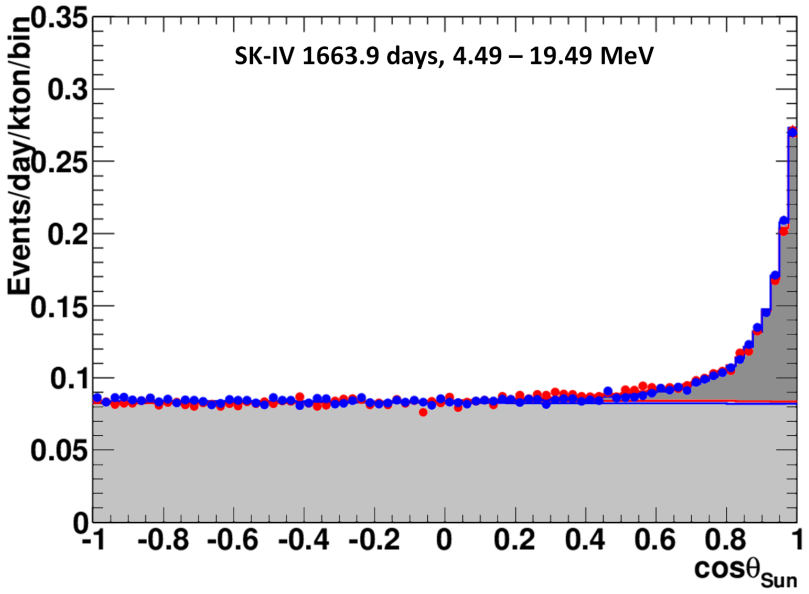

Figure 8.10: The Day and Night $\cos\theta_{\rm Sun}$ distributions for solar neutrino recoil electron candidates with energy $T_e \geq 4.49$ MeV. The Day (Night) information is color-coded in red (blue). The best fit to the background (signal plus background) is given in light (dark) gray.

discussed.

8.4.1 Day-Night Asymmetry A_{DN}

The asymmetry between the day and night flux (or event rate) is termed the "day-night asymmetry," denoted by A_{DN}. It is a useful way to measure the size of the effect that matter in the Earth has on solar neutrino oscillations. The day-night asymmetry is defined for the rate in Eq. 3.19, and is similarly defined for the flux:

$$A_{\rm DN} = \frac{\Phi_D - \Phi_N}{\frac{1}{2}(\Phi_D + \Phi_N)}. \tag{8.9}$$

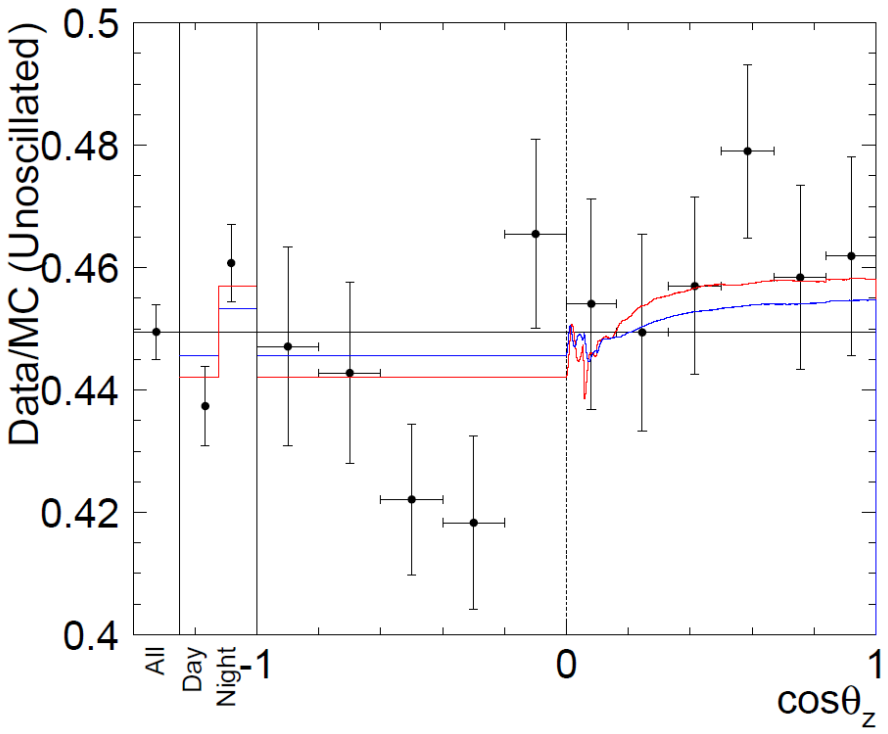

Figure 8.11: The zenith angle dependence of the SK-IV 1664-day solar neutrino interaction rate ratio [42]. The y-axis is the number of events from data divided by the expected number of MC events assuming no oscillations, with an assumed ^{8}B (*hep*) flux of $5.25\times10^6/(\mathrm{cm}^2\ \mathrm{s})$ ($8\times10^3/(\mathrm{cm}^2\ \mathrm{s})$). The errors are statistical only. The day data is equally divided into 5 sub-bins. The night data is divided into five mantle bins and a single core bin. The red (blue) line corresponds to the predicted results of one day bin and 1000 night bins, from the best fit oscillation parameters using all solar (solar + KamLAND) data.

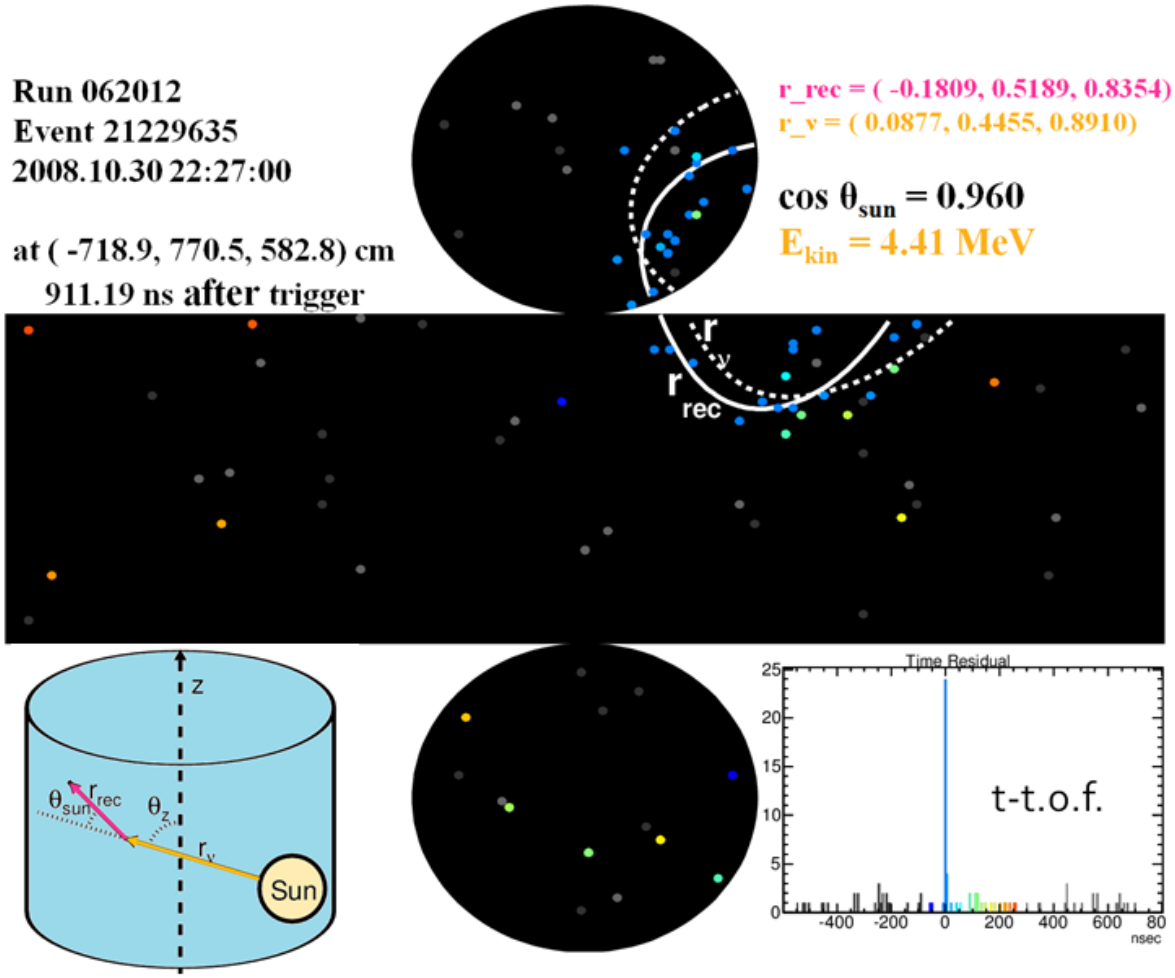

Figure 8.12: An event display for a solar neutrino candidate event. This event is very low energy and has traveled through the Earth. There is a very high likelihood this is an actual solar neutrino, as very stringent cuts were applied, including large MSG, large $\cos\theta_{\rm Sun}$, and very good event reconstruction quality.

The day and night live time for the 1664-day solar analysis day-night asymmetry is 797.43 and 866.48 days respectively, and the measured flux above 4.49 MeV is

$$\begin{aligned} \Phi_D &= (2.250^{+0.030}_{-0.029}(\text{stat.}) \pm 0.038(\text{syst.})) \times 10^6/(\text{cm}^2\ \text{s}), \\ \Phi_N &= (2.364 \pm 0.029(\text{stat.}) \pm 0.040(\text{syst.})) \times 10^6/(\text{cm}^2\ \text{s}). \end{aligned} \tag{8.10}$$

The percent day-night asymmetry in the flux is then

$$A_{DN} = -4.9 \pm 1.8(\text{stat.}) \pm 1.4(\text{syst.})\%. \tag{8.11}$$

The combined asymmetry for each phase is $A_{DN} = -4.1 \pm 1.2 \pm 0.8\%$, but this ignores any correlations between phases. The combined SK day-night asymmetry gives significance of 2.84σ from no day-night effect ($A_{DN} = 0$). The day-night asymmetry results for each SK-Phase and the combined result are given in Table 3.9, along with the day and night live times and the analysis threshold for each phase.

Day-Night Asymmetry Systematic Errors

The primary systematic uncertainties in the day-night asymmetry come from the energy scale, the energy resolution, and the non-flat background shape of the $\cos\theta_{\text{Sun}}$ distribution. Systematic effects in the reconstruction of N_{eff}, and the reconstructed vertex and direction, differ for upward-going and downward-going events. These effects are caused from differences in the detector response as a function of the zenith angle. Also, there is an additional effect from the top-bottom asymmetry. The effect on N_{eff} as a function of $\cos\theta_{\text{Z}}$ can be seen in Fig. 5.25.

The background shape should vary more slowly than variations in A_{DN}, but the different zenith bins need to use different background shape distributions. This is because directional biases from event reconstruction enter into the distributions, since the direction

fitter prefers directions along and perpendicular to the detector symmetry axis [42].

Using the A_{DN} from SK-I as an example, the day-night asymmetry in fractional form is $-0.021 \pm 0.020(\text{stat.}) \pm 0.013(\text{syst.})$. The energy scale and resolution contribute ± 0.012 to the systematic uncertainty while the non-flat background contributes ± 0.004 [44]. Improvements between the SK-I and SK-IV systematic error primarily come from the improvements in the understanding of the absolute energy scale, since the systematic uncertainties from the energy resolution and the background shape are similar for SK-I and SK-IV.

8.4.2 Zenith Flux Measurements

Beyond the Day and Night binned samples, the Night solar sample can be further separated in zenith binning. For the Day bin, it is considered singly, as any matter effect on solar neutrino oscillation due to the atmosphere is negligible. However, it is sometimes divided into five equal sub-bins in $\cos\theta_{\text{Z}}$ (Fig 8.11). This division of the Day bins is performed to check for systematic effects in the Night bins with similar exposure time of the Sun. The Night sub-binning, on the other hand, corresponds to differing matter densities in the Earth and is divided into five "Mantle" bins (M1 - M5) and a single "Core" bin. The boundaries in $\cos\theta_{\text{Z}}$ that define the mantle bins are $\cos\theta_{\text{Z}} = 0$, 0.16, 0.33, 0.5, 0.67, and 0.84. Zenith directions with $\cos\theta_{\text{Z}} \geq 0.84$ are considered to be part of the core bin. The Mantle and Core bins are illustrated in Fig. 8.13. Because the latitude of SK is too far from the equator, solar neutrinos arriving in SK only pass through the outer core of the Earth and not the inner core. The ecliptic plane and the Sun are given as a cartoon in the figure to demonstrate this lack of sensitivity to the inner core.

The zenith sub-divisions of the Night bin have their own correlated background shapes, but have independent $Y_{i\text{Z}}$. They use the same signal shapes as the Day and Night bins. Fig. 8.11 shows the breakdown of the SK-IV 1664-day data set (in the ratio of data to

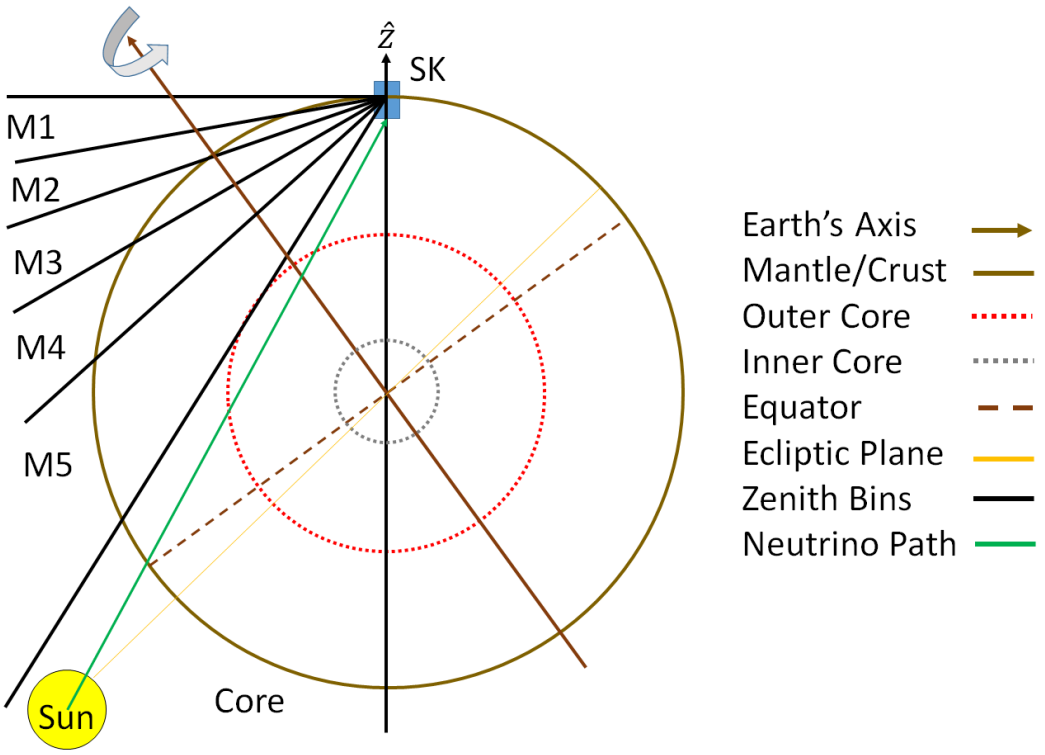

Figure 8.13: Illustration of the Night zenith bins (M1 - M5) and the Core bin. The Sun is included to illustrate SK's lack of sensitivity to the inner core. The ecliptic plane is denoted by the orange line and the neutrino path by the green ray.

unoscillated solar neutrino MC interaction rate) as a function of the zenith direction. Fig. 8.14 shows the similar zenith angle dependence of the flux for SK-I/II/III, assuming a ^{8}B flux of $5.25 \times 10^6/(\mathrm{cm}^2\ \mathrm{s})$.

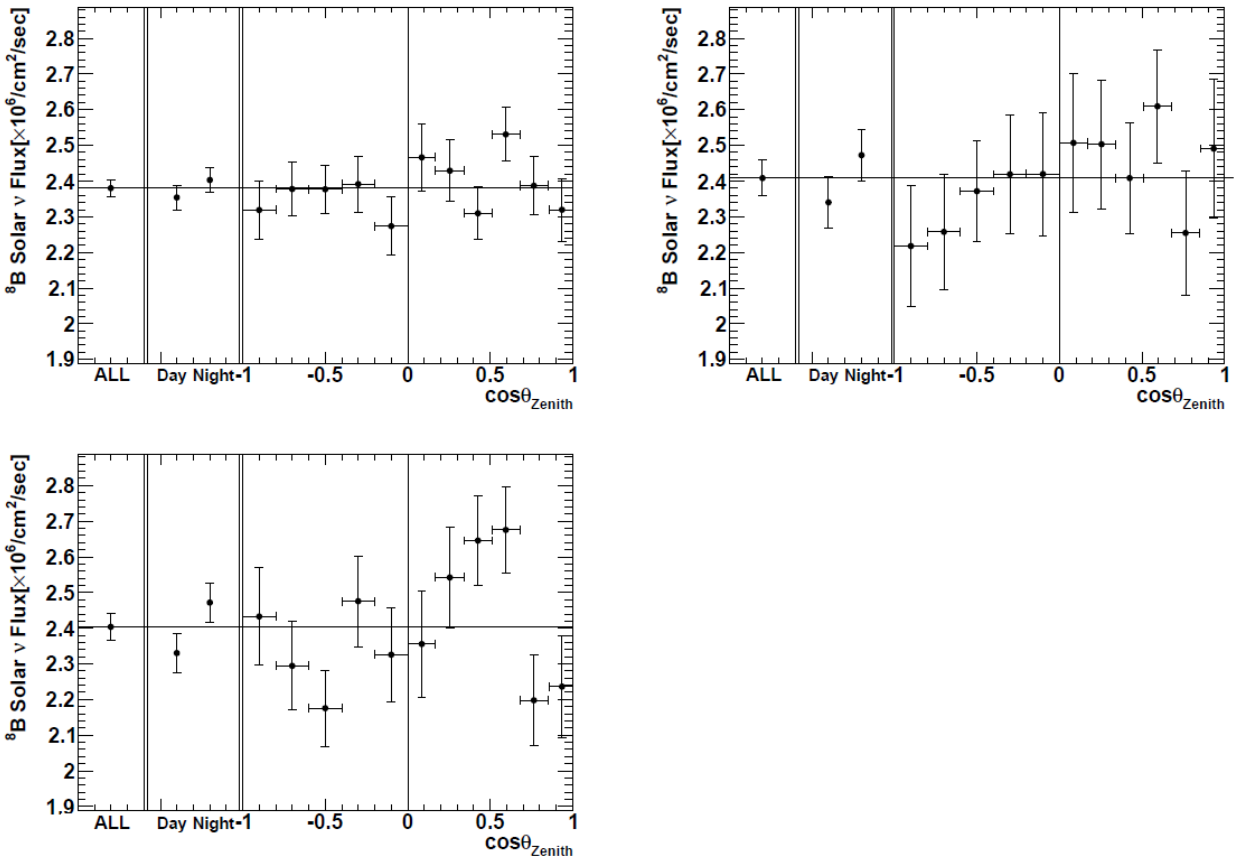

Figure 8.14: The zenith angle dependence of the SK-I (top left), SK-II (top right), and SK-III (bottom left) flux determined from the neutrino interaction rate ratio, data/MC(unoscillated), assuming a ^{8}B flux of $5.25 \times 10^6/(\mathrm{cm}^2\ \mathrm{s})$ [48].

Chapter 9

The Solar Neutrino Spectrum Analysis

The signal extraction method for the neutrino spectrum uses a modified version of the method used in the total flux analysis. The extended maximum likelihood fit (Eq. 8.1) is described in Sec 8.1. Above 7.49 MeV, the likelihood is fit only to a single bin at a time while holding the $Y_i = 1$. This extracts the signal and background events independently of constraints on the spectrum shape. The energy bins below 7.49 MeV are divided up into three MSG sub-samples with boundaries at MSG values of 0.35 and 0.45. Below 7.49 MeV, the index i will denote energy-MSG sub-bins. Since MSG is not used above 7.49 MeV, i will denote energy bins only.

9.1 MSG in the Signal Extraction

For the energy-MSG sub-bins, the background shape PDFs, signal shape PDFs, and Y_i factors are defined independently for each sub-bin. Each of the background shapes for the

sub-samples are derived from fitting to the corresponding background distributions in the final solar data sample. The sub-sample Y_i factors and signal shape PDFs are determined from the solar neutrino MC in the same way as in the flux analysis. For a given energy bin, the three MSG sub-bins are simultaneously fit for three background B_is and a single signal S.

By dividing these lower energy bins into the three MSG samples, background-like events preferentially fall into the lowest MSG bin. Signal-like events are evenly divided among the three MSG bins. This creates a distinction in the signal-to-background ratio in each MSG bin and leads to better signal extraction from the highest MSG bin. This causes the statistical precision of the number of signal events extracted to increase by up to 10% in the energy bins below 7.5 MeV [42]. By looking at the results in the lowest energy ranges (Fig. 9.2), the solar peak is more pronounced in the highest MSG bin.

9.2 Systematic Uncertainties for the Solar Neutrino Spectrum

The energy-uncorrelated systematic uncertainties for each energy bin are determined using the same methods as in the total flux analysis (Sec. 8.2). The additional systematic uncertainty from including MSG in the signal extraction is treated as energy-uncorrelated and will be discussed shortly. When listing the uncertainties for the energy spectrum, the results from the SK-IV 1664-day solar neutrino analysis are used. The total energy-uncorrelated systematic uncertainty for each energy is provided in Table 9.1. They are determined by adding the components of the systematic uncertainty from each source in quadrature. The systematic uncertainties above 7.49 MeV are the same value for each energy bin, and the final column is simply a contraction to save space.

9.2.1 Systematic Uncertainty from Multiple Scattering Goodness

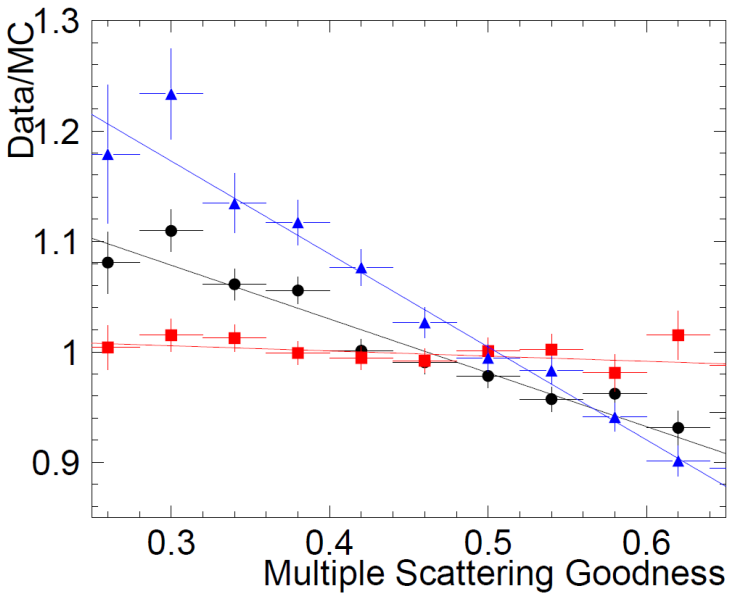

Figure 9.1: The linear scaling functions used in LINAC MC to estimate the systematic uncertainty from MSG on the solar neutrino energy spectrum [48]. The lines are linear fits to the LINAC data divided by MC data points. The red, black, and blue coloring correspond to 4.89, 8.67, and 16.1 MeV (in-tank energy) LINAC events respectively.

Using LINAC data and MC, the systematic uncertainty on the energy spectrum can be estimated by adjusting the MSG distributions in each energy-MSG sub-bin of the solar neutrino MC. The ratio between LINAC data and MC is formed as a function of MSG for various energies, and linear scaling functions are fit to these distributions. The results of this process are plotted in Fig. 9.1. After adjusting the solar neutrino MC with the linear scaling functions, the new signal shapes and signal event expectations Y_i are re-calculated for all sub-samples. The $\cos\theta_{\mathrm{Sun}}$ distributions are then refit with these new inputs. The change in the number of extracted solar neutrino events is taken as the systematic uncertainty due to MSG.

Table 9.1: List of the energy-uncorrelated systematic uncertainties [%] on the spectrum shape measurement for SK-IV [42]. The energy corresponds to the recoil electron kinetic energy in MeV. The SK-IV values are for the 1664-day solar sample. Above 7.49 MeV, the table is contracted as the uncertainties are the same in each energy bin.

Energy [MeV]	3.49-3.99	3.99-4.49	4.49-4.99	4.99-5.49	5.49-5.99	5.99-6.49	6.49-6.99	6.99-7.49	7.49-19.5
Trigger Efficiency	$^{+3.6}_{-3.3}$	±0.8	-	-	-	-	-	-	-
Rec. Goodness (g^2_R)	±0.6	±0.7	$^{+0.6}_{-0.5}$	±0.4	±0.2	±0.1	±0.1	±0.1	±0.1
Hit Pattern	-	-	-	-	-	±0.6	±0.6	±0.6	±0.4
External Event Cut	±0.1	±0.1	±0.1	±0.1	±0.1	±0.1	±0.1	±0.1	±0.1
Vertex Shift	±0.4	±0.4	±0.2	±0.2	±0.2	±0.2	±0.2	±0.2	±0.2
Background Shape	±2.9	±1.0	±0.8	±0.2	±0.1	±0.1	±0.1	±0.1	±0.1
Signal Extraction	±2.1	±2.1	±2.1	±0.7	±0.7	±0.7	±0.7	±0.7	±0.7
Cross Section	±0.2	±0.2	±0.2	±0.2	±0.2	±0.2	±0.2	±0.2	±0.2
MSG	±0.4	±0.4	±0.3	±0.3	±0.3	±1.7	±1.7	±1.7	-
Total	$^{+5.1}_{-4.9}$	±2.6	$^{+2.4}_{-2.3}$	±0.9	±0.9	±2.0	$^{+2.0}_{-1.9}$	±1.9	$^{+0.9}_{-0.8}$

9.3 Results of the Solar Neutrino Spectrum Analysis

The SK-IV 1664-day solar neutrino analysis result is given here in terms of the $\cos\theta_{\rm Sun}$ distributions for each bin i. The energy-MSG sub-bin is displayed for $T_e < 7.49$ MeV. Fig. 9.2 contains the $\cos\theta_{\rm Sun}$ distributions for each energy-MSG sub-bin from the 3.49 - 3.99 MeV bin to the 4.99 - 5.49 MeV bin (in descending order). The left-to-right columns correspond to the MSG ranges: MSG $\in$ [0.00,0.35), MSG $\in$ [0.35,0.45), and MSG $\in$ [0.45, 1.00]. Fig. 9.3 contains the energy-MSG sub-bins from the 5.49 - 5.99 MeV bin to the 6.99 - 7.49 MeV bin (in descending order), with the columns corresponding to the three MSG ranges mentioned for the previous figure. The $\cos\theta_{\rm Sun}$ distributions for the energy bins above $T_e = 7.49$ MeV, where MSG is not applied, are displayed in Fig. 9.4, with energy increasing from left-to-right, top-to-bottom.

The energy-dependent measurements of the solar neutrino recoil electron spectrum for each SK-Phase are given in Table 9.2 and plotted in Fig. 9.5. These measurements are

Table 9.2: The solar neutrino recoil electron spectra from the SK-I, SK-II, SK-III, and SK-IV 1664-day solar analyses in the ratio of the extracted number of events to the predicted unoscillated number of events. The uncertainty is statistical plus energy-uncorrelated systematic errors added in quadrature.

T_e Bin [MeV]	SK-I	SK-II	SK-III	SK-IV (1664 days)
3.49-3.99	–	–	–	$0.4596^{+0.0596}_{-0.0582}$
3.99-4.49	–	–	$0.4476^{+0.1002}_{-0.0962}$	$0.4151^{+0.0304}_{-0.0297}$
4.49-4.99	$0.4529^{+0.0430}_{-0.0416}$	–	$0.4715^{+0.0579}_{-0.0557}$	$0.4894^{+0.0235}_{-0.0230}$
4.99-5.49	$0.4297^{+0.0229}_{-0.0225}$	–	$0.4200^{+0.0388}_{-0.0373}$	$0.4515^{+0.0145}_{-0.0143}$
5.49-5.99	$0.4491^{+0.0184}_{-0.0180}$	–	$0.4569^{+0.0350}_{-0.0335}$	$0.4307^{+0.0120}_{-0.0118}$
5.99-6.49	$0.4436^{+0.0154}_{-0.0151}$	–	$0.4327^{+0.0231}_{-0.0224}$	$0.4423^{+0.0147}_{-0.0146}$
6.49-6.99	$0.4606^{+0.0157}_{-0.0154}$	$0.4386^{+0.0498}_{-0.0477}$	$0.5037^{+0.0248}_{-0.0241}$	$0.4456^{+0.0151}_{-0.0149}$
6.99-7.49	$0.4758^{+0.0163}_{-0.0160}$	$0.4476^{+0.0430}_{-0.0411}$	$0.4244^{+0.0237}_{-0.0229}$	$0.4394^{+0.0154}_{-0.0152}$
7.49-7.99	$0.4567^{+0.0166}_{-0.0162}$	$0.4609^{+0.0372}_{-0.0356}$	$0.4673^{+0.0243}_{-0.0234}$	$0.4544^{+0.0140}_{-0.0137}$
7.99-8.49	$0.4306^{+0.0168}_{-0.0164}$	$0.4729^{+0.0364}_{-0.0348}$	$0.4686^{+0.0258}_{-0.0247}$	$0.4387^{+0.0145}_{-0.0142}$
8.49-8.99	$0.4536^{+0.0180}_{-0.0175}$	$0.4633^{+0.0356}_{-0.0340}$	$0.4200^{+0.0264}_{-0.0250}$	$0.4433^{+0.0154}_{-0.0150}$
8.99-9.49	$0.4635^{+0.0193}_{-0.0187}$	$0.4987^{+0.0384}_{-0.0365}$	$0.4443^{+0.0289}_{-0.0274}$	$0.4306^{+0.0164}_{-0.0158}$
9.49-9.99	$0.4561^{+0.0206}_{-0.0199}$	$0.4742^{+0.0385}_{-0.0364}$	$0.4234^{+0.0307}_{-0.0287}$	$0.4248^{+0.0178}_{-0.0171}$
9.99-10.49	$0.4087^{+0.0214}_{-0.0206}$	$0.4811^{+0.0414}_{-0.0392}$	$0.5294^{+0.0374}_{-0.0349}$	$0.4060^{+0.0192}_{-0.0183}$
10.49-10.99	$0.4718^{+0.0255}_{-0.0243}$	$0.4525^{+0.0425}_{-0.0399}$	$0.4810^{+0.0407}_{-0.0373}$	$0.4305^{+0.0224}_{-0.0214}$
10.99-11.49	$0.4387^{+0.0280}_{-0.0264}$	$0.4693^{+0.0457}_{-0.0426}$	$0.3912^{+0.0444}_{-0.0398}$	$0.4585^{+0.0260}_{-0.0246}$
11.49-11.99	$0.4603^{+0.0330}_{-0.0307}$	$0.4824^{+0.0521}_{-0.0483}$	$0.4785^{+0.0553}_{-0.0493}$	$0.4207^{+0.0289}_{-0.0270}$
11.99-12.49	$0.4654^{+0.0393}_{-0.0361}$	$0.4194^{+0.0537}_{-0.0489}$	$0.4245^{+0.0611}_{-0.0527}$	$0.4223^{+0.0346}_{-0.0318}$
12.49-12.99	$0.4606^{+0.0477}_{-0.0431}$	$0.4617^{+0.0632}_{-0.0567}$	$0.4003^{+0.0733}_{-0.0611}$	$0.4454^{+0.0428}_{-0.0388}$
12.99-13.49	$0.5819^{+0.0640}_{-0.0571}$	$0.4437^{+0.0703}_{-0.0616}$	$0.4223^{+0.0930}_{-0.0744}$	$0.4618^{+0.0547}_{-0.0485}$
13.49-14.49	$0.4747^{+0.0593}_{-0.0524}$	$0.4303^{+0.0658}_{-0.0586}$	$0.6630^{+0.1101}_{-0.0926}$	$0.4857^{+0.0541}_{-0.0481}$
14.49-15.49	$0.7236^{+0.1203}_{-0.1015}$	$0.5625^{+0.1003}_{-0.0867}$	$0.7134^{+0.2007}_{-0.1503}$	$0.4113^{+0.0891}_{-0.0727}$
15.49-19.49	$0.5747^{+0.1731}_{-0.1304}$	$0.6477^{+0.1226}_{-0.1035}$	$0.2124^{+0.2477}_{-0.1215}$	$0.3447^{+0.1416}_{-0.1010}$

described in terms of data divided by the expected unoscillated rate from SSM predictions. The ratio of the measured rate over unoscillated rate is simply referred to as the "rate ratios" ($d^P_{i,\mathrm{Z}}$). The indices correspond to the SK-Phase P, the energy bin i, and the zenith bin Z (if broken down by zenith bin). Details on the SSM predictions are discussed in Sec. 10.1, with the definition of the rate ratios given in Sec. 10.1.3.

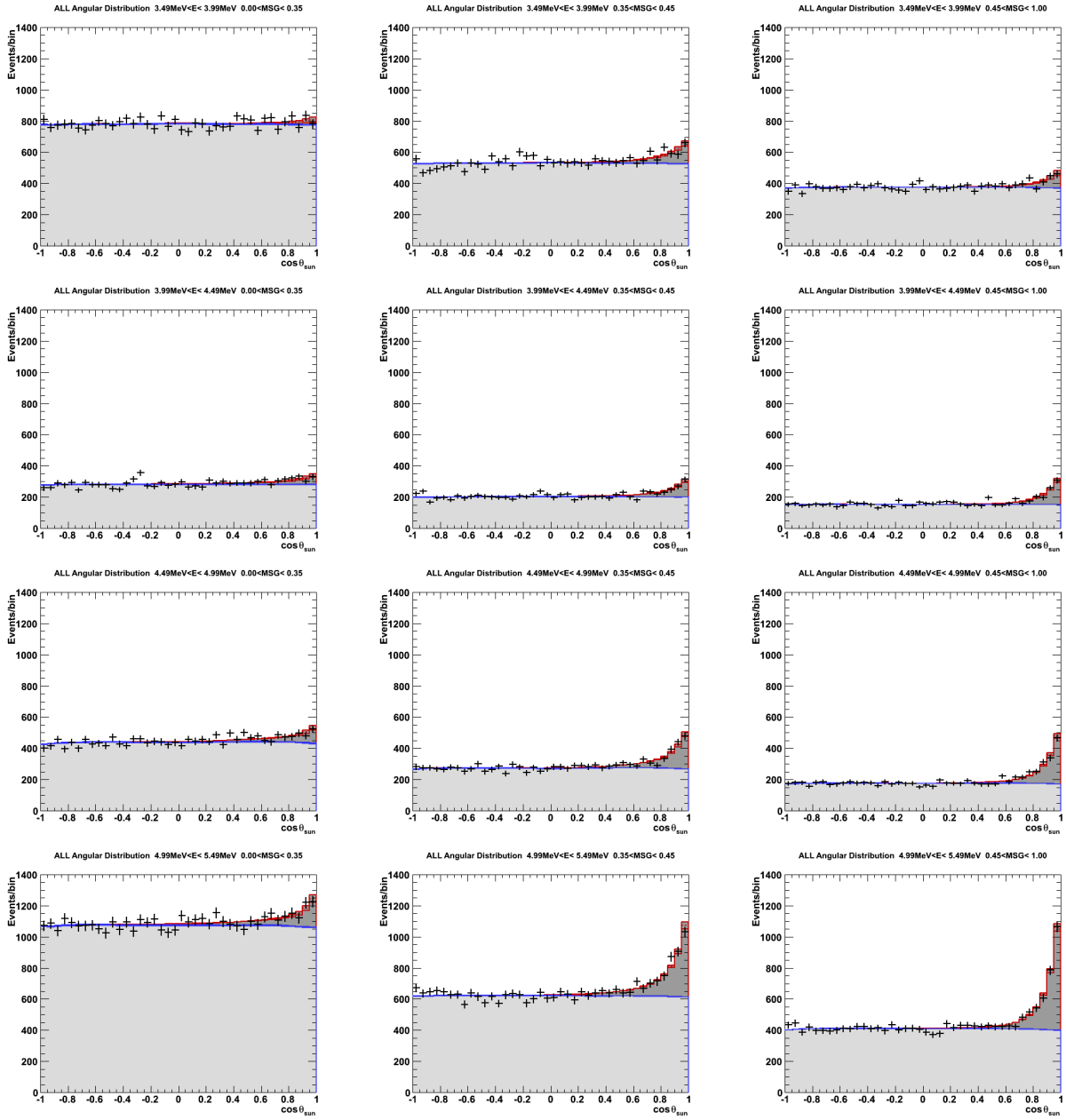

Figure 9.2: The $\cos\theta_{\mathrm{Sun}}$ distributions in each energy-MSG sub-bin from the results of the solar neutrino analysis. The rows correspond to energy bins starting at 3.49 MeV and increase by 0.5 MeV going down. The columns from left to right correspond to the MSG bins: MSG $\in$ [0.00,0.35), MSG $\in$ [0.35,0.45), and MSG $\in$ [0.45, 1.00].

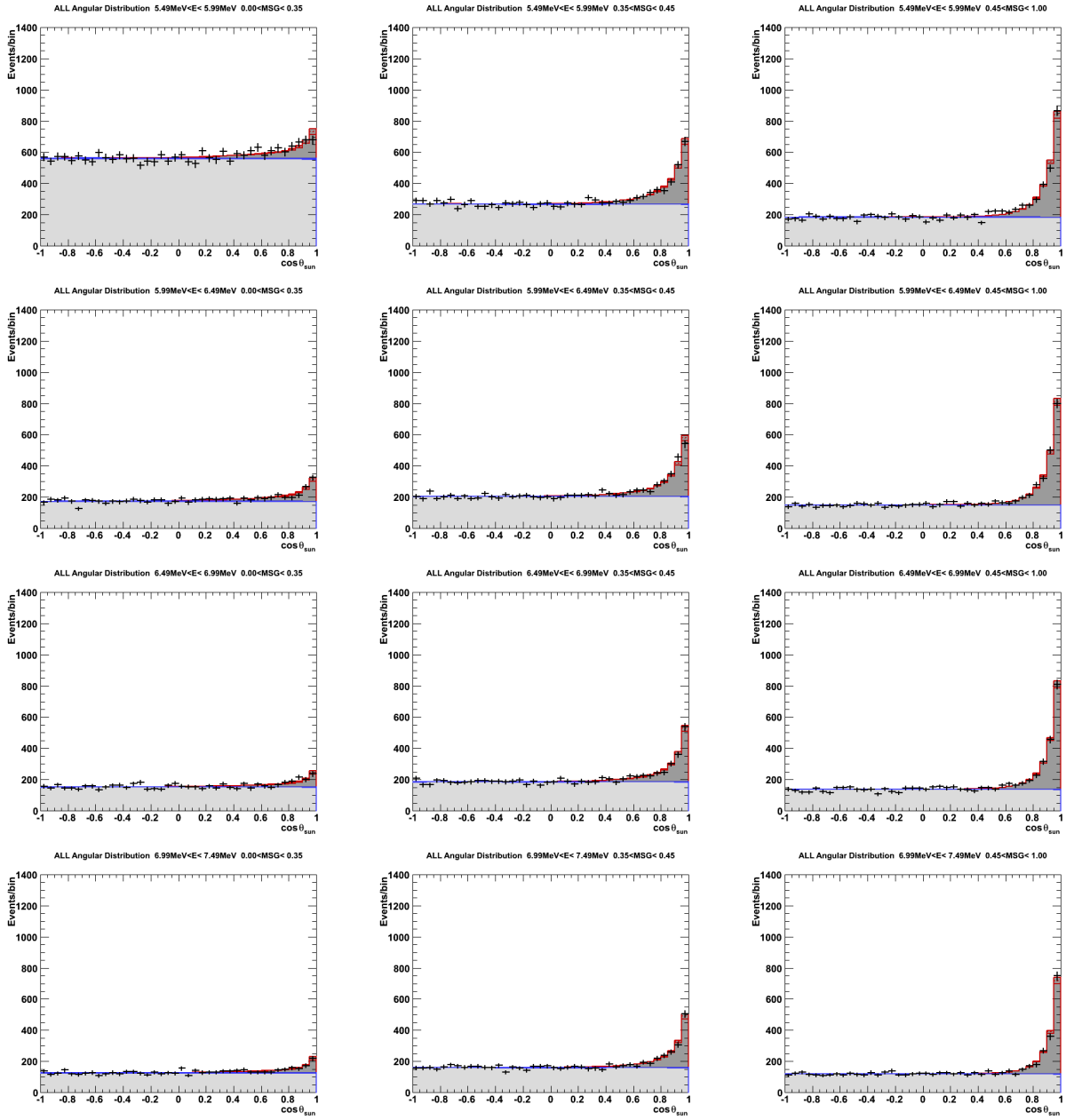

Figure 9.3: The $\cos\theta_{\mathrm{Sun}}$ distributions in each energy-MSG sub-bin from the results of the solar neutrino analysis. The rows correspond to energy bins starting at 5.49 MeV and increase by 0.5 MeV going down. The columns from left to right correspond to the MSG bins: MSG $\in$ [0.00,0.35), MSG $\in$ [0.35,0.45), and MSG $\in$ [0.45, 1.00].

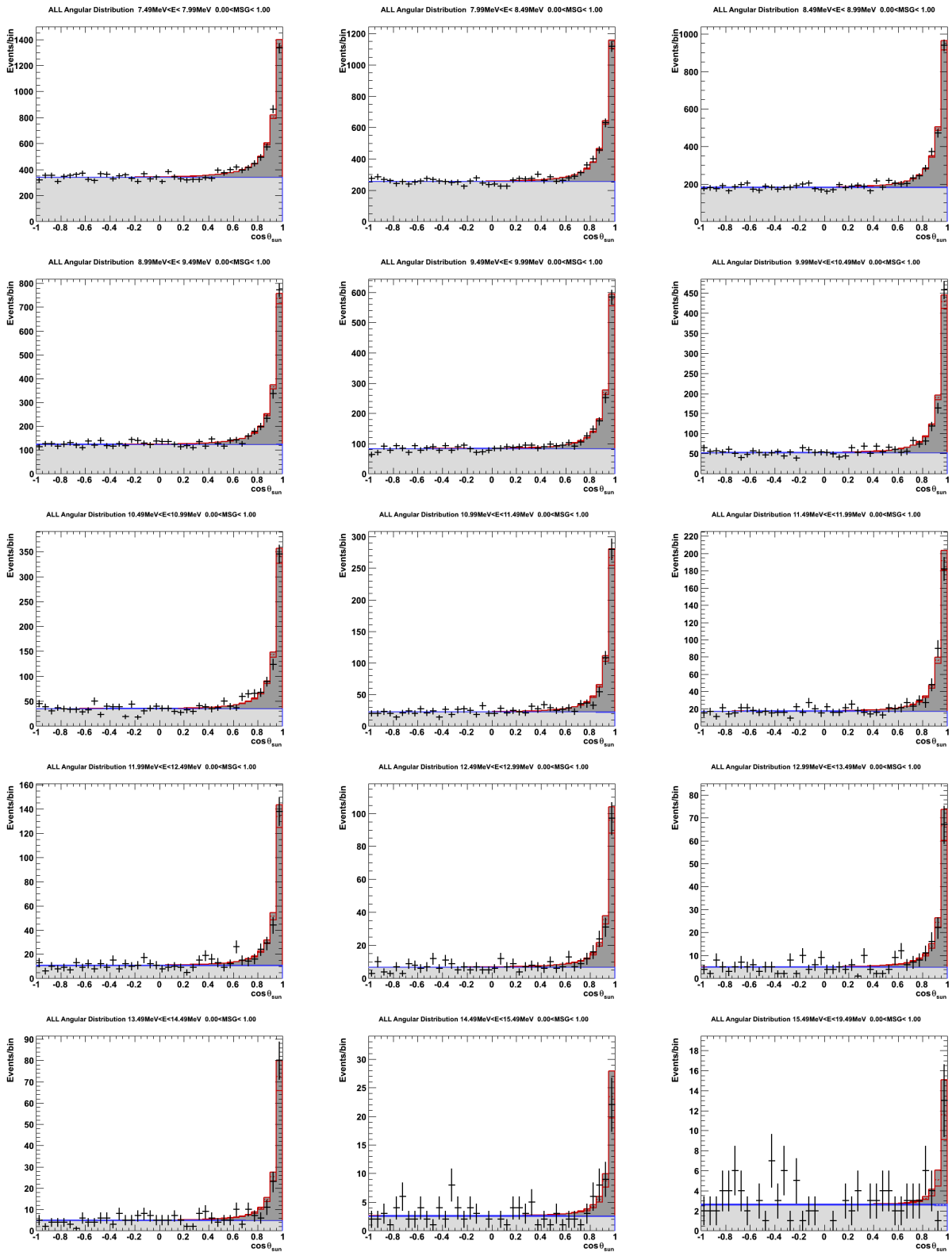

Figure 9.4: Signal Extraction $\cos\theta_{\mathrm{Sun}}$ distributions for the 7.49 MeV to 19.49 MeV recoil electron kinetic energy bins, with MSG $\in$ [0,1].

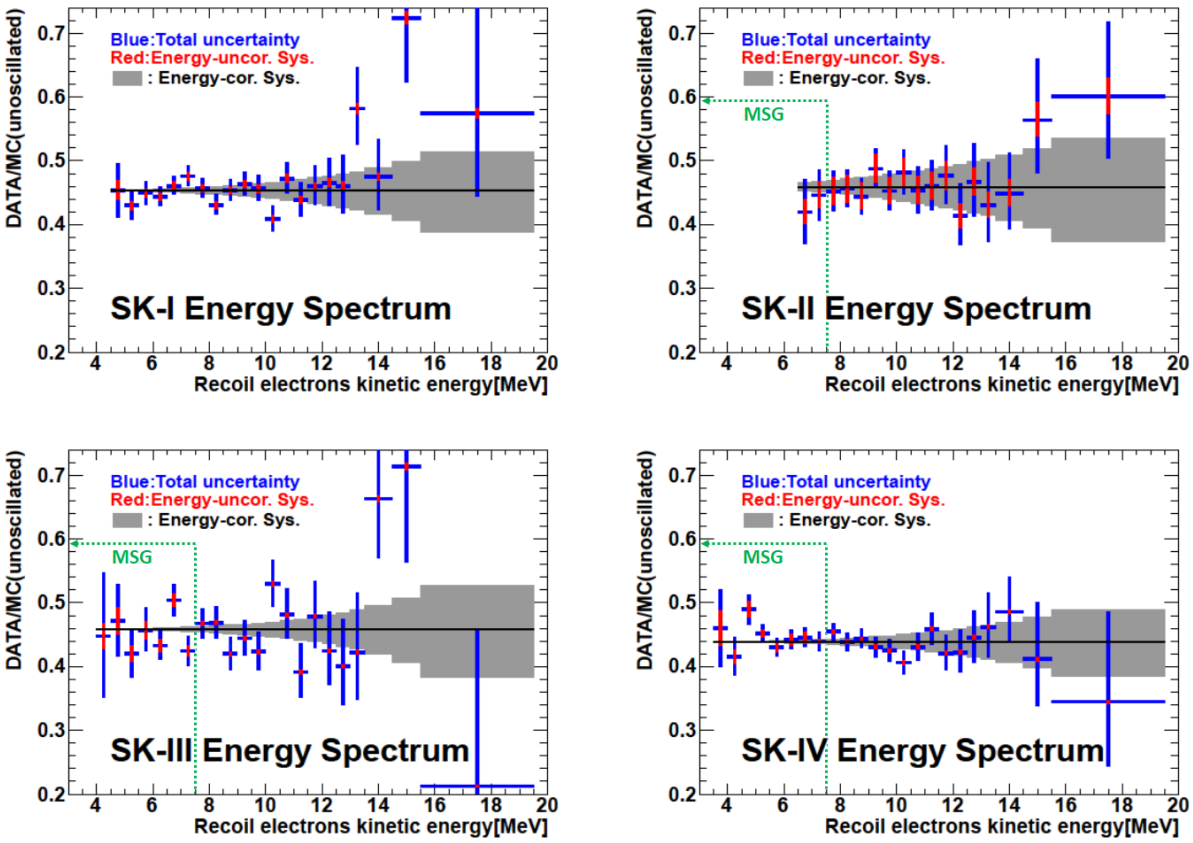

Figure 9.5: The solar neutrino recoil electron spectra for SK-I (top left), SK-II (top right), SK-III (bottom left), and SK-IV 1664-day results (bottom right). The red component of the error bars is the energy-uncorrelated systematic uncertainty, and the blue component is the total by combining the red with the statistical error in quadrature. The gray band is the total energy correlated systematic uncertainties. The dotted green line denotes the region over which MSG is applied for SK-II/III/IV.

9.3.1 Solar Neutrino Zenith Energy Spectrum

In addition to extracting the solar signal by energy and MSG sub-bins, the zenith dependence of the data can be included to construct the day, night, and zenith dependent energy spectra. The SK-IV 1664-day measurement of the energy dependence of the zenith distribution is plotted in Fig. 9.6.

Table 9.3 contains the observed solar neutrino interaction rate in SK for each energy bin at one astronomical unit (AU) using the "All," "Day," and "Night," data samples. The All sample contains all zenith bins, while the Day and Night samples contain the events with $\cos\theta_Z \in$ [-1,0] and $\cos\theta_Z \in (0, 1]$ respectively. The rates are in units of events/kton/day and assume a ^{8}B solar neutrino flux of $5.25 \times 10^6/(\text{cm}^2\ \text{s})$. The rates have also been corrected for reduction efficiencies.

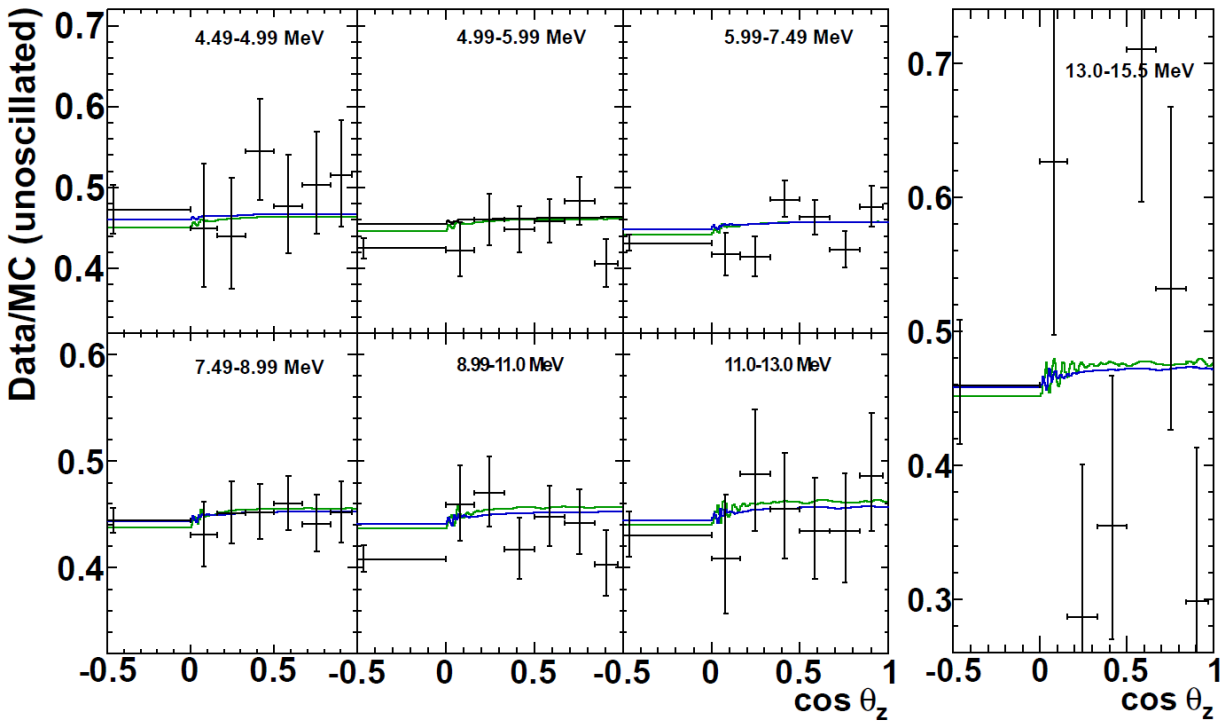

Figure 9.6: The energy dependence of the $\cos\theta_{\rm Sun}$ distribution in Fig. 8.11 for the single day bin, five mantle bins, and single core bin [42]. The green (blue) line corresponds to the predicted results of one day bin and 1000 night bins, from the best fit oscillation parameters using all solar (solar + KamLAND) data. Errors are statistical uncertainties only. The top three energy bins use MSG.

Table 9.3: The event rates observed for each energy bin in units of [events/kton/yr] at 1 AU. The errors are statistical uncertainty only. The expected event rates assume a ^{8}B solar neutrino flux of $5.25 \times 10^6/(\text{cm}^2\ \text{s})$, and the values include the correction to account for the reduction efficiences. Table taken from [42].

Kinetic Energy		Observed Rate		Expected Rate	
T_e	All	Day	Night	^{8}B	*hep*
[MeV]	$\cos\theta_Z \in [-1,1]$	$\cos\theta_Z \in [-1,0]$	$\cos\theta_Z \in (0,1]$		
3.49-3.99	$92.2^{+10.8}_{-10.6}$	$96.0^{+16.8}_{-16.3}$	$81.5^{+14.0}_{-13.6}$	196.8	0.346
3.99-4.49	$76.7^{+5.2}_{-5.1}$	$64.6^{+7.9}_{-7.6}$	$85.2^{+6.9}_{-6.7}$	182.8	0.335
4.49-4.99	$82.1^{+3.4}_{-3.3}$	$79.4^{+5.1}_{-5.0}$	$84.6^{+4.6}_{-4.5}$	167.8	0.323
4.99-5.49	$69.3^{+2.1}_{-2.1}$	$65.9^{+3.1}_{-3.0}$	$72.5^{+3.0}_{-2.9}$	153.3	0.312
5.49-5.99	$59.6^{+1.6}_{-1.6}$	$58.3^{+2.3}_{-2.2}$	$60.5^{+2.2}_{-2.2}$	137.8	0.298
5.99-6.49	$54.2^{+1.4}_{-1.4}$	$51.0^{+2.1}_{-2.0}$	$56.9^{+2.0}_{-2.0}$	121.9	0.282
6.49-6.99	$47.8^{+1.3}_{-1.3}$	$45.7^{+1.9}_{-1.8}$	$49.9^{+1.9}_{-1.8}$	106.8	0.266
6.99-7.49	$40.6^{+1.2}_{-1.1}$	$41.8^{+1.7}_{-1.7}$	$39.5^{+1.6}_{-1.6}$	92.1	0.250
7.49-7.99	$35.7^{+1.0}_{-1.0}$	$35.0^{+1.5}_{-1.5}$	$36.1^{+1.5}_{-1.4}$	78.0	0.232
7.99-8.49	$29.1^{+0.9}_{-0.9}$	$28.6^{+1.3}_{-1.3}$	$28.9^{+1.3}_{-1.2}$	65.2	0.214
8.49-8.99	$24.0^{+0.8}_{-0.8}$	$24.1^{+1.2}_{-1.1}$	$23.7^{+1.1}_{-1.1}$	53.4	0.197
8.99-9.49	$18.5^{+0.7}_{-0.7}$	$17.9^{+1.0}_{-0.9}$	$19.2^{+1.0}_{-0.9}$	42.9	0.179
9.49-9.99	$14.5^{+0.6}_{-0.6}$	$14.5^{+0.9}_{-0.8}$	$14.4^{+0.8}_{-0.8}$	33.8	0.162
9.99-10.49	$10.7^{+0.5}_{-0.5}$	$10.2^{+0.7}_{-0.7}$	$11.1^{+0.7}_{-0.7}$	26.0	0.144
10.49-11.99	$8.43^{+0.43}_{-0.41}$	$7.73^{+0.61}_{-0.56}$	$9.23^{+0.64}_{-0.60}$	19.55	0.128
11.99-11.49	$6.60^{+0.37}_{-0.35}$	$6.60^{+0.54}_{-0.49}$	$6.72^{+0.53}_{-0.49}$	14.34	0.112
11.49-12.99	$4.40^{+0.30}_{-0.28}$	$3.83^{+0.41}_{-0.37}$	$4.89^{+0.44}_{-0.40}$	10.24	0.097
12.99-12.49	$3.04^{+0.25}_{-0.23}$	$3.04^{+0.35}_{-0.31}$	$3.06^{+0.36}_{-0.32}$	7.10	0.083
12.49-13.99	$2.14^{+0.20}_{-0.18}$	$2.41^{+0.31}_{-0.27}$	$1.93^{+0.29}_{-0.25}$	4.80	0.070
13.99-13.49	$1.47^{+0.17}_{-0.15}$	$1.48^{+0.25}_{-0.21}$	$1.47^{+0.25}_{-0.21}$	3.11	0.059
13.49-14.49	$1.59^{+0.17}_{-0.15}$	$1.54^{+0.25}_{-0.21}$	$1.63^{+0.25}_{-0.22}$	3.18	0.088
14.49-15.49	$0.469^{+0.102}_{-0.082}$	$0.486^{+0.151}_{-0.112}$	$0.493^{+0.161}_{-0.121}$	1.117	0.056
15.49-19.49	$0.186^{+0.072}_{-0.051}$	$0.150^{+0.108}_{-0.065}$	$0.203^{+0.113}_{-0.071}$	0.464	0.064

Chapter 10

SK Solar Neutrino Oscillation Analysis

The kinematic reconstruction of the neutrino energy in neutrino-electron elastic scattering interactions in water is prevented by multiple Coulomb scattering of the recoil electrons. However, the recoil electron spectrum can still be used to statistically extract information about the neutrino spectrum, since the electron energy places a lower limit on the neutrino energy. The energy dependence of the elastic scattering cross section (Eq. 2.60) can, in principle, disentangle the ν_e component of the solar neutrino flux from the $\nu_{\mu,\tau}$ component. The ($\nu_{\mu,\tau}$ e) neutral current ES cross section has a softer dependence on the neutrino energy and is a factor of $\sim$6 smaller than the (ν_e e) ES cross section (CC+NC interactions). This means that the recoil electron spectrum depends not only on the flavor content of the flux, but also on the energy dependence of the ES cross section from each neutrino flavor. Because the recoil electron spectrum is dependent on the flavor content of the solar neutrinos, one can predict the recoil electron spectra caused by the survival probability $P_{ee}(E_\nu/\Delta m^2_{21}, \theta_{13}, \theta_{12}, \epsilon^{u,d}_{11}, \epsilon^{u,d}_{12})$. Details about neutrino oscillations are discussed in Ch. 2.

The energy-dependent shape of $P_{ee}(E_\nu)$ will leave an imprint on the spectrum of recoil electrons in SK. $P_{ee}(E_\nu)$ transitions from vacuum-dominated oscillations at low neutrino energy to matter-dominated oscillations at larger energies. Even with a flat $P_{ee}(E_\nu)$, the spectral distortions caused by the ($\nu_{\mu,\tau}$ e) NC interactions will be small, and $P_{ee}(E_\nu)$ can be inferred.

These predicted spectra are compared to the spectra measured by SK. This comparison constrains the oscillation parameters that drive the flavor content through the survival probability (P_{ee}) and the various transition probabilities. While ^{8}B solar neutrinos are the dominant signal for the recoil electron spectrum, the rarer *hep* process also contributes. Because the end-point energy of the *hep* neutrinos is larger than that of the ^{8}B, *hep* neutrinos will distort the higher energy bins of the recoil electron spectra. Therefore, it is necessary to include the *hep* neutrino spectral predictions when trying to constrain the oscillation parameters.

Additional effects from the Earth-matter interactions with solar neutrinos are another signature of matter-effects on neutrino oscillations. These Earth-matter effects must be incorporated into the spectral predictions when trying to compare to the All spectra (Day+Night). The matter effects can also be used to further constrain the oscillation parameters using the day-night asymmetry measured by SK.

Prior to discussing the effects NSI has on the allowed oscillation parameters for solar neutrinos (Ch. 11), the standard case of neutrino oscillations without NSI (i.e. no-NSI) will be covered in this chapter. Also, the solar neutrino recoil electron spectrum will be referred to simply as the "spectrum" in this chapter. When discussing other spectra, such as the neutrino spectra, they will be denoted as such. A block diagram of the analysis framework used for the NSI analysis is illustrated in Fig. 10.1. This framework is used to produce the results described in this chapter.

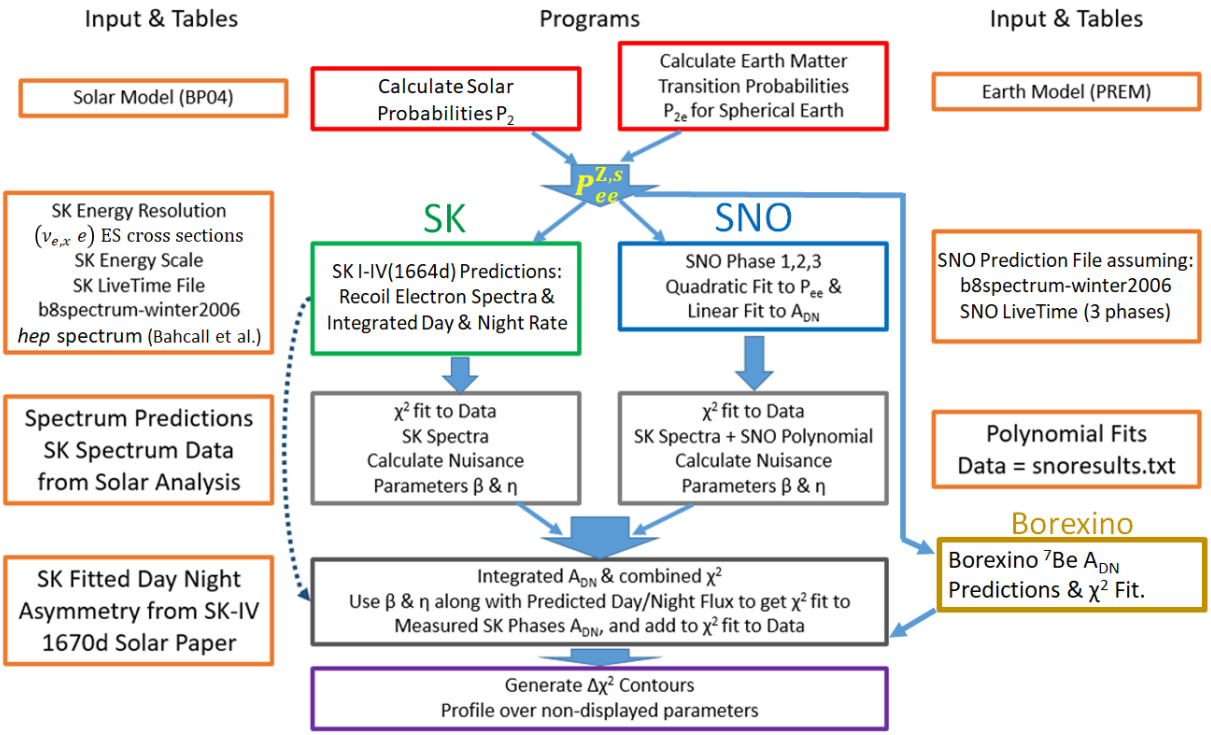

Figure 10.1: A block diagram of the analysis framework used for the SK solar neutrino NSI analysis.

10.1 SK Recoil Electron Spectrum Predictions

To create the SK spectrum predictions, several ingredients are first needed.

- An SSM (see Sec. 3.1 and Sec. 3.2) and a model of the Earth's matter density, which will be used to determine the various probabilities.
- The solar neutrino energy spectrum and flux, discussed in Sec. 3.2.1.
- The $(\nu\ e)$ cross sections, discussed in Sec. 2.3.
- The detector response function, discussed in Sec. 6.2.3.
- The exposure or live time of a detector as a function of zenith bin in $\cos\theta_Z$.

As stated previously, the Winter06 ^{8}B neutrino spectrum [45] and the predicted *hep*

neutrino spectrum from [41] are used in the SK analyses. The numerical calculations for the (ν e) ES cross section including radiative corrections are from [41]. Fig. 10.2 shows the $\cos\theta_Z$ distribution of the live time for each SK phase, where the single Day bin has been divided by 1000 to normalize it to the Night zenith binning. The process used to calculate the survival and transition probabilities for the analysis presented in this work will be discussed next.

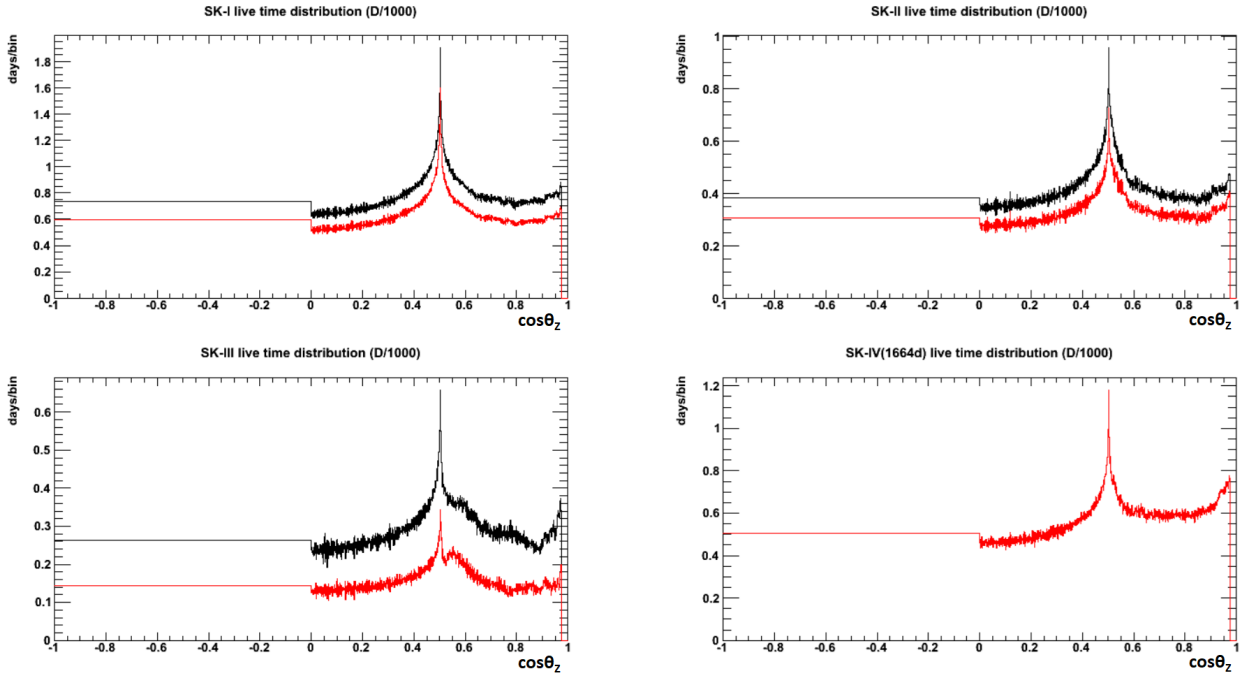

Figure 10.2: The $\cos\theta_Z$ distribution of the live times for the SK solar neutrino analysis. The black (red) lines correspond to the LE (SLE) trigger threshold. The live time of the single Day zenith bin has been divided by 1000 to normalize it to the zenith binning on the Night side. In SK-IV, the live times of the SLE and LE trigger thresholds are the same. The live time for the 31-hit SLE threshold is not displayed.

10.1.1 Solar Neutrino Survival Probability P_{ee} Calculation

As discussed in Sec. 2.1.2, solar neutrinos are produced by the fusion process in the solar core as ν_e. They exit the Sun in either the ν_1 or ν_2 mass eigenstate, with probabilities P_1 and P_2 respectively. Since $P_1 + P_2 = 1$, only one of these probabilities, P_2, will be used. Two sets of radial profiles are needed from an SSM to calculate P_2.

A radial profile is the dependence of a given parameter on the fraction of the solar radius $r = R/R_{\rm Sun}$. These sets of radial profiles are:

1. The fractional contribution each isotope gives to the solar mass. These fractional contributions are determined for spherical shells at r (Fig. 3.2). The metalicity of the Sun, the relative abundance of isotopes larger than helium, is given by these distributions in the SSM table.

2. The fraction of the total flux produced within a spherical shell at r for a solar neutrino species s (Fig. 3.6).

The first set will be referred to as the "mass fraction profiles," and the second set will be referred to as the "fractional flux profiles." The BP2004 SSM profiles are used in the SK solar neutrino oscillation analysis and the solar neutrino NSI analysis. The mass fraction profiles are used to extract the Sun's density profile for electrons, u-quarks, and d-quarks. These density profiles are plotted in Fig. 3.3. With the fermion density profiles, the matter potential (as a function of r) can be used when propagating the neutrino wavefunction through the Sun. The fractional flux profiles are used when calculating P_2 for each solar neutrino species.

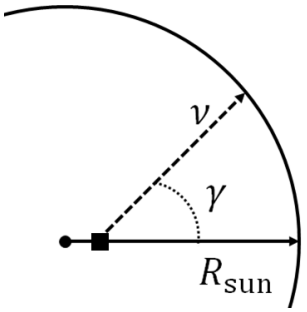

Figure 10.3: Illustration of the angle γ between the direction of neutrino propagation (dashed line) from the ν_e creation point (square) and the solar radius vector (solid ray).

To properly account for variations in the matter density along the potential paths a solar neutrino may take out of the Sun, two sets of binning related to the production location

and neutrino trajectory are used. The first is a binning in the solar radius r that is indexed by k. The radial binning is evenly broken into 16 bins from r = 0 to r = 0.32, with the production (or creation) point of a ν_e being in the center of a bin, i.e. at r = [0.01, 0.03, ..., 0.31]. The second binning is for the neutrino's trajectory through the Sun, defined by $\cos\gamma$ (Fig. 10.3). The binning of $\cos\gamma$ is defined by $\cos\gamma$ = [-1.0, -0.8, ..., 0.8, 1.0]. In all, solar neutrinos are propagated along 176 trajectories through the Sun. For each set of radial-$\cos\gamma$ bins, the neutrino's path is divided into 5000 steps. The matter density along the path is averaged for each step. ^{8}B solar neutrinos are typically produced around $r = 0.04$, well within the boundary of the solar core ($r \leq 0.19$). The minimum (maximum) pathlength through the solar core is $\sim 1.04\times10^5$ (1.60×10^5) km, or 8.19 (12.6) times the diameter of the Earth.

After propagating the neutrino wavefunction along the 11 $\cos\gamma$ directions, $P_{2,k}$ is calculated by averaging over all directions for a given radial bin k. P_2^s for each neutrino species can be calculated using their fractional flux profiles and the set of $P_{2,k}$. The relative contribution to the flux of a solar neutrino species by a given radial bin is extracted from the fractional flux profile. Based on these contributions, a weight f_k^s is determined. The BP2004 SSM f_k^s weights for each radial bin are given in Table 10.1 for the *pp*-chain solar neutrinos. The probabilities are calculated as functions of $E_\nu/\Delta m^2_{21}$. The distinction between the P_2 for each solar neutrino species comes from their fractional flux profile. The probability P_2^s for each species is determined by:

$$P_2^s(E_\nu/\Delta m^2_{21}, \theta_{13}, \theta_{12}, \epsilon_{11}^{u,d}, \epsilon_{12}^{u,d}) = \sum_k f_k^s P_{2,k}. \tag{10.1}$$

The propagation of the ν_1 and ν_2 from the Sun to the Earth can be treated as incoherent for values of $E_\nu/\Delta m^2_{21}$ tested in the SK oscillation [44] and NSI analysis. This means that the solar neutrinos will reach the Earth in the same mass eigenstate they possessed when

they exited the Sun. The survival probability for solar neutrinos arriving at the Earth during the day is then given by

$$P_{ee}^{s,\text{Day}} = \sin^4\theta_{13} + \cos^4\theta_{13} \times P_{ee}^{\text{2-flavor}},$$
$$\text{where} \quad P_{ee}^{\text{2-flavor}} = \sin^2\theta_{12}P_2 + \cos^2\theta_{12}P_1 = \cos^2\theta_{12} - \cos(2\theta_{12})P_2^s(\cos^2\theta_{13}). \tag{10.2}$$

Here, the dependence of P_2^s on the other oscillation parameters has been suppressed in the expression for clarity. Fig. 10.4 displays the difference in the BP2004 ^{8}B and *hep* neutrino $P_{ee}(E_\nu)$ across the range of $\sin^2\theta_{12}$ values for a typical LMA value of Δm^2_{21}. For solar neutrinos detected by SK during the night, the Earth matter effects must be taken into account.

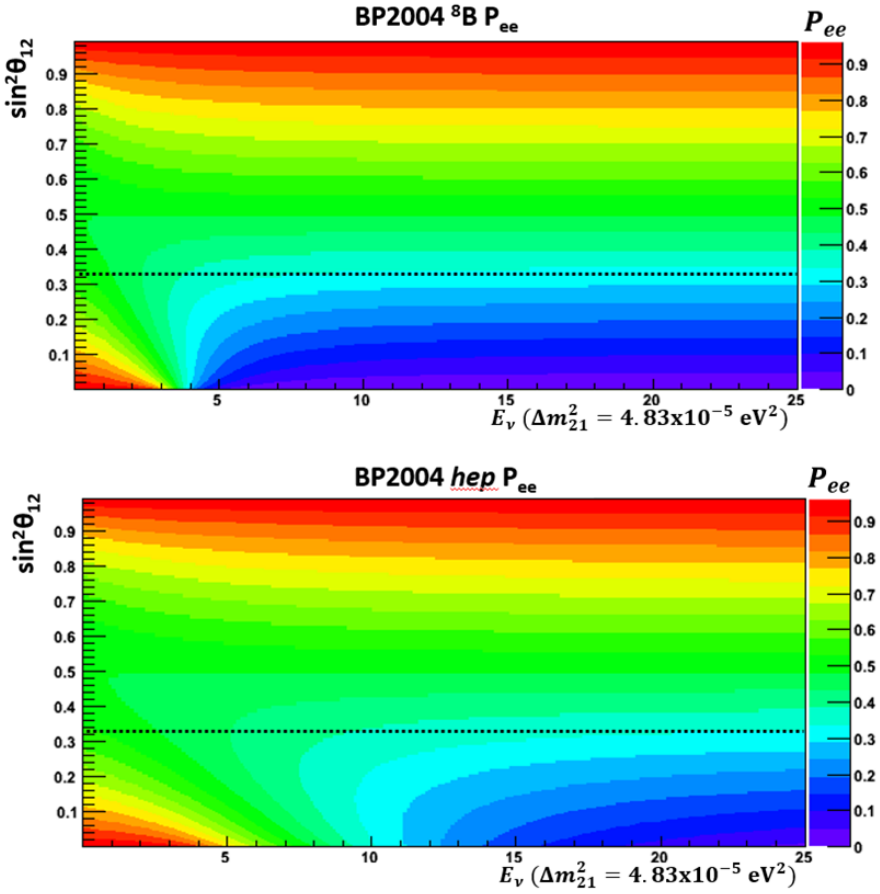

Figure 10.4: The P_{ee} for ^{8}B (top) and *hep* (bottom) solar neutrinos as a function of E_ν and $\sin^2\theta_{12}$. A typical LMA value of Δm^2_{21} has been used to convert $P_{ee}(E_\nu/\Delta m^2_{21})$ to a function of E_ν. The dashed line corresponds to the best fit LMA value of $\sin^2\theta_{12}$.

Table 10.1: The f_k^w weights extracted from the BP2004 SSM [46] ratio flux fraction tables [55] for the *pp*-chain solar neutrinos. This table corresponds to Fig. 3.6.

r-range	k	*pp*	*pep*	^{7}Be	^{8}B	*hep*
0.00-0.02	1	4.64×10^{-3}	1.24×10^{-2}	9.70×10^{-2}	7.29×10^{-2}	1.60×10^{-3}
0.02-0.04	2	2.54×10^{-2}	4.21×10^{-2}	1.30×10^{-1}	2.65×10^{-1}	9.70×10^{-3}
0.04-0.06	3	6.60×10^{-2}	1.03×10^{-1}	2.46×10^{-1}	3.56×10^{-1}	2.89×10^{-2}
0.06-0.08	4	9.95×10^{-2}	1.41×10^{-1}	2.37×10^{-1}	2.06×10^{-1}	5.09×10^{-2}
0.08-0.10	5	1.19×10^{-1}	1.52×10^{-1}	1.65×10^{-1}	7.46×10^{-2}	7.18×10^{-2}
0.10-0.12	6	1.27×10^{-1}	1.44×10^{-1}	9.70×10^{-2}	2.01×10^{-2}	9.01×10^{-2}
0.12-0.14	7	1.25×10^{-1}	1.24×10^{-1}	5.13×10^{-2}	4.41×10^{-3}	1.05×10^{-1}
0.14-0.16	8	1.14×10^{-1}	9.92×10^{-2}	2.52×10^{-2}	8.35×10^{-4}	1.14×10^{-1}
0.16-0.18	9	9.77×10^{-2}	7.30×10^{-2}	1.16×10^{-2}	1.40×10^{-4}	1.16×10^{-1}
0.18-0.20	10	7.74×10^{-2}	4.94×10^{-2}	5.05×10^{-3}	2.14×10^{-5}	1.11×10^{-1}
0.20-0.22	11	5.63×10^{-2}	3.04×10^{-2}	2.05×10^{-3}	2.96×10^{-6}	9.70×10^{-2}
0.22-0.24	12	3.77×10^{-2}	1.71×10^{-2}	7.76×10^{-4}	3.79×10^{-7}	7.86×10^{-2}
0.24-0.26	13	2.34×10^{-2}	8.84×10^{-3}	2.80×10^{-4}	4.58×10^{-8}	6.00×10^{-2}
0.26-0.28	14	1.38×10^{-2}	4.32×10^{-3}	9.27×10^{-5}	5.15×10^{-9}	4.11×10^{-2}
0.28-0.30	15	7.91×10^{-3}	2.03×10^{-3}	2.08×10^{-5}	4.06×10^{-10}	1.86×10^{-2}
0.30-0.32	16	4.35×10^{-3}	9.14×10^{-4}	3.00×10^{-6}	2.01×10^{-11}	5.43×10^{-3}

The shape of solar neutrino P_{ee} is determined by the MSW effect due to the electron density in the Sun. The oscillation parameters $(\sin^2\theta_{12}, \Delta m^2_{21})$ tune the shape in specific ways. The squared mass splitting will stretch or compress the shape of P_{ee}, since it is calculated as a function of $E_\nu/\Delta m^2_{21}$. The deviation between the vacuum-dominated P_{ee} and the matter dominated P_{ee} is tuned by the value of $\sin^2\theta_{12}$. Maximal mixing ($P_{ee} = 0.50$) occurs when $\sin^2\theta_{12} = 0.5$. At maximal mixing, there is no difference between vacuum-dominated and matter-dominated oscillations for neutrinos arriving during the day. By increasing $\sin^2\theta_{12}$, the value of matter-dominated P_{ee} increases and can surpass the value of the vacuum-dominated P_{ee}. Conversely, decreasing $\sin^2\theta_{12}$ deepens the offset between the two regions of P_{ee}. The dependence on the mixing angle θ_{12} is illustrated in Fig. 10.5, where several survival probability curves are plotted as functions of $E_\nu/\Delta m^2_{21}$. The top of the figure shows a typical small mixing angle (SMA) solar neutrino solution P_{ee}. The night-time survival probabiltiy of a neutrino passing through the Earth's core is plotted on top of the day P_{ee} with the difference between the two probabilty curves shaded in gray. The bottom

plot shows a typical P_{ee} curve for a large mixing angle (LMA) solution as a solid line and a darkside (or beyond maximal mixing) P_{ee} as a dash-dotted line. Several of the solar neutrino species are labeled for the various corresponding solar neutrino solutions.

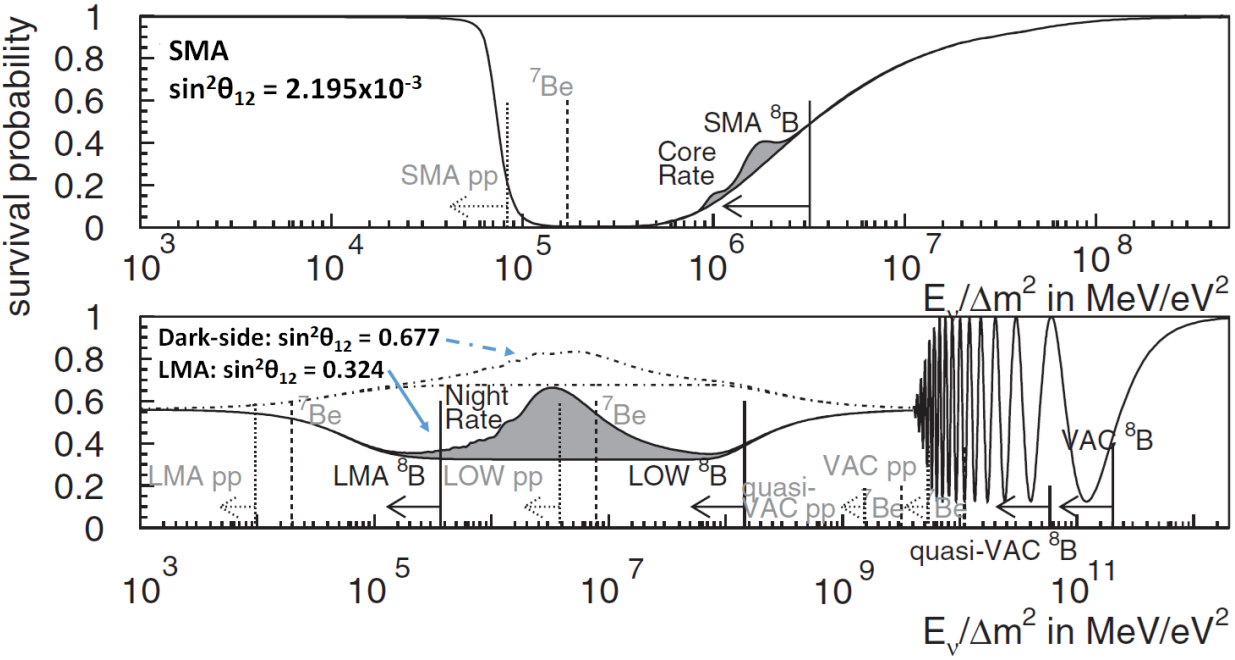

Figure 10.5: The dependence of $P_{ee}(E_\nu/\Delta m^2_{21})$ on $\sin^\theta_{12}$ [44]. The top of the figure shows a typical small mixing angle (SMA) solar neutrino solution P_{ee}. The night-time survival probabiltiy of a neutrino passing through the Earth's core is plotted on top of the day P_{ee} with the difference between the two probabilty curves shaded in gray. The bottom plot shows a typical P_{ee} curve for a large mixing angle (LMA) solution as a solid line and a darkside (or beyond maximal mixing) P_{ee} as a dash-dotted line. Several of the solar neutrino species are labeled for the various corresponding solar neutrino solutions.

10.1.2 Solar Neutrino Transition Probability P_{2e} Calculation

The terrestrial matter effects are taken into account by propagating the neutrino wavefunction through the Earth along the 1000 $\cos\theta_Z$ Night zenith bins (Z). Along the neutrino trajectory, in each of these zenith bins, regions of constant density are first determined by interpolating the matter density profile given by the Preliminary Reference Earth Model (PREM model) [125]. In the PREM model, the Earth is treated as a sphere and the matter

density is given in units of g/cm^3. The matter density profile given by the PREM model is plotted in Fig. 10.6. To determine the regions of constant density along a zenith direction, the running average of the mass density is tracked while stepping through the Earth in one meter increments. If the current density fluctuates more than 0.001 g/cm^3, a new region of constant density is defined. The distance and averaged density of the previous region is saved.

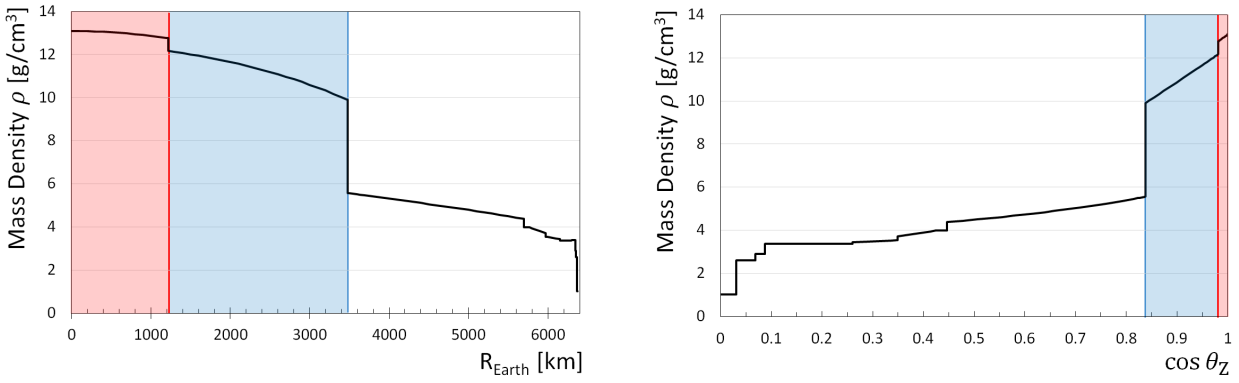

Figure 10.6: The mass density profile from the Preliminary Reference Earth Model [125] as a function of distance from the Earth's center (left) and $\cos\theta_Z$ (right). The red region denotes the inner core, and the blue region denotes the outer core. The mantle region is denoted by the white region, which also includes the crust.

The content of electrons (and quarks) is different between the mantle and core. The PREM model gives the ratios Y_n (the ratio of neutrons to electrons) and Y_e (the ratio of the electron to matter density) based on assumptions about the chemical composition of the mantle and core. The PREM model also assumes that the Earth is electrically neutral. For the mantle (core) region, the PREM model gives $Y_e = 0.497$ (0.468) and $Y_n = 1.012$ (1.137). The number density n_e of electrons is obtained by multiplying Y_e by the mass density and Avogadro's number $N_A = 6.022 \times 10^{23}$. The quark-to-electron ratios, Y_d and Y_u, are listed in Table 10.2. These ratios are obtained by solving the system of equations: $Y_n = n_n/n_e = 2Y_d + Y_u$ and $n_p = n_e \rightarrow 1 = Y_d + 2Y_u$.

As seen in Fig. 10.6, there is an inner and outer part to the Earth's core, which are

Table 10.2: Relevant information from the Preliminary Reference Earth Model [125] for determining the matter potential of neutrinos propagating through the Earth's mantle and/or core. The ratio Y_e of electrons to the matter density ρ is given in the second column. The third (fourth) column contains the ratio $Y_u(Y_d) = n_{u(d)}/n_e$ of the up (down) quark number density to the electron number density.

Region	Y_e [mol/g]	Y_u	Y_d
Mantle	0.497	3.012	3.024
Core	0.468	3.137	3.274

thought to be predominantly composed of a solid and a molten iron-nickel alloy respectively. The PREM model assumes the Y_e and Y_n to be the same in the inner and outer core. The Earth's outer (inner) core is only traversed for neutrino trajectories with $\cos\theta_Z \geq 0.838$ (0.982). Based on the $\cos\theta_Z$ distribution of the SK live time (Fig. 10.2), SK's solar neutrino analysis has sensitivity to the outer core. Because of the relative geometry between SK, the Earth, and the Sun, SK has no sensitivity to neutrinos traversing the inner core (see Fig. 8.13).

The process of calculating the probability of a solar neutrino propagating along a zenith bin Z and arriving at SK in the ν_e flavor eigenstate is as follows:

1. Assume the neutrino begins in the ν_2 mass eigenstate.

2. The neutrino wavefunction is propagated through the Earth along a given zenith bin. The various regions of constant density, defined by the PREM model, supply the densities for the local matter potentials and the pathlengths for propagation. The local matter density is multiplied by N_A and the Y_f factors in Table 10.2 to obtain the local fermion number densities. These are assigned to the local matter potential. The quark contribution to the matter potential is only non-zero with the introduction of NSI.

3. After the neutrino exits the Earth, the transition probability P_{2e} can be determined

by taking the electron component of the neutrino wavefunction.

4. The transition probability P_{2e} is then combined with the probability P_2^s to get the effective two-flavor electron neutrino survival probability

$$\begin{gathered} P_{ee}^{\text{2-flavor,Z},s} = P_1^s \cdot P_{1e}^{\text{Z}} + P_2^s \cdot P_{2e}^{\text{Z}} = \\ (1 - P_2^s)(1 - P_{2e}^{\text{Z}}) + P_2^s \cdot P_{2e}^{\text{Z}} = 1 + 2P_2^s \cdot P_{2e}^{\text{Z}} - P_2^s - P_{2e}^{\text{Z}}. \end{gathered} \tag{10.3}$$

5. $P_{ee}^{\text{2-flavor,Z},s}$ is then three-flavorized via Eq. 2.33:

$$P_{ee}^{\text{Z},s} \equiv \cos^4\theta_{13} \cdot P_{ee}^{\text{2-flavor,Z},s} + \sin^4\theta_{13}. \tag{10.4}$$

This procedure is performed for all zenith bins. Once the zenith-dependent $P_{ee}^{\text{Z},s}$ are calculated (one for the Day and 1000 for the Night), one can determine the corresponding spectrum that should be seen in SK.

10.1.3 Calculation of the Spectrum Predictions

With all the ingredients prepared, the prediction for the solar-neutrino-induced (ν e) ES recoil electron event rate can be determined. For SK-Phase P, energy bin i, and zenith bin Z, the expected event rate is calculated by modifying Eq. 2.66 in the following manner:

$$\text{R}_{i,\text{Z}}^{P,s} = \Phi_{\text{SSM}}^s N_i^P \int_{E_i^{\text{low}}}^{E_i^{\text{high}}} \text{d}E_{obs} \int_{E_\nu} \text{d}E_\nu \int_{E_e} \text{d}E_e \Big(P_{ee}^{\text{Z},s} M^P + \big[1 - P_{ee}^{\text{Z},s}\big] M^P \Big) \tag{10.5}$$

where Φ_{SSM}^s is the flux from the SSM and s corresponds to the ^{8}B or *hep* solar neutrino species. N_i^P is the number of target electrons within the fiducial volume for energy bin i (Sec. 7.4.11). Here, E_e is the true total energy of the recoil electron in SK, E_{obs} is the observed total energy of the recoil electron, and E_i^{high} (E_i^{low}) is the upper (lower) energy bound for the i'th energy bin. The function $M^{P,s} = M^{P,s}(R(E_e, E_{obs}), \phi^s(E_\nu), \frac{d}{dE_e}\sigma_{(\nu\ e)\text{ES}})$

corresponds to "transfer matrices," first employed by the Minos experiment to propagate the neutrino spectrum from the near detector to the far detector [126]. In the SK spectral predictions, these matrices transfer the following effects onto the expected rate of ES events in SK: the SK energy resolution from the detector response (Eq. 6.13), the solar neutrino spectrum $\phi^s(E_\nu)$, and the ES differential cross sections (Sec. 2.3). The function $\phi^s(E_\nu)$ is the energy spectrum for $s = (^8\text{B}, \textit{hep})$ solar neutrinos. It is useful to define $B_{i,\text{Z}}^{P,\text{OSC}}$ and $H_{i,\text{Z}}^{P,\text{OSC}}$ as the ^{8}B and *hep* solar-neutrino-induced event rates corresponding to Eq. 10.5.

The unoscillated event rate is obtained by setting $\Delta m^2_{21} = 0$, which yields $P_{ee} = 1$. There are no matter-induced effects on P_{ee} in this case. The event rate is minimally dependent on the zenith direction through the square of the distance between SK and the neutrino's production point in the Sun. However, the unoscillated event rate will be dependent on energy and energy-related effects such as the cross section and the fiducial volume for the i'th energy bin. It is useful to define the unoscillated rates as $B_{i,\text{Z}}^{P,\ \text{UNOSC}}$ ($H_{i,\text{Z}}^{P,\ \text{UNOSC}}$) expected to be induced by ^{8}B (*hep*) solar neutrinos. Then, the rate ratios for each energy-zenith bin set in a given SK-Phase are defined as:

$$\begin{aligned} b_{i,\text{Z}}^{P} &= \frac{B_{i,\text{Z}}^{P,\text{OSC}}}{B_{i,\text{Z}}^{P,\text{UNOSC}}+H_{i,\text{Z}}^{P,\text{UNOSC}}} \quad \text{expected } ^8\text{B rate ratio} \\ h_{i,\text{Z}}^{P} &= \frac{H_{i,\text{Z}}^{P,\text{OSC}}}{B_{i,\text{Z}}^{P,\text{UNOSC}}+H_{i,\text{Z}}^{P,\text{UNOSC}}} \quad \text{expected } \textit{hep} \text{ rate ratio} \end{aligned} \tag{10.6}$$

The rate ratios for the data can be similarly defined:

$$d_{i,\text{Z}}^{P} = \frac{D_{i,\text{Z}}^{P}}{B_{i,\text{Z}}^{P,\text{MC}}+H_{i,\text{Z}}^{P,\text{MC}}} \quad \text{measured data rate ratio} \tag{10.7}$$

The data rate (D) is the extracted solar neutrino signal (Ch. 9) divided by the corresponding live time. It is divided by the rates derived from the SK solar neutrino MC (Sec. 6.1). The statistical uncertainty for the data rate ratio ($\sigma_{i,\text{Z}}^{P}$) is likewise formed from the statistical error on the extracted signal.

To combine any zenith-energy bin sets, the number of expected events needs to be determined from the corresponding oscillated and unoscillated expected event rates. The expected number of events for a zenith-energy bin is

$$\mathrm{N}_{i,\mathrm{Z}}^{P,s} = \mathrm{R}_{i,\mathrm{Z}}^{P,s} \cdot \tau_{i,\mathrm{Z}}^{P}, \tag{10.8}$$

where $\tau_{i,\mathrm{Z}}^{P}$ is the corresponding live time. This calculation is performed for both the oscillated and unoscillated expectations. The combined rate ratio ($\rho_{\mathrm{comb}}^{P,s}$) for the set of zenith-energy bins one wishes to combine is:

$$\rho_{\mathrm{comb}}^{P,s} = \frac{\sum_{i,\mathrm{Z}} \mathrm{N}_{i,\mathrm{Z}}^{P,s,\mathrm{OSC}}}{\sum_{i,\mathrm{Z}} \mathrm{N}_{i,\mathrm{Z}}^{P,s,\mathrm{UNOSC}}} \ . \tag{10.9}$$

Here, i runs over the desired energy bins, and Z runs over the desired zenith bins. The expected number of events cannot be combined across SK-Phases, since M^P and the live times are different for each phase.

This method is used to predict the rate ratios for each energy bin of the combined spectrum ($\rho_{i,\mathrm{All}}^{P,s}$, All = Day+Night) by summing over the 1001 zenith bins. It is also used to form the Night spectrum by summing over the 1000 Night zenith bins. For each SK-Phase, the predicted ^{8}B rate ratio is b_i^P, and the predicted *hep* rate ratio is h_i^P.

In the "integrated day-night asymmetry" predictions, the total Day rate and total Night rate are compared to determine if there is any extra rate during the day or night. The total Day rate is formed by summing over the energy bins for Z=Day, while the total Night rate is formed by summing over the energy and the 1000 Night zenith bins. These are then combined to get the day-night asymmetry, which is compared to the measured differences in the day and night rates from data.

10.2 The χ^2 Fit of Spectrum Predictions to Data

With the predicted b_i^P and h_i^P spectra for each SK-Phase, one can compare to the spectra measured by SK. The spectrum comparison is a minimized χ^2 fit between the predicted spectrum and the measured spectrum. The predicted spectrum r_i^P is given by

$$r_i^P = \beta \cdot b_e^P + \eta \cdot h_e^P, \tag{10.10}$$

where β and η are nuisance parameters that scale the ^{8}B and *hep* rates respectively. These two nuisance parameters are sometimes referred to as the "flux scaling parameters," and they are constrained by measurements of the corresponding solar neutrino fluxes. Details of the solar oscillation analysis can be found in [44] and in [42].

Energy-Correlated Systematic Uncertainties in the Oscillation Analysis

The energy-correlated uncertainties from the ^{8}B neutrino spectrum shape, absolute energy scale, and energy resolution (Sec. 8.2.2) will shift all the energy bins of the spectra in a correlated manner. These energy-correlated systematic uncertainties for SK-IV are plotted in Fig. 10.7. In the solar oscillation analysis, a spectral distortion factor corresponding to the energy-correlated systematic uncertainties is applied to r_i^P. This is then fit to the measurement $d_i^P \pm \sigma_i^P$. The spectral distortion factor $f_i^P(\tau, \epsilon_P, \rho_P)$ describes the following effects:

- A systematic shift of the ^{8}B neutrino spectrum based on the Winter06 uncertainties (Sec. 8.2.3). The uncertainty in the ^{8}B neutrino spectrum shape leads to a shift in the spectrum by $\sim\pm$100 keV. The shift is scaled by the constrained nuisance parameter τ.
- A deviation of the SK energy scale in phase P (Sec. 8.2.1) is described by the con-

strained nuisance parameter ϵ_P. The uncertainty for the SK-IV absolute energy scale is $\pm 0.54\%$.

- A systematic change in the energy resolution of SK described by the constrained nuisance parameter ρ_P. The energy resolution uncertainty is $\pm 1.0\%$ below 4.89 MeV and $\pm 0.6\%$ above 6.81 MeV [42].

These three systematic nuisance parameters are assumed to be standard Gaussian variables, and are constrained to 0 ± 1. When combining a combined SK spectra fit that includes all experimental phases, the nuisance parameters β, η, and τ are applied simultaneously across each phase.

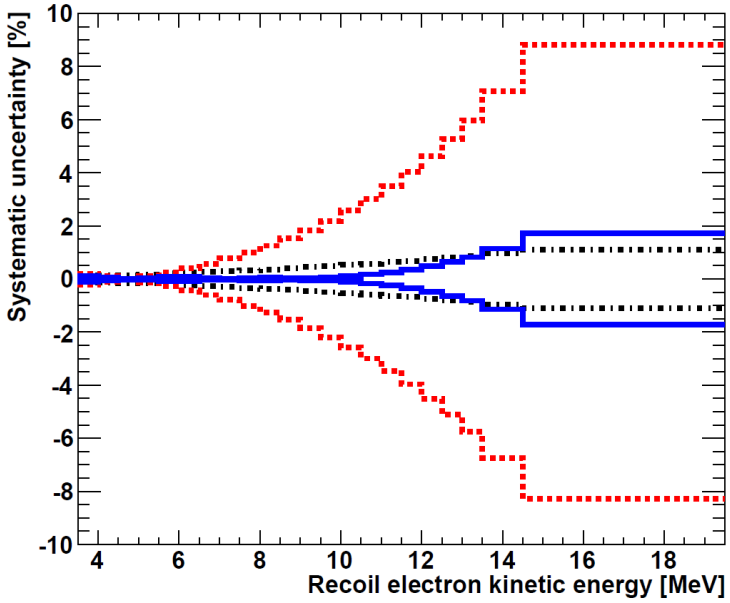

Figure 10.7: The energy-correlated systematic uncertainties for the SK-IV phase [42]. These uncertainties are used in the solar neutrino oscillation analysis. The red, blue, and black lines correspond to the absolute energy scale, energy resolution, and ^{8}B spectrum shape, respectively.

The χ^2 Fit

The $\chi^2_{\rm spec}$ fit to be minimized is

$$\chi^2_P(\beta,\eta) = \sum_{i=1}^{N_P} \left(\frac{d_i^P - f_i^P \cdot r_i^P}{\sigma_i^P} \right)^2, \tag{10.11}$$

where N_P is the number of energy bins for phase P. The spectrum is dependent on the set of oscillation parameters (including NSI) and nuisance parameters:

$$r_i^P = r_i^P(\theta_{13}, \theta_{12}, \Delta m^2_{21}, \epsilon^f_{11}, \epsilon^f_{12}; \beta, \eta)$$

for $f =$ u or d. Minimizing over the five nuisance parameters gives:

$$\chi^2_{{\rm spec},P} = \min_{\tau,\rho_P,\epsilon_P,\beta,\eta} \left[\chi^2_{P,{\rm data}} + \tau^2 + \rho_P^2 + \epsilon_P^2 + \frac{(\beta-\beta_0)^2}{\sigma_\beta^2} + \frac{(\eta-\eta_0)^2}{\sigma_\eta^2} \right], \tag{10.12}$$

where $\beta_0 \pm \sigma_\beta$ and $\eta_0 \pm \sigma_\eta$ are priors for the fit. The constraint on β is motivated by the SNO NC measurement of the ^{8}B solar neutrino flux: $(5.25 \pm 0.20) \times 10^6/({\rm cm}^2\ {\rm s})$ [47]. A weak constraint corresponding to a *hep* flux of $(8 \pm 16) \times 10^3/({\rm cm}^2\ {\rm s})$ [41] is applied to η.

After obtaining the minimum $\chi^2_{{\rm spec},P}$, the energy-independent systematic uncertainties on the total rate (Sec. 8.2) need to be included. These uncertainties are applied independently of f_i^P. An additional parameter α_P is used to incorporate these uncertainties by scaling the a posteriori constraints on the total flux parameters by $\alpha^{-1/2}$, without affecting the minimum χ^2. The form of this parameter was chosen to be:

$$\alpha_P = \frac{\sigma^2_{P,{\rm stat}}}{\sigma^2_{P,{\rm stat}} + \sigma^2_{P,{\rm syst}}}. \tag{10.13}$$

Eq. 10.12 is quadratic in nature due to its dependence on β and η. A 2×2 curvature matrix $\mathbf{C}_P$ is defined to describe the (β,η) parameter space and find the minimum. It can

be used to rewrite Eq. 10.12 in its quadratic form, along with the best fit flux parameters β_{min} and η_{min}:

$$\chi^2_{\text{spec},\alpha_P} = \chi^2_{P,\text{min}} + (\beta - \beta^P_{\text{min}}, \eta - \eta^P_{\text{min}}) \cdot (\alpha_P \mathbf{C}_P) \cdot \begin{pmatrix} \beta - \beta^P_{\text{min}} \\ \eta - \eta^P_{\text{min}} \end{pmatrix}, \tag{10.14}$$

if $\alpha_P = 1$.

To obtain the χ^2 for all phases combined, α_P will take on the form in Eq. 10.13. The systematic uncertainty parameter α_P scales the curvature matrix to account for the energy-uncorrelated uncertainties on the total rate in the spectrum χ^2 fit. By scaling the curvature matrix in this way, the minimum χ^2 and the best-fit (β, η) are preserved. However, this enlarges the uncertainty of the χ^2 constraints on the flux parameters. The SK combined spectrum χ^2 is then obtained by minimizing the following function over all nuisance parameters:

$$\chi^2_{\text{spec}} = \min_{\tau,\rho_P,\epsilon_P,\beta,\eta} \left[\tau^2 + \frac{(\beta - \beta_0)^2}{\sigma^2_\beta} + \frac{(\eta - \eta_0)^2}{\sigma^2_\eta} + \sum_{P=1}^{4} \left(\chi^2_{\text{spec},\alpha_P} + \epsilon^2_P + \rho^2_P \right) \right]. \tag{10.15}$$

The best-fit flux nuisance parameters are used when incorporating the day-night asymmetry in the SK solar neutrino oscillation analysis and the NSI analysis.

When including multiple values of θ_{13}, an additional constraining term is added to the SK χ^2_{spec}: $\left(\frac{\sin^2\theta_{13} - \sin^2\theta^{\text{best}}_{13}}{\sigma_{\sin^2\theta^{\text{best}}_{13}}}\right)^2$. The value of $\sin^2\theta^{\text{best}}_{13}$ and its uncertainty are based on the global best fits from reactor long baseline antineutrino measurements (Table 2.1): $\sin^2\theta_{13} = 0.0216 \pm 0.0003$. In the oscillation analysis, the set of tested values for $\sin^2\theta_{13}$ is: $\sin^2\theta_{13} = [0.000, 0.005, 0.010, \ldots, 0.045, 0.050]$. The penalty from the constraint is added to the χ^2_{spec} at the end when profiling over the non-displayed parameters. Profiling over non-displayed parameters involves collecting the set of χ^2 values from the fits for each point corresponding to the displayed parameter space. The minimum χ^2 value from each set is selected for the χ^2 at that point. For the analysis presented in this work, the θ_{13} constraint is dropped because

θ_{13} is set to $\sin^2\theta_{13} = 0.020$.

10.2.1 Day-Night Asymmetry in the Oscillation Analysis

The SK solar neutrino oscillation has been expanded to allow time-varying signals for the Day and 1000 Night bins. This day-night time-variation effect is incorporated by defining the likelihood:

$$\log L_{\rm DN} = \log L_{\rm with} - \log L_{\rm without}, \tag{10.16}$$

which is the difference in the likelihood with and without the predicted variation between the day and night spectra. It comes from

$$\log L_{\rm with} = (\log L_{\rm with} - \log L_{\rm without}) + \log L_{\rm without} = \log L_{\rm DN} - \frac{1}{2}\chi^2_{\rm spec},$$

since the errors of the energy bins used in the unbinned maximum likelihood fit are Gaussian. This method incorporates the day-night asymmetry into the oscillation analysis in a very precise way. The threshold for the time-variation and day-night asymmetry analysis is 5.0 MeV (7.0 MeV) total energy for SK-I/III/IV (SK-II). $L_{\rm without}$ is simply the sum of the log likelihoods from Eq. 8.1 for each phase: $\log L_{\rm without} = \sum_{P=1}^{4} \log L^P_{\rm without}$. $\log L_{\rm with}$ is also calculated by summing over each phase.

To determine the time-variation likelihood ($L_{\rm with}$), the predicted spectra for each zenith bin and for all phases are recalculated with the best-fit flux and nuisance parameters from the $\chi^2_{\rm spec}$ minimization [43]. The likelihood in Eq. 8.1 is modified to include the zenith-dependent rate ratios to create $L_{\rm with}$:

$$L^P_{\rm with} = e^{-(\sum_i B_i + S)_P} \prod_{i=1}^{N_{\rm bin}} \prod_{j=1}^{n_i} \left(B_i \cdot b_{i,j} + S \cdot Y_i \cdot s_{i,j} \cdot \frac{\rho_{i,\rm Z}}{\rho_{i,\rm All}} \right)_P . \tag{10.17}$$

Here, $(\rho_{i,\rm Z} = \beta_{\rm min} \cdot b_{i,\rm Z} + \eta_{\rm min} \cdot h_{i,\rm Z})$ is the predicted zenith rate ratio spectra, and

($\rho_{i,\mathrm{All}} = \beta_{\mathrm{min}} \cdot b_{i,\mathrm{all}} + \eta_{\mathrm{min}} \cdot h_{i,\mathrm{all}}$) is the predicted spectra after combining over all 1001 zenith bins. The energy-dependent zenith spectrum predictions ($\rho_{i,\mathrm{Z}}/\rho_{i,\mathrm{All}}$) are plotted in Fig 10.8 for $(\sin^2\theta_{12}, \Delta m^2_{21}) = (0.314, 4.84 \times 10^{-5}\ \mathrm{eV}^2)$.

The spectrum prediction and the signal extraction are performed for each set of oscillation parameters, and they are performed independently for each phase. Every candidate recoil electron event in the final solar neutrino sample with an energy above the threshold is fit to minimize the likelihood. The total log likelihood with the time-variation is $\log L_{\mathrm{with}} = \sum_{P=1}^{4} \log L^P_{\mathrm{with}}$. Because the uncertainties in each spectral bin are approximately Gaussian, the time-variation likelihood can be combined with χ^2_{spec} to get the total χ^2: $\chi^2 = \chi^2_{\mathrm{spec}} - 2\log L_{\mathrm{DN}}$. The results for the SK solar neutrino oscillation analysis are discussed in Sec. 3.3.7.

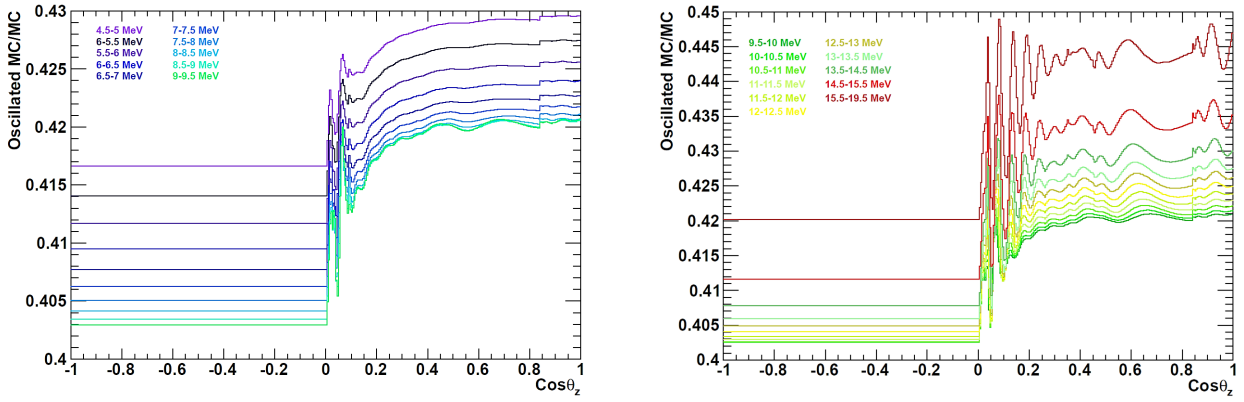

Figure 10.8: The energy dependence of the single day and 1000 night bin predictions used in Eq.10.17: $\rho_{i,\mathrm{Z}}/\rho_{i,\mathrm{All}}$. These predictions are for $(\sin^2\theta_{12}, \Delta m^2_{21}) = (0.314, 4.84 \times 10^{-5}\ \mathrm{eV}^2)$. Figure taken from [48].

Integrated Day-Night Asymmetry

This method of including the day-night variation is very time consuming. The spectral predictions for all four SK-Phases take approximately one week to generate, with no NSI and only one θ_{13} value. Re-running the predictions two more times while performing the

signal extraction for each prediction takes much longer. Because the parameter space is much larger by including the NSI parameters, also including the day-night variations in the solar neutrino NSI analysis is impractical. Instead, we choose to use the day-night asymmetry ($A_{\rm DN}$) of the rates. For each SK-Phase, the measured day-night asymmetry of the rates in SK, the threshold for the $A_{\rm DN}$ analysis, and the live time for the day and night periods are detailed in Table 3.9. In the standard oscillation analysis, the predicted $A_{\rm DN}$ is not used in the likelihood or the χ^2, as the effect is incorporated by the time-variation method.

$A_{\rm DN}$ is predicted during this procedure when calculating $L_{\rm with}$. To predict $A_{\rm DN}$, all energy bins above threshold are combined to form the day and night rate ratios: $b_{\rm D}$, $b_{\rm N}$, $h_{\rm D}$, and $h_{\rm N}$. In effect, the rate ratios have been integrated over energy. The night rate ratios are formed by combining over the 1000 zenith bins. As such, the name "integrated day-night asymmetry" is used here to differentiate this method from other SK analyses related to the day-night asymmetry, such as the amplitude fit method described in [96]. The integrated day-night asymmetry of the data for each phase is:

$$A_{\rm DN}^{P,\rm data} = \frac{d_{\rm D}^P - d_{\rm N}^P}{\frac{1}{2}(d_{\rm D}^P + d_{\rm N}^P)}, \tag{10.18}$$

where D (N) stands for the Day (Night) zenith bin and d corresponds to Eq. 10.7. The statistical uncertainty for $A_{\rm DN}$ is

$$\delta A_{\pm}^{P,\rm data} = \frac{4}{d_{\rm D}^{P\,2} + d_{\rm N}^{P\,2}} \sqrt{d_{\rm N}^{P\,2} \cdot \delta d_{\rm D\pm}^{P\;2} + d_{\rm D}^{P\,2} \cdot \delta d_{\rm N\mp}^{P\;2}}. \tag{10.19}$$

The spectrum prediction software was modified to save the total rate ratio (above threshold) for the day and night of b and h. That way, $(\beta_{\rm min}, \eta_{\rm min})$ may be applied in the calculation for the asymmetry after the SK combined χ^2 spectral fit is complete. The software was additionally modified to save the day and night spectra of the two species, although they are not used in this analysis.

The predicted asymmetry for b and h (Eq. 10.6) is

$$A_{\rm DN}^{P,\rm pred} = 2\frac{(b_{\rm D}^P - b_{\rm N}^P)\beta_{\rm min} + (h_{\rm D}^P - h_{\rm N}^P)\eta_{\rm min}}{(b_{\rm D}^P + b_{\rm N}^P)\beta_{\rm min} + (h_{\rm D}^P + h_{\rm N}^P)\eta_{\rm min}}. \tag{10.20}$$

The predicted values of $A_{\rm DN}$ from this simpler method agree with the corresponding values predicted during the determination of $L_{\rm DN}$.

A simple χ^2 fit between the predictions and the measured asymmetry is performed separately for each phase. These are added to the SK combined χ^2 fit to the spectrum $\chi^2_{\rm spec}$:

$$\chi^2_{\rm S+A} = \chi^2_{\rm spec} + \sum_{P=1}^{4} \chi^2_{\rm P}(A_{\rm DN}). \tag{10.21}$$

10.2.2 Results of the SK Solar Neutrino Oscillation Analysis using Integrated $A_{\rm DN}$

The number of spectral data points fit in the oscillation analysis changes between each phase and corresponds to the lower energy threshold of the spectrum analysis. The spectral data for each SK-Phase is found in Table 9.2. SK-I has a threshold 4.49 MeV and 21 data points. The threshold of SK-II is 6.49 MeV, and the total number of SK-II data points is 17. SK-III (SK-IV) has a threshold of 3.99 (3.49) MeV and 22 (23) data points. In all, the total number of spectral data points used in the SK combined spectral fit is 83. Including the integrated $A_{\rm DN}$, the total number of SK data points in the final fit is 87.

By using the integrated $A_{\rm DN}$ method for including the day-night asymmetry into the total χ^2, the energy and zenith-dependence of the asymmetry is removed. The energy dependence of the day-night asymmetry for the LOW and LMA solutions are opposite in slope: negative for LMA and positive for LOW. This behavior can be observed in Fig. 10.9. This figure shows the LMA (LOW) solution for $\sin^2\theta_{12} = 0.334$ in red (blue) along with the

results of using the integrated A_{DN} denoted by the horizontal lines. It should be noted that the lower statistics at higher energies cause the higher energy bins to have less of an impact on the day-night asymmetry. The zenith dependence of typical LMA and LOW solutions is also different, as illustrated in Fig. 10.10 for several energy ranges of SK-I data [44]. It is the combined zenith and energy dependence of the predictions that, when compared to SK data, disfavors the LOW solution and prefers the LMA solution.

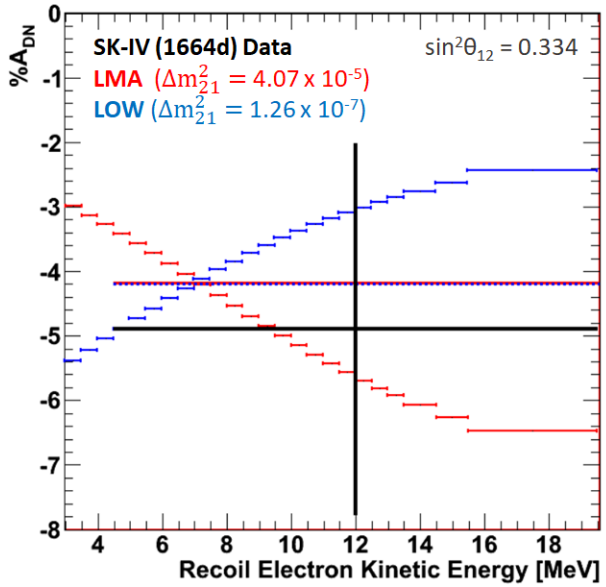

Figure 10.9: The predicted day-night asymmetry of the recoil electron spectrum in SK-IV for the LMA (red) and LOW (blue) solutions. The horizontal lines are the corresponding integrated day-night asymmetry values. The data point is the SK-IV 1664-day A_{DN} measurement of -4.9 $\pm$ 2.88% (statistical and systematic errors combined in quadrature).

The use of the integrated A_{DN} impacts the allowed regions of the $(\sin^2\theta_{12}, \Delta m^2_{21})$ parameter space compared to using L_{DN}. The results of the two methods are plotted in Fig. 10.11. The resulting one through five σ included regions (with two degrees of freedom) from using integrated A_{DN} (L_{DN}) in the analysis are plotted in black (colored) lines. The left side of the figure includes the whole $(\sin^2\theta_{12}, \Delta m^2_{21})$ parameter space (log-scale vertical axis), and the right side of the figure is zoomed into the LMA region (linear scale vertical axis). The regions of the $(\sin^2\theta_{12}, \Delta m^2_{21})$ parameter space referred to in this work are labeled on

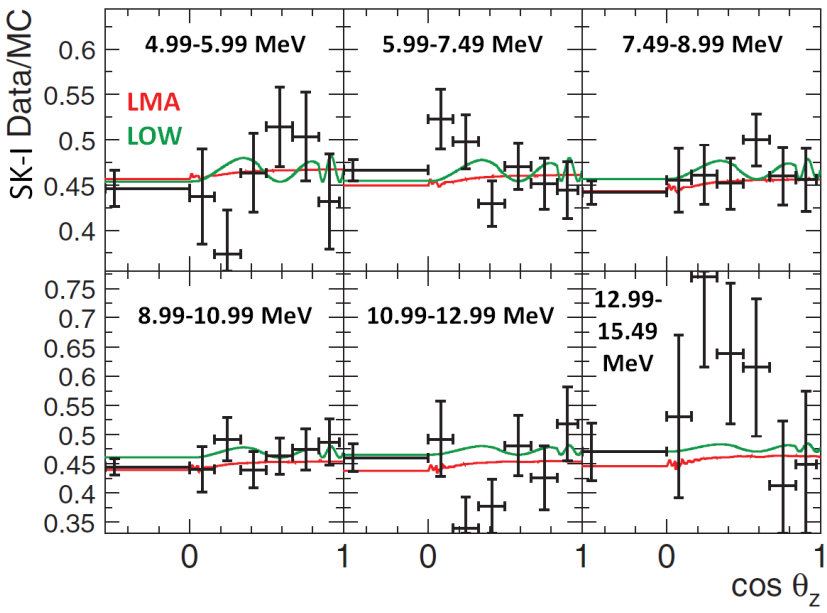

Figure 10.10: The SK-I energy-dependent zenith spectrum, along with the best-fit predictions for the LMA solution (red lines) and the LOW solution (green lines) [44]. These results assume a ^{8}B flux of $5.076\times10^6/(\mathrm{cm}^2\ \mathrm{s})$ and a *hep* flux of $32\times10^3/(\mathrm{cm}^2\ \mathrm{s})$. The predictions are for $\sin^2\theta_{12} = 0.342$ and typical LMA and LOW Δm^2_{21} values. The difference in zenith-dependent behavior of the LMA and LOW predictions is removed when using the integrated A_{DN}.

the left side of the plot, and maximal neutrino flavor-mixing is denoted by the dashed line.

Using either method, the SMA solution ($\sin^2\theta_{12} \simeq 10^{-3} \sim 10^{-2}$) is still excluded at greater than 5σ by SK data. In the LMA region, the shapes of the contours are similar, though they are shifted because they prefer smaller values of Δm^2_{21}. The rougher shapes using the L_{DN} method are predominantly due to the zenith dependence. The best fit LMA $\sin^2\theta_{12}$ is the same in both cases. However, a consequence of this method is the return of the LOW solution. The LOW solution is normally excluded at greater than 3σ by the zenith dependence of the time-variation method. The removal of the zenith information from the integrated A_{DN} actually results in the LOW solution being slightly preferred over the LMA solution. The best fit parameters for both the LMA and LOW solutions using the two methods are written in Table 10.3. In the case reporting the χ^2 for the LOW solution using

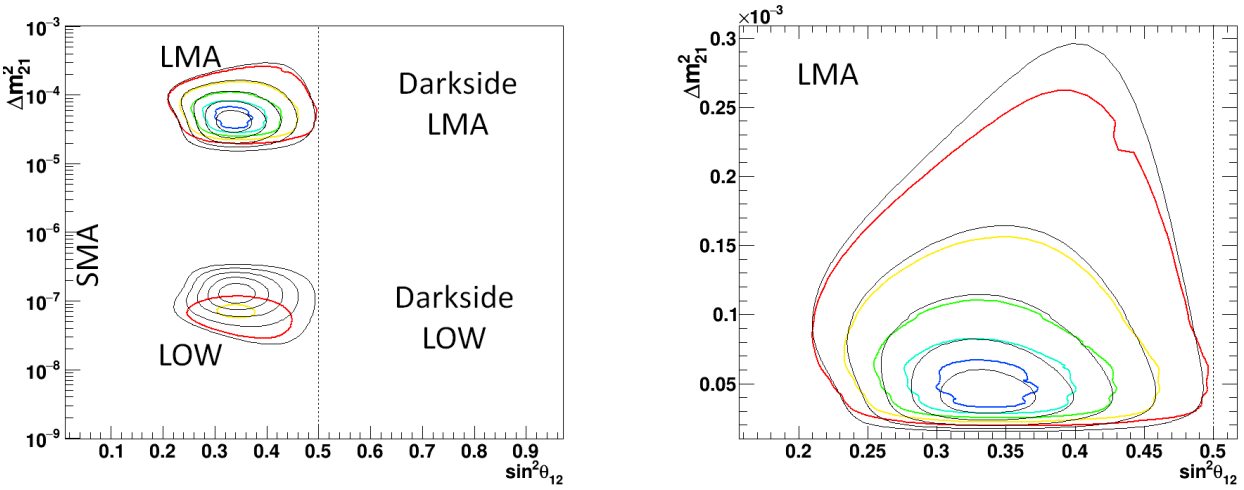

Figure 10.11: Comparison between using integrated A_{DN} (black lines) and L_{DN} (colored lines) in the solar oscillation analysis. $\mathrm{Sin}^2\theta_{13} = 0.020$ is fixed. The allowed values of $(\sin^2\theta_{12}, \Delta m^2_{21})$ are displayed by the one to five σ contours (two d.o.f.). The blue, teal, green, yellow, and red lines correspond to the 1, 2, 3, 4, and 5 σ contours respectively. Left: the allowed parameters of $(\sin^2\theta_{12}, \Delta m^2_{21})$ and labels for the various solar neutrino "solutions" in the parameter space. Right: A zoomed view of the LMA region.

L_{DN}, the same oscillation parameters as the best fit for the integrated A_{DN} method are used. The SK-Only best fit for the LMA (LOW) solution is plotted as a solid red (blue) line in Fig. 10.12 for each phase of SK. The day-night rate asymmetry is also plotted for each phase, along with the predictions for the integrated A_{DN} from the best fit $\chi^2_{\mathrm{S+A}}$. A zoomed-in plot for SK-I/II/III/IV illustration is given in Fig. 10.13. The low energy upturn on the LOW solution comes from the day-night effect and the energy dependence of the ES cross section.

While the shift in Δm^2_{21} is inherent to using the integrated A_{DN} method, Borexino's measurement of the small day-night asymmetry for 862 keV ^{7}Be solar neutrinos strongly constrains the LOW solution. When combining it with the total SK χ^2 from the combined spectral fit and the integrated A_{DN}, the LOW solution is disfavored at greater than 5σ (two degrees of freedom). Additionally, the inclusion of Borexino's data to the fit does not affect the χ^2 in the LMA region. Details of the inclusion of Borexino's measurement for use in the NSI analysis are discussed in Sec. 10.3.3.

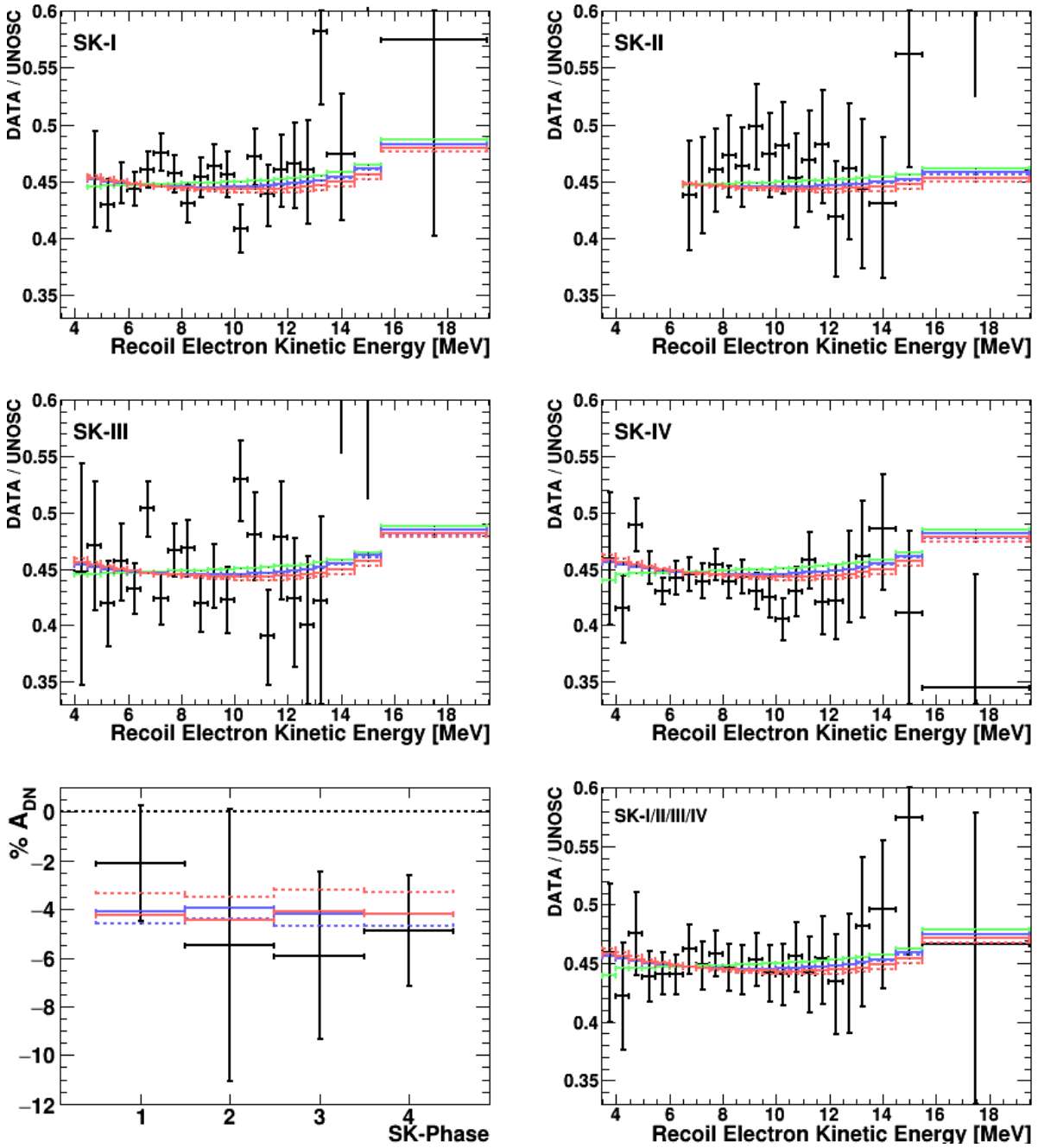

Figure 10.12: The SK Spectra and best-fit predictions (top two rows). The red (blue) lines correspond to the best fit for the LMA (LOW) solution from Table 10.3. The solid (dashed) lines correspond to SK-Only (SK+SNO) best fits using the integrated $A_{\rm DN}$. The green lines correspond to the predictions for a constant value of $P_{ee} = 0.317$ (Sec. 10.2.3). The bottom left plot contains the measured values of the SK day-night rate asymmetry, along with the predicted integrated $A_{\rm DN}$ from the best fit. All errors are statistical and energy-uncorrelated systematic errors combined in quadrature. The bottom right plot is the combined SK-I/II/III/IV spectrum (see caption for Fig. 10.13).

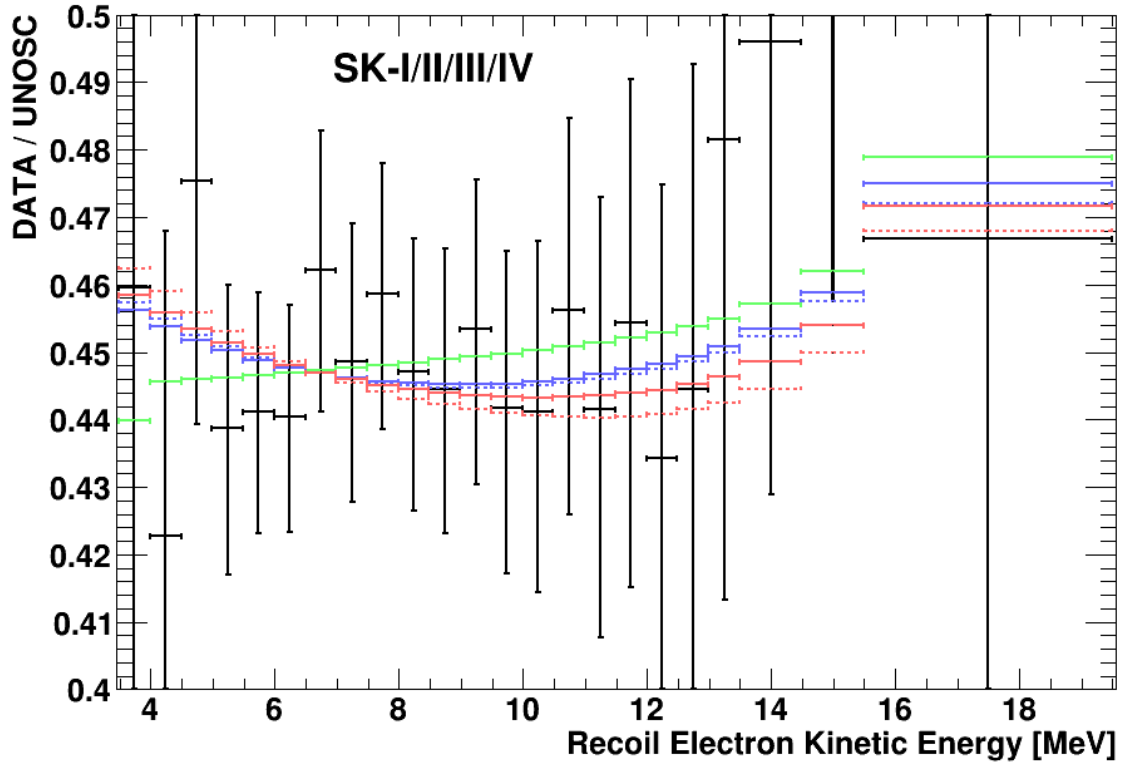

Figure 10.13: The SK-I/II/III/IV1664-day combined recoil electron spectrum. This spectrum is the combination of a given energy bin for each phase weighted by the statistical and energy-uncorrelated error. It is provided for illustrative purposes and should not be used for analysis. The red (blue) lines correspond to the best fit for the LMA (LOW) solution from Table 10.3. The solid (dashed) lines correspond to SK-Only (SK+SNO) best fits using the integrated $A_{\rm DN}$. The green lines correspond to the predictions for a constant value of $P_{ee} = 0.317$ (Sec. 10.2.3). All errors are the combined statistical and energy-uncorrelated systematic errors corresponding to the weighted sum of the errors from each phase.

Table 10.3: The best fit parameters for the oscillation analysis using $L_{\rm DN}$, and the best fit LOW and LMA parameters using integrated $A_{\rm DN}$. $\mathrm{Sin}^2\theta_{13} = 0.020$ is fixed. The final column is the χ^2 value and the number of degrees of freedom for the fit, including θ_{12} and Δm^2_{21} as free parameters. The total SK fit has 83 spectral data points and 4 day-night rate asymmetry data points. The SNO fit has 6 data points. The combined SK+SNO fit has 92 data points, since the ^{8}B NC measurement from SNO is used as a constraint. Also included are the constraints from the fit to SNO's data and the combined SK+SNO fit. For the LOW solution using $L_{\rm DN}$, uncertainties in the oscillation parameters are not included, as the region is excluded at greater than 3σ by the LMA best fit using SK data alone. The χ^2 values between both methods should not be directly compared.

Data	Method	Region	$\sin^2\theta_{12}$	Δm^2_{21} [eV^2]	χ^2/NDF
SK-Only	Integrated	LMA	$0.334^{+0.021}_{-0.010}$	$4.07^{+1.12}_{-0.76} \times 10^{-5}$	69.59/85
	$A_{\rm DN}$	LOW	$0.344^{+0.011}_{-0.021}$	$1.26^{+0.33}_{-0.21} \times 10^{-7}$	69.43/85
SNO		LMA	$0.314^{+0.010}_{-0.010}$	$5.50^{+1.67}_{-1.19} \times 10^{-5}$	1.29/6
		LOW	$0.314^{+0.010}_{-0.020}$	$1.26^{+0.33}_{-0.16} \times 10^{-7}$	0.92/6
SK+SNO	Integrated	LMA	$0.314^{+0.010}_{-0.010}$	$4.90^{+1.13}_{-0.87} \times 10^{-5}$	76.00/90
	$A_{\rm DN}$	LOW	$0.314^{+0.010}_{-0.010}$	$1.38^{+0.13}_{-0.12} \times 10^{-7}$	76.16/90
SK-Only	$L_{\rm DN}$	LMA	$0.334^{+0.021}_{-0.020}$	$4.79^{+1.31}_{-0.52} \times 10^{-5}$	58.73
		LOW	0.334	1.26×10^{-7}	91.10
SK+SNO	$L_{\rm DN}$	LMA	$0.314^{+0.010}_{-0.010}$	$4.84^{+1.54}_{-0.37} \times 10^{-5}$	64.06
		LOW	0.314	1.38×10^{-7}	104.54

10.2.3 Constant P_{ee} Fit to SK Spectrum

In addition to using solar neutrino $P_{ee}(E_\nu)$ to predict the recoil electron spectra, one may substitute the survival probabilities by polynomial and exponential functions for use in the predictions. These functional descriptions provide a model-independent method of describing the shape of $P_{ee}(E_\nu)$. A quadratic function has been employed by SNO to describe their measurement of $P_{ee}^{\rm Day}(E_\nu)$ [47]. SK has performed fits to spectral predictions created from these functional forms of $P_{ee}(E_\nu)$. Details of SK's fits and results are published in [42].

A survival probability of $P_{ee} = 0.317$ corresponds to the survival probability above ~6 MeV for the best fit to all solar neutrino data. This value is used as a constant P_{ee} fit,

Table 10.4: Results from fitting SK data to a constant $P_{ee} = 0.317$, independent of energy. The predicted recoil electron spectra include energy-dependent ES cross sections and day/night corrections. For comparison, the best fit in the LMA region to all four phases of SK is $\chi^2_{\rm spec} = 68.38$.

Fit	SK-I	SK-II	SK-III	SK-IV	Combined
$\chi^2_{\rm spec}$	18.92	5.30	27.94	15.50	69.30

independent of energy, to SK's data. The constant P_{ee} fit yields an average spectrum value of $r = 0.4268$, assuming no oscillations (Eq. 10.10). The differences in the ES cross sections between ν_e and $\nu_{\mu,\tau}$ lead to an upturn at low energy, even for this constant value of P_{ee}. Additional effects on the spectrum are introduced by day/night corrections to the rates and produce a downturn at low energy. These day/night corrections are on the order of $\sim$1.5%. The resulting recoil electron spectra are plotted as green lines in Fig. 10.12 and Fig. 10.13.

The results for the spectral fit $\chi^2_{\rm spec}$ to the constant P_{ee} are given in Table 10.4. The χ^2 values in the table do not include $L_{\rm DN}$ or the integrated $A_{\rm DN}$. The flat-fit results can be used to compare how well the fits for the predicted spectra favor or disfavor a flat spectrum and lack of a strong upturn of P_{ee} predicted by the MSW effect (in the LMA region). The best fit to all four phases of SK using the solar neutrino P_{ee} calculations is $\chi^2_{\rm spec} = 68.38$ for the LMA solution. The best fit favors the MSW upturn at about 0.96σ compared to the constant P_{ee} fit.

10.3 SK+SNO+Borexino $A_{\rm DN}^{^7{\rm Be}}$ Solar Neutrino Oscillation Analysis

10.3.1 SNO's Polynomial ^{8}B Solar Neutrino Analysis

SNO's suggested procedure of analyzing their data and combining with other experiments is described in [47]. Their procedure entails a simultaneous fit to the ^{8}B $P_{ee}^{\rm Day}(E_\nu)$ and the asymmetry in the day and night ^{8}B survival probabilities $A_{ee}(E_\nu)$ centered around $E_\nu = 10$ MeV (Eq. 3.16) and the ^{8}B flux. This fit includes correlations between all six parameters. Table 3.6 details the measured values of the fit coefficients for the SNO data and contains the corresponding correlation matrix. The SNO analysis is discussed in Sec. 3.3.4. The results of SNO's three-phase analysis [47] are displayed in Fig. 3.9 for $\sin^2\theta_{13} = 0$.

For each set of oscillation parameters, SNO simultaneously fits $P_{ee}^{\rm Day}(E_\nu)$ with quadratic functions and the asymmetry $A_{ee}(E_\nu) = 2\frac{P_{ee}^{\rm N}(E_\nu) - P_{ee}^{\rm D}(E_\nu)}{P_{ee}^{\rm N}(E_\nu) + P_{ee}^{\rm D}(E_\nu)}$ with a linear function. In the SK+SNO combined solar neutrino oscillation analysis, the day and 1000 night zenith bin survival probabilities used in the SK analyses are used to predict SNO's polynomial coefficients. The corresponding 1000 night $P_{ee}^{\rm Z}$ are combined based on SNO's $\cos\theta_{\rm Z}$ exposure. SNO's procedure of simultaneously fitting the two polynomial functions is repeated here. The resulting coefficients are compared against the corresponding measurements by SNO (Table 3.6). SNO's contours have been carefully reproduced in the SK solar neutrino oscillation analysis using SNO's prescribed procedure. The 1-5σ allowed SNO contours produced by the SK analysis are plotted in Fig. 10.14 for $\sin^2\theta_{13} = 0.020$. SNO has a slight preference for LOW solution over the LMA, but excludes the SMA solution at 3σ. The best fit points for SNO in the LMA and LOW solutions are given in Table 10.3.

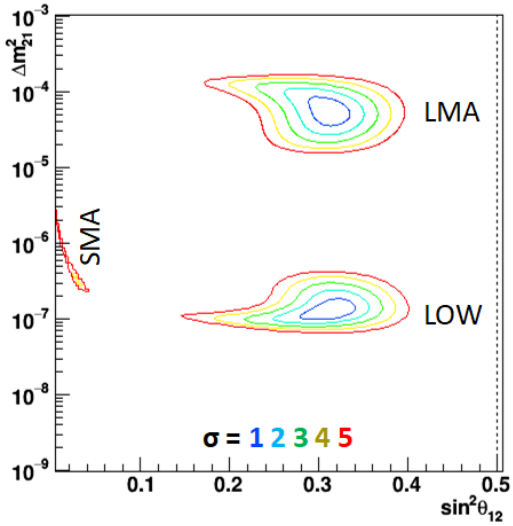

Figure 10.14: The results of the fit to SNO's data (1-5σ included regions). Here, $\sin^2\theta_{13} = 0.020$.

10.3.2 SK+SNO Combined Analysis

SNO measures a similar energy range of ^{8}B solar neutrinos as SK. A combined analysis profits from correlations and is better than simply adding the χ^2 of both experiments. The results of the fit to SNO's measurements can be described using a χ^2 of the same form as Eq. 10.14, and the χ^2 is minimized in the same way. Because the SNO data is being fit to, the β parameter is constrained directly through SNO's ^{8}B flux measurement. The η parameter is constrained based on the BS2005 SSM [57] *hep* flux constraint used by SNO [47]: $(7.9 \pm 1.2) \times 10^3/(\text{cm}^2\ \text{s})$.

By comparing the SK and SNO allowed contours (Fig. 10.15), we see that the SK 1-3σ contours in the LMA region provide a tighter constraint to Δm^2_{21} than SNO's. In the LOW region, the constraint on Δm^2_{21} is more comparable between the two experiments. We also see that SNO's contours more tightly constrain $\sin^2\theta_{12}$ in the LMA and LOW regions than SK. While the SMA solution is only excluded by SNO at greater than 3σ, SK excludes it at greater than 5σ. With the replacement of $-2\log L_{\text{DN}}$ by the sum of the integrated A_{DN} χ^2s, SK no longer disfavors the LOW solution at greater than 3σ, and both SK and SNO

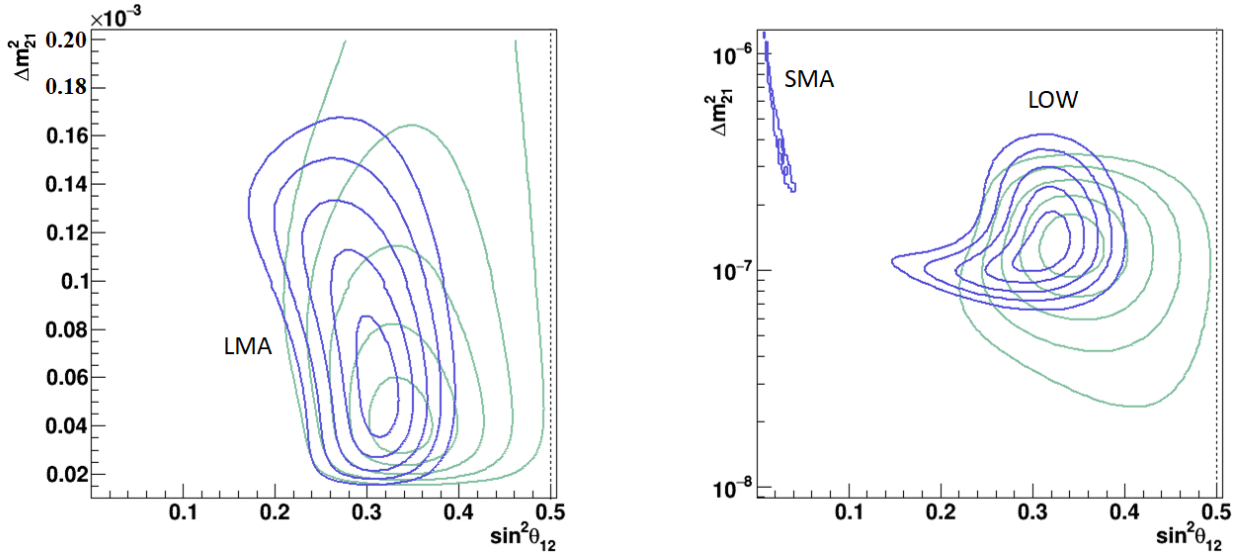

Figure 10.15: The SK-Only (integrated $A_{\rm DN}$) and SNO 1-5σ included regions for the LMA (left) and LOW (right) solutions. The LMA vertical axis is linear scale, while the LOW vertical axis is logarithmic scale.

include parts of the LOW solution at better than 1σ. The Borexino day-night asymmetry measurements discussed earlier will be used to exclude the LOW solution at greater than 5σ in the final combined fit across experiments.

The SK and SNO analyses can be combined by using an SK-like χ^2 fit to the SNO coefficients and adding this fit to the SK combined spectral fit $\chi^2_{{\rm spec},\alpha_P}$ as a fifth phase. When performing this combined fit, SNO's ^{8}B flux measurement is used to directly constrain β. The *hep* flux constraint is set to correspond to the constraint used in SNO's analysis. The resulting SK+SNO $\chi^2_{\rm SK\ spec+SNO}$ is fit to the 83 data points from SK and the five coefficients from SNO. The best-fit nuisance parameters $(\beta_{\rm min}, \eta_{\rm min})$ from the minimized χ^2 fit to SK+SNO are applied to fit the SK integrated $A_{\rm DN}$. The total $\chi^2_{\rm S+A}$ is given by Eq. 10.21, where $\chi^2_{\rm spec} \rightarrow \chi^2_{\rm SK\ spec+SNO}$. The combination of SK and SNO slightly favors the LMA solution over the LOW Solution. The predicted SK-IV spectrum for the best fit to SK+SNO data in the LMA (LOW) solution is plotted as red (blue) dashed lines in Fig. **??**.

10.3.3 The $A_{\mathrm{DN}}^{^7\mathrm{Be}}$ measurement by Borexino

Borexino's measurement of the day-night asymmetry for 862 keV ^{7}Be solar neutrinos ($A_{\mathrm{DN}}^{^7\mathrm{Be}}$) [84] is discussed in Sec. 3.3.5. Using the SK-like definition of $A_{\mathrm{DN}} = -A_{\mathrm{dn}}$ (Eq. 3.17), Borexino measures a day-night asymmetry of

$$A_{\mathrm{DN}}^{^7\mathrm{Be}} = -0.001 \pm 0.012(\mathrm{stat}) \pm 0.007(\mathrm{sys}). \tag{10.22}$$

The same analysis framework used in the SK and SNO predictions is used to determine the survival probabilities. Mono-energetic ^{7}Be 862 keV solar neutrinos are used to calculate the P_2 and P_{ee}^{Day} probabilities. The zenith-dependent probabilities are combined to form P_{ee}^{Night} using the zenith distribution in Fig. 3.10. Instead of using 1000 night zenith bins, the P_{2e}^{Z} are generated corresponding to the binning in θ_{Z} from the figure.

Since the neutrinos are mono-energetic, the differential rate with respect to the recoil electron kinetic energy T_e is proportional to the combination of the survival probabilities and differential cross sections:

$$\frac{dR}{dT_e} \propto \left[P_{ee}^{\mathrm{Z}} \frac{d\sigma_{\nu_e}}{dT_e} + (1 - P_{ee}^{\mathrm{Z}}) \frac{d\sigma_{\nu_x}}{dT_e} \right]. \tag{10.23}$$

Here, $\frac{d\sigma_{\nu_e}}{dT_e}$ is the differential cross section corresponding to (ν_e e) ES, and $\frac{d\sigma_{\nu_x}}{dT_e}$ corresponds to the ($\nu_{\mu,\tau}$ e) ES cross sections. Because the Borexino analysis sets the range of $T_e \in [550\ \mathrm{keV}, 800\ \mathrm{keV}]$, we integrate the cross sections over T_e, up to $T_e^{\mathrm{max}} \simeq$665 keV. As used in the spectrum predictions, the (ν e) cross sections include the radiative corrections from [41].

When calculating the predicted $A_{\mathrm{DN}}^{^7\mathrm{Be}}$, both the flux and the number of target electrons in the detector's fiducial volume (N_e) cancel. After integrating over T_e, the predicted day-

night asymmetry simply becomes

$$A_{\rm DN}^{^7{\rm Be}} = 2\frac{\left[\sigma_{\nu_e}P_{ee}^{\rm D} + \sigma_{\nu_x}(1-P_{ee}^{\rm D})\right] - \left[\sigma_{\nu_e}P_{ee}^{\rm N} + \sigma_{\nu_x}(1-P_{ee}^{\rm N})\right]}{\left[\sigma_{\nu_e}P_{ee}^{\rm D} + \sigma_{\nu_x}(1-P_{ee}^{\rm D})\right] + \left[\sigma_{\nu_e}P_{ee}^{\rm N} + \sigma_{\nu_x}(1-P_{ee}^{\rm N})\right]}. \tag{10.24}$$

Because the reaction that produces ^{7}Be solar neutrinos is the parent reaction to the one that produces ^{8}B solar neutrinos, the production location of the two species of solar neutrinos is similar. However, the energy of the neutrinos differs by approximately an order of magnitude. This means that the shape of equivalent levels of the day-night asymmetry for ^{7}Be 862 keV solar neutrinos will be similar to that of ^{8}B solar neutrinos, except shifted down by about one order of magnitude. The shape of the contours of equal values in $A_{\rm DN}$ are also in good agreement with Fig. 3.11, after accounting for the shift in E_ν between the two species.

A simple χ^2 fit of the predicted ^{7}Be day-night asymmetry to the Borexino measurement is performed, denoted as $\chi^2_{\rm B^7BeA}$. The results of the fit to the Borexino $A_{\rm DN}^{^7{\rm Be}}$ measurement are plotted in Fig. 10.16. The 1-5σ exclusion contours are given, along with the resulting LMA solution of SK+Borexino $A_{\rm DN}^{^7{\rm Be}}$. The 3σ exclusion contours reported by the Borexino collaboration (right side of Fig. 3.10 [84]) were accurately reproduced.

10.4 Results of the SK+SNO+Borexino $A_{\rm DN}^{^7{\rm Be}}$ Solar Neutrino Oscillation Analysis

Because the ratio in Eq. 10.24 removes any dependence on the flux, the correlations in the flux between the ^{7}Be and the ^{8}B (and *hep*) neutrinos from the SSM cancel. Therefore, the day-night asymmetry $\chi^2_{\rm B^7BeA}$ can simply be added to the total $\chi^2_{\rm S+A}$ from the SK combined spectral fit or the SK+SNO fit:

$$\chi^2_{\rm comb} = \chi^2_{\rm S+A} + \chi^2_{\rm B^7BeA}. \tag{10.25}$$

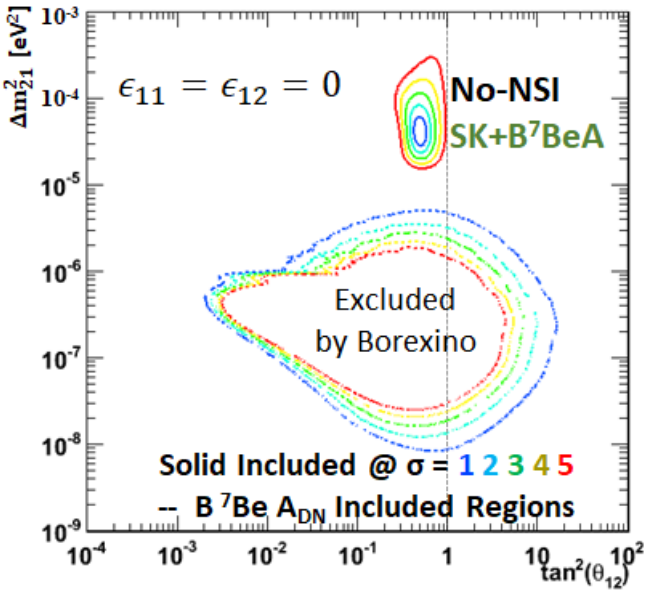

Figure 10.16: The SK+Borexino ^{7}Be $A_{\rm DN}$ results (1-5σ included regions, solid lines), and the excluded Borexino ^{7}Be $A_{\rm DN}$ regions (1-5σ included regions, dashed lines).

The results of the oscillation analysis, the 1-5σ included regions of the $(\sin^2\theta_{12}, \Delta m^2_{21})$ parameter space (two degrees of freedom), are plotted in Fig. 10.17. The top-left plot is the SK-Only with integrated $A_{\rm DN}$ results, while the bottom-left includes the fit to the Borexino $A^{^7{\rm Be}}_{\rm DN}$. The center plots are the SNO results without (center-top) and with (center-bottom) the fit to the Borexino $A^{^7{\rm Be}}_{\rm DN}$. The top-right plot is the SK+SNO results without Borexino. The results of the combined fit (SK+SNO+Borexino $A^{^7{\rm Be}}_{\rm DN}$) are given in the bottom-right plot.

The LOW solution in the combined fit is excluded at greater than 5σ, while leaving the $\chi^2_{\rm comb}$ in the LMA region unaltered from the $\chi^2_{\rm S+A}$ value. Once including NSI in the matter potential, the $\chi^2_{\rm B^7BeA}$ removes any LOW-equivalent solutions that return due to the change in the method of including the SK A_{DN} into the NSI analysis. When including the data from SNO, the same procedure for combining χ^2 applies. In the no-NSI case for SK+SNO, the LOW solution is again excluded while leaving the $\chi^2_{\rm SK+SNO}$ unchanged in the LMA region. The χ^2 for the SK+Borexino LOW solution becomes 625.47, and the χ^2 for the SK+SNO+Borexino fit is 758.50. When combing SK χ^2s (or SK+SNO) with Borexino

in the NSI analysis, LOW-like solutions are strongly disfavored, and only LMA-like solutions remain.

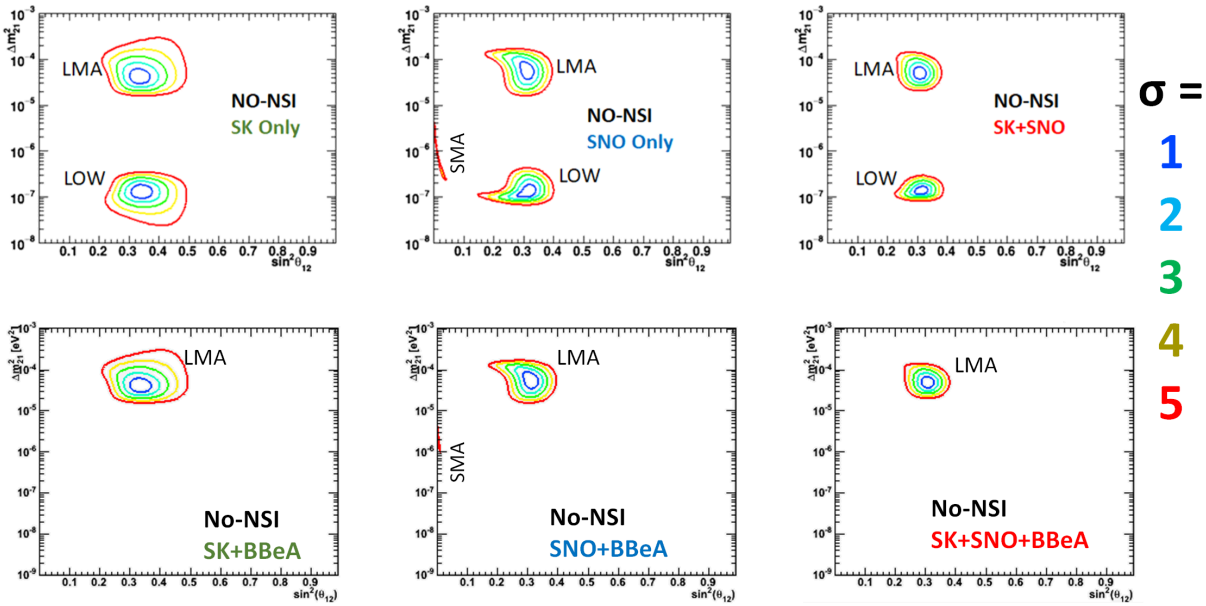

Figure 10.17: The SK+Borexino ^{7}Be A_{DN} results (1-5σ included regions, solid lines), and the excluded Borexino ^{7}Be A_{DN} regions (1-5σ included regions, dashed lines).

Chapter 11

The Solar Neutrino NSI Analysis

The formalism of including NSI into neutrino-matter interactions is discussed in Sec. 2.4. The addition of the effective two-flavor NSI parameters ϵ_{11}^f and ϵ_{12}^f ($f = e$, u, d) into the matter potential (Eq. 2.77) influences the neutrino wavefunction as a solar neutrino propagates through matter.

The NSI Lagrangian (Eq. 2.69) is constructed to leave the charge current interactions that produce solar neutrinos unaffected. This means that the (ν_e D) CC interactions in SNO, the CC antineutrino interactions in the liquid scintillator of KamLAND, and the CC reactions detected by the radiochemical experiments will remain unchanged by the introduction of NSI [16]. Neutrino-electron elastic scattering reactions can be affected by the extra coupling with electrons through $\epsilon_{\alpha\beta}^e$ ($\alpha, \beta = e, \mu, \tau$) from the NSI matter potential in Eq. 2.73:

$$H_{mat}^{NSI} = \sqrt{2} G_F N_e(r) \begin{bmatrix} 1+\epsilon_{ee} & \epsilon_{e\mu} & \epsilon_{e\tau} \\ \epsilon_{\mu e}^* & \epsilon_{\mu\mu} & \epsilon_{\mu\tau} \\ \epsilon_{\tau e}^* & \epsilon_{\tau\mu}^* & \epsilon_{\tau\tau} \end{bmatrix}. \tag{11.1}$$

These $\epsilon_{\alpha\beta}$ parameters are the sum of the contributions from each fermion-neutrino interac-

tions scaled by Y_f, the ratio of the local fermion density N_f by the local electron density N_e (Eq. 2.78):

$$\epsilon_{\alpha\beta} = \epsilon^e_{\alpha\beta} + \epsilon^d_{\alpha\beta} Y_d + \epsilon^u_{\alpha\beta} Y_u = \sum_{f=e,u,d} Y_f \epsilon^f_{\alpha\beta}, \tag{11.2}$$

where $Y_f = N_f/N_e$ for $f = e$, u, d. The $\epsilon^e_{\alpha\beta}$ parameters would modify the cross sections through both the axial and vector currents. The neutrino-electron ES cross sections in SK, Borexino, and SNO (D_2O), and, therefore, the detection reactions, would also be affected by $\epsilon^e_{\alpha\beta}$. In this analysis, any extra contribution due to NSI with electrons in matter is neglected ($\epsilon^e_{\alpha\beta} = \epsilon^e_{11} = \epsilon^e_{12} = 0$) so that the ES cross sections remain unaffected. Only the NSI between solar neutrinos and a single type of quark (u or d) is considered at a time.

The neutral current reaction in SNO could also be affected by NSI, since that reaction is dependent on the axial current. This analysis uses the NC constraint from SNO, as well as their data in the combined fit (SK+SNO+Borexino $A^{^7\mathrm{Be}}_{\mathrm{DN}}$). Any extracted dependence of the $\epsilon^f_{\alpha\beta}$ from either ϵ^f_{11} or ϵ^f_{12} would have to be the vector component $\epsilon^{V,f}_{\alpha\beta}$ (Eq. 2.72). The axial component would need to be set to zero: $\epsilon^{A,f}_{\alpha\beta} = 0 \rightarrow \epsilon^{R,f}_{\alpha\beta} = \epsilon^{L,f}_{\alpha\beta}$. This is the same procedure used by Gonzalez-Garcia and Maltoni [17].

Current experimental constraints to flavor-dependent NSI ($\epsilon^f_{\alpha\beta}$) have been performed by SK using atmospheric data [127] and by the neutrino beam experiments NuTeV [128][129] and CHARM-II [130][131]. These analyses constrain the μ-related terms to be approximately zero, i.e. $\epsilon_{\mu\alpha} = \epsilon_{\beta\mu} \simeq 0$. Additional constraints have been published by the COHERENT neutrino-nucleus elastic scattering experiment [132] for electron-flavor vector-coupled NSI parameters: (ϵ^{dV}_{ee}, ϵ^{uV}_{ee}). The results of the analysis presented in this work can be used in conjunction with the results from these works to obtain limits on $\epsilon^{Vf}_{\alpha\beta}$, for $f =$ u or d. The dependence of ϵ^f_{11} and ϵ^f_{11} on $\epsilon^f_{\alpha\beta}$ and the parameters of U_{PMNS} are given by Eq. 2.82 and Eq. 2.83 respectively. These effective NSI terms modify the two-flavor matter potential in

Eq. 2.41 to become:

$$V_{\rm NSI} = \frac{G_F N_e}{\sqrt{2}} \begin{bmatrix} \cos^2\theta_{13} + Y_f \epsilon^f_{11} & Y_f \epsilon^f_{12} \\ Y_f \epsilon^{f*}_{12} & -\cos^2\theta_{13} - Y_f \epsilon^f_{11} \end{bmatrix}, \tag{11.3}$$

where the NSI parameters in Eq. 2.77 have been written explicitly in terms of ϵ^f_{11} and ϵ^f_{12} (f = u, d). Explicitly writing the effective mixing angle in matter (Eq. 2.80) in terms of ϵ^f_{11} and ϵ^f_{12}, one obtains:

$$\tan(2\theta_{\rm NSI}) = \frac{A(\cos^2\theta_{13} + Y_f\epsilon^f_{11}) - \Delta m^2_{21}\cos(2\theta_{12})}{AY_f\epsilon^f_{12} + \Delta m^2_{21}\sin(2\theta_{12})}, \tag{11.4}$$

where $A = 2\sqrt{2}G_F N_e E_\nu$. Similarly, writing out the explicit dependence of the effective squared mass splitting in matter (Eq. 2.79) in terms of ϵ^f_{11} and ϵ^f_{12}, one gets:

$$\Delta m^2_{\rm NSI} = \sqrt{\left[(A(cos^2\theta_{13} + Y_f\epsilon^f_{11}) - \Delta m^2_{21}\cos(2\theta_{12})\right]^2 + \left[AY_f\epsilon^f_{12} + \Delta m^2_{21}\sin(2\theta_{12})\right]^2}. \tag{11.5}$$

It is the effective NSI parameters ϵ^f_{11} and ϵ^f_{12} (f = u or d) that will be tested in the analysis presented in this work. The extraction of constraints on $\epsilon^f_{\alpha\beta}$ is beyond the results of this analysis, which focuses solely on constraints solar neutrino data place on ϵ^f_{11} and ϵ^f_{12} for f=u or d.

Solar neutrino data, including data from SK and SNO, has been used by theorists to constrain the NSI parameters ϵ^f_{11} and ϵ^f_{12} in Friedland et al. [16] and Gonzalez-Garcia and Maltoni [17]. These analyses constrain Δm^2_{21} using fits to KamLAND data (assuming CPT-invariance and antineutrino-NSI interactions in the Earth's crust). The impact that NSI has on the regions of $(\sin^2\theta_{12}, \Delta m^2_{21})$ allowed by KamLAND's reactor antineutrino measurements are somewhat insensitive to NSI due to the short path of the antineutrino through the Earth's crust. However, NSI does weaken their constraint on Δm^2_{21}, and the "darkside" region ($\sin^2\theta_{12} > 0.5$) agrees with KamLAND's data for more negative values of

ϵ^f_{11} [17][133]. Fig. 11.1 shows the results from Gonzalez-Garcia and Maltoni [17], which uses fits to all available solar and KamLAND data. The left side shows the results for NSI with u-quarks, and the right side shows the results for NSI with d-quarks. The top row shows the allowed regions of $(\sin^2\theta_{12}, \Delta m^2_{21})$, and the bottom row shows the allowed regions of $(\epsilon^f_{\rm D}, \epsilon^f_{\rm N})$. One should note that $\epsilon^f_{11} = -2\epsilon^f_{\rm D}$ and $\epsilon^f_{12} = 2\epsilon^f_{\rm N}$ (Eq. 2.81). The regions of color denote their results using the polynomial fits to SNO's data, while the black lines denote fits to SNO's measured fluxes and spectra. The green shaded regions denote the constraints from atmospheric and long baseline data. Without NSI, the combined solar and KamLAND measurements constrain Δm^2_{21} to be between $\sim 6.9\times10^{-5}$ and $\sim 8.2\times10^{-5}$ eV^2 at 3σ. The slightly weakened Δm^2_{21} constraints for the combined solar and KamLAND measurements are evidenced in this plot.

In both Friedland et al. and in Gonzalez-Garcia and Maltoni, their analysis employs an analytic approximation of P_{ee} instead of tracing the neutrino wavefunction through the Sun (or the Earth). This approximation agrees well with the wavefunction-tracing method for the LMA and darkside regions but breaks down when the adiabaticity of neutrino flavor transition is violated. This violation occurs for small values of $\sin^2\theta_{12} < 0.08$, which corresponds to part of the small mixing angle (SMA) solution of the solar neutrino oscillation parameter space. The analytic method works by considering the effect of the local electron density (and quark density) where the neutrino is created on the matter potential, as the local densities are the dominant contribution to the MSW effect. The survival probability is calculated assuming the exponential solar mass density profile, and the analytic approximation averages out any directional information [16]. The analytic approximation also assumes incoherent propagation of the neutrino mass eigenstate from the Sun to the Earth.

To avoid the breakdown of the analytic approximation, and to test a wider region of the parameter space, the standard method employed by SK of tracing the neutrino wavefunction through matter (Sec. 10.1) is used in the analysis presented here. The implementation of

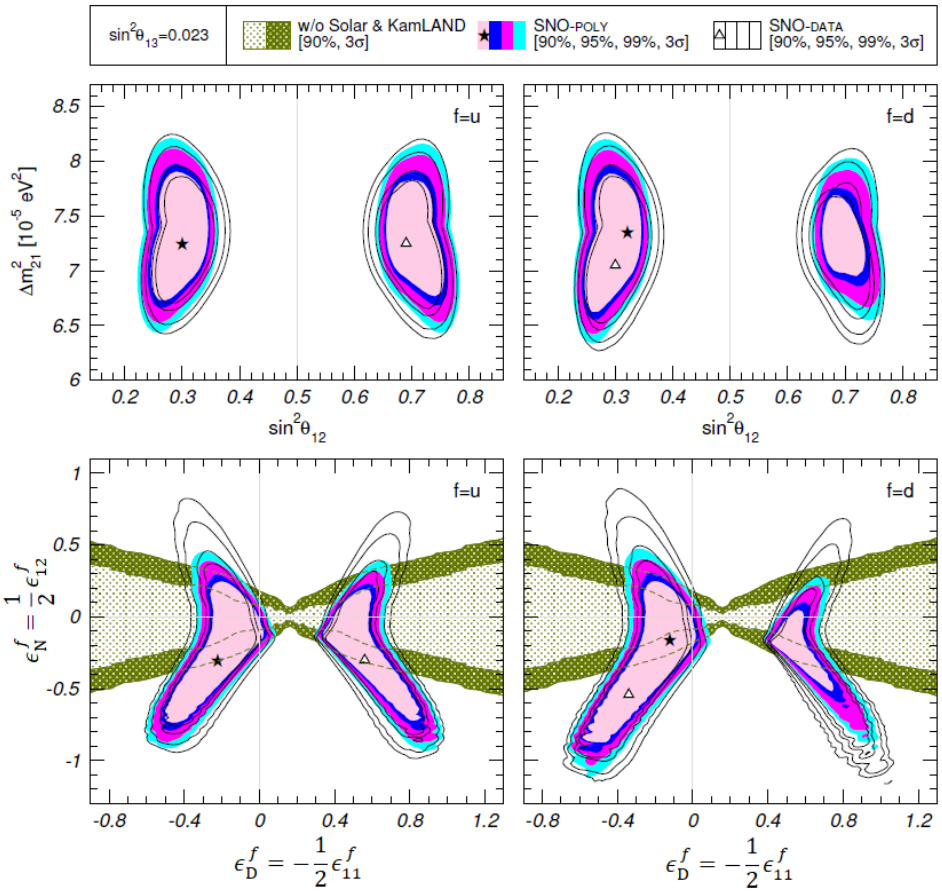

Figure 11.1: The allowed regions for the solar neutrino oscillation parameters $(\sin^2\theta_{12}, \Delta m^2_{21})$ and NSI parameters published by Gonzalez-Garcia and Maltoni [17]. These contours are the result of fitting to all available solar and KamLAND data. The left side shows the results for NSI with u-quarks, and the right side shows the results for NSI with d-quarks. The top row shows the allowed regions of $(\sin^2\theta_{12}, \Delta m^2_{21})$, and the bottom row shows the allowed regions of $(\epsilon^f_{\rm D}, \epsilon^f_{\rm N})$. Here, D (N) stands for the diagonal (non-diagonal) component in the two-flavor NSI matter potential. It should be noted that $\epsilon^f_{11} = -2\epsilon^f_{\rm D}$ and $\epsilon^f_{12} = 2\epsilon^f_{\rm N}$. The regions of color denote their results using the polynomial fits to SNO's data, while the black lines denote fits to SNO's measured fluxes and spectra. The green shaded regions denote the constraints from atmospheric and long baseline data.

NSI into the tracing method of determining P_{ee} was compared to the analytic approximation in LMA-like regions for various sets of $(\epsilon_{11}^f, \epsilon_{12}^f)$ values. The comparisons showed good agreement of less than $\sim$1% deviation in the tested regions. In the analysis presented in this work, KamLAND reactor antineutrino data is not used.

With these choices, we look at the effect the NSI parameters have on SK's predicted recoil electron spectra. We can then use SK's spectra and A_{DN} data, SNO's measured neutrino spectrum, and Borexino's A_{DN} measurement of ^{7}Be solar neutrinos to constrain the allowed values of $(\epsilon_{11}^{u,d}, \epsilon_{12}^{u,d})$ and $(\sin^2\theta_{12}, \Delta m_{21}^2)$. In this analysis, the tested values of $\sin^2\theta_{12}$ are between 10^{-4} and 1, and the tested values of Δm_{21}^2 are between 10^{-9} and 10^{-3} eV^2. The methods of creating the predictions for the three experiments and performing the fits to the data are the same methods used in the no-NSI case described in Ch. 10.

11.1 The Effects of NSI on P_{ee} and Recoil Electron Spectra Predictions

Fig. 11.2 displays the effects that NSI has on the survival probabilities as a function of $E_\nu/\Delta m_{21}^2$. The top four panels are for d-quark NSI, and the bottom four panels are for u-quark NSI. The left side is for $\sin^2\theta_{12} = 0.334$, which corresponds to the best fit LMA point in the no-NSI case. The right side is for a darkside value of $\sin^2\theta_{12} = 0.799$. The first and third panels are for non-zero values of ϵ_{11}^f, and the second and fourth rows are for non-zero values of ϵ_{12}^f.

When analyzing the effect of ϵ_{11}^f and ϵ_{12}^f on the oscillation probabilities and the resulting recoil electron spectral predictions, it is helpful to look at the best fit in the LMA and an equivalent point in the darkside region. Additionally, when one NSI parameter is being evaluated, the other parameter is held to zero. While the effect of NSI on LOW-like solutions

will be discussed, KamLAND's constraints on Δm^2_{21} (assuming CPT-invariance) would remove these solutions from consideration, making them less interesting than the LMA region. Because KamLAND data is not used in this analysis, and in the case of CPT violation, the Borexino $A^{^7\mathrm{Be}}_{\mathrm{DN}}$ measurement removes LOW-like solutions independently of KamLAND.

For this reason, the primary focus of this analysis will be on LMA-like solutions. To simplify the discussion, the NSI between u-quarks and solar neutrinos will be used for example survival probabilities, spectra, and contours. Small differences between using up or down quarks for NSI interactions occur due to the differences in the abundances of the quarks in the Sun where the neutrinos are produced. The differing densities can be seen on the left side of Fig. 3.3. These small differences have a small, though non-negligible, impact on the best-fit points with NSI and the allowed parameters. One aspect of these differences is evidenced in Fig. 11.2 (first and third row) by how rapidly the onset of transitioning between an LMA-like P_{ee} and a darkside-like P_{ee} occurs for a step-size of $\Delta\epsilon^f_{11} = 0.1$. In the d-quark case (first row), the transition is slower, taking five steps. In the u-quark case (third row), the transition is more rapid, occurring in only three steps. The smaller d-quark density causes a slightly finer scanning of the NSI effects than with the larger u-quark density.

The Effect due to ϵ^f_{11}

The NSI parameter ϵ^f_{11} shifts the onset of the MSW effect (matter-dominated oscillations) for $P_{ee}(E_\nu/\Delta m^2_{21})$. For values of $\sin\theta_{12} < 0.5$, positive values of NSI shift the onset of the MSW effect to smaller values of $(E_\nu/\Delta m^2_{21})$. Large values of ϵ^f_{11} compress the transition region of the MSW effect to smaller $(E_\nu/\Delta m^2_{21})$. Large values of ϵ^f_{11} also affect the LOW solution by bringing the P_{ee} out of the suppressed MSW region, which normally occurs at higher $(E_\nu/\Delta m^2_{21})$, to lower values of $(E_\nu/\Delta m^2_{21})$. The LMA region is shifted towards smaller values of $\sin^2\theta_{12}$ and to larger values of Δm^2_{21}.

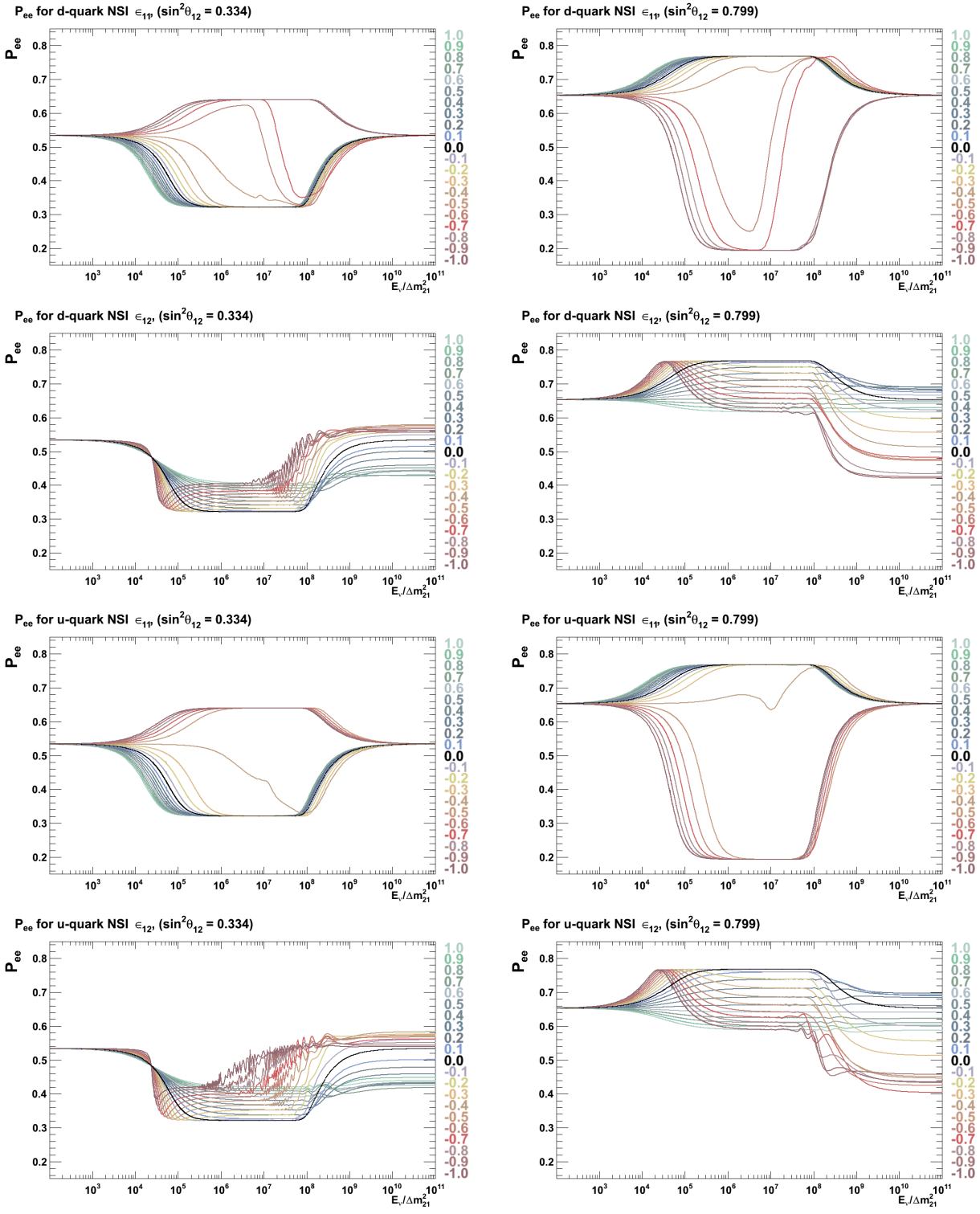

Figure 11.2: ^{8}B solar neutrino $P_{ee}^{\rm Day}(E_\nu/\Delta m^2_{21})$. The top four panels are for (ν d) NSI, and the bottom four panels are for (ν u) NSI. The left (right) side is the effect that NSI has on an LMA (darkside) P_{ee}. The first, second, third, and fourth rows correspond to NSI with $\epsilon^{\rm d}_{11}$, $\epsilon^{\rm d}_{12}$, $\epsilon^{\rm u}_{11}$, and $\epsilon^{\rm u}_{12}$ respectively, while holding the other NSI term to zero.

The situation is reversed for darkside P_{ee}. Large positive values of ϵ^f_{11} tend to slowly increase P_{ee} in the MSW region of $(E_\nu/\Delta m^2_{21})$, while negative values suppress P_{ee}. The effect that ϵ^f_{11} has on the ^{8}B solar neutrino survival probability can be seen in the first and third row of Fig. 11.2. The left side panels of the figure are for the best-fit LMA ($\sin^2\theta_{12} = 0.334$). The effect that $\epsilon^{\rm u}_{11}$ has on the spectral predictions in the four regions of interest (LMA, LOW, darkside LMA, darkside LOW) is displayed in Fig. 11.3. The plotted spectral predictions are the combined ^{8}B and *hep* total rates.

For negative values of ϵ^f_{11}, the effects are reversed. The MSW effect on the LMA P_{ee} is delayed to larger $E_\nu/\Delta m^2_{21}$ and eventually causes the shape to be more darkside-like. The darkside P_{ee} becomes suppressed until it has a similar shape to the no-NSI LMA P_{ee}, and the LMA-like region shifts toward larger values of $\sin^2\theta_{12}$. When the LMA-like region gets close to the maximal mixing boundary at $\sin^2\theta_{12} = 0.5$, the preferred solution is at small values of $\sin^2\theta_{12}$ (the SMA-like solution) where the measured recoil electron spectra do not agree well with the predictions. This occurs because, at maximal mixing, $P^{\rm Day}_{ee} = 0.5$, independent of any matter effects in the Sun. Any Earth-matter-induced effects are only on the level of a few percent. The SK data strongly disfavors maximal mixing case. For NSI-affected spectra, this situation occurs around $\epsilon^f_{11} \simeq -0.4$. Beyond $\epsilon^f_{11} \simeq -0.4$, the LMA-like region is in the darkside of the $\sin^2\theta_{12}$ space. For more negative values of ϵ^f_{11}, the darkside LMA-like region begins to be pulled to higher values of Δm^2_{21}, similar to large positive values of ϵ^f_{11}. The effects on the LOW solution are similar. Fig. 11.4 shows the effect of $\epsilon^{\rm u}_{11}$ on the 1-3σ allowed contours in the $(\sin^2\theta_{12}, \Delta m^2_{21})$ parameter space. These allowed regions are with respect to the minimum χ^2 for the given pair of NSI parameters used to create the spectral and $A_{\rm DN}$ predictions.

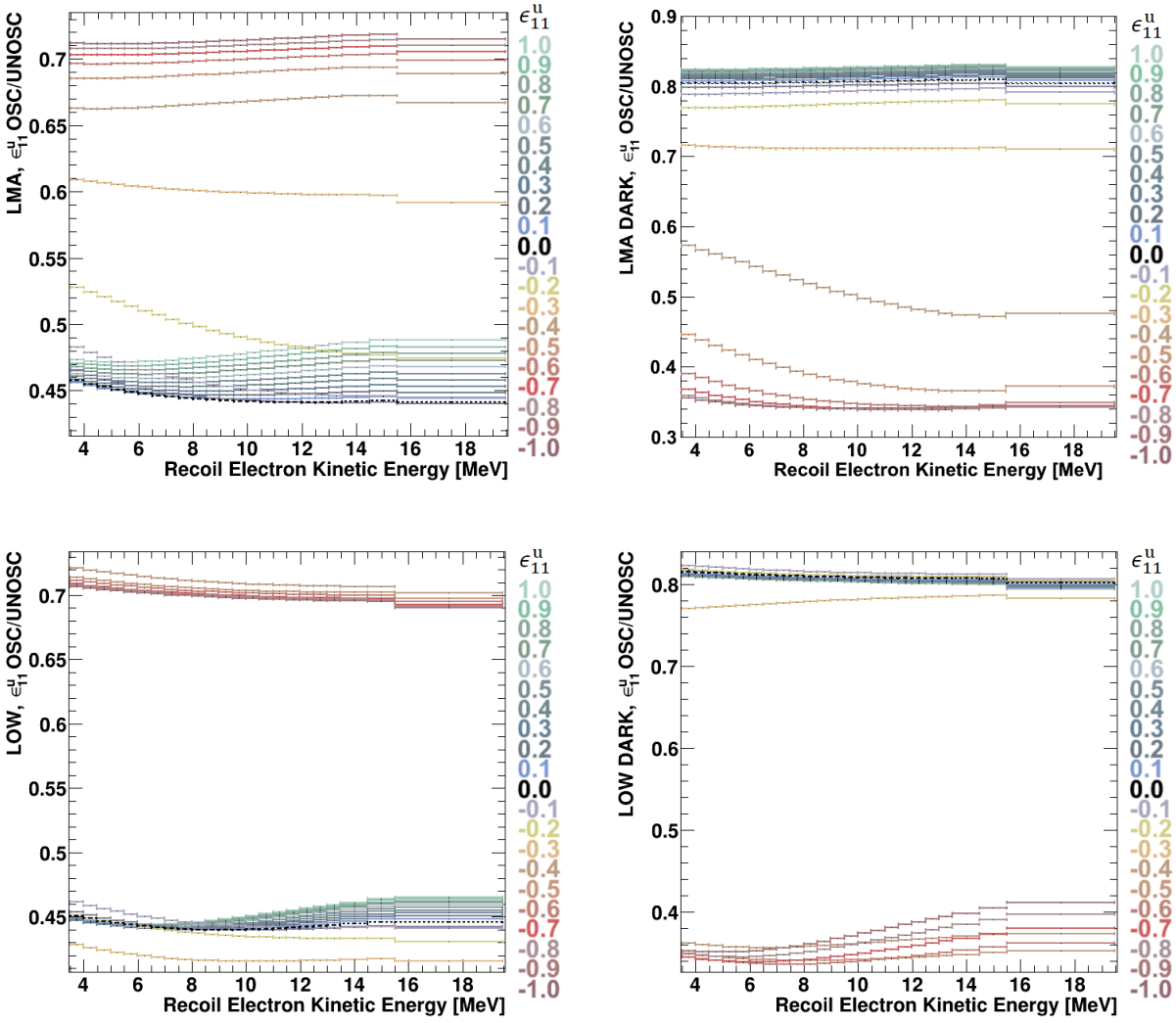

Figure 11.3: The effect of ϵ^u_{11} on the SK-IV recoil electron spectrum predictions for the LMA region (top-right) and LOW region (bottom-left), and the darkside equivalents (darkside LMA = top-right and darkside LOW = bottom-right). On the left $\sin^2\theta_{12} = 0.334$, and on the right $\sin^2\theta_{12} = 0.799$. The top row corresponds to $\Delta m^2_{21} = 4.07 \times 10^{-5}$ eV^2, while the bottom row corresponds to $\Delta m^2_{21} = 1.26 \times 10^{-7}$ eV^2. The spectral predictions include the induced recoil electrons from both ^{8}B and *hep* neutrinos.

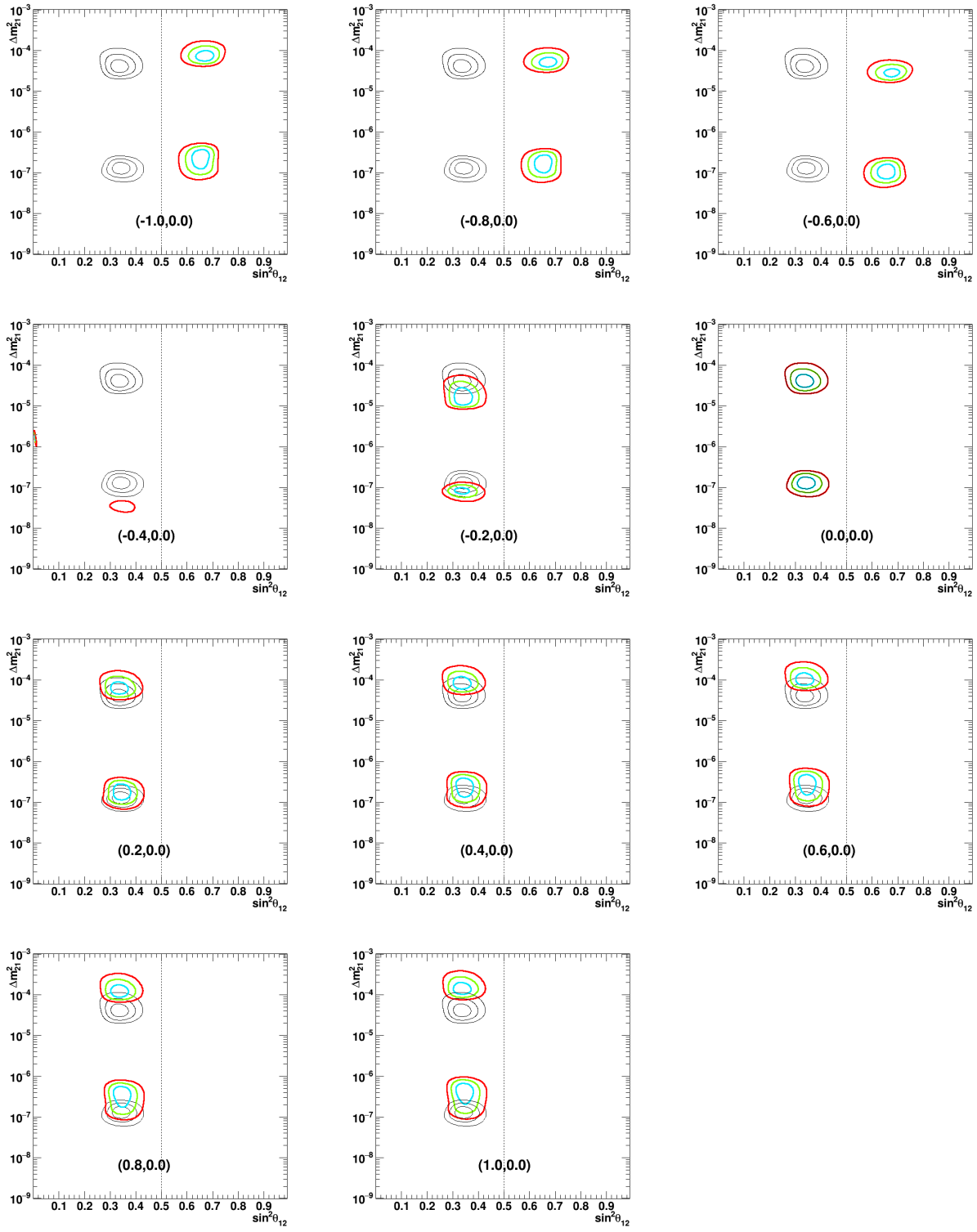

Figure 11.4: The 1-3σ (2 d.o.f.) allowed regions of $(\sin^2\theta_{12}, \Delta m^2_{21})$ for various values of ϵ^{u}_{11} in the SK-Only case. The minimum χ^2 is with respect to the NSI parameters given in each plot. The 1 (cyan), 2 (green) and 3 (red) σ allowed regions for the given NSI case are displayed. The no-NSI contours (black) are displayed for reference.

The Effect due to ϵ_{12}^{f}

The NSI parameter ϵ_{12}^{f} alters the shape of the transition between vacuum-dominated and matter-dominated oscillations caused by the MSW effect. In the LMA region, more positive values of ϵ_{12}^{f} cause the upturn to become shallower, resulting in an increase to P_{ee}. Negative values of ϵ_{12}^{f} cause the upturn to distort into a downturn before rising back up to the corresponding vacuum-dominated value of P_{ee}. This downturn distortion effect can also cause an upswing to larger P_{ee} values at smaller $E_\nu/\Delta m^2_{21}$ than the downturn before returning to the vacuum-dominated values. It also causes the P_{ee} value in the matter-dominated region to be larger than when NSI is not present. The NSI parameter ϵ_{12}^{f} can also cause the onset of small rapid transitions in P_{ee}. Rapid distortions are averaged out when creating the spectral predictions due to energy resolution effects. The effect that ϵ_{12}^{f} has on the ^{8}B solar neutrino survival probability can be seen in the second and fourth rows of Fig. 11.2.

For the darkside P_{ee}, large magnitudes of ϵ_{12}^{f} distort the hump in the onset of the MSW region into a soft downturn. More negative values of ϵ_{12}^{f} cause more of a hump in P_{ee} before falling to lower values that match the positive ϵ_{12}^{f} of the same magnitude. The effect that $\epsilon_{12}^{\mathrm{u}}$ has on the spectral predictions in the four regions of interest (LMA, LOW, darkside LMA, darkside LOW) is displayed in Fig. 11.5.

The effect of ϵ_{12}^{f} on the LMA-like region is complicated, as the LMA-like solution is distorted. Negative values of ϵ_{12}^{f} stretch and break apart the region, while shifting it to lower values of $\sin^2\theta_{12}$. Positive values of ϵ_{12}^{f} stretch the allowed region in $\sin^2\theta_{12}$. The predicted spectra do not agree well with the no-NSI LOW-like spectra, and that region becomes disfavored. Fig. 11.6 shows the effect of $\epsilon_{12}^{\mathrm{u}}$ on the 1-3σ allowed contours in the $(\sin^2\theta_{12}, \Delta m^2_{21})$ parameter space. These allowed regions are with respect to the minimum χ^2 for the given pair of NSI parameters used to create the predictions.

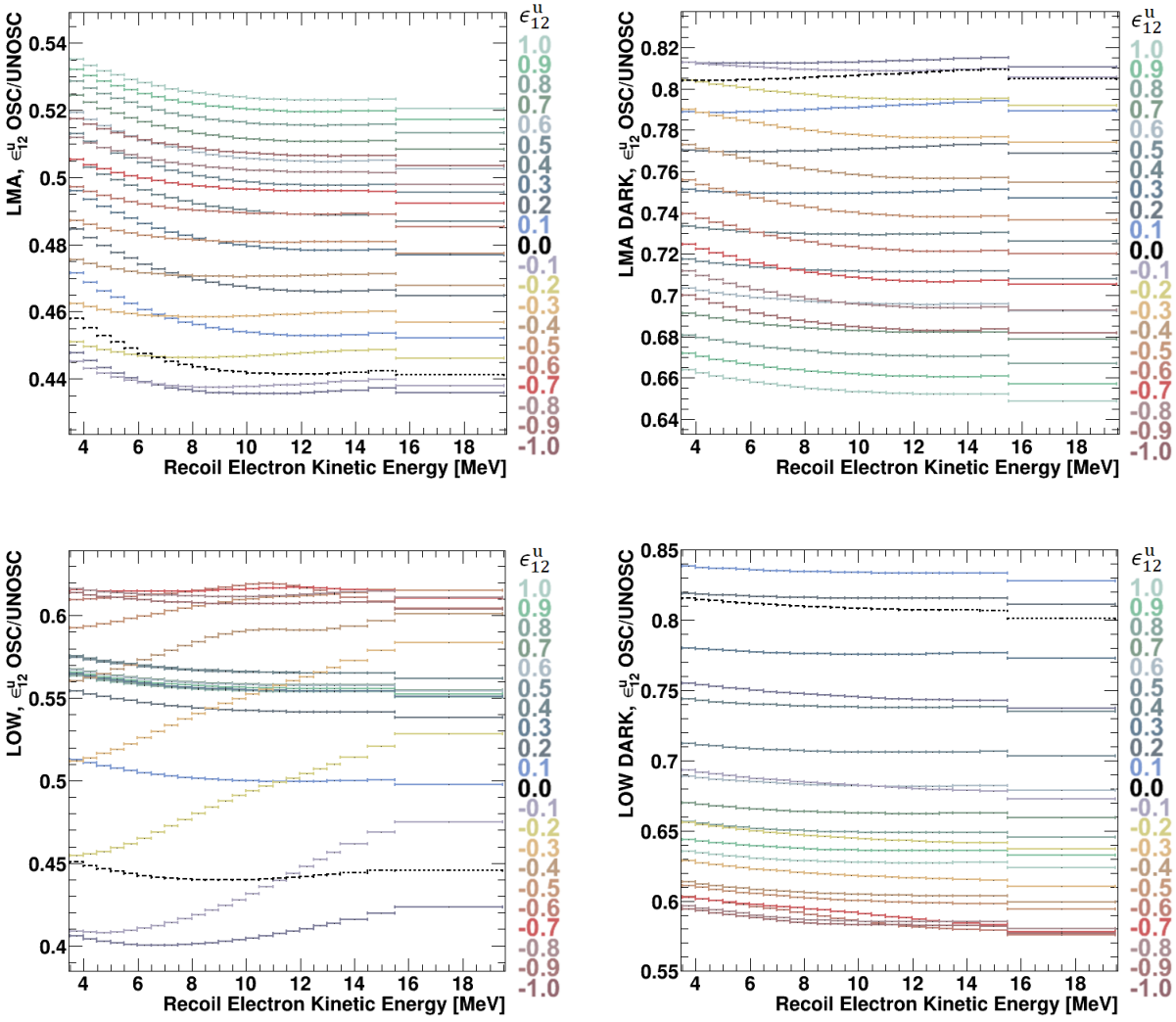

Figure 11.5: The effect of ϵ^u_{12} on the SK-IV recoil electron spectrum predictions for the LMA region (top-right) and LOW region (bottom-left), and the darkside equivalents (darkside LMA = top-right and darkside LOW = bottom-right). On the left $\sin^2\theta_{12} = 0.334$, and on the right $\sin^2\theta_{12} = 0.799$. The top row corresponds to $\Delta m^2_{21} = 4.07 \times 10^{-5}$ eV^2, while the bottom row corresponds to $\Delta m^2_{21} = 1.26 \times 10^{-7}$ eV^2. The spectral predictions include the induced recoil electrons from both ^{8}B and *hep* neutrinos.

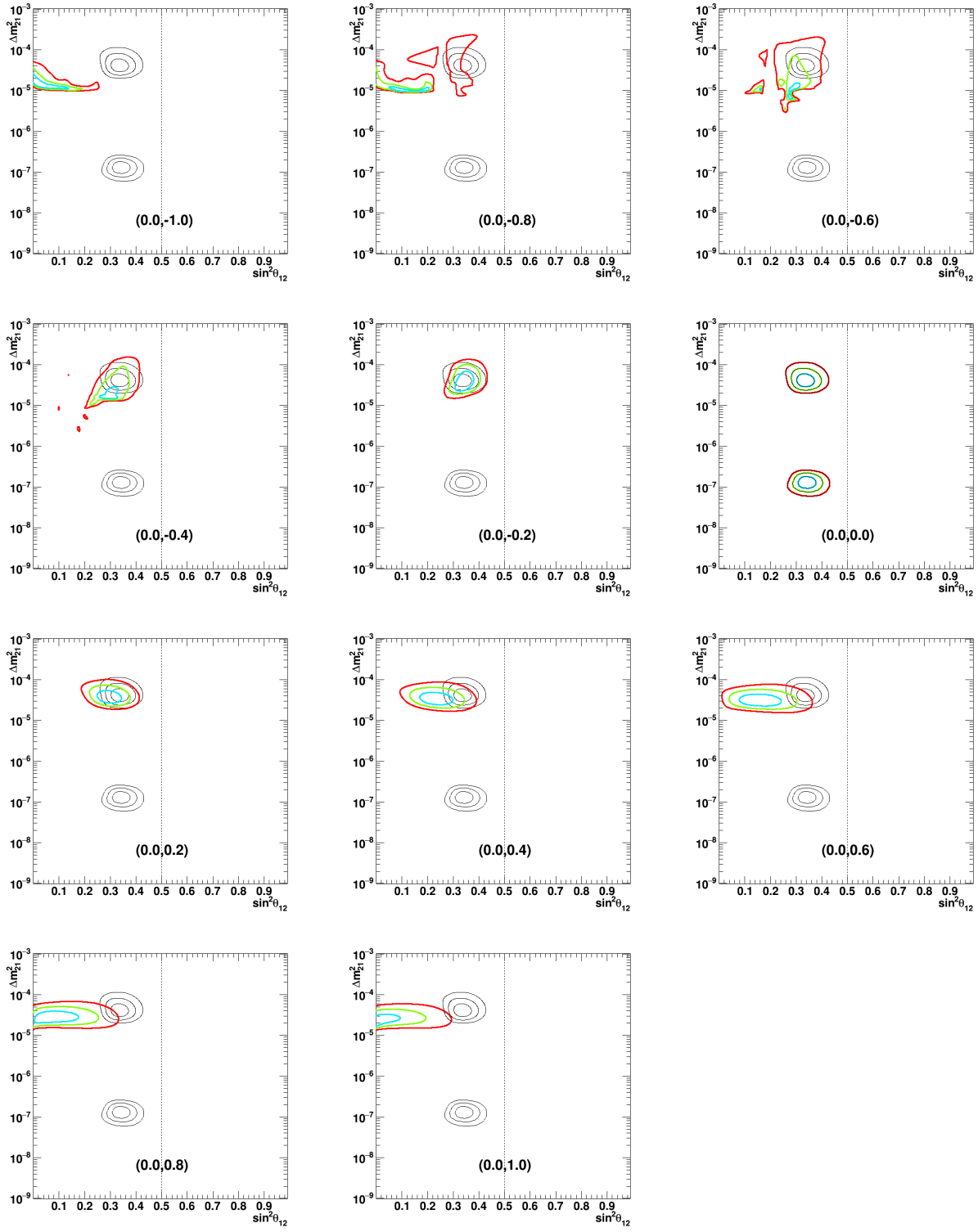

Figure 11.6: The 1-3σ (2 d.o.f.) allowed regions of $(\sin^2\theta_{12}, \Delta m^2_{21})$ for various values of ϵ^{u}_{12} in the SK-Only case. The minimum χ^2 is with respect to the NSI parameters given in each plot. The 1 (cyan), 2 (green) and 3 (red) σ allowed regions for the given NSI case are displayed. The no-NSI contours (black) are displayed for reference.

The combined effect of $(\epsilon^f_{11}, \epsilon^f_{12})$

While a single NSI parameter may be tested at a time, the simultaneous effect of both parameters for a given quark are considered in the analysis presented in this work. When allowing both parameters to be non-zero, the combined effects previously described may occur. The simultaneous effect of both NSI parameters $(\epsilon^{\rm u}_{11}, \epsilon^{\rm u}_{12})$ on the no-NSI LMA best-fit spectral predictions are plotted in Fig. 11.7. The blue lines are the predicted Night spectra induced by ^{8}B solar neutrinos and the red lines are the predicted Day spectra induced by ^{8}B solar neutrinos. The solid-black lines are the total spectra induced by ^{8}B solar neutrinos, and the dashed-black lines are the total spectra induced by both ^{8}B and *hep* solar neutrinos. Fig. 11.8 shows these effects for the darkside LMA spectral predictions.

In both sets of spectral plots, the day-night asymmetry (the difference between the red and blue lines divided by the solid black lines in each bin) can be affected by the NSI parameters and can even become zero. In Fig. 11.7, the bottom-center panel displays a case (0.0, -1.0) when NSI causes the $A_{\rm DN}$ to become zero and even removes spectral distortions. A similar effect can be seen in the bottom left panel (-1.0, -1.0) of the darkside LMA spectral examples in Fig. 11.8.

Fig. 11.9 shows the effect of both $(\epsilon^{\rm u}_{11}, \epsilon^{\rm u}_{12})$ on the 1-3σ allowed contours in the $(\sin^2\theta_{12}, \Delta m^2_{21})$ parameter space. These allowed regions are with respect to the minimum χ^2 for the given pair of NSI parameters used to create the predictions. The plots for the LMA and darkside spectra and the plots for the $(\sin^2\theta_{12}, \Delta m^2_{21})$ parameter space all correspond to the same set of $(\epsilon^{\rm u}_{11}, \epsilon^{\rm u}_{12})$ values.

For negative values of both ϵ^f_{11} and ϵ^f_{12}, the LMA and LOW solutions shift to the darkside, as expected, but also begin to merge. This situation can be seen for the case of $(\epsilon^{\rm u}_{11}, \epsilon^{\rm u}_{12}) = (-1.0, -1.0)$, which is plotted in the lower left of Fig. 11.9. A zoomed-in version of this plot is given in Fig. 11.10. The LMA-like solution is denoted by the black lines

resulting from including the fit to Borexino's $A_{\mathrm{DN}}^{^{7}\mathrm{Be}}$ data. As this plot indicates, LOW-like solutions, such as the lower-left peninsula, are removed by including the fit to Borexino's $A_{\mathrm{DN}}^{^{7}\mathrm{Be}}$ measurement.

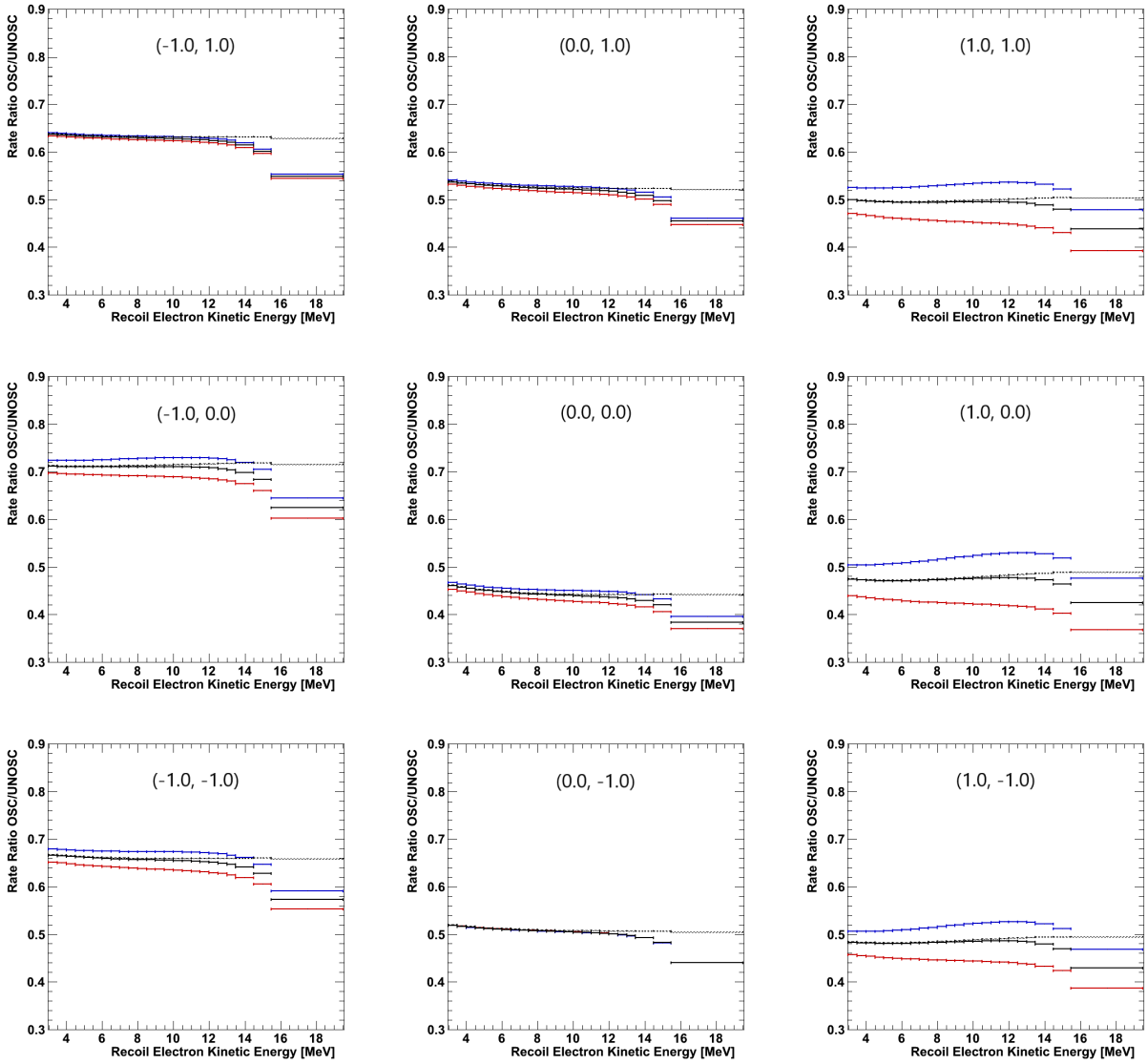

Figure 11.7: The predicted recoil electron spectrum for sets of $(\epsilon^{u}_{11}, \epsilon^{u}_{12})$ at the no-NSI LMA best-fit point. The red (blue) line corresponds to the day (night) spectrum due to ^{8}B neutrinos. The solid black lines correspond to the day and night combined rate. The dashed line is the combined rate including the contribution of *hep* neutrinos to the spectrum.

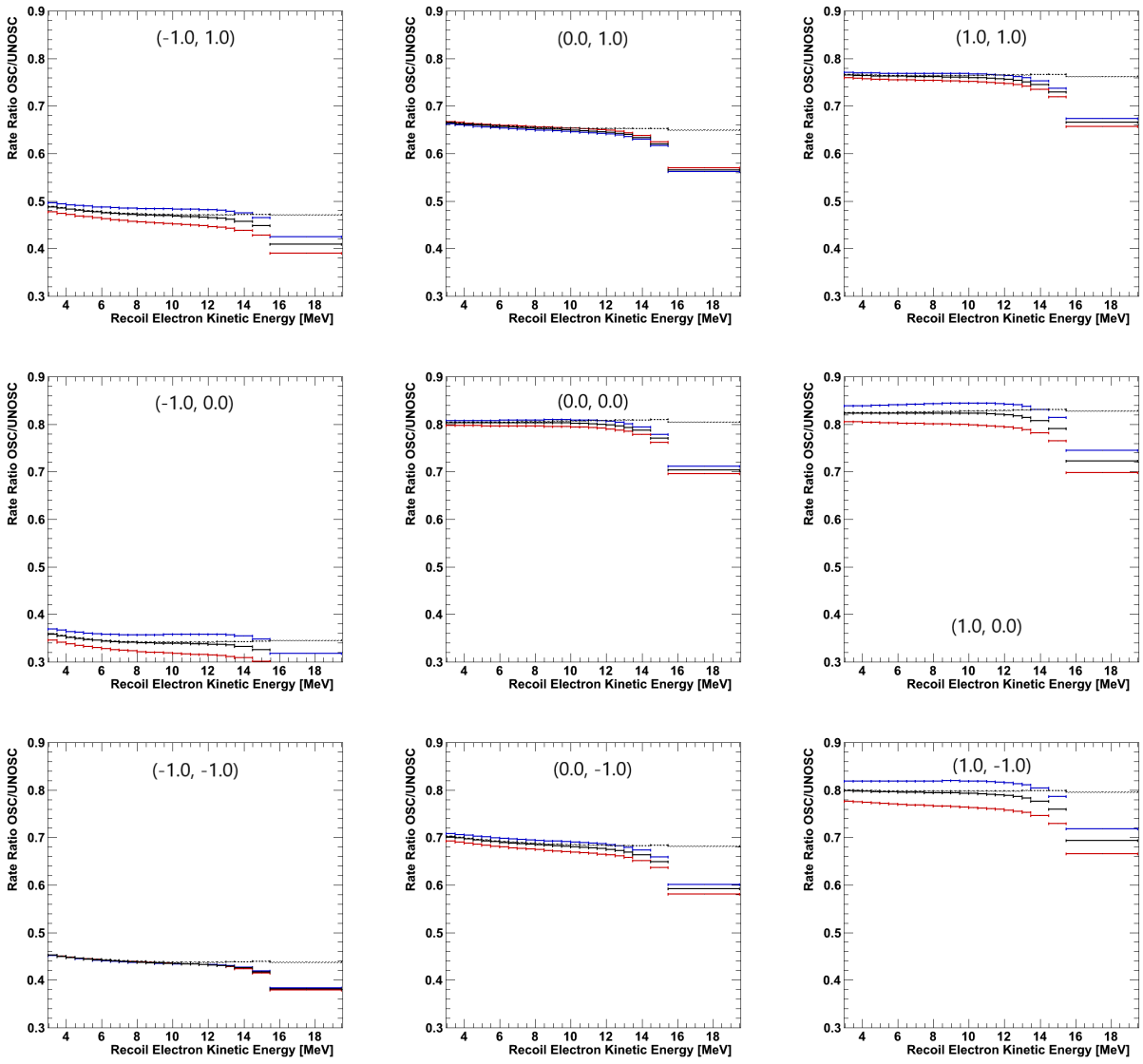

Figure 11.8: The predicted recoil electron spectrum for sets of $(\epsilon^{u}_{11}, \epsilon^{u}_{12})$ at the darkside LMA point of $\sin^2\theta_{12} = 0.799$. The value of Δm^2_{21} is the same as the LMA best-fit point for no-NSI. The red (blue) line corresponds to the day (night) spectrum due to ^{8}B neutrinos. The solid black lines correspond to the day and night combined rate. The dashed line is the combined rate including the contribution of *hep* neutrinos to the spectrum.

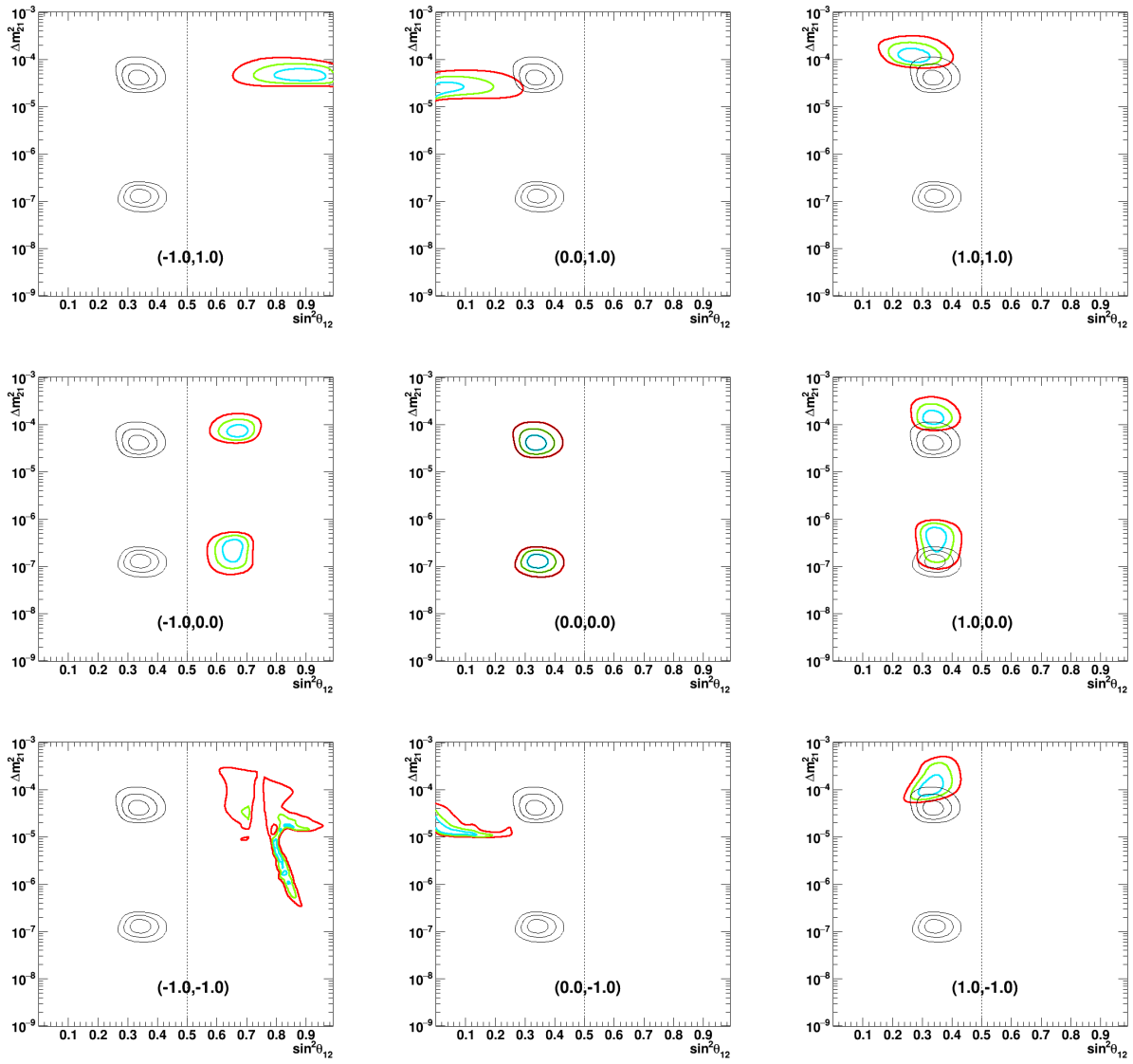

Figure 11.9: The simultaneous effect of non-zero $(\epsilon^u_{11}, \epsilon^u_{12})$ on the oscillation contours. The minimum χ^2 is with respect to the NSI parameters given in each plot.

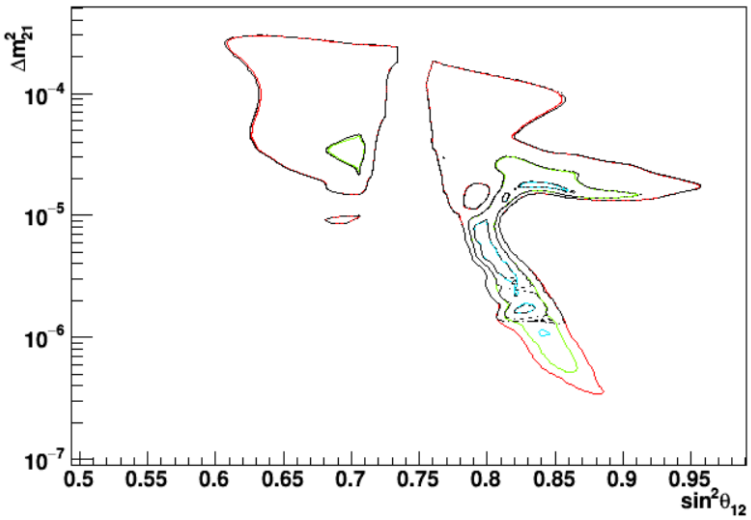

Figure 11.10: The SK-Only 1 (cyan) 2 (green) and 3 (red) σ included regions for $(\epsilon^{u}_{11}, \epsilon^{u}_{12}) = (-1.0, -1.0)$. The black dashed lines are the LMA-like included regions from SK+Borexino $A^{^7Be}_{DN}$. The region without the black dashed lines in the lower right of the figure corresponds to the NSI-equivalent LOW solution that is removed by including the fit to Borexino's data.

11.2 Results of the Solar Neutrino NSI Analysis

The NSI parameter $\epsilon^{u,d}_{11}$ is allowed to range between $-6.$ and $+6.$, while $\epsilon^{u,d}_{12}$ can range between $-7.$ and $+5$. Positive values of ϵ^{f}_{12} are not as well favored by SK data as are negative values. The very large values of the NSI parameters were chosen in an attempt to see if the NSI contours would close at two σ (with 2 d.o.f.). However, they do not close for large values of ϵ^{f}_{11} or ϵ^{f}_{12}, since, based on the work by Gonzalez-Garcia and Maltoni [17], it seems that tight constraints on Δm^2_{21} are needed. For parameter estimation, the two-dimensional contours are drawn for the one, two, and three σ included confidence regions for two degrees of freedom. This corresponds to $\Delta\chi^2$ values of 2.296, 6.180, and 11.829 respectively. The non-displayed parameters are profiled over. When profiling, for each pair of displayed parameters, the minimum χ^2 value for the corresponding set of non-displayed parameters is chosen as the χ^2 for that pair of displayed parameters. The results for SK-Only (including the SNO NC constraint) will be reported first, followed by SK with the addition of the fit to Borexino's $A^{^7Be}_{DN}$ measurement, and finally the combined result of SK+SNO and the fit to $A^{^7Be}_{DN}$. The

results for each case are given in Table 11.1, along with SK+SNO.

Table 11.1: The results of the SK solar neutrino NSI analysis. Each line corresponds to the best fit for the given data set stated in the first column. SK-Only denotes the use of the SK recoil electron spectra and integrated $A_{\rm DN}$ data for SK-I/II/III/IV while using the SNO NC measurement. The SK-Only result is in an LOW-like solution of the $(\sin^2\theta_{12}, \Delta m^2_{21})$ parameter space. SK+Borexino denotes the combined χ^2 of SK-Only result and Borexino's measure of the day-night asymmetry for 862 keV ^{7}Be solar neutrinos. The SK+Borexino result removes LOW-like solutions and the best fit is in an LMA-like solution. SK+SNO denotes the combined fit to SK and SNO data. Combined denotes the combined fit to the SK, SNO, and Borexino measurements. The second column corresponds to the fermion f with which the NSI occur, for the no-NSI case (-), or for up (u) or down (d) quarks. The third and fourth columns are the resulting best-fit NSI parameters ϵ^f_{11} and ϵ^f_{11} (f = u,d) for the fit. Similarly, the fifth and sixth columns are the best-fit $\sin^2\theta_{12}$ and Δm^2_{21}. The value of $\sin^2\theta_{13} = 0.020$ is fixed for this analysis. Results with $\Delta m^2_{21} < 10^{-5}$ eV^2 are in LOW-like solutions, while above this value, they are in LMA-like solutions. The last column contains the χ^2 for the given best-fit point and the number of degrees of freedom (NDF). With no-NSI, there are two degrees of freedom from $\sin^2\theta_{12}$ and Δm^2_{21}. With NSI, two additional degrees of freedom are added: $(\epsilon^f_{11}, \epsilon^f_{12})$, where f = u, d. The bottom table contains the log-likelihood ratio (1 d.o.f) of the NSI best fit and the no-NSI best fit and the corresponding σ-value for SK-Only, SK and Borexino $A^{^7\rm Be}_{\rm DN}$, and the combined fit of SK+SNO with Borexino $A^{^7\rm Be}_{\rm DN}$.

f-Quark NSI	Fitted Data	ϵ^f_{11}	ϵ^f_{12}	$\sin^2\theta_{12}$	Δm^2_{21} [eV^2]	χ^2/NDF
-	SK-Only	0	0	0.3442	1.258×10^{-7}	69.43/85
-	SK+Borexino	0	0	0.3339	4.073×10^{-5}	69.59/86
-	SK+SNO	0	0	0.3137	4.897×10^{-5}	75.99/90
-	Combined	0	0	0.3137	4.897×10^{-5}	76.00/91
u	SK-Only	-2.5	-3.1	0.8519	1.148×10^{-6}	66.77/83
u	SK+Borexino	5.1	-6.4	0.1864	5.957×10^{-5}	66.80/84
u	SK+SNO	-2.2	-1.4	0.9380	1.259×10^{-6}	72.27/88
u	Combined	0.5	-1.0	0.1935	1.175×10^{-5}	72.95/89
d	SK-Only	-3.3	-3.1	0.8835	1.202×10^{-6}	66.18/83
d	SK+Borexino	-2.4	-2.0	0.8340	2.113×10^{-5}	66.83/84
d	SK+SNO	-3.3	-3.1	0.8835	1.202×10^{-6}	70.60/88
d	Combined	-5.1	-6.7	0.7992	8.035×10^{-5}	72.23/89

1 D.O.F. Log-Likelihood Ratio (LLR = $\log\mathcal{L}$(NSI-best) $-$ $\log\mathcal{L}(0.0, 0.0)$) and σ-value.

NSI Quark f	SK-Only		SK+Borexino		SK+SNO+Borexino (Combined Fit)	
	LLR	σ	LLR	σ	LLR	σ
u	1.33	1.63	1.40	1.67	1.53	1.75
d	1.63	1.80	1.38	1.66	1.89	1.94

11.2.1 SK-Only Results

Using SK solar neutrino data (and SNO's NC constraint), the allowed 1-3σ regions (2 d.o.f.) for NSI between solar neutrinos u-quarks or d-quarks are plotted in the top row of Fig. 11.11. The results for the up-quark (down-quark) case are given in the left (right) column. The best-fit point is denoted by the yellow triangle. The top row of Fig. 11.12 contains the allowed values of $\sin^2\theta_{12}$ and Δm^2_{21} from the SK-Only fit, with the u-quark (d-quark) results plotted on the left (right) side of the figure.

Similar to the case with no-NSI, the best-fit point in either case prefers a LOW-like solution, as evidenced by the best fit being disfavored by more than 5σ when including the fit to Borexino's $A^{^7\mathrm{Be}}_{\mathrm{DN}}$. For the u-quark best fit to SK-Only, the $A^{^7\mathrm{Be}}_{\mathrm{DN}}$ fit adds 69.8 units of χ^2, while for the d-quark best fit, the fit adds 35.7 units of χ^2. The expansion of the contours is expected due to the introduction of the two extra parameters, and the disjointed nature is expected due to the effects of ϵ^f_{12}.

The corresponding one-dimensional $\Delta\chi^2$ values for the NSI parameters are plotted in the top row of Fig. 11.13. The ϵ^f_{11} (ϵ^f_{12}) parameter is plotted on the left side (right side) of the figure. The up quark (down quark) results are plotted as a solid blue (black dashed) line. All non-displayed parameters are profiled over.

The resulting SK-Only best fit for up-quark NSI is at $(\epsilon^{\mathrm{u}}_{11}, \epsilon^{\mathrm{u}}_{12}, \sin^2\theta_{12}, \Delta m^2_{21}) = (-2.5, -3.1, 0.8519, 1.148 \times 10^{\text{-}6}\ \mathrm{eV}^2)$ with a χ^2 value of 66.77. The d-quark NSI best-fit location is at $(\epsilon^{\mathrm{d}}_{11}, \epsilon^{\mathrm{d}}_{12}, \sin^2\theta_{12}, \Delta m^2_{21}) = (-3.3, -3.1, 0.8835, 1.202 \times 10^{\text{-}6}\ \mathrm{eV}^2)$ with a χ^2 value of 66.18. The d-quark NSI scenario is slightly favorable to the u-quark scenario, and both are slightly favorable to the case with No-NSI. The one-dimensional log-likelihood ratio

$$\mathrm{LLR} = \log\mathcal{L}(\text{NSI-best}) - \log\mathcal{L}(0.0, 0.0) \tag{11.6}$$

for the u-quark (d-quark) best fit is 1.3 (1.6). The corresponding σ-value is 1.6σ for NSI with up quarks and 1.8σ for NSI with down quarks.

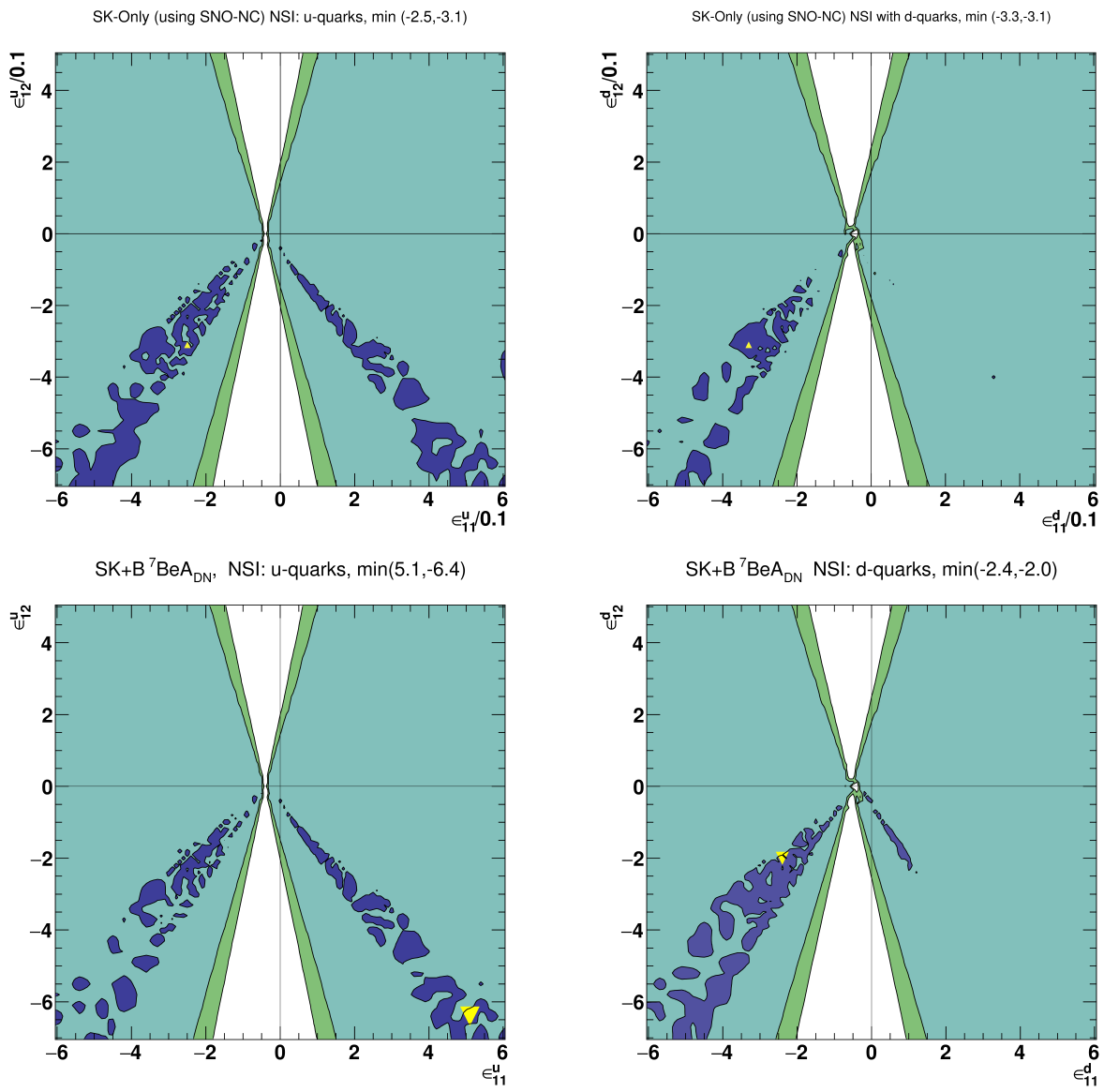

Figure 11.11: The SK-Only (top row) results and SK+ Borexino $A_{\rm DN}^{^7{\rm Be}}$ results (bottom row) for the allowed values of $(\epsilon_{11}^{\rm f}, \epsilon_{12}^{\rm f})$, where f = u, d. The case for NSI with u-quarks is plotted on the left, and the case for NSI with d-quarks is plotted on the right. The 1 (blue), 2 (teal) and 3 (green) σ confidence level allowed regions for the parameters are obtained by profiling over the non-displayed parameters. The top row contains the allowed values of $(\sin^2\theta_{12}, \Delta m^2_{21})$, and the bottom row contains the allowed values of $(\epsilon_{11}^{\rm u,d}, \epsilon_{12}^{\rm u,d})$. The best-fit point is denoted by a yellow triangle. Differences in the allowed regions between the up and down quark cases are due to their differing densities in the Sun (and Earth).

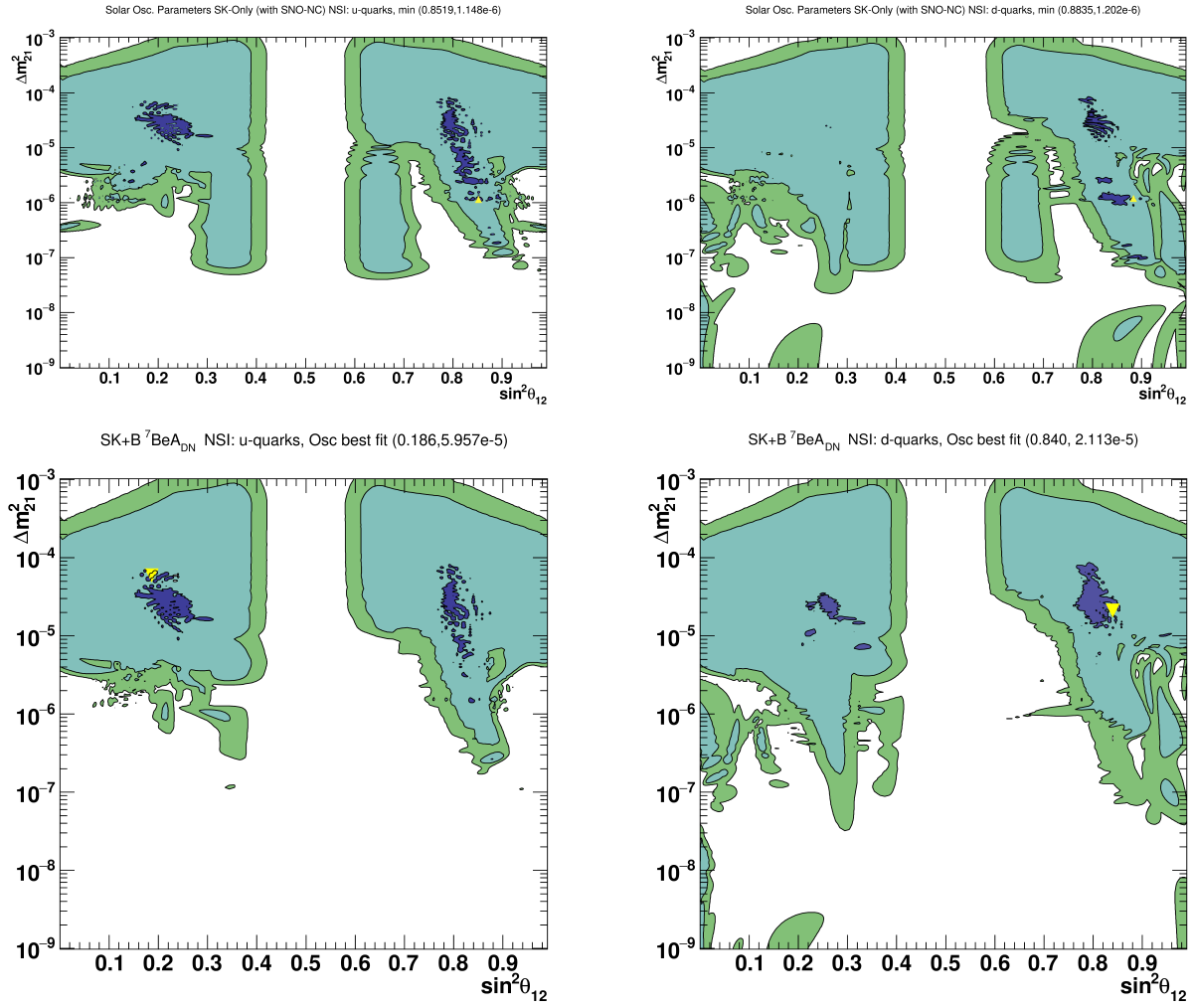

Figure 11.12: The SK-Only (top row) results and SK+ Borexino $A_{\mathrm{DN}}^{^{7}\mathrm{Be}}$ results (bottom row) for the allowed values of $(\sin^2\theta_{12}, \Delta m^2_{21})$ in the case of NSI with u-quarks (left) and d-quarks (right). The 1 (blue), 2 (teal) and 3 (green) σ confidence level allowed regions for the parameters are obtained by profiling over the non-displayed parameters. The best-fit point is denoted by a yellow triangle. Differences in the allowed regions between the up and down quark cases are due to their differing densities in the Sun (and Earth). The best-fit point is in the LOW-like solution on the darkside in both NSI cases for SK-Only. For SK+ Borexino $A_{\mathrm{DN}}^{^{7}\mathrm{Be}}$, LOW-like solutions are removed. The u-quark best-fit point is on the standard LMA side, while the d-quark best-fit point is in the darkside LMA region.

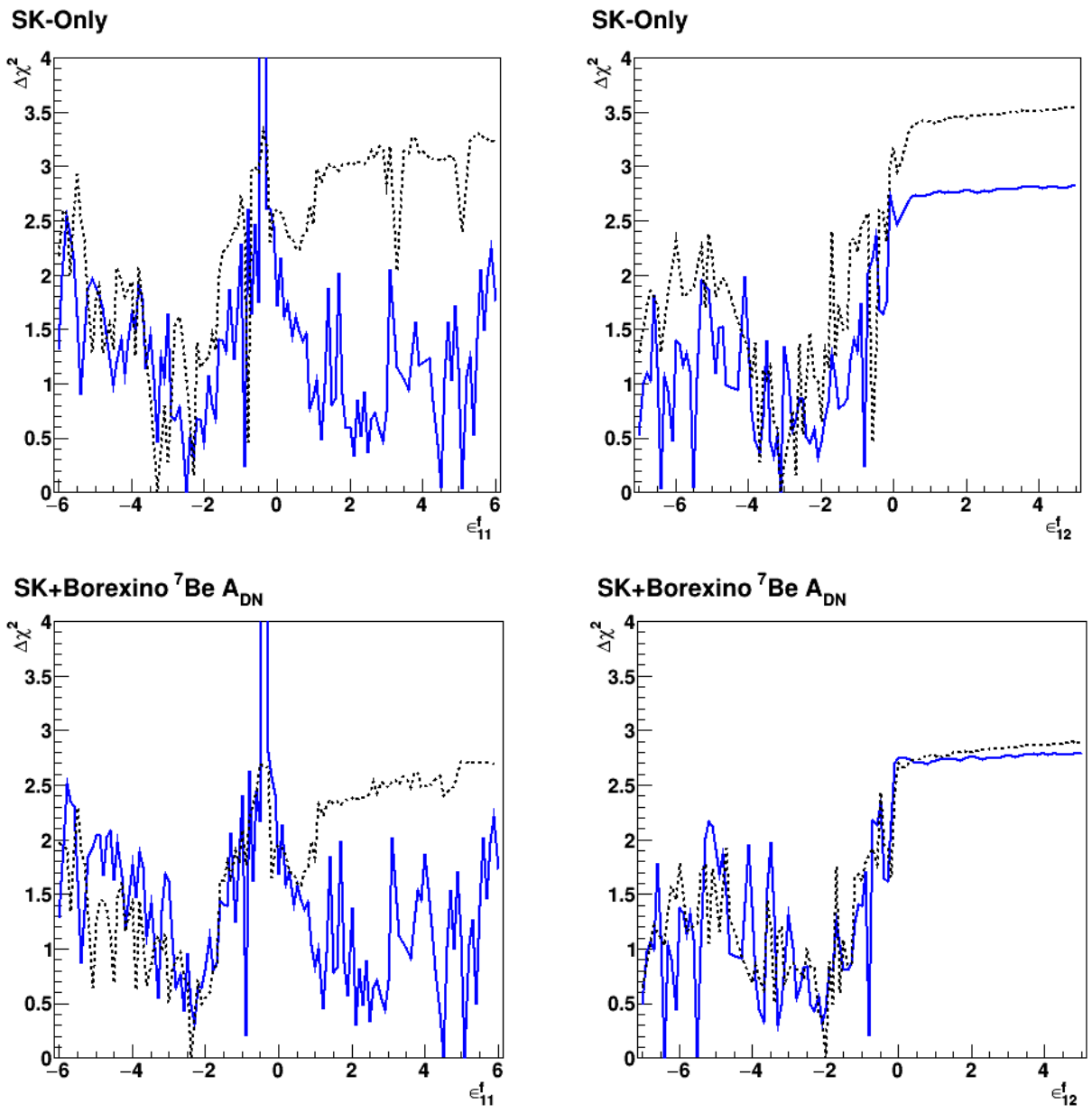

Figure 11.13: The one-dimensional $\Delta\chi^2$ limits for the NSI parameters ϵ^f_{11} (left) and ϵ^f_{12} (right). The top row contains the results from the SK-Only fit, and the bottom row contains the results from the SK + Borexino $A^{^7\mathrm{Be}}_{\mathrm{DN}}$ fit. The u-quark (d-quark) case is plotted with a solid blue (black dashed) line. All non-displayed parameters are profiled over.

11.2.2 SK+Borexino $A_{\mathrm{DN}}^{^7\mathrm{Be}}$

As stated earlier, the addition of the fit to Borexino's measurement of nearly zero $A_{\mathrm{DN}}^{^7\mathrm{Be}}$ [84] removes LOW-like solutions. The allowed NSI contours are plotted in the bottom row of Fig. 11.11, and the allowed $(\sin^2\theta_{12}, \Delta m^2_{21})$ contours are plotted in the bottom row of Fig. 11.12. The 1σ allowed NSI parameters for the u-quark case change a little, and the best fit shifts from the darkside LMA to a value of $\sin^2\theta_{12}$ more similar to standard LMA values. This shift between the standard LMA region and the darkside LMA is reflected in the shift of the best fit in $\epsilon^{\mathrm{u}}_{11}$ from a negative value to a positive value. For the d-quark NSI case, the removal of the LOW-like solutions brings back standard LMA regions of $\sin^2\theta_{12}$, and equivalently allows for more positive values of $\epsilon^{\mathrm{d}}_{11}$. The corresponding one-dimensional $\Delta\chi^2$ values for the NSI parameters are plotted in the bottom row of Fig. 11.13. The ϵ^{f}_{11} (ϵ^{f}_{12}) parameter is plotted on the left side (right side) of the figure. The up quark (down quark) results are plotted as a solid blue (black dashed) line.

The best fit to both SK data and Borexino's day-night asymmetry in the up-quark NSI scenario is at $(\epsilon^{\mathrm{u}}_{11}, \epsilon^{\mathrm{u}}_{12}, \sin^2\theta_{12}, \Delta m^2_{21}) = (5.1, -6.4, 0.1864, 5.957 \times 10^{-5}\ \mathrm{eV}^2)$ with a χ^2 value of 66.80. It prefers a value of $\sin^2\theta_{12}$ less than 0.5, closer to the no-NSI LMA region. The best fit for down quark is at $(-2.4, -2.0, 0.8340, 2.113 \times 10^{-5}\ \mathrm{eV}^2)$ with a χ^2 value of 66.83. The d-quark best fit prefers the darkside LMA solution. By removing LOW-like solutions, the u-quark NSI scenario is barely favorable to the d-quark scenario, since their χ^2 values differ by only 0.06. Again, both NSI cases are slightly favorable to the case without NSI. The resulting LLR for NSI with either up quarks or down quarks is 1.4 (1.7σ).

11.2.3 SK+SNO+Borexino $A_{\mathrm{DN}}^{^7\mathrm{Be}}$

With the combined fit to SK+SNO and including the fit to Borexino's $A_{\mathrm{DN}}^{^7\mathrm{Be}}$, the tension in $\sin^2\theta_{12}$ between the two experiments becomes important. The tension comes from the average value of P_{ee} allowed by the ES rate in SK and the P_{ee} allowed by the rate of (ν D) CC reactions in SNO. These two reactions have different effects at low and high energies. SK has a much larger exposure (fiducial volume $\times$ live time) than SNO and also has a higher rate of low energy solar neutrino-induced ES recoil electrons. This allows SK to place tighter constraints than SNO on the low energy side of the recoil electron spectrum and P_{ee}. In SNO, the 1.4 MeV nuclear threshold of the deuteron breakup is an effective neutrino-energy threshold, and the low energy measurements get smeared out by ES. This weakens SNO's ability to constrain the low energy side of the P_{ee}. However, it creates a stronger constraint on the higher energy side of P_{ee}. The energy of the protons produced by the (ν d) CC reaction in SNO is tightly correlated to the neutrino energy, which gives SNO more statistics for higher energy solar neutrinos.

The allowed NSI contours are given in Fig. 11.14, and the allowed $(\sin^2\theta_{12}, \Delta m^2_{21})$ contours are plotted in Fig. 11.15. One can see there are now holes ($2 < \sigma < 3$ regions, i.e. green regions) which appear in the 2σ included regions (teal). These holes appear due to the squeezing of the LMA-side and darkside contours in Δm^2_{12}, in large part from constraining the larger values of Δm^2_{21}. In the u-quark case, the hole that appears at $(\epsilon^{\mathrm{u}}_{11}, \epsilon^{\mathrm{u}}_{12}) = (-3.5, -2.5)$ is a result of the shrinking peninsula just below $\Delta m^2_{21} = 10^{-5}$, near $\sin^2\theta_{12} \simeq 0.86$.

In the d-quark case, all of the large holes are predominantly a result of the tighter constraints at large Δm^2_{21}. The diagonal holes are also caused, in part, by this effect. The tightened contour around $(\sin^2\theta_{12}, \Delta m^2_{21}) \simeq (0.12, 3 \times 10^{-6})$ contributes to the diagonal holes for $\epsilon^{\mathrm{d}}_{11} > 0$. The lower bound of the horn-like shape on the darkside between $0.66 < \sin^2\theta^2_{12} < 0.75$ and $10^{-5} < \Delta m^2_{21} < 10^{-4}$ eV^2 contributes to the diagonal hole near (-1.5,-2.5)

in the corresponding NSI parameter space.

For the up-quark NSI scenario, the best-fit point to the combined fit again prefers a $\sin^2\theta_{12}$ value near the no-NSI LMA region. It is located at $(0.5, -1.0, 0.1935, 1.175\times10^{-5}\ \mathrm{eV}^2)$ and has a χ^2 value of 72.95. The down quark best fit also prefers the darkside LMA, and it is located at $(-5.1, -6.7, 0.7992, 8.035\times10^{-5}\ \mathrm{eV}^2)$ with a χ^2 value of 72.23. In the combined result, the d-quark NSI scenario is once again more favorable to the u-quark scenario. Their χ^2 values differ by 0.72 units. Similar to the previous fits, both NSI scenarios are slightly more favorable than without NSI. The LLR for the u-quark best fit and the no-NSI best fit is 1.5 (1.8σ). For d-quark NSI, the LLR is 1.9 (1.9σ). In both cases, no-NSI is still included at better than the 95% confidence level.

The one-dimensional $\Delta\chi^2$ results for the NSI parameters from the combined fit are plotted in Fig. 11.16. The ϵ^f_{11} (ϵ^f_{12}) parameter is plotted on the left side (right side) of the figure. The up quark (down quark) results are plotted as a solid blue (black dashed) line.

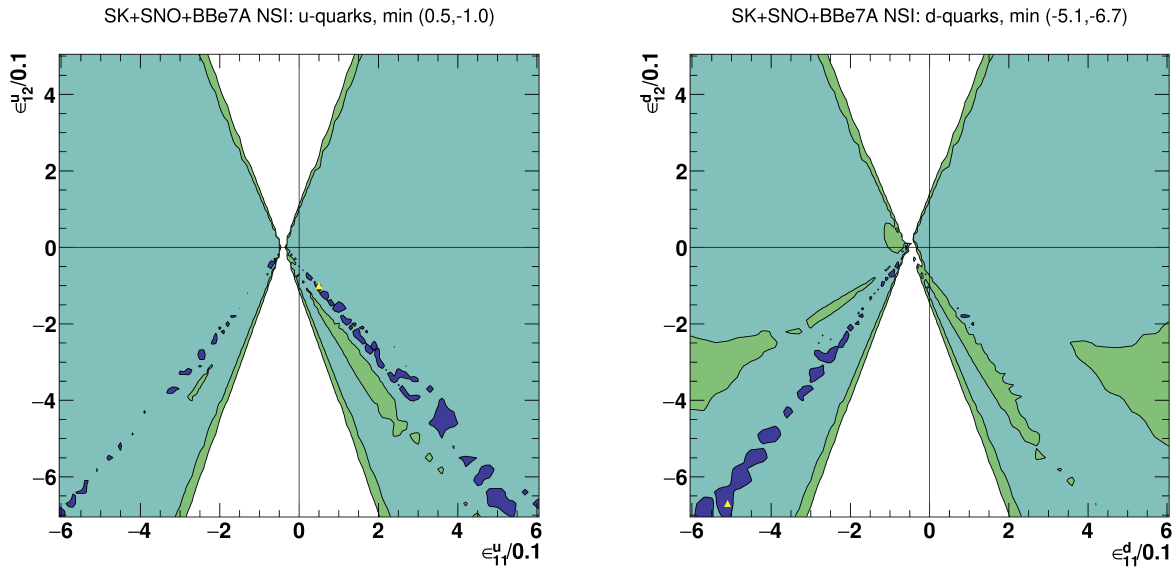

Figure 11.14: The SK + SNO + Borexino $A_{\mathrm{DN}}^{^{7}\mathrm{Be}}$ results for allowed values of $(\epsilon_{11}^{\mathrm{f}}, \epsilon_{12}^{\mathrm{f}})$, where $f = \mathrm{u}, \mathrm{d}$. The case for NSI with u-quarks is plotted on the left, and the case for NSI with d-quarks is plotted on the right. The 1 (blue), 2 (teal) and 3 (green) σ confidence level allowed regions for the parameters are obtained by profiling over the non-displayed parameters. The top row contains the allowed values of $(\sin^2\theta_{12}, \Delta m^2_{21})$, and the bottom row contains the allowed values of $(\epsilon_{11}^{\mathrm{u,d}}, \epsilon_{12}^{\mathrm{u,d}})$. The best-fit point is denoted by a yellow triangle. Differences in the allowed regions between the up and down quark cases are due to their differing densities in the Sun (and Earth).

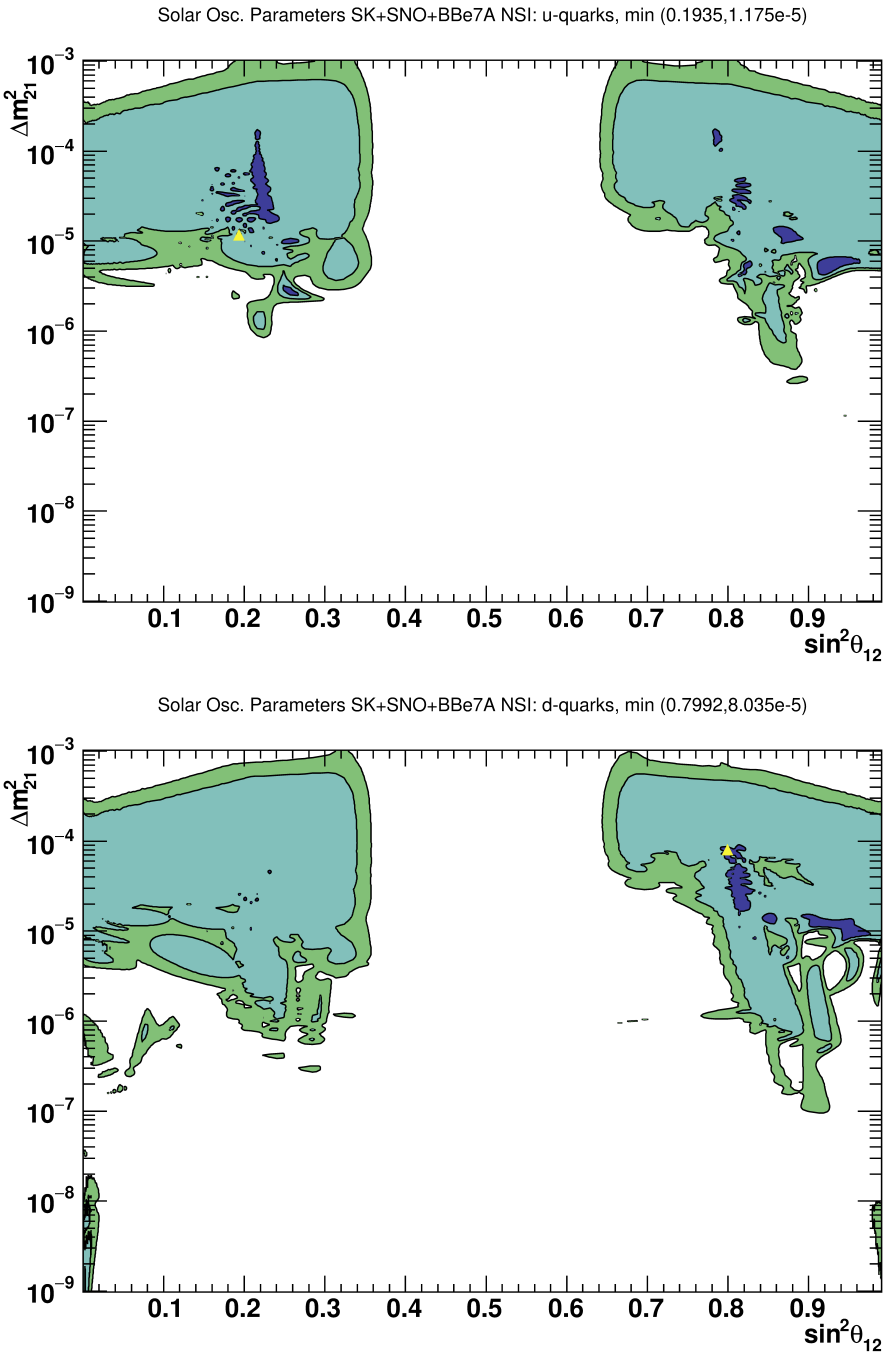

Figure 11.15: The SK + SNO + Borexino $A_{\mathrm{DN}}^{^7\mathrm{Be}}$ results for the allowed values of $(\sin^2\theta_{12}, \Delta m^2_{21})$ in the case of NSI with u-quarks (top) and d-quarks (bottom). The 1 (blue), 2 (teal) and 3 (green) σ confidence level allowed regions for the parameters are obtained by profiling over the non-displayed parameters. The best-fit point is denoted by a yellow triangle. Differences in the allowed regions between the up and down quark cases are due to their differing densities in the Sun (and Earth). The best-fit point is in the LMA-like solution on the darkside in both cases.

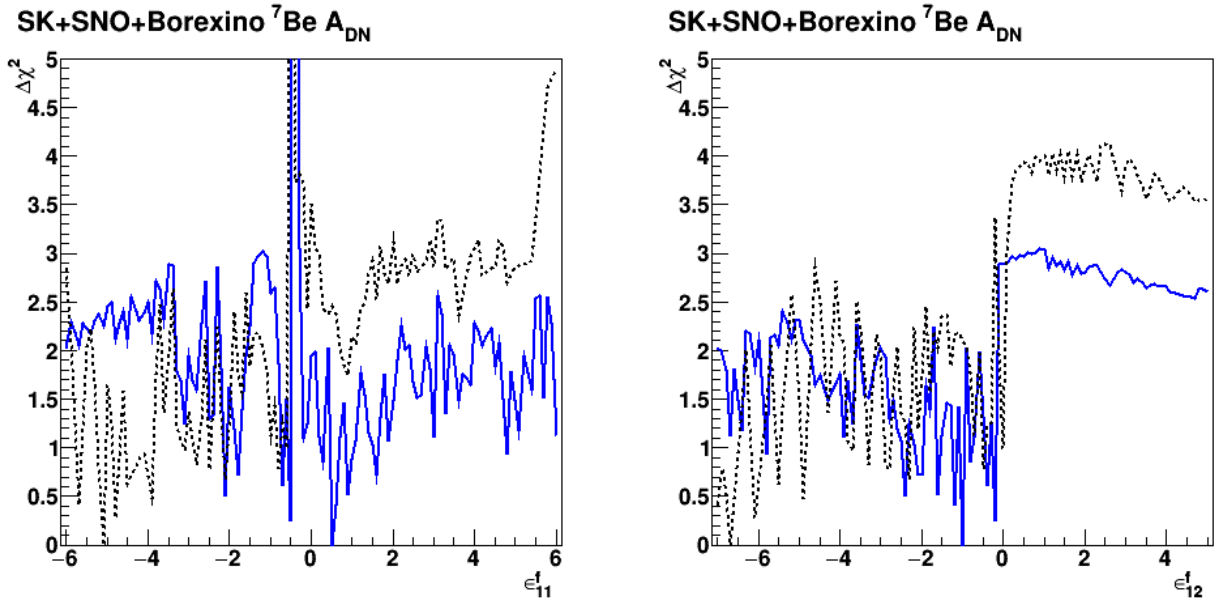

Figure 11.16: The SK + SNO + Borexino $A_{\rm DN}^{^7{\rm Be}}$ one-dimensional $\Delta\chi^2$ limits for the NSI parameters ϵ_{11}^f (left) and ϵ_{12}^f (right). The u-quark (d-quark) case is plotted with a solid blue (black dashed) line. All non-displayed parameters are profiled over.

11.2.4 The Best-Fit Recoil Electron Spectra and Integrated $A_{\rm DN}$ Results

The spectral results for NSI with u-quarks (d-quarks) for each SK-Phase are plotted in Fig. 11.17 with the SK-Only results as solid (dashed) blue lines, and with the SK + Borexino $A_{\rm DN}^{^7{\rm Be}}$ results as solid (dashed) red lines. The day-night asymmetry results are plotted in the bottom-left panel of the figure. The bottom-right panel contains the illustrative combination of SK-I/II/III/IV spectra and best fits. The best fit LMA result (SK + Borexino $A_{\rm DN}^{^7{\rm Be}}$) from the no-NSI case (gray lines) is plotted for comparison. A zoomed version of the lower right panel from Fig. 11.17 is given in Fig. 11.19 along with the constant-value P_{ee} spectrum (green) for comparison.

The results for the combined fit to SK+SNO + Borexino $A_{\rm DN}^{^7{\rm Be}}$ data are plotted in Fig. 11.18 as the solid (dashed) blue lines for the u-quark (d-quark) NSI case. The red lines and gray lines still correspond to the SK + Borexino $A_{\rm DN}^{^7{\rm Be}}$ results with and without NSI from

Fig. 11.17. A zoomed version of the lower right panel from Fig. 11.18 is given in Fig. 11.20 along with the constant-value P_{ee} spectrum (green) for comparison.

Common examples of best-fit survival probabilities are given in Fig. 11.21. The no-NSI P_{ee} are for the best fit to all solar data (green) and to all solar and KamLAND data (blue). The NSI survival probabilities are common examples for good fits for SK+SNO + Borexino $A_{\rm DN}^{^7{\rm Be}}$. The dashed black lines are for the SK+SNO quadratic fit results published in the SK-IV 1664 day paper [42], while the blue band is for an updated result that includes most of the full SK-IV data set (∼2800 days).

The SK-Only best fit with u-quark NSI prediction has a slight downturn below 6.99 MeV, while the SK+Borexino $A_{\rm DN}^{^7{\rm Be}}$ prediction is relatively flat below this energy. The behavior of the d-quark NSI best fits is the opposite to that of the u-quark NSI best fit in both cases. By including the combined fit with SNO, the spectra have a slight upturn, though not to the same scale as the no-NSI LMA case. In all cases, the shape of the spectrum at low energy is flat or has a downturn.

Comparisons of the SK-Only NSI results (and SK + Borexino $A_{\rm DN}^{^7{\rm Be}}$) with the spectrum due to a constant $P_{ee} = 0.317$ (Sec. 10.2.3) demonstrate the central energy region of the spectra has an improved fit over both the no-NSI and constant P_{ee} cases. The energy bins below 4.99 MeV were removed energy bin by energy bin and the fit re-performed for the best-fit results and the constant P_{ee} spectra. The results of the no-NSI (LMA and LOW), SK-Only, and SK + Borexino $A_{\rm DN}^{^7{\rm Be}}$ were checked for both quarks and are reported in Table 11.2 and Table 11.3. As the lower energy bins were removed from the fit, the SK-I/II/III/IV combined spectral fit was consistently better with the NSI cases than with either the constant P_{ee} case or the no-NSI cases. This indicates that the central energy region of the spectral fits, specifically for SK-I and SK-IV, are the dominant contribution to the better χ^2 from the spectral fit.

Table 11.2: The comparisons between the fits to spectra from a constant $P_{ee} = 0.317$ and the best-fit spectra from the no-NSI case (LMA and LOW), and between the spectra from a constant P_{ee} and spectra with NSI effects (SK-Only and SK + Borexino $A_{\rm DN}^{^7{\rm Be}}$). The first table contains the results for fitting to the full spectra. The second table is the results of fitting to the spectra above 4.49 MeV. The difference in the spectral fit χ^2 to the constant P_{ee} spectral fit is given as $\Delta\chi^2_{\rm const} = \chi^2_{\rm spec} - \chi^2_{\rm const}$. Better fits will have positive values of $\Delta\chi^2_{\rm const}$, and poorer fits will have negative values. Dashes indicate fits that are unaffected by changing the lower threshold of the spectral fit. For the 4.49 MeV threshold, three spectral data points have been removed from the fit: one from SK-III and two from SK-IV. For the 4.99 MeV threshold case and the 5.49 MeV threshold case, refer to Table 11.3.

Full Spectral Fits with no ^{8}B flux constraint

Prediction	SK-I/II/III/IV		SK-I		SK-II		SK-III		SK-IV	
Constant P_{ee}	69.30		18.92		5.30		27.94		15.5	
	χ^2	$\Delta\chi^2_{\rm const}$	χ^2	$\Delta\chi^2_{\rm const}$	χ^2	$\Delta\chi^2_{\rm const}$	χ^2	$\Delta\chi^2_{\rm const}$	χ^2	$\Delta\chi^2_{\rm const}$
No-NSI LOW	68.26	1.04	19.32	−0.40	5.45	−0.15	27.97	−0.03	13.97	1.54
No-NSI LMA	68.38	0.92	19.39	−0.47	5.43	−0.13	28.14	−0.20	13.79	1.71
d SK-Only	65.36	3.94	17.82	1.10	5.27	0.03	27.46	0.48	13.40	2.10
d SK+Borexino	64.14	5.16	17.29	1.63	5.08	0.22	27.32	0.62	12.93	2.57
u SK-Only	65.71	3.59	18.06	0.87	5.24	0.06	27.75	0.19	13.13	2.37
u SK+Borexino	64.61	4.69	17.40	1.52	5.07	0.23	27.18	0.76	13.61	1.89

Fits for $T_e > 4.49$ (no ^{8}B flux constraint)

Prediction	SK-I/II/III/IV		SK-I	SK-II	SK-III		SK-IV	
Constant P_{ee}	68.16		-	-	27.94		14.31	
	χ^2	$\Delta\chi^2_{\rm const}$			χ^2	$\Delta\chi^2_{\rm const}$	χ^2	$\Delta\chi^2_{\rm const}$
No-NSI LOW	66.76	1.40	-	-	27.96	−0.02	12.68	1.63
No-NSI LMA	66.74	1.42	-	-	28.12	−0.19	12.39	1.91
d SK-Only	64.36	3.80	-	-	27.46	0.48	12.53	1.78
d SK+Borexino	63.08	5.07	-	-	27.32	0.62	12.01	2.30
u SK-Only	64.55	3.61	-	-	27.74	0.19	12.14	2.17
u SK+Borexino	63.66	4.50	-	-	27.18	0.76	12.77	1.53

Table 11.3: The comparisons between the fits to spectra from a constant $P_{ee} = 0.317$ and the best-fit spectra from the no-NSI case (LMA and LOW), and between the spectra from a constant P_{ee} and spectra with NSI effects (SK-Only and SK + Borexino $A_{\rm DN}^{^7{\rm Be}}$). The first table contains the results for fitting to the spectra above 4.99 MeV. The second table is the results of fitting to the spectra above 5.49 MeV. The difference in the spectral fit χ^2 to the constant P_{ee} spectral fit is given as $\Delta\chi^2_{\rm const} = \chi^2_{\rm spec} - \chi^2_{\rm const}$. Better fits will have positive values of $\Delta\chi^2_{\rm const}$, and poorer fits will have negative values. Dashes indicate fits that are unaffected by changing the lower threshold of the spectral fit. For the 4.99 MeV (5.49 MeV) threshold case, six (nine) spectral data points have been removed from the fit: one, three, and four (two, four, and five) from SK-I, SK-III, and SK-IV respectively. For the 4.49 MeV threshold and full spectral comparisons, refer to Table 11.2.

Fits for $T_e > 4.99$ (no ^{8}B flux constraint)

Prediction	SK-I/II/III/IV		SK-I		SK-II	SK-III		SK-IV	
Constant P_{ee}	63.98		19.39		-	27.78		9.86	
	χ^2	$\Delta\chi^2_{\rm const}$	χ^2	$\Delta\chi^2_{\rm const}$		χ^2	$\Delta\chi^2_{\rm const}$	χ^2	$\Delta\chi^2_{\rm const}$
No-NSI LOW	63.69	0.29	19.33	0.06	-	27.89	−0.11	9.25	0.62
No-NSI LMA	63.89	0.08	19.40	−0.01	-	28.07	−0.29	9.16	0.70
d SK-Only	60.39	3.59	17.80	1.58	-	27.32	0.46	8.28	1.58
d SK+Borexino	59.23	4.74	17.29	2.10	-	27.20	0.58	7.85	2.01
u SK-Only	60.96	3.01	18.05	1.33	-	27.64	0.14	8.22	1.65
u SK+Borexino	59.37	4.61	17.38	2.01	-	27.02	0.76	8.24	1.62

Fits for $T_e > 5.49$ (no ^{8}B flux constraint)

Prediction	SK-I/II/III/IV		SK-I		SK-II	SK-III		SK-IV	
Constant P_{ee}	62.50		18.73		-	27.17		9.02	
	χ^2	$\Delta\chi^2_{\rm const}$	χ^2	$\Delta\chi^2_{\rm const}$		χ^2	$\Delta\chi^2_{\rm const}$	χ^2	$\Delta\chi^2_{\rm const}$
No-NSI LOW	61.98	0.51	18.26	0.47	-	27.02	0.15	8.90	0.12
No-NSI LMA	62.05	0.44	18.21	0.52	-	27.12	0.05	8.90	0.13
d SK-Only	57.69	4.80	16.45	2.28	-	26.45	0.71	7.28	1.74
d SK+Borexino	58.90	3.59	17.02	1.71	-	26.61	0.55	7.69	1.33
u SK-Only	57.90	4.59	16.74	1.99	-	26.41	0.75	7.39	1.63
u SK+Borexino	59.40	3.10	17.15	1.58	-	26.84	0.33	7.76	1.26

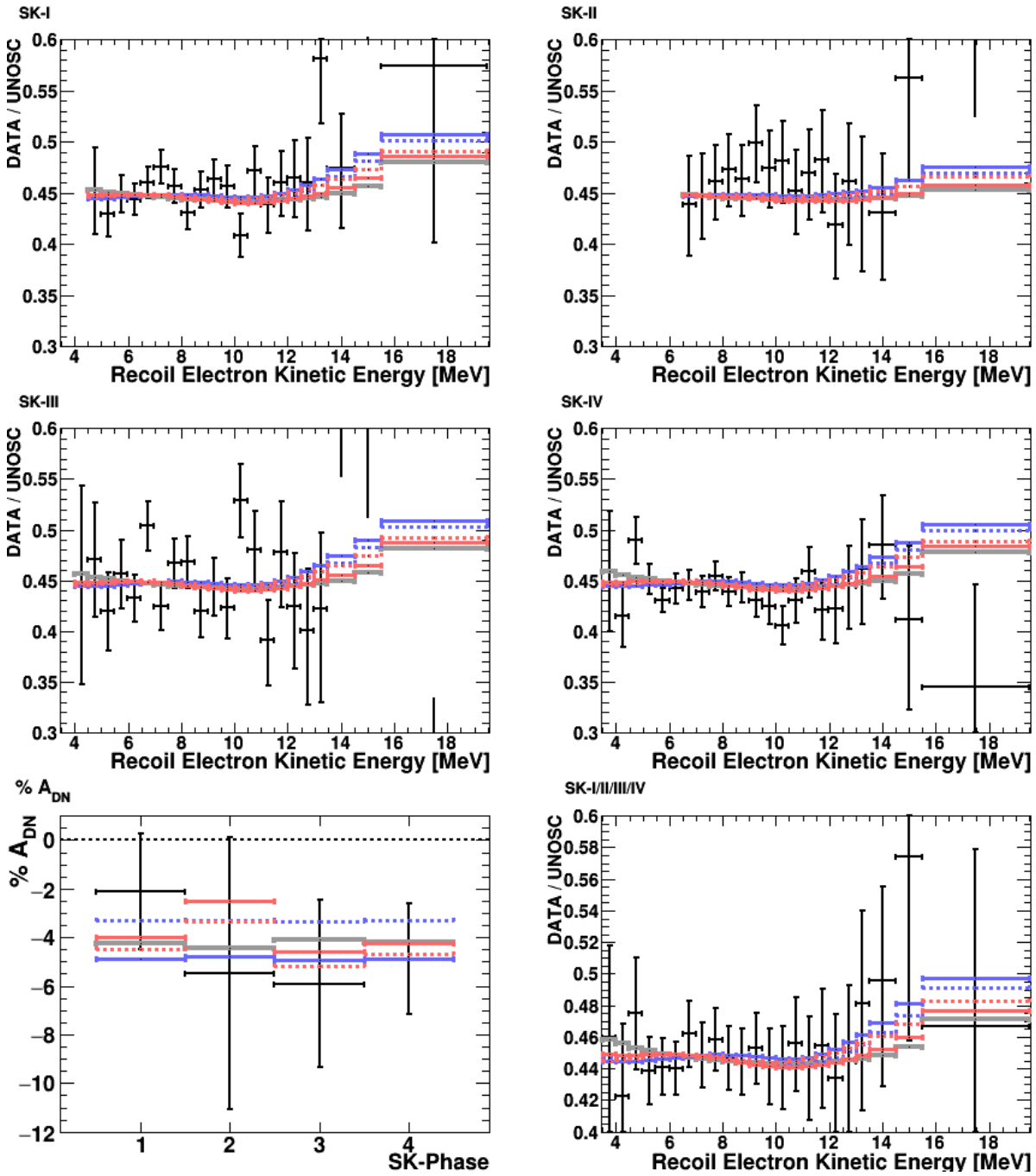

Figure 11.17: The SK Spectra with the best-fit NSI predictions for SK-Only (blue) and SK + Borexino $A_{\mathrm{DN}}^{^{7}\mathrm{Be}}$ (red). The data (black lines) includes statistical and energy-uncorrelated errors added in quadrature. The best fit predictions and data for the integrated A_{DN} are plotted in the bottom left panel. The bottom right panel is the SK-I/II/III/IV combined spectra, which is provided for illustrative purposes. The solid (dashed) lines correspond to NSI with up quarks (down quarks). The LMA best fit for no-NSI (solid gray line) is plotted for comparison.

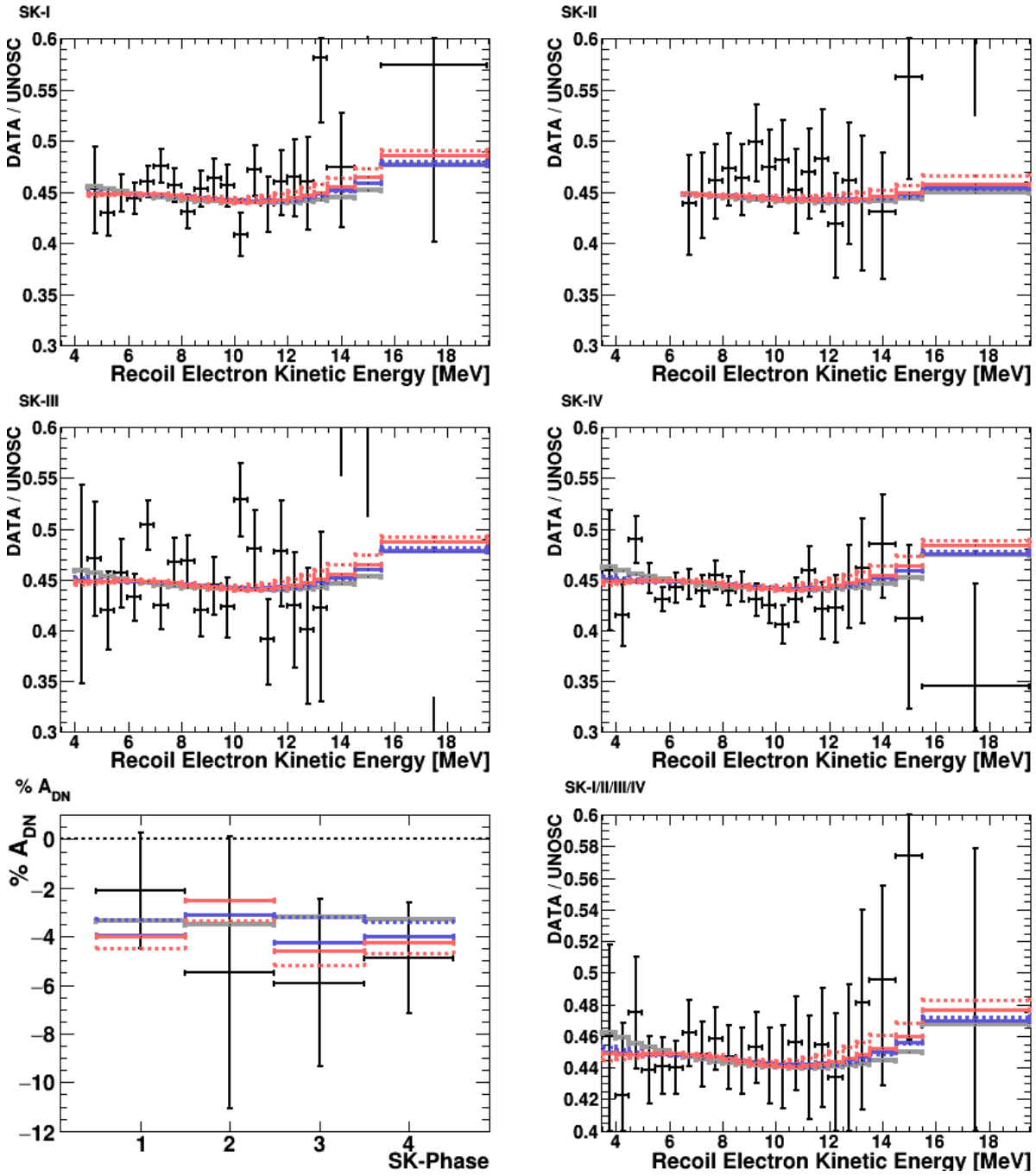

Figure 11.18: The SK Spectra with the best-fit NSI predictions for SK + Borexino $A_{\rm DN}^{^7{\rm Be}}$ (red) and the combined fit to SK+SNO + Borexino $A_{\rm DN}^{^7{\rm Be}}$ (blue). The data (black lines) includes statistical and energy-uncorrelated errors added in quadrature. The best fit predictions and data for the integrated $A_{\rm DN}$ are plotted in the bottom left panel. The bottom right panel is the SK-I/II/III/IV combined spectra, which is provided for illustrative purposes. The solid (dashed) lines correspond to NSI with up quarks (down quarks). The LMA best fit for no-NSI (solid gray line) is plotted for comparison.

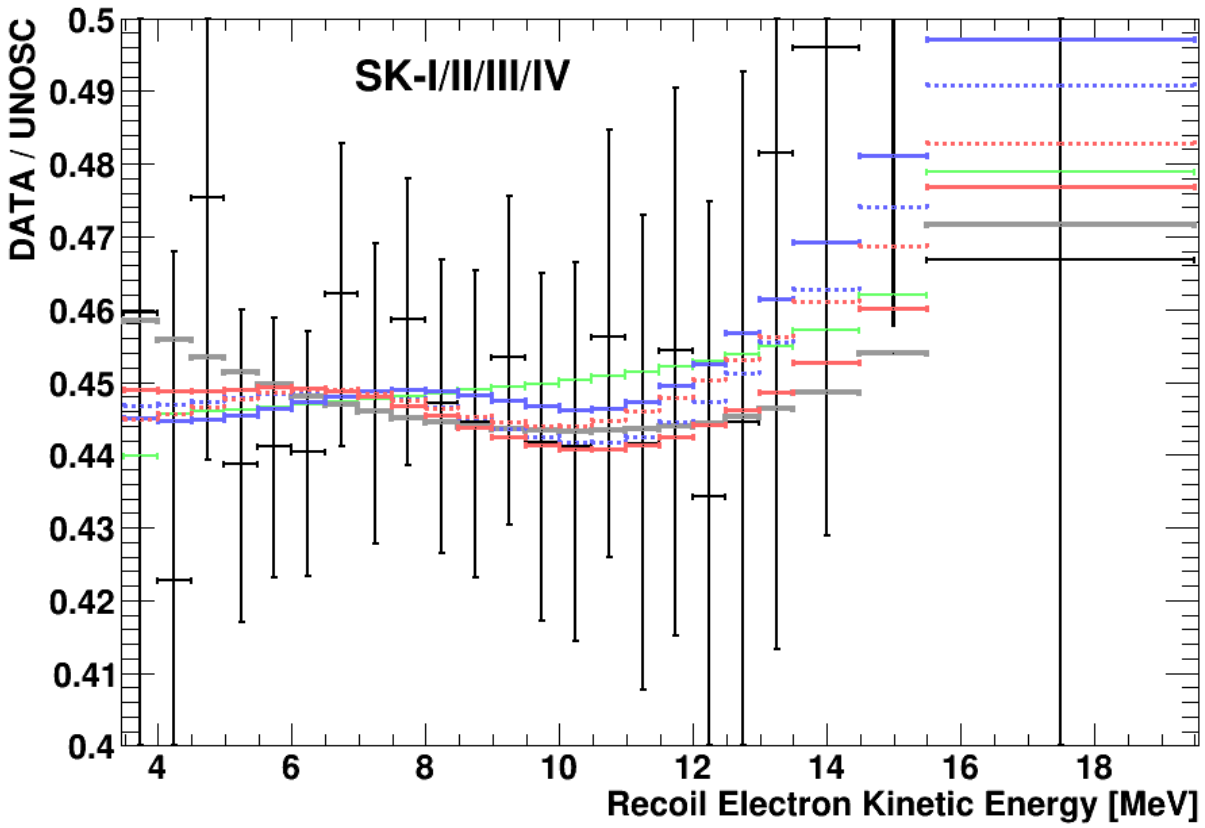

Figure 11.19: The SK-I/II/III/IV1664-day combined recoil electron spectrum. This spectrum is the combination of a given energy bin for each phase weighted by the statistical and energy-uncorrelated error. It is provided for illustrative purposes and should not be used for analysis. The best-fit NSI predictions for SK + Borexino $A_{\rm DN}^{^7{\rm Be}}$ are plotted in red, and the combined fit to SK+SNO + Borexino $A_{\rm DN}^{^7{\rm Be}}$ are plotted blue. The solid (dashed) lines correspond to NSI with up quarks (down quarks). The LMA best fit for no-NSI (solid gray line) and constant-value P_{ee} spectra (solid green line) are plotted for comparison. All errors are the combined statistical and energy-uncorrelated systematic errors corresponding to the weighted sum of the errors from each phase.

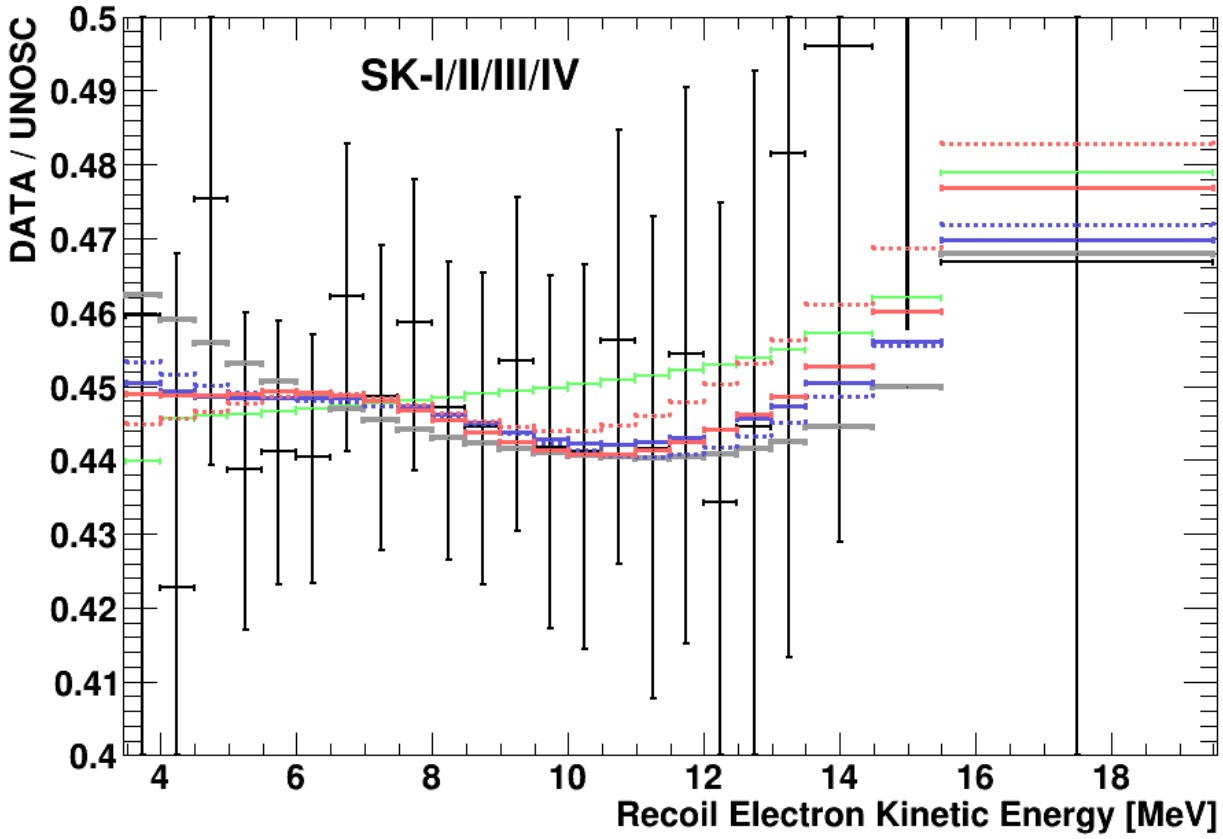

Figure 11.20: The SK-I/II/III/IV1664-day combined recoil electron spectrum. This spectrum is the combination of a given energy bin for each phase weighted by the statistical and energy-uncorrelated error. It is provided for illustrative purposes and should not be used for analysis. The best-fit NSI predictions for SK + Borexino $A_{\rm DN}^{^7{\rm Be}}$ are plotted in red, and the combined best fits to SK+SNO + Borexino $A_{\rm DN}^{^7{\rm Be}}$ are plotted blue. The solid (dashed) lines correspond to NSI with up quarks (down quarks). The LMA best fit for no-NSI (solid gray line) and constant-value P_{ee} spectra (solid green line) are plotted for comparison. All errors are the combined statistical and energy-uncorrelated systematic errors corresponding to the weighted sum of the errors from each phase.

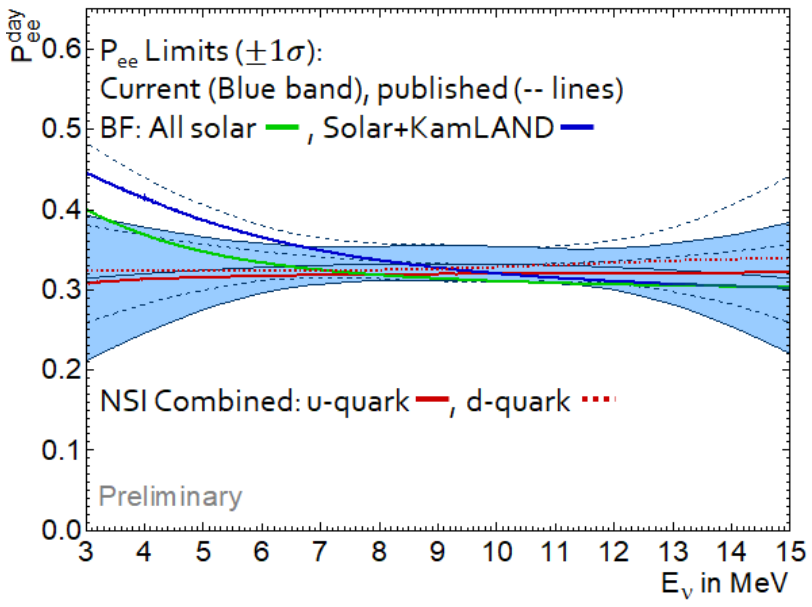

Figure 11.21: The best fit P_{ee} with and without NSI. The NSI survival probabilities are common examples for good fits for SK+SNO + Borexino $A_{\mathrm{DN}}^{^7\mathrm{Be}}$.

11.3 Conclusion and Discussion

Super-Kamiokande data shows a preference for non-standard interactions between ^{8}B (and *hep*) solar neutrinos and up and down quarks in the matter the neutrinos traverse. The results for each combination of fits to data (SK, SNO, and Borexino) are summarized in Table 11.1 for no-NSI, NSI with up quarks, and NSI with down quarks. The fit to SK-I, SK-II, SK-III, and SK-IV spectral and integrated day-night rate asymmetry data prefers the LOW solution with no-NSI at $\chi^2_{\mathrm{S+A}} = 69.43$. In the LMA region, the best-fit point with no NSI gives $\chi^2_{\mathrm{S+A}} = 69.59$. This value is unaffected by including Borexino data (less than 0.01%).

With the two additional degrees of freedom from the NSI parameters, the best-fit $\chi^2_{\mathrm{S+A}}$ is 66.77 (66.18) for u-quarks (d-quarks). In both cases, the darkside LOW-like solution is preferred. SK data is better fit by NSI spectral predictions than no-NSI LOW spectral predictions. The one-dimensional log-likelihood ratio (LLR) comparing NSI to no-NSI (Eq. 11.6) is LLR = 1.3 for up quark NSI and LLR = 1.6 for down quark NSI. The LLR values

result in a σ-value of 1.6σ (1.8σ) for u-quarks (d-quarks). The results for the different data-sets that are fit to and the NSI scenario are listed in Table 11.1. The top sub-table includes the best-fit NSI, $\sin^2\theta_{12}$ and Δm^2_{21} values, and the χ^2/NDF for each fit. The bottom sub-table contains the log-likelihood ratios and corresponding σ-values for each case.

Using the fit to Borexino's $A^{^7\mathrm{Be}}_{\mathrm{DN}}$ removes LOW and LOW-like solutions. After removing LOW-like solutions, the LLR is slightly improved in the u-quark case and the σ-value increases by 0.04σ. In the down quark case, the LLR decreases to 1.4 and has a correspondingly lower σ-value of 1.7σ. After performing a combined fit to SK and SNO's data and incorporating Borexino's $A^{^7\mathrm{Be}}_{\mathrm{DN}}$, the LLR value is better in both cases: LLR = 1.5 (1.7σ) for u-quarks and LLR = 1.9 (1.9σ) for d-quarks. Compared to the SK-Only fit, the combined fit increases the confidence level for the up-quark NSI and down-quark NSI by 0.1σ.

The allowed regions for the parameters in all of the cases are reported, as well as the one-dimensional results for the NSI parameters. In all cases, $\epsilon^f_{12} > 0.1$ is disfavored at more than 1.5σ. Without including SNO data, the NSI best fits prefer flatter spectra at low energy or downturns. By including SNO, the best fits yield spectra with slight upturns, but not as strong as the standard MSW LMA predictions (no-NSI). By comparing to a constant P_{ee} spectral prediction, the better results for the fits using the predictions with NSI can be attributed to the NSI predictions being a better fit for the shape of the spectra above 4.99 MeV than the predicted spectra without NSI (or the constant P_{ee} spectra).

11.3.1 Discussion

The analysis would most benefit from including an NSI analysis of KamLAND's data, since it would greatly constrain the Δm^2_{21} values and could possibly disfavor large values of NSI. Fig. 11.22 shows the effect on the allowed NSI-parameter contours from constraining 6.0×10^{-5} eV$^2 < \Delta m^2_{12} < 9.0 \times 10^{-5}$ eV^2. To properly compare constraints from this anal-

ysis to those performed externally, a KamLAND NSI analysis is crucial. Additionally, an incorporation of $\epsilon^f_{\alpha\beta}$ NSI parameter limits measured in SK's atmospheric NSI analysis [127] and those measured by long baseline neutrino experiments may impact the allowed values of ϵ^f_{11} and ϵ^f_{12}.

An additional benefit of constraining the squared mass splitting would be the reduced calculation time required for this analysis. The framework for this analysis is also currently prepared to test the case for allowing NSI with both quarks at the same magnitude: $\epsilon_{1j} = \epsilon^q_{ij} \times (Y_d \pm Y_u)$ for j=1,2. In these two scenarios, ϵ^q_{1j} would be the free NSI parameters.

SK also has an additional ∼1300 days of SK-IV data, which includes ∼1000 days of low energy, 31-hit trigger threshold data that could be used in this analysis. Several years of even lower energy solar neutrino data (below 3.49 MeV) from the SK Wideband Intelligent Trigger needs to be analyzed and could be incorporated into this analysis. The low energy behavior of the spectra would help to further constrain the shape of the upturn, and the larger statistics for high energy recoil electrons can further constrain the tilt of the spectrum. The smaller statistical errors in the central part of the spectrum will also impact the allowed shape for the NSI spectra. The NSI analysis is ready to be applied to the full SK-I/II/III/IV solar neutrino data set after the SK-IV data set and systematic errors are finalized. The SK-IV spectral and integrated $A_{\rm DN}$ predictions would need to be recalculated with the new full SK-IV period results before performing the $\chi^2_{\rm spec}$ fits.

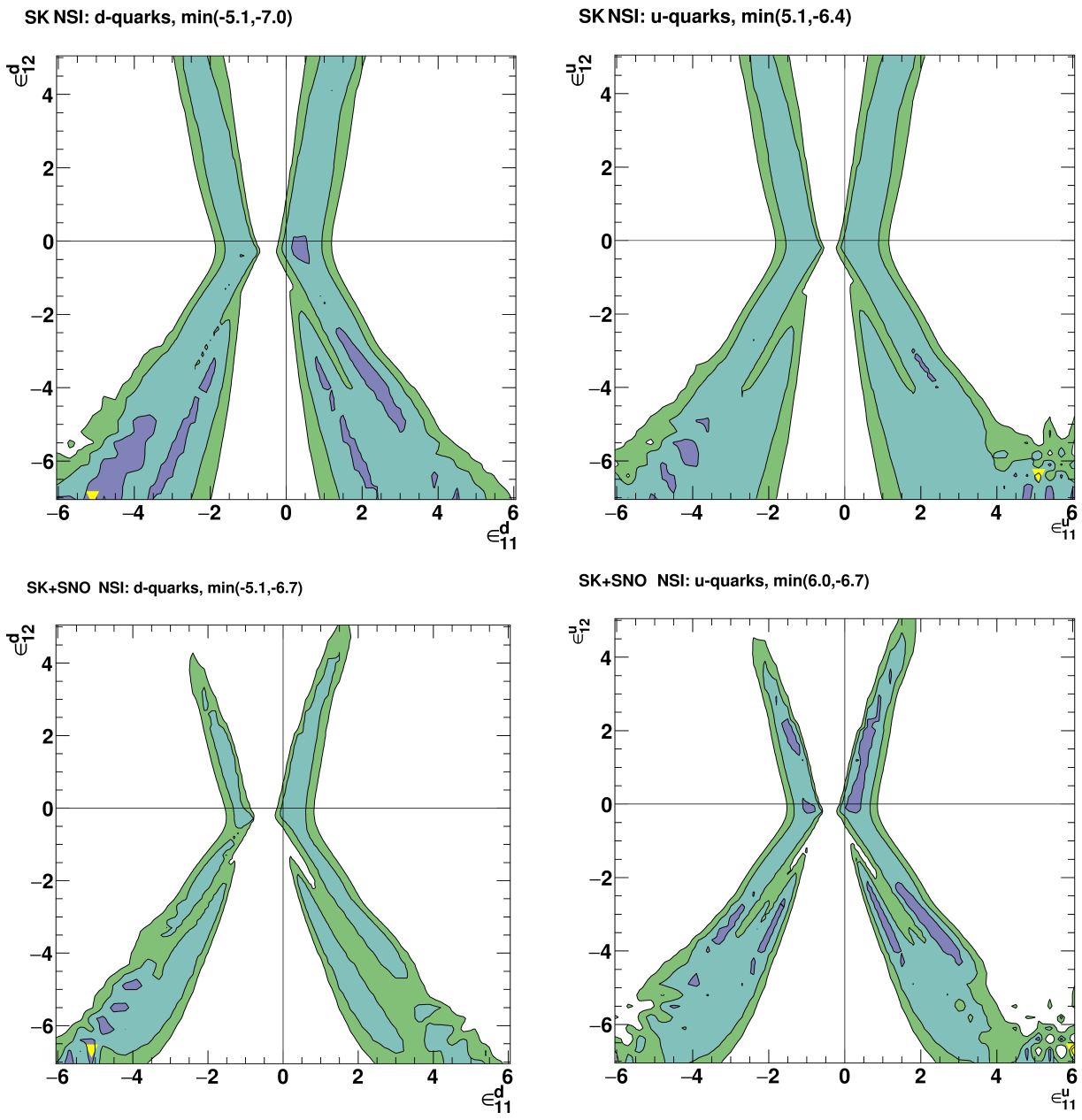

Figure 11.22: The effect on the allowed NSI parameters when enforcing simple constraint: $\Delta m^2_{12} \in (6 \times 10^{-5}, 9 \times 10^{-5})$ eV^2. A KamLAND NSI analysis would help to constrain the allowed values of Δm^2_{12}. However, KamLAND NSI analysis would do more than just constrain the squared mass splitting, as the predicted antineutrino spectra and flux would be changed by the NSI parameters and could be disfavored by fits to their data.

References

[1] The Ice Cube Experiment. **About Neutrinos**. 2018.

[2] The T2K Experiment. **About Neutrinos**. 2013.

[3] Wolfgang Pauli. **Open letter to the group of radioactive people at the Gauverein meeting in Tbingen.** December 1930.

[4] E. Z. Fermi. **Versuch einer Theorie der -Strahlen. I**. *Physik*, **88**, 1934.

[5] Raymond Davis. **Attempt to Detect the Antineutrinos from a Nuclear Reactor by the ^{37}Cl $(\overline{\nu}, e^-)$ ^{37}A Reaction**. *Phys. Rev.*, **97**:766–769, Feb 1955.

[6] Nobel Media AB 2018. **Raymond Davis Jr. – Biographical.** *NobelPrize.org*, Oct 2015.

[7] Bruce T. Cleveland, Timothy Daily, Jr. Raymond Davis, James R. Distel, Kenneth Lande, C. K. Lee, Paul S. Wildenhain, and Jack Ullman. **Measurement of the Solar Electron Neutrino Flux with the Homestake Chlorine Detector**. *The Astrophysical Journal*, **496**(1):505, 1998.

[8] Los Alamos Library. **The Reines-Cowan Experiments – Detecting the Poltergeist**. *Los Alamos Science*, 1997.

[9] C. L. Cowan, F. Reines, F. B. Harrison, H. W. Kruse, and A. D. McGuire. **Detection of the Free Neutrino: a Confirmation**. *Science*, **124**:103–104, 1956.

[10] Kai Zuber. *Neutrino Physics*. CRC Press, 2012.

[11] E. J. Konopinski and H. M. Mahmoud. **The Universal Fermi Interaction**. *Phys. Rev.*, **92**:1045–1049, Nov 1953.

[12] G. Danby, J-M. Gaillard, K. Goulianos, L. M. Lederman, N. Mistry, M. Schwartz, and J. Steinberger. **Observation of High-Energy Neutrino Reactions and the Existence of Two Kinds of Neutrinos**. *Phys. Rev. Lett.*, **9**:36–44, Jul 1962.

[13] K. Kodama et al., The DONuT Collaboration. **Observation of tau neutrino interactions**. *Physics Letters B*, **504**(3):218 – 224, 2001.

[14] K. Kodama et al., The DONuT Collaboration. **Final tau-neutrino results from the DONuT experiment**. *Phys. Rev. D*, **78**:052002, Sep 2008.

[15] J. A. Formaggio and G. P. Zeller. **From eV to EeV: Neutrino cross sections across energy scales**. *Rev. Mod. Phys.*, **84**:1307–1341, Sep 2012.

[16] A. Friedland, C. Lunardini, and C. Pe na Garay. **Solar neutrinos as probes of neutrino-matter interactions**. *Phys. Lett. B*, **594**:347, 2004.

[17] M.C. Gonzalez-Garcia and M. Maltoni. **Determination of matter potential from global analysis of neutrino oscillation data**. *JHEP*, **1309**:152, 2013.

[18] M. Kaplinghat, G. Steigman, and T. P. Walker. **Supernova relic neutrino background**. *Phys. Rev. D*, **62**:043001, Jul 2000.

[19] John F. Beacom and Mark R. Vagins. **Antineutrino Spectroscopy with Large Water Čerenkov Detectors**. *Phys. Rev. Lett.*, **93**:171101, Oct 2004.

[20] M. Aartsen et al., The IceCube Collaboration. **Neutrino emission from the direction of the blazar TXS 0506+056 prior to the IceCube-170922A alert**. *Science*, **361**(6398):147–151, 2018.

[21] S. T. Dye. **Geoneutrinos and the radioactive power of the Earth**. *Reviews of Geophysics*, **50**(3), 2012.

[22] Ziro Maki, Masami Nakagawa, and Shoichi Sakata. **Remarks on the Unified Model of Elementary Particles**. *Progress of Theoretical Physics*, **28**(5):870–880, 1962.

[23] F. P. An et al., The Daya Bay Collaboration. **Measurement of electron antineutrino oscillation based on 1230 days of operation of the Daya Bay experiment**. *Phys. Rev. D*, **95**:072006, Apr 2017.

[24] J. K. Ahn et al., The RENO Collaboration. **Observation of Reactor Electron Antineutrinos Disappearance in the RENO Experiment**. *Phys. Rev. Lett.*, **108**:191802, 2012.

[25] S.H. Seo, The RENO Collaboration. **talk at the TAUP2017 International Workshop,July 24-28, 2017, Sudbury, Canada**. *arXiv:1710.08204*, 2017.

[26] Y. Abe et al., The Double Chooz Collaboration. **Reactor $\bar{\nu}_e$ disappearance in the Double Chooz experiment**. *Phys. Rev. D*, **86**:052008, 2012.

[27] Y. Abe et al., The Double Chooz Collaboration. *JHEP*, **1014**:086, 2014.

[28] T. K. Kuo and J. Pantaleone. **Solar-Neutrino Problem and Three-Neutrino Oscillations**. *Phys. Rev. Lett.*, **57**:1805–1808, Oct 1986.

[29] M. Tanabashi et al., Particle Data Group. **Review of Particle Physics**. *Phys. Rev. D*, **98**:030001, Aug 2018.

[30] F. P An et al., The Daya Bay Collaboration. **New measurement of θ_{13} via neutron capture on hydrogen at Daya Bay**. *Phys. Rev. D*, **93**:072011, Apr 2016.

[31] S.P. Mikheyev and A.Yu. Smirnov. **3 oscillations in matter and solar neutrino data**. *Physics Letters B*, **200**(4):560 – 564, 1988.

[32] G. L. Fogli, E. Lisi, and D. Montanino. **Matter-enhanced three-flavor oscillations and the solar neutrino problem**. *Phys. Rev. D*, **54**:2048–2062, Aug 1996.

[33] L. Wolfenstein. **Neutrino oscillations in matter**. *Phys. Rev. D*, **17**:2369, 1978.

[34] S. P. Mikheyev and A. Y. Smirnov. **Resonance Amplification of Oscillations in Matter and Spectroscopy of Solar Neutrinos**. *Sov. J. Nucl. Phys.*, **42**:913, 1985.

[35] S. Fukuda et al., The Super-Kamiokande Collaboration. **The Super-Kamiokande detector**. *Nuclear Instruments and Methods in Physics Research Section A: Accelerators, Spectrometers, Detectors and Associated Equipment*, **501**(2):418 – 462, 2003.

[36] J Boger et al. **The Sudbury Neutrino Observatory**. *Nuclear Instruments and Methods in Physics Research Section A: Accelerators, Spectrometers, Detectors and Associated Equipment*, **449**(1):172 – 207, 2000.

[37] G. Alimonti et al. **The Borexino detector at the Laboratori Nazionali del Gran Sasso**. *Nuclear Instruments and Methods in Physics Research Section A: Accelerators, Spectrometers, Detectors and Associated Equipment*, **600**(3):568 – 593, 2009.

[38] Sheldon L. Glashow. **The renormalizability of vector meson interactions**. *Nuclear Physics*, **10**:107 – 117, 1959.

[39] Abdus Salam and J. C. Ward. **Weak and electromagnetic interactions**. *Il Nuovo Cimento (1955-1965)*, **11**(4):568–577, Feb 1959.

[40] Steven Weinberg. **A Model of Leptons**. *Phys. Rev. Lett.*, **19**:1264–1266, Nov 1967.

[41] John N. Bahcall, Marc Kamionkowski, and Alberto Sirlin. **Solar neutrinos: Radiative corrections in neutrino-electron scattering experiments**. *Phys. Rev. D*, **51**:6146–6158, Jun 1995.

[42] K. Abe et al., The Super-Kamiokande Collaboration. **Solar neutrino measurements in Super-Kamiokande-IV**. *Phys. Rev. D*, **94**:052010, Sep 2016.

[43] Andrew Renshaw. *First Direct Evidence for Matter Enhanced Neutrino Oscillation, Using Super-Kamiokande Solar Neutrino Data*. PhD thesis, University of California Irvine, 2013.

[44] J. Hosaka et al., The Super-Kamiokande Collaboration. **Solar neutrino measurements in Super-Kamiokande-I**. *Phys. Rev. D*, **73**:112001, Jun 2006.

[45] W. T. Winter, S. J. Freedman, K. E. Rehm, and J. P. Schiffer. **The ^{8}B neutrino spectrum**. *Phys. Rev. C 73.025503*, 2006.

[46] John N. Bahcall and M. H. Pinsonneault. **What Do We (Not) Know Theoretically about Solar Neutrino Fluxes?** *Phys. Rev. Lett. 92, 121301*, 2004.

[47] B. Aharmim et al., The SNO Collaboration. **Combined analysis of all three phases of solar neutrino data from the Sudbury Neutrino Observatory**. *Phys. Rev. C*, **88**:025501, Aug 2013.

[48] Yuki Nakano. *^{8}B solar neutrino spectrum measurement using Super-Kamiokande IV*. PhD thesis, University of Tokyo, 2015.

[49] C. F. "von Weizsäcker". **Über Elementumwandlungen in Innern der Sterne I**. *Physikalische Zeitschrift*, **38**:176191, 1937.

[50] C. F. "von Weizsäcker". **Über Elementumwandlungen in Innern der Sterne II**. *Physikalische Zeitschrift*, **39**:633646, 1938.

[51] H. A. Bethe. **Energy Production in Stars**. *Phys. Rev.*, **55**:434–456, Mar 1939.

[52] V. A. Kuzmin and G. T. Zatsepin. **Upper limit of the spectrum of cosmic rays**. *Proc. of the 9th Int. Conf. on Cosmic Rays*, **2**:1023, 1965.

[53] John N. Bahcall, M. H. Pinsonneault, and Sarbani Basu. **Solar Models: current epoch and time dependences, neutrinos, and helioseismological properties**. *ApJ 555, 2*, 2001.

[54] W. C. Haxton. **The Solar Neutrino Problem**. *Annual Review of Astronomy and Astrophysics*, **33**:459–504, 1995.

[55] John N. Bahcall. **Software and data for solar neutrino research**. http://www.sns.ias.edu/ jnb/SNdata/sndata.html, 2005.

[56] John N. Bahcall. **Neutrino-spectroscopy of the solar interior**. *Phys. Lett.*, **13**:332, 1964.

[57] J. N. Bahcall, A. M. Serenelli, and S. Basu. **NEW SOLAR OPACITIES, ABUNDANCES, HELIOSEISMOLOGY, AND NEUTRINO FLUXES**. *ApJ, 621, L85-L88*, 2005.

[58] C. E. Ortiz, A. García, R. A. Waltz, M. Bhattacharya, and A. K. Komives. **Shape of the ^{8}B Alpha and Neutrino Spectra**. *Phys. Rev. Lett.*, **85**:2909–2912, Oct 2000.

[59] J. Napolitano, S. J. Freedman, J., and Camp. **Beta and neutrino spectra in the decay of ^{8}B**. *Phys. Rev. C*, **36**:298–302, Jul 1987.

[60] Raymond Davis. **Solar Neutrinos. II. Experimental**. *Phys. Rev. Lett.*, **12**:303–305, Mar 1964.

[61] Kenzo Nakamura, Kamiokande-II. **Present Status and Future of Kamiokande**. *Conf. Proc.*, **890928**, 1989.

[62] Kenzo Nakamura et al., Kamiokande-III. **Recent results from Kamiokande solar neutrino observations**. *Nuc. Phys. B - Proc. Supplements*, **31**, 1993.

[63] Y. Fukuda et al., Kamiokande-III. **Solar Neutrino Data Covering Solar Cycle 22**. *Phys. Rev. Lett.*, **77**:1683–1686, Aug 1996.

[64] John N. Bahcall and R. K. Ulrich. **Solar models, neutrino experiments, and helioseismology**. *Rev. Mod. Phys.*, **60**, 1988.

[65] John N. Bahcall and M. H. Pinsonneault. **Standard solar models, with and without helium diffusion and the solar neutrino problem**. *Rev. Mod. Phys.*, **64**, 1992.

[66] John N. Bahcall, M. H. Pinsonneault, and Sarbani Basu. **Solar Models: Current Epoch and Time Dependences, Neutrinos, and Helioseismological Properties**. *The Astrophysical Journal*, **555**:990 – 1012, 2001.

[67] W Hampel et al., The GALLEX Collaboration. **GALLEX solar neutrino observations: results for GALLEX IV**. *Physics Letters B*, **447**:127–133, 02 1999.

[68] M. Altmann et al., The GNO Collaboration. **Complete results for five years of GNO solar neutrino observations**. *Physics Letters B*, **616**(3):174 – 190, 2005.

[69] F. Kaether, W. Hampel, G. Heusser, J. Kiko, and T. Kirsten, The GALLEX Collaboration. **Reanalysis of the Gallex solar neutrino flux and source experiments**. *Physics Letters B*, **685**(1):47 – 54, 2010.

[70] J. N. Abdurashitov et al., The SAGE Collaboration. **Measurement of the solar neutrino capture rate with gallium metal. III. Results for the 2002–2007 data-taking period**. *Phys. Rev. C*, **80**:015807, Jul 2009.

[71] Herbert H. Chen. **Direct Approach to Resolve the Solar-Neutrino Problem**. *Phys. Rev. Lett.*, **55**:1534–1536, Sep 1985.

[72] B. Aharmim et al., The SNO Collaboration. **Determination of the ν_e and total ^{8}B solar neutrino fluxes using the Sudbury Neutrino Observatory Phase I data set**. *Phys. Rev. C*, **75**:045502, Apr 2007.

[73] B. Aharmim et al., The SNO Collaboration. **Electron energy spectra, fluxes, and day-night asymmetries of ^{8}B solar neutrinos from measurements with NaCl dissolved in the heavy-water detector at the Sudbury Neutrino Observatory**. *Phys. Rev. C*, **72**:055502, Nov 2005.

[74] B. Aharmim et al., The SNO Collaboration. **Low-energy-threshold analysis of the Phase I and Phase II data sets of the Sudbury Neutrino Observatory**. *Phys. Rev. C*, **81**:055504, May 2010.

[75] B. Aharmim et al., The SNO Collaboration. **Independent Measurement of the Total Active ^{8}B Solar Neutrino Flux Using an Array of ^{3}He Proportional Counters at the Sudbury Neutrino Observatory**. *Phys. Rev. Lett.*, **101**:111301, Sep 2008.

[76] B. Aharmim et al., The SNO Collaboration. **Measurement of the ν_e and total ^{8}B solar neutrino fluxes with the Sudbury Neutrino Observatory phase-III data set**. *Phys. Rev. C*, **87**:015502, Jan 2013.

[77] S. Andringa et al., The SNO+ Collaboration. **Current Status and Future Prospects of the SNO+ Experiment**. *Advances in High Energy Physics*, **2016**:21, 2016.

[78] M. Anderson et al., The SNO+ Collaboration. **Measurement of the ^{8}B solar neutrino flux in SNO+ with very low backgrounds**. *Phys. Rev. D*, **99**:012012, Jan 2019.

[79] G. Bellini et al., The Borexino Collaboration. **Final results of Borexino Phase-I on low-energy solar neutrino spectroscopy**. *Phys. Rev. D*, **89**:112007, Jun 2014.

[80] C. Arpesella et al., The Borexino Collaboration. **First real time detection of 7Be solar neutrinos by Borexino**. *Physics Letters B*, **658**(4):101 – 108, 2008.

[81] M. Agostini et al. **First Simultaneous Precision Spectroscopy of *pp*, ^{7}Be, and *pep* Solar Neutrinos with Borexino Phase-II**. arXiv:1707.09279v2 [hep-ex], Dec 2017.

[82] G. Bellini et al., The Borexino Collaboration. **Measurement of the solar ^{8}B neutrino rate with a liquid scintillator target and 3 MeV energy threshold in the Borexino detector**. *Phys. Rev. D*, **82**:033006, Aug 2010.

[83] M. Agostini et al. **Comprehensive measurement of *pp*-chain solar neutrinos**. *Nature*, **562**:505–510, 10 2018.

[84] G. Bellini et al. **Absence of a daynight asymmetry in the 7Be solar neutrino rate in Borexino**. *Physics Letters B*, **707**(1):22 – 26, 2012.

[85] M. Agostini et al. **Improved measurement of 8B solar neutrinos with 1.5 kt y of Borexino exposure**. arXiv:1709.00756v1, Sep 2017.

[86] Ivan Esteban, M C. Gonzalez-Garcia, Michele Maltoni, Ivan Martinez-Soler, and Thomas Schwetz-Mangold. **Updated fit to three neutrino mixing: exploring the accelerator-reactor complementarity**. *Journal of High Energy Physics*, **2017**:87, 1 2017.

[87] Michael B. Smy. **The Solar Neutrino Problem and Its Oscillation Solution**. *Modern Physics Letters A*, **17**(33):2163–2178, 2002.

[88] A. Gando et al., The KamLAND Collaboration. **Constraints on θ_{13} from a three-flavor oscillation analysis of reactor antineutrinos at KamLAND**. *Phys. Rev. D*, **83**:052002, Mar 2011.

[89] A. Gando et al., The KamLAND Collaboration. **Reactor on-off antineutrino measurement with KamLAND**. *Phys. Rev. D*, **88**:033001, Aug 2013.

[90] A. Gando et al., The KamLAND Collaboration. ^{7}Be **solar neutrino measurement with KamLAND**. *Phys. Rev. C*, **92**:055808, Nov 2015.

[91] S. Abe et al., The KamLAND Collaboration. **Measurement of the ^{8}B solar neutrino flux with the KamLAND liquid scintillator detector**. *Phys. Rev. C*, **84**:035804, Sep 2011.

[92] Y. Fukuda et al., The Super-Kamiokande Collaboration. **Evidence for Oscillation of Atmospheric Neutrinos**. *Phys. Rev. Lett.*, **81**:1562–1567, Aug 1998.

[93] **The Nobel Prize in Physics 2015 was awarded jointly to Takaaki Kajita and Arthur B. McDonald "for the discovery of neutrino oscillations, which shows that neutrinos have mass.** *NobelPrize.org*, Oct 2015.

[94] J. P. Cravens et al., The Super-Kamiokande Collaboration. **Solar neutrino measurements in Super-Kamiokande-II**. *Phys. Rev. D*, **78**:032002, Aug 2008.

[95] K. Abe et al., The Super-Kamiokande Collaboration. **Solar neutrino results in Super-Kamiokande-III**. *Phys. Rev. D*, **83**:052010, Mar 2011.

[96] A. Renshaw et al., The Super-Kamiokande Collaboration. **First Indication of Terrestrial Matter Effects on Solar Neutrino Oscillation**. *Phys. Rev. Lett.*, **112**:091805, Mar 2014.

[97] Kazuaki Kuroda et al., The KAGARA Collaboration. **Current status of large-scale cryogenic gravitational wave telescope**. **20**:S871, 08 2003.

[98] K. Abe et al., The XMASS Collaboration. **XMASS detector**. *Nuclear Instruments and Methods in Physics Research Section A: Accelerators, Spectrometers, Detectors and Associated Equipment*, **716**:78 – 85, 2013.

[99] S. Umehara et al., The CANDLES Experiment. **Neutrino-less double-β decay of ^{48}Ca studied by CaF_2(Eu) scintillators**. *Phys. Rev. C*, **78**:058501, Nov 2008.

[100] Kiseki Nakamura et al., The NEWAGE Experiment. **Direction-sensitive dark matter search with gaseous tracking detector NEWAGE-0.3b'**. *Progress of Theoretical and Experimental Physics*, **2015**(4):043F01, 2015.

[101] Magro, Lluís Martí, The EGADS Collaboration. **EGADS approaching GADZOOKS!** *EPJ Web of Conferences*, **95**:04041, 2015.

[102] A.G. Thompson, E. Villaescusa, and C.R. Windsor. *Rock Supprot and Reinforcement Practice in Mining*. CRC Press, 1999.

[103] K. Abe et al. **The T2K experiment**. *Nuclear Instruments and Methods in Physics Research Section A: Accelerators, Spectrometers, Detectors and Associated Equipment*, **659**(1):106 – 135, 2011.

[104] Pietro Antonioli et al. **SNEWS: The Supernova Early Warning System**. *New J. Phys.*, **6**:114, 2004.

[105] Giada Carminati, The Super-Kamiokande Collaboration. **The new Wide-band Solar Neutrino Trigger for Super-Kamiokande**. *Physics Procedia*, **61**:666 – 672, 2015. 13th International Conference on Topics in Astroparticle and Underground Physics, TAUP 2013.

[106] Muhammad Elnimr, The Super-Kamiokande Collaboration. **Low Energy ^{8}B Solar Neutrinos with the Wideband Intelligent Trigger at Super-Kamiokande**. *J. Phys.: Conf. Ser.*, **888**, 2017.

[107] Pablo Fernandez. **Status of GADZOOKS!: Neutron tagging in Super-Kamiokande**. The Super-Kamiokande Collaboration, 07 2014. ICHEP2014.

[108] A. Suzuki, M. Mori, K. Kaneyuki, T. Tanimori, J. Takeuchi, H. Kyushima, and Y. Ohashi. **Improvement of 20 in. diameter photomultiplier tubes**. *Nuclear Instruments and Methods in Physics Research Section A: Accelerators, Spectrometers, Detectors and Associated Equipment*, **329**(1):299 – 313, 1993.

[109] L. P. Boivin and D. S. Hanna. **Studies of bis-MSB wavelength shifter for application in a supernova neutrino detector**. *Nuclear Instruments and Methods in Physics Research Section A: Accelerators, Spectrometers, Detectors and Associated Equipment*, **273**(1):397 – 402, 1988.

[110] S. Yamada et al. **Commissioning of the New Electronics and Online System for the Super-Kamiokande Experiment**. *IEEE Transactions on Nuclear Science*, **57**(2):428–432, April 2010.

[111] S.Y.F. Chu, L.P. Ekström, and R.B. Firestone. **The Lund/LBNL Nuclear Data Search**. *webpage*, 1999.

[112] K. Abe et al., The Super-Kamiokande Collaboration. **Calibration of the Super-Kamiokande detector**. *Nuclear Instruments and Methods in Physics Research Section A: Accelerators, Spectrometers, Detectors and Associated Equipment*, **737**:253 – 272, 2014.

[113] Y. Nakano, H. Sekiya, S. Tasaka, Y. Takeuchi, R.A. Wendell, M. Matsubara, and M. Nakahata. **Measurement of radon concentration in super-Kamiokandes buffer gas**. *Nuclear Instruments and Methods in Physics Research Section A: Accelerators, Spectrometers, Detectors and Associated Equipment*, **867**:108 – 114, 2017.

[114] G Pronost, M Ikeda, T Nakamura, H Sekiya, and S Tasaka. **Development of new radon monitoring systems in the Kamioka mine**. *Progress of Theoretical and Experimental Physics*, **2018**(9):093H01, 2018.

[115] M Nakahata et al., The Super-Kamiokande Collaboration. **Calibration of Super-Kamiokande using an electron LINAC: The Super-Kamiokande Collaboration**. *Nuclear Instruments and Methods in Physics Research Section A: Accelerators, Spectrometers, Detectors and Associated Equipment*, **421**(1):113 – 129, 1999.

[116] E Blaufuss et al., The Super-Kamiokande Collaboration. **16N as a calibration source for Super-Kamiokande**. *Nuclear Instruments and Methods in Physics Research Section A: Accelerators, Spectrometers, Detectors and Associated Equipment*, **458**(3):638 – 649, 2001.

[117] R. Brun, F. Bruyant, M. Maire, A. C. McPherson, and P. Zanarini. **GEANT3**. 1987.

[118] Linyan Wan. *Experimental Studies on Low Energy Electron Antineutrinos and Related Physics*. PhD thesis, Tsinghua University, 2018.

[119] Robin M. Pope and Edward S. Fry. **Absorption spectrum (380–700 nm) of pure water. II. Integrating cavity measurements**. *Appl. Opt.*, **36**(33):8710–8723, Nov 1997.

[120] Erik Karl Blaufuss. *Study of the Energy Spectrum of Solar Neutrinos above 5.5 MeV*. PhD thesis, Louisiana State University, 2000.

[121] Michael Smy, The Super-Kamiokande Collaboration. **Low Energy Event Reconstruction and Selection in Super-Kamiokande-III**. *Proc. of the 30th Int. Conf. on Cosmic Rays*, **5**:1279–1282, 2007.

[122] Shirley Weishi Li and John F. Beacom. **Spallation backgrounds in Super-Kamiokande are made in muon-induced showers**. *Phys. Rev. D*, **91**:105005, May 2015.

[123] Y. Zhang et al., The Super-Kamiokande Collaboration. **First measurement of radioactive isotope production through cosmic-ray muon spallation in Super-Kamiokande IV**. *Phys. Rev. D*, **93**:012004, Jan 2016.

[124] K. Bays et al., The Super-Kamiokande Collaboration. **Supernova relic neutrino search at Super-Kamiokande**. *Phys. Rev. D*, **85**:052007, Mar 2012.

[125] A. M. Dziewonski and D. L. Anderson. **Preliminary reference Earth model (PREM)**. *Phys. Earth Plan. Int.*, **25**:297–356, 1981.

[126] A. Para, The MINOS Experiment. **Comments on 'Matrix' and 'Ratio' Methods for the Oscillation Analysis**. *Numi-Note, MINOS-doc-1844-v4*, May 2006.

[127] G. Mitsuka et al., The Super-Kamiokande Collaboration. **Study of nonstandard neutrino interactions with atmospheric neutrino data in Super-Kamiokande I and II**. *Phys. Rev. D*, **84**:113008, Dec 2011.

[128] G. P. Zeller et al., The NuTeV Collaboration. **Precise Determination of Electroweak Parameters in Neutrino-Nucleon Scattering**. *Phys. Rev. Lett.*, **88**:091802, Feb 2002.

[129] G. P. Zeller et al., The NuTeV Collaboration. **Erratum: Precise Determination of Electroweak Parameters in Neutrino-Nucleon Scattering [Phys. Rev. Lett. 88, 091802 (2002)]**. *Phys. Rev. Lett.*, **90**:239902, Jun 2003.

[130] P. Vilain et al., The CHARM II Collaboration. **Precision measurement of electroweak parameters from the scattering of muon-neutrinos on electrons**. *Physics Letters B*, **335**(2):246 – 252, 1994.

[131] P. Coloma, P. B. Denton, M. C. Gonzalez-Garcia, M. Maltoni, and T. Schwetz. **Curtailing the Dark Side in Non-Standard Neutrino Interactions**. *JHEP*, **04**:116, 2017.

[132] D. Akimov et al., The COHERENT Collaboration. **Observation of coherent elastic neutrino-nucleus scattering**. *Science*, **03**, 2018.

[133] Ivan Esteban, M. C. Gonzalez-Garcia, Michele Maltoni, Ivan Martinez-Soler, and Jordi Salvado. **Updated constraints on non-standard interactions from global analysis of oscillation data**. *Journal of High Energy Physics*, **2018**(8):180, Aug 2018.